

NON-LINEAR CONSOLIDATION  
AROUND  
DRIVEN PILES IN CLAYS

Vol. 2113 I  
by

MICHAEL KAVVADAS

DIPLOMA, N.T.U. Athens (EMI), Greece,  
(1977)

S.M., Massachusetts Institute of Technology, U.S.A.  
(1980)

SUBMITTED IN PARTIAL FULFILLMENT  
OF THE REQUIREMENTS FOR THE  
DEGREE OF  
DOCTOR OF SCIENCE

at the  
MASSACHUSETTS INSTITUTE OF TECHNOLOGY  
June 1982

c Massachusetts Institute of Technology, 1982

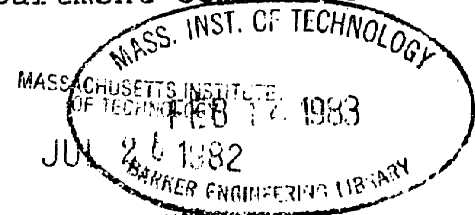
Signature of Author \_\_\_\_\_  
Department of Civil Engineering, December 1981

Certified by \_\_\_\_\_  
M.M. Baligh, Thesis Supervisor

Certified by \_\_\_\_\_  
A.S. Azzouz, Thesis Co-Supervisor

Accepted by \_\_\_\_\_  
Chairman, Department Committee

Eng.



# NON-LINEAR CONSOLIDATION

AROUND

DRIVEN PILES IN CLAYS

by

MICHAEL KAVVADAS

Submitted to the Department of Civil Engineering  
on February 12, 1982 in partial fulfillment  
of the requirements for the Degree of Doctor of Science in  
Civil Engineering

## ABSTRACT

This research represents an effort to develop a better understanding of the mechanisms governing the development of friction along the shafts of long piles driven in clays, because skin friction represents the major portion of the axial load capacity of these piles. The skin friction mobilized during pile loading to failure depends on the sequence of events preceding pile loading, i.e., pile installation and subsequent soil consolidation. Analysis of these events requires the use of a stress-strain relationship to model clay behavior under general undrained and partially drained loading. Thus, this research concentrates on the development of a general stress-strain model for clays and its application in the study of pile installation and subsequent soil consolidation.

A general anisotropic effective stress model for clays, based on the Theory of Incremental Elasto-Plasticity is proposed. The yield surface of the model can be represented by a distorted ellipsoid which may change in size and rotate in the effective stress space thus allowing for changes in soil anisotropy. The proposed model predictions show good agreement with undrained and drained, monotonic and cyclic tests on one-dimensionally normally consolidated and slightly overconsolidated Boston Blue Clay.

The proposed model is used to study pile installation in clays via the Cylindrical Cavity Expansion and the Strain Path methods and the results are compared with the predictions of the Modified Cam-Clay and the Prevost-Levadoux-Baligh soil models. It is shown that, for all soil models, the effective



stress and excess pore pressure distributions predicted by the Strain Path method are very different than the predictions of the Cavity Expansion method.

The predicted effective stress and excess pore pressure distributions immediately after pile installation are used as initial conditions in linear and non-linear consolidation analyses around the pile. Linear analyses show that the total radial stress at the pile wall remains constant during consolidation, which is not in agreement with field measurements around piles. Non-linear analyses using the proposed model give reasonable predictions of the effective stress changes and the excess pore pressure dissipation rates during consolidation. It is shown that during consolidation the soil is initially elastic and only at later times a soft plastic zone develops close to the pile wall.

Thesis Co-Supervisors:

Dr. Mohsen M. Baligh, Associate Professor of Civil Engineering  
Dr. Amr S. Azzouz, Assistant Professor of Civil Engineering

## ACKNOWLEDGEMENTS

The author wishes to extend his deepest appreciation to:

Professors M. M. Baligh and A. S. Azzouz, his thesis co-supervisors, for numerous discussions during the course of this research;

Professor C. C. Ladd for reviewing carefully every chapter of this thesis and providing many constructive comments;

Professors J. J. Connor, R. V. Whitman and M. P. Cleary for serving in his thesis committee;

Many other members of the faculty and staff of MIT have also helped the author. In particular, special thanks go to his longtime friend and colleague Spiro Pollalis for various discussions and considerable help in the preparation of this thesis, as well as Mr. Mike Morrisson for his help with the field data of Boston Blue Clay.

Finally, the author wishes to express his sincere gratitude to his parents for constant guidance, love and support and to Theresa Morrissey for her patience, encouragement and for typing a significant portion of this thesis. Her application of English scholarship to deciphering the text will be remembered by the author.

December 28, 1981  
Cambridge, Massachusetts

TABLE OF CONTENTS

	<u>Page</u>
TITLE PAGE .....	1
ABSTRACT .....	2
ACKNOWLEDGEMENTS .....	4
TABLE OF CONTENTS .....	5
LIST OF TABLES .....	11
LIST OF FIGURES .....	16
<u>CHAPTER 1</u> : INTRODUCTION .....	32
<u>CHAPTER 2</u> : EXISTING APPROACHES FOR ESTIMATING THE LIMITING SKIN FRICTION OF DRIVEN PILES IN CLAYS .....	38
2.1 EMPIRICAL APPROACHES .....	38
2.1.1 Total Stress Approaches: The $\alpha$ -method .....	38
2.1.2 Effective Stress Approaches: The $\beta$ -method ..	40
2.1.3 Mixed Approaches .....	45
2.1.4 Conclusions .....	47
2.2 RATIONAL APPROACHES .....	50
2.2.1 General .....	50
2.2.2 In Situ Conditions prior to Pile Driving ...	54
2.2.3 Effects of Pile Installation .....	57
2.2.4 Effects of Soil Consolidation .....	87
2.2.5 Effects of Pile Loading .....	122
<u>CHAPTER 3</u> : PLASTICITY THEORY FOR SOILS .....	188
3.1 INTRODUCTION .....	188
3.2 GENERAL CONCEPTS OF THE INCREMENTALLY LINEARIZED PLASTICITY THEORY FOR SOILS .....	199
3.2.1 The Elastic Part of the Elastoplastic Deformation of Soils .....	203
3.2.2 The Plastic Part of the Elastoplastic Deformation of Soils .....	205
3.3 THE MODIFIED CAM-CLAY MODEL .....	221

3.3.1	Introduction .....	221
3.3.2	Yield Function and Flow Rule .....	223
3.3.3	Anisotropic Characteristics of the MCC model .....	225
3.3.4	Hardening Characteristics .....	229
3.3.5	The Elastoplastic Modulus H .....	231
3.3.6	Effective Stress Path for Undrained Tests ...	234
3.3.7	Prediction of $K_o$ .....	236
3.3.8	The Critical State .....	238
3.3.9	The Soil Friction Angle and the MCC model ...	243
3.3.10	Input Parameters for the MCC model .....	246
<b>CHAPTER 4:</b>	<b>THE PROPOSED MODEL .....</b>	<b>254</b>
4.1	INTRODUCTION .....	254
4.2	THE YIELD SURFACE AND THE YIELD FUNCTION .....	257
4.2.1	Experimental Evidence .....	257
4.2.2	The Form of the Yield Surface and its Properties .....	260
4.3	HARDENING RULES .....	267
4.3.1	Hardening Characteristics of the Proposed model .....	267
4.3.2	The Consistency Condition .....	270
4.4	SOIL ANISOTROPY .....	272
4.4.1	Introduction .....	272
4.4.2	Quantitative Description of Anisotropy .....	273
4.4.3	Anisotropic Features of the Proposed model ..	284
4.5	TRANSFORMED VARIABLES FOR THE DESCRIPTION OF THE PROPOSED MODEL .....	286
4.6	A FAILURE CRITERION FOR PEAK AND CRITICAL STATES ..	290
4.7	RADIAL EFFECTIVE STRESS PATHS .....	298
4.8	UNDRAINED STRESS PATHS .....	308

	<u>Page</u>
4.9 INPUT PARAMETERS FOR THE PROPOSED MODEL .....	314
<u>CHAPTER 5: EVALUATION OF THE PROPOSED MODEL</u> .....	328
5.1 INTRODUCTION .....	328
5.2 EVALUATION OF THE MODEL PARAMETERS .....	329
5.2.1 The Consolidation Parameter $\lambda$ .....	329
5.2.2 The Elastic Parameters $\kappa$ and $G$ .....	330
5.2.3 The $K_o$ -value .....	331
5.2.4 The Friction Angles .....	332
5.2.5 The Rate of Change of the Anisotropy .....	333
5.2.6 The Parameters $\alpha$ and $\beta$ .....	337
5.2.7 The Parameter $c$ .....	339
5.3 THE INITIAL VALUES OF THE STATE VARIABLES .....	342
5.4 STRESS-STRAIN-STRENGTH PREDICTIONS .....	344
5.4.1 Normally $K_o$ -consolidated BBC .....	344
5.4.2 $K_o$ -overconsolidated BBC .....	353
5.5 SUMMARY AND CONCLUSIONS .....	357
<u>CHAPTER 6: STEADY STATE PILE INSTALLATION</u> .....	399
6.1 INTRODUCTION .....	399
6.2 SOIL MODEL AND METHOD OF ANALYSIS .....	401
6.2.1 Soil Model .....	401
6.2.2 Method of Analysis .....	402
6.3 STRAINS IN THE SOIL DURING PILE INSTALLATION ....	410
6.4 PREDICTED STRESS AND PORE PRESSURE CHANGES IN THE SOIL DURING CONSOLIDATION .....	413
6.5 COMPARISON WITH MEASUREMENTS .....	419
6.5.1 The Shape of the Pore Pressure Distribution .....	419
6.5.2 Comparison between Measurements and Predictions in BBC .....	420
6.6 SUMMARY AND CONCLUSIONS .....	427

	<u>Page</u>
<u>CHAPTER 7: LINEAR AND NON-LINEAR SOIL CONSOLIDATION</u> .....	450
7.1 INTRODUCTION .....	450
7.2 BIOT'S THEORY OF CONSOLIDATION .....	453
7.2.1 General .....	453
7.2.2 The Conservation of Momentum .....	454
7.2.3 The Conservation of Mass .....	455
7.2.4 Rendulic's Consolidation Theory .....	460
7.3 AN ANALYTICAL SOLUTION FOR THE LINEAR CONSOLIDATION AROUND PILES .....	462
7.4 A WEIGHTED RESIDUALS FORMULATION FOR NON- LINEAR CONSOLIDATION AND ITS FINITE ELEMENT IMPLEMENTATION .....	466
7.4.1 Introduction .....	466
7.4.2 A Weighted Residuals Formulation for Soil Consolidation .....	467
7.4.3 The Finite Element Implementation .....	472
7.4.4 Finite Element Implementation for the Radial Consolidation around Piles .....	477
<u>CHAPTER 8: RADIAL CONSOLIDATION ANALYSES AROUND A PILE         DRIVEN IN BOSTON BLUE CLAY</u> .....	481
8.1 INTRODUCTION .....	481
8.2 NON-LINEAR CONSOLIDATION ANALYSES IN NORMALLY CONSOLIDATED BOSTON BLUE CLAY .....	484
8.3 NON-LINEAR CONSOLIDATION ANALYSES IN SLIGHTLY OVERCONSOLIDATED BOSTON BLUE CLAY .....	494
8.4 COMPARISON WITH MEASUREMENTS .....	497
8.5 COMPARISON BETWEEN LINEAR AND NON-LINEAR CONSOLIDATION SOLUTIONS .....	501
8.6 SUMMARY AND CONCLUSIONS .....	504
<u>CHAPTER 9: SUMMARY AND CONCLUSIONS</u> .....	528
<u>REFERENCES</u> .....	544

	<u>Page</u>
<u>APPENDIX A</u> : INVERSION OF THE INCREMENTAL STRESS- STRAIN RELATIONSHIPS FOR ELASTO-PLASTIC SOILS .....	559
<u>APPENDIX B</u> : STRAIN HARDENING AND STRAIN SOFTENING .....	561
<u>APPENDIX C</u> : RADIAL STRESS PATHS IN SOFT CLAYS .....	563
<u>APPENDIX D</u> : THE FLUID MASS FLUX VECTOR .....	571
<u>APPENDIX E</u> : UNCOUPLING OF THE CONSOLIDATION EQUATION IN THE CASE OF IRROTATIONAL DISPLACEMENT FIELDS .....	573
<u>APPENDIX F</u> : AN ANALYTICAL SOLUTION FOR THE LINEAR CONSOLIDATION AROUND PILES .....	577
<u>APPENDIX G</u> : FINITE ELEMENT IMPLEMENTATION OF NON-LINEAR SOIL CONSOLIDATION .....	580
G.1    THE ALGORITHM .....	580
G.2    THE 'ELASTIC' STIFFNESS MATRIX .....	589
G.3    NON-DIMENSIONALIZATION OF THE FINITE ELEMENT EQUATIONS .....	591
<u>APPENDIX H</u> : COMPUTER PROGRAMS .....	593
H.1    INTRODUCTION .....	593
H.2    A COMPUTER PROGRAM FOR LABORATORY STRAIN CONTROLLED TESTS .....	595
H.2.1 Program Description .....	595
H.2.2 User's Manual .....	596
H.2.3 Program Listing .....	598
H.3    A COMPUTER PROGRAM FOR THE UNDRAINED EXPANSION OF A CYLINDRICAL CAVITY .....	602
H.3.1 Program Description .....	602
H.3.2 User's Manual .....	602
H.3.3 Program Listing .....	605
H.4    A COMPUTER PROGRAM FOR PILE DRIVING USING THE STRAIN PATH METHOD .....	608

	<u>Page</u>
H.4.1 Program Description .....	608
H.4.2 User's Manual .....	608
H.4.3 Program Listing .....	611
H.5 A COMPUTER PROGRAM TO COMPUTE PORE PRESSURES DUE TO GIVEN EFFECTIVE STRESSES .....	614
H.5.1 Program Description .....	614
H.5.2 User's Manual .....	614
H.5.3 Program Listing .....	615
H.6 PROGRAM NON-CAP FOR NON-LINEAR ONE-DIMENSIO- NAL CONSOLIDATION AROUND A PILE USING THE FINITE ELEMENT METHOD .....	617
H.6.1 Program Description .....	617
H.6.2 User's Manual .....	618
H.6.3 Program Output .....	621
H.6.4 Program Listing .....	622
H.7 SUBROUTINE LIBRARY .....	646
H.7.1 Program Description .....	646
H.7.2 Contents of Unit 09 .....	646
H.7.3 Program Listing .....	650
<u>BIOGRAPHY</u> .....	666



## LIST OF TABLES

<u>Table No.</u>	<u>Title</u>	<u>Page</u>
2.1	Terzaghi and Peck (1967) Classification of Clays. ....	139
2.2	Limiting Skin Friction Values into Stiff to very Stiff Clays (After Tomlinson, 1971) ..	140
2.3	Summary of Available Solutions for Cylindrical and Spherical Cavity Expansion (After Levadoux, 1980) .....	141
2.4	Comparison of Stress Path and Strain Path Methods (After Levadoux, 1980) .....	142
2.5	Normalized Total Radial Stress Changes after Linear Consolidation around a Pile for various Initial Excess Pore Pressure Distributions (After Baligh and Kavvadas, 1980) .....	143
2.6	Total and Effective Radial Stress Changes after Consolidation at $r = \lambda R$ according to Linear Solutions (After Baligh and Kavvadas, 1980) ...	144
2.7	Model Parameters and Predictions of the Cam-Clay model for Resedimented $K_o$ -consolidated Boston Blue Clay (After Baligh and Kavvadas, 1980) .....	145
2.8	Simplifying Assumptions in the Analysis of the Shaft Resistance of Piles in Clays .....	148

LIST OF TABLES (continued)

<u>Table No.</u>	<u>Title</u>	<u>Page</u>
2.9	Backfigured Friction Angles from Direct Simple Shear Tests (After Baligh and Kavvadas, 1980) ..	149
2.10	Equations for Predicting the Friction Angle and the Undrained Shear Strength of Normally Consolidated Clays based on the Cam-Clay model when Elastic Strains are neglected .....	150
3.1	Modified Cam-Clay Model Predictions of $K_o$ for Different Values of the Friction Angle $\bar{\phi}$ and the ratio $\lambda/\kappa (=C_c/C_s)$ .....	248
3.2	Relations Between the Strength Parameters of the Mohr-Coulomb and Modified Cam-Clay Models ..	249
3.3	Input Parameters for the Modified Cam-Clay Model .....	250
3.4	Incremental Stress-Strain Relations for the MCC Model .....	251
4.1	Transformed Variables for the Proposed Model ...	317
4.2	Data at Peak and Critical Conditions from $\overline{CK}_oU(C)$ and $\overline{CK}_oU(E)$ Triaxial Tests on Normally Consolidated Boston Blue Clay (Data from Ladd and Varallyay, 1965) .....	318
4.3	Requirements for (H+KQP) along Various Paths ...	319
5.1	Classification Data of Boston Blue Clay (After Ladd and Varallyay, 1965) .....	361

LIST OF TABLES (continued)

<u>Table No.</u>	<u>Title</u>	<u>Page</u>
5.2	Measured $\lambda$ Values from Consolidation Tests on Normally Consolidated Boston Blue Clay (Data from Ladd and Varallyay, 1965) .....	362
5.3	Data at Peak and Critical Conditions from $\overline{CK}_O U(C)$ and $\overline{CK}_O U(E)$ Triaxial Tests on Normally Consolidated Boston Blue Clay (data from Ladd and Varallyay, 1965) .....	363
5.4	Evaluation of the Parameter $\alpha$ of the Proposed Model from the Undrained Shear Strength of $\overline{CK}_O U$ Triaxial Extension Tests on Normally Consolidated BBC. ....	364
5.5	Evaluation of the Parameter $\beta$ of the Proposed Model from the Critical State Undrained Shear Strength of $\overline{CK}_O U$ Triaxial Compression Tests on Normally Consolidated BBC .....	365
5.6	Classification Data of St. Alban (Champlain) Clay (Data from Leroueil et al, 1979) .....	366
5.7	Input Parameters and Initial Values of the State Variables used in the Predictions of the Stress-Strain-Strength Behavior of $K_O$ -consolidated BBC ...	367
5.8	Measured and Predicted Undrained Shear Strengths and Effective Friction Angles for $K_O$ -consolidated Undrained Triaxial Tests on Boston Blue Clay .....	368
5.9	Measured and Predicted Undrained Shear Strengths and Effective Friction Angles for $K_O$ -consolidated	

LIST OF TABLES (continued)

<u>Table No.</u>	<u>Title</u>	<u>Page</u>
	Undrained Plane Strain Tests on BBC .....	369
5.10	Measured and Predicted Undrained Shear Strengths and Effective Friction Angles for $K_o$ -consolidated Undrained Direct Simple Shear Tests on BBC .....	370
5.11	Measured and Predicted Peak Undrained Shear Strengths for $K_o$ -overconsolidated Undrained Tests on BBC (OCR = 2) .....	371
6.1	Radial Coordinates of the nodal Points far behind the Tip of the Pile, used to model Pile Installation via the Cavity Expansion and the Strain Path methods .....	432
6.2	Measured values of the Excess Pore Pressure and of the Radial Stress at the Pile Wall in Boston Blue Clay .....	433
7.1	Cartesian Components of the Various Matrices Describing Field Quantities .....	479
7.2	Basic Shape Functions for One-Dimensional Bar Elements .....	480
8.1	Normalized Radial Coordinates of nodal Points used in the Finite Element Solution of Radial Consolidation around a long Cylindrical Pile ....	508
C.1	Measured $\lambda$ Values from Consolidation Tests on Normally Consolidated BBC (Data after Ladd and Varallyay, 1965) .....	566

LIST OF TABLES (continued)

<u>Table No.</u>	<u>Title</u>	<u>Page</u>
G.1	Dimensionless Finite Element Equation and Related Matrices .....	592

## LIST OF FIGURES

<u>Fig. No.</u>	<u>Title</u>	<u>Page</u>
1.1	Free Body of an Axially Loaded Pile .....	37
2.1	Compilation of $\alpha$ -factors ( $\alpha=f_s/s_u$ ) by Peck (1958), Woodward et al (1961) and API (1975). $s_u$ obtained from Unconfined Compression Tests. ....	151
2.2	Compilation of $\alpha$ -factors by Tomlinson (1971). For Description see Table 2.2 .....	152
2.3	Relationship between average Adhesion Factor $\alpha$ , and Undrained Shear Strength for Driven Piles in Clay. (after Flaate, 1968). $s_u$ obtained from Field Vane Tests .....	153
2.4	Average Adhesion Parameter $\alpha$ versus $s_u$ (after Flaate and Selnes, 1977). $s_u$ obtained from Field Vane Tests. ....	154
2.5	Average Shaft Friction vs Midheight Depth for Driven Piles in Soft to Medium Clays. (after Burland, 1973) .....	155
2.6	Skin Friction factor $\beta$ vs Depth for Soft to Medium Clays (after Meyerhof, 1976) .....	156
2.7	Observed Side Friction vs Adjusted Effective Vertical Stress (after Flaate and Selnes, 1977) ....	157
2.8	$\beta$ Adhesion Factor versus Plasticity Index (after Bea, 1975) .....	158

LIST OF FIGURES (continued)

<u>Fig. No.</u>	<u>Title</u>	<u>Page</u>
2.9	Frictional Capacity $\lambda$ , vs. Pile Penetration (after Vijayvergiya and Focht, 1972). $s_u$ obtained from miniature vane tests or unconfined compression .....	159
2.10	Relationship between the Limiting Skin Friction and the mean Effective Stress (at failure) at the Pile-Soil Interface .....	160
2.11	Sequence of Events in the Life of a Pile Driven in Clay. ....	161
2.12	$K_o$ of Normally Consolidated Clays vs. (a) Friction Angle and (b) Plasticity Index (after Ladd and Edgers, 1972) .....	162
2.13	Variation of $K_o$ exponent 'n' with Plasticity Index (after Esrig et al, 1978) .....	163
2.14	Comparison of Predicted Stress-Strain curves for $\overline{CK}_o U$ Undrained Expansion of a Cylindrical Cavity in Normally Consolidated BBC (after Levadoux, 1980) .....	164
2.15	Predicted Stress Distributions after Undrained Expansion of a Cylindrical Cavity in Normally Consolidated BBC (after Levadoux, 1980) .....	165

LIST OF FIGURES (continued)

<u>Fig. No.</u>	<u>Title</u>	<u>Page</u>
2.16	Effects of Strain Softening on the Stress Distributions after Expansion of a Cylindrical Cavity in Normally Consolidated BBC (after Levadoux, 1980) .....	166
2.17	Comparison of Predicted Stress Distributions after Expansion of a Cylindrical Cavity: Modified Cam-Clay and Elastic-Perfectly Plastic materials (after Levadoux, 1980) .....	167
2.18	Comparison of three Predictions for the Stress Distributions after Undrained Expansion of a Cylindrical Cavity in Normally Consolidated BBC (after Levadoux, 1980) .....	168
2.19	Application of the Strain Path method to deep steady Pile Penetration in Clays (after Levadoux, 1980) .....	169
2.20	Predicted Deformation Pattern around a 60° Pile assuming no shearing resistance of the Soil (after Levadoux, 1980) .....	170
2.21	Strain Paths of selected Elements during Penetration of a 60° Pile (after Levadoux, 1980) .....	171
2.22	Predicted Deviatoric Stress Path during steady	



LIST OF FIGURES (continued)

<u>Fig. No.</u>	<u>Title</u>	<u>Page</u>
	Penetration of a 60° Pile in Normally Consolidated BBC (after Levadoux, 1980) .....	172
2.23	Predicted Shear Induced Pore Pressures during Steady Pile Penetration in Normally Consolidated BBC (18° and 60° tips) (after Levadoux, 1980) .....	173
2.24	Predicted Excess Pore Pressures during steady Pile Penetration in Normally Consolidated BBC (18° and 60° tips) (after Levadoux, 1980) ..	174
2.25	Predicted vs. measured normalized Excess Pore Pressures along the Face and Shaft of 18° and 60° Piles during Steady Penetration in BBC (after Levadoux, 1980) .....	175
2.26	Predicted vs measured Distribution of Normalized Excess Pore Pressures during Penetration in Clays (after Levadoux, 1980) .....	176
2.27	Excess Pore Pressure Measurements due to Pile Installation in Clays - Case Histories (after Baligh and Levadoux, 1980) .....	177
2.28	Excess Pore Pressure Measurements due to Pile Installation in Clays - Simplified Distributions (after Levadoux, 1980) .....	178

LIST OF FIGURES (continued)

<u>Fig. No.</u>	<u>Title</u>	<u>Page</u>
2.29	Field Data on Increase of Bearing Capacity with time for Friction Piles in Clay (after Baligh and Kavvadas, 1980) .....	179
2.30	Initial Pore Pressure Distributions used in the Linear Consolidation Analysis (after Baligh and Kavvadas, 1980) .....	180
2.31	Effect of Initial Excess Pore Pressure Distri- bution on Dissipation around an impervious cylinder (after Levadoux, 1980) .....	181
2.32	Effective and Total stress paths predicted by linear elastic solutions ( $\bar{\nu}=1/3$ ) at the pile wall during Consolidation around a Pile (after Baligh and Kavvadas, 1980) .....	182
2.33	The Engineering model (Esrig et al, 1977) .....	183
2.34	Stress Paths for Cavity Expansion and Consoli- dation for a Soil Element at the Pile Wall. Cam-Clay predictions (after Randolph et al, 1978) ..	184
2.35	Decay of Pore Pressures with time at the Pile Wall for various Constitutive Laws (after Randolph et al, 1978) .....	185
2.36	Changes in Radial Stress with time at the Pile Wall, for various Constitutive laws (after Randolph et al, 1978) .....	186
2.37	Stress States for Failure in the Soil under various assumptions (after Baligh and Kavvadas, 1980) .....	187

LIST OF FIGURES (continued)

<u>Fig. No.</u>	<u>Title</u>	<u>Page</u>
3.1	Flow Chart of the Incremental Algorithm for an inviscid Effective Stress-Strain Soil model based on Plasticity Theory .....	252
3.2	The Yield Surface of the Modified Cam-Clay model and Characteristic Effective Stress Paths .....	253
4.1	Limit State Curve for St. Louis (Champlain) Clay (after Leroueil, 1977) .....	320
4.2	Limit State Curve for St. Alban (Champlain) Clay (after Leroueil, 1977) .....	321
4.3	The Yield Surface of (a) the Proposed model and (b) an "equivalent" Modified Cam-Clay model in a general tensorial Effective Stress space .....	322
4.4a	The Yield Surface of the Proposed model for a $K_o$ -consolidated State represented in a transformed Triaxial Effective Stress Space .....	323
4.4b	The Yield Surface of the Proposed model for a $K_o$ -consolidated State represented in a $\bar{p}$ -q Effective Stress Space .....	324
4.5	The Yield Surface of the Proposed model in (a) the Effective Stress space and, (b) the Deviatoric subspace .....	325
4.6	Geometrical Representation of the Yield Surface and the Failure Cones of the Proposed model .....	326

LIST OF FIGURES (continued)

<u>Fig. No.</u>	<u>Title</u>	<u>Page</u>
4.7	Values of the Coefficient X used in the Proposed model .....	327
5.1	Secant Shear modulus predicted by the Proposed model at various levels of axial strain during $K_o$ -consolidated Undrained Triaxial Compression Tests on a Clay with the Properties of Normally Consolidated Boston Blue Clay .....	372
5.2	Measured $K_o$ -values of Resedimented Normally Consolidated samples of BBC using two Plane Strain Apparatuses (after Ladd et al, 1971) .....	373
5.3	Proposed model Prediction of the change in anisotropy during one-dimensional consolidation of an initially isotropically normally consolidated sample .....	374
5.4	Proposed model Prediction of the Effective Stress Path during one-dimensional straining of an initially normally consolidated sample .....	375
5.5	Proposed model Prediction of the Mean Effective Stress vs. volumetric strain curves during one-dimensional straining of an initially isotropic normally consolidated sample .....	376
5.6	Proposed model Prediction of the change in anisotropy during $K'_o$ -consolidation of an initially $K_o$ -consolidated sample with properties similar to Boston Blue Clay .....	377
5.7	Proposed model Predictions of the Effective Stress Path during $K'_o$ -consolidation of an initially $K_o$ -consolidated sample .....	378

LIST OF FIGURES (continued)

<u>Fig. No.</u>	<u>Title</u>	<u>Page</u>
5.8	Proposed model Prediction of the mean Effective Stress vs. Volumetric Strain curves for $K'_0$ -consolidation of an initially $K_0$ -consolidated sample .....	379
5.9	Proposed model Prediction of the Effective Stress Paths of $K_0$ -consolidated undrained Triaxial Extension tests on Normally Consolidated Boston Blue Clay .....	380
5.10	Proposed model Prediction of the Effective stress paths of $K_0$ -normally consolidated undrained Triaxial Compression tests for various values of the parameter $\beta$ .....	381
5.11	Schematic Procedure for Evaluating the Parameter $c$ of the Proposed model .....	382
5.12	Proposed model Prediction of the Effective Stress Paths of $K_0$ -normally consolidated undrained Triaxial Compression tests for various values of the parameter $c$ .....	383
5.13	Proposed model Prediction of the Effective Stress Paths of $K_0$ -normally consolidated undrained Triaxial Extension tests for various values of the parameter $c$ .....	384
5.14	Predicted and Measured stress-strain curves for undrained Triaxial Compression and Extension Tests on $K_0$ -normally consolidated resedimented BBC (data from Ladd and Varallyay, 1965) .....	385
5.15	Predicted and Measured Effective Stress Paths for undrained Triaxial Compression and Extension tests on $K_0$ -normally consolidated resedimented Boston Blue Clay .....	386

LIST OF FIGURES (continued)

<u>Fig. No.</u>	<u>Title</u>	<u>Page</u>
5.16	Predicted and Measured stress-strain curves for undrained Plane Strain Compression and Extension tests on $K_0$ -normally consolidated resedimented BBC (data from Ladd et al, 1971) .....	387
5.17	Predicted and Measured Effective Stress Paths for undrained Plane Strain Compression and Extension tests on $K_0$ -normally consolidated resedimented BBC (data from Ladd et al, 1971) .....	388
5.18	Predicted and Measured stress-strain curves for undrained Direct Simple Shear tests on $K_0$ -normally consolidated resedimented BBC .....	389
5.19	Predicted and Measured Effective Stress Paths for Undrained Direct Simple Shear tests on $K_0$ -normally consolidated resedimented BBC .....	390
5.20	Proposed model Prediction of the Evolution of the Mohr circle of stress during a $K_0$ -normally consolidated undrained Direct Simple Shear test on resedimented BBC .....	391
5.21	Proposed model Prediction of the effect of shear stress reversal during undrained Direct Simple Shear tests on a $K_0$ -normally consolidated clay with properties similar to BBC .....	392
5.22	Measured and Predicted stress-strain curves for an undrained Cyclic Triaxial test on $K_0$ -normally consolidated resedimented BBC .....	393
5.23	Measured and Predicted Effective Stress Paths for an undrained Cyclic Triaxial test on $K_0$ -normally consolidated resedimented BBC .....	394

LIST OF FIGURES (continued)

<u>Fig. No.</u>	<u>Title</u>	<u>Page</u>
5.24	Proposed model Predictions of the Effective Stress Paths for various consolidation tests on an initially $K_o$ -normally consolidated clay with properties similar to BBC .....	395
5.25	Proposed model Predictions of the stress-strain curves and the Effective Stress Paths of $K_o$ -consolidated undrained Triaxial Compression and Extension tests for overconsolidated resedimented BBC (OCR=2) .....	396
5.26	Measured values and Proposed model Predictions of the stress-strain curves and the Effective Stress Paths of $K_o$ -consolidated undrained Plane Strain Compression and Extension tests for overconsolidated resedimented BBC (OCR=2) .....	397
5.27	Measured values and Proposed model Predictions of the stress-strain curves and the Effective Stress Paths of $K_o$ -consolidated undrained Direct Simple Shear tests for overconsolidated resedimented BBC (OCR=2) .....	398
6.1	Stress-strain curves predicted by various models during an undrained Cylindrical Cavity Expansion in normally consolidated BBC .....	434
6.1c	Effective Stress Paths predicted by various models during an undrained Cylindrical Cavity Expansion in normally consolidated BBC .....	435
6.2	Application of the Strain Path method to deep steady Pile Installation using an Effective Stress model .....	436

LIST OF FIGURES (continued)

<u>Fig. No.</u>	<u>Title</u>	<u>Page</u>
6.3	Distribution of (a) the radial and (b) the circumferential strains far behind the pile tip, predicted according to the Cavity Expansion and the Strain Path methods .....	437
6.4	Axial and Shear strain far behind the Pile tip, predicted according to the Strain Path method .....	438
6.5	Distributions of the Radial Effective Stress far behind the Pile tip, predicted according to the Cavity Expansion and the Strain Path methods ....	439
6.6	Distributions of the Shear Stress in the horizontal plane, far behind the Pile tip, predicted according to the Cavity Expansion and the Strain Path methods .....	440
6.7	Distributions of the Axial Effective Stress far behind the Pile tip, predicted according to the Cavity Expansion and the Strain Path methods .....	441
6.8	Distributions of the Excess Pore Pressure far behind the Pile tip, predicted according to the Cavity Expansion and the Strain Path methods .....	442
6.9	Distributions of the Radial Total Stress far behind the Pile tip, predicted according to the Cavity Expansion and the Strain Path methods .....	443
6.10	Excess Pore Pressure measurements due to Pile Installation in Clays - Case Histories .....	444
6.11	Effect of (a) the Overconsolidation Ratio and (b) the Elastic Shear modulus on the distributions of the excess Pore Pressure predicted according to the Strain Path method, using the Proposed model ....	445



LIST OF FIGURES (continued)

<u>Fig. No.</u>	<u>Title</u>	<u>Page</u>
6.12	Proposed model Prediction of the stress-strain curves and the Effective Stress Paths during an undrained Cylindrical Cavity Expansion in BBC for various overconsolidation ratios .....	446
6.13	Effect of the OCR on the distributions of (a) the Radial Effective Stress and (b) the Axial Effective Stress predicted according to the Strain Path method using the Proposed model .....	447
6.14	Effect of the OCR on the distributions of (a) the Total Radial Stress and (b) the Shear Stress in the horizontal Plane, predicted according to the Strain Path method using the Proposed model .....	448
6.15	Effective Stresses immediately after Pile Installation predicted by the Proposed model (for $K_o$ -consolidated BBC) in conjunction with the Strain Path method .....	449
8.1	Predicted excess Pore Pressure dissipation and Radial Stress changes at the pile wall during Linear Consolidation. Initial conditions computed via the Strain Path method in conjunction with the proposed model for normally consolidated Boston Blue Clay .....	509
8.2	Predicted Locations of the Elasto-Plastic Boundary around a Pile, during consolidation of a soil with the properties of BBC .....	510

LIST OF FIGURES (continued)

<u>Fig. No.</u>	<u>Title</u>	<u>Page</u>
8.3	Proposed model predictions of the Pore Pressure dissipation and the Radial Stress changes at the pile wall during consolidation of a soil with the properties of normally consolidated BBC. Initial conditions via: (a) Cavity Expansion and (b) Strain Path methods .....	511
8.4	Modified Cam-Clay model Predictions of the Pore Pressure dissipation and the Radial Stress changes at the pile wall during consolidation of a soil with the properties of normally consolidated BBC. Initial conditions via: (a) Cavity Expansion and (b) Strain Path methods .....	512
8.5	Proposed model predictions of the excess Pore Pressure dissipation (at various time factors) during consolidation of a soil with the properties of normally consolidated BBC. Initial conditions via: (a) Cavity Expansion and (b) Strain Path methods .....	513
8.6	Modified Cam-Clay model Predictions of the excess Pore Pressure dissipation (at various time factors) during consolidation of a soil with the properties of normally consolidated BBC. Initial conditions via: (a) Cavity Expansion and (b) Strain Path methods ....	514
8.7	Proposed model predictions of the Radial Effective Stress changes (at various time factors) during consolidation of a soil with the properties of normally consolidated BBC. Initial conditions computed via: (a) Cavity Expansion and (b) Strain Path methods .....	515

LIST OF FIGURES (continued)

<u>Fig. No.</u>	<u>Title</u>	<u>Page</u>
8.8	Modified Cam-Clay model predictions of the Radial Effective stress changes (at various time factors) during consolidation of a soil with the properties of normally consolidated BBC. Initial conditions via: (a) Cavity Expansion and (b) Strain Path methods .....	516
8.9	Proposed model Predictions of (a) the effective stress path and (b) the stress-strain curve for an element located at the pile wall during consolidation of a soil with the properties of normally consolidated BBC. Initial conditions via the Strain Path method .....	517
8.10	Modified Cam-Clay model Predictions of (a) the Effective Stress Path and (b) the Stress-Strain curve for an element located at the pile wall during consolidation of a soil with the properties of normally consolidated BBC. Initial conditions via the Cavity Expansion method .....	518
8.11	Proposed model Predictions of the Pore Pressure and the Radial Stress changes at the Pile wall during consolidation of a soil with the properties of slightly overconsolidated BBC. Initial conditions computed via the Strain Path method .....	519
8.12	Proposed model Predictions of the Pore Pressure dissipation (at various time factors) during consolidation of a soil with the properties of slightly overconsolidated BBC. Initial conditions computed via the Strain Path method .....	520

LIST OF FIGURES (continued)

<u>Fig. No.</u>	<u>Title</u>	<u>Page</u>
8.13	Proposed model predictions of the radial effective stress changes (at various time factors) during consolidation of a soil with the properties of slightly overconsolidated BBC. Initial conditions computed via the Strain Path method .....	521
8.14	Effective Stresses after soil consolidation predicted by the Proposed model (in conjunction with the Strain Path method) for $K_0$ -consolidated BBC .....	522
8.15	Comparison of the measured normalized excess pore pressure dissipation curves at the pile wall, with the proposed model predictions for a soil with the properties of BBC and initial conditions computed via the Strain Path method .....	523
8.16	Comparison of the measured radial effective stress at the pile wall, with the proposed model predictions for a soil with the properties of BBC and initial conditions computed via the Strain Path method .....	524
8.17	Comparison of the measured normalized Radial Total Stress at the pile wall, with the proposed model predictions for a soil with the properties of Boston Blue Clay and initial conditions computed via the Strain Path method .....	525
8.18	Comparison of the Stress and Pore Pressure changes at the pile wall predicted by the proposed model, with the predictions of an 'equivalent' linear elastic soil model for a clay with the properties of normally consolidated BBC .....	526

LIST OF FIGURES (continued)

<u>Fig. No.</u>	<u>Title</u>	<u>Page</u>
8.19	Comparison of the Stress and Pore Pressure changes at the pile wall predicted by the proposed model, with the predictions of an 'equivalent' linear elastic soil model for slightly overconsolidated BBC .....	527
C.1	Mean Effective Stress vs. Volumetric Strain for Radial Stress Paths with various stress ratios. St. Alban sensitive clay (depth=5m) .....	567
C.2	Mean Effective Stress vs. Volumetric Strain for Radial Stress Paths with various stress ratios. St. Alban sensitive clay (depth=5.7m) .....	568
C.3	Mean Effective Stress vs. Volumetric Strain for Radial Stress Paths with various stress ratios. St. Louis sensitive clay .....	569
C.4	Mean Effective Stress vs. Volumetric Strain for Radial Stress Paths with various Stress ratios. Rang de Fleuve sensitive clay .....	570

\*\*\*\*\*

# CHAPTER 1

## INTRODUCTION

Piles represent an important foundation type, especially in difficult soil conditions (e.g., soft clays) and hostile environments (e.g., offshore). The prediction of the ultimate axial capacity of a single pile is the first step in deep foundation design. A free body diagram of an axially loaded pile is shown in Fig. 1.1. Soil resistance is provided at the tip (point resistance) and along the shaft (skin friction). For long piles in clays, the point resistance usually represents a small fraction of the pile capacity and, for most practical purposes, is adequately predicted by existing methods, e.g., Skempton (1951), Meyerhof (1951), McClelland (1974), API (1975), Vesic (1975). On the other hand, the major portion of pile capacity is derived from skin friction along the shaft, especially when no competent end bearing layer exists. Therefore, the limiting skin friction,  $f_s$ , that can be provided by the soil is of primary importance in the design of piles.

This research represents part of a continuing effort at MIT to develop a better understanding of the mechanism of the axial capacity of piles driven in clays. Past research was primarily concerned with estimating the excess pore pressures in the clay during pile penetration (Levadoux and Baligh, 1980) and studying the pore pressure dissipation after pile penetration using a linear, elastic, isotropic soil model (Baligh and Levadoux, 1980). This research is aimed at esti-

mating the pore pressure dissipation and the effective stress changes after pile penetration using non-linear, elastoplastic, anisotropic constitutive models for clays.

This study can be divided into three parts: the first (Chapter 2) provides background material on existing approaches for estimating the limiting skin friction of driven piles in clays; the second (Chapters 3, 4 and 5), presents and evaluates constitutive models, based on Plasticity Theory, for predicting the stress-strain-strength behavior of clays under general loading conditions; finally, the third (Chapters 6, 7 and 8) studies pile installation and performs linear and non-linear consolidation analyses around piles driven in soft clays using the soil models discussed in the second part of this study.

Chapter 2 presents and critically discusses existing approaches for estimating the limiting skin friction of driven piles in clays. Currently, design procedures rely basically on empirical methods because of the complicated and very little understood mechanism of soil deformation and stressing around piles. Rational approaches realize that the limiting skin friction,  $f_s$ , of driven piles is basically controlled by the values of the effective stresses at (and close to) the pile-soil interface after pile installation and soil consolidation is completed and hence, attempt to understand the mechanism governing  $f_s$  by analyzing the sequence of events during the life of the pile. It is thus concluded that esti-

mates of the effective stresses at (and close to) the pile-soil interface after soil consolidation is completed are very sensitive to the characteristics of the soil model used in the analysis of pile installation and consolidation. Hence, a constitutive law that can reliably model soil behavior under general (undrained and partially drained) loading conditions is necessary to obtain realistic estimates of the effective stresses around the pile after consolidation is completed.

Chapter 3 presents the concepts of Plasticity Theory necessary in developing constitutive laws for soils and critically discusses the Modified Cam-Clay model (Roscoe and Burland, 1968).

Chapter 4 proposes a non-linear, elastoplastic, anisotropic soil model based on Plasticity Theory. The proposed model generalizes many of the features of the Modified Cam-Clay model in order to more realistically represent certain aspects of soil behavior (e.g.,  $K_0$ -consolidation, stress-strain and strength anisotropy, strain softening, etc.).

Chapter 5 evaluates the proposed model by comparing its predictions with the measured behavior of resedimented  $K_0$ -consolidated samples of Boston Blue Clay (BBC) in selected laboratory tests (isotropic and one-dimensional consolidation, undrained triaxial, undrained plane strain and undrained direct simple shear). The proposed model gives reasonable predictions of the measured stress-strain-strength behavior of BBC and is shown to be superior to the Modified Cam-Clay



model.

Chapter 6 studies the changes of the effective stresses and the pore pressure far behind the tip of a cylindrical, closed end, driven pile due to installation (driving) in a clay with properties similar to those of Boston Blue Clay. Two methods of analysis are used: the undrained cylindrical cavity expansion (e.g., Randolph et al, 1978a) and the strain path method (Baligh et al, 1978). It is shown that the method of analysis significantly influences the magnitude of the changes in the effective stresses and the pore pressure at (and close to) the pile-soil interface.

Chapter 7 studies the theory of linear and non-linear soil consolidation (Biot's theory of consolidation). As an application of the general theory it presents an analytical solution for the linear (radial) consolidation around a cylindrical pile. Finally, it presents a Weighted Residuals formulation for the non-linear consolidation and its numerical implementation via the Finite Element Method.

Chapter 8 uses the initial distributions of the pore pressures and the effective stresses estimated in Chapter 6 and performs linear and non-linear consolidation analyses around piles in a soil with properties similar to those of Boston Blue Clay. The proposed method of analysis uses the Finite Element numerical scheme developed in Chapter 7 in conjunction with the Modified Cam-Clay and the proposed models and estimates the pore pressure dissipation rates and effec-

tive stress changes around the pile during and after consolidation.

Finally, Chapter 9 summarizes the findings of all previous chapters.

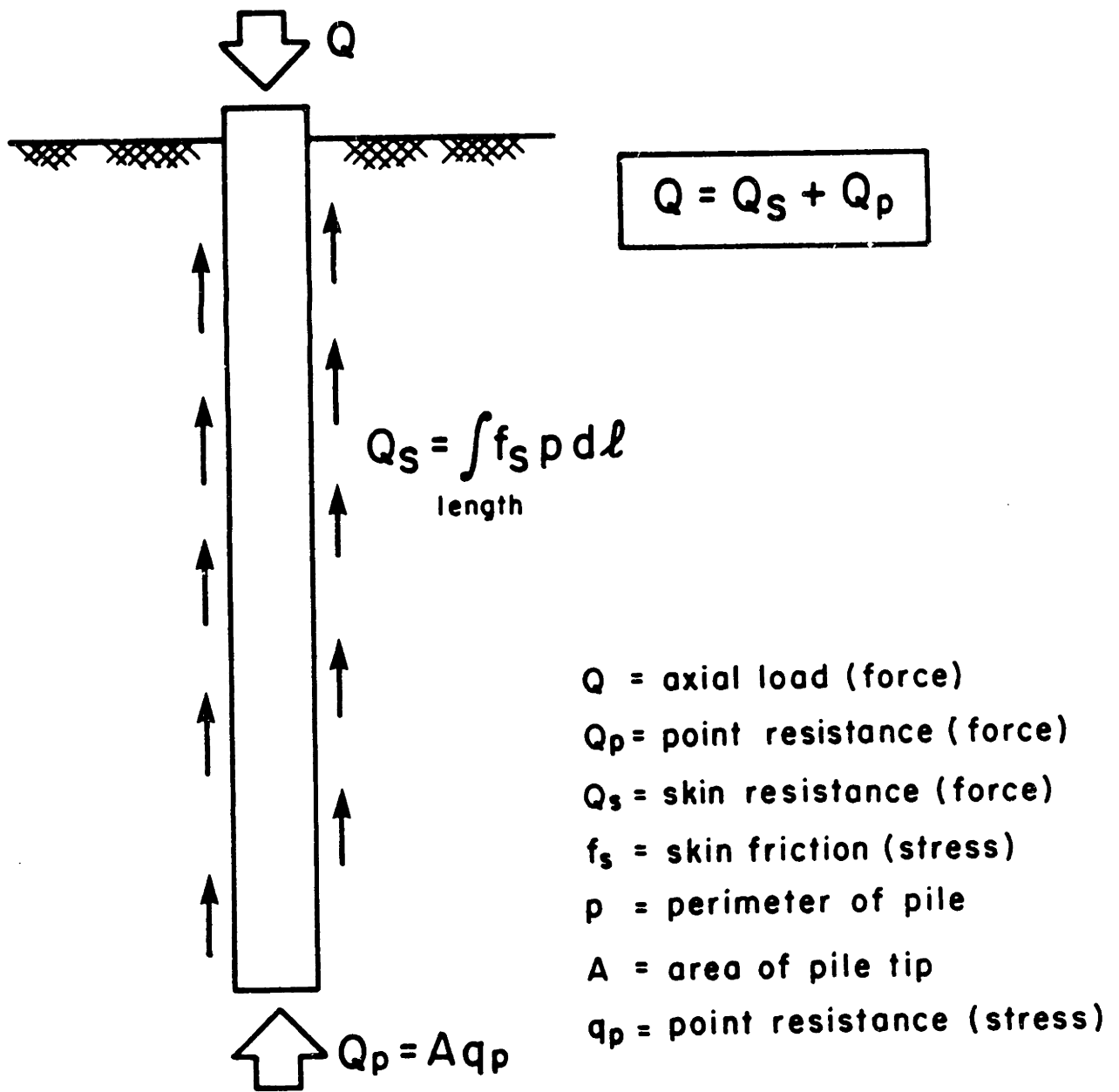


Figure 1.1: Free body of an axially loaded pile.

## CHAPTER 2

### EXISTING APPROACHES FOR ESTIMATING THE LIMITING SKIN FRICTION OF DRIVEN PILES IN CLAYS

Rational estimates of the limiting skin friction along pile shafts are difficult to obtain because of the very complicated mechanism of pile-soil interaction. Therefore, early design methods relied on empirical approaches. The following review applies to driven piles in soft clays (the Terzaghi and Peck, 1967, classification of clays is shown in Table 2.1).

#### 2.1 EMPIRICAL APPROACHES

##### 2.1.1 TOTAL STRESS APPROACHES: THE $\alpha$ -METHOD

In "Total Stress" methods, the limiting skin friction,  $f_s$ , is expressed as a fraction of the undrained shear strength,  $s_u$ , of the virgin clay:

$$f_s = \alpha s_u \quad (2.1)$$

where  $\alpha$  is an empirical parameter backfigured from the results of pile load tests. Therefore, the parameter  $\alpha$  combines the effect of all factors affecting the limiting skin friction e.g., the type of clay, dimensions and method of installation of the pile, time effects, etc.

Terzaghi and Peck (1967) indicate that the soil adjacent

to a pile driven into soft clay becomes stronger than the surrounding soil because of consolidation. They suggest that  $\alpha$  equals unity when the undrained shear strength is determined by means of unconfined compression tests on clay samples (recovered prior to pile driving).

Peck (1958) and Woodward et al. (1961) recommend different values of  $\alpha$  (Fig. 2.1) mostly based on pile load tests in stiff clays ( $s_u > 0.75$  TSF). Typically,  $\alpha$  is less than unity and decreases with increasing undrained shear strength of the soil. The undrained shear strength is again obtained from unconfined compression tests. In Fig. 2.1 the API (1975) recommended curve is also shown. It can be seen that the values of  $\alpha$  decrease from 1.0 for soft clays (where  $s_u < 0.25$  TSF) to 0.5 in stiff clays (where  $s_u > 0.75$  TSF).

Tomlinson (1971) provides design values of the parameter  $\alpha$  for piles driven into stiff to very stiff clays, as shown in Table 2.2 and Fig. 2.2.

Flaate (1968), after a comprehensive analysis of a number of pile load tests\*, suggests that,  $\alpha$ , depends not only on the average undrained shear strength of the clay, but also on the plasticity index,  $I_p$ , as shown in Fig. 2.3.

Flaate and Selnes (1977) compiled results of 44 pile load tests performed mainly on timber piles (length 8-16m) driven

---

\*Very few tests were analyzed in the stiff to very stiff range of clay strength ( $s_u > 0.5$  TSF).

into soft to medium Norwegian clays, and compared the unit average shaft resistance (after subtracting the estimated point resistance) with values of the undrained shear strength measured by means of the field vane test. Figure 2.4 presents their data and clearly indicates that significant scatter and uncertainty exist in the selection of an adequate value of  $\alpha$  ( $0.4 < \alpha < 1.6$ ). They thus suggest the use of an Effective Stress Approach which is presented in Section 2.1.3.2.

Figures 2.1 through 2.4 indicate that the proposed values of  $\alpha$  by different investigators are quite different and hence, estimates of the skin friction of piles in clays by the  $\alpha$ -method involve significant uncertainties. In addition, the designer must estimate the undrained shear strength,  $s_u$ , of the clay, which represents additional uncertainties because of the dependence of  $s_u$  on the type of test, sample disturbance, etc.

### 2.1.2 EFFECTIVE STRESS APPROACHES: THE $\beta$ -METHOD

It is widely accepted that soil failure is controlled by effective stresses. Therefore, it appears reasonable to estimate the limiting skin friction of piles by means of effective stress methods.

Several authors (Zeevaert, 1959; Eide et al., 1961; Chandler, 1968) proposed equations of the following form for estimating the limiting skin friction of driven piles in

cohesive soils:

$$f_s = K \cdot \tan \bar{\theta} \cdot \bar{\sigma}_{vo} \quad (2.2)$$

where:  $K$  = an earth pressure coefficient (often assumed equal to  $K_o$ , prior to pile driving);

$\bar{\theta}$  = an effective friction angle, equal to the pile-soil interface friction angle,  $\bar{\delta}$ , for failure at the interface and, discussed in Section 2.2.5.2 for failure in the soil.

$\bar{\sigma}_{vo}$  = the in situ vertical effective stress.

Burland (1973) studied the skin friction of driven piles in soft clays and made the following assumptions:

- 1) After consolidation (i.e., dissipation of the excess pore pressures generated by pile driving), the radial effective stress acting on the pile shaft is approximately equal to the in situ horizontal effective stress prior to pile installation.
- 2) The pore pressures generated in the soil by subsequent loading of the pile (i.e., by shearing) are sufficiently small and can be neglected.

Consequently, he combined the effect of  $K_o$  and  $\bar{\theta}$  in one parameter  $\beta$ ,

$$\beta = K_o \cdot \tan \bar{\theta} \quad (2.3)$$

and rewrote Eq. 2.2 in the following form;

$$f_s = \beta \bar{\sigma}_{vo} \quad (2.4)$$

where  $K_o$  is the coefficient of earth pressure at rest.

$$(K_o = \bar{\sigma}_{ho} / \bar{\sigma}_{vo}).$$

For normally consolidated clays, Jaky (1944) proposes the well-known relationship:

$$K_o \approx 1 - \sin \bar{\phi} \quad (2.5)$$

where  $\bar{\phi}$  is the effective friction angle of the soil.

Substituting Eq. 2.5 into Eq. 2.3 and assuming that skin friction is controlled by the friction angle of the soil, we get for normally consolidated (N.C.) clays:

$$\beta = (1 - \sin \bar{\phi}) \cdot \tan \bar{\phi} \quad (2.6)$$

Figure 2.5 shows data obtained by Burland (1973) from pile load tests on short piles in soft to medium clays. The range of  $\beta$  values is 0.25 to 0.40 with an average of 0.32. According to Eq. 2.6, this range corresponds to a back-figured friction angle,  $\bar{\phi}$ , of 21° to 40°\* for N.C. clays.

Vesic (1970) analyzed the results of load tests on instrumented driven piles in clays and found that the local ultimate unit skin friction,  $f_s$ , is roughly proportional to depth (or the effective overburden stress) along most of the shaft, which is consistent with the  $\beta$ -method.

---

\* Values of  $\beta$  larger than 0.30 do not correspond to any angle  $\bar{\phi}$  (from Eq. 2.6). Therefore, clays are overconsolidated or Eq. 2.6 is not applicable.



Meyerhof (1976) compiled data from pile load tests performed by various investigators in soft to medium clays (see Fig. 2.6) and concluded that the factor  $\beta$  decreases with the pile length. For short cylindrical piles  $\beta = 0.2$  to  $0.4$  and for long piles  $\beta = 0.1$  to  $0.25$ . The values of  $\beta$  for short piles are in reasonable agreement with results reported by Burland (1973) (see Fig. 2.5).

The cause for the decrease in  $\beta$  with pile length is controversial. One explanation is provided by Meyerhof (1976), who argues that significant deformations are required to develop the average limiting skin friction along the shaft of long piles. These deformations cause large slippage between pile and soil\* and hence the appropriate average effective friction angle,  $\bar{\phi}$ , along the shaft approaches the residual value. The latter is significantly smaller than the peak value of  $\bar{\phi}$ .

Finally, Flaate and Selnes (1977) generalized Eq. 2.4 to include overconsolidated clays and suggested the following expression:

$$f_s = \beta \sqrt{\text{OCR}} \cdot \bar{\sigma}_{vo} \quad (2.7)$$

The correlation (see Fig. 2.7) for 44 pile load tests in soft to medium Norwegian clays (normally and over-consolidated) with

---

\* Especially at shallow depths.

lengths less than 25m, corresponds to  $\beta$  values similar to the ones obtained by Burland (1973) and Meyerhof (1976) for soft to medium clays ( $\beta = 0.20 - 0.40$ ). However, Burland (1973) reports that the use of a similar equation\* for short driven piles in heavily overconsolidated London clay generally underestimates the limiting skin friction by as much as 50%,\*\* and suggests the use of the method with caution. For normally consolidated clays he suggests  $\beta = 0.3$  for pile penetration less than 50 ft,  $\beta = 0.15$  for pile penetration larger than 200 ft, and interpolation for intermediate depths.

Bea (1975) reports laboratory tests on model steel piles (1/2 in dia.) run in a triaxial cell (2 1/8 in dia. soil sample), which show that the limiting skin friction,  $f_s$ , is sensitive to soil composition and pile roughness, but relatively insensitive to the rate of loading and to load cycling. In addition, when full drainage is allowed, undisturbed and remolded soils have virtually the same  $f_s$ . He also reports results from six in situ tests on driven steel pipe piles in clays. The average adhesion factor,  $\beta$ , for these tests, is plotted in Fig. 2.8 versus the average Plasticity Index,  $I_p$ , of the clays penetrated. Clearly,  $\beta$  decreases with  $I_p$  in Fig. 2.8. However, case 1 showing significant effect of  $I_p$ , involves a much longer pile and hence the effect of pile length

---


$$*\beta = (1 - \sin \bar{\phi}) \cdot \tan \bar{\phi} \cdot \sqrt{\text{OCR}}$$

\*\*He reports values of  $\beta$  in the range of 0.8 to 1.2.

represents an important factor not to be neglected in this correlation.

### 2.1.3 MIXED APPROACHES

#### 2.1.3.1 The $\lambda$ -Method

Vijayvergiya and Focht (1972) empirically correlated the skin friction,  $f_s$ , to both the vertical effective stress and the undrained shear strength:

$$f_s = \lambda(\bar{\sigma}_{vo} + 2s_u) \quad (2.8)$$

where  $f_s$ ,  $\bar{\sigma}_{vo}$  and  $s_u$  are the average values of limiting skin friction, vertical effective stress, and undrained shear strength (miniature vane and/or unconfined compression tests) along the pile shaft, respectively.

Backfigured values of  $\lambda$  from forty-two pile load tests\* are shown in Fig. 2.9.

The effect of pile penetration (depth) on  $\lambda$  is similar to the effect on  $\beta$  discussed earlier. However, the scatter of  $\lambda$  in Fig. 2.9 is significantly less than that of  $\beta$  in Fig. 2.6.

Esrig and Kirby (1978) correctly indicate that, like all empirical methods, the  $\lambda$ -method is largely influenced by the data base. They state that data from short piles (penetration less than 15m) are generally from piles driven into overconsolidated clays, whereas the data from very long piles (like the ones used in offshore work) are from piles driven into slightly overconsolidated and normally consolidated clays.

\*Run on 15 different clays by various investigators.

This might provide another explanation of the decrease of  $\beta$  (Fig. 2.6) and  $\lambda$  (Fig. 2.9) with depth.

### 2.1.3.2 Flaate and Selnes' (1977) Method

Meyerhof (1976) states that the excess pore pressures induced by pile loading to failure (after dissipation of the excess pore pressures induced by driving) are very low (in the range of only about  $0.2 s_u$  to  $0.5 s_u$  at the pile shaft). Consequently, the skin friction of the pile is governed by the drained strength of the clay near the pile surface. Based on a similar argument, Bjerrum (1973) proposes the following expression for the skin friction,  $f_s$ , based on Hvorslev's parameters  $\bar{\phi}_e$ ,  $\bar{c}_e$ :

$$f_s = \mu (D \bar{\sigma}_{hf} \tan \bar{\phi}_e + \bar{c}_e \bar{\sigma}_e) \quad (2.9)$$

where  $\mu$  = a coefficient for time rate effects  
 $D$  = mobilization factor for the frictional resistance  
 $\bar{\sigma}_{hf}$  = the effective horizontal stress at failure acting on the pile shaft  
 $\bar{\sigma}_e$  = equivalent consolidation pressure

Starting from this expression, assuming that  $\bar{\sigma}_{hf} = \bar{\sigma}_{ho} = K_o \bar{\sigma}_{vo}$  and using the correlations of Hvorslev parameters with plasticity index  $I_p$  established by Bjerrum (1973), Flaate and Selnes (1977) propose the following expression:

$$f_s = U_L [(0.3 - 0.001I_p) \sqrt{OCR} \bar{\sigma}_{vo} + 0.008I_p s_u] \quad (2.10)$$

in which  $U_L$  is a factor (accounting for the reduction in mobilized skin friction with increased pile length  $L$ ), given by the relationship\*:

$$U_L = \frac{L + 20}{2L + 20} \quad (2.11)$$

and OCR is the overconsolidation ratio.

Comparing the computed and observed values of skin friction from 44 pile load tests on a variety of soft and medium Norwegian clays, Flaate and Selnes show that their method (Eq. 2.10) provides more accurate predictions than the  $\alpha$ ,  $\beta$ , or  $\lambda$  methods. <sup>not available</sup>

#### 2.1.4 CONCLUSIONS

The prediction of skin friction on piles is extremely difficult because of the complicated nature of the soil-pile interaction. Designs are presently performed on the basis of conservative engineering intuition developed by repeated trials and the results of load tests, mostly on single piles. All methods involve serious assumptions, mainly regarding the magnitude of the radial effective stress acting at the pile-soil interface at failure. The limiting skin friction is related to either the in situ (virgin) undrained shear strength of the clay ( $\alpha$ -method) or the vertical effective stress in

---

\* L in meters

the ground ( $\beta$ -method) or a combination of the two ( $\lambda$ -method).

The effect of all other soil and pile parameters on the limiting skin friction is combined into empirical coefficients ( $\alpha$ ,  $\beta$ , or  $\lambda$ ) which are evaluated from pile load tests.

The common use of these very different methods in practice clearly indicates that the mechanism of skin friction on piles is far from being understood.

The following support this argument:

- 1) The  $\alpha$  and  $\beta$  methods, although equally accepted by the profession, imply totally different mechanisms of shearing during pile loading: The first assumes that limiting skin friction is controlled by the in-situ undrained shear strength prior to pile installation, and the second attempts to relate the limiting skin friction to the effective radial stress acting at the pile-soil interface during shearing of the pile.
- 2) It is unlikely that the effects of clay structure and its compressibility, sensitivity, creep characteristics as well as the pile type and its method of installation and history of loading can all be described by a single parameter ( $\alpha$ ,  $\beta$  or  $\lambda$ ).

In addition to uncertainties in the mechanism of skin friction, the data base on which the empirical correlations

are founded can involve significant errors and/or scatter due to:

- 1) Inadequate estimates of soil properties and more specifically the value of the undrained shear strength;
- 2) Variable degrees of dissipation of the excess pore pressures induced by pile driving when pile load tests are conducted;
- 3) Variable rates of pile loading during load testing;
- 4) Questionable methods of estimating the effect of point resistance especially for short piles (where the contribution of point resistance to the total load is significant).

In conclusion, empirical methods for estimating design values of the skin friction of piles in clays should be used with caution. More rational approaches are needed in order to improve the reliability of designs.

## 2.2 RATIONAL APPROACHES

### 2.2.1 GENERAL

It is widely accepted that effective stresses control the shear strength of soils. Thus, rational approaches for estimating the limiting skin friction,  $f_s$ , attempt to estimate the effective stresses controlling the shearing resistance along pile shafts. Because of kinematic constraints, the shear surface of slippage is at, or parallel to, the pile-soil interface. Different assumptions regarding the stress state at failure result in different values of the limiting skin friction,  $f_s$ . Two examples are presented:

- 1) Assuming a frictional failure criterion (of the Coulomb type), and knowing that shear surfaces are vertical, the only stress needed to estimate  $f_s$  is the radial effective stress at (and close to) the pile-soil interface at failure,  $\bar{\sigma}_{hf}$ :

$$f_s = \bar{\sigma}_{hf} \cdot \tan \bar{\theta} \quad (2.12)$$

where  $\bar{\theta}$  is a friction angle. If slippage develops at the pile-soil interface, then  $\bar{\theta} = \bar{\delta}$ , where  $\bar{\delta}$  is the interface friction angle. On the other hand, when slippage develops in the soil,  $\bar{\theta}$  is a complicated



function of the soil friction angle,  $\bar{\phi}$ , (see Section 2.2.5).

- 2) Assuming that the soil adjacent to the pile is in a failure state obeying the Extended Mises criterion (as adopted in the Modified Cam-Clay model, Roscoe and Burland, 1968), and that slippage takes place at the pile-soil interface, Figure 2.10 shows that:

$$f_s = \frac{M}{2} \bar{\sigma}_f \cos \bar{\delta} \quad (2.13)$$

where  $M$  is a failure parameter of the Modified Cam-Clay model\*,  $\bar{\delta}$  is the interface friction angle and  $\bar{\sigma}_f$  the mean effective stress at failure. Eq. 2.13 is reported by Esrig et al. (1977) and is discussed in Section 2.2.5.

Clearly, Eq. 2.13 introduces more parameters and assumptions regarding the state of stress in the soil adjacent to the pile at failure than Eq. 2.12 (e.g., the vertical and tangential effective stresses in addition to the radial effective stress) and thus adds to the uncertainties in the estimated values of  $f_s$ .

Friction angles such as  $\bar{\delta}$  and  $\bar{\phi}$  can be determined from laboratory tests and hence can be estimated within reasonably narrow limits. On the other hand, the effective stresses acting on the shaft at failure represent a major uncertainty in predicting

---

\*  $M$  is related to the effective friction angle,  $\bar{\phi}$ , obtained from triaxial compression tests by:

$$M = \frac{6 \cdot \sin \bar{\phi}}{3 - \sin \bar{\phi}}$$

$f_s$  and require a careful study of the sequence of events prior to pile loading (in situ conditions, pile installation, soil consolidation and shearing). Furthermore, since soil behavior cannot be described by the stresses on one plane (tractions) only, comprehensive soil models involving the full state of stress (on three mutually perpendicular planes) are needed.

The General Effective Stress Method (Kirby et al., 1977, 1979; Esrig et al., 1977, 1978, 1979; Randolph et al., 1979a,b; Liefer et al., 1979; Wroth et al., 1979; Carter et al., 1979c; WCC, 1978) is a rational approach for estimating the limiting skin friction of driven piles in clay and is based on effective stress concepts. Figure 2.11 shows the sequence of events that require investigation before the effective stresses along pile shafts at failure can be estimated:

- a) In situ conditions prior to pile driving; i.e., the values and directions of the in situ principal effective stresses, the stress history (overconsolidation ratio), etc.
- b) Changes in stresses and properties of the soil due to pile installation. Pile installation induces significant shearing (remolding) of the soil in the immediate vicinity of the pile, and causes high excess pore pressures and a significant reduction

in effective horizontal stresses\*.

- c) Changes in stresses and properties of the soil due to consolidation after pile driving. Dissipation of excess pore pressures increases\* the effective stresses in the vicinity of the pile-soil interface and hence increases the shaft resistance of the pile.
- d) Changes in stresses during pile loading to failure.

The remaining of this Chapter (Sections 2.2.2 through 2.2.5) discusses these aspects in detail.

---

\* in soft clays

## 2.2.2 IN SITU CONDITIONS PRIOR TO PILE DRIVING

Most sedimentary soils are deposited in horizontal layers under conditions of no lateral strains (i.e., one-dimensional vertical compression). Consequently, they are expected to exhibit rotational anisotropy in the horizontal plane, with the principal directions in horizontal and vertical planes. Under special circumstances (e.g., slopes of the continental shelf or deltaic fans), soils may be deposited in non-horizontal layers.\* In these latter cases, the initial state of stress is complicated and difficult to estimate.

In horizontal layers, the initial state of stress at an element of soil is characterized by the following three parameters:

- a) The vertical total stress  $\sigma_{vo}$
- b) The static pore pressure,  $p_o$
- c) The ratio,  $K_o$ , of the horizontal to vertical effective stresses

$$K_o = \bar{\sigma}_{ho} / \bar{\sigma}_{vo} \quad (2.14)$$

The vertical total stress,  $\sigma_{vo}$ , is obtained from measurements of the unit weight of the soil which can be estimated with reasonable accuracy.

The static pore pressure,  $p_o$ , is commonly determined

---

\* Tectonic motions may also change the orientation of bedding planes.

by assuming hydrostatic conditions. In unusual circumstances (e.g., strata undergoing consolidation or in cases involving artesian pressures), this assumption is not justified and direct measurements of  $p_o$  are required (by installing piezometers). Therefore, errors in the estimated vertical effective stresses are principally caused by uncertainties in  $p_o$ . This is particularly true in offshore work where  $p_o$  cannot be routinely measured.

The last parameter characterizing the state of stress is  $K_o$ . For normally consolidated clays (NC), Jaky (1944) proposes:

$$K_o = 1 - \sin \bar{\phi} \quad (2.15)$$

where  $\bar{\phi}$  is the effective friction angle. Ladd et al. (1977) found that Eq. 2.15 applies reasonably well to a wide variety of normally consolidated clays tested in the laboratory. Figure 2.12 shows plots of  $K_o$  vs.  $\bar{\phi}$  and also  $K_o$  vs. plasticity index for normally consolidated clays.

For overconsolidated clays (OC), Ladd et al. (1977) propose:

$$K_o(OC) = K_o(NC) (OCR)^n \quad (2.16)$$

in which OCR is the overconsolidation ratio:

$$\text{OCR} = \bar{\sigma}_{vm} / \bar{\sigma}_{vo} \quad (2.17)$$

and the maximum past pressure  $\bar{\sigma}_{vm}$  is determined from routine consolidation (oedometer) tests or CRSC\* tests, by means of empirical methods. Sample disturbance may obscure and underestimate the maximum past pressure. This latter effect is particularly important in offshore work where good quality samples are very difficult to obtain.

During simple unloading from a normally consolidated state, a value of the exponent  $n = 0.41$  (Eq. 2.16) provides a good fit for existing experimental data (Ladd et al., 1977). The variation of the exponent with  $I_p$  for a variety of clays is shown in Fig. 2.13 (after Esrig et al., 1978). This figure is basically the same as Fig. 32 of Ladd et al. (1977).

For stress paths different from simple unloading, the precise geologic history of a deposit has a significant influence on the lateral stress (Wroth, 1975). The parameter  $K_0$  can no longer be uniquely related to OCR, and must be obtained by direct measurements. However, existing methods of measuring  $K_0$  are not reliable in onshore work and do not exist offshore and the subject is still in the research stage.

---

\* Constant Rate of Strain Consolidometer.

### 2.2.3 EFFECTS OF PILE INSTALLATION

Pile installation causes severe straining of the soil and drastic changes in the soil stresses. A rational estimate of the shaft resistance of piles requires that the mechanism of installation be understood and then formulated in a comprehensive method to perform predictions.

Pile driving in saturated clays is a very difficult two-dimensional dynamic problem because of the complicated behavior of soils and the large strains and large stress gradients associated with pile penetration. Therefore, complete solutions\* are not available and existing solutions are based on simplifying assumptions regarding problem geometry, soil behavior, and/or the mode of deformation.

#### 2.2.3.1 Cavity Expansion Approaches

The expansion of a cylindrical cavity in an infinite saturated transversely-isotropic clay mass is a simple one-dimensional problem that can be easily treated. Since cavity expansion represents a cornerstone in the "general effective stress method" proposed by Esrig et al. and Carter et al. to simulate pile installation, a detailed description of the method is presented.

#### Literature Review

Table 2.3 summarizes existing solutions for the expansion of cylindrical cavities and spherical cavities (in an isotropic

---

\* Including the variation with time of stresses, pore pressures, strains, and deformations in the soil.

material) obtained by various investigators for estimating the bearing capacity of deep foundations (point resistance), interpreting pressuremeter tests, and analyzing pile installation effects.

Closed-form solutions are available for simple constitutive relations of the soil (e.g., when the soil is assumed to be elastic-perfectly plastic). For more realistic behavioral soil models, Ladanyi (1963) developed a numerical method for obtaining total stresses and pore pressures at different radii after expansion of a cylindrical (or spherical) cavity in an infinite medium. As a first approximation, he utilizes the curves of shear stress vs shear strain and mean effective stress vs shear strain from a  $\overline{\text{CIU}}$  triaxial compression test to simulate the soil behavior during cavity expansion. The equation of equilibrium is numerically integrated so that general (nonlinear) stress-strain curves can be considered. However, Ladanyi's numerical method is only applicable to an isotropic medium, initially under an isotropic state of stress, in which the vertical stress increment is related to the radial and circumferential stress increments by the equation:

$$\Delta\sigma_z = \frac{1}{2}(\Delta\sigma_r + \Delta\sigma_\theta). \quad (2.18)$$

Butterfield and Bannerjee (1970) approximate the stress distribution around the shaft of a long driven pile by superimposing the stresses due to expansion of a cylindrical cavity to the



stresses caused by a uniform boundary shear (vertical shaft friction). The shear stress distribution at different radii is obtained directly by integrating the equation of vertical equilibrium and by imposing the boundary conditions at the pile-soil interface. The addition of shaft friction does not represent significant complications.

Unfortunately, the results presented by Butterfield and Bannerjee are in error.\* They neglect conservation of volume and hence overestimate the stress changes in the elastic zone by a factor of four. The theoretical derivations conducted by Butterfield and Bannerjee have been corrected by Levadoux (1980) who shows that:

- (1) the radius of the plastic zone is not significantly affected by the shaft friction\*\*
- (2) the radial stress increase (above its initial value) at the cavity wall is reduced by approximately 10% for typical values of the rigidity index ( $I_R = G/s_u = 50-200$ ), when a shaft friction equal to the undrained shear strength,  $s_u$ , is considered.

Carter et al. (1979c) employ the finite element technique for predicting the stresses due to pile driving which is modelled by simple cylindrical cavity expansion. They utilize:

---

\* See discussion by Randolph and Carter (1979).

\*\* A shaft friction equal to the undrained shear strength,  $s_u$ , increases the radius of the plastic zone by less than 0.5% when the rigidity index,  $I_R = G/s_u$ , is greater than 50 (as compared to the case of no shaft friction).

- a) An elastic-perfectly plastic material model (for checking their numerical results against closed-form solutions), and
- b) The modified Cam-Clay model.

After conducting parametric studies by varying the overconsolidation ratio (OCR) on a hypothetical clay with engineering properties similar to those of Boston Blue Clay, they conclude that:

- a) The ratio of the limit pressure (i.e., the limiting radial stress at the soil-pile interface) to the undrained shear strength  $\sigma_l/s_u$ , as well as the ratio of the limit excess pore pressure (at the soil-pile interface) to the undrained shear strength,  $\Delta p/s_u$  are nearly independent of the OCR. This conclusion is basically due to:

- 1) The solution of the cavity expansion problem ( $\sigma_l/s_u$  and  $\Delta p/s_u$ ) is controlled by the stiffness ratio  $G/s_u$  that determines the size of the plastic zone.
- 2) Carter et al. (1979c) assume that the shear modulus  $G$  is proportional to the vertical effective overburden pressure  $\bar{\sigma}_{v0}$  and to the overconsolidation ratio OCR. Writing  $G/s_u$  in the form:

$$\frac{G}{s_u} = \left[ \frac{G}{\bar{\sigma}_{vo}} \right] \cdot \left[ \frac{\bar{\sigma}_{vm}}{\bar{\sigma}_{vo}} \right]^{-1} \cdot \left[ \frac{\bar{\sigma}_{vm}}{s_u} \right] = \left[ \frac{G}{\bar{\sigma}_{vo}} \right] \cdot (OCR)^{-1} \cdot \left[ \frac{\bar{\sigma}_{vm}}{s_u} \right] \quad (2.19)$$

and assuming that  $G = \alpha \cdot \bar{\sigma}_{vo} \cdot (OCR)$  where  $\alpha$  is a constant of proportionality, we get:

$$\frac{G}{s_u} = \alpha \cdot (OCR) \cdot (OCR)^{-1} \cdot \left[ \frac{\bar{\sigma}_{vm}}{s_u} \right] = \alpha \cdot \left[ \frac{\bar{\sigma}_{vm}}{s_u} \right] \quad (2.20)$$

Therefore, the stiffness ratio  $G/s_u$  only depends on the ratio  $(\bar{\sigma}_{vm}/s_u)$  which varies slightly\* with OCR, for constant void ratio.

- b) For high values of OCR ( $> 8$ ) tensile circumferential effective stresses,  $\bar{\sigma}_\theta$ , are predicted at intermediate radii (between 6 and 15 pile radii). Otherwise ( $OCR < 8$ ),  $\bar{\sigma}_\theta$  remains positive.

The predictions of Carter et al. in the case of  $OCR = 1$  are subsequently compared with results of other soil models.

Massarsch and Broms (1977) and Massarsch (1978) investigate the development of vertical cracks in the soil around a pile during driving. They model pile installation by the expansion of a cylindrical cavity in an elastic-perfectly plastic material and estimate the excess pore pressure by means of Henkel's equation (1960). From the results of their analyses, they conclude that:

---

\* for low OCRs

- (1) cracks caused by hydraulic fracturing can develop in clay (especially in normally consolidated clay) during pile driving, and
- (2) these cracks are vertical, independently of the coefficient of lateral earth pressure at rest,  $K_0$ .

The analyses performed by Massarsch and Broms are very crude and, as pointed out by Carter and Randolph (1979), they lead to unrealistic effective stresses. Moreover, the pore pressures are based on Henkel's equation proposed in 1960 that he later corrected (Henkel and Wade, 1966). Levadoux (1980) shows that, contrary to Massarsch and Brom's conclusion, fracturing is unlikely to occur. Furthermore, the method of analysis used by Massarsch and Broms is not reliable because of a) the very idealized soil model used can only provide approximate total stress distributions, and b) the excess pore pressure in the plastic zone is very sensitive to the estimated values of the A parameter which depends significantly on the strain level.

Carter et al. conducted similar parametric analyses on a hypothetical clay using critical state concepts. They conclude that tensile circumferential effective stresses appear away from the pile only for large values of the overconsolidation ratio (OCR = 8) and, thus, contradict Massarsch and Broms' conclusions.

Tensile effective stresses may indeed appear during pile driving. However, more careful estimates of effective stresses

must be performed before the occurrence of hydraulic fracturing can be ascertained.

### Effect of Soil Model on Cylindrical Cavity Solutions

The major computational simplification offered by the undrained Cylindrical Cavity Solutions is that the strain increments everywhere in the soil can be estimated from kinematic constraints (i.e., incompressibility) with no reference to soil behavioral laws or stress equilibrium equations. Once the strain increments are estimated, a soil model is needed at each soil element to compute the corresponding stress increments. Specifically, in the problem of the undrained expansion of a cylindrical cavity, there are only two independent deviatoric total stress components. Consequently, a deviatoric stress model which relates:

(1) The shear stress  $\left[ \frac{\sigma_r - \sigma_\theta}{2} \right]$  vs radial

(or tangential) strain  $\epsilon_r (= -\epsilon_\theta)$ ;

(2) The vertical deviatoric stress  $s_z (= \sigma_z - \sigma_{oct})$

vs.  $\epsilon_r$ .

when supplemented with:

(3) A shear induced pore pressure model,  $\Delta p_s$  vs.  $\epsilon_r$  suffices to predict stresses and pore pressures in the soil during the expansion of a cavity, from zero radius, in a saturated (incompressible) clay, with given initial stresses (i.e., the vertical total stress  $\sigma_{v0} = \bar{\sigma}_{v0} + p_0$ ; the horizontal total stress  $\sigma_{h0} = K_0 \bar{\sigma}_{v0} + p_0$ ; and the pore pressure,  $p_0$ , before expansion).

Assuming normalized behavior (with respect to the vertical consolidation stress,  $\bar{\sigma}_{vc}$ ), the solid lines (labelled #1) in Fig. 2.14 present the three required relationships for normally consolidated BBC.

The deviatoric stresses  $(\sigma_r - \sigma_\theta)/2\bar{\sigma}_{vc}$  and  $s_z/\bar{\sigma}_{vc}$  vs.  $\epsilon_r (= -\epsilon_\theta)$  are predicted by the deviatoric stress model proposed by Levadoux and Baligh (1980), based on parameters derived from laboratory tests on normally consolidated resedimented BBC. Furthermore, the relationship  $\Delta p_s/\bar{\sigma}_{vc}$  vs.  $\epsilon_r$  is predicted by the pore pressure model proposed by Levadoux and Baligh (1980), also based on laboratory test results on normally consolidated resedimented BBC.

Stresses and pore pressures in the soil due to cavity expansion are obtained by means of the numerical method described by Levadoux (1980). Integration of the equilibrium equation begins at a radius equal to 200 times the final radius of the cavity ( $r = 200R$ ) where conditions at infinity are imposed:

$\sigma_z = \bar{\sigma}_{vo} + p_o$ ; and  $\sigma_r = \sigma_\theta = K_o \bar{\sigma}_{vo} + p_o$ . Using 105 intervals (i.e., 106 nodal points), the interval length equals  $10R$  at  $r = 200R$  and decreases with  $1/(r-R)$  to provide better resolution in zones of high stress gradients near the cavity wall. At each nodal point, the natural radial strain,  $\epsilon_r$ , is calculated and

the corresponding values of  $\frac{(\sigma_r - \sigma_\theta)}{2}$ ,  $s_z$ , and  $\Delta p_s$  are evaluated by means of the curves (labelled #1) in Fig. 2.14. The calculations proceed until  $r = 1.003R^*$ . The solution accuracy was checked by increasing the outer boundary radius and the number of intervals. Differences in stresses less than 0.1% were considered acceptable.

---

\*The natural radial strain,  $\epsilon_r$ , increases to infinity when  $r \rightarrow R$ .

The predicted distributions of stresses and pore pressures due to the expansion of a cylindrical cavity (from zero radius) in normally consolidated Boston Blue Clay are plotted in Fig. 2.15 which shows that:

- (1) The peak undrained shear strength is reached at a radius  $r = 3.4R$ . This follows from Fig. 2.14 which indicates that the peak strength is reached at  $\epsilon_r = 4.4\%$  and, for an incompressible soil,  $\epsilon_r \approx \frac{1}{2}(R/r)^2$
- (2) The effect of cavity expansion extends to very large radii. For example,  $\sigma_r$  and  $\sigma_\theta$  experience a 4% change from their initial value at  $r = 100R$ . This is caused by the relatively large initial tangent modulus used in the model ( $G_i = 183\bar{\sigma}_{v0}$ , Fig. 2.14).
- (3) At the cavity wall,  $\sigma_r$ ,  $\sigma_z$ , and  $\sigma_\theta$  are the major, intermediate and minor principal stresses, respectively.\*
- (4) The excess pore pressure,  $\Delta p$ , is significant (5% of  $\bar{\sigma}_{v0}$ ) up to 20R.
- (5) The shear induced pore pressure,  $\Delta p_s$ , is a small fraction (about 25%) of the total excess pore pressure,  $\Delta p$ .
- (6) The minor effective principal stress,  $\bar{\sigma}_\theta$ , remains compressive at any radius. No hydrofracture is therefore expected. When the peak strength of the soil is reached ( $r \approx 3.4R$ ),  $\bar{\sigma}_\theta$  is reduced to 16% of its initial value.

---

\*This also applies to the effective stresses.



Strain-softening behavior is difficult to measure reliably in the laboratory, especially at the large strains expected near the cavity wall. In order to evaluate the effects of uncertainties in strain-softening behavior, results were obtained for a perfectly plastic material (no strain-softening or hardening beyond the peak strength) and compared to the strain-softening soil treated above. Figure 2.16 illustrates the effect of strain-softening. As expected, the two analyses yield identical results for large radii ( $r > 3.4R$ ) where the pre-peak stress-strain relationships for the two soils are the same. At small radii ( $r < 3.4R$ ), strain-softening reduces the gradients of stresses such that at the cavity wall  $\sigma_r/\bar{\sigma}_{vo}$  is reduced by 8.5%.

#### Existing Solutions

Randolph et al. (1978a) employ the finite element technique to analyze the expansion of a cylindrical cavity from zero radius using the "modified Cam-Clay" model for soil behavior (Roscoe and Burland, 1968; Schofield and Wroth, 1968). Since the finite element program used by Randolph et al. does not account for the large strains associated with a cavity expanded from a zero radius, they double the radius  $R_0$  of an existing cavity and then utilize an approximate procedure to extrapolate the results between  $2R_0$  and  $\sqrt{3}R_0$  (final radius of the fictitious cavity with initial zero radius).

The total and effective stress distributions predicted by Randolph et al. (1978a) for a normally consolidated deposit with

"properties similar to BBC" are represented by the solid lines in Fig. 2.17. For the sake of comparison, the three stress-strain curves utilized by Randolph et al. were backfigured from their results (in Fig. 2.17) and plotted in Fig. 2.14. The procedure followed herein to obtain these curves consisted of:

- (1) Compute the strains at a selected number of normalized radii,  $r/R$  [ $\epsilon_r = -\epsilon_\theta \approx \frac{1}{2}(R/r)^2$ ]
- (2) Evaluate  $(\sigma_r - \sigma_\theta)/2$ ,  $s_z$  and  $\Delta p_s$  from the given value of  $\bar{\sigma}_r$ ,  $\bar{\sigma}_\theta$ ,  $\bar{\sigma}_z$ , and  $\Delta p$  (in Fig. 4.4) and the

equations:

$$\sigma_r - \sigma_\theta = \bar{\sigma}_r - \bar{\sigma}_\theta \quad (2.21)$$

$$s_z = \sigma_z - \sigma_{\text{oct}} = \frac{1}{3}(2\bar{\sigma}_z - \bar{\sigma}_r - \bar{\sigma}_\theta) \quad (2.22)$$

$$\Delta u_s = -\frac{1}{3}(\Delta\bar{\sigma}_r + \Delta\bar{\sigma}_\theta + \Delta\bar{\sigma}_z) \quad (2.23)$$

The modelling of the shear behavior of soils by means of the elastic perfectly-plastic model is particularly attractive in cavity expansion problems because closed form solutions are available. The stress-strain curves labelled #3 in Fig. 2.14 represent the behavior of an elastic perfectly-plastic material described by  $G = 25\bar{\sigma}_{vc}$  and  $\nu = 0.50$  in the elastic range and by  $s_u = 0.34\bar{\sigma}_{vc}$  at failure. These parameters were utilized by Randolph et al. in their modified Cam-Clay predictions. A comparison between the stress-strain curves according to the Cam-Clay model (curves 2 in Fig. 2.14) and those of the elastic perfectly-plastic material (curves 3 in Fig. 2.14) shows that:

- (1) The variation in  $\frac{(\sigma_r - \sigma_\theta)}{2}$  vs  $\epsilon_r$  is virtually identical in the two models with the Cam-Clay providing a smoother transition between "elastic" and "plastic" behavior.
- (2) The elastic perfectly-plastic material predicts no change in  $s_z$  until failure is reached and then  $s_z$  drops suddenly to zero. The Cam-Clay predicts a sharp, but continuous decrease in  $s_z$  until  $\epsilon_r \approx 2.6\%$  when  $s_z$  vanishes.
- (3) The elastic perfectly-plastic model does not predict the shear-induced pore pressures,  $\Delta p_s$  (lower diagram of Fig. 2.14).

The total and effective\* stresses due to cavity expansion as predicted by the elastic perfectly-plastic model are shown by the dashed lines in Fig. 2.17. One notes that:

- (1) The total stresses predicted by the elastic perfectly-plastic model are very similar to the Cam-Clay solutions (upper diagram in Fig. 2.17), but (a) are slightly larger in the critical state region ( $r < 5.2R$ ) because of the higher stress resistance  $\frac{(\sigma_r - \sigma_\theta)}{2}$  in the transition between elastic and perfectly plastic behavior ( $0.5 < \epsilon_r < 3.0\%$  in the upper diagram of Fig. 2.14), and (b) exhibit a sharply different behavior between the elastic and plastic regions ( $r_p = 8.6R =$  radius of the

---

\*Assuming  $\Delta p = \Delta \sigma_{oct}$ , i.e.,  $\Delta p_s = 0$ .

plastic zone) whereas the Cam-Clay predicts a smooth variation of stresses throughout the field. This is especially clear for  $\sigma_z$  which is governed by the relationship between  $s_z$  vs  $\epsilon_r$  shown in Fig. 2.14.

(2) By neglecting the shear induced pore pressures,  $\Delta p_s$ , the elastic perfectly-plastic model predicts slightly lower pore pressures and, hence higher effective stresses (lower diagram in Fig. 2.17). However, had  $\Delta p_s$  been introduced, the inverse would have taken place.

In conclusion, predictions obtained by the Cam-Clay model for the expansion of a cylindrical cavity are practically the same as those predicted with the elastic perfectly-plastic model. This is due to the overriding influence of the relationship between  $\frac{\sigma_r - \sigma_\theta}{2}$  and  $\epsilon_r$  on the results. Fig. 2.14 indicates that this relationship is virtually the same in the two models.

### Comparison of Predictions

Fig. 2.18 compares predictions of the radial stresses,  $\sigma_r$ , and the excess pore pressures,  $\Delta p$ , in the soil as obtained by: a) the models proposed by Levadoux and Baligh (1980); b) Randolph et al. for the Cam-Clay (dashed lines), and c) the elastic perfectly-plastic material (dotted lines).

The radial total stress  $\sigma_r$  during expansion of a cylindrical cavity is controlled by the shear resistance  $\frac{(\sigma_r - \sigma_\theta)}{2}$  of the soil and radial equilibrium:

$$\frac{d\sigma_r}{dr} = - \left( \frac{\sigma_r - \sigma_\theta}{r} \right) \quad (2.24)$$

Noting that  $d[\log(r/R)] = dr/(2.3r)$ , Eq. 2.24 becomes:

$$\frac{d\sigma_r}{d[\log r]} = -2.3(\sigma_r - \sigma_\theta) \quad (2.25)$$

This equation indicates that the slope of the curve of  $\sigma_r$  vs  $\log(r/R)$  is proportional to the shear resistance of the soil  $\frac{(\sigma_r - \sigma_\theta)}{2}$  at the strain level  $\epsilon_r$  considered [ $\epsilon_r \approx \frac{1}{2}(R/r)^2$ ].

This observation is useful in comparing predictions of different models in Fig. 2.18.

(1) At large radii ( $r > 10R$ ,  $\epsilon_r < 0.5\%$ ), the model\* predicts higher radial stresses because its shear resistance (or stiffness) at low strains is larger than the Cam-Clay (Fig. 2.14).

(2) Near the cavity wall ( $r < 10R$ ,  $\epsilon_r > 0.5\%$ ), the model\* predicts a smaller rate of increase with  $\log(r/R)$  because its shear resistance is lower than the Cam-Clay (or the elastic perfectly-plastic) model (Fig. 2.14).

(3) In spite of a much lower strength (see Fig. 2.14) the model\* predicts practically the same value of  $\sigma_r$  at the cavity wall (within 10%) as the Cam-Clay (or the elasto-plastic model). The higher initial stiffness of this model\* reduces the effect of a much smaller strength.

The excess pore pressures generated by undrained cavity expansion are caused by: (a) shear induced pore pressures,  $\Delta p_s$ ,  
\*by Levadoux and Baligh (1980)

and (b) changes in octahedral (or isotropic) total stress,  $\Delta\sigma_{\text{oct}}$ .

The lower diagram in Fig. 2.14 shows that the two models predict virtually identical  $\Delta p_s$  up to  $\epsilon_r = 2\%$  and that at larger strains, the maximum discrepancy is less than  $0.15\bar{\sigma}_{v0}$ . On the other hand, the changes in isotropic total stress,  $\Delta\sigma_{\text{oct}}$ , are much more difficult to predict from the stress-strain curves in Fig. 2.14.

In summary, the soil model used to predict stresses and pore pressures in the soil due to expansion of a cylindrical cavity has an effect on the results. However, this effect is believed to be small compared to the uncertainties associated with selecting adequate soil parameters for predictions in a particular deposit (Azzouz et al., 1980).

#### Limitations of Cavity Expansion Approaches

The modelling of pile installation by means of the expansion of a cylindrical cavity is very attractive because of the resulting simplifications in the analysis. Randolph et al. (1978, 1979) measured radial soil displacement in pile model tests and conclude that the cylindrical cavity expansion theory can be used with confidence to estimate the radial stresses in the soil caused by pile installation. However, serious doubts regarding the validity of this approach must be noted: (1) Randolph et al. neglect the importance of the strain path followed by soil elements to reach their final state of strain. The following section shows that although soil particles move

monotonically away from the pile axis, the radial strain decreases slightly behind the tip. Such an unloading can produce a drastic change in the state of stress. Pore pressure measurements at different locations on the tip and along the shaft behind it indicate that the clay experiences significant unloading which support, at least qualitatively, these predictions and, (2) the cavity expansion neglects vertical strains,  $\epsilon_{zz}$ , and shear strains,  $\epsilon_{rz}$ , which might be important.

In summary, the cavity expansion approach should be considered as a convenient but crude method for predicting the effects of pile installation.

### 2.2.3.2 The Strain Path Method (Baligh, 1975)

Deep pile installation in clays is essentially a "strain-controlled" problem where strains and deformations are primarily imposed by kinematic requirements. For this type of problem, Baligh (1975) proposes an approximate method of solution called the "Strain path method". This method is based on concepts similar to the well known "stress path method" (Lambe, 1967) and consists of four basic steps: a) estimate the initial stresses; b) estimate an approximate strain field satisfying conservation of volume, compatibility and boundary velocity requirements; c) evaluate the deviatoric stresses at a selected number of elements by performing laboratory tests on samples subjected to the same strain paths or, alternatively, by using an appropriate soil behavioral model, and; d) estimate the octahedral (isotropic) stresses by integrating the equilibrium equations.

Table 2.4 compares the strain path method with the stress path method to identify their strong similarities. As indicated in Table 2.4, the strain path method is an approximate method because the estimated stresses will not, in general, satisfy the equilibrium requirements, unless the estimated strain field is identical to the actual one.



## The Strain Path Method in Pile Installation

Figure 2.19 describes the steps for evaluating stresses and pore pressures in the soil due to deep pile installation in saturated clays by means of the strain path method, using a deviatoric stress-strain soil model:

- 1) Estimate a velocity field\* satisfying the conservation of volume (or mass) requirement and the boundary conditions.
- 2) From the velocity field determine the soil deformations by integration along streamlines. Figure 2.20 shows the deformation of a square grid due to steady penetration of a pile with a  $60^\circ$  tip as determined by Levadoux and Baligh (1980) after neglecting the shearing resistance of the soil (i.e., assuming the soil to behave as an ideal fluid and pile driving can be simulated by steady penetration).
- 3) Compute the strain rates,  $\dot{\epsilon}_{ij}$ , along the streamlines by differentiating the velocities with respect to the spacial coordinates.
- 4) Integrate the strain rates,  $\dot{\epsilon}_{ij}$ , along streamlines to determine the strain path ( $\epsilon_{ij}$ ) of different soil elements.

---

\*The velocity field describes the velocity of soil particles as they move around the pile.

Figure 2.21 shows the deviatoric\* strain paths of three soil elements (initially located at  $r_0/R = 0.2$ , 0.5 and 1.0 from the axis) due to penetration of a  $60^\circ$  cone (Fig. 2.20). Clearly, the paths are complicated and involve large strains with strain reversals.

5) Estimate the initial stresses,  $(\sigma_{ij})_0$ , and initial pore pressures,  $p_0$ , in the soil prior to cone penetration.

6) Compute the deviatoric stresses,  $s_{ij}$ , and the shear-induced pore pressures,  $\Delta p_s$ , along streamlines.

Levadoux and Baligh (1980) developed the necessary mathematical models to estimate  $s_{ij}$  and  $\Delta p_s$  due to the complicated strain paths imposed by cone penetration taking into consideration the anisotropic inelastic nonlinear behavior of clays. Using soil parameters obtained from laboratory tests on normally consolidated resedimented Boston Blue Clay, Levadoux and Baligh (1980) predict: a) The deviatoric stress paths.

Fig. 2.22 shows the stress path for an element initially located at a radius  $r_0 = 25R$  due to steady penetration of a pile with a  $60^\circ$  tip. For comparison, the paths corresponding to (idealized) Direct Simple Shear (DSS) and Pressuremeter (PR) modes of shearing are also shown in

---

\*No volumetric straining takes place during undrained shearing of a saturated soil.

Fig. 2.22. Clearly, pile penetration subjects the soil to very complicated stress paths consisting of a combination of triaxial compression, DSS and PR modes. b) The shear induced pore pressures. Fig.

2.23 compares the predicted contours of  $\Delta p_s$  due to the penetration of piles having 18° and 60° tips with cylindrical cavity solutions.\*

- 7) (a) From equilibrium considerations, compute the total stresses,\*\*  $\sigma_{ij} (= s_{ij} + \delta_{ij} \sigma_{oct})$ , given the deviatoric stresses,  $s_{ij}$ . This requires the determination of the octahedral stresses,  $\sigma_{oct}$ . Since the assumed strains are not exact, the estimated values of  $\sigma_{oct}$  are approximate because they depend on the integration path, i.e., on the direction where equilibrium is satisfied; radial, axial, etc.

(b) From  $s_{ij}$  and  $\Delta p_s$ , compute the effective stresses,

$$\bar{\sigma}_{ij} [= (\bar{\sigma}_{ij})_o + \Delta \bar{\sigma}_{ij}; \Delta \bar{\sigma}_{ij} = \Delta s_{ij} - \Delta p_s \delta_{ij}] \quad (2.26)$$

- 8) From  $\sigma_{oct}$  and  $p_s$  determine the penetration pore pressures  $p_i (= p_o + \Delta p_i; \Delta p_i = \Delta \sigma_{oct} + \Delta p_s)$ .

---

\*According to the same soil model.

\*\* $\delta_{ij}$  = Kronecker delta: = 0 when  $i \neq j$ ; = 1 when  $i = j$   
and,  $\sigma_{oct} = 1/3 \sigma_{ii}$ .

## Predictions of Penetration Pore Pressures

Figure 2.24 shows the distribution of excess pore pressures,  $\Delta p_i$ , during penetration of piles with  $18^\circ$  and  $60^\circ$  tips based on soil properties obtained from laboratory tests on resedimented normally consolidated Boston Blue clay. In order to obtain these solutions by the strain path method, displacements and strains were determined by assuming the soil to offer no shearing resistance (i.e., to behave as an ideal fluid, Fig. 2.20 and 2.21) and the octahedral stresses were computed by satisfying equilibrium in the radial direction. Results in Fig. 2.24 indicate that:

- 1) The excess pore pressures,  $\Delta p_i$ , are significant even at large distances from the tip. These pore pressures are principally due to the increase in octahedral stresses, i.e., the contribution of  $\Delta p_s$  is small (about 20%, see Fig. 2.23).
- 2) The soil can be divided into two zones: (a) An inner zone where the pore pressure gradients are high and the strains are sufficiently large to cause failure of the soil, and (b) An outer zone where the strains are smaller, the soil is in a pre-peak state\* and the excess pore pressures are not significantly dependent on the tip angle. The boundary between

---

\*but far from being in an elastic (linear) state as assumed by simple bilinear elasto-plastic models.

the inner and outer zones is roughly given by the contour of the octahedral strain\*  $\gamma_{oct} = 2\%$  located at a radius approximately equal to  $5R$ .

- 3) Far behind the cone tip, the excess pore pressures are higher than estimated by cavity expansion solutions\*\* in the outer zone and lower than cavity expansion solutions in the inner zone.

### Comparison with Measurements

A detailed discussion of various predictions obtained by applying the strain path method to pile penetration is given by Levadoux (1980). However, the method is capable of estimating pore pressures that can be compared with measurements. Other "stress" measurements are very difficult (if not impossible) to conduct with available tools.

The solid lines in Fig. 2.25 present the same predictions of penetration excess pore pressures,\*\*\*  $\Delta p_i$ , at different locations on the face and shaft behind  $18^\circ$  and  $60^\circ$  tips after normalization by the excess pore pressure on the shaft,  $\Delta p_{(sh)}$  i.e.,  $\Delta p_i / \Delta p_{(sh)}$  approaches unity at a sufficiently large

---


$$*\gamma_{oct} = 1/3 [(\epsilon_r - \epsilon_\theta)^2 + (\epsilon_\theta - \epsilon_z)^2 + (\epsilon_z - \epsilon_r)^2 + 6\epsilon_{rz}]^{1/2}$$

$\gamma_{oct}$  is approximately equal to the radius of Mohr circle of strain.

\*\* Using the same soil model and soil parameters corresponding to normally consolidated BBC.

\*\*\* As in Fig. 2.24.

distance behind the tip. Fig. 2.25 also shows in situ measurements of  $\Delta p_i / \Delta p_{(sh)}$  conducted in a Boston Blue Clay deposit\* at Saugus, Massachusetts using model piles with a 3.8 cm diameter. Fig. 2.25 indicates that, even though predictions are based on laboratory test data on resedimented normally consolidated BBC, they provide good agreement with measurements in the natural deposit having overconsolidation ratios OCR = 3, 2 and 1.3. Attempts to extend this result to the upper clay having an OCR > 3 were prevented by the large scatter of measured penetration pore pressures,  $\Delta p_i$ , (due to inherent soil variability) as compared to the small average values of  $\Delta p_i$ .

In order to check the predicted penetration pore pressures at some distance from pile shaft, measurements of  $p_i$  in the soil around the cone are required. Such measurements are very difficult to obtain in situ because of: (a) the interference between the measuring device and soil deformations, and; (b) the uncertainties in alignments which can introduce significant errors in the estimated radial distances. Attempts to perform such measurements in BBC by means of two model piles with 3.8 cm diameter were unsuccessful. Therefore, predictions of  $\Delta p / (\Delta p)_{sh}$  in the soil are compared with measurements conducted around a cylindrical pile (21.9 cm in diameter) jacked into Champlain Clay (Roy et al., 1979). The measurements are

---

\*Described in detail by Levadoux and Baligh, 1980.

quite consistent and reliable and, because of the small size of the piezometers (Geonor M-600) compared to the pile,\* are hopefully less sensitive to the errors mentioned above (piezometer-soil interaction and alignment). Furthermore, the excess pore pressure measured along the shaft of the pile  $(\Delta p)_{sh} \approx 2\bar{\sigma}_{vo}$  is very close to that measured in BBC behind conical tips,  $(\approx 2.1\bar{\sigma}_{vo})$ .

Figure 2.26 compares the predicted radial distribution of excess pore pressure at a sufficiently large distance ( $z \approx 14R$ ) behind  $18^\circ$  and  $60^\circ$  tips during penetration in normally consolidated BBC to measurements in Champlain Clay. Results in Fig. 2.26 show that:

- 1) The predicted radial distributions of pore pressures behind the  $18^\circ$  and  $60^\circ$  tips are almost identical and hence suggest the tip angle has a minor effect on the results;
- 2) The agreement between predictions and measurements is remarkable, in view of (a) the approximations in the strain path method, (b) the uncertainties in the field measurements (in particular at small radii) and especially, (c) the difference in behavior between resedimented BBC ( $OCR=1$ ) used for predictions and the extremely sensitive Champlain Clay ( $OCR \approx 2$ ) where measurements are made.

---

\*The pile diameter is about 6.5 times that of the piezometer.

Results in Fig. 2.26 are very encouraging since they suggest that the normalized excess pore pressure distribution during pile installation is not very sensitive to soil type or stress history (OCR). This is further supported by the results in Fig. 2.27 showing that measurements in Champlain Clay (case d) are not unique but are similar to measurements in seven other clay deposits. The first six cases in Fig. 2.27 involve displacement piles whereas cases g and h consist of H piles. In cases a, b, c and d, measurements are conducted in the soil surrounding the pile. In cases c, d, e and f measurements on the pile shaft are available. Properties of the eight clays are given by Baligh and Levadoux (1980) and cover a wide range of soil types. One notes in Fig. 2.27 that:

- 1) In a given clay deposit, measurements of pore pressures in the soil surrounding the pile exhibit significant scatter. This is especially clear in cases b and c, and is probably caused by the measurement difficulties discussed earlier.
- 2) Significant excess pore pressures [ $\Delta p_i(r) \geq 0.2 \bar{\sigma}_{vo}$ , say] develop within a radius  $r = 20R$  (i.e.,  $r/R = 20$ ) around the pile and measurable excess pore pressures extend to  $r = 50R$  or even  $80R$ . However, it is difficult to ascertain the effect of the measuring probe-soil interaction on these data.



- 3) Little correlation can be established between  $\Delta p_i(r)/\bar{\sigma}_{v0}$  and the clay type (as described by the plasticity index  $I_p$ , say), or its overconsolidation ratio (OCR), or its undrained shear strength ( $s_u$ ), or its structure or sensitivity ( $S_t$ ), or the method of pile installation (driving vs. jacking), or the size or cross section of the pile\*, or the depth of measurements (i.e., confining stress).
- 4) Few data points are available in the vicinity of the pile ( $R < r < 5R$ );
- 5) In spite of the very different conditions (soil and pile) in cases a, b, c, d, g and h, results between  $r = 5R$  and  $r = 20R$  fall within a well defined band.

Figure 2.28 shows the band including most of the test data for  $r > 5R$ . A reasonably good fitting of the data between  $r = 5R$  and  $r = 20R$  can be achieved by either a logarithmic distribution\*\* or a linear distribution. Pore pressures beyond  $r = 20R$  are small and can probably be neglected in analyses of single piles.

---

\*For H piles, the radius  $R$  was selected as half the pile width.

\*\*A logarithmic distribution means that  $\Delta p_i$  is proportional to  $\log r$  and hence is represented by a linear relationship in a plot of  $\Delta p_i$  vs.  $\log r$ ; as in Fig. 2.28.

Noting that the logarithmic initial excess pore pressure distribution is derived by elasto-plastic cylindrical cavity expansion solutions, the straight line in Fig. 2.28 corresponds to a clay with  $G/s_u = 400$  and  $s_u/\bar{\sigma}_{vo} = 0.68$  (i.e.,  $G/\bar{\sigma}_{vo} = 272$ ). This ratio of  $G/s_u$  is much higher than estimated by many investigators in analyzing cavity expansion problems even though  $s_u = 0.68 \bar{\sigma}_{vo}$  is excessively high especially for the soft clays ( $OCR \approx 1$ ) in cases a and b. Therefore, special care is needed in selecting the shear modulus,  $G$ , for cavity expansion problems. A more realistic soil model than the bilinear elasto-plastic behavior can reduce this difficulty.

In summary, existing measurements in clays due to pile installation indicate that significant pore pressures develop up to  $r = 20R$ . The measurement scatter and the lack of sufficient data near the pile ( $R < r < 5R$ ) prevent reliable estimates of the spatial variation of excess pore pressures

### 2.2.3.3 Summary and Conclusions

1. The effects of pile installation on soil deformations, stresses and properties are difficult to estimate because of the large displacements (and strains) associated with pile penetration, the complicated properties of natural clays and the large gradients of stresses and strains near

the tip. Open-ended pipe piles, commonly used offshore, present an additional difficulty because of uncertainties in the formation of a soil plug moving with the pile during driving.

2. Cylindrical cavity expansion solutions, utilized by most researchers, represent a simple one-dimensional approach to pile installation that basically assumes soil deformations to be in the radial direction only. This simplification enables more realistic non-linear soil properties to be considered.
  - a) Because of the simplicity of the problem, relatively simple total stress models (e.g., bilinear or hyperbolic) can provide predictions as reliable as more comprehensive models (e.g., the modified Cam-Clay model). However, reasonable engineering judgement must be exercised in choosing an adequate model and appropriate values of its soil parameters.
  - b) Predictions of interest basically depend on the soil (or input) parameters utilized for predicting cavity expansion in a given soil.
3. Predictions of one-dimensional cavity expansion solutions are evaluated by means of more realistic two-dimensional strain-path solutions in simulating the steady penetration of piles (with  $18^\circ$  and  $60^\circ$  tips). Results of this comparison indicate that, by neglecting the actual strain path of

soil elements, the cavity expansion approach can be quite misleading. In particular, cavity expansion solutions predict:

- a) Unrealistic magnitudes and directions of the principal stresses, the extent and magnitude of soil disturbance, and the distribution of excess pore pressures, especially near the pile shaft ( $R < r < 5R$ ).
- b) Reasonable deformations, stresses and pore pressures at some distance from the pile shaft ( $r > 5R$ ).

## 2.2.4 EFFECTS OF SOIL CONSOLIDATION

### 2.2.4.1 Introduction

The shaft resistance of piles in clays increases with time due to pore pressure dissipation and soil consolidation. Bjerrum et al. (1960) report results of pile load tests in Sweden, performed by Wendel at the turn of the century, showing that the bearing capacity of piles driven in soft clay increased rapidly with time and reached a maximum value in less than a month. Similar findings are reported by Terzaghi and Peck (1967). Cummings et al. (1950) present water content measurements around piles driven in a soft clay that clearly demonstrate that water migrates horizontally with time after pile installation. Seed et al. (1955, 1957) report test results on six-inch diameter steel cylindrical, open-ended piles driven into San Francisco Bay mud showing also a decrease of the water content in the clay adjacent to the pile and a six-fold increase in bearing capacity over a period of thirty days. Bjerrum et al. (1958) indicate that the soil around permeable wooden piles "sets up" (i.e. consolidates) much faster than around impervious ones, e.g., steel. Additional data from pile load tests reported by Housel, 1950; Eide et al., 1961; Stermac et al., 1969; McClelland, 1969; and Flaate, 1972; are shown in Fig. 2.29.

A significant increase in the shaft resistance after pile installation can be observed. However, the time to reach the maximum resistance varies significantly because of different soil\* and pile\*\* conditions.

The objective of soil consolidation analyses around pile shafts is to estimate the changes in the effective stresses at (and close to) the pile-soil interface after consolidation because of their effect on the shaft resistance during pile loading. Such estimates are also helpful in understanding the mechanism of consolidation in order to assess the validity of assumptions made by simplified procedures for estimating the limiting skin friction. Pore pressure dissipation rates are needed to estimate the time required for the pile to "set up" and thus obtain its full resistance. This information is essential in evaluating and using pile load test results.

The modeling of soil consolidation around pile shafts is complicated because of the following reasons:

1) Soil Nonlinearity.

During consolidation, changes in soil compressibility and in its permeability take place. In the special case when the ratio of these two parameters remains

---

\*e.g., permeability, compressibility

\*\*e.g., radius, permeability

sensibly constant, the coefficient of consolidation does not change significantly and dissipation can be treated by means of linear formulations (especially for dissipation rates). However, for real clays, the coefficient of consolidation in the overconsolidated range (below the maximum past pressure) can easily be 10 to 20 times higher than the virgin compression range. The change in the coefficient of consolidation during dissipation not only affects dissipation rates, but also appears to have an important effect on the residual stresses after consolidation (Randolph et al., 1978a).

2) Remolding (Soil Disturbance)

Penetration causes severe straining of the soil in the vicinity of the pile and small disturbances at a radius of 10 to 20 diameters from the shaft. Since shearing of the soil can seriously change its subsequent compressibility (during consolidation), the effect of nonhomogeneous (non-uniform) soil straining prior to consolidation must be considered in nonlinear solutions.

3) The Shearing Stress Level During Consolidation.

Soil compressibility depends on the shearing stresses during consolidation. An increase in the level of shearing during consolidation to keep the effective stresses near a "failure" condition causes the soil\* to compress with a high compressibility and hence a low coefficient of consolidation. On the other hand, a constant (or decreasing) shearing level causes the soil to have a lower compressibility and hence a high coefficient of consolidation, at least in the early dissipation stages.

The level of shearing during consolidation cannot be determined a priori but is part of the solution. The effect of this shear is believed to be especially important on the residual stresses after dissipation.

4) Soil Anisotropy.

Because of their mode of deposition and subsequent stress and environmental histories, natural clays exhibit varying degrees of anisotropy in permeability and compressibility.

---

\*Normally consolidated or slightly overconsolidated clays.



5) Soil Creep.

Soils exhibit a time-dependent behavior during undrained shearing (undrained creep), drained consolidation (secondary compression), and drained shearing (drained creep).

In view of the above difficulties, simplifications of the problem geometry and/or the soil behavior models are required in consolidation analyses. A common simplification consists of treating the central portion of a single pile shaft\* and assume that consolidation takes place primarily due to radial water flow and radial soil deformations, i.e., under conditions of plane strain and axial symmetry. The simplest soil model available to conduct consolidation analyses assumes that the soil skeleton behaves as a linear isotropic (and hence elastic) material. Most of the early existing solutions for consolidation around pile shafts utilize this model and hence neglect soil non-linearities and the effect of creep and installation remolding. Solutions based on the (linear) Theory of Elasticity are presented and discussed in the next section.

---

\* And hence neglect the upper portion affected by the ground surface and the lower portion near the tip.

### 2.2.4.2 Linear Solutions\*

Sills (1975) shows that, for a linear isotropic (elastic) soil, radial consolidation around piles is an inherently uncoupled problem. This means that pore pressure dissipation can be determined without the need to consider soil deformations or stresses and, the set of Biot consolidation equations (Biot, 1941) can be reduced\*\* to the heat equation, commonly referred to as the Terzaghi-Rendulic consolidation equation (Terzaghi, 1943; Rendulic, 1936):

$$c \nabla^2 p = \frac{\partial p}{\partial t} \quad (2.27)$$

where  $p$  is the excess pore water pressure,  $c$  is the coefficient of radial consolidation\*\*\* given by:

$$c = \frac{k}{\gamma_w} \cdot \frac{\bar{E}(1-\bar{\nu})}{(1-2\bar{\nu})(1+\bar{\nu})} = \frac{k}{\gamma_w} \cdot \frac{2G(1-\bar{\nu})}{(1-2\bar{\nu})} = \frac{k}{\gamma_w} \cdot \frac{3K(1-\bar{\nu})}{(1+\bar{\nu})} \quad (2.28)$$

and the differential operator  $\nabla^2$  is defined as:

$$\nabla^2 = \frac{\partial^2}{\partial r^2} + \frac{1}{r} \frac{\partial}{\partial r} \quad (2.29)$$

---

\*The term "linear" means that the coefficient of consolidation is a constant.

\*\*Without further simplifying assumptions.

\*\*\*  $k$  = permeability coefficient.

$\gamma_w$  = unit weight of water.

$E, \bar{\nu}$  = Young's modulus and drained Poisson's ratio.

$G, K$  = Shear and Bulk moduli.

Carslaw and Jaegar (1959) provide analytic solutions for Eq. 2.27, using the technique of separation of variables. Soderberg (1962) and Banerjee (1970) use a finite difference approximation of the differential operators in Eq. 2.27 to determine the dissipation rates for various initial excess pore pressure distributions, without computing changes of total and effective stresses\* during consolidation. However, Soderberg (1962) erroneously assumes that the mean total stress remains constant during consolidation in order to uncouple the Biot equations, whereas, Baligh and Kavvadas, 1980 show that the mean total stress decreases during consolidation\*\*. Soderberg's assumption does not affect the form of the resulting "heat equation" (Eq. 2.27) but the coefficient of consolidation he utilizes ( $= kK/\gamma_w$ ), differs by almost a factor of two from the value (Eq. 2.28) derived by other researchers (e.g. Randolph et al., 1979c).

Wroth (1976) presents a closed form solution for the stresses after consolidation, which was extended by Randolph et al. (1979c) to determine soil stresses during consolidation using an infinite series expansion of Bessel functions.

---

\* Which are of main interest for the pile problem.

\*\* According to Linear Elasticity Theory the decrease of the mean total stress at the end of consolidation is equal to about 40% of the initial value of the excess pore pressure (at any radius).

The initial distribution of excess pore pressures for consolidation analyses are the pore pressures caused by pile installation and are difficult to estimate accurately (Section 2.2.3). Baligh and Kavvadas (1980) performed a parametric study by means of simple one-dimensional linear uncoupled consolidation solutions around impervious cylindrical cavities to study the effect of the following factors:

- 1) The "size" of the soil zone around the pile where penetration pore pressures develop (see Figure 2.30);
- 2) The shape of the initial excess pore pressure distribution. They considered three cases: constant, linear and logarithmic distributions with the radial coordinate (see Figure 2.30);
- 3) The location of boundary drainage.

Figure 2.31 shows the normalized\* excess pore pressures  $\Delta p / (\Delta p_i)_{sh}$  during consolidation\*\* for various shapes of the initial distribution. The following remarks can be made:

- 1) For a constant initial spatial variation, significant time is required before excess pore pressures at the cavity wall start to decrease; however, for a logarithmic initial distribution high pore pressure gradients occur at the cavity wall and thus, excess pore pressures decrease rapidly.

\*Normalized with respect to the initial value of the excess pore pressure at the pile shaft  $(\Delta p_i)_{sh}$ .

\*\* Obtained from the previous analyses.

- 2) For all three types of variation, the soil can be divided into two zones. In the inner zone, pore pressures decrease, whereas in the outer zone, pore pressures initially increase and then decrease.

This indicates that, during consolidation, soil elements close to the wall tend to be loaded (i.e., effective stresses increase) and soil elements at greater distances from the wall tend to first be unloaded and then reloaded.

- 3) The initial excess pore pressure distribution has an important effect on dissipation, especially at early times. It can be generally concluded that the logarithmic distribution gives faster dissipation rates than the linear and the linear faster than the constant variation.

The effect of the "size" of the soil zone where pore pressures develop during penetration is also significant. Doubling the size of this zone decreases the dissipation rates (at 50% consolidation) by about a factor of seven. On the contrary, the location of the outer drainage boundary\* has a negligible effect on dissipation, especially during early consolidation stages. Consequently, errors in numerical solutions caused by analyses of finite domains are not very significant, at least in the early stages of dissipation.

---

\*the pile wall is assumed impervious.

In addition to pore pressure dissipation rates, Randolph et al. (1979a,c) investigated stress changes during linear consolidation. They conclude that:

At the pile-soil interface,  $\epsilon_{\theta} = \epsilon_z = 0$  and thus, the soil is deforming one dimensionally. The total radial stress at the interface remains constant during consolidation, i.e., excess pore water pressures are gradually converted into radial effective stress.\* This important prediction contradicts unpublished in situ measurements obtained by MIT in a slightly over-consolidated ( $OCR \approx 1.2$ ) deposit of Boston Blue Clay. During reconsolidation around a model pile (3.8cm in diameter) the total radial stress decreased by 30 to 50%. This decrease is very significant in the predicted effective stresses on the shaft.

Additional interesting predictions of linear solutions (described in detail by Baligh and Kavvadas, 1980) are:

- 1) || At any radius, the vertical effective stress increases with time:

$$\Delta \bar{\sigma}_z = \frac{\bar{\nu}}{1-\bar{\nu}} (-\Delta p) > 0 \quad (2.30)$$

where  $\bar{\nu}$  is Poisson's ratio of the soil skeleton; and, the total vertical stress decreases with time:

---

\*A proof of this interesting result is given by Baligh and Kavvadas, 1980.

$$\Delta\sigma_z = -\frac{(1-2\bar{\nu})}{(1-\bar{\nu})} (-\Delta p) < 0 \quad (2.31)$$

2) Defining  $\Delta s$  and  $\Delta \bar{s}$  by the expressions:

$$\Delta s \equiv \Delta\left(\frac{\sigma_r + \sigma_\theta}{2}\right) = \frac{\Delta\sigma_r + \Delta\sigma_\theta}{2} \quad (2.32)$$

$$\Delta \bar{s} \equiv \Delta\left(\frac{\bar{\sigma}_r + \bar{\sigma}_\theta}{2}\right) = \frac{\Delta\bar{\sigma}_r + \Delta\bar{\sigma}_\theta}{2} \quad (2.33)$$

we get at any time:

$$\frac{\Delta s}{\Delta \bar{s}} = - (1-2\bar{\nu}) \quad (2.34)$$

This ratio is equal to  $-1/3$  for the reasonable value of  $\bar{\nu} = 1/3$ . This implies the stress paths shown in Fig. 2.32 for the pile wall and that, at any radius, the changes after consolidation are given by:

$$\Delta s_{\text{final}} \sim -0.25(\Delta p_i) \quad (2.35)$$

$$\Delta \bar{s}_{\text{final}} \sim 0.75(\Delta p_i)$$

where  $\Delta p_i$  are the initial excess pore pressures.

3) Defining the shear increment,  $\Delta t$ , by the expression:

$$\Delta t \equiv \Delta\left(\frac{\sigma_r - \sigma_\theta}{2}\right) = \frac{\Delta\sigma_r - \Delta\sigma_\theta}{2} \quad (2.36)$$

Baligh and Kavvadas (1980), show that at any time:

$$\frac{\Delta t}{-\Delta s} = 1 + \frac{2(1 - \bar{\nu})}{(1 - 2\bar{\nu})} \cdot \frac{\Delta \sigma_r}{(-\Delta p)} \quad (2.37)$$

which can be either positive or negative depending on the magnitude of the ratio  $\Delta \sigma_r / (-\Delta p)$ . Numerical computations show that in general  $\Delta t / (-\Delta s)$  is positive\* at small distances (less than two to three\*\* pile radii) and negative\* at larger distances. Specifically at the pile-soil interface, the total radial stress does not change, and hence, Eq. 2.37 gives that at any time:

$$\frac{\Delta t}{-\Delta s} = 1 \text{ (at the pile shaft)} \quad (2.38)$$

This means that at the pile shaft the soil is loading in shear (the total stress path rises with a 45° slope, as shown in Fig. 2.32). Using Eq. 2.34 and 2.38, we get:

$$\frac{\Delta t}{\Delta \bar{s}} = 1 - 2\bar{\nu} \text{ (at the pile shaft)} \quad (2.39)$$

which is equal to 1/3 for a Poisson's ratio equal to 1/3. This means that linear solutions predict

---

\* Positive values mean that soil is loading in shear and negative that it is unloading in shear.

\*\* Depending on the initial assumed excess pore pressures.



that the effective stress path ( $\bar{s} - t$  plot) at the pile-soil interface, rises with a slope\* approximately equal to 1/3 (Fig. 2.32).

- 4) At any radius, the mean effective stress  $\bar{\sigma}$  increases during consolidation:

$$\Delta\bar{\sigma} = \frac{1 + \bar{v}}{3(1 - \bar{v})} (-\Delta p) > 0 \quad (2.40)$$

and for  $\bar{v} = 1/3$ , after consolidation:

$$\Delta\bar{\sigma}_{\text{final}} = 0.67 (\Delta p_i) \quad (2.41)$$

This means that approximately\*\* 2/3 of the initial excess pore pressure are "locked in" as an increase in the mean effective stress during consolidation.

- 5) After consolidation, total stresses decrease everywhere\*\*\* in the soil. Table 2.5 shows that this applies for all three assumed initial pore pressure distributions (constant, linear logarithmic) regardless of the "size" parameter  $\lambda$  describing the radius of zone where excess pore pressures develop due to pile installation.

---

\* The slope is solely controlled by the Poisson's ratio.

\*\* Depending on the Poisson's ratio, only.

\*\*\* Except at the pile wall where  $\Delta\sigma_r = 0$ .

Table 2.6 gives magnitudes of  $\Delta\sigma_r$  after consolidation for various values of the "size",  $\lambda$ , and Poisson's ratio,  $\bar{\nu}$ .

Linear solutions discussed above show that stress changes during consolidation depend essentially on ~~Poisson's ratio~~ of the soil. However, the concept of Poisson's ratio for soils can be quite controversial, especially since almost all natural clay deposits are anisotropic (Bishop et al., 1977). Furthermore, linear solutions predict that the total radial stress at the pile wall does not change during consolidation. This leads to large increases in the effective radial stress and hence unrealistically high skin friction,  $f_s$ .

Leifer et al. (1979) consider the soil around the pile to have a compressibility that varies with the radius from the pile axis. A higher compressibility close to the pile results in a smaller increase in the effective radial stress\* after consolidation at the pile-soil interface than that predicted by linear solutions with spatially constant compressibility. Linear solutions predict loading in shear close to the pile and unloading away from the pile which justifies spatial distribution of compressibility (i.e., high compressibility related with

---

\*Hence lower  $f_s$ , as desired.

loading and low with unloading. Therefore, Leifer et al. used a higher compressibility at small radii (i.e. for  $R < r < \mu R$  where  $\mu$  is a parameter and  $R$  the pile radius) and a lower compressibility in the remaining domain, and computed stress changes after consolidation using the initial excess pore pressure distribution around a cylindrical cavity obtained for an elastic-perfectly plastic material, neglecting shear induced pore pressures. They found that:

- 1) An increased compressibility at small radii results in a significant decrease of  $\Delta\bar{\sigma}$ , compared with linear solutions with constant compressibility.

For example, a linear variation of the bulk modulus between zero at the pile wall and a certain positive value at  $r = \mu R$  gives\* a  $\Delta\bar{\sigma}$  (at the cavity boundary after consolidation) equal to only 30% of the initial excess pore pressures  $\Delta p_i$ , whereas a linear analysis with constant bulk modulus gives 60% of  $\Delta p_i$ .

- 2) The mean effective stress at the pile-soil interface is not significantly affected by the size parameter  $\mu$  and/or the assumed distribution of soil

---

\*The bulk modulus was kept constant (and equal to the value at  $r = \mu R$ ) for  $r > \mu R$ .

compressibility, except when the modulus at the interface approaches zero. However, the mean effective stress at the interface is sensitive to the assumed value of Poisson's ratio,  $\bar{\nu}$ . For example, when  $\bar{\nu}$  increases from 0.3 to 0.4 the mean effective stress at the interface increases by 50%.

It should be realized that it is very difficult, if not impossible, to rationally assign and experimentally check spatial variations of compressibility. In addition, by appropriately choosing compressibilities and Poisson's ratio, any desired value of  $\Delta\bar{\sigma}_r$  at the pile wall can be obtained and thus a wide range of  $f_s$  can be reached. This significantly restricts the applications of the method in practice.

During the last few years significant attempts to include non-linearities in the consolidation analyses around piles have been made. These efforts can be divided into two groups:

- 1) Engineering models, which involve assumptions regarding the direction of the stress path and the magnitude of effective stress changes during consolidation (Section 2.2.4.3).
- 2) Comprehensive non-linear solutions involving non-linear soil models (Section 2.2.4.4).

### 2.2.4.3 Engineering Models

Engineering models involving mechanical elements, e.g. springs, are useful in developing a better engineering feeling for complicated continua problems. Esrig et al. (1977), Kirby et al. (1977) and Esrig et al. (1979), developed an engineering model to study stress changes due to consolidation around piles. Based on cylindrical cavity expansion solutions in an elastic-perfectly plastic soil<sup>\*</sup>, the region around the pile is divided into two zones (Fig. 2.33):

- 1) An inner plastic or yielded zone ( $R < r < R_p$ ), where pile installation causes large strains and excess pore pressures, and
- 2) An outer elastic zone ( $r > R_p$ ), where the strains are small enough not to cause soil yielding and no excess pore pressures develop. Since the model considers stress changes at the end of consolidation<sup>\*\*</sup> only, the outer region can be replaced by an array of linear springs with stiffness directly related

---

\* Shear induced pore pressures are neglected.

\*\* i.e., disregarding pore pressure dissipation rates or stress changes during consolidation.

to the elastic properties\* of the outer zone.

(Timoshenko and Goodier, 1951).

The radius  $R_p$  of the elastic-plastic boundary is assumed to be equal to the size of the yielded region predicted by cavity expansion solutions in an elastic-perfectly plastic soil. Dissipation of the positive excess pore pressures generated by pile driving (or cavity expansion) within the yielded zone, is associated with an outward migration of water and hence an inward movement of the elastic-plastic boundary. As the boundary moves inwards, the stress in the springs gradually decreases and hence the radial total stress decreases ( $r > R_p$ ). Esrig et al. (1978) further state that:

"No changes in total stress are assumed as occurring in the classical Terzaghi formulation of consolidation; the Terzaghi formulation was utilized by Soderberg (1962) and others for the pile problem and, therefore, those solutions cannot be relied upon to provide insight into stress changes due to reconsolidation."

This appears to imply that linear consolidation solutions predict no changes in total stress during pore pressure dissipation. However, Eqs. 2.30 through 2.41 show that such solutions do predict changes in all components of total stresses\*\* and that Soderberg's assumptions are in error (see Table 2.6).

\* Which are, however, difficult to estimate or measure (Azzouz et al., 1980).

\*\* With the exception of the total radial stress at the pile-soil interface.

The following discussion presents the additional assumptions made by Esrig et al. (1977), Kirby et al. (1977) and Esrig et al. (1979), in the development of this model, and a critique of their implications.

1. After consolidation is completed, the springs in Fig. 2.33 are assumed to return to their position prior to pile driving (i.e. before cavity expansion). This implies that the elastic zone ( $r > R_p$ ) is completely unloaded and that at  $r = R_p$  the decrease in the radial total (or effective) stress,  $\Delta\sigma_r (= \Delta\bar{\sigma}_r)$  during consolidation equals\* the undrained shear strength of the clay,  $s_u$ .

This assumption contradicts results of linear solutions presented by Baligh and Kavvadas, 1980, indicating that, after consolidation is completed, the changes\*\*  $\Delta\sigma_r (= \Delta\bar{\sigma}_r)$  at  $r = R_p$ :

- a) Depend on the initial distribution of the excess pore pressures in the plastic zone (due to cavity expansion), the effective Poisson's ratio and to a limited extent on  $R_p$ .

---

\* If cavity expansion is analysed assuming an elastic-perfectly plastic material.

\*\* With respect to the condition before consolidation but after expansion.

b) For a logarithmic initial pore pressure distribution\* the changes  $\Delta\sigma_r = \Delta\bar{\sigma}_r = 0.11$  to  $0.08 \bar{\sigma}_{v0}$  when  $R_p = 20R$  and  $\bar{v}$  is between 0.25 and 0.35. For normally consolidated clays (where  $s_u$  is equal to about  $0.25\bar{\sigma}_{v0}$ ) this implies that  $\Delta\sigma_r = \Delta\bar{\sigma}_r = 0.44$  to  $0.32s_u$  rather than  $\Delta\sigma_r = \Delta\bar{\sigma}_r = s_u$ .

This clearly indicates that linear solutions predict much lower reductions in  $\Delta\sigma_r$  and that the neglected residual compression in the springs (of Fig. 2.33) after dissipation of excess pore pressures is significant. The radial stresses at  $r = R_p$  have a major effect on the stresses acting on the pile shaft after consolidation. Finally, the effect of soil non-linearities on  $\Delta\sigma_r$  (at  $r = R_p$  after consolidation) is not fully evaluated by existing solutions, but is not believed to change linear predictions significantly.

2. During consolidation, the clay in the yielded (inner) zone is assumed to behave as normally consolidated\*\*

---

\* As predicted by an elastic-perfectly plastic model when shear induced pore pressures are neglected.

\*\* With properties depending only on the value of the mean effective stress at the beginning of consolidation.



clay, regardless of its overconsolidation ratio (OCR) prior to pile driving. This assumption is based on the fact that the clay is sheared to large strain levels and that sufficient remolding takes place to erase the clay's "memory of its initial stress history."

Kirby et al. (1977) state that:

"Because the soil has amnesia it should behave as a normally consolidated soil during subsequent reconsolidation and, therefore, reconsolidate along the Critical State Line in  $e-\bar{\sigma}$  space. To do so requires that the stresses follow the Critical State Line (CSL) in  $q-\bar{\sigma}$  space."

This appears to suggest that consolidation along the CSL is a consequence of the assumption that soil behaves like normally consolidated. However, consolidation along the CSL takes place only if a soil model without a cap (e.g. the extended Mises perfectly plastic model) is used but does not follow from Critical State concepts (Schofield and Wroth, 1968). In fact, Critical State models can accommodate normally consolidated behavior (i.e. stress point lying on the yield surface), away from the CSL because of the existence of the cap. In addition, both linear and non-linear comprehensive consolidation solutions predict consolidation paths which lie away from the critical

state line\*.

- 3) The distribution of the change in the mean effective stress,  $\Delta\bar{\sigma}$ , in the inner yielded region has the same shape as the initial distribution of the excess pore pressures. Baligh and Kavvadas, 1980 show that this assumption is in agreement with linear solutions.

Using the previous assumptions and significant engineering judgement Esrig, Kirby and their co-workers conclude that:

- 1) For normally consolidated clays, the mean effective stress at the pile-soil interface after consolidation, is approximately equal to the mean effective stress prior to pile driving.
- 2) For heavily overconsolidated soils (OCR greater than about 10) the mean effective stress at the pile-soil interface after consolidation is approximately equal to the mean effective stress at the end of pile driving.

*No AP effects.*

↙ In summary, existing engineering models involve severe assumptions often contradicting results of comprehensive analyses and otherwise difficult to evaluate by existing theories and/or measurement techniques. Therefore, they should be used, with extreme care, to develop a better understanding of the mechanisms of soil consolidation around pile shafts, but not to provide quantitative predictions.

\*See Figure 2.32 for linear solutions and Miller et al. (1978) and Randolph et al. (1978b) for non-linear solutions.

#### 2.2.4.4 Non-linear Consolidation Analyses

##### Analysis by Miller et al. (1978)

Miller et al. (1978) performed non-linear radial, plane-strain consolidation analyses for the soil around a single pile shaft, using a Critical State non-linear model (the modified Cam-Clay model), and assuming that soil was isotropically consolidated before pile installation. They approximated the differential operators of the coupled consolidation equations\* with an implicit finite difference scheme in the radial dimension and an explicit scheme in time, and solved by calculating displacements and pore pressures, computing strain and stress increments from the displacements, updating total strains and stresses and repeating the calculations until excess pore pressures dissipate.

The main objective of Miller's study was to evaluate predictions of the engineering model (Esrig et al., 1977, Kirby et al., 1977) and, in particular, check the assumption that the effective stress path follows the Critical State line during consolidation. Therefore, they selected four different hypothetical initial effective stress distributions\*\*

---

\* For the case of radial, plane-strain consolidation, the field equations reduce to two equations involving as unknowns:

- a) The radial displacement;
- b) The excess pore pressure.

\*\* Lying in the normally and overconsolidated regions and on the Critical State line.

and the same\* initial excess pore pressure distribution, corresponding to the expansion of a cylindrical cavity.\*\*

Results of this study showed that for a soil element at the pile-soil interface:

- 1) The radial effective stress, at the end of consolidation, ~~is~~ the major principal stress and the vertical and circumferential effective stresses are approximately equal.
- 2) Regardless of the assumed initial effective stress distribution, the effective stress path during consolidation approaches the one-dimensional consolidation line, corresponding to the  $K_0$ -value predicted\*\*\* by the Cam-Clay model. However, the final stress state on the  $K_0$ -line depends on the initial effective stress distribution.\*\*\*\*

These results clearly indicate that an effective stress path along the Critical State Line during consolidation (as assumed by the engineering model of Esrig et al., 1977 and Kirby et al., 1977) is not adequate. Furthermore, by assuming

---

\* Because they thought that the direction of the stress path followed by the soil at the pile wall is independent of the shape of the initial pore pressure distribution.

\*\* Using also the Cam-Clay model.

\*\*\* For the input parameters used.

\*\*\*\* And on the initial pore pressure distribution.

that at the pile wall:  $\tau_{rz} = \epsilon_{\theta} = \epsilon_z = 0$ , the one-dimensional straining condition obviously leads to a stress path approaching the  $K_0$ -condition.

The final stress state at all radii, after consolidation is completed, depends on:

- 1) The constitutive law (i.e., model) used.
- 2) The boundary conditions imposed at the far-field (specified tractions or displacements). Miller et al. (1978) assumed that stresses at the far-field are not affected by pile installation and consolidation.
- 3) Initial values of effective stresses.
- 4) The magnitude and shape of the initial excess pore pressure distribution.

At distances away from the pile-soil interface, Miller et al. (1978) find that:

- 1) Consolidation is no longer one-dimensional (i.e. the stress path is not directed towards the  $K_0$ -line). In general, the circumferential strain,  $\epsilon_{\theta}$ , is compressive, i.e. soil moves inwards during consolidation.
- 2) At the end of consolidation the radial effective stress at the pile wall is slightly smaller than away from the pile. This suggests that the pile-soil interface is the surface of least shearing

resistance and thus the most likely shearing surface during pile loading. However, this result depends on: (a) the soil model used for the consolidation analyses; (b) the initial effective stress and pore pressure distribution; and (c) the friction angle along various shear surfaces and hence should be utilized with caution especially since the gradients of  $\bar{\sigma}_r$  after consolidation obtained by Miller et al. (1978) are very small near the pile wall.

Analysis by Carter et al. and Randolph et al.

(a) Introduction

Carter et al. (1977), Randolph et al. (1978b, 1979b) and Carter et al. (1979a,c) use the Finite Element technique of spatial discretization in a coupled consolidation analysis which allows for both material and geometric non-linearities.\* Their method may be used whenever the soil can be modeled by an effective stress-strain law in an incremental (or rate) form. They studied both effective stress changes and pore pressure dissipation rates during radial plane-strain consolidation around a single pile by using three material laws:

\* i.e., non-linear material laws and finite strains, respectively. Finite strains are needed to solve the problem of expansion of a cylindrical cavity.

- 1) An elastic material with properties\*  $G/s_u = 50$ ;  
 $\bar{v} = 0.3$ .
- 2) An elastic-perfectly plastic material yielding according to the Tresca criterion ( $\sigma_1 - \sigma_3 = 2s_u$ ) with properties  $G/s_u = 50$ ;  $\bar{v} = 0.3$ .
- 3) The modified Cam-Clay model with properties "similar to Boston Blue Clay". For the normally consolidated clay they used the data shown in the fourth column of numbers in Table 2.7. For an overconsolidated clay they assume that  $G/\bar{\sigma}_{vo}$  is proportional to the OCR\*\* and that for all OCR's the void ratio, before pile driving, is the same.

The investigation by Carter et al. and Randolph et al. is very similar to the study of Miller et al. (1978) with the following differences:

- 1) Miller et al. used finite differences to solve the coupled consolidation equations, whereas Carter et al. and Randolph et al. used finite elements.
- 2) Carter et al. and Randolph et al. studied the elastic-perfectly plastic model, in addition to other soil models.
- 3) Carter et al. and Randolph et al. studied the effect of varying the overconsolidation ratio of the soil and some soil parameters (e.g., the elastic shear

---

\*The specific value of  $s_u$  used is not of interest since all results are normalized <sup>u</sup> with  $s_u$ .

\*\*This means that  $G$  is practically independent of OCR for constant void ratio.

modulus  $G$ ).

- 4) Carter et al. and Randolph et al. give more detailed diagrams of (effective and total) stress changes during consolidation, as well as pore pressure dissipation curves.

The initial state of stress in the soil prior to pile installation is given by point B (Fig. 2.34) on the  $K_0$ -line for the normally consolidated soil and by points on the line AB for overconsolidated soils. Pile installation is simulated by a cylindrical cavity expansion and causes significant straining of the soil near the pile shaft. Therefore, according to the Critical State concepts, the effective stress state at (and close to) the pile wall is located at point X on the Critical State Line (which is defined by its slope  $M = 1.2$ , corresponding to  $\bar{\phi} = 30^\circ$  for triaxial compression tests). Thus paths like BX and AX represent\* pile installation for various OCR's.

Consolidation analyses performed by Randolph et al., 1978b, using the elastic and elastic-perfectly plastic models utilize the initial stresses and excess pore pressure distributions which correspond to cylindrical cavity

---

\*Since the undrained shear strength is practically independent of OCR for the same void ratio. (Randolph et al. 1978b)



expansion solutions for an elastic-perfectly plastic soil (neglecting shear induced pore pressures). On the other hand, for analyses performed by the Cam-Clay model the initial stress and excess pore pressure distributions were predicted by the Cam-Clay model.

(b) Pore Pressure Dissipation Rates.

Figure 2.35 shows pore pressure dissipation curves at the pile wall for the linear, elastic-perfectly plastic and the Cam-Clay model (normally consolidated and heavily overconsolidated) computed by Randolph et al. (1978b). The predicted dissipation rates by the various models are very similar, especially those corresponding to the linear, elastic-perfectly plastic and the Cam-Clay (normally consolidated) models. This is rather surprising because of the differences in compressibilities between the various models (compressibility after yielding vs. elastic compressibility). The dissipation curve corresponding to the heavily overconsolidated Cam-Clay model is evidently affected by the lower initial magnitudes of the excess pore pressures\*. However, if the pore pressures are normalized by the shaft initial excess pore pressures, no significant effect of OCR on dissipation rates will be found.

(c) Changes of the Radial Stress at the Pile Wall.

Figure 2.36 shows the changes in the radial stress (total and effective) with time at the pile wall:

\*Mainly because of negative shear induced pore pressures during undrained shearing.

- 1) The linear model predicts no changes in the total radial stress at the pile wall during consolidation, (Baligh and Kavvadas, 1980).
- 2) The elastic-perfectly plastic model predicts a small decrease of the total radial stress at the pile wall after consolidation, that depend on  $G/s_u$  (e.g. 12% decrease for  $G/s_u = 50$ ).
- 3) The Cam-Clay model also predicts a small decrease of the total radial stress at the pile wall after consolidation (about 15% for the normally consolidated and 12% for the heavily overconsolidated soil).
- 4) According to the Cam-Clay model, changes of the effective radial stress at the pile wall during consolidation are independent of the OCR. However, the value of  $\bar{\sigma}_r/s_u$  after consolidation is affected by the assumed value of the elastic shear modulus,  $G$ , and typically decreases from 4.8 (for  $G/s_u = 100$ ) to 4.0 (for  $G/s_u = 20$ ).

#### (d) Effective Stress Paths

According to the Cam-Clay model, during consolidation, soil elements at (and close to) the pile wall<sup>\*</sup>, work-harden by expanding the yield surface, whereas soil elements away

---

\* For  $r$  less than two to three pile radii.

from the pile unload elastically (i.e. the stress point retreats from the yield surface). Thus, most of the soil unloads elastically. This behavior might explain why pore pressure dissipation rates are insensitive to the model used (linear vs. non-linear), as shown in Fig. 2.35.

Figure 2.34 shows the (total and effective) stress paths during consolidation for a soil element at the pile wall according to Cam-Clay model predictions and indicates that:

- 1) The effective stress path,  $XW$ , during consolidation is insensitive to the overconsolidation ratio\* prior to pile driving. This is a direct result of the Critical State concepts requiring that failure "erases soil memory" as expressed by its stress history.
- 2) The effective stress path,  $XW$ , tends towards the one-dimensional consolidation line corresponding to the  $K_0$ -value predicted by the Cam-Clay model (0.627 for the soil properties used by Randolph et al. 1978b, as shown in Table 2.7).
- 3) For the normally consolidated case, the mean effective stress in a soil element at the pile wall increases after consolidation is completed, by approximately 55% of the initial value of the excess pore pressure\*\*

\*Note that all paths correspond to the same void ratio.

\*\*Since Cam-Clay is known to overestimate the value of  $K_0$  (0.627 vs. the more reasonable value of 0.55 for Boston Blue Clay), a model that predicts more accurate  $K_0$ -values is expected to provide lower increases in the mean effective stress.

which is in the range of values predicted by linear elastic solutions. Also, the shear stress,  $q$ , decreases slightly, whereas linear solutions predict an increase of  $q$  at the pile wall.

#### 2.2.4.5 Summary and Conclusions

1. After pile installation, the dissipation of excess pore pressures and the consolidation of the soil around the shaft is an important step in estimating the skin friction,  $f_s$ , of piles, primarily because of the changes in the effective stresses acting on the pile shaft.
2. Existing measurements of the shaft resistance of piles driven in clays show a significant increase in  $f_s$  with time after installation and hence indicate that the radial effective stress acting on the pile shaft,  $\bar{\sigma}_h$ , increases during consolidation.
3. Most of the existing solutions consider only radial water flow and radial soil deformations, assume that the soil adjacent to the pile remains in contact with the pile during consolidation and neglect shear stresses at the pile-soil interface ( $\tau_{rz} = 0$ ). These assumptions imply that, at the pile-soil interface, the soil is subjected to one-dimensional straining ( $\epsilon_\theta = \epsilon_z = \tau_{rz} = 0$ ) and thus its stress path approaches the one-dimensional  $K_0$ -line regardless of the initial location of the stress point

and the specific stress-strain model used in the analyses.

4. Because of simplicity most of the existing consolidation solutions are linear, i.e. the soil is assumed to be linear and isotropic (and therefore elastic). Linear solutions predict that, at the pile-soil interface, the total horizontal stress,  $\sigma_h$ , remains constant during consolidation. This, together with the assumption  $\tau_{rz} = \epsilon_\theta = \epsilon_z = 0$  (discussed in item 3 above) implies that at the pile wall:

- a) During consolidation,  $\bar{\sigma}_h$  increases by an amount equal to the excess pore pressure  $\Delta p_i$  (at the interface), caused by pile installation.

Measurements of  $\Delta p_i$  in a number of case histories indicate that  $\Delta p_i \sim 2\bar{\sigma}_{vo}$ . This means that according to linear theories  $\bar{\sigma}_h$  after consolidation is at least\* equal to  $2\bar{\sigma}_{vo}$ . Such a value of  $\bar{\sigma}_h$  is believed to be excessively high in view of measured values of  $f_s$  unless  $\bar{\sigma}_h$  decreases significantly during loading.

- b) The remaining principal effective stresses, are strictly controlled by Poisson's ratio

$$(\Delta\bar{\sigma}_\theta = \Delta\bar{\sigma}_z = \frac{\bar{\nu}}{(1-\bar{\nu})} \Delta\bar{\sigma}_h).$$

---

\* Because  $\bar{\sigma}_h$  after pile installation is neglected.

These stresses are only important in models requiring the full state of stress (not only  $\bar{\sigma}_h$ ) to be known at the soil element adjacent to the pile (e.g. Critical State models) in order to estimate the skin friction,  $f_s$ .

5. A number of attempts have been made in the last few years to introduce soil non-linearity in order to reduce predicted values of  $\bar{\sigma}_h$  at the pile wall after consolidation. Leifer et al. (1979) conducted a parametric study to show that a spatially variable soil compressibility can reduce  $\bar{\sigma}_h$  at the wall. However, the use of their results in practice is prevented by the many uncertainties in the assumed distribution of compressibility.
6. Engineering approximations of the effective radial stress at the pile wall after consolidation is completed were obtained by Esrig, Kirby and their co-workers assuming that the soil consolidates along the Critical State Line, i.e., a prescribed path of void ratio, shear stress and mean effective stress. More importantly they assumed that after consolidation, soil stresses at some distance from the pile return to their values prior to pile installation and thus, they predicted that, for normally consolidated soils, the radial effective stress at the pile wall after consolidation is approximately equal to the in situ horizontal stress prior to pile installation.
7. More comprehensive non-linear solutions were obtained by Miller et al. (1978) and at Cambridge University by Randolph

and his co-workers, using the modified Cam-Clay model. They found that at the pile-soil interface the soil consolidates along the one-dimensional  $K_0$ -line (instead of the Critical State line, as assumed under item 6 above) and that  $\sigma_h'$  decreases slightly (10-20%) regardless of the overconsolidation ratio prior to pile driving.

8. The problem of soil consolidation after pile driving is still far from being solved satisfactorily. A better understanding of the mechanism of the consolidation around piles is required via more accurate soil behavioral models and comprehensive non-linear solutions in conjunction with in situ measurements of total and effective stresses at the pile-soil interface during consolidation.

## 2.2.5 EFFECTS OF PILE LOADING

### 2.2.5.1 Simplifying Assumptions and Location of the Shear Surface

Soil-pile interaction during pile loading is complicated and hence simplifications are needed. Table 2.8 lists three common simplifying assumptions. Assumption (1) reduces pile loading to a one-dimensional problem where the only spacial coordinate is the radial distance,  $r$ , from the pile axis. Assumptions (1) and (2) imply that the surface where slippage takes place (shear surface) is parallel to the pile shaft (i.e., vertical for vertical piles) and hence two alternatives present themselves:

(A). The shear surface is located at the pile-soil interface.

Slippage at the pile-soil interface means that the soil did not reach a failure condition\* and the limiting skin friction,  $f_s$ , can be written as:

$$f_s = \bar{\sigma}_{hf} \cdot \tan \bar{\delta} \quad (2.42)$$

where:  $\bar{\sigma}_{hf}$  = the effective horizontal stress on the pile shaft at failure.

$\bar{\delta}$  = the pile-soil interface friction angle.

---

\*and hence Mohr circles and criteria for soil failure are not particularly helpful.



Estimates of the friction angle,  $\bar{\delta}$ , can be obtained with difficulty from special laboratory tests where shearing between the soil and the pile material is imposed. On the other hand, estimates of  $\bar{\sigma}_{hf}$  depend on the stress state in the soil element adjacent to the pile and soil deformability, i.e. its stress-strain behavior. Estimates of  $\bar{\sigma}_{hf}$  are discussed subsequently.

(B). The shear surface is located in the soil.

If slippage takes place in the soil, the interface properties\* do not affect the limiting skin friction,  $f_s$ . Adding assumption (3) to assumptions (1) and (2) in Table 2.8,  $f_s$  now represents the limiting soil resistance "close" to the pile wall when the shear surface is parallel to the pile (i.e. vertical). Estimates of  $f_s$ , therefore, depend on the soil conditions\*\* before pile loading (i.e., after consolidation), the mode of shearing (undrained, drained or partially drained) and the effect of shearing on the stress state in the soil located "near" the pile wall.

If pile loading is sufficiently rapid to allow no water flow from the clay during shearing, an undrained shearing mode takes place and the compressibility of the clay can be

\* e.g. pile material and its surface roughness, ... etc.

\*\* stress state and properties.

neglected (i.e. it behaves as an incompressible solid). Under "undrained" shearing conditions, the magnitude of  $f_s$  can be estimated by total or effective stress approaches. In a total stress approach  $f_s$  depends on the soil conditions before shearing (i.e. after consolidation) but this dependence is difficult to estimate rationally without consideration of effective stresses. On the other hand, an effective stress approach is more fundamental, applies to undrained, drained and partially drained conditions and enables  $f_s$  to be written in the form:

$$\underline{f_s = f_s(\bar{\sigma}_{hf}, \bar{c}, \bar{\phi})} \quad (2.43)$$

i.e. as a function of the effective stress,  $\bar{\sigma}_{hf}$ , acting on the shear surface at failure, the effective cohesion intercept,  $\bar{c}$ , and the effective friction angle of the soil,  $\bar{\phi}$ . Neglecting  $\bar{c}$  in the soil adjacent to the pile wall represents a reasonable assumption for normally consolidated and slightly overconsolidated clays, especially in view of the large straining (remolding) caused by pile installation. Therefore, Eq. 2.43 can be written in the simpler form:

$$f_s = \bar{\sigma}_{hf} \cdot f(\bar{\phi}) \quad (2.44)$$

The following section investigates the dependence of  $f_s$  on  $\bar{\phi}$  (i.e., the function  $f$ ) and the major uncertainties associated with estimating the effective horizontal stress at failure,  $\bar{\sigma}_{hf}$ .

### 2.2.5.2 Dependence of the Limiting Skin Friction on the Soil Friction Angle

For "undrained" conditions, the three assumptions listed in Table 2.8 imply that soil shearing around the pile exhibits strong similarities with the ideal\* Direct Simple Shear (DSS) conditions of laboratory testing; namely the only non-vanishing strain around the pile is the shear strain  $\gamma_{rz}$  vs.  $\gamma_{xz}$  in the DSS test. Therefore, in discussing the dependence of  $f_s$  on  $\bar{\phi}$  in Eq. 2.44, we can use previous studies establishing the relationship between  $\tau_{xz}$  and  $\bar{\phi}$  in "undrained" DSS tests at failure. Ladd and Edgers (1972) studied the implications of three types of assumptions regarding the stress state at failure in DSS tests. All assumptions define failure as the state leading to a Mohr circle of effective stresses touching the Coulomb envelope with an inclination given by  $\bar{\phi}$ . When translated into the shearing conditions of the soil around the pile, these assumptions are:

- 1) The shear surface of slippage coincides with the plane of maximum obliquity\*\* (in terms of effective stresses). Noting that the shear surface is vertical, Fig. 2.37a illustrates the failure effective stress state according to this assumption and shows that:

$$f_s = \bar{\sigma}_{hf} \tan \bar{\phi} \quad (2.45)$$

- 2) The shear stress on the slippage surface is larger

\*neglecting non-uniform stress distributions.

\*\*i.e., the maximum ratio of shear stress to normal stress.

than the shear stress on any other plane. Fig. 2.37b illustrates the location of the origin of planes  $O_p$  implied by this assumption (which is consistent with the associated plasticity theory for a frictionless material) and shows that:

$$f_s = \bar{\sigma}_{hf} \cdot \sin \bar{\phi} \quad (2.46)$$

- 3) During soil shearing, total stress-increments are proportional to the strain-increments. Since the only non-vanishing strain during shearing is  $\gamma_{rz}$ , the only total stress altered by pile loading is  $\tau_{rz}$  and in particular the two normal total stresses  $\sigma_r$  and  $\sigma_z$  remain unchanged (i.e. pure shear total stress increments are applied). Figure 2.37c illustrates the implications of this assumption for the case when the horizontal radial stress exceeds the vertical stress and shows that:

$$f_s = \left[ \left( \frac{\bar{\sigma}_{vc} + \bar{\sigma}_{hc}}{2} - \Delta p_f \right)^2 \cdot \sin^2 \bar{\phi} - \left( \frac{\bar{\sigma}_{hc} - \bar{\sigma}_{vc}}{2} \right)^2 \right]^{1/2} \quad (2.47)$$

where  $\bar{\sigma}_{vc}$  and  $\bar{\sigma}_{hc}$  are the vertical ( $\bar{\sigma}_z$ ) and horizontal radial ( $\bar{\sigma}_r$ ) effective stresses at the end of consolidation respectively.

Based on these three assumptions, Table 2.9 shows the values of the friction angle  $\bar{\phi}$  backfigured by Ladd and Edgers (1972)

from measurements of the shear stress and the effective normal stress on the shear surface (i.e. equivalent to  $f_s$  and  $\bar{\sigma}_{hf}$  on the pile shaft) at failure\* in DSS tests conducted on two normally consolidated clays. Clay A is a lean resedimented Boston Blue Clay and clay B is a plastic deltaic (natural) clay. Clearly, assumption (3) can significantly overestimate  $\bar{\phi}$  and hence appears unreasonable.

Ladd and Edgers (1972) estimate that  $\bar{\phi} = 30^\circ$  for clay A and  $\bar{\phi} = 25^\circ$  for clay B. Therefore, both assumptions (1) and (2) underestimate  $\bar{\phi}$  but the difference between assumptions (1) and (2) is relatively small ( $1.3^\circ$  to  $2^\circ$  in  $\bar{\phi}$ ). Kenney (1966) and Schmertmann (1963) report undrained and drained DSS test results on normally consolidated quick clays. The tests were run with instrumented reinforced rubber membrane, thus enabling the full state of stress to be described by measurements. At failure\*\*, conditions close to those in assumption (2) were obtained (see Fig. 2.37b).

The dependence of the limiting skin friction on the friction angle of the clay is also studied by Randolph and Wroth (1981). This is discussed in Section 2.2.5.3c.

---

\* i.e. at maximum shear stress.

\*\* Corresponding to the maximum measured horizontal shear stress during the DSS test.

In conclusion, the analogy between the undrained shearing of the soil adjacent to pile shafts and the DSS test results suggests that:

- a) Significant rotation of the principal planes takes place during pile loading.
- b) The magnitude of  $f_s$  probably falls between values estimated by assumptions (1) and (2), i.e.:

$$\sin \bar{\phi} \leq \frac{f_s}{\bar{\sigma}_{hf}} \leq \tan \bar{\phi} \quad (2.48)$$

- c) For normally consolidated clays, adequate estimates of  $\bar{\phi}$  in Eq. 2.48 are on the low side and probably in the range of 20° to 25°.

#### 2.2.5.3 Effect of Shearing on the Effective Stresses

A major difficulty in estimating reliable values of  $f_s$  on pile shafts is caused by the uncertainties in estimating the horizontal effective stresses (Eq. 2.44 and 2.48). At failure, the horizontal effective stress,  $\bar{\sigma}_{hf}$ , can be written as:

$$\bar{\sigma}_{hf} = \bar{\sigma}_{hc} + \Delta\bar{\sigma}_{hf}$$

(2.49)

$$\Delta\bar{\sigma}_{hf} = \Delta\sigma_{hf} - \Delta p_f$$

where  $\bar{\sigma}_{hc}$  = effective horizontal stress after soil consolidation

$\Delta\sigma_{hf}$ ,  $\Delta p_f$  = changes in total horizontal stress and pore pressure caused by pile loading.

#### (a) Linear Isotropic Elasticity

Solutions based on linear isotropic elasticity are relatively simple to obtain and, in some cases, can provide insight into the important aspects of geotechnical problems. Therefore, in addition to the assumptions in Table 2.8, it is further assumed that during pile loading:

- 1) The clay is sheared in an undrained mode, i.e. no water flow takes place, excess pore pressures do not dissipate and the clay is incompressible.
- 2) The soil behaves as a linear isotropic material. Therefore, excess pore pressures are equal to the change in octahedral (mean) total stress,  $\Delta\sigma$ . In particular:

$$\text{if } \Delta\sigma = 0 \text{ then } \Delta p = 0. \quad (2.50)$$

3) After consolidation, the principal directions are in the radial, tangential and vertical directions. This is consistent with cavity expansion approaches.

Equilibrium considerations in the vertical direction during pile loading, together with the assumptions above and assumption (1) in Table 2.8, require that the shear stress  $\tau_{rz}$  at any radius,  $r$ , be given by:

$$\tau_{rz} = \Delta\tau_{rz} = \frac{R}{r} \cdot f_s \quad (2.51)$$

where:  $f_s$  = the limiting skin friction at the pile-soil interface, and

$R$  = pile radius

Finally, using the assumptions in Table 2.8 and assumptions (1), (2) above one can show\* that all other effective and total stress increments during pile loading, vanish at all radii, i.e.:

$$\Delta p_f = \Delta\bar{\sigma}_{rf} = \Delta\bar{\sigma}_{\theta f} = \Delta\bar{\sigma}_{zf} = 0 \quad (2.52)$$

Thus, the radial (horizontal) effective stress at failure is equal to the radial effective stress after consolidation is completed, i.e.:

\*it is also assumed that pile loading has no effect on the stress conditions at infinity.



$$\bar{\sigma}_{hf} = \bar{\sigma}_{hc} \quad \text{and} \quad \sigma_{hf} = \sigma_{hc} \quad (2.53)$$

and pile loading imposes a pure shear total stress increment and hence corresponds to assumption (3), (in Section 2.2.5.2 regarding the state of stress at failure. However, assumption (3) is believed to be unrealistic and thus one or more of the assumptions used to derive Eq. 2.52 are not reasonable.

Since soils rarely exhibit a linear behavior, the usefulness of linear solutions depends on the importance of soil non-linearities in affecting the response under consideration. For non-linear material laws, estimates of  $f_s$  require an analysis of the stresses around the pile, based on a comprehensive soil model and the stress state after consolidation is completed as initial conditions.

Alternatively estimates of  $f_s$  can be obtained by assuming the state of stress during pile loading.

#### (b) Solutions Based on Critical State Concepts

Esrig et. al. (1979) apply the Critical State concepts to estimate the limiting skin friction,  $f_s$ . They assume that:

- (1) The clay is sheared in an undrained mode, i.e., no water flow takes place, excess pore pressures do not dissipate and the clay is incompressible during pile loading.

- (2) Slippage takes place at the pile-soil interface (i.e., the shear surface is located at the interface) and thus:

$$f_s = \bar{\sigma}_{hf} \cdot \tan \bar{\delta} \quad (2.54)$$

where:  $\bar{\sigma}_{hf}$  = the effective horizontal stress acting on the pile-soil interface the failure.

$\bar{\delta}$  = the interface friction angle

- (3) After consolidation is completed, the state of the soil adjacent to the pile is represented by a point on the Critical State Line (CSL), which is characterized by a parameter M equal to:

$$M = \frac{6 \cdot \sin \bar{\delta}}{3 - \sin \bar{\delta}} \quad (2.55)$$

This implies that during pile loading (a) the mean effective stress,  $\bar{\sigma}$ , at a soil element adjacent to the pile wall, does not change, i.e.:

$$\bar{\sigma}_f = \bar{\sigma}_c \quad (2.56)$$

where,  $\bar{\sigma}_f$ ,  $\bar{\sigma}_c$ , are the mean effective stresses at the pile wall at failure and after consolida-

tion, respectively, and (b) no "shear induced"\* pore pressures,  $\Delta p_s$ , develop.

Changes of the mean total stress,  $\Delta\sigma$ , during pile loading (and thus pore pressures) cannot be estimated without comprehensive analyses of the state of stress around the pile. In order to investigate the changes in mean normal total stress caused by pile loading, Esrig et. al. (1979), performed finite element analyses for an elastic pile in an elastic medium, assuming constant soil and pile properties with depth and no slippage at the pile-soil interface. Despite obvious limitations, these analyses provide interesting parametric studies of the effects of pile to soil moduli and the length to diameter ratio of the pile. For typical situations corresponding to long steel piles in clays they find that the change in mean

---

\*The pore pressure change during undrained loading,  $\Delta p$ , is equal to the sum of:

(a) The change of the total mean stress,  $\Delta\sigma$ .

(b) The shear-induced pore pressure  $\Delta p_s$ .

$$\text{i.e.: } \Delta p = \Delta\sigma + \Delta p_s \quad (2.57)$$

$$\text{where: } \Delta p_s = - \Delta\bar{\sigma}$$

total stress is limited to 5 to 10% of the undrained shear strength of the soil,

- (4) The pile-soil interface is the plane of maximum obliquity (i.e., maximum ratio of shear stress to normal effective stress).
- (5) At failure\* the intermediate effective principal stress,  $\bar{\sigma}_{2f}$ , is equal to either the minimum effective principal stress,  $\bar{\sigma}_{3f}$ , or the maximum effective principal stress,  $\bar{\sigma}_{1f}$ .

Using the previous assumptions, the limiting skin friction,  $f_s$ , can be estimated by the expression\*\* proposed by Esrig et. al. (1979)

$$f_s = \frac{M}{2} \cdot \bar{\sigma}_c \cdot \cos \bar{\delta} \quad (2.58)$$

where:  $\bar{\sigma}_c$  = the mean effective stress at the pile-soil interface after consolidation is completed

$\bar{\delta}$  = the pile-soil interface friction angle

M = Critical state parameter (Eq. 2.55)

\*Assumption (5) is implied by the relation:

$$q_f = \sigma_{1f} - \sigma_{3f}$$

which is used during the derivation of Eq. 2.58. In general:

$$q_f = \frac{1}{\sqrt{2}} \{(\sigma_{1f} - \sigma_{2f})^2 + (\sigma_{2f} - \sigma_{3f})^2 + (\sigma_{3f} - \sigma_{1f})^2\}^{1/2}$$

\*\*The derivation is illustrated in Fig. 2.10.

or, by using Eq. 2.55, Eq. 2.58 can also be written:

$$f_s = \left( \frac{3 - 3 \sin^2 \bar{\delta}}{3 - \sin \bar{\delta}} \right) \cdot \bar{\sigma}_c \cdot \tan \bar{\delta} \quad (2.59)$$

which is approximately\* equal to:

$$f_s \approx \bar{\sigma}_c \cdot \tan \bar{\delta} \quad (2.60)$$

for values of  $\bar{\delta}$  less than  $27^\circ$ . Compared with Eq. 2.54 and noting Eq. 2.56, Eq. 2.60 implies that the mean effective stress acting at the pile-soil interface after consolidation is completed,  $\bar{\sigma}_c$ , is approximately equal to the horizontal effective stress acting at the pile-soil interface at failure.

The validity of some of the assumptions made by Esrig et. al. (1979) is questionable. Assumption (3) is extensively discussed in Sections 2.2.4.3 and 2.2.4.4. Assumption (4) is also discussed\*\* in Section 2.2.5.2. Furthermore, Eq. 2.55 relating the Critical State parameter M with the pile-soil interface friction angle,  $\bar{\delta}$ , is highly suspect because of the following reasons:

- (a) A Critical State soil condition cannot be associated with a failure at the interface, simply

---

\*within 6% error

\*\*Assuming that failure occurs at the interface (Assumption (2)), there is no reason for the interface to be a plane of maximum obliquity.

because a Critical State soil condition is independent of the pile-soil interface friction angle,  $\bar{\delta}$ . Thus a relationship between the Critical State parameter  $M$  and  $\bar{\delta}$  is most unusual.

- (b) Baligh and Kavvadas (1980) show that Eq. 2.55 should be used to relate the Critical State parameter  $M$  with the friction angle of the soil in triaxial compression. Since the mode of failure during pile loading is not believed to be close to a triaxial compression mode, equations other than Eq. 2.55 appear more appropriate (see Table 2.10).

Finally in order to check assumption (5), comprehensive analyses of the state of stress around a loaded pile are required.

(c) Solutions Based on the Assumptions of Randolph and Wroth (1981)

Randolph and Wroth (1981) realized that the mode of shearing in the soil during undrained axial loading of a (vertical) pile is that of a pure shear strain with zero extension directions (i.e., directions of no normal strain) coinciding with the axial (vertical) and radial (horizontal) directions. They further used experimental evidence\* (for dense sands) indicating that rupture occurs along the zero

---

\*Arthur et al. (1977) and Budhu (1979)

extension directions and also that rupture planes tend to form on planes of maximum stress obliquity and concluded that during pile shearing the direction of one of the planes of maximum stress obliquity (at peak  $f_s$  and at the Critical State) will coincide with either the vertical or the horizontal direction. More specifically, they concluded that:

- (a) At the state of maximum applied shear stress (i.e., at maximum  $f_s$ ) failure is initiated by the formation of rupture planes parallel to the initial direction\* of the major principal stress. In the case of a driven pile they believe that after soil consolidation the radial stress will be larger than the vertical and circumferential stresses. Thus, when a vertical driven pile is loaded axially, failure is initiated when one of the planes of maximum stress obliquity is horizontal, which means that at maximum  $f_s$

$$\frac{f_s}{\bar{\sigma}_{hf}} = \frac{\sin\bar{\phi} \cos\bar{\phi}}{1 + \sin^2\bar{\phi}} < \sin\bar{\phi} \quad (2.61)$$

---

\*i.e., before shearing

Data from DSS tests\* on normally consolidated Boston Blue Clay reported by Ladd and Edgers (1972) show that, at maximum  $f_s$ , the ratio  $f_s/\bar{\sigma}_{hf}$  ranges between 0.34 and 0.35 which means that  $\bar{\phi} = 28^\circ - 32^\circ$  (from Eq. 2.61). These values compare well with the values of  $\bar{\phi}$  measured in undrained triaxial compression tests on Boston Blue Clay.

- (b) At large axial displacements of the pile (i.e., at large values of shear strain locally in the soil close to the pile) the boundary conditions forced on the soil by the pile cause a discontinuity of displacement in the vertical direction i.e., the rupture surface is vertical. Thus, at the Critical State one of the planes of maximum obliquity is vertical, which means that

$$\frac{f_s}{\bar{\sigma}_{hf}} = \tan\bar{\phi} \quad (2.62)$$

This is consistent with assumption (1) of Ladd and Edger (1972) and, as discussed in Section 2.2.5.2, underestimates  $\bar{\phi}$ .

---

\*The mode of shearing in the DSS test is similar to the mode of shearing during undrained axial loading of driven piles and thus, Eq. 2.61 can be applied.



Undrained Shear Strength* $s_u$ (TSF)	Description
0 - 0.125	Very soft
0.125 - 0.25	Soft
0.25 - 0.50	Medium
0.50 - 1.0	Stiff
1.0 - 2.0	Very stiff

\* $s_u$  obtained from unconfined compression tests.

Table 2.1: Terzaghi and Peck (1967) Classification of Clays.

Case	Soil Conditions	Penetration Ratio* L/D	$a = \frac{f_s}{s_u}$
I	Sands of sandy gravels overlying stiff to very stiff clays	< 20	1.25
		> 20	Use curve 1 in Fig. 2.2
II	Soft clays or silts overlying stiff to very stiff clays	< 20	0.40
		> 20	0.70
III	Stiff to very stiff cohesive soils without overlying strata	< 20	0.40
		> 20	Use curve 2 in Fig. 2.2

\* L = length of pile

D = diameter of pile

Note:  $\alpha$ -values are not applicable to H-section piles.

$s_u$  obtained from unconfined compression tests.

Table 2.2: Limiting skin friction values into stiff to very stiff clays (after Tomlinson, 1971).

Author	Cavity		Material Model	Initial Stresses	Proposed Applications	Remarks
	Cyl.	Sph.				
Bishop, Hill and Mott (1945)	x	x	Elastic-plastic (Von Mises) strain hardening	Not considered (presumably isotropic)	Metal indentation	Closed form solution; ex- perimental results of copper indentation compare well with theory; use natural strains.
Chadwick (1959)		x	Elastic-perfectly plastic (Tresca)	Isotropic	Cylindrical cavity expansion in soils and metals	Considers both loading (expansion) and unloading (contraction) of a spherical cavity.
Gibson and Anderson (1961)	x		Elastic-perfectly plastic (Tresca)	$\sigma_r = \sigma_\theta$	Interpretation of the pressuremeter test	Closed form solution
Ladanyi (1963)	x	x	Experimental stress and mean effective stress vs. strain curves determined from triaxial test	Isotropic	- Stress distribution around cavities - Bearing capacity of deep foundations - Excess pore pressure distribution around driven piles	- Numerical integration of equilibrium equations - Predicts both total stresses and pore pressures.
Butterfield and Bannerjee (1970)	x		Elastic-perfectly plastic (Von Mises)	Isotropic	- Stress and pore pressure distributions around driven piles	- Closed form solution - Consider boundary shear stresses (shaft friction) - <b>ERROR</b> in equations (do not satisfy the conservation of volume; see Appendix A for correct solution).
Bequelin et al. (1972)	x		General (non linear) stress- strain curve	$\sigma_r = \sigma_\theta$	Pressuremeter test	Provide a method of inter- pretation of the pressure- meter test (i.e., obtain stress-strain curve from expansion curve).
Ladanyi (1972)	x		General stress- strain curve	$\sigma_r = \sigma_z$	Pressuremeter test	Same as above.
Palmer (1972)	x		General stress- strain curve	$\sigma_r = \sigma_\theta$	Pressuremeter test	Same as above.
Vesic (1972)	x	x	Elastic-perfectly plastic	Isotropic	- Ultimate cavity pressure - Evaluation of pressure- meter tests - Evaluation of excess pore pressures due to pile driving	- Considers volume change for drained expansion - Evaluates pore pressures and total stresses for undrained expansion
Prevost and Hogg (1975)	x		Elastic-plastic (Von Mises) w/ isotropic hardening or softening	Isotropic	Pressuremeter test	- Provide mathematical expressions for the yield function to obtain closed form solution of stresses.
Carter, Randolph and Wroth (1978)	x		Modified cam- clay	K condition	Stress distribu- tion along the shaft of a driven pile	Finite element analysis

NOTE: All references consider a) an incompressible isotropic homogeneous non viscous material (unless otherwise indicated)  
b) plane strain deformations in the cylindrical cavity expansion with  $\Delta\sigma_r = 4(\Delta\sigma_r + \Delta\sigma_\theta)$

Table 2.3: Summary of cylindrical and spherical cavity expansion solutions (After Levadoux, 1980)

Stress Path Method	Strain Path Method
<b>APPLICATIONS</b>	
Surface Problems	Deep Problems
<b>STEPS</b>	
<ol style="list-style-type: none"> <li>1. Estimate initial stresses</li> <li>2. Estimate incremental stresses</li> <li>3. Perform stress path tests on samples (or use adequate soil model) to obtain strains at selected locations.</li> <li>4. Estimate deformations by integrating strains</li> </ol>	<ol style="list-style-type: none"> <li>1. Estimate initial stresses</li> <li>2. Estimate incremental strains</li> <li>3. Perform strain path tests on samples (or use adequate soil model) to obtain deviatoric stresses at selected locations.</li> <li>4. Estimate octahedral (isotropic) stresses by integrating equilibrium equations.</li> </ol>
<b>APPROXIMATION</b>	
<p>In step 2, stresses are approximate thus leading to strains not satisfying compatibility requirements. i.e., deformations in step 4 depend on strain integration path.</p>	<p>In step 2, strains are approximate thus leading to stresses not satisfying all equilibrium conditions. i.e., octahedral stresses in step 4 depend on equilibrium integration path.</p>

Table 2.4: Comparison of stress path and strain path methods, (After Levadoux, 1980)

INITIAL PORE PRESSURE DISTRIBUTION	$(-\Delta\sigma_r)/(p_i)_{eh}$	
	$R \leq r < \lambda R$	$r > \lambda R$
CONSTANT	$\frac{(1-2\bar{\nu})}{2(1-\bar{\nu})} \left\{ 1 - \left(\frac{R}{r}\right)^2 \right\}$	$\frac{(1-2\bar{\nu})}{2(1-\bar{\nu})} (\lambda^2 - 1) \left(\frac{R}{r}\right)^2$
LINEAR	$\frac{(1-2\bar{\nu})}{2(1-\bar{\nu})} \cdot \frac{1}{(\lambda-1)} \left\{ \lambda \left[ 1 - \left(\frac{R}{r}\right)^2 \right] + \frac{2}{3} \left[ \left(\frac{R}{r}\right)^2 - \left(\frac{r}{R}\right) \right] \right\}$	$\frac{(1-2\bar{\nu})}{2(1-\bar{\nu})} \cdot \frac{1}{(\lambda-1)} \left\{ (\lambda^2 - 1) \lambda + \frac{2}{3} \left[ 1 - \lambda^2 \left(\frac{r}{R}\right) \right] \right\} \left(\frac{R}{r}\right)^2$
LOGARITHMIC	$\frac{(1-2\bar{\nu})}{2(1-\bar{\nu})} \left\{ \left[ 1 - \left(\frac{R}{r}\right)^2 \right] \cdot \left[ 1 + \frac{1}{2\lambda n} \right] + \frac{1}{\lambda n} \ln \left(\frac{R}{r}\right) \right\}$	$\frac{(1-2\bar{\nu})}{2(1-\bar{\nu})} \left\{ \frac{(\lambda^2 - 1)}{2\lambda n} - 1 \right\} \left(\frac{R}{r}\right)^2$

Table 2.5: Normalized total radial stress changes after linear consolidation around a pile for various initial excess pore pressure distributions. (After Baligh and Kavvasdas, 1980)

TABLE 2.6

TOTAL AND EFFECTIVE RADIAL STRESS CHANGES AFTER CONSOLIDATION AT $r = \lambda R$ ACCORDING TO LINEAR SOLUTIONS			
$\bar{\nu}$	$\lambda^{(1)}$	$(-\Delta\sigma_r) / (p_i)_{sh} = (-\Delta\bar{\sigma}_r) / (p_i)_{sh}$ at $r = \lambda R$ ; $t = \infty$	
		CONSTANT	LOGARITHMIC
0.25	10	0.3300	0.1200
	20	0.3325	0.1161
	30	0.3329	0.1146
0.35	10	0.2285	0.0831
	20	0.2302	0.0804
	30	0.2305	0.0793
(1) for an elastic-perfectly plastic material $\lambda = (G/s_u)^{1/2}$			

Table 2.6: Total and effective radial stress changes after consolidation at  $r = \lambda R$  according to linear solutions. (After Baligh and Kavvas, 1980)

input parameters	Beece and Burland (1968) (1)		Carter et al. (1979c) (1) Baniolph et al. (1978b)		Laboratory tests on resedimented BIC	comments
	elastic strains neglected	elastic strains included	elastic strains neglected	elastic strains included		
$\lambda$	0.15	0.15	0.15	0.15	-	slope of the virgin, $e$ vs. $\ln \bar{\sigma}$
$\kappa$	0.00	0.03	0.00	0.03	-	slope of rebound, $e$ vs. $\ln \bar{\sigma}$
$M$	-	-	1.20	1.20	-	see note (2)
$\bar{\psi}$	30°	30°	-	-	-	see definitions
$K_0$ (1)	0.55	0.55	0.55	0.55	-	value used in analyses; see note (2)
$e_0$	1.16	1.16	1.16	1.16	-	equivalent to using critical state void ratio $e_{ce}$
$\frac{G}{E}$ (1)	-	2.17	-	2.17	-	
equivalent input parameters						
CR (1)	0.160	0.160	0.160	0.160	0.17 ± 0.03	compression ratio CR = $\Delta \epsilon_c / (\Delta \log \bar{\sigma}_c)$ (at $e_0 = 1.16$ )
RR (1)	0.000	0.032	0.000	0.032	0.025 - 0.05	recompression ratio RR = $-\Delta \epsilon_c / (\Delta \log \bar{\sigma}_c)$ (at $e_0 = 1.16$ )
$\bar{\psi}_{TC}$	30°	30°	30°	30°	29° - 33° (13)	at max obliquity
predictions						
$K_0$ (1)	0.671	0.627	0.671	0.627	0.50 - 0.55	normally consolidated clay
$\bar{\psi}(TE)$	30°	30°	48.5° (1)	48.5° (1)	35° - 40° (11)	
$\bar{\psi}(PSC)$	30°	30°	43.8° (1)	43.8° (1)	34° (11)	at max obliquity (from $\bar{C}_{\theta}^U$ tests)
$\bar{\psi}(PSE)$	30°	30°	43.8° (1)	43.8° (1)	34° (11)	
$S_u/\bar{\sigma}_{vo}$ (TC)	0.270	0.295 (1)	0.270	0.295 (1)	0.328 (11)	$\bar{C}_{\theta}^U$ triaxial compression peak strength
$S_u/\bar{\sigma}_{vo}$ (TE)	0.256	0.264 (1)	0.270	0.295 (1)	0.130 (11)	$\bar{C}_{\theta}^U$ triaxial extension peak strength
$S_u/\bar{\sigma}_{vo}$ (PSC)	0.296 (1)	0.310 (1)	0.312	0.340 (1)	0.335 (11)	$\bar{C}_{\theta}^U$ plane strain compression peak strength
$S_u/\bar{\sigma}_{vo}$ (PSE)	0.296 (1)	0.310 (1)	0.312	0.340 (1)	0.175 (11)	$\bar{C}_{\theta}^U$ plane strain extension peak strength
$S_u/\bar{\sigma}_{vo}$ (PH)	0.296 (1)	0.223 (1)	0.312	0.340 (1)	0.210 (11)	$\bar{C}_{\theta}^U$ pressurometer
$S_u/\bar{\sigma}_{vo}$ (DSS)	0.296 (1)	0.310 (1)	0.312	0.340 (1)	0.200 (11)	$\bar{C}_{\theta}^U$ direct simple shear

Table 2.7: Model parameters and predictions of the Cam-Clay model for resedimented  $K_0$ -normally consolidated Boston Blue Clay. (After Balogh and Kavvasas, 1980)

TABLE 2.7 (Cont.)

DEFINITIONS

$$(1) \quad q = \frac{1}{\sqrt{2}} \{ (\bar{\sigma}_1 - \bar{\sigma}_2)^2 + (\bar{\sigma}_2 - \bar{\sigma}_3)^2 + (\bar{\sigma}_3 - \bar{\sigma}_1)^2 \}^{1/2}; \quad q \geq 0$$

$$(2) \quad \bar{\sigma} = \frac{1}{3} (\bar{\sigma}_1 + \bar{\sigma}_2 + \bar{\sigma}_3); \quad \bar{\sigma}_1, \bar{\sigma}_2, \bar{\sigma}_3 \text{ are major, intermediate and minor principal effective stresses } (\bar{\sigma}_1 \geq \bar{\sigma}_2 \geq \bar{\sigma}_3)$$

$$(3) \quad \bar{\phi} = \arcsin \left[ \frac{\bar{\sigma}_{1f} - \bar{\sigma}_{3f}}{\bar{\sigma}_{1f} + \bar{\sigma}_{3f}} \right] \quad \text{or} \quad \frac{\bar{\sigma}_{1f}}{\bar{\sigma}_{3f}} = \frac{1 + \sin \bar{\phi}}{1 - \sin \bar{\phi}} = N_{\phi};$$

subscript f refers to failure (according to a failure criterion)

$$(4) \quad s_u = \frac{\bar{\sigma}_{1f} - \bar{\sigma}_{3f}}{2}$$

NOTES

(1) Assuming Mohr-Coulomb failure criterion:

- $\bar{\phi}$  is independent of failure mode
- The yield surface is an ellipse with an associated flow rule, but, at failure, violates incompressibility requirement

(2) Assuming Extended Mises criterion:

- $M = \frac{q_f}{\sigma_f}$

- M is evaluated from triaxial compression test ( $\bar{\sigma}_2 = \bar{\sigma}_3$ )

$$\bar{\phi} \text{ (TC)} = \arcsin \frac{3M}{6 + M}$$



TABLE 2.7 (Cont.)

- The yield surface is an ellipse with an associated flow rule;

therefore, in plane strain failures  $\bar{\sigma}_{2f} = \frac{1}{2} (\bar{\sigma}_{1f} + \bar{\sigma}_{3f})$

(3) For  $M = 1.2$  we have:

- neglecting elastic strains:  $K_o = 0.671$

- without neglecting elastic strains:  $K_o = 0.627$

(4)  $K$  is the bulk elastic modulus:  $K = \frac{\bar{\sigma}(1+e)}{\kappa}$

We assume  $\frac{K}{G} = \frac{2(1+\bar{\nu})}{3(1-2\bar{\nu})}$  and  $\bar{\nu} = 0.3$

(5)  $CR = \frac{2.3\lambda}{(1+e)}$   $RR = \frac{2.3\kappa}{(1+e)}$

(6)  $\bar{\phi}_{(TE)} = \arcsin \left( \frac{3M}{6-M} \right)$

(7)  $\bar{\phi}_{(PSC)} = \bar{\phi}_{(PSE)} = \arcsin \left( \frac{M}{\sqrt{3}} \right)$

(8) Assuming  $\bar{\sigma}_{2f} = \frac{1}{2} (\bar{\sigma}_{1f} + \bar{\sigma}_{3f})$

(9) Numerically evaluated

(10) Numerical computation of  $\bar{\sigma}_{1f}$ ,  $\bar{\sigma}_{2f}$ ,  $\bar{\sigma}_{3f}$ , yielded that  $\bar{\sigma}_{2f} \neq \frac{1}{2} (\bar{\sigma}_{1f} + \bar{\sigma}_{3f})$

(11) After Ladd et al. (1977)

- (1) The pile shaft is circular and sufficiently long, such that:
  - (a) the effects of pile tip and ground surface can be neglected, i.e.  $\epsilon_z = 0$  and,
  - (b) the problem exhibits rotational symmetry, i.e. no dependence on the circumferential coordinate,  $\theta$ .
- (2) The pile material is very rigid compared to the soil.
- (3) When the shear surface of slippage develops in the soil adjacent to the pile, its radial distance,  $\Delta R$ , from the pile wall is small compared to the pile radius  $R$ , i.e.  $\Delta R/R \ll 1$ .

Table 2.8: Simplifying assumptions in the analysis of the shaft resistance of piles in clays.

Soil Type	(1) $f_s / \bar{\sigma}_{hc}$	Assumption (2) at failure	Backfigured $\bar{\phi}$ at max shear stress	$f_s / \bar{\sigma}_{hf}$	Estimated $\phi$ by Ladd and Edgers (1972)
A Normally Consolidated CL Boston Blue Clay ( $K_o = 0.50$ )	0.200	①	19.3°	0.351	30°
		②	20.6°		
		③	90°		
B Normally Consolidated CH Clay ( $K_o = 0.65$ )	0.250	①	22.6	0.417	25°
		②	24.6°		
		③	45.9°		

- (1) At maximum shear stress  $f_s$
- (2) ① Shear surface coincides with plane of maximum obliquity  
 ② Shear stress on shear surface is a maximum  
 ③ Total stress increments are proportional to strain increments.

Table 2.9: Backfigured friction angles from Direct Simple Shear Tests.  
 (After Baligh and Kavvas, 1980)

(Undrained shear strength)  $s_u = \left| \sigma_{1f} - \sigma_{3f} \right| / 2$

(For triaxial compression and extension)  $s_u = q_f / 2$

(For all plane strain modes)  $= q_f / \sqrt{3}$

$$q_f = \eta \bar{\sigma}_f$$

$$\bar{\sigma}_f = \frac{2a}{1 + (\eta/M)^2}$$

$$a = \frac{1}{2\bar{\sigma}_0} \left[ \bar{\sigma}_0^2 + \frac{q_0}{M^2} \right]$$

$$\bar{\sigma}_0 = \left( \frac{1 + 2K_0}{3} \right) \bar{\sigma}_{v_0}$$

$$q_0 = (1 - K_0) \bar{\sigma}_{v_0}$$

	Assumed Failure Criterion	
	Extended Von Mises	Mohr-Coulomb
Input parameters	$M(=\eta) \text{ and } K_0$	$\bar{\phi}, K_0$
Triaxial compression	$\sin \bar{\phi} = \frac{3M}{6+M}$	$\eta = M = \frac{6 \sin \bar{\phi}}{3 - \sin \bar{\phi}}$
Triaxial extension	$\sin \bar{\phi} = \frac{3M}{6-M}$	$\eta = \frac{6 \sin \bar{\phi}}{3 + \sin \bar{\phi}}$
All plane strain failures	$\sin \bar{\phi} = \frac{M}{\sqrt{3}}$	$\eta = \sqrt{3} \sin \bar{\phi}$

$$q = \frac{1}{\sqrt{2}} \{ (\bar{\sigma}_1 - \bar{\sigma}_2)^2 + (\bar{\sigma}_2 - \bar{\sigma}_3)^2 + (\bar{\sigma}_3 - \bar{\sigma}_1)^2 \}^{1/2}$$

$$\bar{\sigma} = \frac{1}{3} (\bar{\sigma}_1 + \bar{\sigma}_2 + \bar{\sigma}_3)$$

Table 2.10: Equations for predicting the friction angle ( $\bar{\phi}$ ) and the undrained shear strength ( $s_u$ ) of normally consolidated clays based on the Cam-Clay model when elastic strains are neglected.

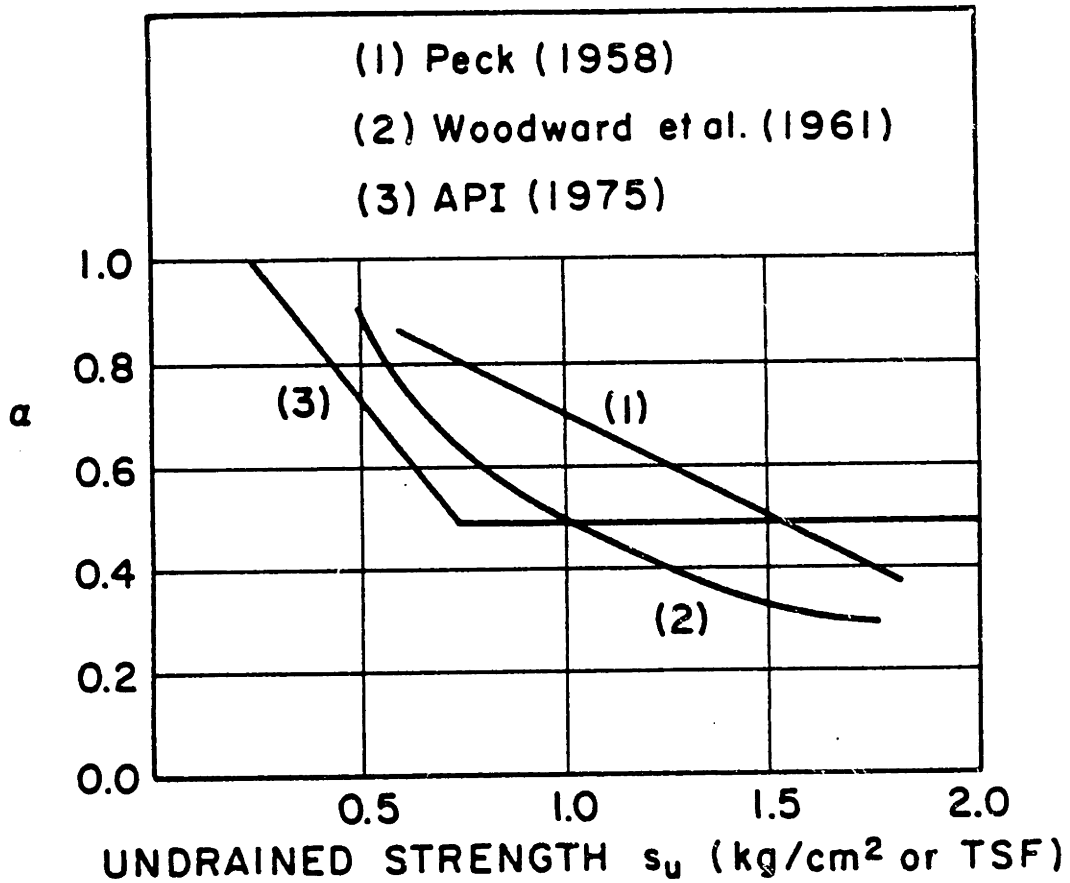


Figure 2.1: Compilation of  $\alpha$ -factors ( $\alpha=f_s/s_u$ ) by Peck (1958), Woodward, et al., (1961) and API (1975).  $s_u$  obtained from unconfined compression tests.

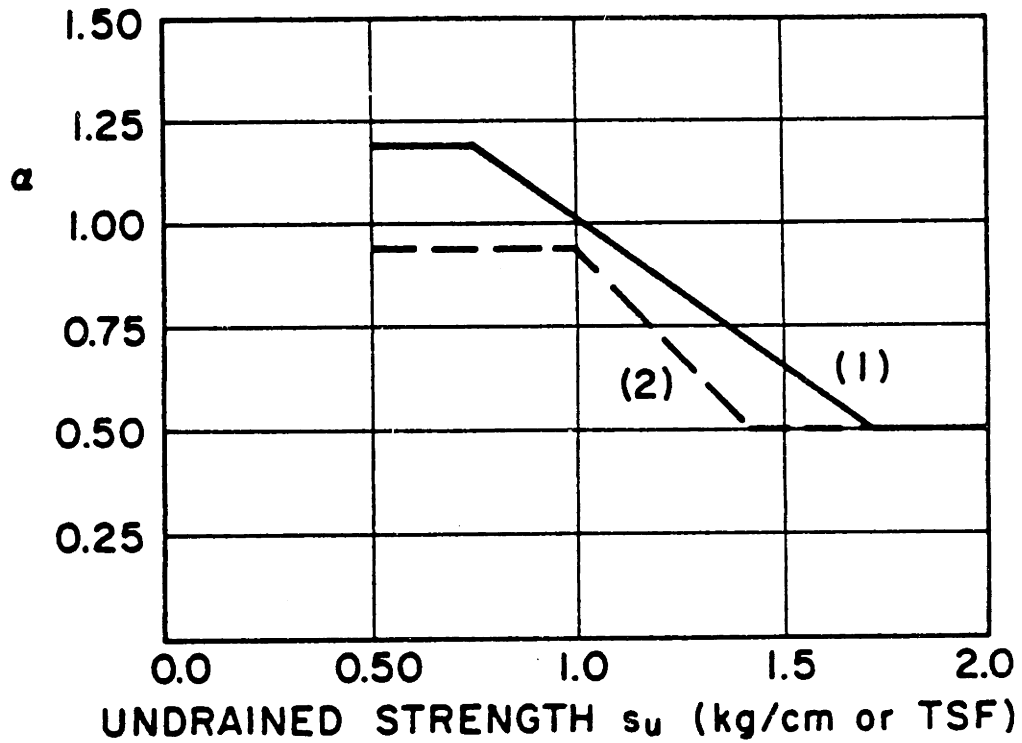


Figure 2.2: Compilation of  $\alpha$ -factors ( $\alpha=f_s/s_u$ ) by Tomlinson (1971). For description see Table 2.2.

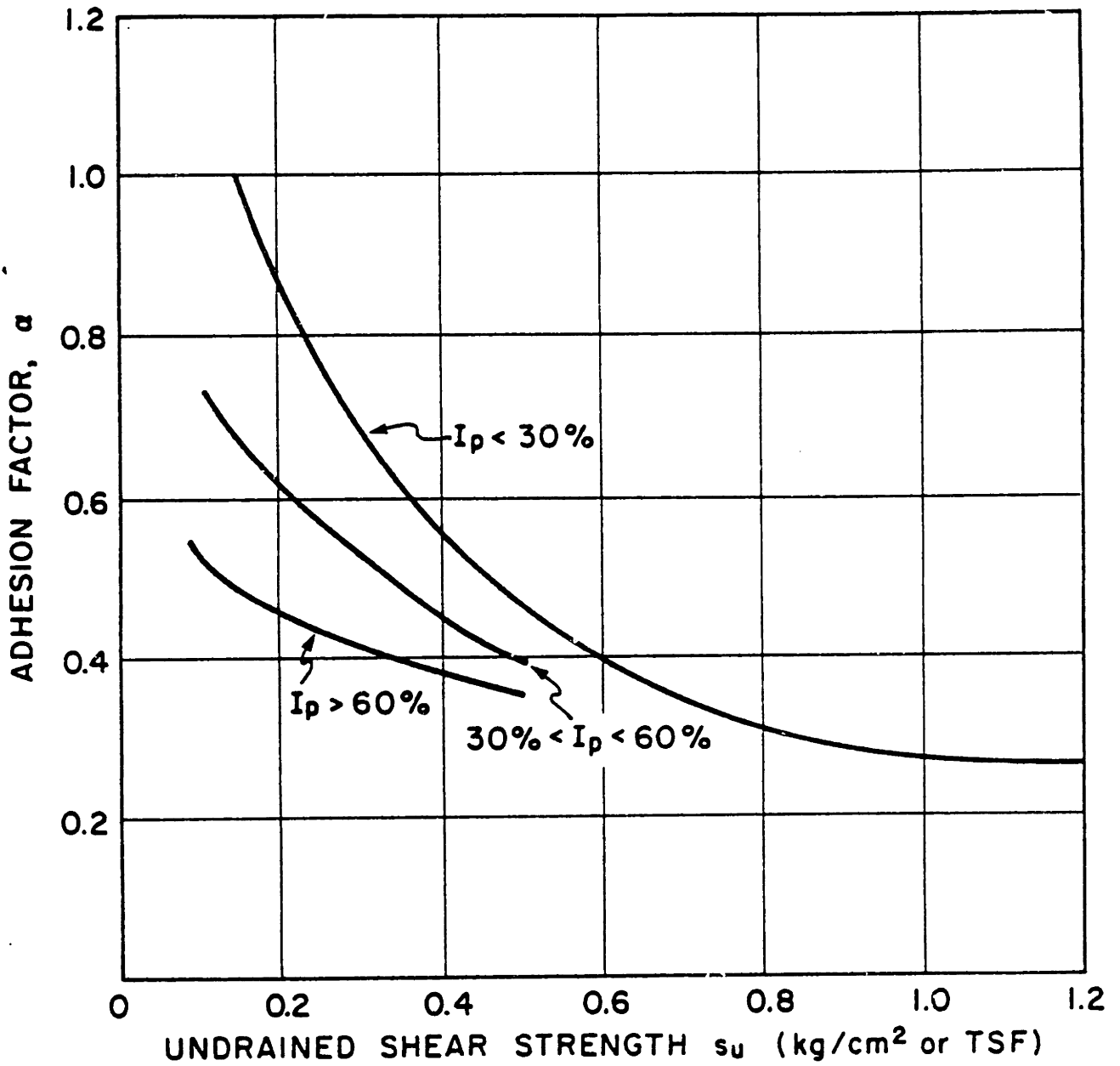


Figure 2.3: Relationship between average Adhesion Factor  $\alpha$ , and undrained shear strength for driven piles in Clay. (After Flaate, 1968).  $s_u$  obtained from field vane tests.

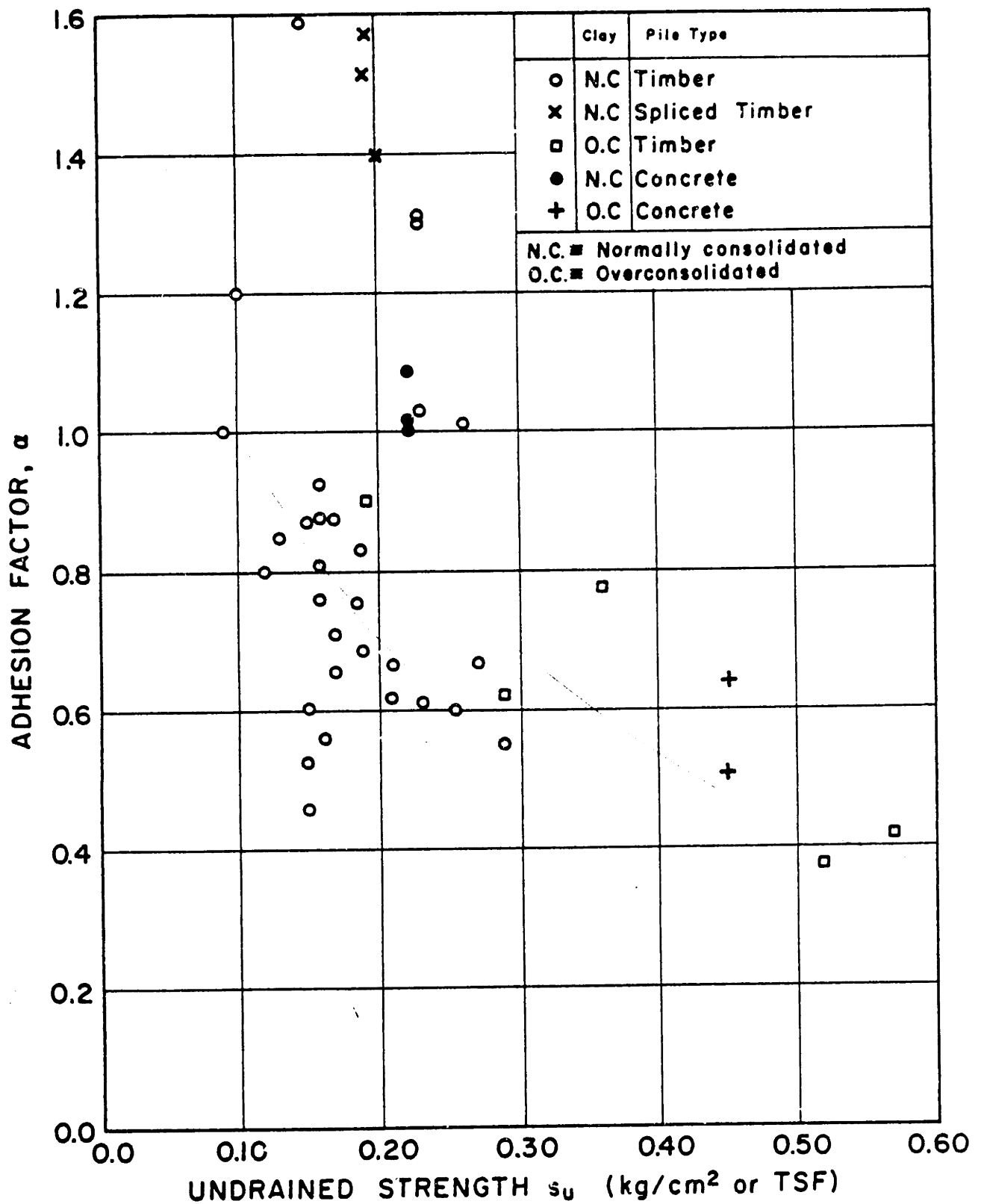


Figure 2.4: Average Adhesion parameter  $\alpha$  versus  $s_u$  (After Flaate and Selnes, 1977).  $s_u$  obtained from field vane tests.



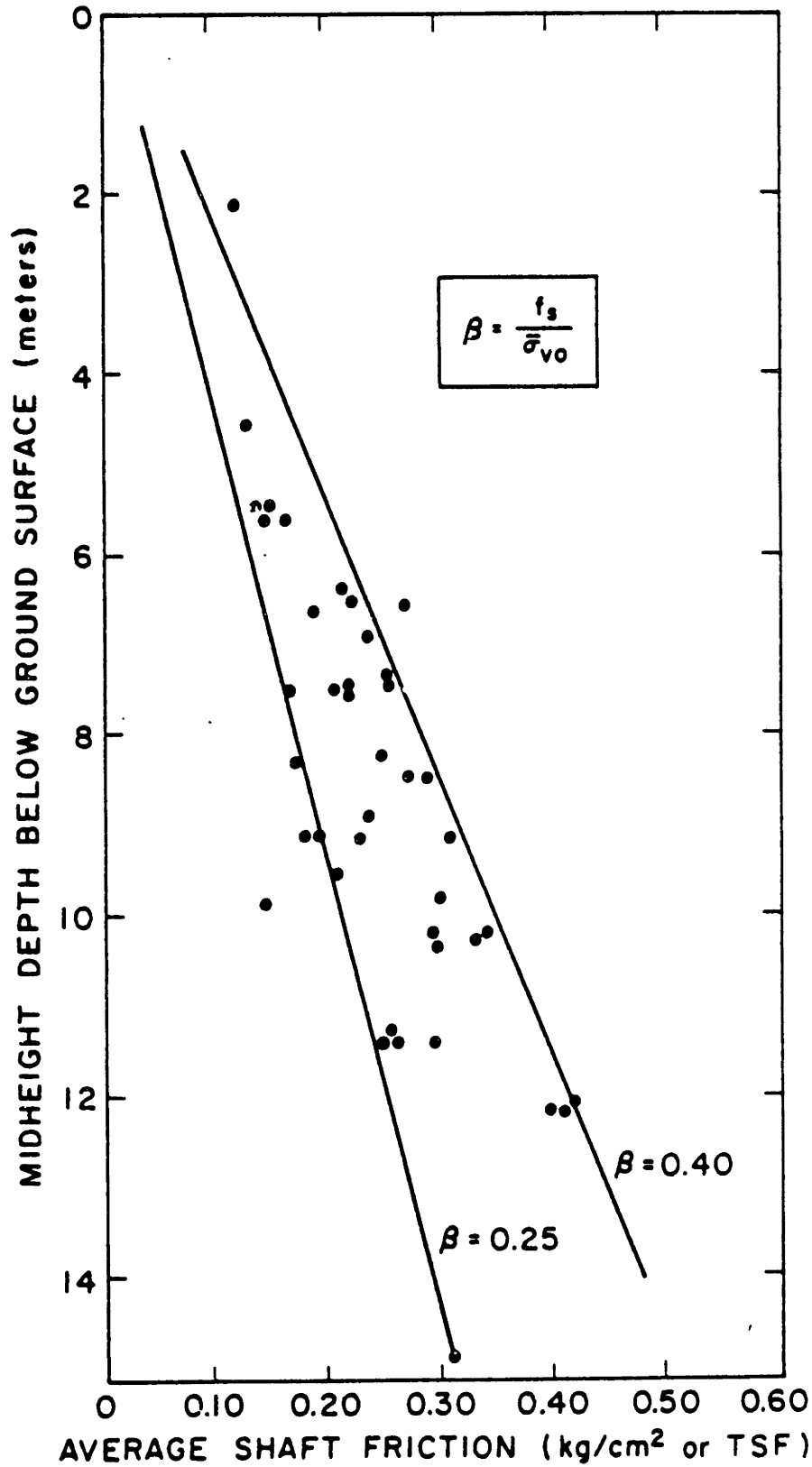


Figure 2.5: Average shaft friction vs midheight depth for driven piles in soft to medium clays (After Burland, 1973).

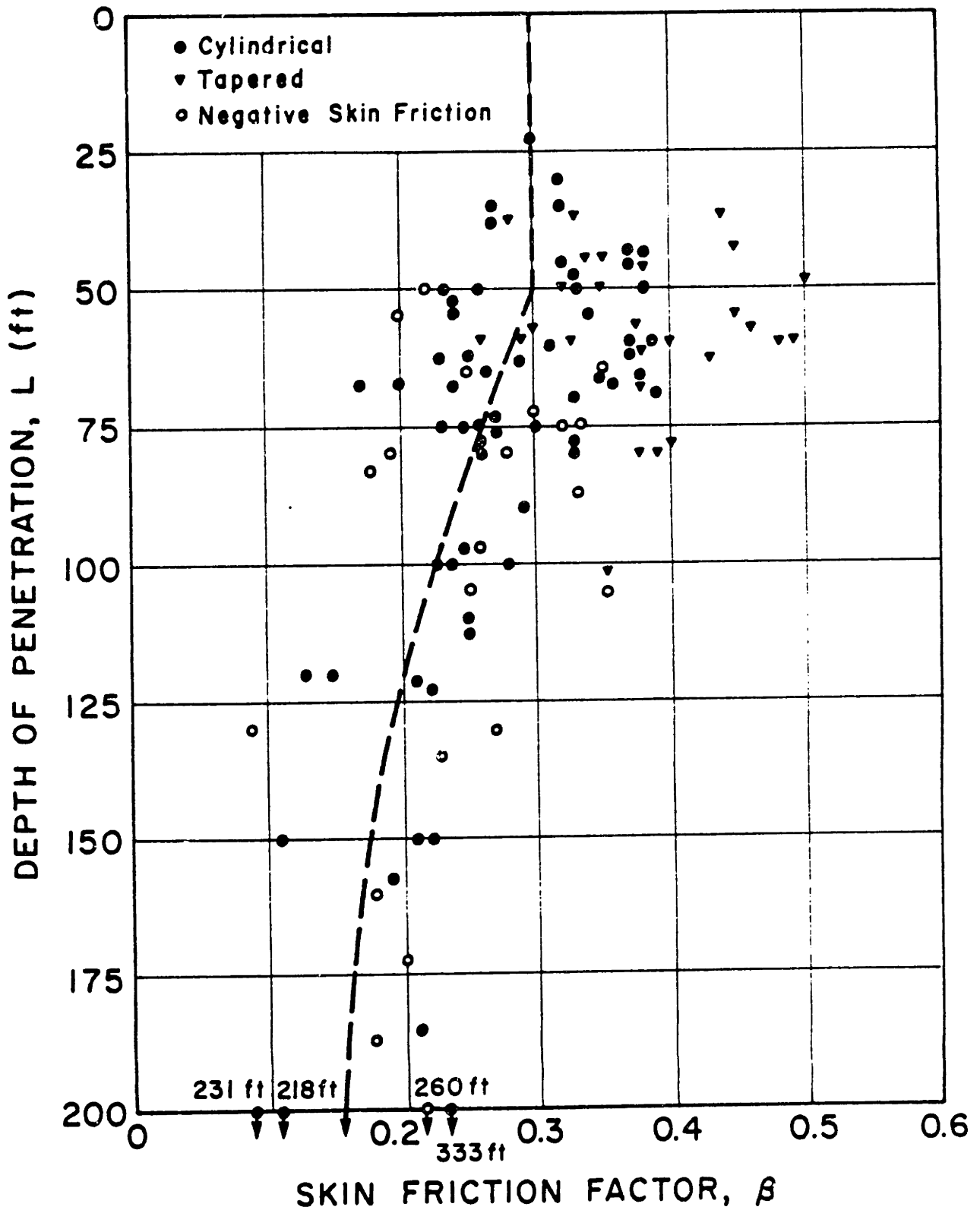


Figure 2.6: Skin friction factor  $\beta$  vs depth for soft to medium clays (After Meyerhof, 1976).

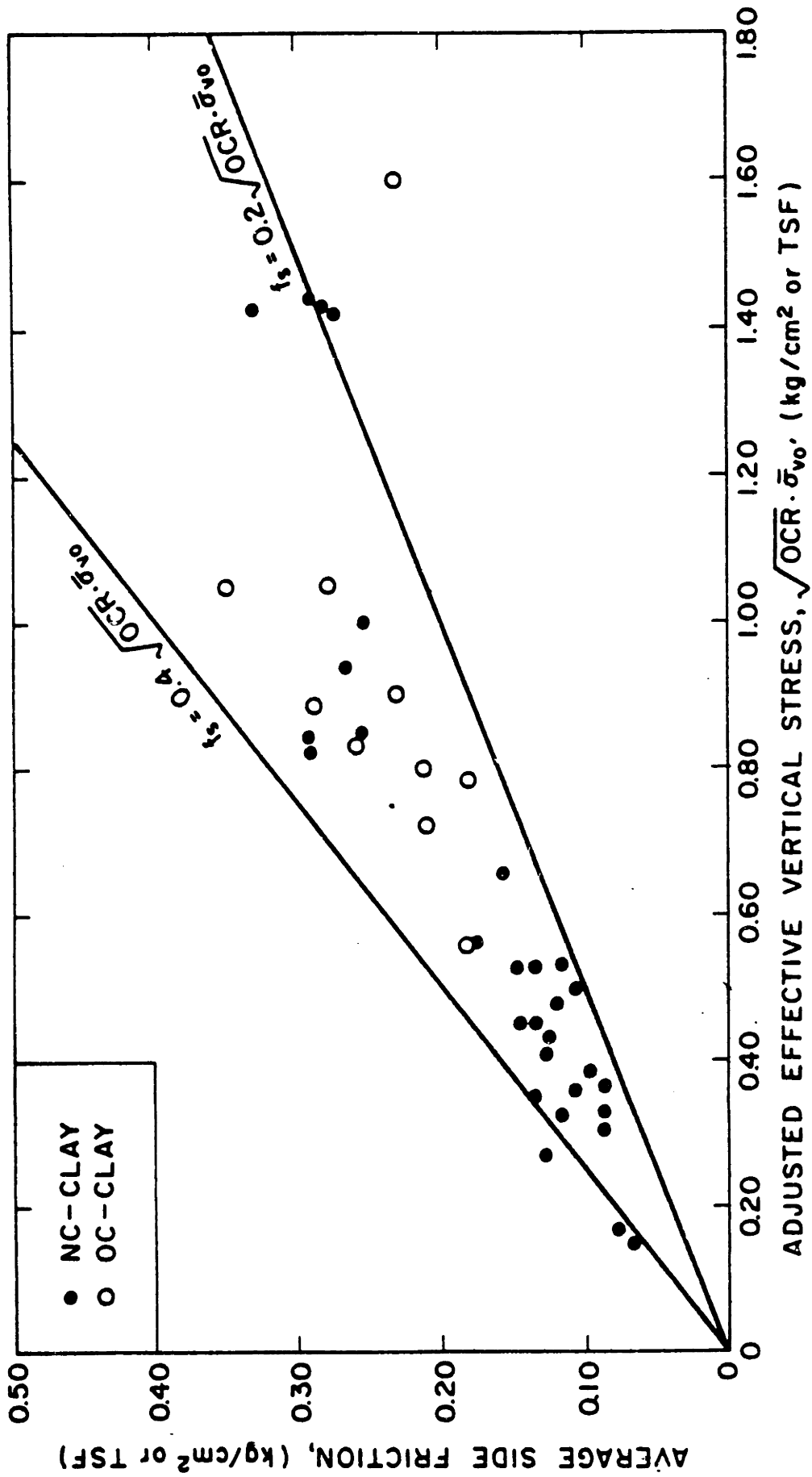


Figure 2.7: Observed side friction vs adjusted effective vertical stress (After Flaate and Selnes, 1977).

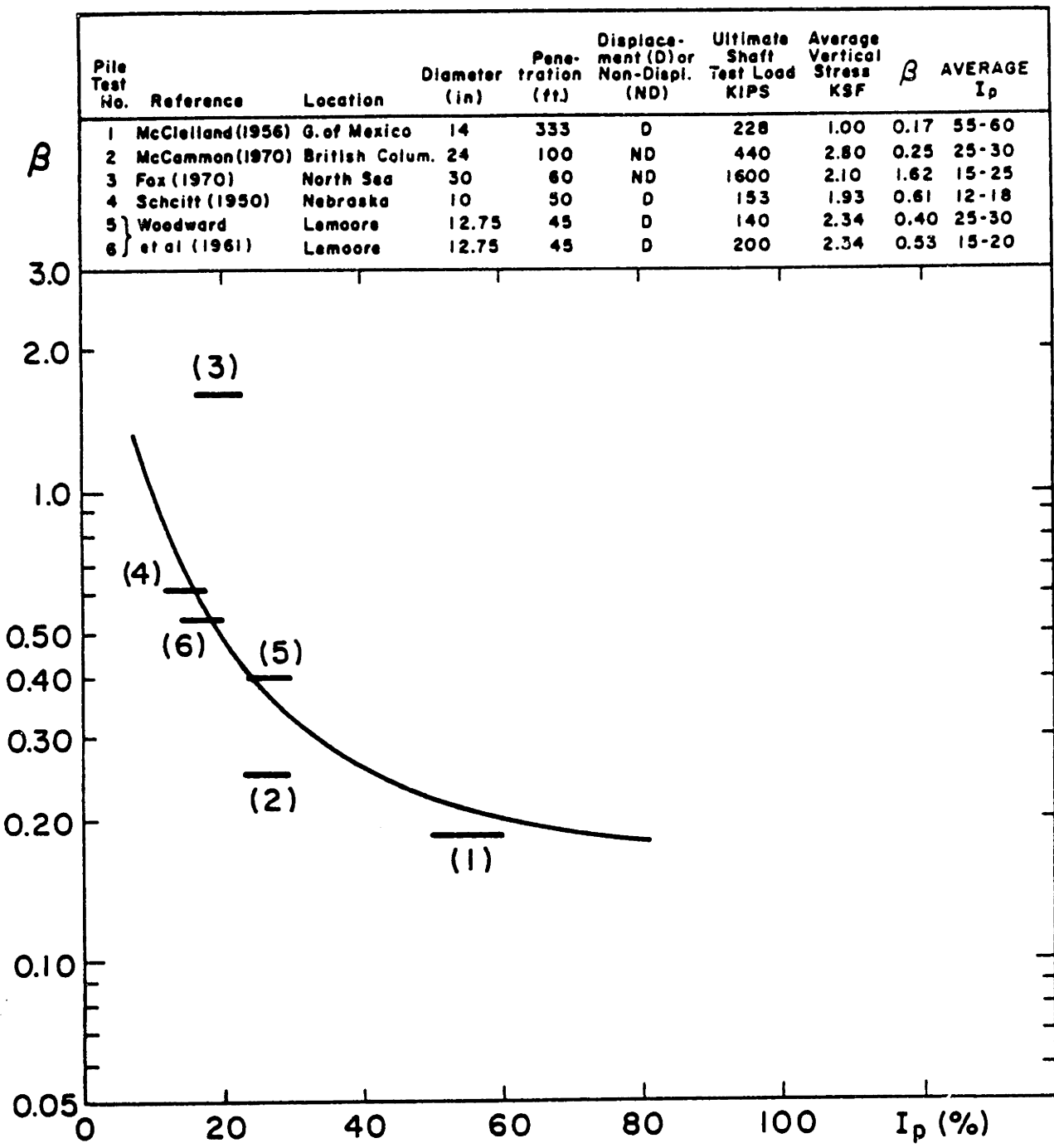


Figure 2.8:  $\beta$  Adhesion Factor versus Plasticity Index (After Bea, 1975).

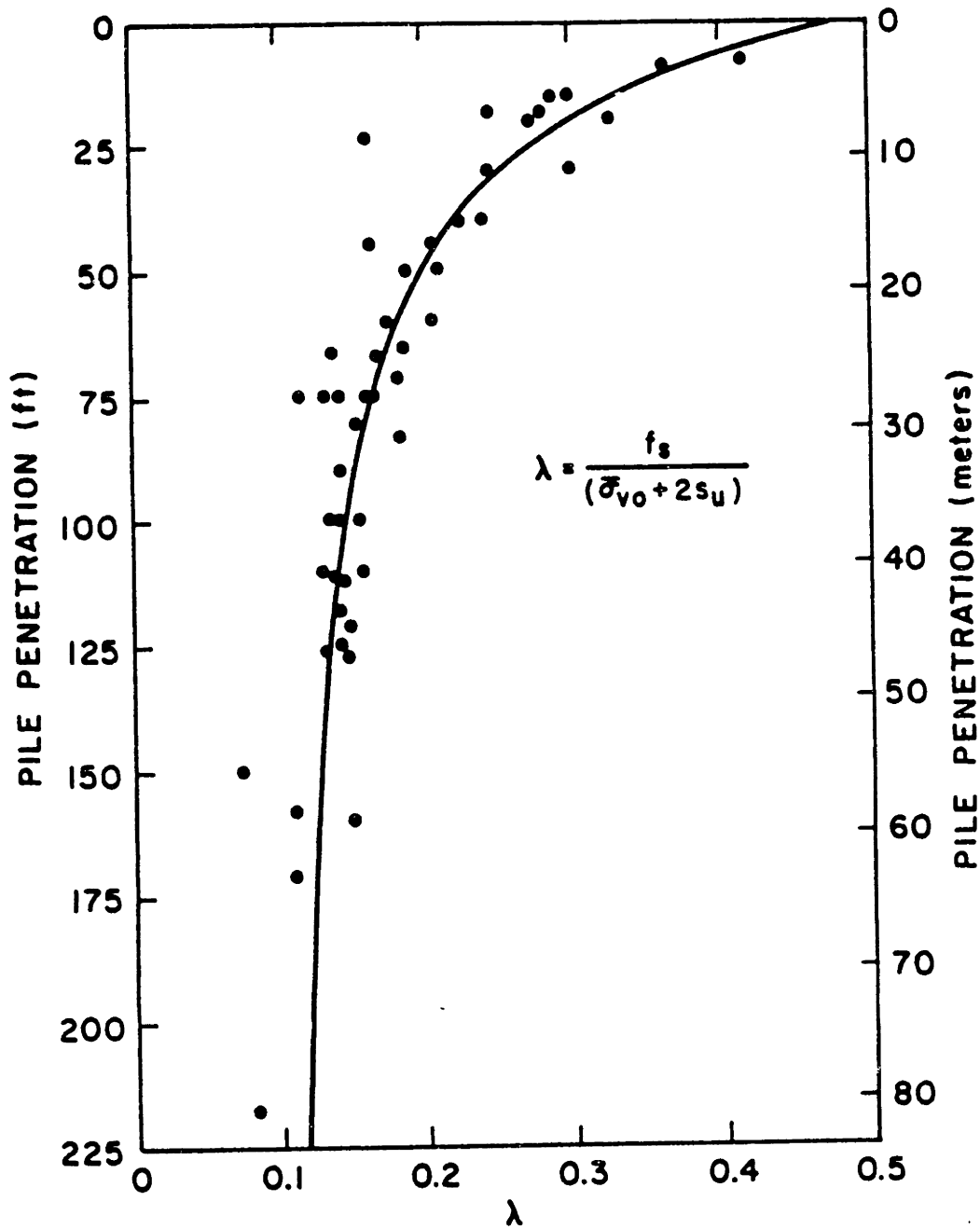
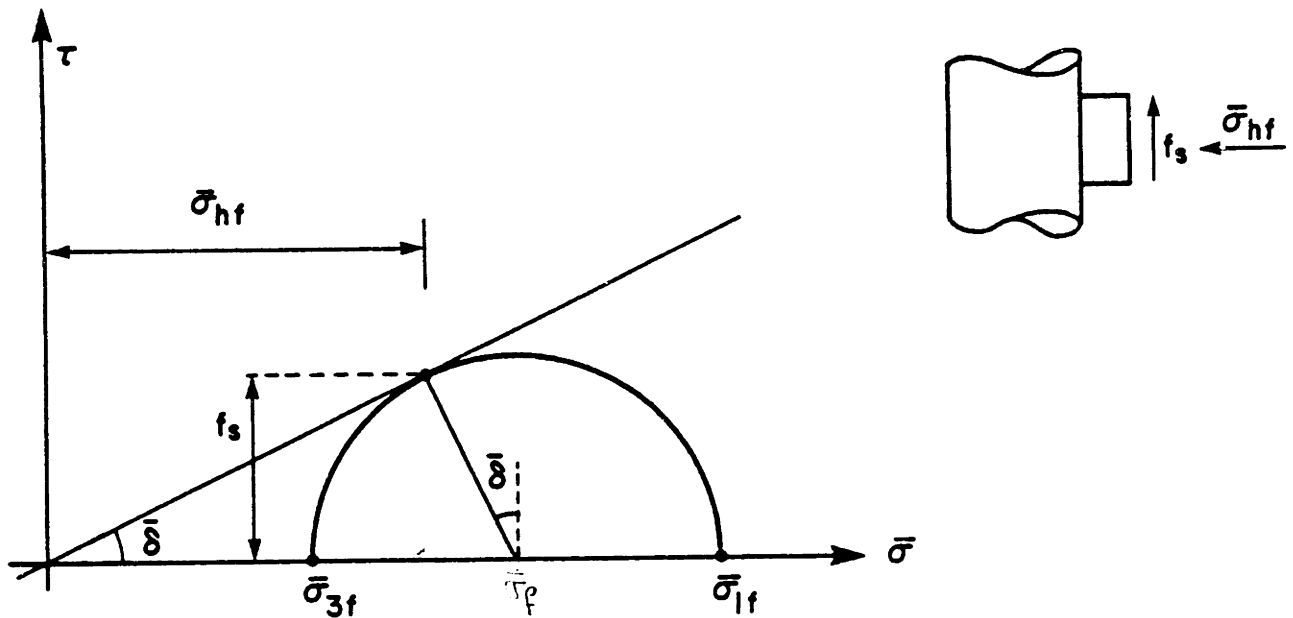


Figure 2.9: Frictional capacity,  $\lambda$ , vs. pile penetration (After Vijayvergiya and Focht, 1972).  $s_u$  obtained from miniature vane test or unconfined compression.



$$f_s = \left( \frac{\bar{\sigma}_{1f} - \bar{\sigma}_{3f}}{2} \right) \cos \bar{\delta}$$

Modified Cam-Clay (for  $\bar{\sigma}_{2f} = \bar{\sigma}_{3f}$ ):  $q_f = \bar{\sigma}_{1f} - \bar{\sigma}_{3f} = M\bar{\sigma}_f$

where:  $M = \frac{6 \cdot \sin \bar{\phi}}{3 - \sin \bar{\phi}}$

so:  $f_s = \frac{M}{2} \bar{\sigma}_f \cos \bar{\delta}$  (2.13)

**Fig. 2.10:** Relation between the limiting skin friction and the mean effective stress (at failure) at the pile-soil interface

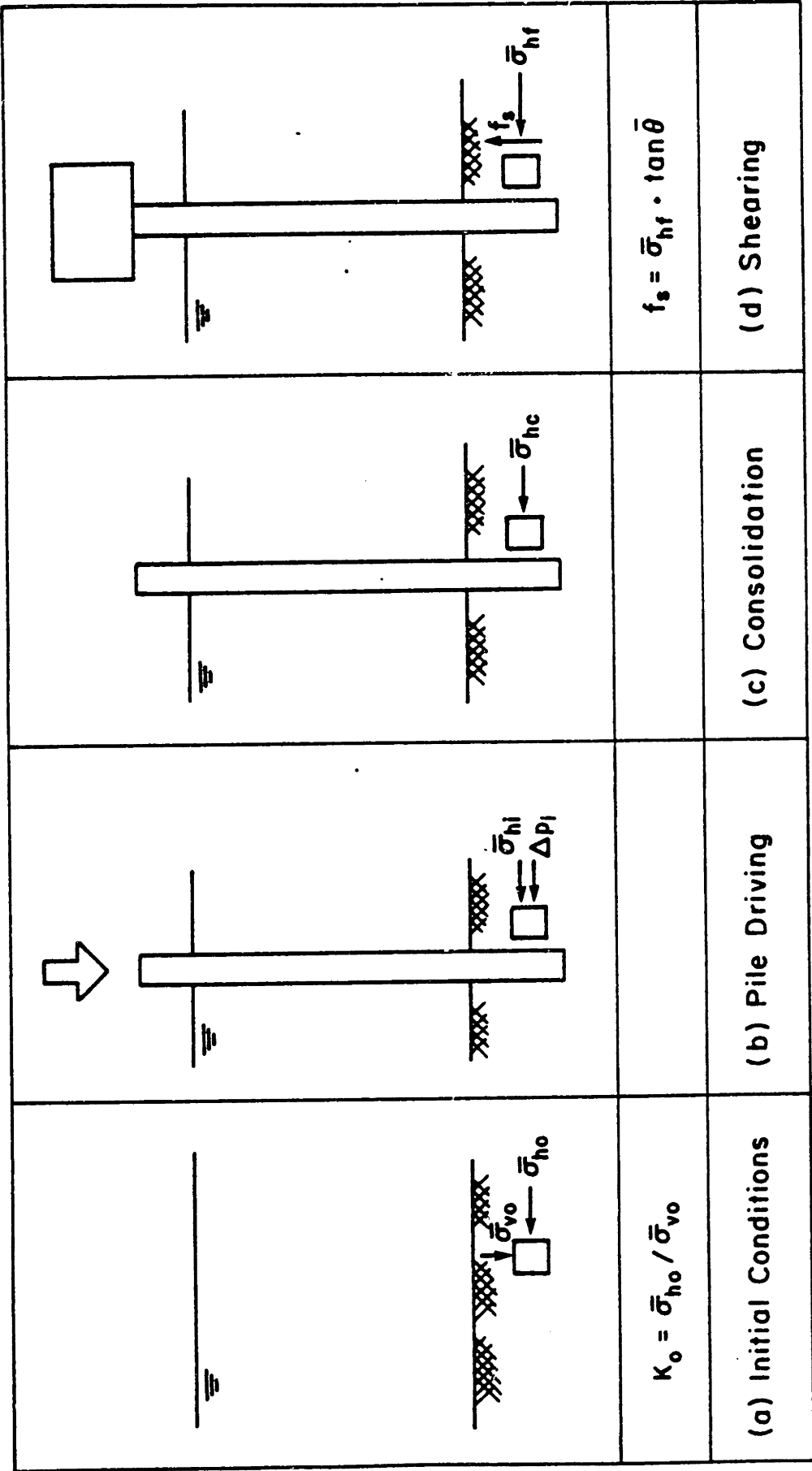


Figure 2.11: Sequence of events in the life of a pile driven in clay.

Re-molded	Un-disturbed	REFERENCE
○		Brooker & Ireland (1965)
□	■	R. Ladd (1964)
○	●	Bishop (1958)
	◆	Simons (1958)
	▲	Campanella & Vaid (1972)
⊙		Compiled by Wroth (1972)
	▼	Geot. Eng. Inc. (1976)
☆		Abdelhamid & Krizek (1976)

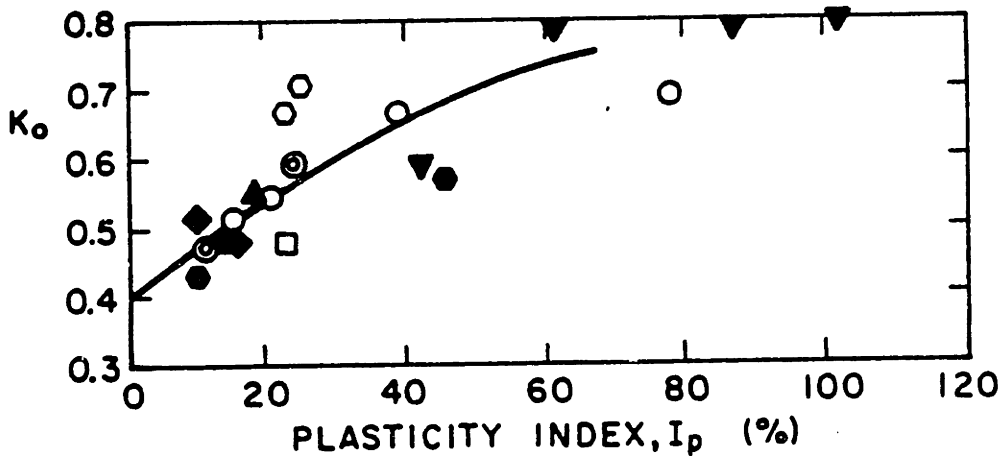
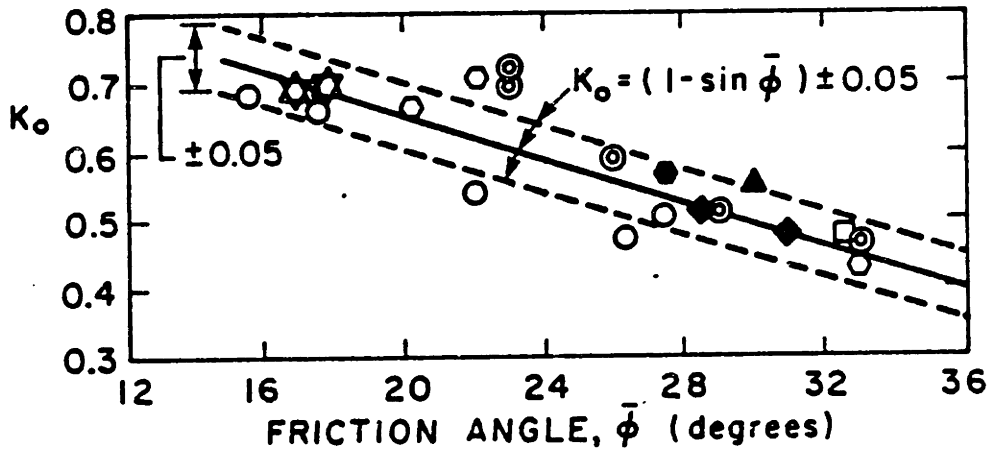


Figure 2.12:  $K_0$  of normally consolidated clays vs (a) friction angle and (b) Plasticity Index. (After Ladd and Edgers, 1972).



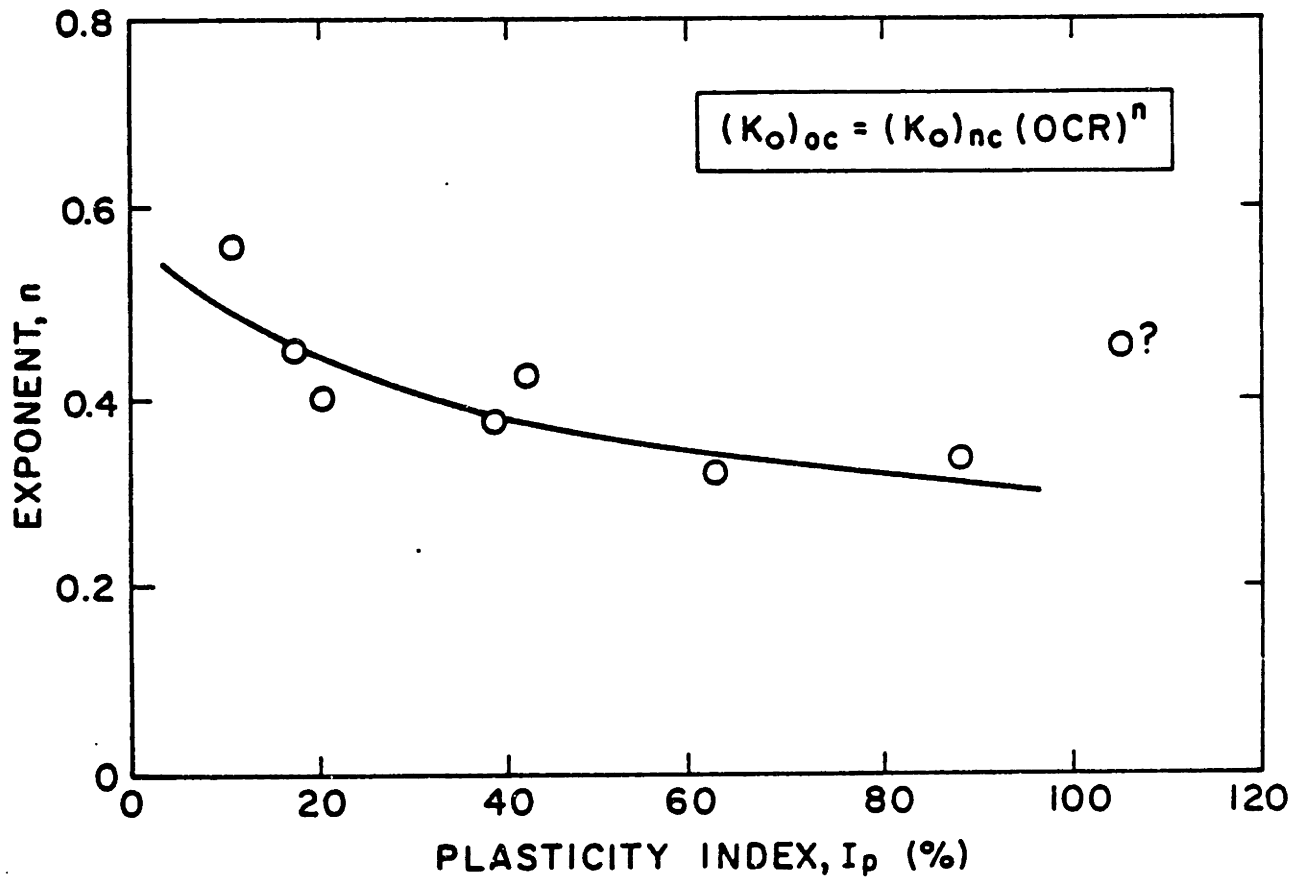


Figure 2.13: Variation of  $K_o$  exponent 'n' with Plasticity Index. (After Esrig et al., 1978)

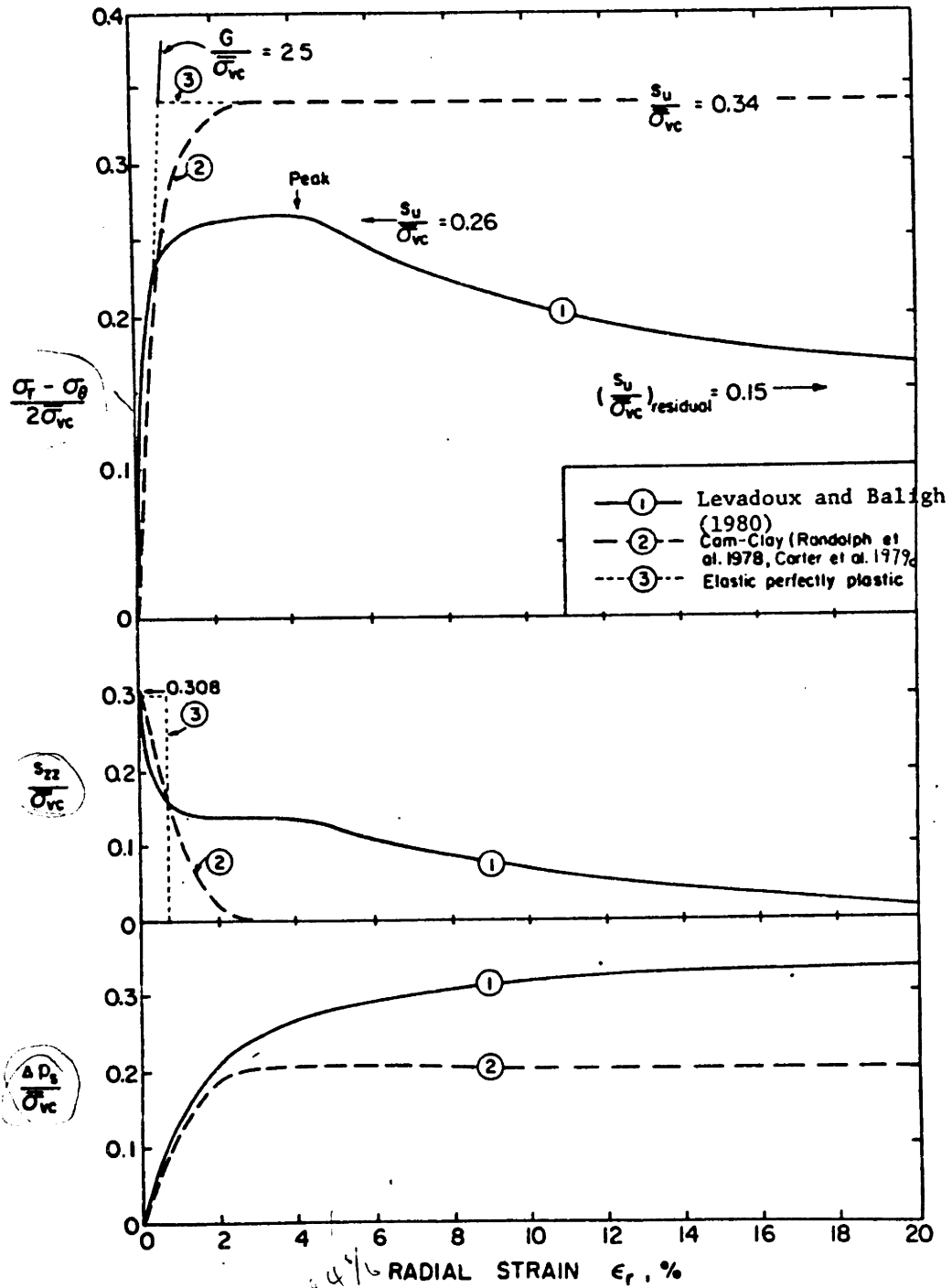


Figure 2.14: Comparison of predicted stress-strain curves for CK U undrained expansion of a cylindrical cavity in normally consolidated Boston Blue Clay. (After Levadoux, 1980)

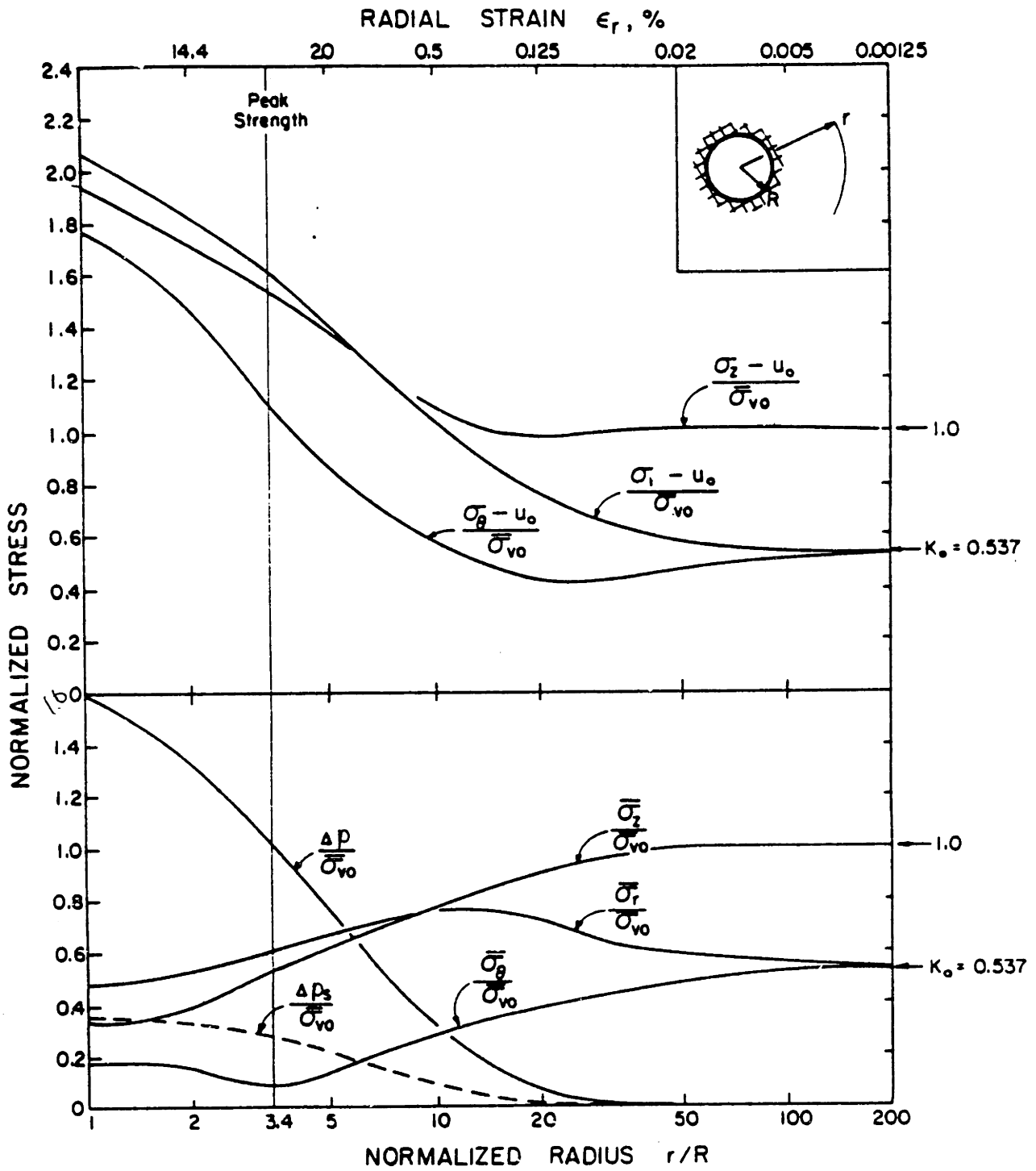


Figure 2.15: Predicted stress distributions after undrained expansion of a cylindrical cavity in normally consolidated BBC. (After Levadoux, 1980)

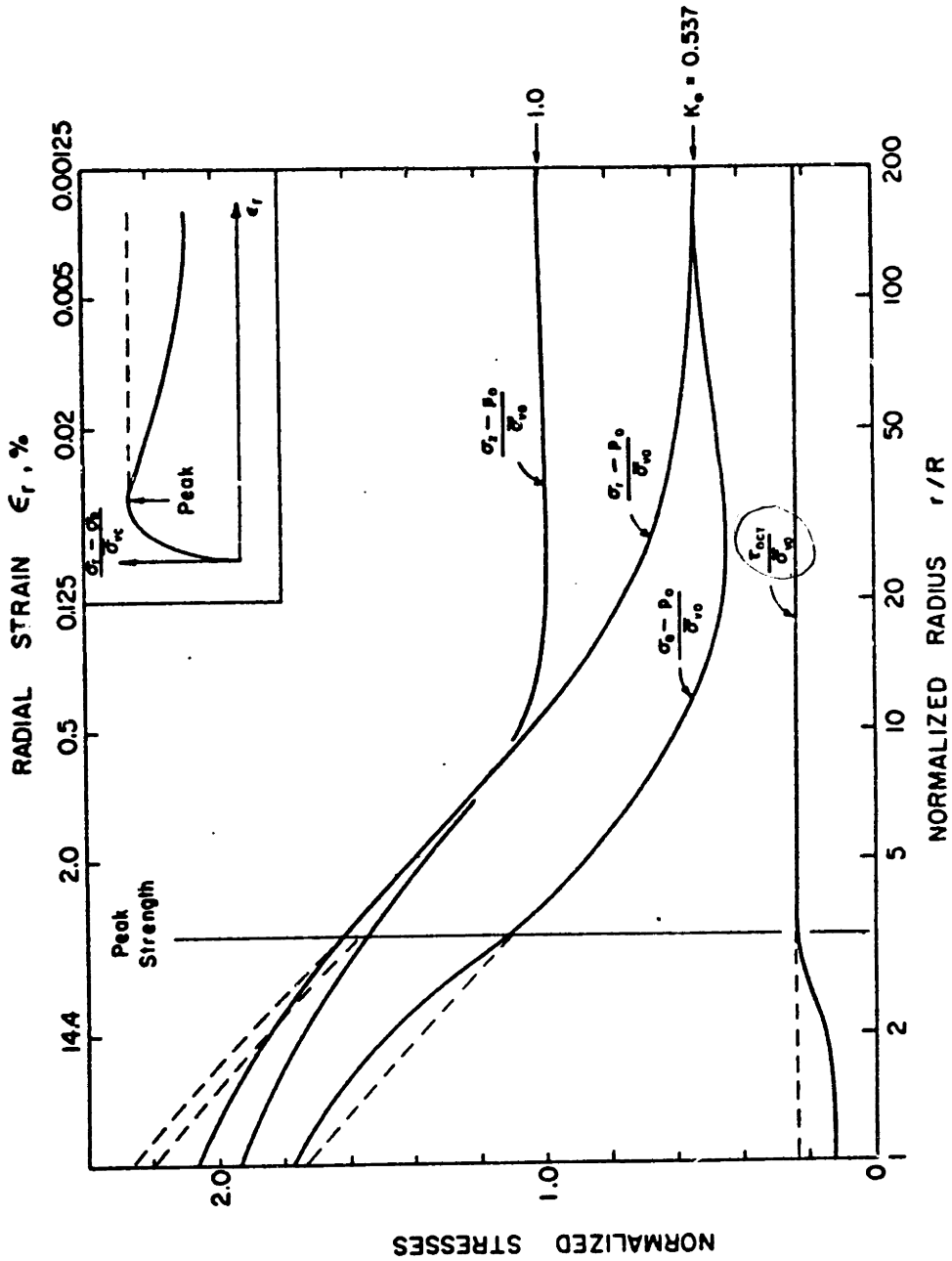


Figure 2.16: Effects of strain-softening on the stress distributions after expansion of a cylindrical cavity in normally consolidated Boston Blue Clay. (After Levadoux, 1980)

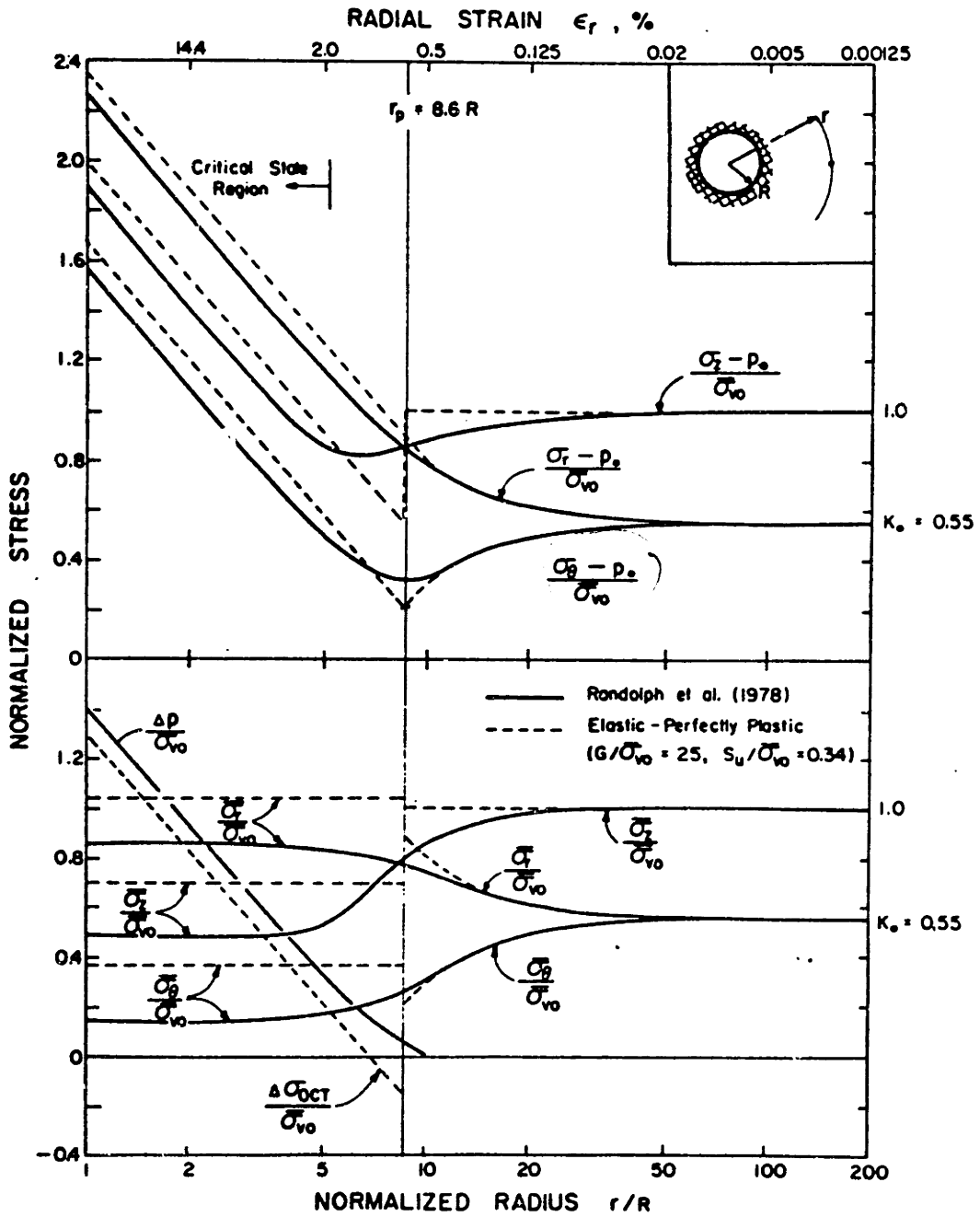


Figure 2.17: Comparison of predicted stress distributions after expansion of a cylindrical cavity: modified Cam-Clay and elastic-perfectly materials (OCR = 1). (After Levadoux, 1980)

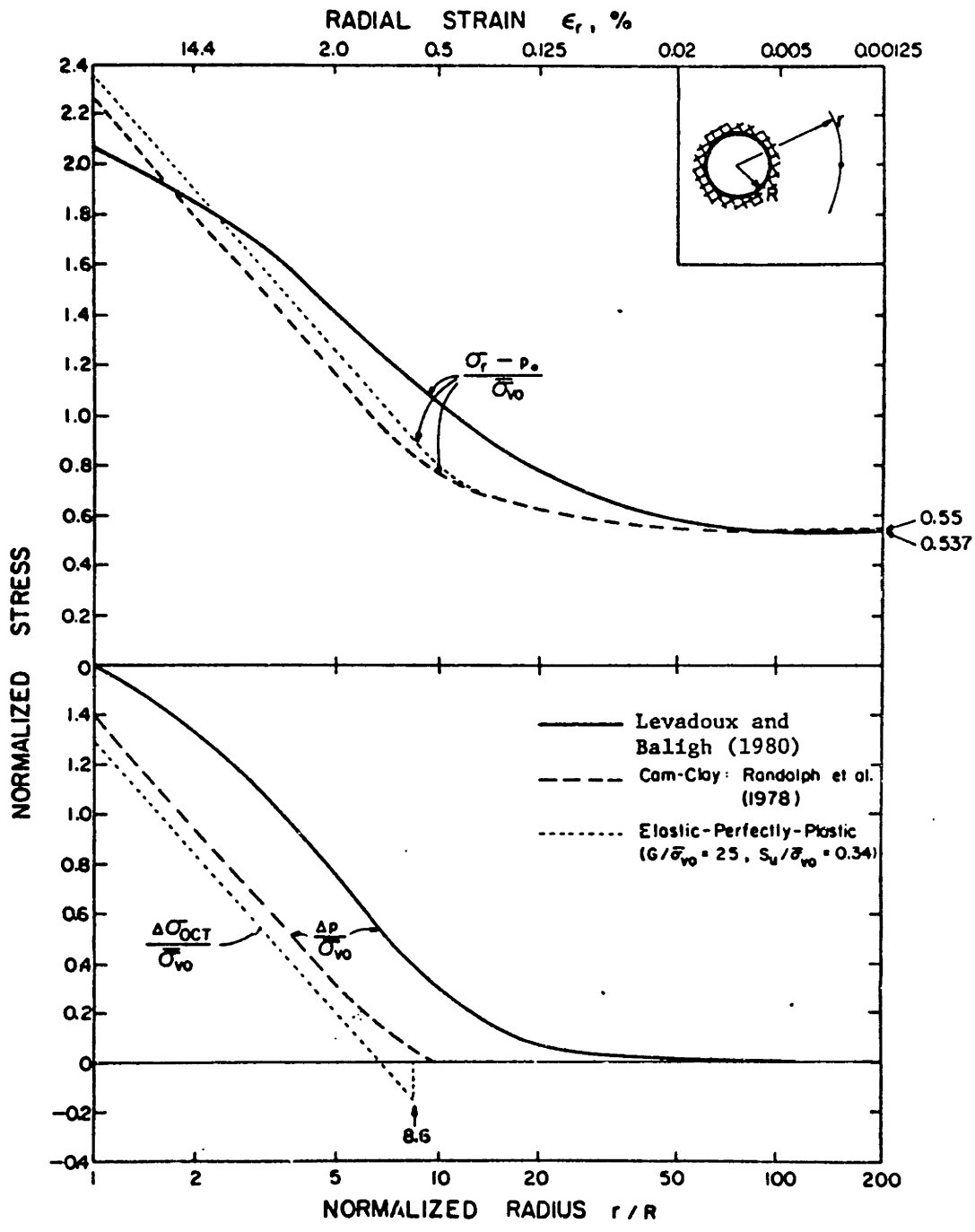


Figure 2.18: Comparison of three predictions for the stress distributions after undrained expansion of a cylindrical cavity in normally consolidated Boston Blue Clay. (After Levadoux, 1989)

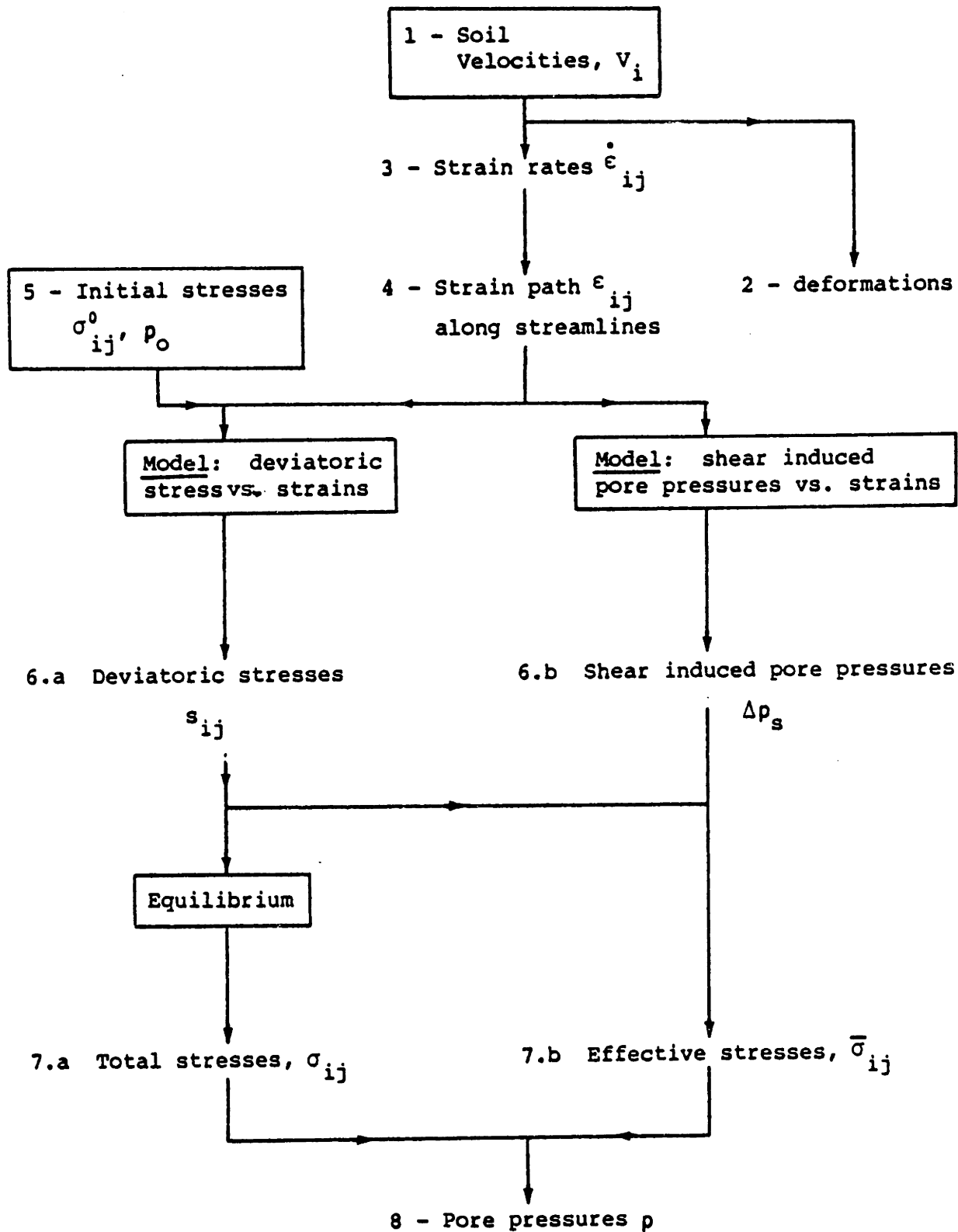


Figure 2.19: Application of the strain path method to deep steady pile penetration in clays.

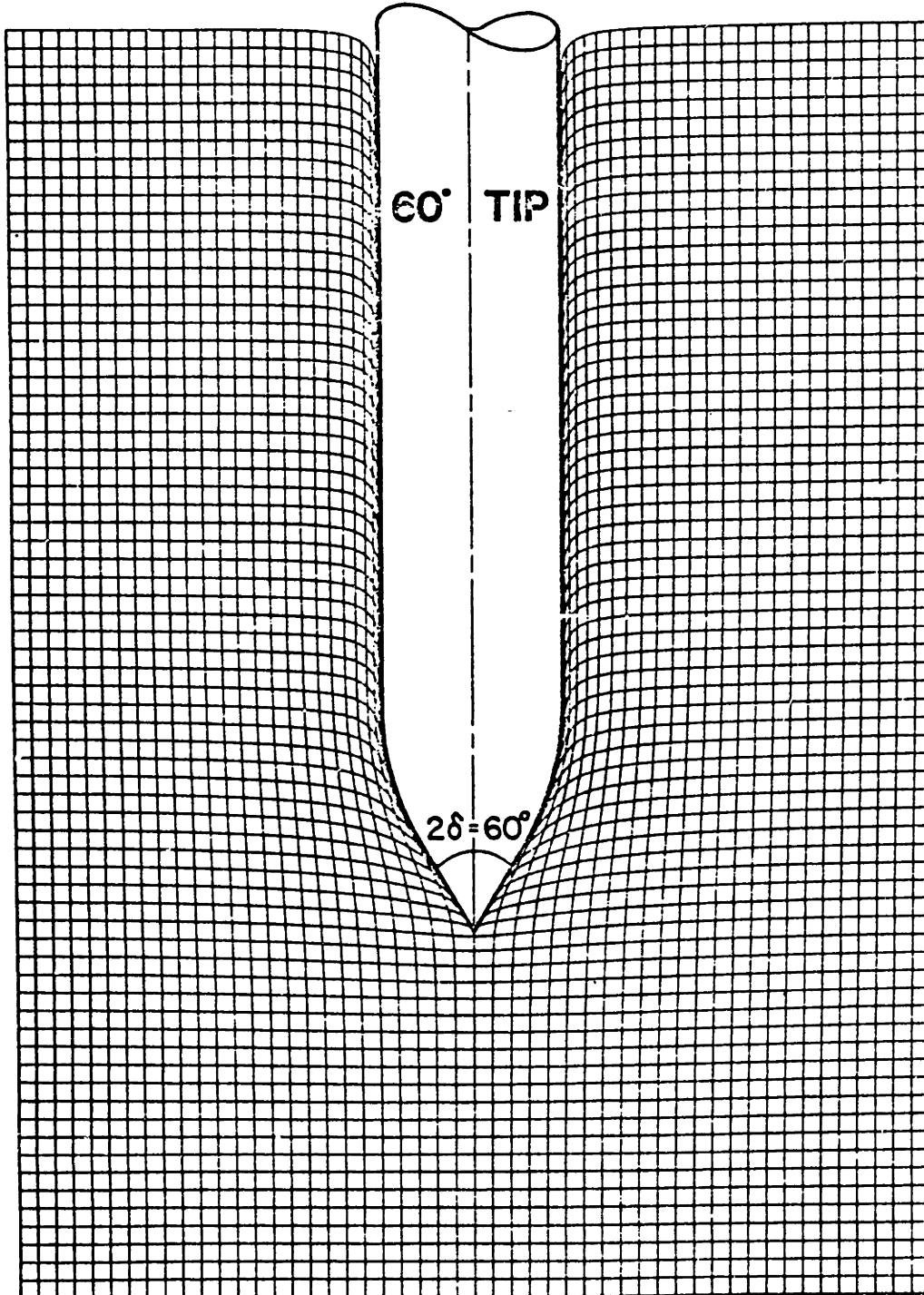


Figure 2.20: Predicted deformation pattern around a 60° pile assuming no shearing resistance of the soil. (After Levačoux, 1980)



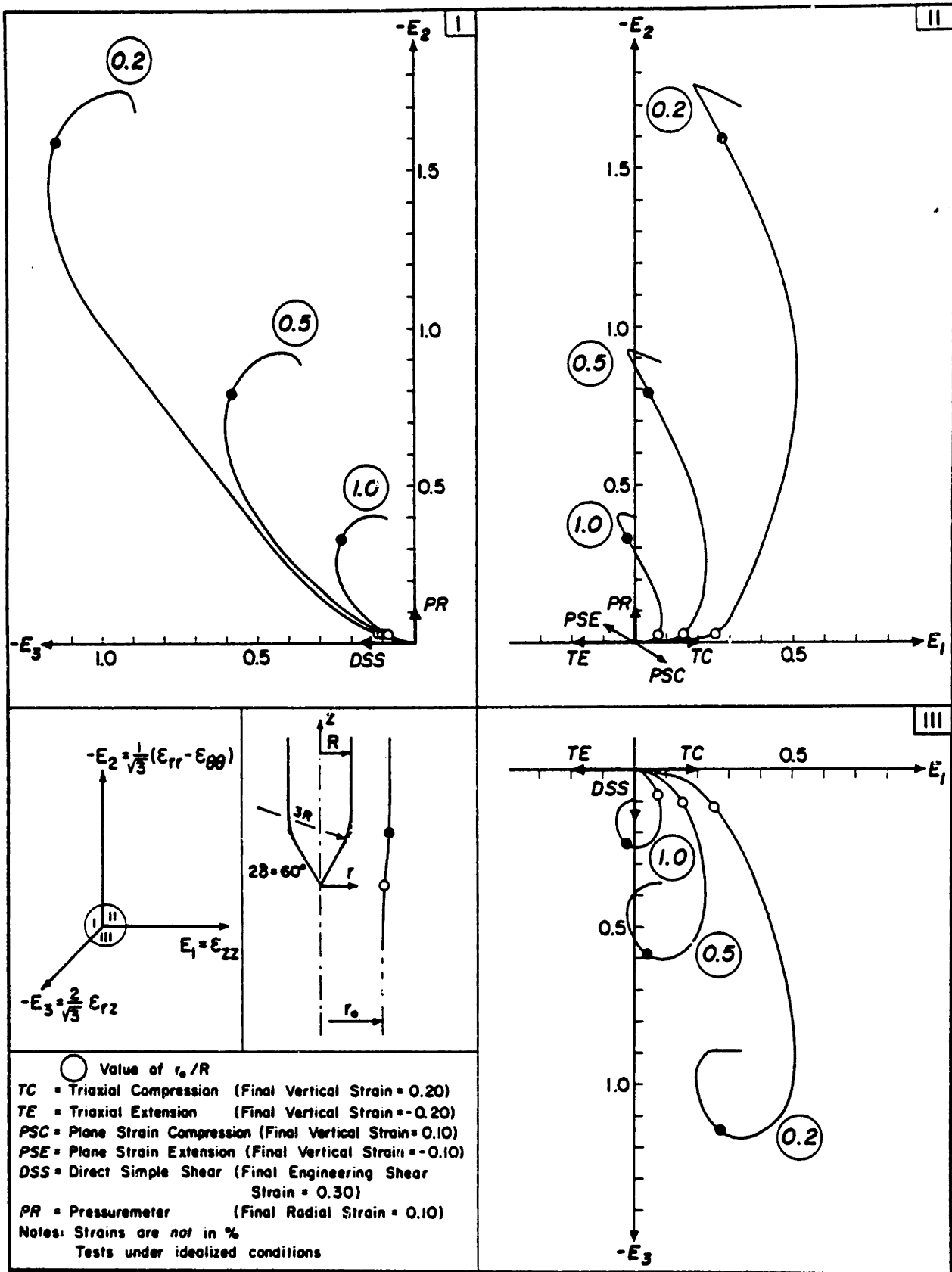


Figure 2.21: Strain paths of selected elements during penetration of a 60° pile. (After Levadoux, 1980)



CYLINDRICAL  
CAVITY  
EXPANSION

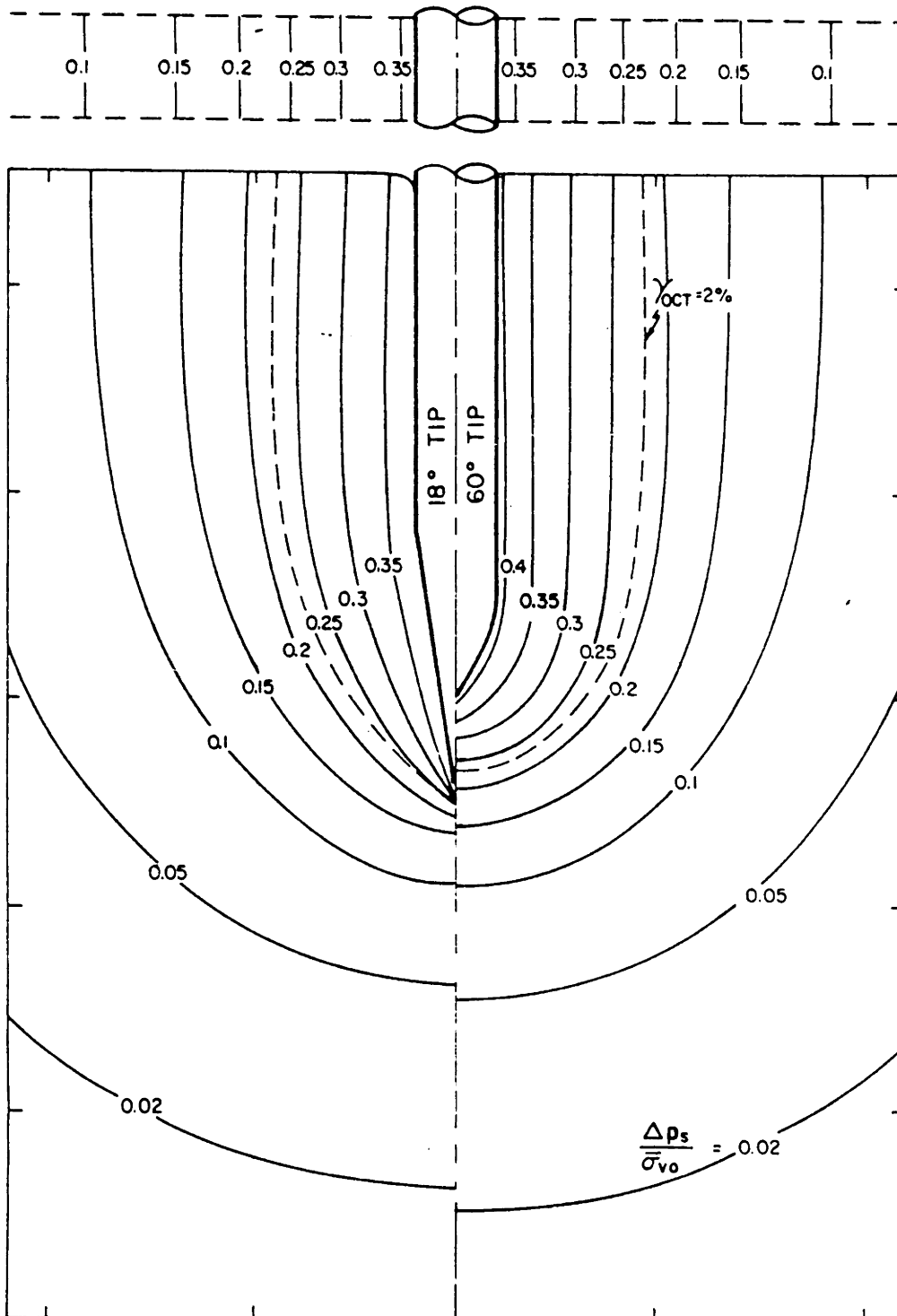


Figure 2.23: Predicted shear induced pore pressures during steady pile penetration in normally consolidated Boston Blue Clay (18° and 60° tips). (After Levadoux, 1980)

CYLINDRICAL  
CAVITY  
EXPANSION

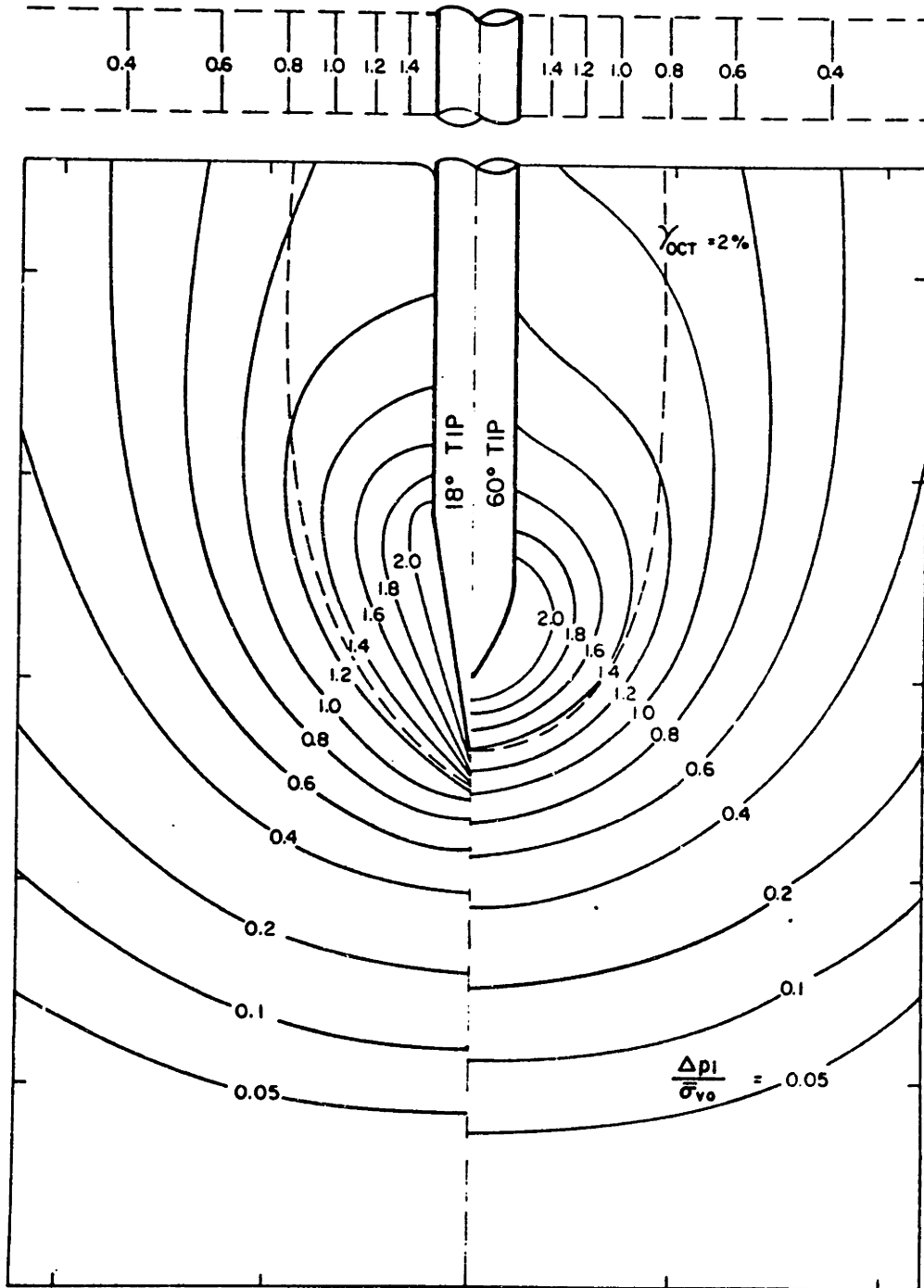


Figure 2.24: Predicted excess pore pressures during steady pile penetration in normally consolidated Boston Blue Clay (18° and 60° tips). (After Levadoux, 1980)

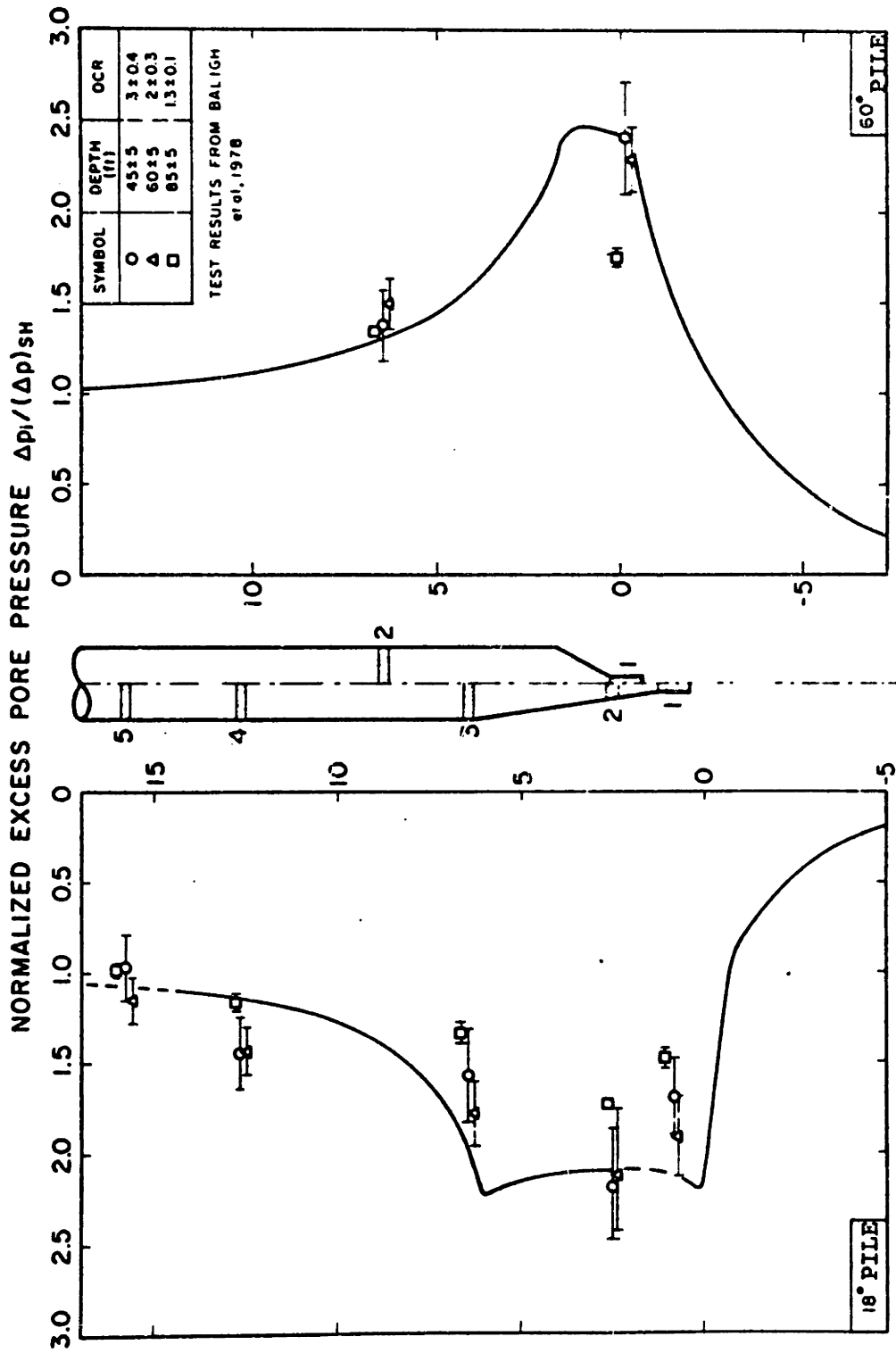


Figure 2.25: Predicted vs measured normalized excess pore pressures along the face and shaft of 18° and 60° piles during steady penetration in Boston Blue Clay. (After Levadoux, 1980)

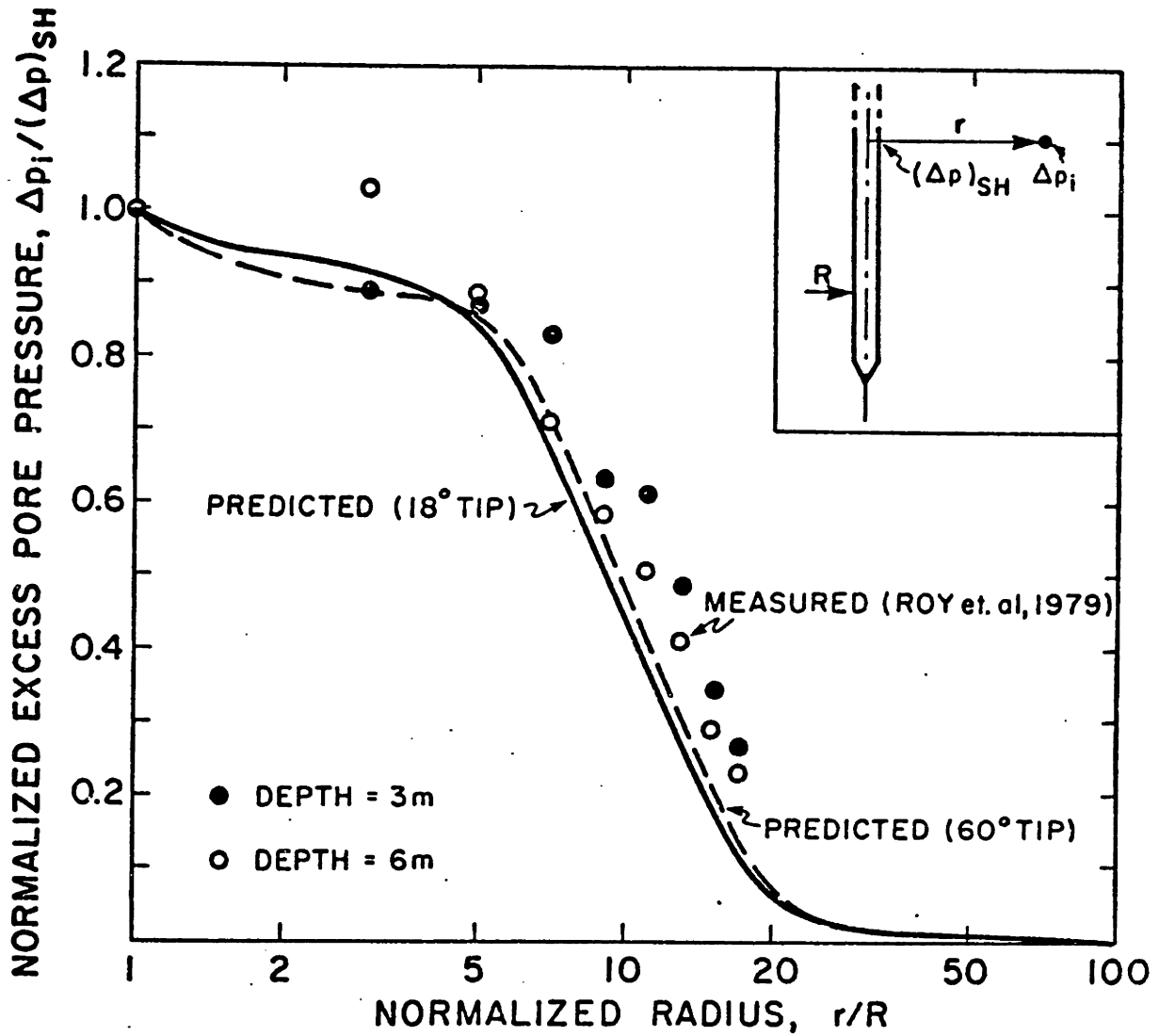


Figure 2.26: Predicted vs measured distribution of normalized excess pore pressures during penetration in clays. (After Levadoux, 1980)

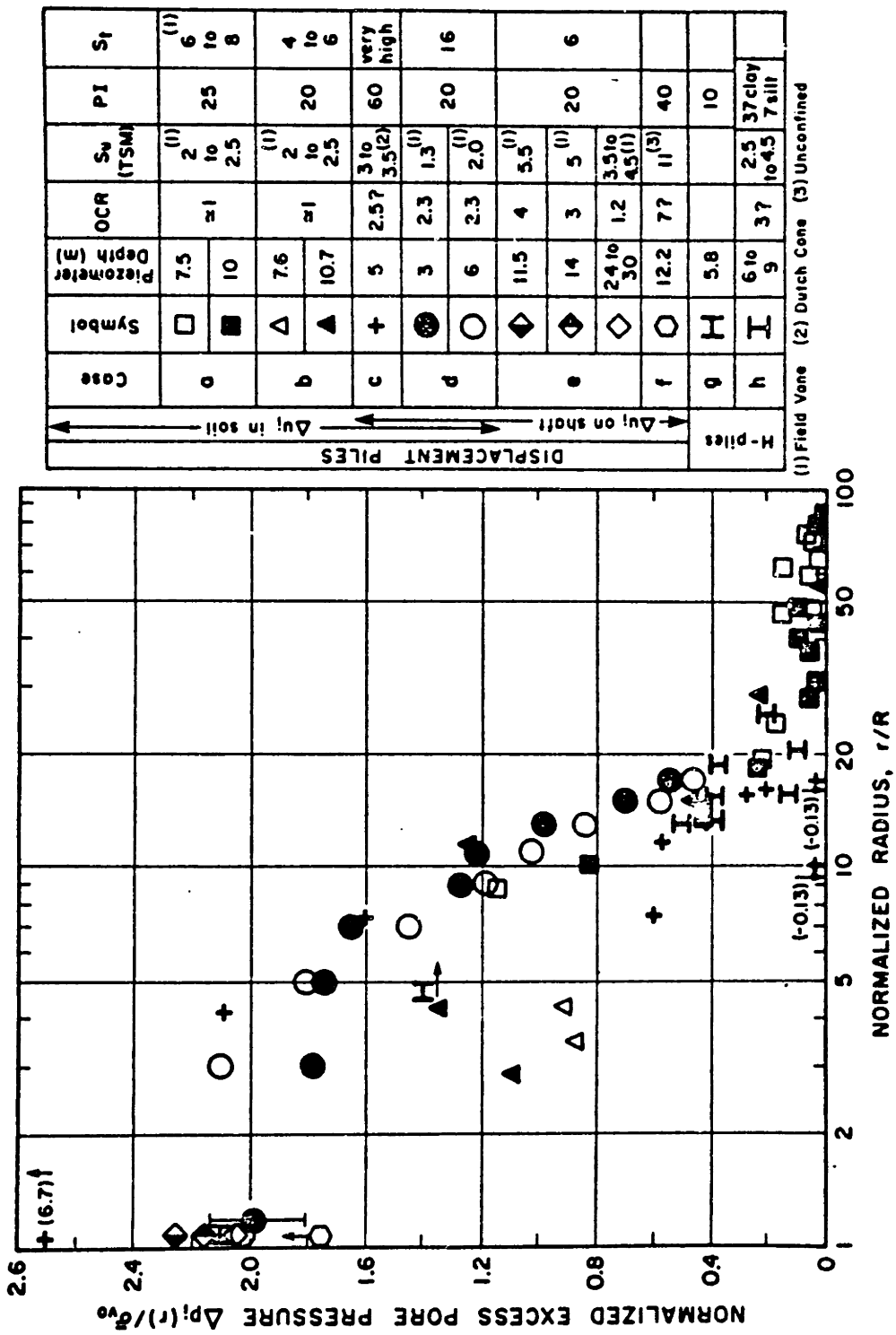


Figure 2.27: Excess pore pressure measurements due to pile installation in clays - Case histories. (After Baligh and Levagoux, 1980)

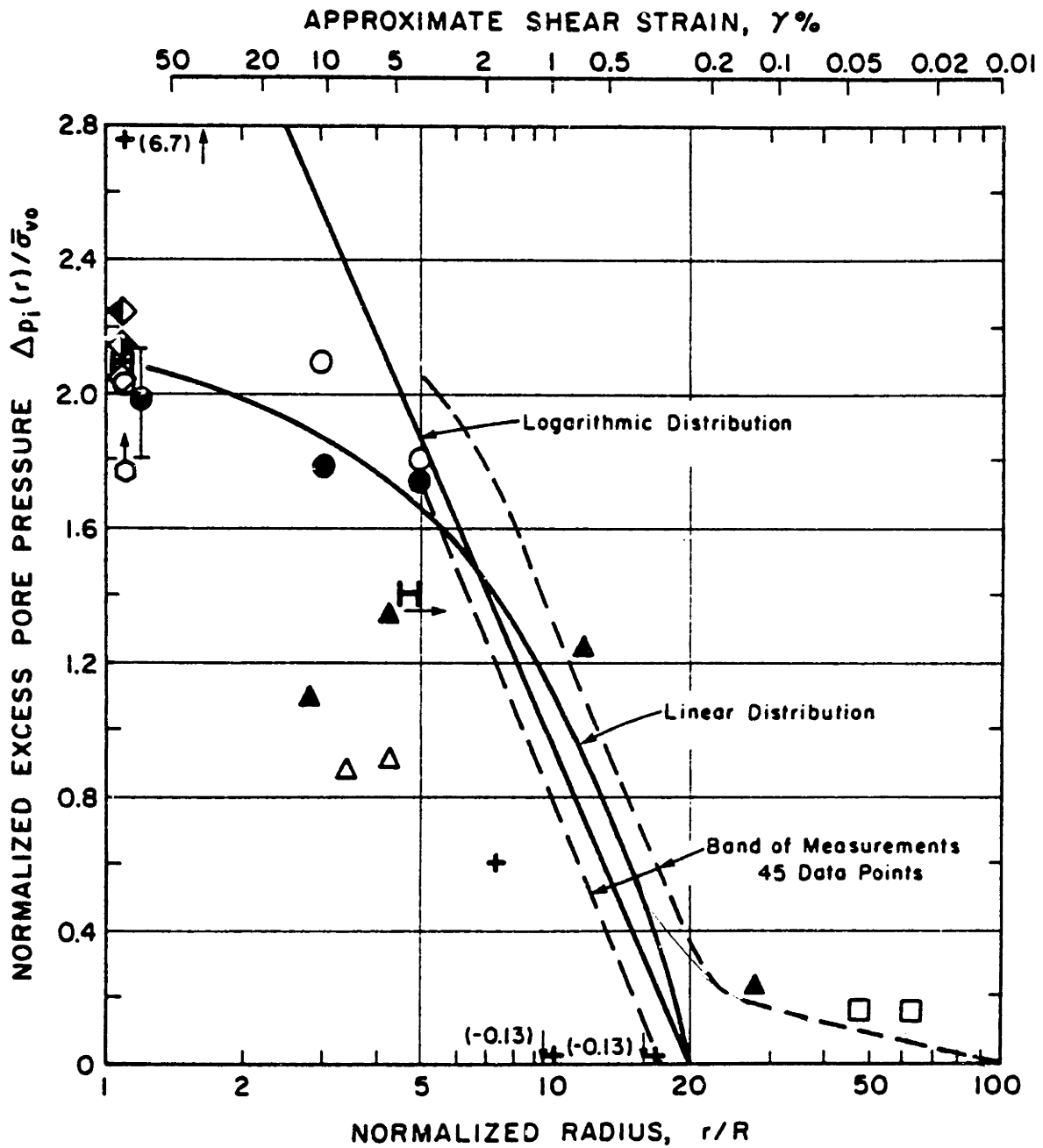


Figure 2.28: Excess pore pressure measurements due to pile installation in clays - Simplified distributions, (After Levadoux, 1980)



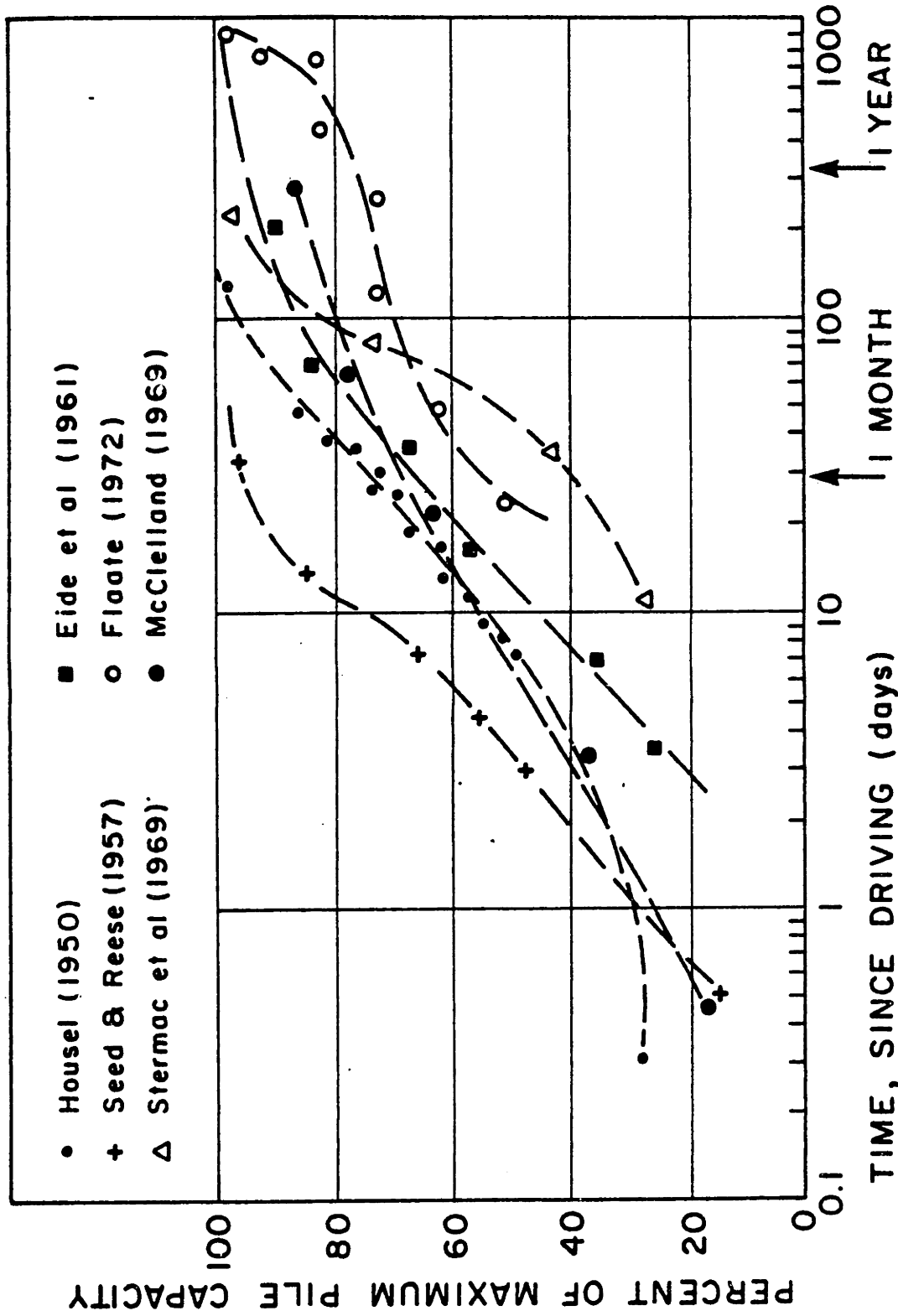
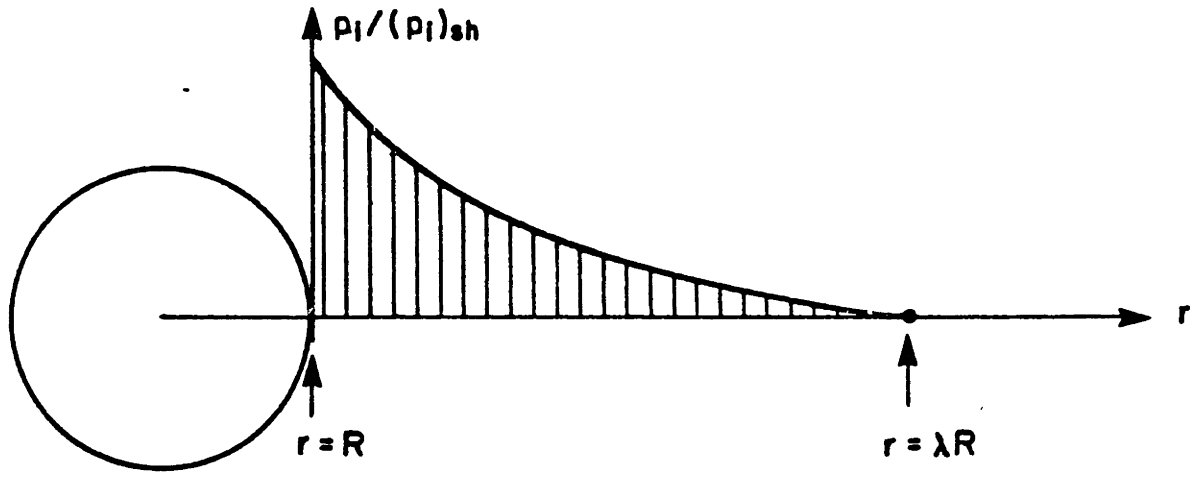


Figure 2.29: Field data on increase of bearing capacity with time for friction piles in clay. (After Baligh and Kavvadas, 1980)



PORE PRESSURE DISTRIBUTION TYPE	$p_i / (p_i)_{sh}$	
	$R < r < \lambda R$	$r > \lambda R$
CONSTANT	1	0
LINEAR	$\frac{1}{\lambda - 1} \left( \lambda - \frac{r}{R} \right)$	0
LOGARITHMIC	$1 - \frac{1}{\ln \lambda} \cdot \ln \left( \frac{r}{R} \right)$	0

Note:  $(p_i)_{sh}$  is the initial pore pressure at the pile shaft.

Figure 2.30: Initial pore pressure distributions used in the linear consolidation analysis. (After Baligh and Kavvas, 1980)

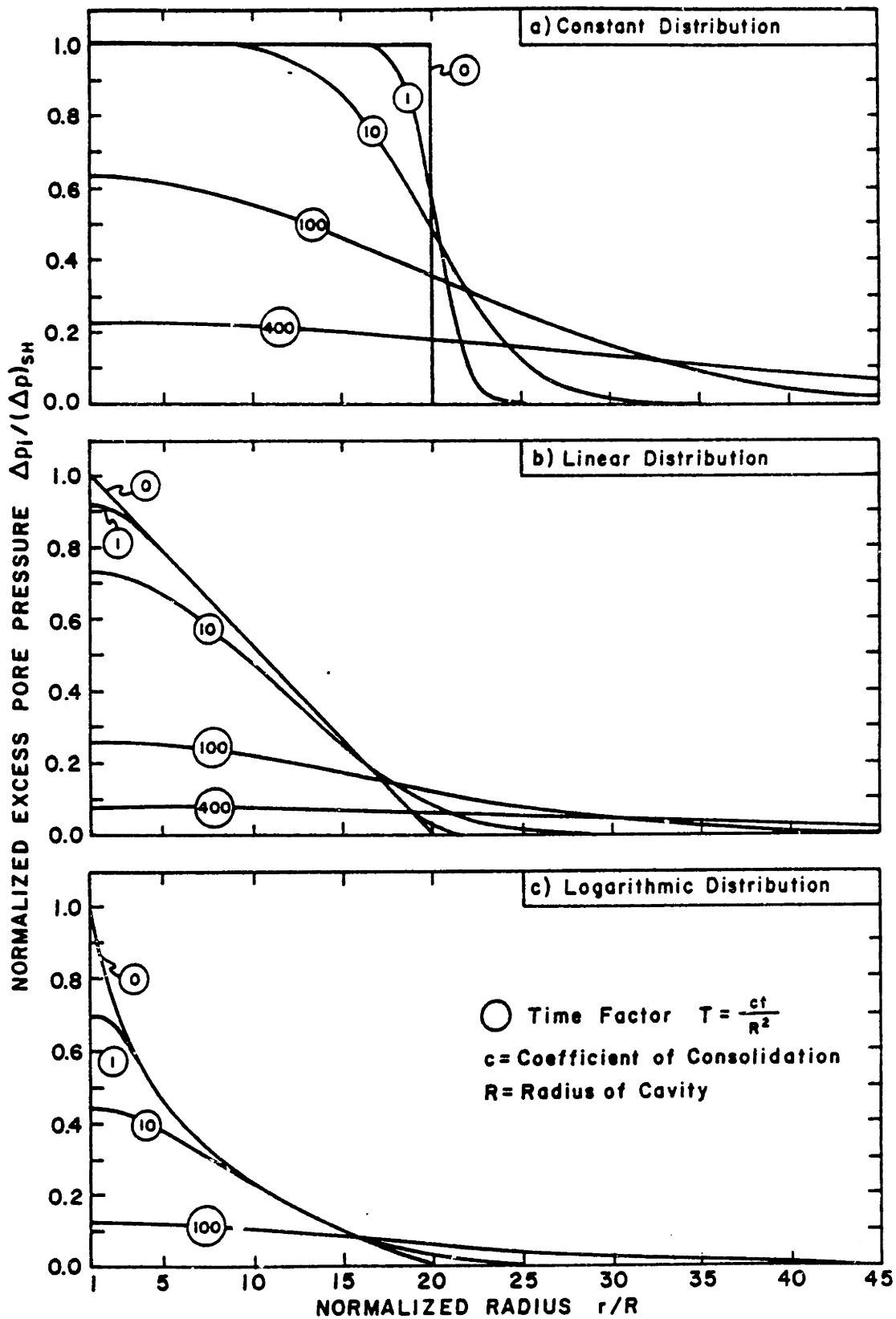


Figure 2.31: Effect of initial excess pore pressure distribution on dissipation around an imperious cylinder. (After Levadoux, 1980)

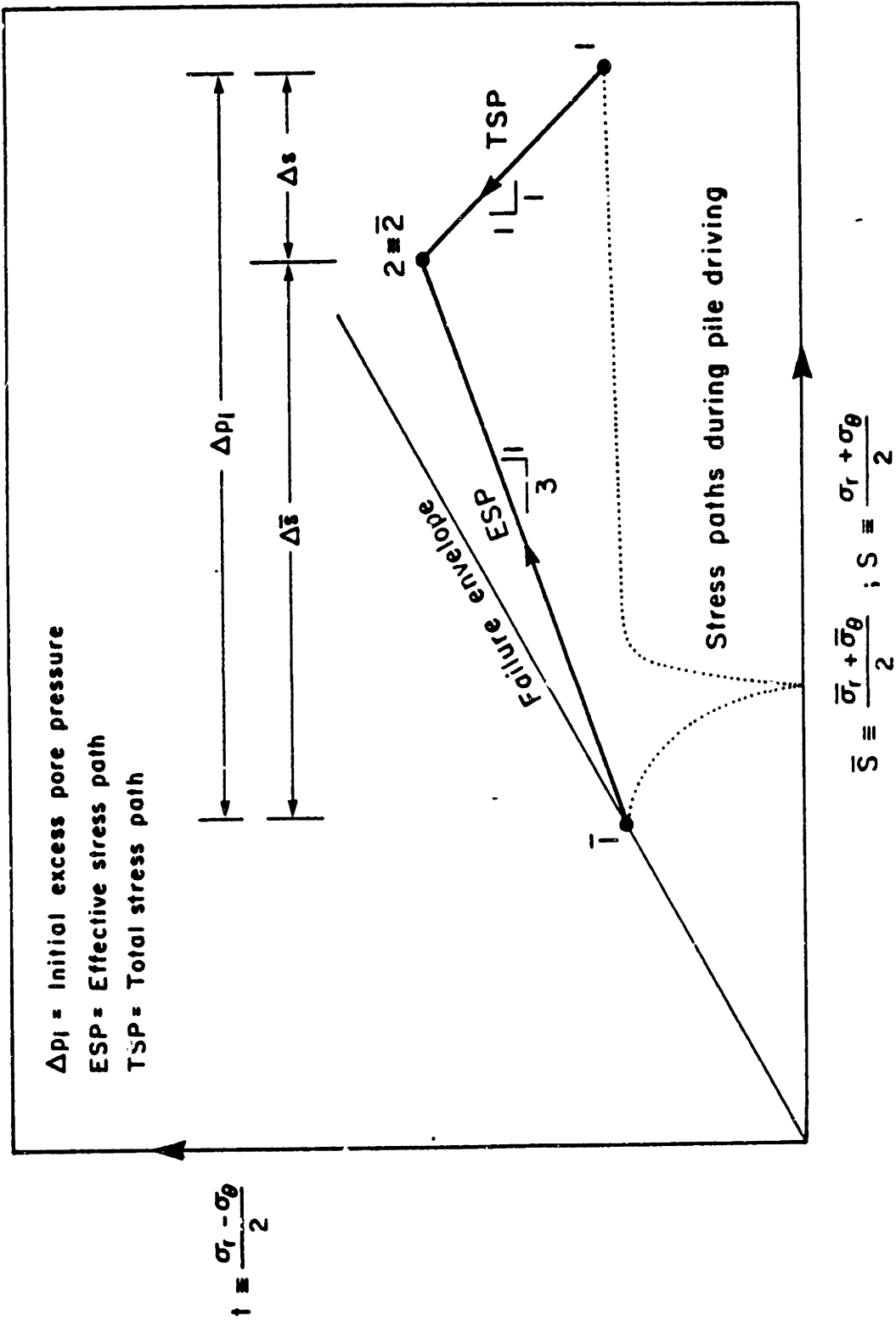


Figure 2.32: Effective and total stress paths predicted by linear elastic solutions ( $\bar{\nu}=1/3$ ) at the pile wall during consolidation around a pile. (After Baligh and Kavvadas, 1980)

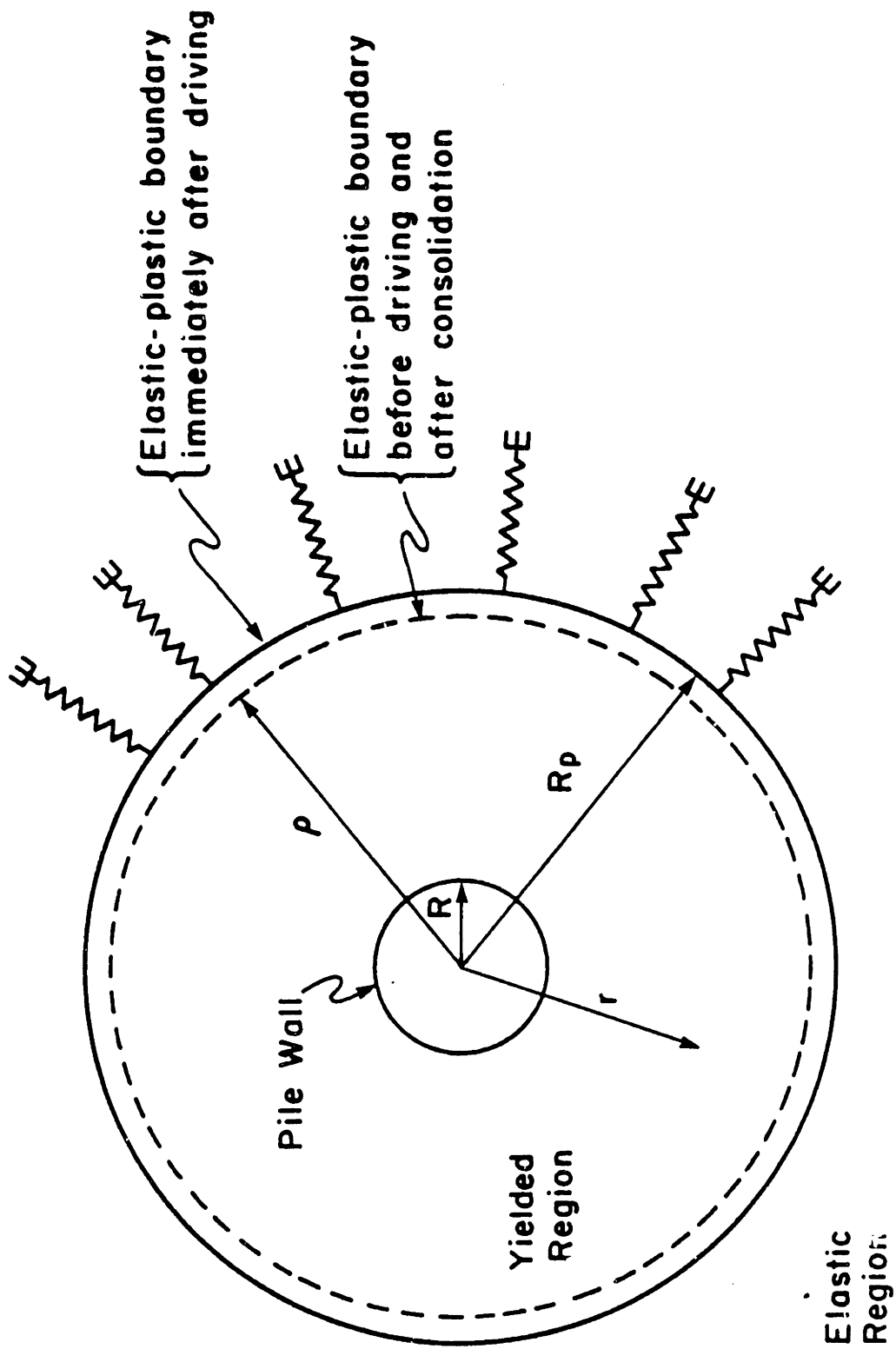


Figure 2.33: The engineering model (Esrig et al., 1977).

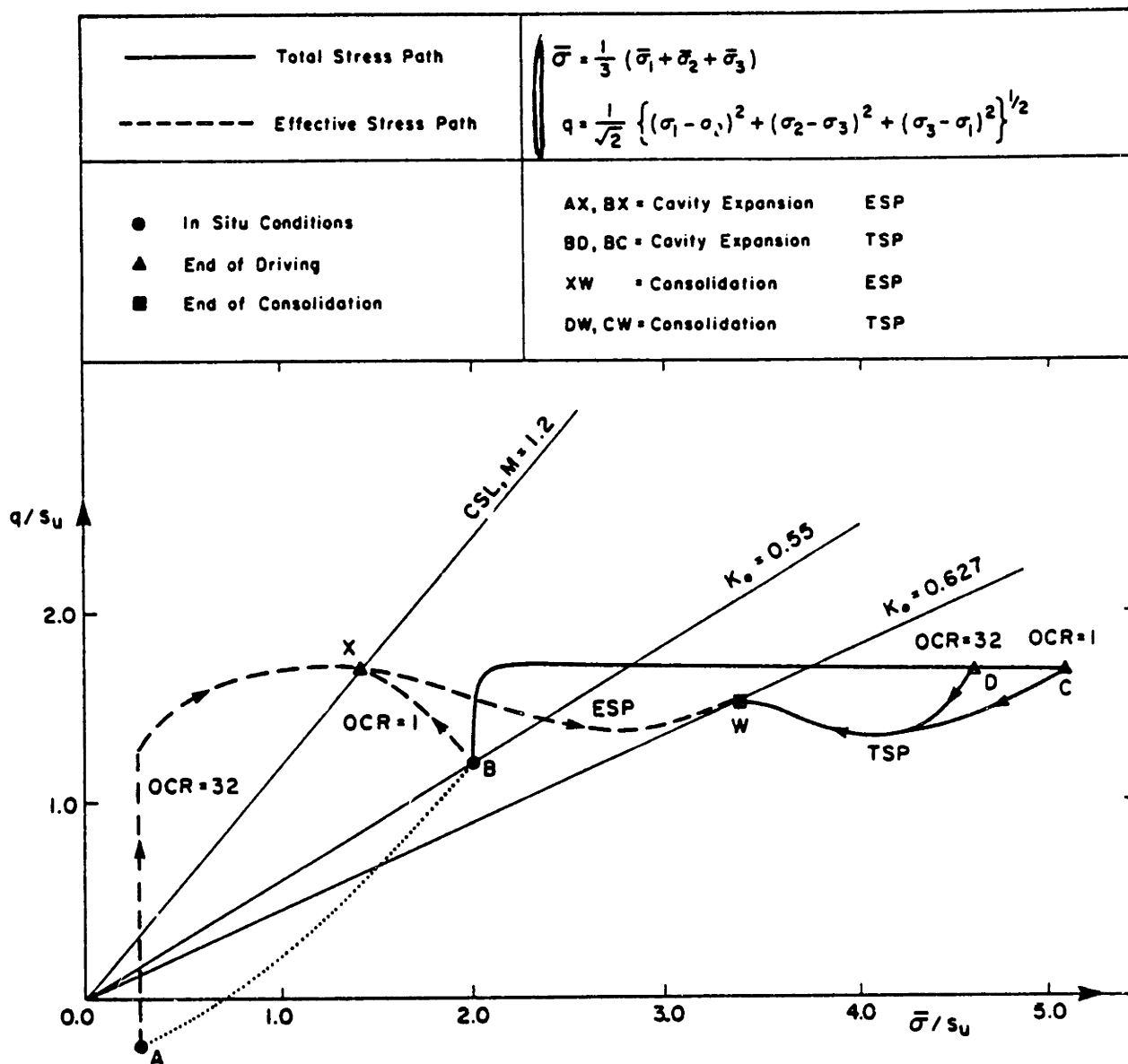


Figure 2.34: Stress paths for cavity expansion and consolidation for a soil element at the pile wall. Cam-Clay predictions (After Randolph et al., 1978b).

Code	Type of Model	Properties	T	Remarks
-----	Linear Elastic	$G/s_u = 50$		$R = \text{Pile Radius}$ $m = \frac{\kappa}{(1+e)\bar{\sigma}_{av}}$
-----	Elastic-Perfectly Plastic	$\bar{\nu} = 0.3$		
.....	Cam-Clay OCR=1	Table 2.7	$\frac{k}{\gamma_w} \cdot \frac{1}{mR^2} \cdot t$	
-----	Cam-Clay OCR=32	Table 2.7 + $\frac{G}{\bar{\sigma}_{vc}} \propto \text{OCR}$		

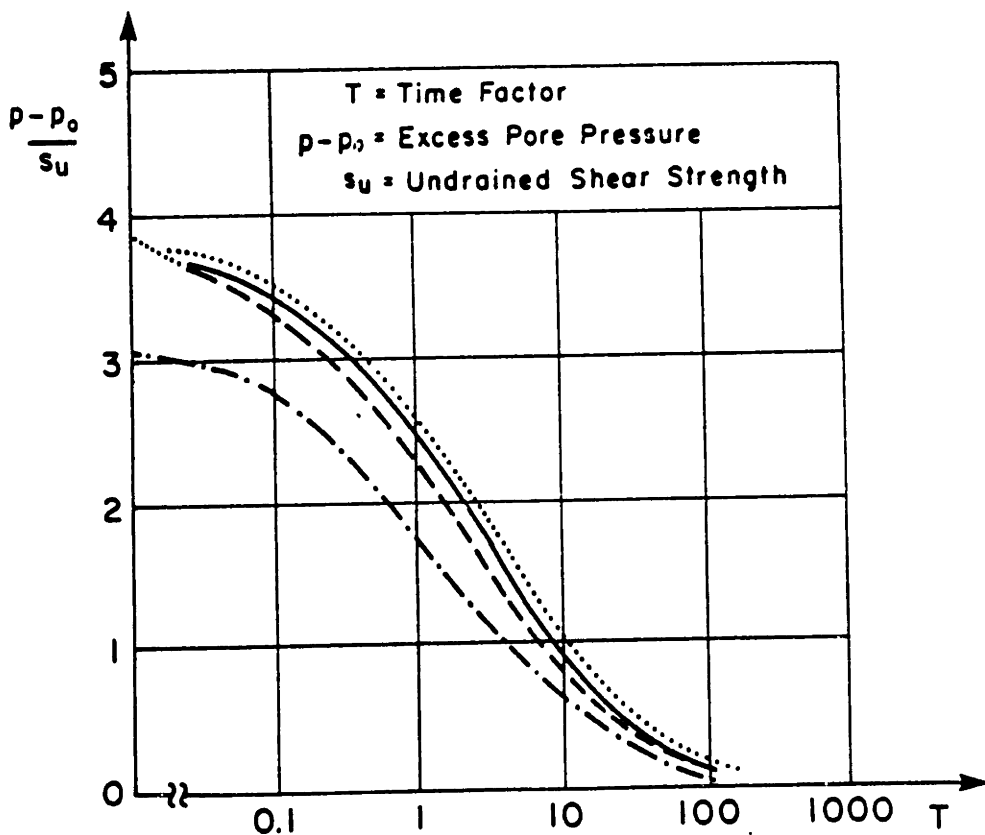


Figure 2.35: Decay of pore pressures with time at the pile wall for various constitutive laws (After Randolph et al., 1978b).

Code	Type of Model	Properties	T	Remarks
----	Linear Elastic	$G/s_u = 50$		$R = \text{Pile Radius}$  $m = \frac{\kappa}{(1+e)\bar{\sigma}_{av}}$
—	Elastic-Perfectly Plastic	$\bar{\nu} = 0.3$	$\frac{k}{\gamma_w} \cdot \frac{2G}{R^2} \frac{(1-\bar{\nu})}{(1-2\bar{\nu})} \cdot t$	
.....	Cam-Clay OCR=1	Table 2.7		
-----	Cam-Clay OCR=32	Table 2.7 + $\frac{G}{\bar{\sigma}_{vc}} \propto \text{OCR}$	$\frac{k}{\gamma_w} \cdot \frac{1}{mR^2} \cdot t$	

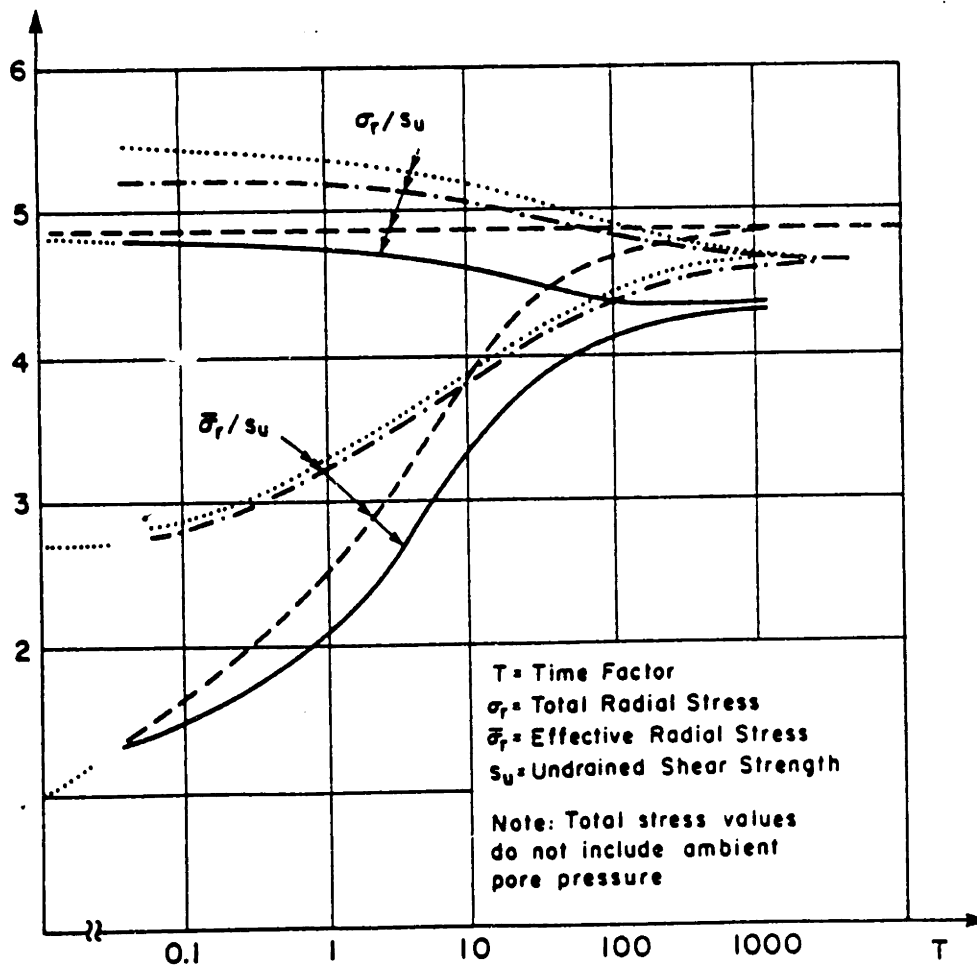


Figure 2.36: Changes in radial stress (total and effective) with time at the pile wall, for various constitutive laws (After Randolph et al., 1978b).



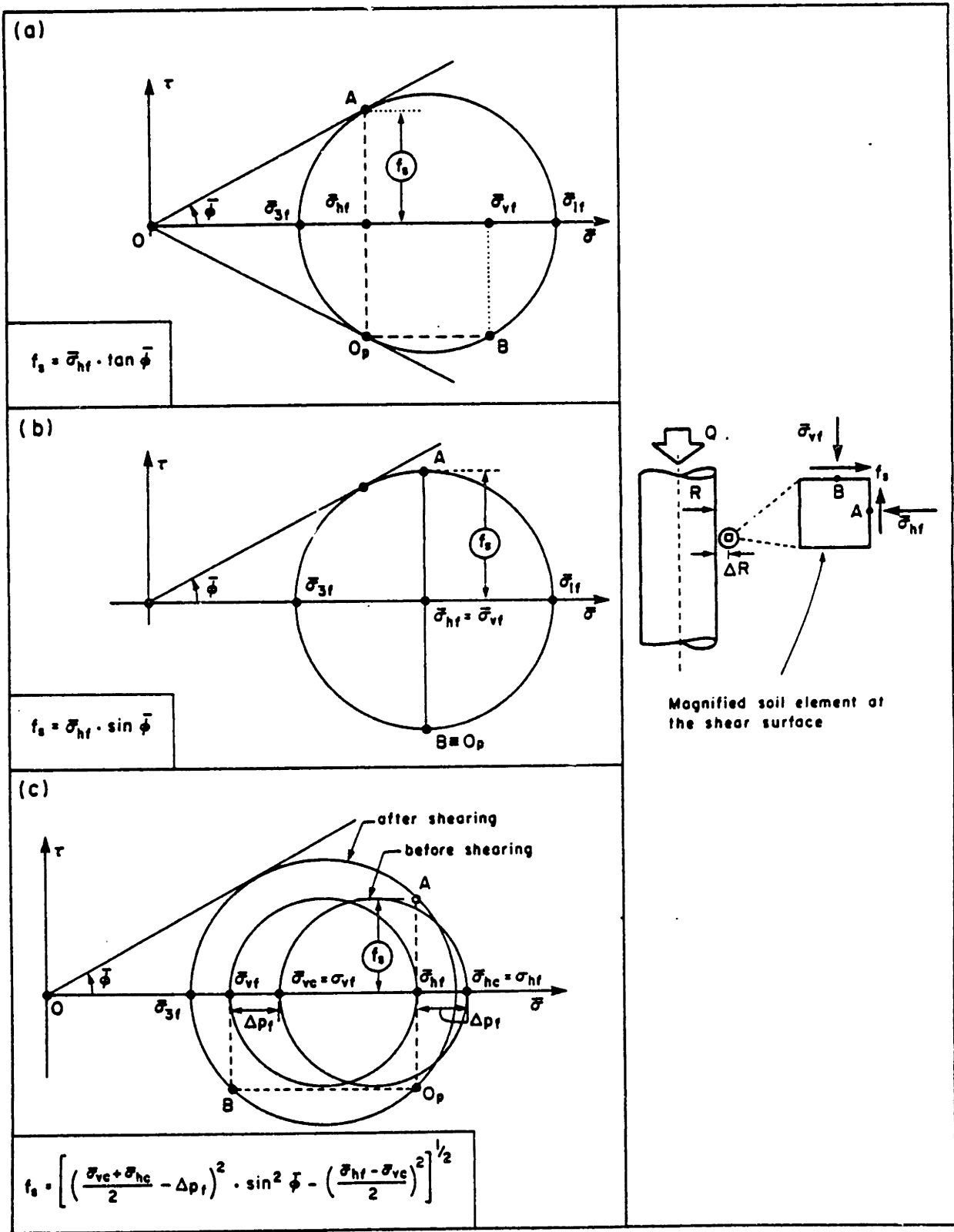


Figure 2.37: Stress states for failure in the soil under various assumptions. (After Baligh and Kavvas, 1980)

CHAPTER 3  
PLASTICITY THEORY FOR SOILS

3.1 INTRODUCTION

It is important in geotechnical engineering to be able to make realistic predictions of the behavior of prototype soil structure interacting systems (e.g., shallow and deep foundations, embankments or dams made of earth materials and/or resting on soil, underground openings, etc.). In principle, such predictions require the solution of Boundary Value Problems, i.e., the solution of a set of Field Equations in conjunction with appropriate Constitutive Laws. Both field equations and constitutive laws for soils are highly complex. This is discussed below:

1. Field Equations for Soils

The field equations for soils are the same as the field equations of Classical Mechanics, i.e.:

- (i) The Equilibrium Equations, which are derived from the Momentum Conservation law and,
- (ii) The Mass Conservation Equation, which is derived from the Mass Conservation law.

These equations are quite complicated in the case of Solid Mechanics problems (i.e., problems involving one-phase materials), but they become almost intractable in the case of soils which usually must be considered as multi-phase materials.

---

\* Assuming isothermal conditions.

The simplest case to study is when fully drained\* conditions prevail (or when the soil is dry). In such cases, soils can be treated as one-phase materials, which means that the standard procedures of Solid Mechanics are directly applicable. Unfortunately, such conditions are rare for cohesive deposits and hence, partially and fully saturated clays under undrained or partially drained conditions represent a large number of practical problems. In most of these cases, soils must be treated as multi-phase materials.

## 2. Constitutive Equations for Soils

These basically refer to the stress-strain-strength-time relationships governing the behavior of soils. They are highly complex because:

- (i) Soils exhibit non-linear and inelastic (hysteretic) behavior even at low stress levels and immediately following a load reversal (e.g., Hardin, 1972).
- (ii) Soils are frictional materials\*\* and thus, unlike metals whose response only depends on the deviatoric stresses, soil behavior also depends on the mean normal effective stress\*\*\* (Terzaghi, 1923).  
This feature is sometimes called pressure dependency.
- (iii) In soils, shearing causes a tendency for volume change. During drained shearing, dense sands and

---

\* i.e., the application of the external loads is sufficiently slow so that no significant excess pore pressures develop during deformation.

\*\* When treated in terms of effective stresses.

\*\*\* Loosely speaking, effective stress is the portion of the applied (total) stress which is carried by the solid phase.

highly overconsolidated clays tend to dilate, whereas loose sands and normally consolidated clays contract (e.g., Lambe and Whitman, 1969). However, after significant shearing, soils tend to approach a condition of no volume change (e.g., Rowe, 1971). When drainage is prevented (i.e., under undrained conditions), negative (decreased) pore pressures develop during shearing of dilatant soils and positive (increased) pore pressures develop in contracting soils.

- (iv) Soils are anisotropic due to their structure, depositional environment and subsequent straining (e.g., Duncan and Seed, 1966a,b, Arthur and Menzies, 1972, Arthur, et al., 1977).
- (v) In certain modes of deformation,\* soils exhibit unstable behavior (i.e., they strain soften). This type of behavior violates Drucker's Stability Postulate (Drucker, 1959) and thus creates problems of existence and uniqueness in the solution of boundary value problems (e.g., Prevost and Hoeg, 1975).
- (vi) Some soils exhibit time dependent behavior and thus require the use of the real time scale of load application in their constitutive description (e.g., Prevost, 1976). In the present context, time

---

\* For example, during undrained triaxial (or plane strain) compression tests starting from a  $K_0$ -condition.

dependency refers to the constitutive equations (i.e., it includes creep, relaxation, etc.) and not to time dependent phenomena (e.g., consolidation) which arise from the form of the field equations rather than the form of the constitutive law and thus, take place even when time independent constitutive relations are assumed for the soil (e.g., in the case of linear isotropic elastic soils).

Such extremely complex field equations and constitutive laws make analytical solutions of practical boundary value problems intractable. Thus, for many years since the beginning of modern Soil Mechanics, solutions of practical problems were obtained by making simplifications such as:

- (i) Treat the problem either as a stability (i.e., look for equilibrium under the ultimate load) or a deformation (i.e., look for the deformations under the working load) problem.
- (ii) Use simplified constitutive laws, such as Linear Isotropic Elasticity (for deformation problems) or Rigid-Perfect Plasticity (for stability problems).\*
- (iii) Approximately satisfy some of the Field Equations (e.g., in conventional slope stability analyses, equilibrium is only satisfied in a global sense).

These simplifications had been justified in view of the need for solutions, even though they might be crude. Such

---

\* In conjunction with the powerful bounding theorems of Plasticity.

solutions, when coupled with judgement based on the experience of the user, can be used with success in soil engineering analyses.

In the last two decades, with the development of computational analysis techniques and the availability of large digital computers, analytical solutions no longer represent the only method of predicting prototype soil-structure behavior. Numerical solutions can be obtained without the need to make simplifying assumptions, and thus predictions should in principle be more realistic. However, there are reasons why such numerical techniques do not always give accurate predictions:

- (i) There are few, if any, general purpose computer programs that can be used under general boundary and stress conditions, are fully debugged, reasonably economical and well documented.
- (ii) There are uncertainties in the assumed soil profile because of (a) soil inhomogeneity, (b) limited sampling and (c) testing inability to measure all pertinent stress-strain-time relationships for each soil type.
- (iii) There is concern about the reliability and capability of many of the presently available constitutive relationships to adequately model soil behavior.

These factors serve to inhibit continued progress in developing improved predictive procedures and also cause concern among the profession as to whether or not detailed numerical

analyses (e.g., by using the Finite Element method and sophisticated soil constitutive laws) are justified by the level of confidence in the obtained predictions.

It is thus required to improve (a) computer programs, (b) sampling and testing techniques and (c) the reliability of soil constitutive relations by developing new soil models which incorporate the significant aspects of soil behavior and/or improving existing models. Chapters 3, 4 and 5 of this study focus on this last item, as they relate to (a) the development of a Plasticity Theory framework for the constitutive description of clayey soils, and (b) the application of the theory in the design of a stress-strain-strength model for clays which incorporates most of the significant aspects of clay behavior.

Some general concepts on the constitutive description of soils follow.

We will first introduce the notion of the soil element, which is a volume of soil sufficiently small so that the assumption that it is subjected to uniform stresses is reasonable and, sufficiently large so that the soil can be treated as a continuum (i.e., the particulate\* nature of the soil does not appear). Thus, all constitutive descriptions of soil refer to the soil element and then, the soil medium is treated as a continuous field of soil elements.

We will then introduce the notion of the effective

---

\* i.e., soil is comprised of discrete particles, forming a matrix which is called the "soil skeleton".

stress (Terzaghi, 1923),  $\bar{\sigma}$ , which\* is basically the portion of the total applied stress carried by the solid phase (soil skeleton). If  $\underline{\sigma}$  is the total stress tensor,  $p$  is the pore pressure and  $\underline{I}$  the unit second order tensor (Kronecker delta), then, for saturated (or dry) soils, the effective stress tensor is defined by:

$$\bar{\sigma} \equiv \underline{\sigma} - p\underline{I} \quad (3.1)$$

where compressive stresses (and pressures) are considered positive. We will further postulate the so-called "Effective Stress Principle" which was stated by Terzaghi (1936) as:

"All measurable effects of a change of stress, such as compression, distortion and a change of shearing resistance, are exclusively due to changes in the effective stresses."

This means that if we consider a soil element and subject it to either of two load sequences which have identical effective stress paths,\*\* then both will give identical deformations. The significance of the above statement will become evident if we consider two load sequences which do not have identical effective stress paths but have, for example, identical total stress paths\*\*\* (but different pore pressure), or identical

---

\* In the following, tensor quantities are denoted with an undertilda, whereas scalar quantities have no sign below them.

\*\* The values of the total stress and pore pressure may be different.

\*\*\* These can be achieved, for example, if one loading sequence is drained and the other is undrained.



deviatoric stress paths\* (but different mean effective stress).

It is evident that the deformations associated with the two load sequences will be different.

Using the previous argument we can say that effective stresses control soil behavior and thus, any comprehensive constitutive law for soils should relate effective stresses (or increments of effective stresses) with strains\*\* (or increments of strains). Furthermore, since the effective stresses are carried by the soil skeleton (solid matrix) it follows that constitutive relations for soils associate stresses of the soil skeleton with strains (of the soil skeleton) and thus they describe the constitutive behavior of the soil skeleton.

Having decided that soil constitutive relations should associate effective stresses (or increments of effective stresses) with strains (or increments of strains) it remains to decide on the specific form of these relationships. It seems impossible (Hill, 1950, Naghdi, 1960) to write a relationship between the effective stress  $\bar{\sigma}$  and the associated strain  $\underline{\epsilon}$  which is valid for non-proportional loading\*\*\*

\* These can be achieved, for example, if one loading sequence is drained and the other is undrained.

\*\* Kavvadas (1980) shows that in the special case of undrained deformation of soils, a total (or deviatoric) stress constitutive law can equivalently be used because the values of the pore pressures are constrained by the incompressibility requirement.

\*\*\* i.e., for an effective stress path with variable direction in the stress space.

because such a relation cannot adequately account for the path dependency of soils. On the contrary, the path dependency of soils can be treated via the so-called "Incremental (or Rate) Formulations" which relate an infinitesimal increment  $d\bar{\sigma}$  of the effective stress tensor with the associated infinitesimal increment  $d\varepsilon$  of the strain tensor, via an equation of the form:

$$d\bar{\sigma} = \bar{C} : d\varepsilon \quad (3.2a)$$

or its inverse:

$$d\varepsilon = \bar{S} : d\bar{\sigma} \quad (3.2b)$$

where\*  $\bar{C}$  and  $\bar{S}$  are proportionality fourth order tensors and ":" denotes the double contraction\*\* of indices of the associated tensors. Tensors  $\bar{C}$  and  $\bar{S}$  are the so-called current (tangent) stiffness and compliance tensors, respectively. For Linear Soil Models these tensors do not vary during the deformation process. On the contrary, in Non-Linear Elasticity and in Plasticity, the stiffness and compliance tensors vary during deformation, which means that their components

---

\* Eqs. 3.2 are still only formal expressions. Specific forms of the tensors  $\bar{C}$  and  $\bar{S}$  will be given in subsequent sections.

\*\* See e.g., Malvern (1969).

depend on the current (effective) stress and/or strain state. Furthermore, Eqs. 3.2 are commonly\* "incrementally linearized" in the sense that they are linear in the (infinitesimal) stress and strain increments which basically means that  $\bar{C}$  and  $\bar{S}$  do not depend on the imposed (infinitesimal) increments of stress and strain. In this thesis we will only study Incrementally Linearized Theories.

In discussing non-linear soil models we will assume that the soil skeleton is inviscid, which means that time effects are excluded from the constitutive description of the soil skeleton\*\*. Hence, the stiffness and compliance tensors do not depend on time and thus, for convenience, we can substitute the infinitesimal increments of stress and strain ( $d\bar{\sigma}$  and  $d\bar{\epsilon}$ ), by their time rate of changes ( $\dot{\bar{\sigma}}$ ,  $\dot{\bar{\epsilon}}$  respectively). Then, Eqs. 3.2 can be written:

$$\dot{\bar{\sigma}} = \bar{C} : \dot{\bar{\epsilon}} \quad ; \quad \dot{\bar{\epsilon}} = \bar{S} : \dot{\bar{\sigma}} \quad (3.3)$$

The specific form of the stiffness and compliance tensors depends on the particular soil model used. Before we specialize to particular soil models, however, we will present some

---

\* i.e., most Plasticity Theories have this feature mainly for simplicity.

\*\* e.g., creep and relaxation phenomena are excluded. However, consolidation phenomena can still be studied because, as discussed previously, they arise from the field equations and not from the constitutive law used for the soil.

concepts of the Incrementally Linearized Plasticity Theory which are universal, in the sense that they are used (or can be used) by most soil models.

3.2 GENERAL CONCEPTS  
OF THE INCREMENTALLY LINEARIZED  
PLASTICITY THEORY FOR SOILS

It is a well established experimental fact that soils exhibit inelastic behavior, even at low stress levels (e.g., Hardin, 1972). Inelasticity basically means that if a soil element is subjected to a cycle of application and removal of an infinitesimal effective stress increment then, only part of the strain that occurred during the application of the stress is recovered when the stress is removed. Thus, it seems reasonable to divide\* the total strain increment corresponding to the imposition of an infinitesimal (effective) stress increment in two portions:

- (i) A portion which is reversible, i.e., it is recovered upon removal of the infinitesimal (effective) stress increment. We will call this portion the "elastic" strain increment\*\* and denote it with a right superscript "e".
- (ii) The remaining portion which is irreversible, i.e., it is not recovered upon removal of the infinitesimal (effective) stress increment.  
We will call this portion the "plastic" strain

---

\* as is commonly done in Plasticity Theory.

\*\* As it was stated previously, infinitesimal increments (denoted by a preceding "d") and time rates of change (denoted by a superdot) will be used interchangeably.

increment and denote it with a right superscript "p". Thus:

$$\dot{\tilde{\epsilon}} \equiv \dot{\tilde{\epsilon}}^e + \dot{\tilde{\epsilon}}^p \quad (3.4)$$

We will further define the volumetric component of the strain increment (total, elastic and plastic, respectively) by:

$$\dot{\tilde{\epsilon}} \equiv \dot{\tilde{\epsilon}} : \underline{\underline{I}} \quad (3.5a)$$

$$\dot{\tilde{\epsilon}}^e \equiv \dot{\tilde{\epsilon}}^e : \underline{\underline{I}} \quad (3.5b)$$

$$\dot{\tilde{\epsilon}}^p \equiv \dot{\tilde{\epsilon}}^p : \underline{\underline{I}} \quad (3.5c)$$

which is basically the sum of the normal components of the associated tensor\*, i.e., the trace of the tensor.

The deviatoric part of the strain increment (total, elastic and plastic, respectively) is then defined by:

$$\dot{\tilde{\epsilon}} \equiv \dot{\tilde{\epsilon}} - \frac{1}{3} \dot{\tilde{\epsilon}} \underline{\underline{I}} \quad (3.6a)$$

$$\dot{\tilde{\epsilon}}^e \equiv \dot{\tilde{\epsilon}}^e - \frac{1}{3} \dot{\tilde{\epsilon}}^e \underline{\underline{I}} \quad (3.6b)$$

$$\dot{\tilde{\epsilon}}^p \equiv \dot{\tilde{\epsilon}}^p - \frac{1}{3} \dot{\tilde{\epsilon}}^p \underline{\underline{I}} \quad (3.6c)$$

---

\* For example, in Cartesian components:

$$\dot{\tilde{\epsilon}} : \underline{\underline{I}} = \dot{\tilde{\epsilon}}_x + \dot{\tilde{\epsilon}}_y + \dot{\tilde{\epsilon}}_z$$

Combining Eqs. 3.5 and 3.6, it can be easily shown that the decomposition of the (total) strain increment into elastic and plastic components (Eq. 3.4) also holds for the volumetric and deviatoric components, separately, i.e.:

$$\dot{\underline{\epsilon}} = \dot{\underline{\epsilon}}^e + \dot{\underline{\epsilon}}^p \quad (3.7a)$$

$$\dot{\underline{\underline{\epsilon}}}} = \dot{\underline{\underline{\epsilon}}}}^e + \dot{\underline{\underline{\epsilon}}}}^p \quad (3.7b)$$

Analogously, for the effective stress tensor  $\bar{\underline{\sigma}}$ , we will define the mean effective stress:

$$\bar{\sigma} \equiv \frac{1}{3} (\bar{\underline{\sigma}} : \underline{\underline{I}}) \quad (3.8a)$$

and the deviatoric stress:

$$\underline{\underline{s}} \equiv \bar{\underline{\sigma}} - \bar{\sigma} \underline{\underline{I}} \quad (3.8b)$$

and then, for the effective stress increments:

$$\dot{\bar{\sigma}} = \frac{1}{3} (\dot{\bar{\underline{\sigma}}} : \underline{\underline{I}}) \quad (3.9a)$$

$$\dot{\underline{\underline{s}}} = \dot{\bar{\underline{\sigma}}} - \dot{\bar{\sigma}} \underline{\underline{I}} \quad (3.9b)$$

The main reason for using general tensorial stress and strain measures is that we aim at developing soil models that can be used in studying general three-dimensional stress paths.

Furthermore, since we plan to study anisotropic soil models, principal stress and strain spaces are inadequate because the physical directions of load application are important\*. In the present study, we will use a general effective stress space comprised of a "hyperplane" containing the components of the stress deviator  $\underline{s}$  and an axis orthogonal to the hyperplane representing the mean effective stress  $\bar{\sigma}$ . This space is better than a space which contains the components of the effective stress tensor  $\bar{\underline{\sigma}}$  because it is a direct extension of the deviatoric stress space ( $\underline{s}$ ) commonly used in metal Plasticity. In fact, the effect of confinement\*\* is taken into consideration by simply adding an extra dimension ( $\bar{\sigma}$ ) to the  $\underline{s}$ -space. Furthermore, as shown subsequently, the use of the  $(\underline{s}, \bar{\sigma})$  space results in compact forms of the incremental stress-strain relations.

The decomposition of the strain increment in elastic and plastic parts (Eqs. 3.4 and 3.7) is very useful since it enables studying the Elastic and Plastic components of soil deformation separately. Thus, instead of pursuing constitutive relations between  $\dot{\bar{\underline{\sigma}}}$  and  $\dot{\underline{\epsilon}}$  (as Eq. 3.3 suggests) we can aim towards two separate sets of constitutive relations:

- (i) Relations between  $\dot{\bar{\underline{\sigma}}}$  and  $\dot{\underline{\epsilon}}^e$  which describe the elastic part of soil deformation, and

---

\* Principal spaces can only be used for stress paths not involving rotations of the principal stress axes.

\*\* which is expressed by the derivative with respect to  $\bar{\sigma}$ .



- (ii) Relations between  $\dot{\bar{\sigma}}$  and  $\dot{\bar{\epsilon}}^p$  which describe the plastic part of soil deformation.

If these relations are given, we can determine the elastic and plastic strain increments ( $\dot{\bar{\epsilon}}^e$  and  $\dot{\bar{\epsilon}}^p$  respectively) associated with the application of any infinitesimal effective stress increment  $\dot{\bar{\sigma}}$ . The following sections study these (two) relations.

### 3.2.1 THE ELASTIC PART OF THE ELASTOPLASTIC DEFORMATION OF SOILS

For most load sequences, the elastic (reversible) part of soil deformation is much smaller than the plastic (irreversible) part. Thus, sophistication in the constitutive description of the elastic part of soil deformation is not usually justified\* and simple, isotropic (linear or non-linear) models have commonly been used (e.g., Roscoe and Burland, 1968, Davis and Mullenger, 1978). Therefore, we will subsequently study an isotropic model, involving only two independent parameters and having the form\*\*:

$$\dot{\bar{\sigma}} = K \dot{\bar{\epsilon}}^e \quad (3.10a)$$

$$\dot{\bar{s}} = 2G \dot{\bar{\epsilon}}^e \quad (3.10b)$$

---

\* especially if we do not concentrate in soil behavior under cyclic loads.

\*\* Using the standard sign convention of Soil Mechanics, compressive strains are positive.

where  $K$  is an elastic bulk modulus and  $G$  an elastic shear modulus.

Results of oedometer tests\* on typical clays\*\* indicate that during rebound the change of the void ratio is proportional to the change of the logarithm of the mean effective stress, which means that:

$$K = \frac{1 + e_o}{\kappa} \bar{\sigma} \quad (3.10c)$$

where  $e_o$  is the initial void ratio and  $\kappa$  a material constant related to the swelling index\*\*\*  $C_s$  by:

$$\kappa = (0.434) C_s \quad (3.10d)$$

The elastic modulus  $G$  affects the initial\*\*\*\* stiffness and the stiffness of the unloading portion of the shear stress-strain curve during undrained deformation. The Modified Cam-Clay (MCC) model\*\*\*\*\* neglects elastic shear strains which means that  $G$  is equal to infinity. However, such an assumption

---

\* subjecting samples to one-dimensional straining.

\*\* i.e., not very sensitive or expansive or highly overconsolidated ( $OCR < 5-10$ )

\*\*\* The slope of the  $e-\log \bar{\sigma}$  line is:

$$C_s = de/d(\log \bar{\sigma})$$

\*\*\*\* i.e., at very low strain levels

\*\*\*\*\* Roscoe and Burland, 1968

tion is both unrealistic and causes numerical problems\*.

Therefore, in the context of this thesis we will assume that the ratio:  $\frac{G}{K}$  is constant and is dictated by an "elastic" Poisson's ratio\*\*. Thus, both K and G are functions of the current level of the mean effective stress (see also Eq. 3.10c) which means that the elastic portion of the soil deformation is non-linear (but isotropic).

### 3.2.2 THE PLASTIC PART OF THE ELASTO-PLASTIC DEFORMATION OF SOILS

#### 3.2.2.1 Incremental Stress-Strain Relations

The plastic part of soil deformation represents the relationship between the plastic component of the strain increment ( $\dot{\tilde{\epsilon}}^p$ ) and the corresponding effective stress increment ( $\dot{\tilde{\sigma}}$ ). The most general form of this relationship is:

$$\dot{\tilde{\epsilon}}^p \equiv \Lambda \dot{\tilde{P}} \quad (3.11)$$

where  $\Lambda$  is a scalar quantity controlling the magnitude of the plastic strain increment and  $\tilde{P}$  is a second order tensor that specifies the direction\*\*\* of the plastic strain increment in the strain space. For Incrementally Linearized Plasticity

---

\* The elasto-plastic compliance tensor  $\tilde{S}$  is singular which means that the stiffness tensor  $\tilde{C}$  does not exist.

\*\* Since  $2G/K = 3(1-2\bar{\nu})/(1+\bar{\nu})$  where  $\bar{\nu}$  is the "elastic" Poisson's ratio.

\*\*\* i.e., the principal axes of  $\dot{\tilde{\epsilon}}^p$  and  $\dot{\tilde{P}}$  coincide.

Theories considered herein, it can be shown\* (based on Eq. 3.11) that:

- (i)  $\dot{P}$  is independent\*\* of  $\dot{\underline{\underline{\sigma}}}$  and,
- (ii)  $\dot{\Lambda}$  can be written as a linear combination of the components of the effective stress increment  $\dot{\underline{\underline{\sigma}}}$ , i.e.:

$$\dot{\Lambda} \equiv \frac{1}{H} (\underline{\underline{Q}} : \dot{\underline{\underline{\sigma}}}) \quad (3.12)$$

where, H is an elastoplastic modulus\*\*\* and  $\underline{\underline{Q}}$  is a second order tensor which controls the magnitude of the plastic strain increment. In fact, if the applied effective stress increment  $\dot{\underline{\underline{\sigma}}}$  is perpendicular to  $\underline{\underline{Q}}$  (i.e., if  $\underline{\underline{Q}} : \dot{\underline{\underline{\sigma}}} = 0$ ) then  $\dot{\Lambda} = 0$  which means that no plastic strains occur. The other extreme case is when  $\dot{\underline{\underline{\sigma}}}$  is parallel to  $\underline{\underline{Q}}$  and then  $\underline{\underline{Q}} : \dot{\underline{\underline{\sigma}}}$  is a maximum, which means that the plastic strain increment is also a maximum. Finally, if the direction of the stress increment  $\dot{\underline{\underline{\sigma}}}$  lies between the previous two extremes, the plastic strain increment is non-zero but less than the previous maximum.

It is convenient (Prevost, 1978) to decompose  $\underline{\underline{P}}$  and  $\underline{\underline{Q}}$  in

---

\* excluding the trivial case:  $\underline{\underline{P}} = \dot{\underline{\underline{\sigma}}}$ , which is unrealistic.

\*\* This means that the direction of the plastic strain increment depends only on the current state and not on the applied effective stress increment.

\*\*\* evidently independent of  $\dot{\underline{\underline{\sigma}}}$  but may depend on the current state

their volumetric ( $P, Q$ ) and deviatoric ( $\underline{P}', \underline{Q}'$ ) components\*:

$$P \equiv \underline{P} : \underline{I} ; \quad Q \equiv \underline{Q} : \underline{I} \quad (3.13a)$$

$$\underline{P}' \equiv \underline{P} - \frac{1}{3} P \underline{I} ; \quad \underline{Q}' \equiv \underline{Q} - \frac{1}{3} Q \underline{I} \quad (3.13b)$$

and then\*\*, it can be shown that Eq. 3.11 can be written separately for the volumetric and deviatoric components in the form:

$$\dot{\underline{\epsilon}}^P = \dot{\Lambda} P \quad (3.14)$$

$$\dot{\underline{\epsilon}}^P = \dot{\Lambda} \underline{P}' \quad (3.15)$$

Furthermore, combining Eqs. 3.12, 3.14, 3.15 and 3.9 we get:

$$\dot{\Lambda} = \frac{1}{H} (\underline{Q}' : \dot{\underline{s}} + Q \dot{\bar{\sigma}}) \quad (3.16)$$

which gives the magnitude of the plastic strain increment in terms of the applied increments of the deviatoric stress  $\dot{\underline{s}}$  and mean effective stress  $\dot{\bar{\sigma}}$ , separately. Finally, combining Eqs. 3.11 and 3.12 we get:

$$\dot{\underline{\epsilon}}^P = \frac{1}{H} (Q : \dot{\underline{\sigma}}) \underline{P} \quad (3.17)$$

---

\* in a fashion analogous to the decomposition of the strain increment in volumetric and deviatoric components (see Eqs. 3.5 and 3.6)

\*\* using Eqs. 3.5c and 3.6c

which gives the constitutive relation for the plastic part of soil deformation (relating  $\dot{\underline{\underline{\epsilon}}}^P$  to  $\dot{\underline{\underline{\sigma}}}$ ) provided that  $H$ ,  $\underline{Q}$ ,  $\underline{P}$  are known\*. The values of these functions and their evolution during soil deformation depend on the specific soil model used and they will be studied for the Modified Cam-Clay (MCC) model (in Section 3.3) and for a model proposed in Chapters 4 and 5. In the present chapter we discuss the features of these functions that are common in most of the existing soil models.

Equation 3.17 suffices to evaluate the plastic component of the strain increment, for a given effective stress increment. However, in the application of constitutive laws to the solution of boundary value problems via numerical methods\*\*, the problem is posed inversely: Given the applied strain increment  $\dot{\underline{\underline{\epsilon}}}$  (or its components  $\dot{\underline{\underline{\epsilon}}}$  and  $\dot{\underline{\underline{\epsilon}}}$  from Eqs. 3.5a and 3.6a), it is required to compute the corresponding effective stress increment  $\dot{\underline{\underline{\sigma}}}$  (or its components  $\dot{\underline{\underline{\sigma}}}$  and  $\dot{\underline{\underline{s}}}$ , from Eq. 3.9). Appendix A shows that\*\*\* these are given by the following expressions:

$$\dot{\underline{\underline{\sigma}}} = K\{\dot{\underline{\underline{\epsilon}}} - \dot{\underline{\underline{\Lambda}}} \underline{P}\} \quad (3.18a)$$

$$\dot{\underline{\underline{s}}} = 2G\{\dot{\underline{\underline{\epsilon}}} - \dot{\underline{\underline{\Lambda}}} \underline{P}'\} \quad (3.18b)$$

---

\*  $H$ ,  $\underline{Q}$ ,  $\underline{P}$  are functions of the current state of the element.  
 \*\* e.g., the Finite Element or the Finite Difference methods.  
 \*\*\* basically inverting the elastoplastic compliance to get the stiffness tensor, in a compact form

where

$$\dot{\Lambda} = \frac{2G(\dot{Q}' : \dot{\underline{e}}) + K Q \dot{\epsilon}}{H + 2G(\dot{Q}' : \dot{\underline{P}}') + K Q P} \quad (3.18c)$$

Eq. 3.18a gives the increment of the mean effective stress in terms of the increments of the volumetric and deviatoric strain,  $\dot{\epsilon}$  and  $\dot{\underline{e}}$  respectively. Eq. 3.18b gives the increment of the deviatoric stress in terms of the same increments of strain. Eqs. 3.18 are linear in the (effective) stress and strain increments (note that  $\Lambda$  is also a linear function of the strain increments) and can be directly used in a numerical scheme provided that  $K$ ,  $G$ ,  $P$ ,  $\underline{P}'$ ,  $Q$ ,  $\underline{Q}'$  and  $H$  are known at each stress state.

### 3.2.2.2 Elastic and Elastoplastic States

Section 3.2.2.1 discussed that upon the application of external loads, soils undergo deformations that, in general, involve both elastic (reversible) and plastic (irreversible) components (see e.g., Eq. 3.4). However, experimental evidence indicates that certain stress paths cause negligible irreversible strains. For example, consider a clay sample that is first  $K_0$ -consolidated\* and then rebounded to an overconsolidated state ( $OCR = 2$ , say). Experimental evidence shows that, for typical clays, subsequent small effective stress changes in the oedometer apparatus cause small irrever-

---

\* one-dimensional straining in the oedometer apparatus

sible deformations, which basically means that the swelling and recompression\* indices are approximately equal. Thus, for constitutive laws that do not concentrate in modelling soil behavior under repeated (cyclic) loads, it is reasonable to assume\*\* that the swelling and recompression indices are equal, or equivalently, that starting from an overconsolidated state in the oedometer apparatus, small effective stress changes cause only reversible (elastic) strains. In order to set up a framework, Plasticity Theory generalizes\*\*\* the previous conclusion and assumes that there exist soil states such that the application of any infinitesimal effective stress increment causes only reversible (elastic) strains. Such states are called elastic states. For example, overconsolidated states are elastic states but the notion of the elastic state is broader than the common definition of the overconsolidated state. Any state which is not elastic will be called an elastoplastic state and for these states there is at least one possible effective stress increment that causes both elastic and plastic strain increments\*\*\*\*. For example, any normally consolidated state is

---

\* The swelling and recompression indices are defined as the change of the void ratio per log cycle of mean effective stress during rebound and recompression (respectively) in the oedometer apparatus.

\*\* for modelling purposes.

\*\*\* The generalization is that although experimental evidence only exists for certain stress paths (e.g., oedometer), Plasticity Theory assumes that there exist states such that purely reversible strains occur for any stress path.

\*\*\*\* However, some stress changes from an elastoplastic state may cause only elastic strain changes.



an elastoplastic state; in fact, any stress change from a normally consolidated state which leads to a new normally consolidated state (virgin compression) gives a soft response (i.e., causes both elastic and plastic strains) and any stress change from a normally consolidated state which leads to an overconsolidated state (rebound) gives a stiff response (i.e., causes only elastic strains).

### 3.2.2.3 Plastic Loading and Elastic Unloading

Commonly, the notions of loading and unloading of a soil element are related to the increase and decrease (respectively) of the applied stresses\*. However, in some deformation sequences certain stress components increase while others decrease. Since such deformation sequences are common in many practical Boundary Value problems, the commonly used notions of loading and unloading are inadequate. It is thus essential in the development of the framework for Constitutive models to define loading and unloading unambiguously.

We say that the application of an infinitesimal effective stress increment represents a plastic loading condition (or that it causes yielding) if both plastic and elastic strains occur, and represents an elastic unloading condition if only elastic strains occur\*\*. According to the previous definitions:

---

\* or of a specific stress component which is considered significant in the problem

\*\* Note that plastic strains without some elastic strains never occur in Plasticity Theories.

- (i) Any infinitesimal effective stress change from an elastic (e.g. overconsolidated state) causes elastic unloading.
- (ii) An infinitesimal effective stress change from an elastoplastic (e.g. normally consolidated) state may cause either plastic loading or elastic unloading. In fact, a rebound from a normally consolidated state causes elastic unloading, whereas a stress change from a normally consolidated state leading to a new normally consolidated state (virgin compression) causes plastic loading\*.

In order to illustrate the differences between these definitions and the commonly used notions of loading and unloading, consider the following two tests:

- (i) An isotropically normally consolidated sample sheared in a drained mode in a triaxial test where the cell pressure is kept constant and the axial stress is increased.
- (ii) An isotropically normally consolidated sample sheared in a drained mode in a triaxial test where the cell pressure is kept constant and the axial stress is decreased.

---

\* A general (quantitative) criterion to distinguish between plastic loading and elastic unloading from elastoplastic states (for a given strain increment) is presented in Section 3.2.2.4.

According to the commonly used definitions, the first test is a loading test and the second an unloading test. On the other hand, according to the above definitions both tests represent plastic loading tests since plastic strains are expected in both tests. In the following, and unless explicitly stated, the definitions of plastic loading and elastic unloading introduced in this section will be used.

#### 3.2.2.4 The Yield Function and its Applications

The yield function ( $f$ ) is a scalar function of the state of a soil element\* which is introduced in Plasticity Theory for the following reasons:

(a) Distinguish between elastic and elastoplastic states.

As discussed in Section 3.2.2.2, soil behavior at elastic states is different than soil behavior at elastoplastic states. The yield function ( $f$ ) is a mathematical device capable of distinguishing between elastic and elastoplastic states since it is commonly defined such that its value is negative for an elastic state and zero for an elastoplastic state. Positive values of the yield function cannot occur for any state. Since a zero value of the yield function identifies an elastoplastic state and normally consolidated states are elastoplastic states, then the equation:

---

\* i.e., a function of the effective stresses and other variables characterizing the state of the soil element which are called state variables.

$$f(\text{state}) = 0 \quad (3.19a)$$

is valid for all normally consolidated states. Eq. 3.19a represents a surface in an effective stress space (e.g. the  $s - \bar{\sigma}$  space) which is called the yield surface. It thus follows that normally consolidated states are represented by points on the yield surface. On the other hand, any point in the interior\* of the yield surface gives

$$f(\text{state}) < 0 \quad (3.19b)$$

and thus represents an elastic state. However, overconsolidated states are elastic states which means that overconsolidated states are represented by points in the interior of the yield surface.

In summary:

- (i) The yield surface is usually represented by a (closed) surface in an effective stress space.
- (ii) Elastoplastic (e.g. normally consolidated) states are represented by points on the yield surface.
- (iii) Elastic (e.g. overconsolidated) states are represented by points in the interior of the yield surface.

---

\* In order to avoid ambiguities regarding the interior and exterior of the yield surface, the yield surface is usually chosen to be a closed surface.

Finally, it is interesting to note that since the yield surface distinguishes between normally and overconsolidated states, it is identical to the experimental "Limit State Surface" used by Tavenas and Leroueil (1977) and Tavenas et al (1978, 1979).

- (b) Define the second order tensor  $\underline{Q}$  and a criterion for plastic loading and elastic unloading from elastoplastic states.

Sections 3.2.2.2 and 3.2.2.3 showed that starting from a state on the yield surface (normally consolidated state), elastic unloading causes the stress point to retreat from the yield surface\* and produces no plastic strains, whereas any effective stress increment directed towards the outside of the yield surface causes plastic loading, leads to a new elastoplastic state\*\* and produces plastic strains. As a limiting case, it is desirable that an effective stress increment tangent to the yield surface\*\*\* causes no plastic strains, and thus the magnitude of the plastic strain increment has a continuous transition at the boundary between plastic loading and elastic unloading paths (starting from elastoplastic states). This requirement is satisfied if  $\underline{Q}$  is defined as the

---

\* i.e. the effective stress increment is directed towards the inside of the yield surface.

\*\* on the yield surface which however may have changed in position because hardening (see Section 3.3) may occur.

\*\*\* i.e.,  $\dot{\underline{\sigma}}$  is such that:

$$(\partial f / \partial \underline{\sigma}) : \dot{\underline{\sigma}} = 0$$

gradient of the yield function at the stress point representing the current stress state of the soil element\*, i.e.:

$$\underline{\underline{Q}} = \frac{\partial f}{\partial \underline{\underline{\sigma}}} \quad (3.20a)$$

Combining with Eqs. 3.13 it can be shown that\*\* the volumetric and deviatoric components of  $\underline{\underline{Q}}$  are given by:

$$Q = \frac{\partial f}{\partial \bar{\sigma}} \quad (3.20b)$$

$$\underline{\underline{Q}}' = \frac{\partial f}{\partial \underline{\underline{s}}} - \frac{1}{3} \left( \frac{\partial f}{\partial \underline{\underline{s}}} : \underline{\underline{I}} \right) \underline{\underline{I}} \quad (3.20c)$$

Having defined  $\underline{\underline{Q}}$  as the gradient of the yield function at the stress point we can now establish a quantitative criterion to distinguish between plastic loading and elastic unloading from elastoplastic states.

Section 3.2.2.3 discussed that an infinitesimal effective stress increment from an elastoplastic state may cause either plastic loading or elastic unloading and for the case of elastic unloading:

- (i) The plastic strain increment vanishes, i.e.:

$$\underline{\underline{\dot{\epsilon}}}^p = \underline{\underline{0}} \quad (3.21a)$$

$$\underline{\underline{\dot{\epsilon}}} = \underline{\underline{\dot{\epsilon}}}^e \quad (3.21b)$$

---

\* i.e.  $\underline{\underline{Q}}$  is perpendicular to the yield surface at the stress point. Note that this has nothing to do with normality since normality specifies the relation between  $\underline{\underline{P}}$  and  $\underline{\underline{Q}}$ .

\*\* Using the chain rule of differentiation in Eq. 3.20a.

(ii) The new state is elastic (overconsolidated) i.e. the stress point lies inside the yield surface, which means that the stress point retreats from the yield surface during elastic unloading. Since  $\underline{Q}$  is directed towards the outer normal to the yield surface, it immediately follows that during elastic unloading from an elastoplastic state

$$\underline{Q} : \dot{\underline{\sigma}} < 0 \quad (3.21c)$$

Using Eqs. 3.13, 3.9b and 3.21c we can show that:

$$\underline{Q}' : \dot{\underline{s}} + \underline{Q}\dot{\underline{\sigma}} < 0 \quad (3.21d)$$

and via Eqs. 3.10 and 3.21b we get the following criterion for elastic unloading from elastoplastic states:

$$2G(\underline{Q}' : \dot{\underline{\epsilon}}) + K\underline{Q}\dot{\underline{\epsilon}} < 0 \quad (3.22a)$$

and the conjugate criterion for plastic loading:

$$2G(\underline{Q}' : \dot{\underline{\epsilon}}) + K\underline{Q}\dot{\underline{\epsilon}} \geq 0 \quad (3.22b)$$

This concludes the general concepts of Incrementally Linearized Plasticity Theory. The necessary ingredients are

now available to design various soil models.

The differences between these models consist of:

- (i) The dependence of the yield function on the stress state (i.e. the form of the yield function).
- (ii) The evolution of the yield function during deformation (i.e. the hardening rules).
- (iii) The form of the tensor  $\underline{P}$  (i.e. the plastic flow rule) and,
- (iv) The form of the elastoplastic modulus  $H$  and its evolution during deformation.

Despite these differences, the algorithm used to solve the basic problem of Incremental Plasticity\* is essentially the same. Figure 3.1 shows the flow-chart of this algorithm which involves the following steps:

- (1) The value of a 'flag' is examined to check if the current state of the soil element is elastic (i.e. the stress point is in the yield surface) or elastoplastic (i.e. the stress point is on the yield surface). If the state is elastic go to step (5), otherwise continue.

---

\* which, as discussed before, is to evaluate the effective stress increment  $\underline{\sigma}$  (and thus the new stress state  $\underline{\sigma}$ ) corresponding to a (small) applied strain increment  $\underline{\epsilon}$ .



- (2) The criterion distinguishing between plastic loading and elastic unloading (Eq. 3.22) is employed. If the strain increment causes elastic unloading go to step (5), otherwise continue.
- (3) After computing  $\tilde{P}$ ,  $H$  and  $\tilde{\Lambda}$ , the elastoplastic incremental stress-strain relations (Eqs. 3.18) are used to compute the effective stress increment corresponding to the applied strain increment.
- (4) The effective stress state is updated, and then, using the hardening rules, the remaining state variables are updated and the algorithm is exited.
- (5) This step is reached if the state of the soil element is elastic or if elastic unloading takes place, and basically involves the use of the elastic incremental stress-strain relations (Eqs. 3.10) in order to compute the effective stress increment corresponding to the applied strain increment.
- (6) The new effective stress state ( $\tilde{\sigma}^N$ ) is examined to see if the associated stress point is still inside the yield surface\*, or on the yield surface\*\*, or if it has crossed the

---

\* i.e.  $f(\tilde{\sigma}^N) < 0$

\*\* i.e.  $f(\tilde{\sigma}^N) = 0$

yield surface\*. In the first two cases the 'flag' is set appropriately\*\*, the effective stress state is updated and the algorithm is exited. However if the stress point has crossed the yield surface, it means that the applied strain increment is too large and the following procedure must be followed:

- (7) The point of intersection with the yield surface is computed and the fraction of the applied strain increment which would lead to this stress state\*\*\* (via Eq. 3.10) is evaluated.
- (8) The stress state is updated using the point of intersection with the yield surface as the new stress state and then, the remaining strain increment is evaluated by subtracting the strain increment required to reach the yield surface from the applied strain increment. Finally the 'flag' is appropriately set and the algorithm transfers to step (3).

As an application of the concepts discussed in Section 3.2, Section 3.3 studies the Modified Cam-Clay (MCC) model.

---

\* i.e.  $f(\bar{\sigma}^N) > 0$

\*\* in order to be used in the following call of the algorithm.

\*\*\* i.e. the point of intersection with the yield surface.

### 3.3 THE MODIFIED CAM-CLAY MODEL

#### 3.3.1 INTRODUCTION

The Modified\* Cam-Clay (MCC) model, developed by Roscoe and his co-workers at Cambridge University (Roscoe and Burland, 1968) represents one of the early attempts to develop comprehensive constitutive laws for soils. The model is valuable because it was designed on the basis of actual clay behavior\*\* and can adequately model some important characteristics of natural clays (e.g. volumetric hardening, Critical State).

Section 3.3 describes the main features of the MCC model\*\*\* in order to:

- (i) Illustrate an application of the concepts of Plasticity Theory developed in Section 3.2.
- (ii) Assess the advantages and disadvantages of the MCC model and thus exhibit the need for further developments.
- (iii) Utilize the MCC model as a base for the development of a new model proposed in Chapters 4 and 5. This model represents a natural extension of the MCC model in order to obtain

---

\* The original Cam-Clay model (Roscoe et al, 1958, Roscoe and Poorooshasb, 1963, Roscoe et al, 1963) was modified by Roscoe and Burland in 1968 to provide more realistic predictions by changing the shape of the yield surface.

\*\* Mainly for isotropically consolidated clays.

\*\*\* Comparisons of model predictions with laboratory tests are presented in Chapter 5.

more realistic predictions without adding significant complications to the basic Cam-Clay Theory.

- (iv) Compare the predictions of the proposed model not only with actual measurements on laboratory specimens but also with the predictions of the MCC model.

The following description of the main features of the MCC model, based on modern concepts of Plasticity Theory, differs\* from the approach presented in the Roscoe and Burland (1968) paper in order to hopefully bring out the most important aspects of the model more clearly.

Section 3.2 stated that the development of an elasto-plastic model requires (in addition to the general concepts):

- (i) Specific forms of the elastoplastic modulus  $H$  and the second order tensors\*\*  $\underline{Q}$  and  $\underline{P}$  and,
- (ii) The evolution of the state variables (other than the effective stress) during deformation.

These will be presented in the remaining sections of this Chapter.

---

\* but leads to the same final results as the Cambridge approach to the issue which is based on the Differential Geometry of Surfaces.

\*\*  $\underline{Q}$  controls the direction of the effective stress increment for which the plastic flow is a maximum and  $\underline{P}$  is the direction of the plastic flow.

### 3.3.2 YIELD FUNCTION AND FLOW RULE

The MCC model adopts an ellipsoidal yield surface, symmetric about the hydrostatic axis in an effective stress space. Figure 3.2a shows the yield surface of the MCC model in an effective stress space comprised of the deviatoric stress subspace\*  $\underline{s}$  and the mean effective stress  $\bar{\sigma}$ . The yield function for such a yield surface is given by the following expression:

$$f(\bar{\sigma}, \underline{s}; \bar{\alpha}) \equiv \underline{s} : \underline{s} - c^2 \bar{\sigma} (2\bar{\alpha} - \bar{\sigma}) \quad (3.23a)$$

or:

$$\hat{f}(\bar{\sigma}, r; \bar{\alpha}) \equiv r^2 - c^2 \bar{\sigma} (2\bar{\alpha} - \bar{\sigma}) \quad (3.23b)$$

where:

$r$  is called the invariant stress deviator\*\* and is proportional to the second invariant of the stress deviator  $J_2$

$$r = \{\underline{s} : \underline{s}\}^{1/2} = \sqrt{2} J_2 \quad (3.23c)$$

$c$  is a material constant; namely the ratio of the axes of the ellipsoid, and

---

\* The scalar (invariant) stress measure  $r$  (Eq. 3.23c) can also be used instead of the deviatoric stress subspace.  
 \*\*  $r^2 = \frac{1}{3} \{(\sigma_x - \sigma_y)^2 + (\sigma_y - \sigma_z)^2 + (\sigma_z - \sigma_x)^2\} + 2\{\tau_{xy}^2 + \tau_{yz}^2 + \tau_{zx}^2\}$

$\bar{\alpha}$  is a size (hardening) state variable controlling the size of the yield surface. Changes of  $\bar{\alpha}$  during deformation allow the yield surface to expand and thus allow the strength of the soil to increase with consolidation. The hardening parameter  $\bar{\alpha}$  and its evolution during deformation are discussed in Section 3.3.4.

A comparison of Eq. 3.23 with the equation of the yield surface given by Roscoe and Burland (1968) shows that:

$$c = \sqrt{2/3} M \quad (3.23d)$$

where M is the parameter utilized by Roscoe and Burland to describe the ratio of the axes of the yield surface\*.

Using Eqs. 3.20 for the specific yield function of this model (Eq. 3.23a), we directly get for the components of  $\underline{Q}$ :

$$Q = 2c^2 (\bar{\sigma} - \bar{\alpha}) \quad (3.24a)$$

$$\underline{Q}' = 2\underline{s} \quad (3.24b)$$

Furthermore, the model employs an associated flow rule, which means that:

$$\underline{P} = \underline{Q} ; \underline{P}' = \underline{Q}' \quad (3.25)$$

---

\* and also the soil friction angle as will be shown in Section 3.3.8.

Thus, the direction of the plastic strain increment (given by  $\underline{P}$  in Eq. 3.11) coincides with the direction of the normal\* to the yield surface (given by  $\underline{Q}$  according to Eq. 3.20a). Hence, for example, if the stress state is hydrostatic (represented by point A in Fig. 3.2) the plastic strain increment is purely volumetric (i.e.  $\dot{\underline{\epsilon}}^P = \underline{0}$  since  $\underline{P}' = \underline{Q}' = \underline{0}$  for this point). On the other hand, for a stress state represented by a point at the top of the ellipsoid (point F in Fig. 3.2) the plastic strain increment is purely deviatoric (i.e.  $\dot{\underline{\epsilon}}^P = \underline{0}$  since  $\underline{P} = \underline{Q} = \underline{0}$  for this point). Finally for any other point between A and F the normality rule requires that plastic flow has both volumetric and deviatoric components.

### 3.3.3 ANISOTROPIC CHARACTERISTICS OF THE MCC MODEL

In the following, we will extensively use the notion of the rotation of principal axes. When we say that the principal axes (e.g. of stress or strain) do not rotate, we mean that the frame of the three (orthogonal) axes does not rotate in space\*\*, i.e. the major, intermediate and minor quantities (e.g. stresses or strains) are considered as a group and even if their directions are interchanged\*\*\*, we will still say

---

\* This kind of flow rule is commonly referred to as the normality rule.

\*\* This is the common definition of the rotation of principal axes used in Applied Mechanics (e.g. Shield and Ziegler, 1958, Mroz, 1967, Prevost, 1977, Prevost, 1978) and will be used here because it helps unify the concepts about anisotropy.

\*\*\* such as in a  $K_0$ -consolidated triaxial extension test.

that the principal axes have not rotated. If we want to study problems where the direction of a specific principal value is fixed we will explicitly state that (e.g. we will say that the direction of the major principal stress does not rotate).

The MCC model has the following isotropic/anisotropic features:

(1) The yield function of the MCC model (Eq. 3.23b) depends on stress only via invariant quantities; namely the first invariant of the effective stress tensor (i.e. the mean effective stress  $\bar{\sigma}$ ) and the second invariant of the stress deviator (i.e.  $r$  or  $J_2$  as Eq. 3.23c suggests). Thus, the yield function is independent of the physical directions of the principal stresses, which means that the MCC model predicts isotropic yielding, i.e. if a certain stress state causes yielding\* of the material, then any other stress state of the same magnitude but rotated with respect to the previous one\*\* will also cause yielding. This is simply because both stress states have the same values of the stress invariants.

(2) The tensor  $\underline{P}$  gives the direction of the plastic strain increment (Eq. 3.11). However, according to the MCC model,  $\underline{P} = \underline{Q}$  (normality rule) and the principal axes of  $\underline{Q}$

---

\* i.e. corresponds to a stress point on the yield surface.

\*\* i.e. having the same stress components but in a different frame of orientation.



coincide with the principal axes of the stress deviator (as Eq. 3.24 suggests). Furthermore, since the effective stress tensor and the stress deviator share the same principal axes, it follows that the MCC model predicts that:

The principal axes of the plastic strain increment coincide with the principal stress axes.

When applied to tests involving no rotation of the principal axes\*, the MCC model predicts that:

- (i) The principal axes of the plastic strain do not rotate and coincide with the principal stress axes because, as shown above, the principal axes of the plastic strain increment coincide with the principal stress axes which do not rotate.
- (ii) The principal axes of the elastic strain do not rotate and coincide with the principal stress axes because, for isotropic elasticity, the principal axes of the elastic strain coincide with the principal stress axes.

Finally, combining the last two conclusions we can say that the MCC model predicts that:

---

\* such as any test conducted in the classical triaxial and plane strain apparatuses.

For all tests that do not cause rotations of the principal stress axes, the principal strain axes do not rotate and always coincide with the principal stress axes.

This conclusion is very significant and basically shows that the anisotropic characteristics of the MCC model are limited\*. Its consequences will be studied in Chapter 4\*\* but for the moment we can say that the conclusion is not always realistic. In fact, tests on sands performed in the Directional Shear Cell show\*\*\* that if the sand was previously deformed along a set of axes different than the current principal stress axes, then the principal strain axes initially coincide with the axes of the previous deformation and during stressing gradually rotate towards the current principal stress axes.

Even though the MCC model has a lot of isotropic features\*\*\*\* the model is not isotropic since isotropy means complete lack of preferred directions in space. On the contrary, the MCC model does have preferred directions; namely the current principal stress directions and all the previous

---

\* In fact, any isotropic model would predict the same kind of behavior.

\*\* where the anisotropic characteristics of the MCC model are compared with these of the model proposed in Chapter 4 and the anisotropy expected by natural clays.

\*\*\* e.g. Arthur et al (1980).

\*\*\*\* e.g. isotropic yielding, principal strain axes coinciding with the principal stress axes when the last do not rotate, etc.

discussions exhibited their existence\*. However, since the model only recognizes the current principal stress directions, it has no memory\*\* of the preferred directions of its past deformation history\*\*\*. Thus, the MCC model cannot predict the anisotropy existing prior to the application of stresses during a test aimed to measuring the anisotropic behavior.

### 3.3.4 HARDENING CHARACTERISTICS

The hardening characteristics of a model describe the evolution of the parameters specifying the size, shape and orientation of the yield surface during plastic deformation. Since  $\bar{\alpha}$  is the only parameter of the yield surface of the MCC model, the hardening rules specify the evolution of  $\bar{\alpha}$  during plastic deformation. The model adopts the so-called  $\Rightarrow$  isotropic hardening rule (Hill, 1950; Hodge, 1955) which allows the yield surface to expand\*\*\*\* in the stress space (without changing its shape) homothetically with the origin O (Fig. 3.2) representing the pole.

The MCC model assumes that plastic loading along a

---

\* e.g. the principal axes of the plastic strain increment always coincide with the current principal stress axes.

\*\* This is a feature common to all models whose yield function depends on stress only via the invariants.

\*\*\* e.g. the principal directions of any previous straining are past preferred directions.

\*\*\*\* during loading only.

radial\* stress path (in an effective stress space) gives a linear relation between the void ratio  $e$  and the natural logarithm of the mean effective stress  $\bar{\sigma}$ , with slope  $\lambda$ :

$$\lambda = -de/d(\ln\bar{\sigma}) \quad (3.26a)$$

where  $\lambda$  is related to the virgin compression index  $C_c$  via:

$$\lambda = (0.434) \cdot C_c \quad (3.26b)$$

Furthermore, Fig. 3.2a shows that for plastic loading along radial paths, the hardening parameter  $\bar{\alpha}$  is proportional to the mean effective stress  $\bar{\sigma}$  and thus:

$$\begin{aligned} de^P &= de - de^e = -\lambda \cdot d(\ln\bar{\sigma}) + \kappa d(\ln\bar{\sigma}) = \\ &= -(\lambda - \kappa) d(\ln\bar{\sigma}) = -(\lambda - \kappa) d(\ln\bar{\alpha}) \end{aligned}$$

or:

$$\dot{e}^P = -(\lambda - \kappa) \frac{\dot{\bar{\alpha}}}{\bar{\alpha}} \quad (3.27)$$

where  $\dot{e}^P$  is the irreversible (plastic) part of the increment of the void ratio,  $\frac{\dot{\bar{\alpha}}}{\bar{\alpha}}$  is the increment of the size parameter  $\bar{\alpha}$

---

\* i.e. a stress path for which the effective stresses are at a constant ratio during deformation, e.g. isotropic consolidation or one-dimensional consolidation of normally consolidated clays.

and  $\kappa$  is related to the swelling ratio, via:

$$\kappa = (0.434) \cdot C_s \quad (3.28)$$

However, from the definition of the void ratio\*:

$$\dot{e}^p = -(1 + e_0) \dot{\epsilon}^p \quad (3.29)$$

where  $e_0$  is the initial void ratio and  $\dot{\epsilon}^p$  is the volumetric component of the plastic strain increment. Combining Eqs. 3.27 and 3.29 we get the following form of the isotropic hardening rule for the MCC model:

$$\frac{\dot{\alpha}}{\alpha} = \frac{(1 + e_0)}{(\lambda - \kappa)} \frac{\dot{\epsilon}^p}{\alpha} \quad (3.30a)$$

or using Eq. 3.14:

$$\frac{\dot{\alpha}}{\alpha} = \frac{(1 + e_0)}{(\lambda - \kappa)} \frac{\dot{\epsilon}^p}{\alpha} \quad (3.30b)$$

### 3.3.5 THE ELASTOPLASTIC MODULUS H

Section 3.2 stated that the stress point remains on the yield surface during plastic loading. Thus, the effective stress increment  $\dot{\bar{\sigma}}$  and the change of the size of the yield

---

\* Note that compressive strains are positive according to the Standard Soil Mechanics convention.

surface must be such that,  $f = 0$  continuously. This is expressed by Prager's consistency condition (Prager, 1956) which specifies that:

$$\dot{f}(\bar{\sigma}; \bar{\alpha}) = 0 \quad (3.31a)$$

and using the chain rule (and Eq. 3.20a):

$$\underline{Q} : \underline{\dot{\sigma}} + \frac{\partial f}{\partial \bar{\alpha}} \dot{\bar{\alpha}} = 0 \quad (3.31b)$$

or, using Eqs. 3.30b, 3.12 and solving for H:

$$H = \left( \frac{1 + e_0}{\lambda - \kappa} \right) \cdot \left( - \frac{\partial f}{\partial \bar{\alpha}} \right) \cdot \bar{\alpha} P \quad (3.32a)$$

where (via Eq. 3.23a):

$$\frac{\partial f}{\partial \bar{\alpha}} = - 2c^2 \bar{\sigma} \quad (3.32b)$$

and P is given by (Eqs. 3.25 and 3.24a):

$$P = 2c^2 (\bar{\sigma} - \bar{\alpha}) \quad (3.32c)$$

In the portion FAF' of the yield surface (Fig. 3.2a),  $\bar{\sigma} > \bar{\alpha}$  and thus  $P > 0$ . This means that the elastoplastic modulus H is positive along this part of the yield surface. More specifically, H reaches a maximum value at point A and decreases as

the stress point moves towards point F where it vanishes (since  $\bar{\sigma} = \bar{\alpha}$ ). Points F and F' are characteristic points of the yield surface. Section 3.3.8 shows that these points are associated with the Critical State condition\*. The geometrical loci of the Critical States are represented by the Critical State Lines (lines OF and OF' in Fig. 3.2a).

Soil elements that are initially normally consolidated or overconsolidated with an overconsolidation ratio\*\* (OCR) less than two, when sheared in an undrained mode, reach the portion FAF' of the yield surface\*\*\*. The elastoplastic modulus H is non-negative in this portion of the yield surface. Furthermore, Appendix B shows that for the MCC model\*\*\*\*, a positive value of H implies strain hardening behavior which basically means that the effective stresses increase with continued plastic deformation\*\*\*\*\*. Thus, the MCC model predicts that shearing of normally consolidated and lightly overconsolidated clays (OCR < 2) is monotonically strain

---

\* i.e. the condition where further shear strains occur without changes of the applied stresses.

\*\* In the following, the overconsolidation ratio is defined by the ratio of the maximum mean effective stress ever carried by the soil to the mean effective stress immediately before shearing.

\*\*\* The mean effective stress does not change during undrained shear from elastic states (interior of the yield surface) since Eq. 3.10a suggests that  $\bar{\sigma} = 0$ .

\*\*\*\* Actually Appendix B shows that this is true for any model equipped with an associated flow rule (normality rule).

\*\*\*\*\* Appendix B gives an exact definition for strain hardening and strain softening.

hardening until failure. Chapter 5 shows experimental data indicating that soils may strain soften for certain modes of deformation. This kind of behavior cannot be predicted by the MCC model.

### 3.3.6 EFFECTIVE STRESS PATH FOR UNDRAINED TESTS

Fig. 3.2a shows the geometric representation of an elasto-plastic stress state (point R on the yield surface) in the effective stress space ( $\underline{s}, \bar{\sigma}$ ) and Fig. 3.2b shows the geometric representation of the same state in an  $e - \bar{\sigma}$  space (where  $e$  is the void ratio). The model assumes that for each such state, the tip A of the yield surface (Fig. 3.2a) is represented in an  $e - \bar{\sigma}$  space by the intersection of the virgin isotropic consolidation curve\* with the isotropic rebound curve\*\* through the stress point (Fig. 3.2b). It is then evident from Fig. 3.2 that:

$$\bar{\sigma}_0 = 2\bar{\alpha} \quad (3.33a)$$

where  $\bar{\sigma}_0$  is the value of the (isotropic) effective stress at the tip of the yield surface.

Defining  $\eta$  as the ratio of the invariant stress deviator  $r$  (Eq. 3.23c) to the mean effective stress  $\bar{\sigma}$ , i.e.:

$$\eta \equiv r/\bar{\sigma} \quad (3.33b)$$

---

\* having slope  $\lambda$  in an  $e - \ln \bar{\sigma}$  plot.

\*\* having slope  $\kappa$  in an  $e - \ln \bar{\sigma}$  plot.



the equation of the yield surface (Eq. 3.23b) can be expressed by:

$$\frac{\bar{\sigma}}{\bar{\sigma}_0} = \frac{c^2}{c^2 + \eta^2} \quad (3.34)$$

which is identical to the equation of the yield surface given by Roscoe and Burland (1968), i.e. an ellipsoid.

A particularly useful stress measure\* is the mean effective stress  $\bar{\sigma}_e$  of the point E (Fig. 3.2b) on the virgin isotropic consolidation line, corresponding to the same void ratio as the current state (point R). Since the void ratio remains constant along an undrained path, the value of  $\bar{\sigma}_e$  also remains constant and thus, each undrained path corresponds to a specific value of  $\bar{\sigma}_e$ , in the same way that each undrained path corresponds to a specific value of the void ratio. Furthermore, assuming that both the virgin isotropic consolidation and the rebound curves are straight lines in an  $e-\ln\bar{\sigma}$  plot (with slopes  $\lambda, \kappa$  respectively), we have (see Fig. 3.2b):

$$\lambda \ln \left( \frac{\bar{\sigma}_e}{\bar{\sigma}_0} \right) = \kappa \ln \left( \frac{\bar{\sigma}}{\bar{\sigma}_0} \right) \quad (3.35a)$$

or

$$\frac{\bar{\sigma}}{\bar{\sigma}_e} = \left( \frac{\bar{\sigma}}{\bar{\sigma}_0} \right)^{1 - \frac{\kappa}{\lambda}} \quad (3.35b)$$

---

\* especially in studying undrained stress paths.

Combining Eqs. 3.34 and 3.35b we get:

$$\frac{\bar{\sigma}}{\bar{\sigma}_e} = \left( \frac{c^2}{c^2 + \eta^2} \right)^{1 - \frac{\kappa}{\lambda}} \quad (3.36)$$

Equation 3.36 provides the effective stress path during undrained shear of a clay with void ratio  $e$  associated with a specific value of  $\bar{\sigma}_e$  (from Fig. 3.2b).

### 3.3.7 PREDICTION OF $K_0$

Most natural sedimentary clays are deposited under conditions of zero lateral strain and consequently this "at rest" condition represents the starting point for most practical problems. The principal stresses are assumed to act in the vertical and horizontal directions and the coefficient of earth pressure at rest ( $K_0$ ) is defined as the ratio of the horizontal to the vertical effective stress. Since the  $K_0$ -condition is very often encountered in practice, any realistic model should either accurately predict the value of  $K_0$  or, alternatively, consider  $K_0$  as an input material constant.

The MCC model can predict  $K_0$  for normally consolidated clays. In fact, using the incremental stress-strain relations (Eqs. 3.18) and the values of  $\underline{P}$  and  $\underline{Q}$  computed for the MCC model in the previous sections, it can be shown\* that  $K_0$  can be computed from the solution of the following quadratic

---

\* Neglecting the effect of elastic shear strains, i.e. for  $G = \infty$

equation:

$$AK_o^2 + BK_o + C = 0 \quad (3.37a)$$

where

$$A = 6 \frac{\kappa}{\lambda} - 2c^2 - 3 \quad (3.37b)$$

$$B = - (3 \frac{\kappa}{\lambda} + 2c^2 + 3) \quad (3.37c)$$

$$C = - 3 \frac{\kappa}{\lambda} - \frac{c^2}{2} + 6 \quad (3.37d)$$

Section 3.3.9 shows that the material constant  $c$  is related to the soil friction angle  $\bar{\phi}$  at the critical state via the following relation:

$$c = \frac{2\sqrt{6} \sin \bar{\phi}}{3 - \sin \bar{\phi}} \quad (3.38)$$

which is obtained by matching the friction angle  $\bar{\phi}$  of a tri-axial compression test and the MCC strength parameter\*  $c$ . Thus, the predicted value of  $K_o$  is a function of the ratio  $\kappa/\lambda$  and  $\bar{\phi}$ . Table 3.1 shows values of  $K_o$  predicted by Eq. 3.37 for different values of the ratio  $\lambda/\kappa$  ( $= C_c/C_g$ ) and  $\bar{\phi}$ . Comparing these predictions with the experimentally measured  $K_o$ -value for normally consolidated Boston Blue Clay\*\* (Ladd et al,

---

\* The strength parameter  $c$  is related to  $M$  via Eq. 3.23d.

\*\*  $\bar{\phi} \approx 30^\circ$  and  $\lambda/\kappa \approx 6$

1971) we can clearly see that the MCC model overestimates  $K_0$  by about 15-20% (measured value 0.53 to 0.55). However, the predicted trends are correct. Ladd et al (1977) show that, in general, the  $K_0$ -value decreases with increasing friction angle  $\bar{\phi}$ .

### 3.3.8 THE CRITICAL STATE

Experimental observations show that, when sheared, soils eventually\* reach a state where deformation takes place under constant effective stresses and no further volume changes (i.e. no further volumetric strains). This is often called the Critical State Condition\*\* (Schofield and Wroth, 1968, Roscoe and Burland, 1968) and basically defines the failure of the soil element.

The MCC model predicts that at the Critical State:

- (i) The void ratio  $e$  and the associated mean effective stress  $\bar{\sigma}$  correspond to points located on a straight line (in a  $e-\ln\bar{\sigma}$  plot) which is parallel to the virgin isotropic consolidation line (Critical State Line in Fig. 3.2b).
- (ii) Critical States are represented in an effective stress space (e.g. the  $s - \bar{\sigma}$  space of

---

\* i.e. at large strains

\*\* Usually the Critical State Condition corresponds to the state of maximum obliquity, where the ratio of the shear stress to the mean effective stress is a maximum.

Fig. 3.2a) by a circular cone with apex at the origin, axis along the hydrostatic line and passing through the peak points of the yield surface (points F and F' in Fig. 3.2a\*).

In fact, a point which is located at the peak of the yield surface (e.g. point F in Fig. 3.2a) has the following properties:

- (i) The direction normal to the yield surface has no component along the mean effective stress (hydrostatic) axis, i.e.  $\partial f / \partial \bar{\sigma} = 0$  or,  $Q = 0$  which means that also  $P = 0$ .
- (ii) Since  $P = 0$  the plastic strain increment is purely deviatoric (i.e.  $\dot{\epsilon}^P = 0$ , because of Eq. 3.14) which means that there are no plastic volumetric strains.
- (iii) There is no hardening, i.e. there are no further changes of the size of the yield surface (because of Eq. 3.30b and since  $P = 0$ ).
- (iv) The elastoplastic modulus H vanishes (because of Eq. 3.32a).
- (v) According to Eqs. 3.18b and 3.18c

$$\underline{Q}' : \underline{\dot{s}} = 0$$

This means that the deviatoric stress

---

\* In Fig. 3.2a the cone is represented by the Critical State Lines OF and OF'.

increment is tangent to the yield surface, and since the yield surface does not expand, it follows that no further changes\* of the deviatoric (shear) stresses can take place.

(vi) During undrained shear, the mean effective stress does not change (see Eq. 3.18a).

(vii) From Fig. 3.2a it is clear that:

$$\eta \equiv r/\bar{\sigma} = c \quad (3.39a)$$

This is the equation governing the Critical State Condition.

(viii) Combining Eq. 3.39a with the equation of the Effective Stress Path for Undrained shear (Eq. 3.36) we get:

$$\bar{\sigma} = \bar{\sigma}_e \left(\frac{1}{2}\right)^{1 - \frac{\kappa}{\lambda}} \quad (3.39b)$$

and:

$$r = c \bar{\sigma}_e \left(\frac{1}{2}\right)^{1 - \frac{\kappa}{\lambda}} \quad (3.39c)$$

which give the values of the mean effective stress  $\bar{\sigma}$  and the invariant stress deviator  $r$  at undrained failure for all modes of deformation.

The failure criterion of the MCC model (Eq. 3.39a) is purely isotropic since both  $r$  and  $\bar{\sigma}$  are quantities invariant with

---

\* Evidently, the principal stress axes do not rotate, too.

respect to rotations of the coordinate axes. However, most soils are anisotropic and thus an isotropic failure criterion is not generally satisfactory in describing their failure characteristics\*.

In the triaxial test\*\*, using Eq. 3.23c we get:

$$r = \sqrt{\frac{2}{3}} (\sigma_v - \sigma_h) \quad (3.40)$$

where  $\sigma_v$  and  $\sigma_h$  are the vertical and horizontal stresses, respectively. Thus, if we define the undrained shear strength in the triaxial mode by:

$$s_u = \frac{1}{2} |\sigma_v - \sigma_h|_f \quad (3.41)$$

where subscript "f" denotes the "at failure" condition, then:

$$s_u = \sqrt{\frac{3}{2}} c \bar{\sigma}_e \left(\frac{1}{2}\right)^{2 - \frac{\kappa}{\lambda}} \quad (3.42a)$$

or (via Eq. 3.23d):

$$s_u = M \bar{\sigma}_e \left(\frac{1}{2}\right)^{2 - \frac{\kappa}{\lambda}} \quad (3.42b)$$

---

\* See Chapter 5 for comparisons of MCC predictions with laboratory test data.

\*\* both in compression and extension and for any state along the stress path

Equations 3.42 give the undrained shear strength in the triaxial mode in terms of the material constants ( $c$  or  $M$ ,  $\lambda$ ,  $\kappa$ ) and the void ratio (or equivalently  $\bar{\sigma}_e$ ). It is thus evident that the model predicts the same value of  $s_u$  for both triaxial compression and extension tests, i.e. it fails to predict strength anisotropy. Furthermore, the values of  $r$  in plane strain and\* triaxial modes are related by:

$$r(\text{plane strain}) = (2/\sqrt{3}) \cdot r(\text{triaxial}) \quad (3.42c)$$

at failure, since the MCC model predicts that the intermediate principal stress is equal to the average of the maximum and minimum principal stresses at failure. Thus, the undrained shear strengths in plane strain and triaxial modes predicted by the MCC model are related via:

$$s_u(\text{plane strain}) = (2/\sqrt{3}) s_u(\text{triaxial}) \quad (3.42d)$$

i.e. the MCC model predicts that the undrained shear strength in plane strain is 15% higher than that in the triaxial mode.

We will finally give an equation for the undrained shear strength of overconsolidated clays in terms of the overconsolidation ratio (OCR):

---

\* both compression and extension



If  $\bar{\sigma}_c$  is the mean effective stress immediately before shearing, then combining Eqs. 3.42b and 3.35b\* we get:

$$\frac{s_u}{\bar{\sigma}_c} = M \cdot \left(\frac{1}{2}\right)^{2 - \frac{\kappa}{\lambda}} \cdot \left(\frac{\bar{\sigma}_o}{\bar{\sigma}_c}\right)^{1 - \frac{\kappa}{\lambda}} \quad (3.43a)$$

or, since  $\bar{\sigma}_o/\bar{\sigma}_c$  is the overconsolidation ratio\*\* (OCR):

$$\frac{s_u}{\bar{\sigma}_c} = M \cdot \left(\frac{1}{2}\right)^{2 - \frac{\kappa}{\lambda}} \cdot (\text{OCR})^{1 - \frac{\kappa}{\lambda}} \quad (3.43b)$$

### 3.3.9 THE SOIL FRICTION ANGLE AND THE MCC MODEL

The Mohr-Coulomb criterion is widely used in Soil Mechanics and describes the failure condition of the soil in terms of a friction angle  $\bar{\phi}$ . More specifically, the Mohr-Coulomb criterion assumes that failure of the soil takes place when the ratio of the shear stress  $\tau$  to the normal effective stress  $\bar{\sigma}_n$  on any plane reaches the value:

$$\frac{\tau}{\bar{\sigma}_n} = \tan \bar{\phi} \quad (3.44)$$

where the friction angle  $\bar{\phi}$  is a material constant. On the

---

\*  $\bar{\sigma} \equiv \bar{\sigma}_c$

\*\* Defined in terms of mean effective stress instead of vertical effective stress (as is common in Soil Mechanics)

contrary, the MCC model uses a failure criterion associated with the Critical State condition, i.e., it assumes that failure occurs when the ratio of the invariant stress deviator  $r$  (defined by Eq. 3.23c) to the mean normal effective stress  $\bar{\sigma}$  is equal\* to:

$$\frac{r}{\bar{\sigma}} = c \quad (= \sqrt{\frac{2}{3}} M) \quad (3.45)$$

Although the Mohr-Coulomb and MCC failure criteria are different, they basically have the same philosophy: they both assume that failure takes place when the ratio of some measure of shear stress ( $\tau$  or  $r$  respectively) to some measure of normal stress ( $\bar{\sigma}_n$  or  $\bar{\sigma}$  respectively) reaches a certain value (related to the strength parameter of each model,  $\bar{\phi}$  and  $M$  respectively). However, these stress measures are different and thus the two failure criteria are different. In fact, the Mohr-Coulomb failure criterion is represented by an irregular hexagonal pyramid and the MCC criterion is represented by a circular cone\*\* in the effective stress space.

It is desirable to relate the strength parameters  $\bar{\phi}$  and  $M$  of the two failure criteria for two reasons:

---

\* See Eq. 3.39a

\*\* It is thus identical to the so-called "extended Mises criterion" which is basically the transformation of the Mises cylindrical yield surface to a cone in order to include dependence of soil failure on the confinement.

- (i) Standard laboratory tests give the failure condition via a friction angle  $\bar{\phi}$ . Thus,  $\bar{\phi}$  could directly be used to evaluate the MCC strength parameter M.
- (ii) Compare the predictions of the Mohr-Coulomb and MCC failure criteria.

Unfortunately, since the criteria are different it is impossible to establish general relationships between  $\bar{\phi}$  and M that are valid for all modes of deformation. Therefore, the following procedure for matching the two criteria\* will be used:

- (i) Write one failure criterion (i.e. Eq. 3.44 or 3.45) and express the stress measures that appear (i.e.  $\bar{\sigma}_n, \bar{\sigma}, r, \tau$ ) in terms of the stress components (e.g. the Cartesian components).
- (ii) Apply the relations between the stress components for the specific mode of deformation that the criteria will be matched (e.g.  $\bar{\sigma}_x = \bar{\sigma}_z$  in the triaxial mode of shearing).
- (iii) Repeat steps (i) and (ii) above for the other failure criterion.
- (iv) Eliminate the stress components between the two resulting expressions (one for

---

\* in some mode of deformation of our choice, e.g. triaxial compression, triaxial extension, etc.

each criterion) and hence reach a relation between the strength parameters of the two criteria.

Table 3.2 gives these relations when the two criteria are matched in the triaxial compression (TC), triaxial extension (TE) and plane strain (PS) modes of deformation. These relations are quite useful. For example, suppose  $\bar{\phi} = 30^\circ$  was measured in a triaxial compression test. Matching the MCC strength parameter M with the friction angle  $\bar{\phi}$  in triaxial compression we have:

$$M = \frac{6 \sin \bar{\phi}}{3 - \sin \bar{\phi}} \quad (3.46)$$

and hence, when  $\bar{\phi} = 30^\circ$ , we get  $M = 1.2$ . Using the MCC strength parameter M computed before, the MCC failure criterion predicts:

$$\sin \bar{\phi} = \frac{3M}{6 - M} \quad (3.47)$$

for the friction angle in triaxial extension. Therefore, for  $M = 1.2$  we get  $\bar{\phi} = 48.6^\circ$ .

### 3.3.10 INPUT PARAMETERS FOR THE MCC MODEL

Table 3.4 shows the input parameters required to utilize the MCC model to predict soil behavior, as well as the use of these parameters and methods to determine them from conventional laboratory tests. The model requires two consolidation parameters (namely  $C_c$  and  $C_s$ ), a strength parameter (M), the

elastic shear modulus ( $G$ ) and the initial void ratio ( $e_0$ ).

In numerical implementations of the MCC model via the Finite Element Method, the values of the state variables at each integration point are also required, i.e.:

- (i) The current effective stress tensor  $\bar{\sigma}$   
(or its isotropic and deviatoric components  $\bar{\sigma}$  and  $\underline{s}$  respectively).
- (ii) The size  $\bar{\alpha}$  of the yield surface.

Using the model parameters and state variables described above, the general procedure\* presented in Section 3.2.2.4 (and in Fig. 3.1) can be used to estimate the effective stress increment  $\dot{\bar{\sigma}}$  (or its components  $\dot{\bar{\sigma}}$  and  $\dot{\underline{s}}$ ) caused by a given strain increment  $\dot{\underline{\epsilon}}$ . Table 3.4 summarizes the required equations in the case of the MCC model.

---

\* valid for any soil model

**Modified Cam-Clay Model Predictions of  $K_0$  for Different Values  
of the Friction Angle  $\bar{\phi}$  and the Ratio  $\lambda/\kappa$  ( $= C_c/C_s$ )**

$\bar{\phi}$ / $\lambda/\kappa$	10.0	8.0	6.0	5.0
24°	0.753	0.835	0.932	0.991
26°	0.719	0.781	0.873	0.964
28°	0.684	0.720	0.783	0.882
30°	0.650	0.654	0.663	0.692
32°	0.616	0.586	0.524	0.406

Notes: (i)  $\bar{\phi}$  is matched with the Cam-Clay strength parameter  $M$  (or  $c$ ) in the triaxial compression mode of failure.

(ii) Elastic shear strains neglected ( $G = \infty$ )

**Table 3.1: Modified Cam-Clay Model Predictions of  $K_0$  for Different Values  
of the Friction Angle  $\bar{\phi}$  and the Ratio  $\lambda/\kappa$  ( $= C_c/C_s$ )**

Relations Between the Strength Parameters of the  
Mohr-Coulomb and Modified Cam-Clay Models

Matching Mode of Deformation	Relations* Between $\bar{\phi}$ and M
TC	$M = \frac{6 \sin \bar{\phi}}{3 - \sin \bar{\phi}} ; \sin \bar{\phi} = \frac{3M}{6 + M}$
TE	$M = \frac{6 \sin \bar{\phi}}{3 + \sin \bar{\phi}} ; \sin \bar{\phi} = \frac{3M}{6 - M}$
PS**	$M = \sqrt{3} \sin \bar{\phi} ; \sin \bar{\phi} = \frac{M}{\sqrt{3}}$

\* Elastic strains are neglected.

\*\* It is assumed that at failure:  $\bar{\sigma}_2 = \frac{1}{2} (\bar{\sigma}_1 + \bar{\sigma}_3)$   
where  $\bar{\sigma}_1, \bar{\sigma}_2, \bar{\sigma}_3$  are the major, intermediate  
and minor principal stresses.

Table 3.2: Relations Between the Strength Parameters of the  
Mohr-Coulomb and Modified Cam-Clay Models

Input Parameters for the Modified Cam-Clay Model

Parameter	Used for	How to obtain
M or c	Shape of yield surface	From friction angle $\bar{\phi}$ (see Section 3.3.9 and Table 3.2)  $c = \sqrt{2/3} M$
$C_c$ or $\lambda$	Changes of size of the yield surface	From virgin isotropic compression curve:  $\lambda = (0.434) \cdot C_c = de/d(\lambda \bar{\sigma})$
$C_s$ or $\kappa$	Changes of size of the yield surface	From isotropic rebound curve:  $\kappa = (0.434) \cdot C_s = de/d(\lambda \bar{\sigma})$
G	Elastic shear modulus	From small strain region of any interpretable test (see Section 3.2.1)
$e_o$	Initial void ratio	Laboratory measurement

Table 3.3: Input Parameters for the Modified Cam-Clay Model



Incremental Stress-Strain Relations  
for the MCC Model

$\kappa = 0.434 C_s$ $\lambda = 0.434 C_c$	$c = \sqrt{2/3} M$ $K = \frac{1 + e_o}{\kappa} \bar{\sigma}$
$\dot{\underline{\underline{\epsilon}}} = \dot{\underline{\underline{\epsilon}}} : \underline{\underline{I}}$	$\dot{\underline{\underline{\epsilon}}} = \dot{\underline{\underline{\epsilon}}} - \frac{1}{3} \dot{\underline{\underline{\epsilon}}} \underline{\underline{I}}$
$Q = P = 2c^2 (\bar{\sigma} - \bar{\alpha})$	$\underline{\underline{Q}}' = \underline{\underline{P}}' = 2\underline{\underline{s}}$
$H = 2c^2 \bar{\sigma} \bar{\alpha} \left( \frac{1 + e_o}{\lambda - \kappa} \right) P$	
$\dot{\underline{\underline{\Lambda}}} = \frac{2G(\underline{\underline{Q}}' : \dot{\underline{\underline{\epsilon}}}) + KQ \dot{\underline{\underline{\epsilon}}}}{H + 2G(\underline{\underline{Q}}' : \underline{\underline{P}}') + KQP}$	
$\dot{\bar{\sigma}} = K[\dot{\underline{\underline{\epsilon}}} - \dot{\underline{\underline{\Lambda}}}P]$	$\dot{\underline{\underline{s}}} = 2G[\dot{\underline{\underline{\epsilon}}} - \dot{\underline{\underline{\Lambda}}}\underline{\underline{P}}']$
$\dot{\bar{\alpha}} = \left( \frac{1 + e_o}{\lambda - \kappa} \right) \bar{\alpha} \dot{\underline{\underline{\Lambda}}} P$	
$\bar{\sigma} = \bar{\sigma} + \dot{\bar{\sigma}}$ $\underline{\underline{s}} = \underline{\underline{s}} + \dot{\underline{\underline{s}}}$	$\bar{\alpha} = \bar{\alpha} + \dot{\bar{\alpha}}$

Table 3.4: Incremental Stress-Strain Relations  
for the MCC Model

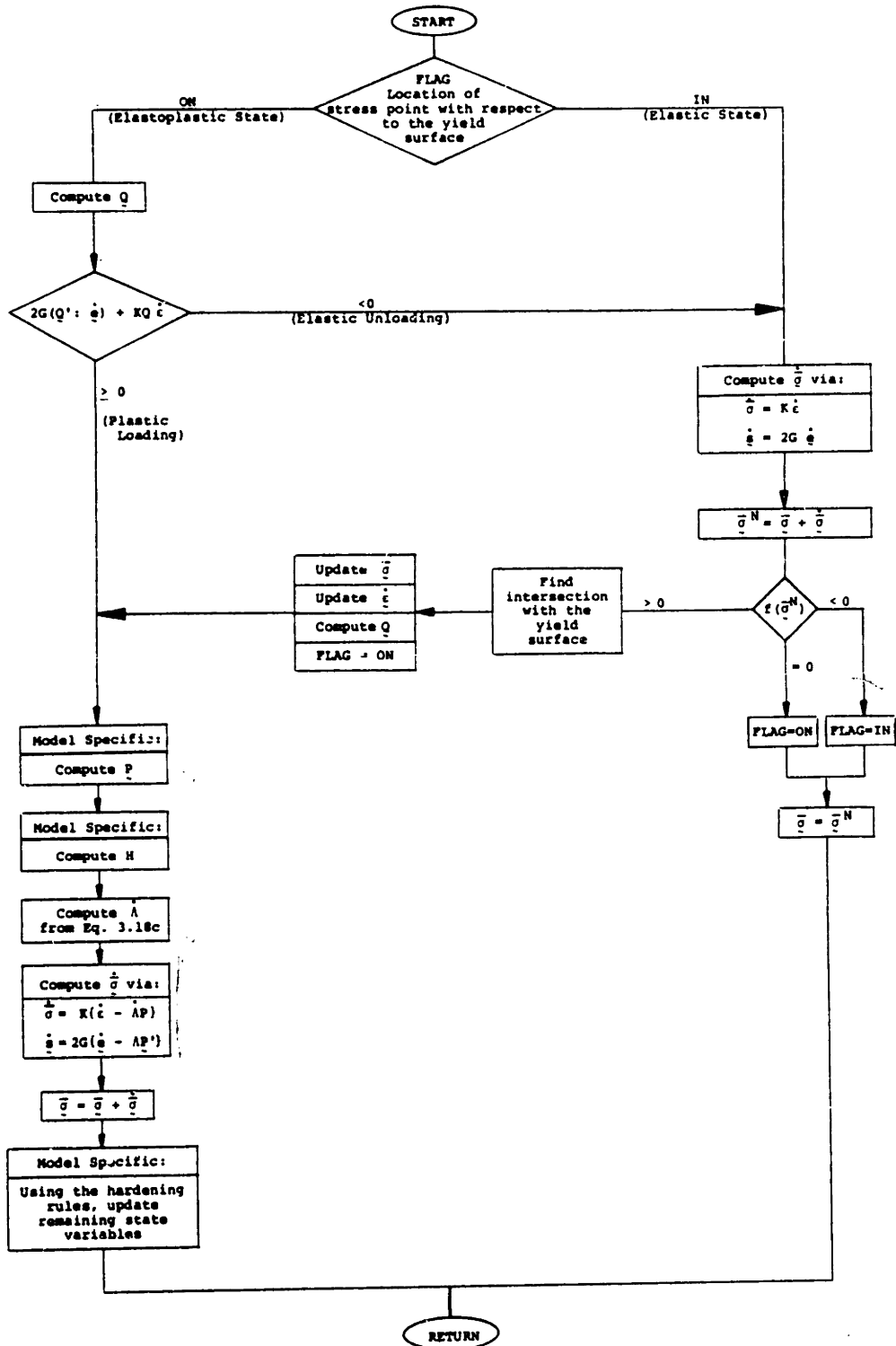


**Fig. 3.1:** Flow chart of the incremental algorithm for an inviscid effective stress-strain soil model based on Plasticity Theory

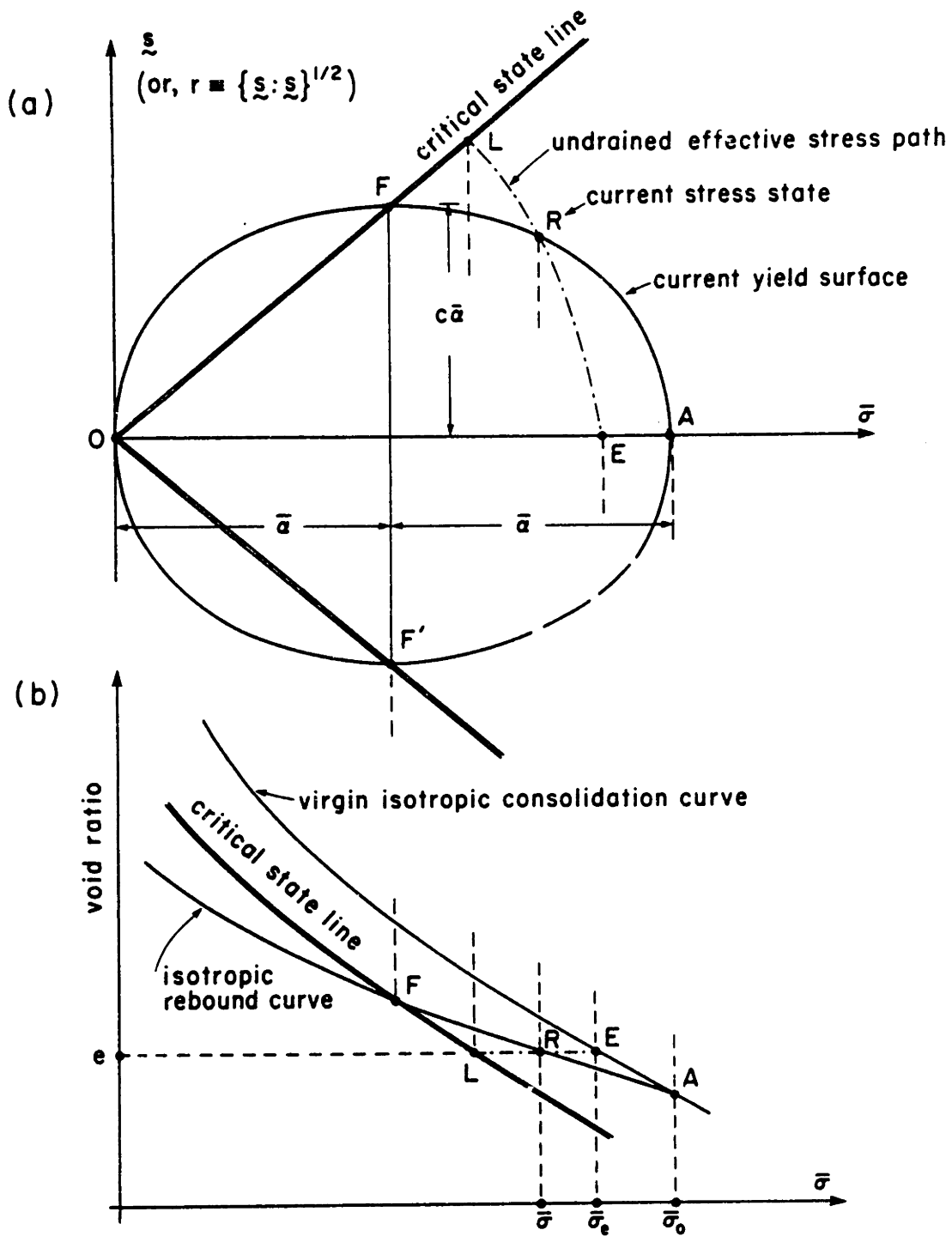


**Fig. 3.2:** The yield surface of the Modified Cam-Clay model and characteristic effective stress paths

CHAPTER 4  
THE PROPOSED MODEL

4.1 INTRODUCTION

Chapter 5 evaluates the Modified Cam-Clay (MCC) model\* and shows its serious limitations in predicting the stress-strain-strength behavior of the  $K_0$ -normally consolidated resedimented Boston Blue Clay in selected laboratory tests (e.g., Undrained Triaxial, Plane Strain and Direct Simple Shear). It is thus evident that the MCC model is too simple to predict the behavior of natural clays\*\*. The main limitations of the MCC model are:

- (i) For normally consolidated and lightly over-consolidated clays ( $OCR < 2$ ) the model does not predict strain softening.
- (ii) The model overpredicts the value of the coefficient of earth pressure at rest ( $K_0$ ). Since the  $K_0$ -condition is very important\*\*\*, more realistic  $K_0$ -values are needed.
- (iii) The yield function adopted by the MCC model depends only on the (first and second) invariants of the effective stress tensor; this

---

\* discussed in Section 3.3

\*\* especially these deposited under  $K_0$  conditions

\*\*\* it represents the initial condition for most practical problems

significantly restricts the ability of the model to describe the anisotropic stress-strain behavior of most natural clays and, more specifically:

- (a) It cannot simulate the memory that clays have of their history of straining. The only preferred directions that the model takes into consideration are the current principal stress directions.
- (b) It cannot simulate the strength anisotropy commonly exhibited by most natural clays (e.g., it predicts the same value of the undrained shear strength in triaxial compression and triaxial extension modes of deformation).

In order to get more realistic predictions of the stress-strain-strength behavior of natural clays significant improvements are required. The present chapter proposes a soil model which attempts to remedy the limitations of the MCC discussed above. The MCC model will be used as a base for the development of the proposed model for the following reasons:

- (i) It is based on studies of actual clay behavior and hence incorporates the effects of the confining stress, void ratio as well as the concept of the Critical State.

- (ii) It has a solid theoretical formulation (Plasticity Theory) and thus it can be used for describing general stress conditions\* (e.g. three-dimensional and involving rotations of the principal axes).
- (iii) It is a reasonably simple model, amenable to further development without significant changes of the basic computational algorithm (Fig. 3.1).
- (iv) The model parameters required to characterize the soil (and hence solve problems) can be determined by means of existing laboratory tests.
- (v) Predictions of the model for isotropically consolidated clays have been favorable (Roscoe and Burland, 1968).

The remaining sections of this chapter illustrate the main features of the proposed model.

---

\* it has been applied to the solution of Boundary Value Problems by Simpson and Wroth, 1972, Wroth et al, 1974, Miller et al, 1978, Randolph et al, 1979, etc.

## 4.2 THE YIELD SURFACE AND THE YIELD FUNCTION

### 4.2.1 EXPERIMENTAL EVIDENCE

Section 3.3.2 indicated that the yield surface adopted by the MCC model has its axis oriented along the hydrostatic line\* (see Fig. 3.2a). Recent data indicate that this assumption needs serious reevaluation.

- (i) Leroueil (1977), Tavenas and Leroueil (1977) and Leroueil et al (1979), experimentally studied the behavior of the (lean sensitive) Champlain clay\*\* deposits in the St. Lawrence lowland and the Ottawa valley in Canada. They checked the possible applicability of the concepts of yielding\*\*\*, by studying the effects of the initial (anisotropic)  $K_0$ -consolidation on the shape of the yield surface. In order to define the yield surface (or curve), they used (a) radial\*\*\*\* stress paths with various stress ratios starting from an overconsolidated

---

\* this is the so-called space diagonal of a space comprised of the components of the effective stress tensor

\*\* also called Leda Clay

\*\*\* as defined in Plasticity (see Section 3.2.2.3)

\*\*\*\* i.e., stress paths geometrically represented by a straight line passing through the origin

state\*, and (b) undrained triaxial tests starting from the same state. A point on the yield surface (or on the Limit State Curve, according to their nomenclature), was defined by an abrupt change in the slope of the stress-strain curve, i.e., the transition from a stiff (elastic) state to a soft (elastoplastic) state.

Figures 4.1 and 4.2 show the zones of probable yield curves in a two-dimensional (shear stress vs. "mean" normal effective stress) stress space. Tavenas and Leroueil (1977) concluded that:

"The shape of this experimental yield locus strongly differs from the theoretical shape of the yield locus in the Cam-Clay models. In particular, if the yield locus appears to have a more or less elliptical shape, this ellipse is not centered on the isotropic line but rather on a line close to the  $K_0$ -line of the normally consolidated clay, the intersection of the yield locus with the  $K_0$ -line corresponding roughly with the pre-consolidation state of stress."

and also that:

"These findings are consistent with the concepts of the Cam-Clay model but not with the details of that model. The main differences come from the fact that the Cam-Clay model has been developed,

---

\* obtained via the undrained rebound of block samples to a hydrostatic stress state during the process of sampling.



and is applicable, for isotropic materials for which the yield locus is centered on the isotropic stress axis. In natural clays, deposition and pre-consolidation develop under  $K_0$ -stress conditions. As a consequence, the clay structure is organized anisotropically and it is logical to admit that the stress conditions causing volumetric yield of that structure should be referred to the  $K_0$ -condition, and thus, that the yield locus of a natural clay, should be centered on the  $K_0$ -line."

- (ii) Wood (1981), performed true triaxial tests on normally consolidated Boston Blue Clay and investigated stress paths similar to the undrained expansion of a long cylindrical cavity. He attempted to match laboratory measurements with the predictions of the MCC model, and concluded that:

"This model is not particularly successful in matching the observed response.. Cam-Clay is an isotropically hardening model, founded historically largely on data from conventional triaxial compression tests on isotropically consolidated samples. Anisotropically consolidated samples are expected to behave anisotropically (Lewin, 1973) and a qualitative indication of the observed behavior might be associated with a rather long slender constant volume surface centered on the one-dimensional consolidation path rather than the squat constant volume surface implied by Cam-Clay, centered on the stress space diagonal."

- (iii) Finally, Ko and Sture (1980) in their state-of-the-art paper on "Data Reduction and Application for Analytical Modelling", critically review the Cam-Clay model and conclude:

"The model performs best for clays that have initially experienced isotropic consolidation. A  $K_0$ -consolidation history frequently results in yield loci which seem to be centered on the  $K_0$ -line rather than the hydrostatic axis. Such behavior can only be modelled by anisotropic hardening models."

In summary, experimental evidence strongly suggests that for  $K_0$ -consolidated clays, the yield surface should be centered along the  $K_0$ -line rather than the hydrostatic line assumed by the MCC model.

Generalizing the experimental evidence we will use the following working hypothesis:

Soil elements consolidated along a radial stress path can be described by a model with a yield surface oriented\* along the (radial) stress path of the consolidation.

Evidently, the hypothesis includes isotropic consolidation,  $K_0$ -consolidation as well as consolidation paths along any other radial direction.

#### 4.2.2 THE FORM OF THE YIELD SURFACE AND ITS PROPERTIES

The proposed model adopts a yield surface which is shown in Fig. 4.3a for the case of a soil element\*\* A, normally consolidated along a radial stress path with direction

$$\underline{\beta} \equiv \underline{b} + \underline{1} \quad (4.1)$$

\* in the effective stress space

\*\* denoted by points  $A_1$  and  $A_2$  is parts (a) and (b) of the figure

in the effective stress space  $(\underline{s}, \bar{\sigma})$ , where  $\underline{\beta}$  is a symmetric second order tensor with unit isotropic component ( $\underline{I}$ ) and a deviatoric component equal to\*  $\underline{b}$ . The yield surface of an "equivalent" MCC model is shown for comparison in Fig. 4.3b.

The yield surface of the proposed model has the following properties:

- (i) It is a distorted ellipsoid in the  $(\underline{s}, \bar{\sigma})$  space\*\* with axis along the direction  $\underline{\beta}$  of the radial stress path as suggested by Tavenas and Leroueil (1977), Ko and Sture (1980) and Wood (1981).
- (ii) The yield function associated with this yield surface is given by

$$f(\bar{\sigma}, \underline{s}; \bar{\alpha}, \underline{b}) \equiv (\underline{s} - \bar{\sigma}\underline{b}) : (\underline{s} - \bar{\sigma}\underline{b}) - c^2 \bar{\sigma} (2\bar{\alpha} - \bar{\sigma}) \quad (4.2)$$

i.e., it is a function of the effective stress state (namely, the mean effective stress  $\bar{\sigma}$  and the stress deviator  $\underline{s}$ ) and the hardening state variables  $\bar{\alpha}$  and  $\underline{b}$ ,

---

\* Since  $\underline{I}$  is a unity, we can always use  $\underline{b}$  (instead of  $\underline{\beta}$ ) to describe the direction of the radial stress path.

\*\* It also looks like a distorted ellipsoid in a stress space comprised of the (cartesian) effective stress components.

representing the size and orientation of the yield surface respectively. Finally  $c$  is a material constant representing the ratio of the axes of the yield surface.

- (iii) The intersection of the yield surface with any deviatoric subspace (e.g. the hyperplane  $xx$  in Fig. 4.5a) is a "hypersphere" (shown in Fig. 4.5b) centered at the point where the radial stress path (with direction  $\beta$ ) intersects the deviatoric subspace (point C in Fig. 4.5).
- (iv) A soil element\* A, normally consolidated along the direction  $\beta$ , is located at the tip of the yield surface and has stress components:

$$\underline{s} = 2\bar{\alpha}\underline{b} \quad (4.3a)$$

$$\bar{\sigma} = 2\bar{\alpha} \quad (4.3b)$$

- (v) The yield surface of the proposed model reduces to the yield surface of the MCC model when the orientation tensor  $\underline{b}$  vanishes (i.e., if  $\underline{\beta} = \underline{I}$ ) implying isotropic consolidation.

---

\* represented by points  $A_1$  and  $A_2$  in parts (a) and (b) of Fig. 4.3 respectively.

(vi) The yield function of the proposed model does not depend on the stress solely via invariant quantities\* because of the existence of tensor  $\underline{b}$ . In fact, the tensor  $\underline{b}$  introduces preferred directions other than the principal stress directions and thus allows a more realistic simulation of anisotropic soil behavior (see Section 4.4). For this reason we will refer to it as the anisotropy tensor.

Using the yield function of the proposed model (Eq. 4.2) and Eqs. 3.20, the volumetric and deviatoric components ( $Q$  and  $Q'$  respectively) of the gradient  $\underline{Q}$  of the yield function\*\* are given by

$$\left\| \begin{aligned} Q &= 2c^2 \left( \bar{\sigma} - \sqrt{\frac{2}{3}} \bar{\alpha} \right) - 2(\underline{s} - \bar{\sigma} \underline{b}) : \underline{b} & (4.4a) \\ Q' &= 2(\underline{s} - \bar{\sigma} \underline{b}) & (4.4b) \end{aligned} \right.$$

More specifically, for a point located at the tip of the yield surface,

---

\*The MCC model depends on stress solely via invariant quantities; namely:

$$\bar{\sigma} \equiv \frac{1}{3}(\bar{\sigma} : \underline{I}) \quad \text{and} \quad r \equiv (\underline{s} : \underline{s})^{1/2}$$

as discussed in Section 3.3.

\*\*  $\underline{Q}$  is in the direction normal to the yield surface at the  $\underline{\tilde{s}}$  stress point (see Section 3.2.2.3). Its components are defined by Eqs. 3.13.

$$Q = 2c^2 \bar{\alpha}$$

$$Q' = 0$$

which basically means that the direction normal to the yield surface at the tip, is parallel to the  $\bar{\sigma}$ -axis (see Fig. 4.3). Note that Eqs. 4.4 reduce to Eqs. 3.24 for  $b = 0$  (i.e., for the case of the MCC model).

Figure 4.4 shows the representation of the yield surface (for a  $K_0$ -consolidated sample) in two stress spaces useful in studying the stress paths followed in the conventional triaxial test. Figure 4.4a shows the representation of the yield surface in a stress space comprised of the mean effective stress and the shear stress acting on the sample. Figure 4.4b shows the representation of the same yield surface in the more conventional  $(q/\bar{\sigma}_{v0}, \bar{p}/\bar{\sigma}_{v0})$  space where:

$$q \equiv \frac{\sigma_v - \sigma_h}{2} \quad (4.5a)$$

$$\bar{p} \equiv \frac{\bar{\sigma}_v + \bar{\sigma}_h}{2} \quad (4.5b)$$

Evidently, the ellipsoidal shape of the yield surface is distorted differently in each of the stress spaces.

Attempts to model soil behavior by means of yield surfaces oriented along axes other than the hydrostatic are also reported in the literature. Ohta and Wroth (1976) presented a model with a yield surface\* which is permanently oriented along the line of the initial anisotropic consolidation of the clay. Pender (1978), Ghaboussi and Momen (1979), and Hashiguchi (1979) also used rotated yield surfaces to account for the initial anisotropic consolidation of natural clays. However, predictions of most of these models\*\* had limited success because we believe that a yield surface permanently oriented along the  $K_0$ -line can adequately predict the behavior of  $K_0$ -consolidated clays only right after consolidation. In fact, after significant shearing or subsequent consolidation under a different stress ratio there is no reason for the yield surface to remain oriented along the  $K_0$ -line. For example, consider a soil element which is initially  $K_0$ -normally consolidated in situ. According to the previous discussion, the state of this element can be represented by a yield surface oriented along the  $K_0$ -line. The soil element is then removed from the ground (perfect sampling), i.e., the shear stress applied in situ is removed under constant volume, leaving the element in an overconsolidated isotropic stress state. Since

---

\* they used the shape of the yield surface adopted by the original Cam-Clay model (Roscoe et al, 1963)

\*\* Some of these models are just conceptual and the associated papers do not give any comparisons with measured soil behavior.

the undrained removal of the shear stress causes elastic unloading, the yield surface is not altered and remains oriented along the  $K_0$ -line. The soil element is subsequently isotropically consolidated by applying an all-around isotropic stress (e.g. by increasing the cell pressure in the triaxial apparatus). We believe that during this isotropic consolidation the soil gradually erases its memory of the previous ( $K_0$ -consolidated) state and acquires the features of the new (isotropic) stress path (i.e., the soil has fading memory). Thus, the yield surface must gradually rotate towards the isotropic consolidation line and, since  $b$  defines the orientation of the axis of the yield surface,  $b$  will, in general, change both in magnitude and in direction (i.e. its principal axes will rotate). The changes of  $b$  along certain stress paths give a convenient way to take into consideration the changes of anisotropy during soil deformation.



### 4.3 HARDENING RULES

#### 4.3.1 HARDENING CHARACTERISTICS OF THE PROPOSED MODEL

The hardening characteristics of a Plasticity model specify the evolution of the size, shape, location and orientation of the yield surface during plastic loading\*. In the proposed model hardening is described by the hardening parameters  $\bar{\alpha}$  and  $\bar{b}$  which control the size and orientation of the yield surface respectively\*\*. The evolution of these hardening parameters is described by the following hardening rules:

(1) The Isotropic Hardening Rule:

The isotropic hardening rule of the proposed model specifies the evolution of the size of the yield surface during plastic loading and has the form:

$$\frac{\dot{\bar{\alpha}}}{\bar{\alpha}} = \phi \bar{\alpha} \dot{\epsilon}^p \quad (4.6a)$$

i.e., it is basically a volumetric\*\*\* hardening rule, analogous to the hardening rule of the MCC model (Eq. 3.30a) with the only difference that now  $\phi$  is a dimensionless function of

---

\* By convention, elastic unloading causes no hardening which means that the size, shape, location and orientation of the yield surface do not change.

\*\* The shape of the yield surface does not change during deformation. The location of the yield surface also does not change since it always passes through the point of zero stress (origin).

\*\*\* since the change of the size of the yield surface is proportional to the plastic volumetric strain increment

the state variables to be evaluated subsequently (see Eq. 4.10).

(2) The Kinematic Hardening Rule:

The kinematic hardening rule of the proposed model specifies the evolution of the orientation of the yield surface during plastic loading and has the form:

$$\dot{\underline{b}} = \psi \left[ \frac{1}{\alpha} (\underline{s} - \bar{\sigma} \underline{b}) \right] \dot{\underline{\epsilon}}^P \quad (4.6b)$$

where  $\psi$  is a dimensionless material constant that controls the rate at which the soil erases its memory of its history preferred directions, i.e., the rate at which it alters its anisotropy. The magnitude of the change in anisotropy ( $\dot{\underline{b}}$ ) is proportional to the plastic volumetric strain increment ( $\dot{\underline{\epsilon}}^P$ ) which means that the kinematic hardening rule is volumetric. The direction of the change in anisotropy is assumed parallel to the direction of  $(\underline{s} - \bar{\sigma} \underline{b})$  for the following reasons:

- (i)  $\dot{\underline{b}}$  is a second order deviatoric tensor and thus it can only be controlled by the deviatoric components of the state variables\*, i.e., in the case of the proposed model, the stress deviator  $\underline{s}$  and the anisotropy tensor  $\underline{b}$ .

---

\* for incrementally linearized theories the direction of  $\dot{\underline{b}}$  cannot depend on the directions of  $\dot{\underline{\epsilon}}^P$  and/or  $\dot{\underline{s}}$ .

- (ii) When the principal axes of stress ( $\underline{s}$ ) and anisotropy ( $\underline{b}$ ) coincide, no rotations of the principal directions of anisotropy are expected (see Section 4.4.2) and hence, the principal axes of  $\dot{\underline{b}}$  must coincide with the principal axes of  $\underline{b}$ , as Eq. 4.6b suggests.
- (iii) We believe that during soil deformation the principal axes of anisotropy rotate towards the principal stress axes (see Section 4.4.2). Equation 4.6b shows that the proposed model has this feature, as illustrated in Fig. 4.5: Figure 4.5a shows the yield surface of the proposed model, the stress point P corresponding to a soil element on the yield surface and the deviatoric hyperplane xx through P. Figure 4.5b shows the intersection of the yield surface with the deviatoric hyperplane xx. It is then easy to show that:

$$\overline{CP} = \underline{s} - \overline{\sigma b}$$

and combining with Eq. 4.6b we get that the yield surface rotates toward P, i.e., the current stress state or, equivalently, that the principal axes of anisotropy rotate towards the principal stress axes.

(iv) We believe that consolidation along a radial stress path is the only deformation sequence that preserves soil anisotropy (i.e.,  $\dot{\underline{b}} = \underline{0}$ ). The kinematic hardening rule of the proposed model is consistent with this assumption because for radial stress paths

$$\underline{s} = \bar{\sigma} \underline{b}$$

as Eqs. 4.3 suggest.

#### 4.3.2 THE CONSISTENCY CONDITION

During plastic loading from an elastoplastic state\* the stress point remains on the yield surface. (see Section 3.2.2.3). Thus, the changes of size, shape, location and orientation of the yield surface must be such that  $f = 0$  both before and after the application of the effective stress increment  $\dot{\underline{\sigma}}$ . This is expressed by Prager's consistency condition (Prager, 1956):

$$\dot{f}(\bar{\sigma}; \bar{\alpha}, \underline{b}) = 0 \quad (4.7)$$

Using the chain rule of differentiation and Eq. 3.20a we get:

$$\dot{Q} : \dot{\underline{\sigma}} + \frac{\partial f}{\partial \bar{\alpha}} \dot{\bar{\alpha}} + \frac{\partial f}{\partial \underline{b}} : \dot{\underline{b}} = 0 \quad (4.8)$$

---

\* i.e., a state on the yield surface

where (via Eq. 4.2):

$$\frac{\partial f}{\partial \bar{\alpha}} = - 2c^2 \bar{\sigma} \quad (4.9a)$$

and,

$$\frac{\partial f}{\partial \bar{b}} = - 2\bar{\sigma}(\bar{s} - \bar{\sigma}\bar{b}) \quad (4.9b)$$

Finally substituting from Eqs. 4.9 and 4.6 in Eq. 4.8 and using Eqs. 3.14, 3.12 and 4.2 we get:

$$\phi = \frac{1}{\bar{\alpha}} \left\{ \frac{1}{2c^2 \bar{\sigma}} \left( \frac{H}{P} \right) - \psi \left( \frac{\bar{\sigma}}{\bar{\alpha}} \right) (2\bar{\alpha} - \bar{\sigma}) \right\} \quad (4.10)$$

which is used to estimate  $\phi$ , provided that  $H$  has been evaluated (see Section 4.8).

## 4.4 SOIL ANISOTROPY

### 4.4.1 INTRODUCTION

Ample experimental data indicate that soil behavior is, in general, anisotropic which means that soil properties are associated with certain preferred\* directions in space (e.g.: Casagrande and Carillo, 1944; Mitchell, 1976; Oda and Koishikawa, 1977; Martin and Ladd, 1975; Krizek, 1977; Arthur et al, 1977; Prevost, 1978; Ladd, 1980). The following describes various attempts to define the sources and mechanisms of soil anisotropy.

Casagrande and Carillo (1944) distinguished between two forms of anisotropy in soils: inherent and induced anisotropy. Inherent anisotropy was defined as a "physical characteristic inherent in the material and entirely independent of the applied stresses", whereas induced anisotropy was defined as "due exclusively to the strain associated with the applied stresses". The classification of Casagrande and Carillo is conceptually pleasing because it separates the effects of "soil structure"\*\* giving rise to inherent anisotropy and the effects of pre-straining causing induced anisotropy. However, this classification provides little help in quantifying soil anisotropy

---

\* with respect to a set of fixed coordinate axes.

\*\* According to Lambe (1958), has two components: the orientation and distribution of particles in the soil, i.e., its fabric; and the nature, magnitude and orientation of the interparticle forces.

for purposes of predicting behavior. For example, a soil involving no induced anisotropy must have experienced an isotropic stress history (involving no shearing). Such conditions are not encountered in either natural or man-made soils and hence inherent anisotropy cannot be measured.

Ladd (1980) has distinguished between certain forms of anisotropy as follows:

- (i) Inherent: that caused by initial one-dimensional deposition and subsequent  $K_0$ -consolidation and,
- (ii) Initial: that existing prior to the application of stresses during a test aimed at measuring anisotropic behavior.

Ladd's inherent anisotropy results from both Casagrande and Carillo's inherent and induced anisotropy for a one-dimensional consolidation stress path and basically is the anisotropy that a  $K_0$ -consolidated soil possesses. On the other hand, Ladd's initial anisotropy is basically the anisotropy that a soil possesses at any stage during deformation and may result from both Casagrande and Carillo's inherent and induced anisotropy.

#### 4.4.2 QUANTITATIVE DESCRIPTION OF ANISOTROPY

At any stage during deformation, soil anisotropy implies the existence of preferred directions due to:

- (i) The soil memory of its history:

During deposition and one-dimensional consolidation, gravity imposes a preferred direction,

and any subsequent straining of the soil imposes additional preferred directions; namely the principal directions of the applied strain increments. These preferred directions will be called history preferred directions, since they basically contain the memory that soil has of its history.

(ii) The current stress state of the soil:

Also imposes preferred directions; namely the principal stress directions\*.

The grouping of the factors causing anisotropy in these two classes is useful in quantifying anisotropy for the purpose of predicting soil behavior by means of mathematical models. In fact, Section 3.3.3 indicated that the MCC model incorporates anisotropic characteristics caused by the current principal stress directions but lacks history preferred directions. By introducing the anisotropy tensor  $b$  in the proposed model, the history preferred directions can be taken into consideration\*\*.

In summary, the anisotropic features of the proposed model are fully described by:

---

\* The only tensor with no preferred directions is the isotropic tensor.

\*\* The use of a single tensor to describe all history preferred directions is probably an oversimplification of soil behavior. However, we believe that such a model can provide acceptable predictions especially since in most natural soil deposits the directions of deposition and prestraining coincide.



- (i) The effective stress tensor  $\bar{\sigma}$  and,
- (ii) The anisotropy tensor  $\underline{b}$ .

The following examples illustrate the importance of  $\bar{\sigma}$  and  $\underline{b}$ .

(1) Example 1 (Isotropic Consolidation):

Consider a remolded\* clay sample that is subjected to isotropic consolidation. During isotropic consolidation the effective stress is isotropic,  $\underline{b} = \underline{0}$ \*\* and hence, like the MCC model, the proposed model predicts isotropic behavior, i.e., purely volumetric strains. This result appears reasonable provided that the soil has no inherent anisotropy as defined by Casagrande and Carillo, 1944 (see Section 4.4.1). Clearly, neither the MCC model nor the proposed model can incorporate this type of inherent anisotropy.

(2) Example 2 ( $K_0$ -Consolidation):

Consider a clay sample deposited along the vertical (y) direction and consolidated under no horizontal strains ( $K_0$ -consolidation). Then, the stress point lies on the  $K_0$ -line and the yield surface is oriented along the  $K_0$ -line, which means that:

$$\bar{\sigma}_x = \bar{\sigma}_z = K_0 \bar{\sigma}_y ; \bar{\sigma}_{xy} = \bar{\sigma}_{yz} = \bar{\sigma}_{zx} = 0 \quad (4.11a)$$

---

\* Remolding completely erases the soil memory and thus it erases soil anisotropy.

\*\* since the radial stress path is along the hydrostatic axis (see Eq. 4.3a)

and using Eqs. 4.3:

$$b_x = b_z = -\frac{b_y}{2} = -\frac{1 - K_0}{1 + 2K_0}; \quad b_{xy} = b_{yz} = b_{zx} = 0 \quad (4.11b)$$

Note that in Eq. 4.11b the anisotropy tensor  $\underline{b}$  has only one independent component, the same principal directions as  $\bar{\underline{\sigma}}$  but is different than\*  $\bar{\underline{\sigma}}$ . The anisotropy exhibited by this clay is called inherent anisotropy according to Ladd\*\* (1980). The proposed model can describe this type of anisotropy because both  $\underline{b}$  and  $\bar{\underline{\sigma}}$  are non-hydrostatic. The MCC model can also describe this type of anisotropy because for a  $K_0$ -consolidated state,  $\bar{\underline{\sigma}}$  and  $\underline{b}$  have the same principal directions. Thus, although the MCC does not possess history preferred directions (i.e.  $\underline{b} = 0$ ) the anisotropy of a  $K_0$ -consolidated state can be described via the current (non-hydrostatic) effective stress tensor.

### (3) Example 3 (Radial Stress Paths):

Consider a remolded clay sample which is consolidated along an arbitrary radial path in the stress space (as in Example 2 but not necessarily along the  $K_0$ -line). According to the proposed model (see Section 4.3.1) consolidation along a radial stress path preserves the orientation of the yield

---

\* $\bar{\underline{\sigma}}$  has dimensions of stress and  $\underline{b}$  is dimensionless.  
 \*\* but not according to Casagrande and Carillo (1944)

surface in the stress space\* which means that the anisotropy is not altered ( $\dot{b} = 0$ ). Furthermore, according to the proposed model, consolidation along a radial stress path is the only loading sequence that preserves soil anisotropy.

(4) Example 4 (Tests in the Triaxial Cell):

Consider the hypothetical case of a clay sample initially  $K_0$ -normally consolidated (in the vertical direction) and tested in the triaxial cell with the vertical (y) axis of the sample along the axis of the cell. For any stress path (drained or undrained, monotonic or cyclic) in the triaxial cell, the proposed model predicts\*\* that:

- (i) The principal axes of anisotropy (i.e., of  $\tilde{b}$ ) do not rotate and coincide with the axes of the cell, i.e.:

$$b_{xy} = b_{yz} = b_{zx} = 0$$

- (ii) The clay remains cross-anisotropic, i.e.:

$$b_x = b_z$$

- (iii) The principal axes of strain coincide with the principal axes of anisotropy (i.e., the axes of the cell).

---

\*  $b = s/\bar{\sigma}$  where  $s$ ,  $\bar{\sigma}$  are the deviatoric and mean effective stresses.

\*\* because of Eq. 4.6b and since no shear stresses are applied on the faces of the sample

It is thus evident that, for tests in the Triaxial Cell, the anisotropy tensor has two independent components ( $b_x$  and  $b_y$ ) and, at any stage during deformation, the magnitudes of these components depend on the history of the effective stresses (as dictated by Eq. 4.6b).

The MCC model predicts (see Section 3.3.3) that for tests in the Triaxial Cell, the principal axes of strain coincide with the principal stress axes (i.e. the axes of the cell) which is identical to the prediction of the proposed model.

(5) Example 5 (Tests in the True Triaxial Apparatus):

Consider the hypothetical case of a clay sample initially  $K_0$ -normally consolidated (in the vertical direction) and tested in a True Triaxial Apparatus (TTA); (e.g., Sture and Desai, 1979) with the vertical axis of the sample along the vertical (y) axis of the apparatus. For any stress path (drained or undrained) in the TTA, the principal stress axes coincide with the axes of the apparatus and thus, with the initial principal axes of anisotropy.

The proposed model predicts (see Eq. 4.6b) that:

- (i) The principal axes of anisotropy (i.e. of  $\underline{b}$ ) do not rotate and coincide with the axes of the apparatus, i.e.:

$$b_{xy} = b_{yz} = b_{zx} = 0$$

- (ii) The principal axes of strain coincide with the principal axes of anisotropy (i.e. with the axes of the apparatus).

It is thus evident that for tests in the TTA the anisotropy tensor has three independent components ( $b_x$ ,  $b_y$  and  $b_z$ ) and, at any stage during deformation, the magnitudes of these components depend on the history of the effective stresses (as dictated by Eq. 4.6b).

The MCC model predicts (see Section 3.3.3) that for tests in the TTA, the principal axes of strain coincide with the principal stress axes (i.e. the axes of the cell) which is identical to the prediction of the proposed model.

(6) Example 6 (Tests in the Directional Shear Cell):

The Directional Shear Cell (DSC); (e.g., Arthur et al, 1977) imposes the following conditions on the faces of a cubical sample:

- (i) Plane Strain in the vertical (y) direction,  
i.e.:

$$\epsilon_y = \tau_{xy} = \tau_{zy} = 0$$

- (ii) Independently controlled normal stresses  $\sigma_x$  and  $\sigma_z$  on the lateral surfaces of the sample.
- (iii) The principal stress axes can rotate continuously in the x-z plane. This is achieved by applying shear stresses  $\tau_{xz}$  on the lateral surfaces of the sample.

Consider the hypothetical case of a clay sample initially  $K_0$ -normally consolidated (in the vertical direction) and tested

in the DSC with the vertical axis of the sample along the vertical (y) axis of the apparatus. It is evident that, initially, the principal axes of anisotropy coincide with the axes of the apparatus and the sample is cross-anisotropic in the x-z plane, as Eqs. 4.11 suggest. The sample is then sequentially subjected to three Stages of loading in the DSC:

Stage 1:

Stage 1 involves shearing (drained or undrained) in the x-z plane with the principal stress axes along the axes of the apparatus (i.e.,  $\tau_{xz} = 0$ ) and leads to a new state with  $\bar{\sigma}_x \neq \bar{\sigma}_z$ . The proposed model then predicts

$$b_x \neq b_z ; b_{xz} = 0$$

which means that:

- (i) The sample is no longer cross-anisotropic but shearing in the x-z plane has induced preferred direction along the x and z axes without rotating the principal axes of anisotropy.
- (ii) The principal stress axes coincide with the principal axes of anisotropy.

The MCC model also predicts this type of anisotropy\* because it happens that the principal axes of anisotropy coincide with

---

\* although  $b_{xz} = 0$

the principal stress axes and thus, the MCC model describes the anisotropy via the preferred directions of the (non-hydrostatic) stress tensor.

Stage 2:

Stage 2 involves the removal of the shear stress in the x-z plane and leads to a new state with isotropic stresses in the x-z plane (i.e.,  $\bar{\sigma}_x = \bar{\sigma}_z$ ). The MCC model predicts that after the removal of the shear stress, the sample is again cross-anisotropic in the x-z plane\*. On the contrary, the proposed model predicts that the sample is not cross-anisotropic (because  $b_x \neq b_z$ ) and the principal axes of anisotropy coincide with the axes of the apparatus. In fact, the removal of the shear stress involves elastic unloading which, according to the proposed model causes no hardening. Hence, the orientation of the yield surface is not altered, which means that the anisotropy remains unchanged.

In summary, the sequence of Stage 1 shearing and Stage 2 unloading introduces preferred directions (history preferred directions) in the plane of symmetry of a previously cross-anisotropic clay sample, thus inducing initial anisotropy (Ladd, 1980). The proposed model predicts this type of anisotropy (via the anisotropy tensor  $b$ ) whereas the MCC model fails to predict it. However, the MCC model can predict

---

\* since  $\bar{\sigma}_x = \bar{\sigma}_z$ ,  $\tau_{xz} = 0$  and the principal stress directions are the only preferred directions of the MCC model

some types of initial anisotropy since, it predicts the anisotropy induced after Stage 1 shearing.

Stage 3:

Stage 3 involves shearing (drained or undrained) in the x-z plane with fixed directions of the principal stress axes, different than the axes of the apparatus (i.e.,  $\tau_{xz} \neq 0$ ) and thus, not coinciding with the principal axes of anisotropy\*.

The proposed model predicts (see Section 4.3.1) that during Stage 3 shearing:

- (i) The principal axes of anisotropy gradually rotate in the x-z plane towards the principal stress axes.
- (ii) The principal axes of the strain increment gradually rotate in the x-z plane towards the principal stress axes. Initially, the principal axes of the strain increment coincide with the principal axes of anisotropy (i.e. with the axes of the apparatus) since these are the only\*\* preferred directions in the x-z plane. With continued shearing, the principal axes of the strain increment are dictated by both the principal axes of aniso-

---

\* After Stage 2, the principal axes of anisotropy coincide with the axes of the apparatus.

\*\* The stress state is initially isotropic in the x-z plane.



tropy and the principal stress axes and, since the principal axes of anisotropy rotate towards the principal stress axes, the principal axes of the strain increment also rotate towards the principal stress axes.

On the contrary, the MCC model predicts that the principal axes of the strain increment coincide with the principal stress axes (see Section 3.3.3), i.e., do not rotate.

Regarding predictions of the directions of the principal axes of the strain increment, Stage 3 shearing in the DSC revealed differences between the MCC and the proposed models, whereas shearing in the Triaxial Cell and the True Triaxial Apparatus (see Examples 4 and 5 above) indicated identical behavior. These differences emanate from the fact that the MCC model does not take into consideration the history preferred directions and thus, the differences can only be revealed when the history preferred directions (i.e., the principal axes of  $b$ ) are distinct from the principal stress directions, as in the case of Stage 3 shearing in the DSC. On the contrary, shearing in the Triaxial Cell and the True Triaxial Apparatus cannot separate the effects of history preferred directions and principal stress directions since they always coincide. In order to achieve conditions where the history preferred directions (i.e., the principal axes of anisotropy) are dis-

tinct from the principal stress axes\*, some laboratories test samples "cut" at varying angles to the principal axes of anisotropy and shear the samples by applying (or thinking that they apply) stress changes with principal axes along the geometrical axes of the sample. However, such tests give highly non-uniform stresses and strains inside the sample posing significant problems in interpreting the test data. In fact, since the principal axes of stress and anisotropy are distinct, the principal axes of strain in general do not coincide with the principal stress axes\*\*. However, the Triaxial Cell compels the principal axes of stress and strain to coincide at all times with the geometrical axes of the sample; hence non-uniform stresses and strains in the sample.

#### 4.4.3 ANISOTROPIC FEATURES OF THE PROPOSED MODEL

Based on the discussions of the previous sections, the present section summarizes the anisotropic features of the proposed model\*\*\*:

##### Feature 1 (for strains):

The directions of the principal axes of the plastic strain

---

\* using conventional Triaxial Cells

\*\* As discussed before, the principal strain axes lie between the principal stress and anisotropy directions.

\*\*\* For comparison, the corresponding features of the MCC model are (see Section 3.3.3): The principal axes of the plastic strain increment always coincide with the principal stress directions. Furthermore, in a test that does not involve rotations of the principal stress directions, the principal axes of strain do not rotate and coincide with the principal stress axes.

increment depend on the directions of (a) the principal stress axes and (b) the principal axes of anisotropy (i.e., b).

When the principal stress and anisotropy axes coincide, the principal axes of the plastic strain increment also coincide with them. Furthermore, in a test that does not involve rotations of the principal stress axes and if the principal axes of anisotropy initially coincide with the principal stress axes, then the principal strain axes do not rotate and coincide with the principal stress axes.

Feature 2 (for anisotropy changes):

The application of an infinitesimal effective stress increment causes the principal axes of anisotropy to, in general, rotate towards the principal stress axes. If specifically, the principal axes of anisotropy coincide with the principal stress axes, then the principal axes of anisotropy do not rotate during the application of an infinitesimal effective stress increment. Furthermore, in a test that does not involve rotations of the principal stress axes, and if the principal axes of anisotropy initially coincide with the principal stress axes, then the principal axes of anisotropy do not rotate and coincide with the principal stress axes.

#### 4.5 TRANSFORMED VARIABLES FOR THE DESCRIPTION OF THE PROPOSED MODEL

In presenting the general concepts of Plasticity Theory and in describing the MCC and the proposed models we used general tensorial spaces: the effective stress space  $(\underline{s}, \bar{\sigma})$ , the strain space  $(\underline{e}, \epsilon)$  and the components  $(Q', Q)$ ,  $(P', P)$  and  $(b, l)$  of the  $\underline{Q}$ ,  $\underline{P}$  and  $\underline{\beta}$  tensors respectively. For the sake of simplicity in the numerical implementation of the proposed model\*, we now introduce a set of transformed variables for the tensorial quantities mentioned above. Table 4.1 presents the transformed variables for the effective stress tensor  $\bar{\sigma}$ , the strain tensor  $\underline{\epsilon}$ , the gradient of the yield surface  $\underline{Q}$ , the plastic flow direction  $\underline{P}$  and the anisotropy tensor  $\underline{\beta}$ . Each transformed variable involves six components: one isotropic component (namely  $\bar{\sigma}$ ,  $\epsilon$ ,  $Q$ ,  $P$ ,  $l$  respectively) and five deviatoric components (e.g.,  $S_1, S_2, S_3, S_4$  and  $S_5$  are the transformed deviatoric components of stress).

The transformed variables offer many advantages:

- (i) It can be shown that all the tensor relations of Chapters 3 and 4 can be written in terms of the transformed variables in a form completely analogous to their tensorial form. For example it can be shown that:

---

\* as well as the MCC model

$$\underline{\underline{s}} : \underline{\underline{s}} = \sum_{i=1}^5 S_i^2 \quad (4.12a)$$

$$(\underline{\underline{s}} - \bar{\sigma}\underline{\underline{b}}) : (\underline{\underline{s}} - \bar{\sigma}\underline{\underline{b}}) = \sum_{i=1}^5 (S_i - \bar{\sigma}b_i)^2 \quad (4.12b)$$

$$\underline{\underline{Q}}' : \dot{\underline{\underline{e}}} = \sum_{i=1}^5 Q_i \dot{E}_i \quad (4.12c)$$

$$\underline{\underline{Q}}' : \dot{\underline{\underline{s}}} = \sum_{i=1}^5 Q_i \dot{S}_i \quad (4.12d)$$

$$\underline{\underline{P}}' : \underline{\underline{Q}}' = \sum_{i=1}^5 P_i Q_i \quad (4.12e)$$

$$Q_i = \frac{\partial f}{\partial S_i} \quad (4.12f)$$

$$\dot{E}_i = \dot{E}_i^e + \dot{E}_i^p \quad (3.4 \text{ bis})$$

$$\dot{E}_i^p = \dot{\Lambda} P_i \quad (3.15 \text{ bis})$$

$$\dot{S}_i = 2G\{\dot{E}_i - \dot{\Lambda}P_i\} \quad (3.18 \text{ bis})$$

$$\dot{b}_i = \psi \left[ \frac{1}{\alpha} (S_i - \bar{\sigma}b_i) \right] \dot{\epsilon}^p \quad (4.6 \text{ bis})$$

(ii) Most of the practical problems can be solved in convenient subspaces involving a reduced number of variables. For example:

- (a) Any triaxial test can be represented in the  $(\bar{\sigma}, S_1)$  two-dimensional stress space, since

$$S_2 = S_3 = S_4 = S_5 = 0$$

Then, the yield functions of the MCC and the proposed models (Eqs. 3.23a and 4.2 respectively) can be written:

$$f_1 \equiv S_1^2 - c^2 \bar{\sigma} (2\bar{\alpha} - \bar{\sigma}) = 0 \quad (4.13a)$$

$$f_2 \equiv (S_1 - \bar{\sigma} b_1)^2 - c^2 \bar{\sigma} (2\bar{\alpha} - \bar{\sigma}) = 0 \quad (4.13b)$$

where:

$$\bar{\sigma} = (\bar{\sigma}_v + 2\bar{\sigma}_h) / 3 \quad (4.14a)$$

$$S_1 = (\bar{\sigma}_v - \bar{\sigma}_h) \sqrt{2} / \sqrt{3} \quad (4.14b)$$

Equations 4.13 show that the two-dimensional representation of the yield surface of the MCC model is an ellipse and the two-dimensional representation of the yield surface of the proposed model is a distorted (rotated) ellipse as shown in Fig. 4.4a.

(b) Any true triaxial (or plane strain) test can be represented in the  $(\bar{\sigma}, S_1, S_2)$  three-dimensional stress space since

$$S_3 = S_4 = S_5 = 0$$

(c) Any DSC test can be represented in the  $(\bar{\sigma}, S_1, S_2, S_3)$  four-dimensional stress space since:

$$S_4 = S_5 = 0$$

(d) Any plane strain (or axisymmetric) Boundary Value problem can be studied in the  $(\bar{\sigma}, S_1, S_2, S_3)$  four-dimensional stress space.

(iii) The transformed variables for all quantities in Table 4.1 have exactly the same format\*, which significantly simplifies their use in computational algorithms.

---

\* Mroz (1967) also used transformed stress quantities to study plane stress problems. Prevost (1977) used the same quantities to study plane strain and axisymmetric problems. However, the transformed variables used by these investigators do not have the uniformity of the variables in Table 4.1.

4.6 A FAILURE CRITERION FOR PEAK  
AND CRITICAL STATES

The MCC model predicts that normally consolidated clays strain harden when sheared\* and eventually reach a "Critical State" where further deformation takes place under constant effective stresses and volume. The geometrical representation of the Critical States in the  $(\underline{s}, \bar{\sigma})$  effective stress space is a circular conical surface with its apex at the origin, its axis along the  $\bar{\sigma}$ -axis and is given by the equation:

$$h(\bar{\sigma}, \underline{s}) \equiv \underline{s} : \underline{s} - k^2 \bar{\sigma}^2 = 0 \quad (4.15a)$$

where k is a material constant describing the strength of the clay\*\*. Using the transformed variables introduced in Section 4.5, Eq. 4.15a can be written:

$$h(\bar{\sigma}, S_i) \equiv \sum_{i=1}^5 S_i^2 - k^2 \bar{\sigma}^2 = 0 \quad (4.15b)$$

and specifically for the triaxial test:

$$h(\bar{\sigma}, S_1) \equiv S_1^2 - k^2 \bar{\sigma}^2 = 0 \quad (4.16)$$

---

\* The model predicts the same type of behavior for slightly overconsolidated clays ( $OCR < 2$ ) when sheared in an undrained fashion.

\*\* Section 3.3.9 shows that:

$$k \equiv c = \sqrt{2/3} M$$

where M is the MCC model strength parameter.



Equation 4.16 describes a set of two lines in the  $(\bar{\sigma}, S_1)$  space: A line with slope (+k) representing the Critical State condition in triaxial compression and a line with slope (-k) representing the Critical State condition in triaxial extension. Since the two Critical State lines have the same slope with respect to the  $\bar{\sigma}$ -axis (i.e.,  $S_1 = \pm k\bar{\sigma}$ ), the Critical State criterion is isotropic\*. Experimental results show that an isotropic criterion is inadequate to describe failure\*\* of natural clays: Table 4.2 shows failure data from undrained triaxial compression and extension tests on  $K_0$ -normally consolidated resedimented samples of Boston Blue Clay reported by Ladd and Varallyay (1965). The data show that the values\*\*\* of  $S_1/\bar{\sigma}$  at failure are different in triaxial compression and in extension. Thus, a failure criterion that allows different input values of  $S_1/\bar{\sigma}$  at failure in triaxial compression and extension is required. Such a criterion can be obtained if the Critical State cone of the MCC model is rotated in the stress space by introducing a deviatoric tensor  $\xi$  (material

---

\* Section 3.3.9 shows that an isotropic Critical State criterion does not imply the same friction angle in triaxial compression and extension.

\*\* The term failure in this section indicates either the peak strength condition or the Critical State condition.

\*\*\* In a triaxial test with  $\bar{\sigma}_x = \bar{\sigma}_z$  it can be shown that:

$$S_1 = (\bar{\sigma}_y - \bar{\sigma}_x) \sqrt{2}/\sqrt{3} ; \bar{\sigma} = (\bar{\sigma}_y + 2\bar{\sigma}_x)/3 \quad (4.17a)$$

and then:

$$S_1/\bar{\sigma} = \sqrt{6}(1 - K_\sigma)/(1 + 2K_\sigma) \quad (4.17b)$$

where  $K_\sigma \equiv \bar{\sigma}_x/\bar{\sigma}_y$  is the effective stress obliquity.

constant). Then, the failure criterion of the proposed model can be written

$$h(\bar{\sigma}, \underline{s}) \equiv (\underline{s} - \bar{\sigma}\underline{\xi}) : (\underline{s} - \bar{\sigma}\underline{\xi}) - k^2 \bar{\sigma}^2 = 0 \quad (4.18a)$$

or, (using the transformed variables):

$$h(\bar{\sigma}, S_i) = \sum_{i=1}^5 (S_i - \bar{\sigma}\xi_i)^2 - k^2 \bar{\sigma}^2 = 0 \quad (4.18b)$$

where, the transformed measures  $\xi_i$  (of  $\underline{\xi}$ ) are analogous to the transformed measures  $b_i$  of the anisotropy tensor  $\underline{b}$  (Table 4.1). Equations 4.18 represent a cone in an effective stress space, with its apex at the origin and its axis along the line with direction  $(\underline{\xi} + \underline{I})$ . The failure criterion of the proposed model introduces the following material constants: (i) The scalar  $k$  and (ii) the deviatoric tensor  $\underline{\xi}$  or, equivalently, its transformed components  $\xi_i$ ,  $i = 1, 2, 3, 4, 5$ . These material constants are to be evaluated from laboratory tests.

In triaxial shearing modes, the failure criterion (Eq. 4.18b) is given by:

$$(S_1 - \bar{\sigma}\xi_1)^2 = k^2 \bar{\sigma}^2 \quad (4.19a)$$

or,

$$S_1/\bar{\sigma} = \xi_1 \pm k \quad (4.19b)$$

where the plus (+) sign holds for compression and the minus (-) sign for extension. The two material constants ( $k, \xi_1$ ) can be estimated from the values of the friction angle in triaxial compression ( $\bar{\phi}_C$ ) and extension ( $\bar{\phi}_E$ ) as follows:

$$\xi_1 = \frac{1}{2} (C_C - C_E) \quad (4.20a)$$

$$k = \frac{1}{2} (C_C + C_E) \quad (4.20b)$$

where:

$$C_C = \sqrt{\frac{2}{3}} \frac{6 \sin \bar{\phi}_C}{3 - \sin \bar{\phi}_C} \quad (4.21a)$$

$$C_E = \sqrt{\frac{2}{3}} \frac{6 \sin \bar{\phi}_E}{3 + \sin \bar{\phi}_E} \quad (4.21b)$$

It is interesting to note that the failure criterion of the proposed model reduces to the Critical State criterion of the MCC if the friction angles  $\bar{\phi}_C$  and  $\bar{\phi}_E$  do not vary independently but are related via the expression

$$\frac{6 \sin \bar{\phi}_E}{3 + \sin \bar{\phi}_E} = \frac{6 \sin \bar{\phi}_C}{3 - \sin \bar{\phi}_C} \quad (4.22)$$

predicted by the MCC model (see Table 3.2). In this case:

$C_C = C_E \equiv c$  and then:

$$\xi_1 = 0 \quad ; \quad k = c$$

which gives the Critical State criterion of the MCC model (compare Eqs. 4.19a and 4.16).

For the sake of simplicity, we will assume that  $\xi_2 = \xi_3 = \xi_4 = \xi_5 = 0$  which means that the strength anisotropy\* is controlled by its magnitude in the triaxial stress subspace  $(\bar{\sigma}, S_1)$ . This assumption is made because:

- (i) The evaluation of the parameters  $\xi_i$  (for  $i \neq 1$ ) requires tests other than the standard triaxial (e.g. plane strain, DSS and true triaxial) which cannot be routinely performed and,
- (ii) Available experimental strength data are not sufficient and/or reliable for shearing modes other than the triaxial.

In addition to specifying triaxial friction angles in compression and extension separately as input, the failure criterion of the proposed model offers another advantage compared to the MCC model: By introducing two nested cones, one for the peak strength condition and the other for the Critical State condition, the peak and Critical State friction angles\*\* can be used as input. Thus, the parameters  $\xi_1^P, k^P$  of the inside cone (representing the peak strength condition) can be evaluated by using the peak strength friction angles in triaxial compression and extension, whereas the parameters  $\xi_1^C, k^C$  of the outside cone (representing the Critical State condition) can be evaluated by using the Critical State friction angles

---

\* fully described by the tensor  $\xi$   
\*\* in both triaxial compression and extension

in triaxial compression and extension. The two nested conical surfaces divide the effective stress space into three regions:

- (i) the region inside the peak strength cone (strain hardening or pre-peak domain),
- (ii) the region between the peak strength and the Critical State cones (strain softening or post-peak domain) and,
- (iii) the region outside the Critical State cone, which is inaccessible.

Figure 4.6a shows the geometrical representation of the yield surface of the proposed model and the two nested cones (AOB and AOD) in the effective stress space ( $\underline{s}, \bar{\sigma}$ ). Figure 4.6b represents the intersection of the effective stress space with a deviatoric hyperplane  $xx$  (orthogonal to the  $\bar{\sigma}$ -axis) through the stress point  $P$ . The circle with center  $C$  and passing through  $P$  in Fig. 4.6b represents the intersection of the yield surface with the deviatoric hyperplane  $xx$ . The circles with diameters  $AB$  and  $AD$  in Fig. 4.6b represent the intersections of the peak strength and the Critical State cones respectively, with the deviatoric hyperplane  $xx$ . The two cones are tangent along the line  $OA$  indicating that there is no strain softening in the triaxial extension mode of deformation. The stress point  $P$  is in the strain softening region of the effective stress space since it is located between the peak strength and the Critical State cones (see Fig. 4.6b). In order to quantitatively keep track of the position of the

stress point relative to the two failure cones, the proposed model introduces the scalar variables  $r_c$  and  $r_p$ , such that (see Fig. 4.6b):

$$\overrightarrow{PR}_p = r_p \cdot \overrightarrow{CR}_p$$

$$\overrightarrow{PR}_c = r_c \cdot \overrightarrow{CR}_c$$

or in general,

$$\overrightarrow{PR} = r \cdot \overrightarrow{CR}$$

where  $r$  denotes either  $r_p$  or  $r_c$  (i.e. either of the two cones).

It is then evident that:

- (i) If the stress point lies at the tip of the yield surface:

$$r = 1$$

- (ii) If the stress point lies inside the cone:

$$0 < r < 1$$

- (iii) If the stress point lies on the cone:

$$r = 0$$

- (iv) If the stress point lies outside the cone:

$$r < 0$$

Thus, the various regions in the effective stress space correspond to the following values of  $r_c$  and  $r_p$ :

(i) Radial stress paths:

$$r_c = r_p = 1$$

(ii) Strain hardening domain:

$$0 < r_p \leq 1 ; 0 < r_c \leq 1$$

(iii) Peak strength condition:

$$r_p = 0 ; 0 < r_c < 1$$

(iv) Strain softening domain:

$$r_p < 0 ; 0 < r_c < 1$$

(v) Critical State condition:

$$r_p \leq 0 ; r_c = 0$$

The value of  $r$  for each stress state  $(\bar{\sigma}, S_i; i=1,2,3,4,5)$  is estimated via simple geometric considerations\* and is equal to:

$$r = \frac{A + B - \sqrt{B^2 + AC}}{B - \sqrt{B^2 + AC}} \quad (4.23a)$$

where

$$A = C^2 (2\bar{\alpha} - \bar{\sigma}) \quad (4.23b)$$

$$B = \sum_{i=1}^5 (b_i - \xi_i) (S_i - \bar{\sigma}b_i) \quad (4.23c)$$

$$C = \bar{\sigma} \left\{ k^2 - \sum_{i=1}^5 (b_i - \xi_i)^2 \right\} \quad (4.23d)$$

---

\* since  $\overrightarrow{CP} = \underline{s} - \bar{\sigma}\underline{b}$  (see Fig. 4.6b)

#### 4.7 RADIAL EFFECTIVE STRESS PATHS

Radial Effective Stress Paths consist of effective stress paths where the ratio of any two effective stress components is constant along the path. Thus, they can be geometrically represented (in an effective stress space) by a straight line passing through the origin.

We will study the behavior of the proposed model along radial stress paths in order to:

- (i) discuss some restrictions that such paths impose on the elastoplastic modulus  $H$ , and
- (ii) formulate the flow rule of the proposed model.

These are discussed in the following sections.

##### 4.7.1 THE ELASTOPLASTIC MODULUS $H$

The proposed model predicts that for radial stress paths, the stress point is located at the tip of the yield surface (see Section 4.2), which means that:

$$\underline{Q}' = \underline{Q} \quad (4.24)$$

and, combining with Eq. 3.18c, we get that the magnitude of  $\dot{\Lambda}$  along radial stress paths is:

$$\dot{\Lambda} = \frac{KQ}{H + KQP} \dot{\epsilon} \quad (4.25)$$

Hence, Eq. 3.18a shows that the relation between the increments



of the mean effective stress and the volumetric strain, is:

$$\frac{\dot{\sigma}}{\sigma} = \frac{KH}{H + KQP} \dot{\epsilon} \quad (4.26)$$

Appendix C presents results of consolidation tests\* on various clays that support the validity of the following working hypothesis:

For a normally consolidated clay subjected to any radial effective stress path, there exists a linear relationship between the void ratio (e) and the natural logarithm of the mean effective stress ( $\bar{\sigma}$ ).

This means that\*\*:

$$\frac{\dot{\sigma}}{\sigma} = \frac{1 + e_0}{\lambda} \bar{\sigma} \dot{\epsilon} \quad (4.27)$$

Combining Eqs. 4.26, 4.27 and 3.10c we get:

$$H + KQP = \left(\frac{\lambda}{\kappa}\right) \left(\frac{1 + e_0}{\lambda - \kappa}\right) \bar{\sigma} QP \quad (4.28)$$

which gives a restriction on the magnitude of the elastoplastic modulus H along any radial stress path. Finally, combining

---

\* on cylindrical samples following radial stress paths such that  $\bar{\sigma}_x = \bar{\sigma}_z$  and  $\sigma_{xy} = \sigma_{yz} = \sigma_{zx} = 0$  (y is the direction of the axis of the samples)

\*\* since  $\dot{e} = -(1 + e_0)\dot{\epsilon}$ , where  $e_0$  is the initial void ratio

Eqs. 4.28, 4.25 and 3.10c, we get:

$$\dot{\Lambda} = \left(\frac{\lambda-\kappa}{\lambda}\right) \frac{1}{P} \dot{\epsilon} \quad (4.29)$$

and using Eqs. 3.14:

$$\dot{\epsilon}^e = \frac{\kappa}{\lambda} \dot{\epsilon} \quad (4.30a)$$

$$\dot{\epsilon}^p = \left(1 - \frac{\kappa}{\lambda}\right) \dot{\epsilon} \quad (4.30b)$$

Equations 4.30 specify the reversible and irreversible components of a (total) volumetric strain increment  $\dot{\epsilon}$  during any radial stress path, as predicted by the proposed model for a normally consolidated clay. For typical clays, the ratio  $\lambda/\kappa$  ranges between 5 and 10 which means that only 10-20% of the total volumetric strain is reversible.

#### 4.7.2 THE FLOW RULE OF THE PROPOSED MODEL

Substitution of the value of  $\dot{\Lambda}$  for radial stress paths (Eq. 4.29) in the incremental stress-strain relations (Eqs. 3.18a,b) gives the following form of the incremental stress-strain relations along any radial stress path:

$$\dot{\underline{s}} = 2G \left\{ \left(\frac{e}{\epsilon}\right) - \left(\frac{\lambda-\kappa}{\lambda}\right) \left(\frac{P'}{P}\right) \right\} \dot{\epsilon} \quad (4.31a)$$

$$\dot{\underline{\sigma}} = K \left(\frac{\kappa}{\lambda}\right) \dot{\epsilon} \quad (4.31b)$$

or, dividing by parts:

$$\left(\frac{\dot{s}}{\dot{\sigma}}\right) = \frac{2G}{K} \left\{ \left(\frac{\kappa}{\lambda}\right) \left(\frac{\dot{e}}{\dot{\varepsilon}}\right) - \left(\frac{\lambda-\kappa}{\kappa}\right) \left(\frac{P'}{P}\right) \right\} \quad (4.32)$$

or, solving for  $(P'/P)$ :

$$\frac{P'}{P} = \left(\frac{\lambda}{\lambda-\kappa}\right) \left\{ \left(\frac{\dot{e}}{\dot{\varepsilon}}\right) - \left(\frac{2G}{K}\right)^{-1} \left(\frac{\kappa}{\lambda}\right) \left(\frac{\dot{s}}{\dot{\sigma}}\right) \right\} \quad (4.33a)$$

and using the transformed variables:

$$\frac{P_i}{P} = \left(\frac{\lambda}{\lambda-\kappa}\right) \left\{ \left(\frac{\dot{E}_i}{\dot{\varepsilon}}\right) - \left(\frac{2G}{K}\right)^{-1} \left(\frac{\kappa}{\lambda}\right) \left(\frac{\dot{S}_i}{\dot{\sigma}}\right) \right\} \quad (4.33b)$$

for  $i = 1, 2, 3, 4, 5$ . Equations 4.33 give the required form of the flow rule (i.e.,  $P$ ) along radial stress paths, as a function of the stress and the (corresponding) strain ratios ( $\dot{s}/\dot{\sigma}$  and  $\dot{e}/\dot{\varepsilon}$  respectively) of the radial path.

Some specific examples of radial stress paths will now be discussed:

(i) Isotropic Consolidation:

During isotropic consolidation, both the stress and strain ratios ( $\dot{s}/\dot{\sigma}$  and  $\dot{e}/\dot{\varepsilon}$  respectively) vanish and then, Eqs. 4.33 give

$$P' = 0$$

(ii) One-dimensional ( $K_0$ ) Consolidation:

During  $K_0$ -consolidation, straining is prevented along the x and z directions, say, while the stress is increased in the y-direction. Using the transformed strain variables (see Table 4.1) we get:

$$E_2 = E_3 = E_4 = E_5 = 0 \quad (4.34a)$$

$$\frac{E_1}{\epsilon} = \frac{\dot{E}_1}{\dot{\epsilon}} = \sqrt{\frac{2}{3}} \quad (4.34b)$$

Furthermore,  $\bar{\sigma}_x = \bar{\sigma}_z$  and thus\*:

$$S_2 = S_3 = S_4 = S_5 = 0 \quad (4.35a)$$

$$\frac{S_1}{\sigma} = \frac{\dot{S}_1}{\dot{\sigma}} = \sqrt{6} \frac{1 - K_0}{1 + 2K_0} \quad (4.35b)$$

Finally, substituting from Eqs. 4.34 and 4.35 in Eq. 4.33b, we get:

$$P_2 = P_3 = P_4 = P_5 = 0 \quad (4.36a)$$

$$\frac{P_1}{P} = \sqrt{\frac{2}{3}} \left( \frac{\lambda}{\lambda - \kappa} \right) \left\{ 1 - \left( \frac{2G}{K} \right)^{-1} \left( \frac{\kappa}{\lambda} \right) \frac{3(1 - K_0)}{(1 + 2K_0)} \right\} \quad (4.36b)$$

---

\*  $K_0 \equiv \bar{\sigma}_x / \bar{\sigma}_y$

which represents the required form of the flow rule along  $K_0$ -consolidation paths\*. It is interesting to note that since  $P_1 \neq 0$  for  $K_0$ -consolidation paths, the required flow rule is non-associated (i.e.,  $\tilde{P}$  is not proportional to  $\tilde{Q}$ ) because  $Q_1 = 0$  for all radial stress paths.

The proposed model adopts the following flow rule\*\*:

$$\int P \equiv 2c^2 \bar{\alpha} r_c \quad (4.37a)$$

$$\int \tilde{P}' \equiv c^2 x (\tilde{Q}' + r_c \tilde{S}) \quad (4.37b)$$

or, using the transformed variables (see Table 4.1)

$$P_i = c^2 x (Q_i + r_c S_i) \quad (4.37c)$$

for  $i = 1, 2, 3, 4, 5$ , where  $x$  is evaluated by considering  $K_0$ -consolidation paths, as follows:

For any radial stress path the proposed model predicts:

$$\tilde{Q}' = 0 ; r_c = 1 ; \bar{\sigma} = 2\bar{\alpha}$$

---

\* in terms of the material constants  $K_0, \lambda, \kappa, (2G/K)$   
 \*\* valid for any stress path (radial and not)

and then, Eqs. 4.37 give:

$$\frac{P_1}{P} = x \left( \frac{S_1}{\sigma} \right) \quad (4.38)$$

Finally, Eqs. 4.38, 4.36b and 4.35b give

$$x = \left( \frac{\lambda}{\lambda - \kappa} \right) \left\{ \frac{1 + 2K_0}{3(1 - K_0)} - \left( \frac{2G}{K} \right)^{-1} \left( \frac{\kappa}{\lambda} \right) \right\} \quad (4.39)$$

i.e., an expression for  $x$  in terms of the material constants  $\lambda$ ,  $\kappa$ ,  $K_0$  and  $(2G/K)$ .

The flow rule presented above (Eq. 4.37) was chosen for the following reasons:

(i) It describes the desired features at the Critical State:

(a) At the Critical State,  $r_c = 0$  (see Section 4.6) and then, the flow rule of the proposed model gives:

$$P = 0$$

Hence, Eqs. 3.14 and 4.6 give:

$$\dot{\alpha} = 0$$

$$\dot{\tilde{b}} = 0$$

at the Critical State, which means that the proposed model predicts that the clay deforms with no further altera-

tions of its yield surface, i.e., with no further changes of the anisotropy. In addition, Eq. 4.8 then gives:

$$\underline{Q} : \dot{\underline{\sigma}} = 0$$

and using Eq. 3.12 we get:

$$H = 0$$

which means that the elastoplastic modulus  $H$  vanishes at the Critical State.

- (b) At the Critical State, the non-associated flow rule in Eq. 4.37 reduces to an associated (normality) rule\*. There is experimental evidence in support of such behavior: Lade and Duncan (1978) and Lade and Musante (1978) performed drained tests on loose and dense Monterey sand and undrained tests on remolded Grundite clay using a cubical, rigid boundary, true triaxial device in which each of the three principal stresses can be varied independently. They measured the directions of the strain increment vectors before and at the Critical State and con-

---

\* for  $r_c = 0$ , Eqs. 4.37 give that  $\underline{P}$  is proportional to  $\underline{Q}$ .

cluded that: (1) before the Critical State is reached, the direction of the deviatoric component of the strain increment may deviate significantly from normality and (2) at the Critical State, the direction of the deviatoric component of the strain increment nearly satisfies normality.

(ii) It gives good predictions for  $K'_O$ -consolidation paths:

A  $K'_O$ -consolidation path is a radial effective stress path where strains are prevented in the y-direction, say, while equal stresses are applied in the x and z directions. Using the transformed variables (see Table 4.1) we get:

$$E_2 = E_3 = E_4 = E_5 = 0 \quad (4.40a)$$

$$\frac{E_1}{\epsilon} = \frac{\dot{E}_1}{\dot{\epsilon}} = - \frac{1}{\sqrt{6}} \quad (4.40b)$$

and\*

$$S_2 = S_3 = S_4 = S_5 = 0 \quad (4.41a)$$

---

\* Burland (1967) defined

$$K'_O \equiv \bar{\sigma}_x / \bar{\sigma}_y \quad (4.43)$$

for this stress path



$$\frac{s_1}{\sigma} = - \sqrt{6} \frac{K'_o - 1}{1 + 2K'_o} \quad (4.41b)$$

Substituting from Eqs. 4.41b and 4.40b in Eqs. 4.38 and 4.33b and using Eq. 4.39 we get:

$$K'_o = \frac{1 + K_o}{2K_o} \quad (4.42)$$

which gives the value of  $K'_o$  predicted by the proposed model as a function of  $K_o$ . Lewin and Burland (1970) and Lewin (1973) performed  $K_o$  and  $K'_o$  consolidation tests on a remolded clayey silt (Llyn Brianne slate dust) and measured

$$K_o = 0.56 ; K'_o = 1.39$$

This value of  $K'_o$  is exactly predicted by the proposed model (Eq. 4.42).

#### 4.8 UNDRAINED STRESS PATHS

Undrained conditions prevail, when the time scale of application of the external loads is too short to allow exchanges of pore fluid between neighboring soil elements.

For soft soils, it is commonly assumed that the compressibilities of the pore fluid and the solid phase are negligible compared to the compressibility of the soil skeleton\*, which means that the undrained deformation is incompressible, i.e.:

$$\dot{\epsilon} = 0 \quad (4.43)$$

Using this condition, the incremental stress-strain relations (Eqs. 3.18) can be written as follows for the case of undrained plastic loading:

$$\dot{\bar{\sigma}} = - K \dot{\Lambda} P \quad (4.44a)$$

$$\dot{\underline{s}} = 2G\{\dot{\underline{e}} - \dot{\Lambda} \underline{P}'\} \quad (4.44b)$$

where :

$$\dot{\Lambda} = \frac{2G(Q' : \dot{\underline{e}})}{H + 2G(Q' : \underline{P}') + KQP} \quad (4.44c)$$

Premultiplying Eq. 4.44b by  $\underline{Q}'$  and using Eq. 4.44c, we get:

---

\* In such a case, Skempton's B parameter (Skempton, 1954) is equal to unity.

$$\frac{(\underline{Q}' : \underline{\dot{s}})}{2G(\underline{Q}' : \underline{\dot{e}})} = \frac{H + KQP}{H + KQP + 2G(\underline{Q}' : \underline{P}')} \quad (4.45)$$

Experimental results from undrained tests on normally consolidated\* clays show that the mean effective stress decreases during shear (i.e.,  $\dot{\bar{\sigma}} < 0$ ). This means that  $\dot{\Lambda}$  must\*\* be positive during undrained plastic loading. However, in such cases the numerator of Eq. 4.44c is positive (see Section 3.2.2.4b) which means that the denominator must also be positive, i.e.:

$$H + KQP + 2G(\underline{Q}' : \underline{P}') > 0 \quad (4.46)$$

Thus, the sign of the left-hand-side expression in Eq. 4.45 is controlled by the sign of  $H + KQP$ .

The left-hand-side expression in Eq. 4.45 represents a normalized\*\*\* stiffness of the shear stress vs. shear strain curve for undrained plastic loading. In fact,  $(\underline{Q}' : \underline{\dot{s}})$  and  $(\underline{Q}' : \underline{\dot{e}})$  are the projections of the shear stress and shear strain increments respectively, on the direction of  $\underline{Q}'$  and their ratio gives the elastoplastic shear modulus for undrained plastic loading\*\*\*\*. In order to study the possible values of

---

\* as well as slightly overconsolidated

\*\* from Eq. 4.44a and since  $P \geq 0$  (see Eq. 4.37a)

\*\*\* normalized with the elastic shear modulus  $2G$

\*\*\*\* in the case of undrained testing in the triaxial apparatus, the left-hand-side expression of Eq. 4.45 gives  $\dot{S}_1/2GE_1$  which is evidently a normalized shear modulus.

this modulus, we will study the various parts of the shear stress-strain curve of a normally consolidated clay sample subjected to undrained shear;

(i) Initial condition:

The clay is initially normally consolidated along a radial stress path ( $\dot{Q}' = 0$ ) and Eq. 4.45 gives:

$$\frac{(\dot{Q}' : \dot{s})}{2G(\dot{Q}' : \dot{e})} = 1 \quad (4.47)$$

which means that the initial stiffness of the shear stress-strain curve during undrained deformation is controlled by the elastic shear modulus  $G$ .

(ii) Strain hardening region:

Appendix B shows (see Eq. B.1) that during strain hardening

$$\dot{Q}' : \dot{s} + Q\dot{\sigma} > 0 \quad (4.48a)$$

In addition, (a) experimental evidence suggests that  $\dot{\sigma} < 0$  during undrained deformation of normally consolidated clays and (b) the proposed model predicts that  $Q > 0$  for normally consolidated clays. Combining the above, we can see that during strain hardening

it is required that

$$\underline{Q}' : \underline{\dot{s}} > 0 \quad (4.48b)$$

Furthermore, for plastic undrained loading (see Section 3.2.2.4b)

$$\underline{Q}' : \underline{\dot{e}} > 0 \quad (4.48c)$$

Combining Eqs. 4.48b, 4.48c, 4.46 and 4.45 we get that in the strain hardening region

$$H + KQP > 0 \quad (4.48d)$$

which means that (from Eq. 4.45)

$$0 < \frac{(\underline{Q}' : \underline{\dot{s}})}{2G(\underline{Q}' : \underline{\dot{e}})} < 1 \quad (4.48e)$$

i.e., the elastoplastic shear modulus in the strain hardening region is positive but smaller (as expected) than the initial modulus.

(iii) Peak strength condition:

In the triaxial mode of deformation, the peak strength condition is reached when the only independent component of the stress deviator\*

---

\* which is equal to the maximum shear stress acting on the sample

reaches a peak value or, equivalently, when its time rate of change vanishes. For more general stress paths, the peak strength condition is reached when\*

$$\underline{Q}' : \underline{\dot{s}} = 0 \quad (4.49a)$$

Then, Eq. 4.45 gives the following criterion for the peak strength condition:

$$H + KQP = 0 \quad (4.49b)$$

(iv) Strain softening region:

In the strain softening region we require

$$\underline{Q}' : \underline{\dot{s}} < 0$$

while

$$\underline{Q}' : \underline{\dot{e}} > 0$$

since we have plastic loading. Thus,

$$\frac{(\underline{Q}' : \underline{\dot{s}})}{2G(\underline{Q}' : \underline{\dot{e}})} < 0$$

which means that the criterion for strain softening is (see Eq. 4.45):

$$H + KQP < 0$$

---

\* Eq. 4.49a reduces to the previous definition of the peak strength condition in the triaxial mode of shearing.

(v) Critical State condition:

At the Critical State (see Section 4.7.2):

$$H = P = 0$$

which means that:

$$H + KQP = 0$$

or (via Eq. 4.45):

$$\underline{Q}' : \underline{\dot{s}} = 0$$

while

$$\underline{Q}' : \underline{\dot{e}} > 0$$

since we have plastic loading.

Table 4.3 summarizes the requirements for the quantity  $(H + KQP)$  discussed above and in Section 4.7.1.

Using all these requirements, we will adopt the following form\* for the elastoplastic modulus  $H$  of the proposed model.

$$H + KQP = 2c^{2\bar{\alpha}} \left(\frac{\lambda}{\kappa}\right) \left(\frac{1 + e_0}{\lambda - \kappa}\right) r_p \{2\bar{\alpha} + (2\bar{\alpha} - \bar{\sigma})X\}P \quad (4.55)$$

where  $X$  depends on the difference  $(r_c - r_p)$  as shown in Fig. 4.7.

---

\* valid for any stress path

#### 4.9 INPUT PARAMETERS FOR THE PROPOSED MODEL

This section summarizes the required input parameters for the proposed model and briefly discusses the aspects of the model controlled by each of these parameters. Chapter 5 gives an extensive description of the input parameters as well as, the tests required for their evaluation and typical values for normally consolidated Boston Blue Clay.

The proposed model requires the following input parameters (material constants):

- (i)  $\lambda$  - the slope of the straight line representing the relationship between the void ratio and the natural logarithm of the mean effective stress for radial stress paths on normally consolidated clays (see Section 4.7.1).
- (ii)  $\kappa$  - the slope of the straight line representing the relationship between the void ratio and the natural logarithm of the mean effective stress for isotropic rebound tests. It basically controls the elastic bulk modulus  $K$  (see Section 3.2.1).
- (iii)  $(2G/K)$  - the ratio of the elastic shear modulus  $G$  to the elastic bulk modulus  $K$ . It controls the initial stiffness and the stiffness of the unloading portion of the shear stress-strain curve during undrained deformation (see Section 3.2.1).



- (iv)  $K_o$  - the ratio of the lateral to the axial effective stress for one-dimensional consolidation in the axial direction (see Section 4.7).
- (v)  $\bar{\phi}_{TC}^P$  - the friction angle at the Peak Strength condition in the triaxial compression mode of shearing (see Section 4.6).
- (vi)  $\bar{\phi}_{TC}^C$  - the friction angle at the Critical State condition in the triaxial compression mode of shearing (see Section 4.6).
- (vii)  $\bar{\phi}_{TE}^P$  - the friction angle at the Peak Strength condition in the triaxial extension mode of shearing (see Section 4.6).
- (viii)  $\bar{\phi}_{TE}^C$  - the friction angle at the Critical State condition in the triaxial extension mode of shearing (see Section 4.6).
- (ix)  $\psi$  - parameter controlling the rate of rotation of the yield surface in the effective stress space, i.e., the rate of change of material anisotropy (see Section 4.3.1).
- (x)  $\alpha$  - parameter controlling the effective stress path of  $K_o$ -normally consolidated undrained triaxial extension tests (see Section 4.8).
- (xi)  $\beta$  - parameter controlling the effective stress path of  $K_o$ -normally consolidated undrained triaxial compression tests (see Section 4.8).

- (xii)  $c$  - the ratio of the axes of the yield surface (see Section 4.2.2).

In the solution of problems by means of the proposed model, the initial values of the state variables are also required.

The proposed model involves the following state variables:

- (i) The effective stress tensor,  $\bar{\sigma}$ , consisting of its six components, or, equivalently, the mean effective stress  $\bar{\sigma}$  and the five transformed stress variables  $S_1, S_2, S_3, S_4$  and  $S_5$  (see Table 4.1). For many practical problems, less than five transformed variables are required. For example, in plane strain and axisymmetric problems,  $S_4$  and  $S_5$  vanish.
- (ii) The size  $\bar{\alpha}$  of the yield surface.
- (iii) The (deviatoric) soil anisotropy tensor  $\underline{b}$  consisting of its five transformed variables  $b_1, b_2, b_3, b_4$  and  $b_5$  (see Table 4.1). For many practical problems, less than five transformed variables are required. For example in plane strain and axisymmetric problems,  $b_4$  and  $b_5$  vanish (see Eq. 4.6b).

In most practical problems the initial state consists of the  $K_0$ -consolidated state. The values of the state variables for this state are given in Table 5.8b.

Effective Stress	Strain	Yield Surface Gradient	Plastic Flow Direction	Anisotropy
$(\bar{\sigma}, \bar{\sigma})$	$(\bar{\epsilon}, \bar{\epsilon})$	$(\bar{Q}, \bar{Q})$	$(\bar{P}, \bar{P})$	$(\bar{b}, 1)$
$\bar{\sigma} \equiv \frac{1}{3} (\bar{\sigma}_x + \bar{\sigma}_y + \bar{\sigma}_z)$	$\bar{\epsilon} \equiv \epsilon_x + \epsilon_y + \epsilon_z$	$\bar{Q} \equiv Q_x + Q_y + Q_z$	$\bar{P} \equiv P_x + P_y + P_z$	1
$S_1 \equiv \frac{1}{\sqrt{6}} (2\bar{\sigma}_y - \bar{\sigma}_x - \bar{\sigma}_z)$	$E_1 \equiv \frac{1}{\sqrt{6}} (2\epsilon_y - \epsilon_x - \epsilon_z)$	$Q_1 \equiv \frac{1}{\sqrt{6}} (2Q_y - Q_x - Q_z)$	$P_1 \equiv \frac{1}{\sqrt{6}} (2P_y - P_x - P_z)$	$b_1 \equiv \frac{1}{\sqrt{6}} (2b_y - b_x - b_z)$
$S_2 \equiv \frac{1}{\sqrt{2}} (\bar{\sigma}_z - \bar{\sigma}_x)$	$E_2 \equiv \frac{1}{\sqrt{2}} (\epsilon_z - \epsilon_x)$	$Q_2 \equiv \frac{1}{\sqrt{2}} (Q_z - Q_x)$	$P_2 \equiv \frac{1}{\sqrt{2}} (P_z - P_x)$	$b_2 \equiv \frac{1}{\sqrt{2}} (b_z - b_x)$
$S_3 \equiv \sqrt{2} \bar{\sigma}_{xy}$	$E_3 \equiv \sqrt{2} \epsilon_{xy}$	$Q_3 \equiv \sqrt{2} Q_{xy}$	$P_3 \equiv \sqrt{2} P_{xy}$	$b_3 \equiv \sqrt{2} b_{xy}$
$S_4 \equiv \sqrt{2} \bar{\sigma}_{yz}$	$E_4 \equiv \sqrt{2} \epsilon_{yz}$	$Q_4 \equiv \sqrt{2} Q_{yz}$	$P_4 \equiv \sqrt{2} P_{yz}$	$b_4 \equiv \sqrt{2} b_{yz}$
$S_5 \equiv \sqrt{2} \bar{\sigma}_{zx}$	$E_5 \equiv \sqrt{2} \epsilon_{zx}$	$Q_5 \equiv \sqrt{2} Q_{zx}$	$P_5 \equiv \sqrt{2} P_{zx}$	$b_5 \equiv \sqrt{2} b_{zx}$

Table 4.1: Transformed Variables for the Proposed Model

$\overline{CK}_O \overline{U}$	Failure Condition	Test Number	$K_\phi$	$K_\sigma$ Average	$\overline{\phi}$	$S_1/\overline{\sigma}$
TC	Peak	CK <sub>O</sub> UC - 1	0.3861	0.3922	25.88°	0.83423
		CK <sub>O</sub> UC - 2	0.3984			
	Critical ( $\epsilon_y = 8\%$ )	CK <sub>O</sub> UC - 1	0.3082	0.2899	33.40°	1.10084
		CK <sub>O</sub> UC - 2	0.2717			
TE	Peak	CK <sub>O</sub> UE - 1	8.00	6.10	45.91°	-0.9464
	Critical ( $\epsilon_y = 8\%$ )	CK <sub>O</sub> UE - 4	4.20			

Note:  $K_\sigma \equiv \overline{\sigma}_x/\overline{\sigma}_y$  ;  $\overline{\sigma}_x = \overline{\sigma}_z$  (triaxial)

Table 4.2: Data at Peak and Critical Conditions  
From CK<sub>O</sub>U(C) and CK<sub>O</sub>U(E) Triaxial Tests on  
Normally Consolidated Boston Blue Clay  
(Data from Ladd and Varallyay, 1965)

Path	Radial Consolidation	Undrained Loading			
		Strain Hardening	Peak Strength	Strain Softening	Critical State
Mode					
Mode Characteristics	$r_p = 1$ $r_c = 1$	$r_p > 0$ $r_c > 0$	$r_p = 0$ $r_c > 0$	$r_p < 0$ $r_c > 0$	$r_p < 0$ $r_c = 0$
Value of H + KQP	$\left(\frac{\lambda}{\kappa}\right) \left(\frac{1+e_0}{\lambda - \kappa}\right) \bar{\sigma}_{QP} > 0$	> 0	= 0	< 0	= 0

Table 4.3: Requirements for (H + KQP) Along Various Paths

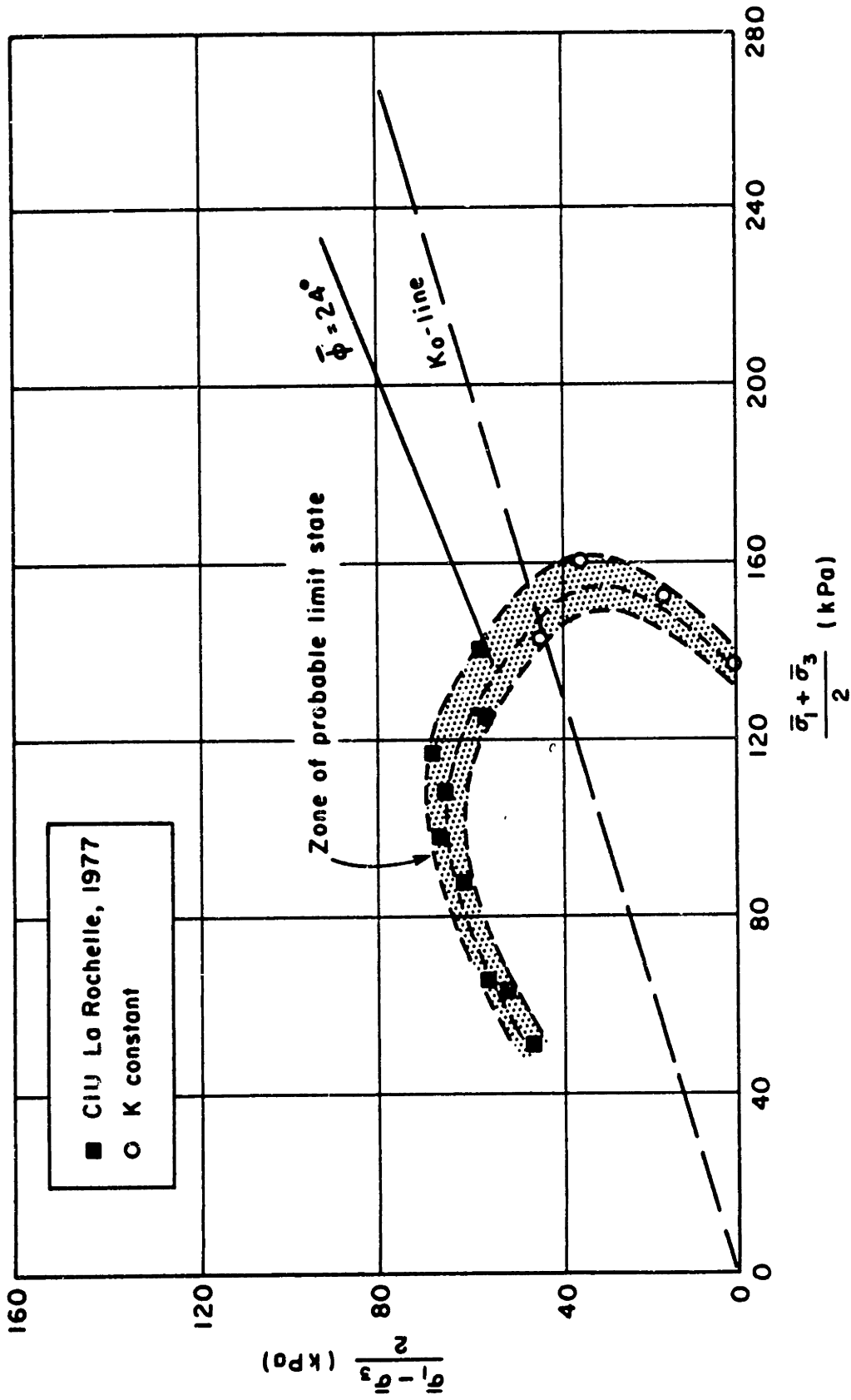


Fig. 4.1: Limit state curve for St. Louis (Champlain) Clay.  
 After Leroueil (1977)

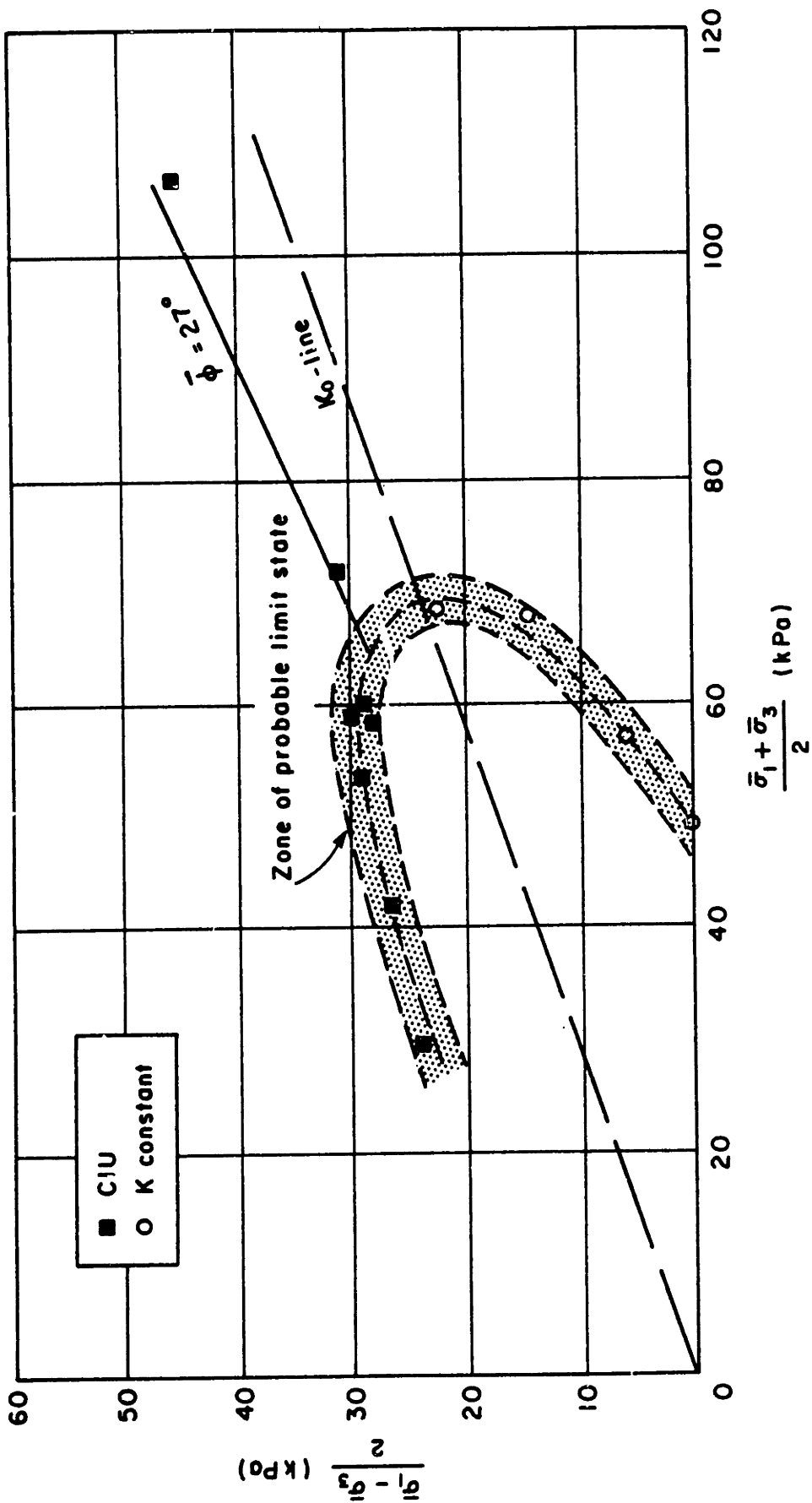
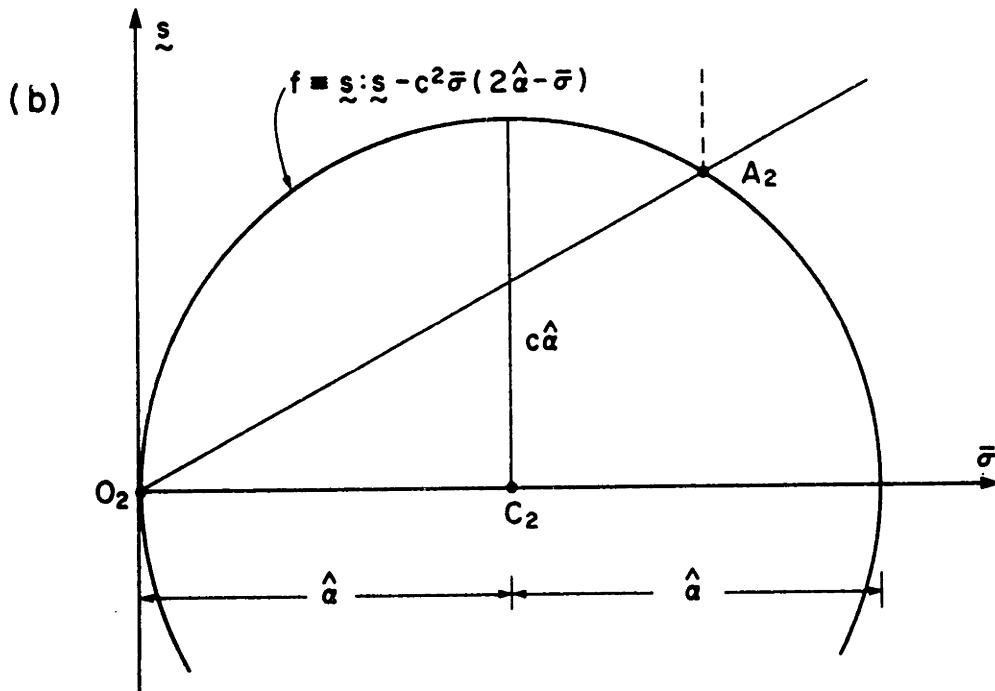
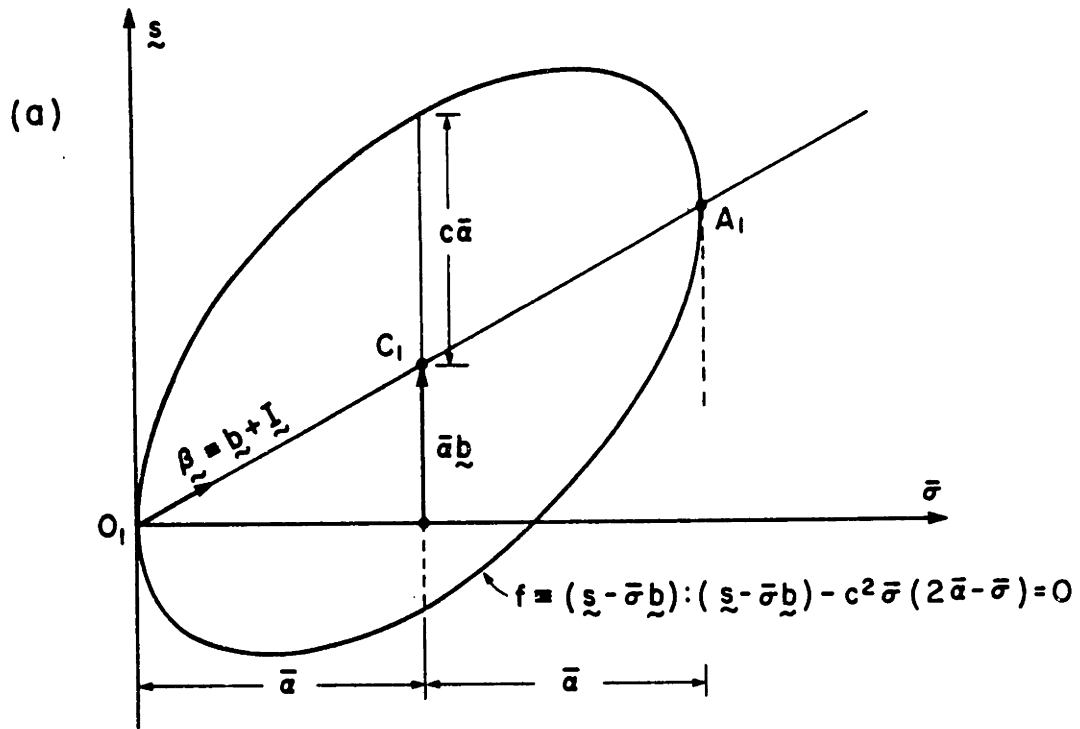
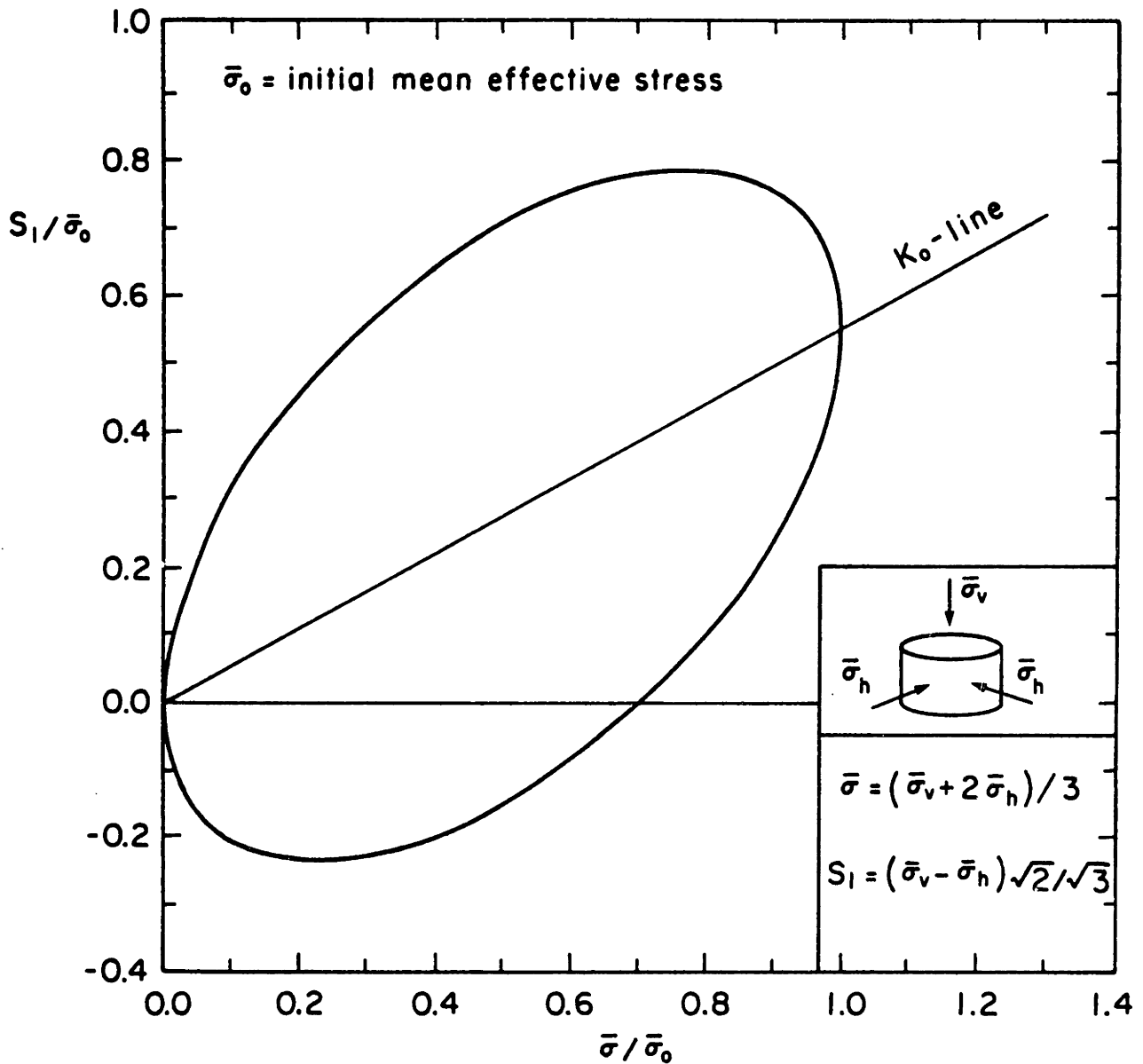


Fig. 4.2: Limit state curve for St. Alban (Champlain) Clay.  
After Leroueil (1977)



**Fig. 4.3:** The yield surface of (a) the proposed model and (b) an "equivalent" Modified Cam-Clay model in a general tensorial effective stress space





Note:  $K_0 = 0.534$  and  $c = 0.866$  was used.

Fig. 4.4a:

The yield surface of the proposed model for a  $K_0$ -consolidated state represented in a transformed triaxial effective stress space

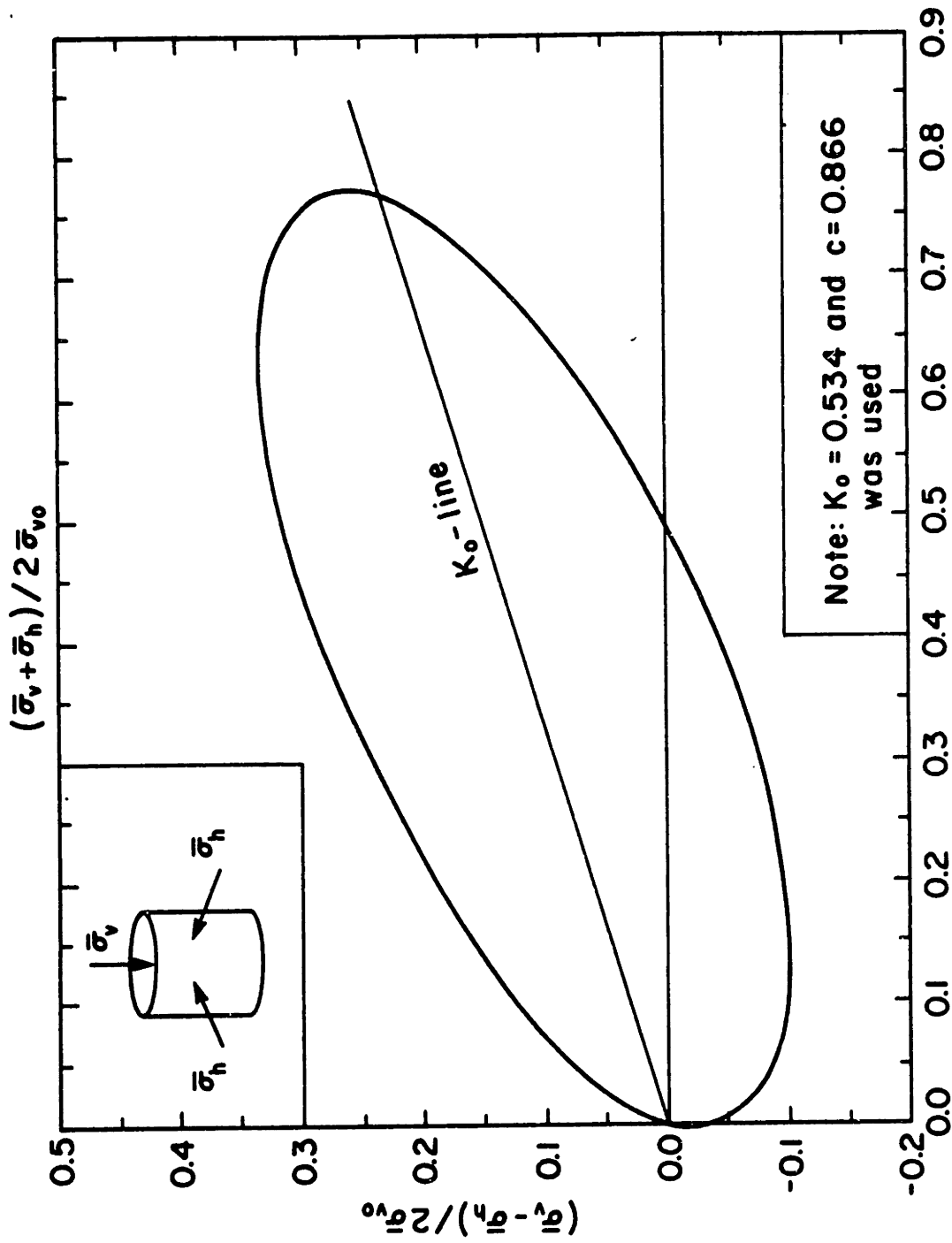


**Fig. 4.4b:** The yield surface of the proposed model for a  $K_0$ -consolidated state represented in a  $\bar{p}$ - $\bar{q}$  effective stress space

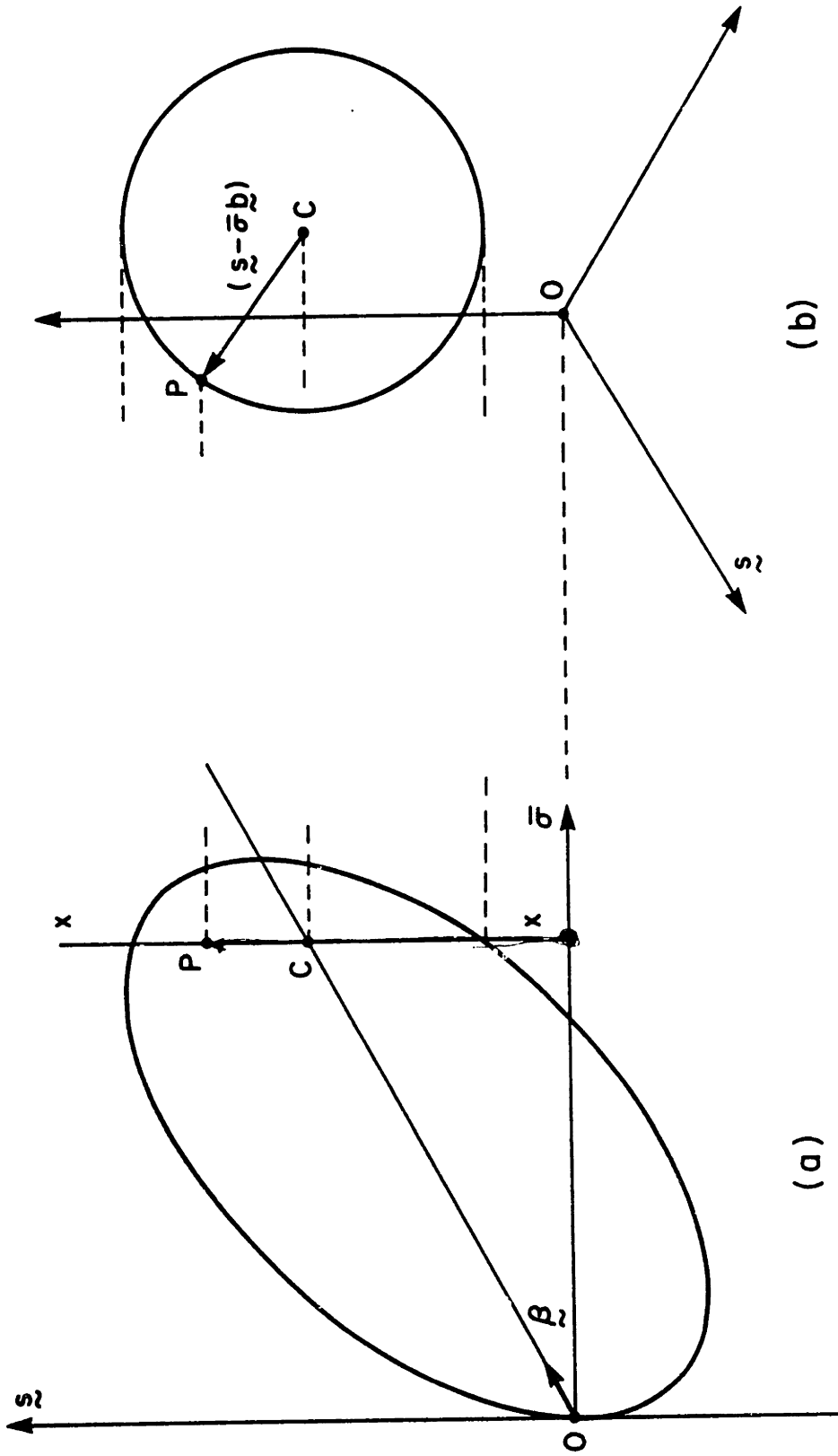


Fig. 4.5: The yield surface of the proposed model in (a) the effective stress space and, (b) the deviatoric subspace.

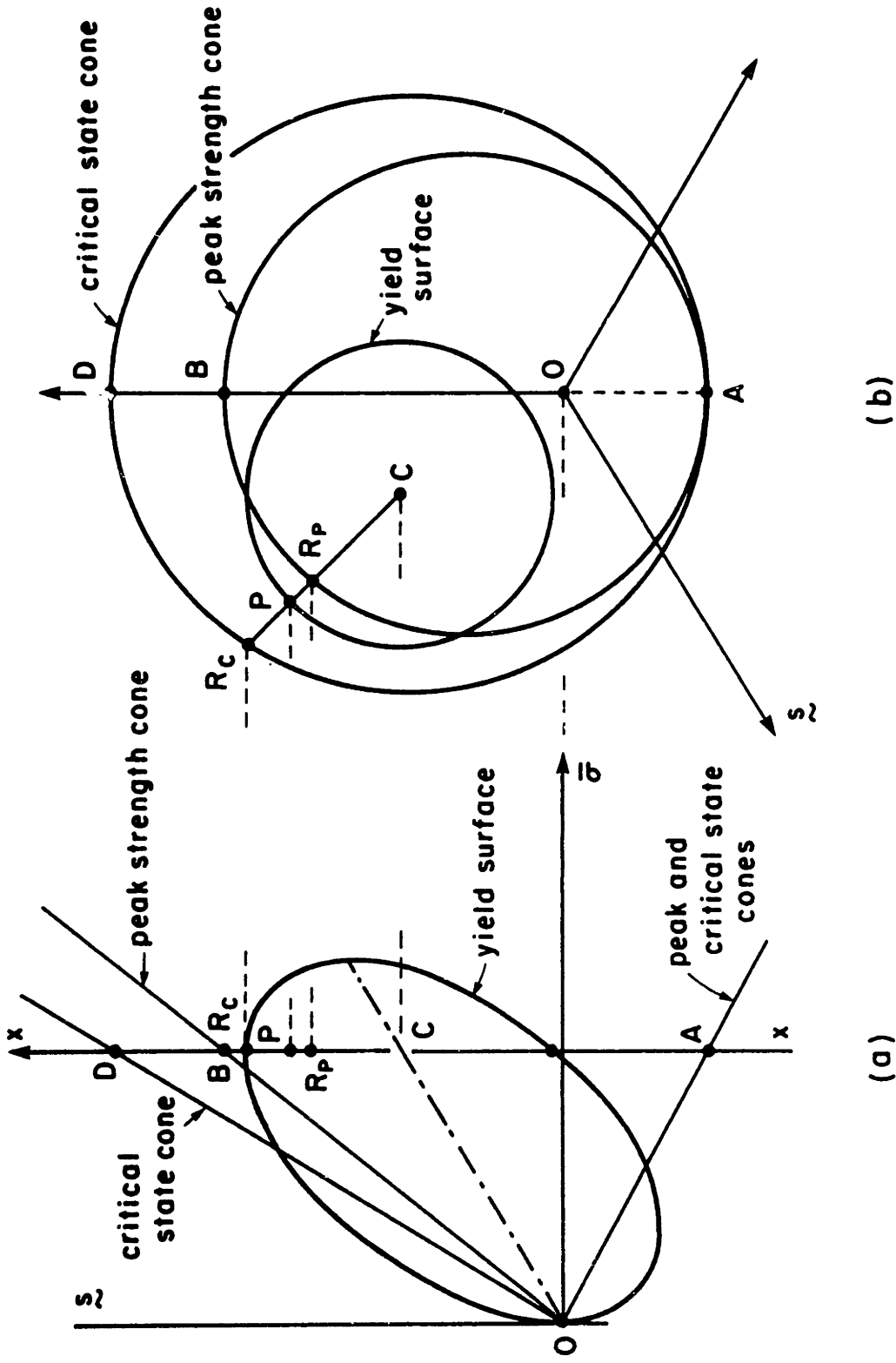


Fig. 4.6: Geometrical representation of the yield surface and the failure cones of the proposed model.

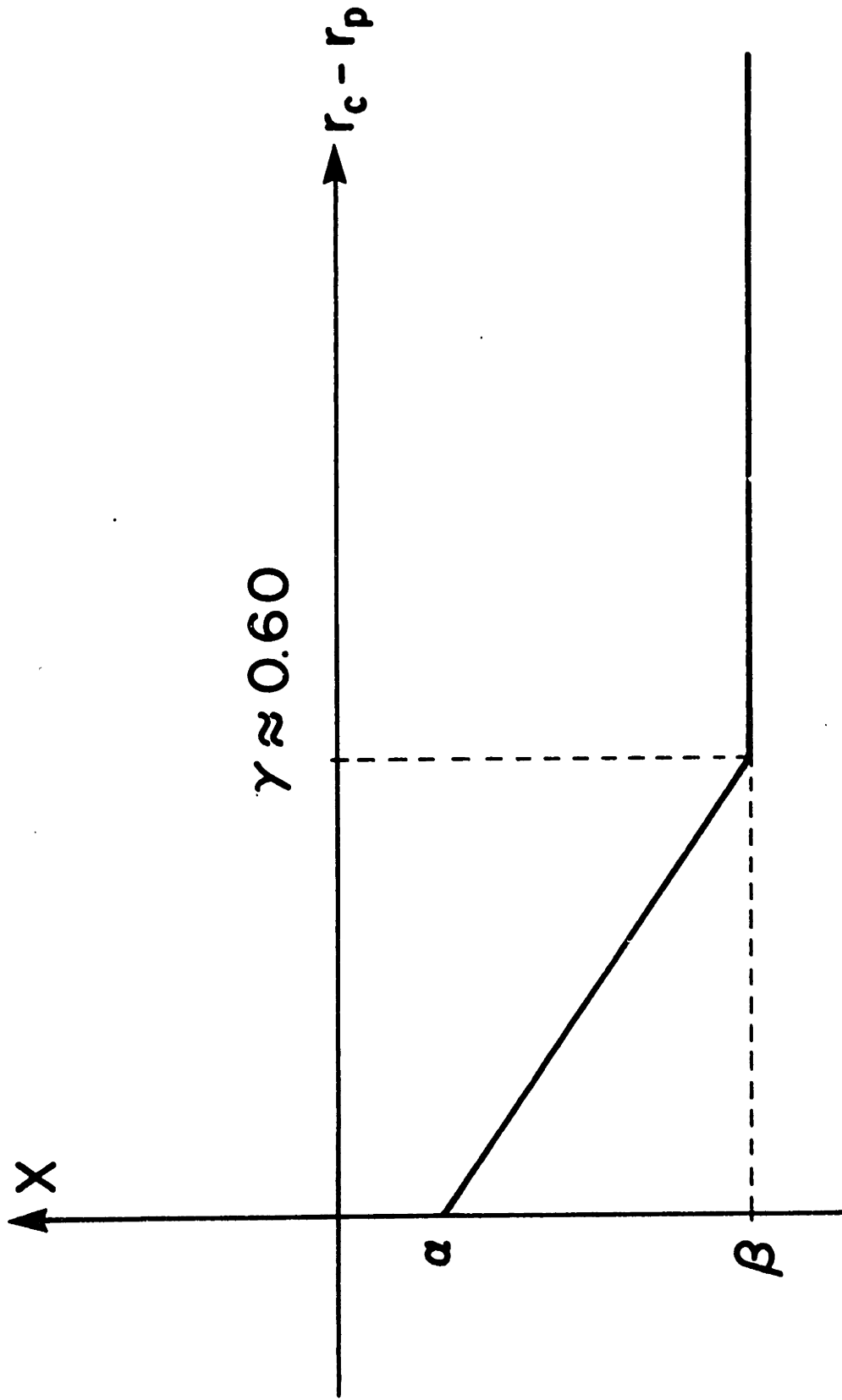


Fig. 4.7: Values of the coefficient  $X$  used in the proposed model (see Eq. 4.55).

## CHAPTER 5

### EVALUATION OF THE PROPOSED MODEL

#### 5.1 INTRODUCTION

Chapter 4 proposes a stress-strain-strength model for soils based on modern concepts of Plasticity Theory and the observed behavior of soft clays (e.g. volumetric hardening, stress-strain and strength anisotropy, strain softening, Critical State, etc). This Chapter evaluates the proposed model by comparing its predictions with the behavior of resedimented  $K_0$ -normally consolidated and lightly overconsolidated Boston Blue Clay (BBC), measured under controlled laboratory conditions. Natural clay from the MIT campus was airdried, ground and mixed to insure uniformity. The dust was then mixed with salt water (16 grams per liter) at a high liquidity index and was one-dimensionally consolidated to give 12 inch dia. "block samples" that were then trimmed and used in the strength testing program.

BBC is a lean post-glacial marine clay that has been extensively studied at MIT. Kenney (1964) presents a detailed description of the geologic history of the post-glacial marine deposits in the Boston area. Table 5.1 presents classification data of BBC performed according to Lambe (1951) and reported by Ladd and Varallyay (1965).

## 5.2 EVALUATION OF THE MODEL PARAMETERS

### 5.2.1 THE CONSOLIDATION PARAMETER $\lambda$

The material constant  $\lambda$  is the slope of the straight line representing the relationship between the void ratio ( $e$ ) and the natural logarithm of the mean effective stress ( $\bar{\sigma}$ ) for an isotropic consolidation path on the normally consolidated clay, i.e.,

$$\lambda = -\Delta e / \Delta \ln \bar{\sigma} \quad (5.1)$$

Experimental evidence (see e.g. Appendix C) indicates that other radial \* stress paths (e.g.  $K_o$ -consolidation paths) give similar values of the slope of the  $e$ - $\ln \bar{\sigma}$  curve. Table 5.2 shows values of  $\lambda$  measured in isotropic,  $K_o$ - and  $1/K_o$ -consolidation \*\* tests on resedimented BBC, \*\*\* reported by Ladd and Varallyay (1965). The data show significant scatter ( $\lambda = 0.17 \pm 0.07$ ). We select  $\lambda = 0.17$  as a reasonable average to be used in the predictions. Since the virgin compression index  $C_c$  is related to  $\lambda$  by the equation:

$$C_c = \lambda / 0.434 \quad (5.2)$$

the selected value of  $\lambda$  corresponds to  $C_c = 0.392$ .

---

\* see definition in Section 3.3.4

\*\*  $1/K_o$  consolidation paths are triaxial paths with

$$\bar{\sigma}_h / \bar{\sigma}_v = 1/K_o = \text{constant}$$

\*\*\* for the stress range of 2 to 6 ksc

## 5.2.2 THE ELASTIC PARAMETERS $\kappa$ AND G

The material constant  $\kappa$  is the slope of the straight line representing the relationship between the void ratio ( $e$ ) and the natural logarithm of the mean effective stress ( $\bar{\sigma}$ ) for isotropic rebound tests on clays.  $\kappa$  is related to the swelling index  $C_s$  by the equation:

$$C_s = \kappa / 0.434 \quad (5.3)$$

Koutsoftas and Ryan (1970) report  $C_s = 0.06 \pm 0.04$  for undisturbed BBC rebounded to overconsolidation ratios less than four. These values correspond to  $\kappa = 0.026 \pm 0.017$ . For monotonic shearing paths, the model predictions are relatively insensitive to the value of  $\kappa$ , because  $\kappa$  mainly controls the elastic bulk modulus  $K$  of the clay (see Eq. 3.10c) and, elastic deformations usually represent a small portion of the total deformation. Thus, we select  $\kappa = 0.034$  (it corresponds to a ratio  $\lambda/\kappa = 5$ ).

The elastic shear modulus  $G$  controls the initial stiffness and the stiffness of the unloading portion of the shear stress-strain curve during undrained deformation of clays but, has a negligible effect on the predicted effective stress path (and thus, on the predicted strength of the clay). Section 3.2.1 discussed that, according to the proposed model,  $G$  is proportional to the mean effective stress  $\bar{\sigma}$  (i.e., normalized behavior is assumed), which means that the ratio  $G/K$  is a constant.

Figure 5.1 shows the values of the secant shear modulus predicted by the proposed model at various levels of the axial



strain in  $K_0$ -consolidated undrained triaxial compression tests, plotted vs. the assumed elastic shear modulus  $G$ . For axial strains larger than 0.1%, the predicted secant shear modulus is insensitive to the value of the model parameter  $G$ . Since 0.1% is usually a lower limit of measurable strains in standard laboratory setups, the proposed model predictions of monotonic tests on the normally consolidated clay are insensitive to the selected value of  $G$ . Levadoux (1980) reports values of the secant shear modulus of BBC at low strain levels. Based on these data, we select  $G/\sqrt{\sigma_{v0}} = 150$  as an input parameter in the proposed model.

### 5.2.3 THE $K_0$ -VALUE

Figure 5.2 shows values of  $K_0$  reported by Ladd et al (1971) for normally consolidated resedimented BBC, measured during the consolidation stage of  $K_0$ -consolidated Undrained Plane Strain tests. Clearly, the data exhibit significant scatter and the various methods of measuring  $K_0$  give different results. Ladd et al (1971) suggest that the Cell Pressure method gives the most reliable results. We select  $K_0 = 0.534$  as a reasonable average to be used in predictions.

#### 5.2.4 THE FRICTION ANGLES

The proposed model can use different values of the friction angle at the Peak Strength and the Critical States in both the triaxial compression and extension modes of deformation as input parameters (i.e., four distinct values). For the purposes of this model, we associate the "Critical State" with the state where the diameter of the Mohr circle of strain is equal to  $12\%$  \* since, the necking or bulging of laboratory samples at high strain levels causes difficulties in interpreting the data. Table 5.3 presents measured values of the Peak Strength and the Critical State friction angles from  $K_0$ -consolidated undrained triaxial compression (TC) and triaxial extension (TE) tests on resedimented normally consolidated BBC, reported by Ladd and Varallyay (1965). For the purposes of the proposed model we will use the average values given in the third column of numbers in Table 5.3. Ladd (1981) suggests that a triaxial extension friction angle equal to  $45.91^\circ$  is too high because of necking during testing of some samples in triaxial extension. A value equal to  $38^\circ$  would be more reasonable. A parametric study was performed to study the effect of the selected triaxial extension friction angle on the predicted stress-strain curve and the value of the predicted

---

\* this is equivalent to vertical strains equal to  $8\%$  and  $6\%$  for undrained Triaxial and Plane Strain tests respectively and, shear strain equal to  $12\%$  in undrained Direct Simple Shear tests.

undrained shear strength in triaxial extension. \*\* The study shows that the effect on the predicted stress-strain curve and the effective stress path is very small: typically, by changing the friction angle from  $45.91^\circ$  to  $38^\circ$ , the predicted normalized undrained shear strength changes from 0.142 to 0.130 which is still within the band of the measurements (see Fig. 5.14).

Based on Eqs. 4.20, 4.21 and the selected values of  $\bar{\phi}$  (separately for the Peak Strength and the Critical States) we get the following values of the parameters describing the Peak Strength (denoted by a superscript "p") and the Critical State (denoted by a superscript "c") failure cones (see Section 4.6):

$$\xi_1^p = -0.05608 \quad k^p = 0.89031 \quad (5.4a)$$

$$\xi_1^c = 0.07723 \quad k^c = 1.02362 \quad (5.4b)$$

#### 5.2.5 THE RATE OF CHANGE OF THE ANISOTROPY

The proposed model takes into consideration soil anisotropy by allowing changes of the orientation of the yield surface in the stress space during deformation. The orientation of the yield surface is described by a deviatoric, symmetric, second order anisotropy tensor  $b$ , with "transformed" components  $b_i$ ,  $i=1,2,3,4,5$  (see Table 4.1). The material constant  $\psi$  controls the rate of change of the anisotropy tensor  $b$  (see Eq. 4.6b),

---

\*\* the effect on other modes of deformation is expected to be less significant

i.e., it controls the rate with which the soil erases its memory of its previous state and acquires the anisotropic features of the new state.

The following procedure can be used to evaluate the material constant  $\psi$ : An initially isotropically consolidated sample \* is one-dimensionally ( $K_0$ ) consolidated in the vertical (y) direction. During this one-dimensional straining, it is expected that the component  $b_1$  of the anisotropy tensor gradually changes and asymptotically tends towards the value corresponding to a virgin  $K_0$ -consolidation path (i.e.,  $b_1=0.551$ ). Figure 5.3 shows the proposed model prediction of the changes of  $b_1$  plotted vs. the volumetric strain applied during  $K_0$ -consolidation, for various values \*\* of the parameter  $\psi$ . Experimental measurements of the orientation of the yield surface (i.e., of  $b_1$ ) at some level of the applied volumetric strain, \*\*\* are sufficient to estimate  $\psi$  by matching the measured value of  $b_1$  with one of the curves shown in Fig. 5.3. Since such data are not currently available for BBC, it is assumed that 30% volumetric strain during  $K_0$ -consolidation of an initially isotropically consolidated sample changes its anisotropy (i.e.,  $b_1$ ) such that the final value of  $b_1$  approaches 0.551 (corresponding to a virgin

---

\* For an isotropically consolidated sample, the yield surface is oriented along the hydrostatic axis, i.e.,  $b_1=b_2=b_3=b_4=b_5=0$ .

\*\* the values of the other model parameters used are shown in Table 5.7.

\*\*\* following the procedure described by Leroueil et al (1979) and summarized in Section 4.2.1

$K_0$ -consolidated sample) within 10%. Thus,  $\psi = 14$  is selected.

Figure 5.4 shows the effective stress path for  $K_0$ -consolidation tests corresponding to various values of the parameter  $\psi$  as predicted by the proposed model. The predicted effective stress path gradually tends towards the  $K_0$ -line with a rate increasing for higher values of  $\psi$ . Figure 5.5 shows the corresponding relationship between the mean effective stress ( $\bar{\sigma}$ ) and the volumetric strain ( $\epsilon$ ) where we note:

- (i) The effect of  $\psi$  on the  $\epsilon$ - $\log \bar{\sigma}$  relationship is not significant.
- (ii) After a short transition region, the relationship  $\epsilon$ - $\log \bar{\sigma}$  can be represented by a straight line with a slope corresponding to the virgin compression index  $C_c$ .

In order to further demonstrate the ability of the proposed model to predict changes of soil anisotropy by changing the orientation of the yield surface in the stress space, the proposed model is used to predict the response in the following test: An initially  $K_0$ -consolidated sample is subjected to a  $K_0'$ -consolidation path by preventing strains in the vertical (y) direction and increasing the stress in the horizontal direction ( $\bar{\sigma}_x = \bar{\sigma}_z$ ). Figures 5.6 through 5.8 show the proposed model predictions for this path. Figure 5.6 shows the component  $b_1$  of the anisotropy tensor plotted vs. the applied volumetric strain for various values \* of the parameter  $\psi$ . Initially  $b_1 = 0.551$  (i.e., the value corresponding to a virgin

---

\* the values of the other model parameters are those shown in Table 5.7

$K'_0$ -consolidated state) and, with  $K'_0$ -straining, the anisotropy gradually changes and asymptotically tends towards the value  $b_1 = -0.276$  which is the proposed model prediction for virgin  $K'_0$ -consolidation radial paths (see Eqs. 4.41b and 4.42). The selected value  $\psi = 14$  again appears to give a reasonable rate of reorientation of the yield surface on the basis that the value of  $b_1$  at 30% volumetric strain is within 10% of  $b_1$  corresponding to the virgin  $K'_0$ -consolidation path. Figure 5.7 shows the predicted effective stress path for the selected value  $\psi = 14$ . The initial stress state is denoted by A and lies on the  $K_0$ -line. During  $K'_0$ -consolidation, the effective stress path tends towards the  $K'_0$ -line predicted by the proposed model. Figure 5.8 shows the predicted relationship between the mean effective stress  $\bar{\sigma}$  and the volumetric strain during  $K'_0$ -consolidation of an initially  $K_0$ -consolidated sample. We note that:

- (i) The  $\epsilon - \log \bar{\sigma}$  relationship is quite insensitive to the value of the parameter  $\psi$ .
  - (ii) After a short transition region, the  $\epsilon - \log \bar{\sigma}$  relationship is a straight line with slope corresponding to the virgin compression index  $C_c$ .
- Comparison of Figs. 5.5 and 5.8 shows that the transition region is more pronounced in the case of the  $K'_0$ -consolidation path than in the case of the  $K_0$ -consolidation path. This should be expected because, in the second case, the soil starts with an isotropic structure which is not going to change much upon the

application of  $K_0$ -stresses whereas, in the first case, the soil starts with an anisotropic structure \* and one expects higher compressibility upon the application of  $K_0'$ -stresses in the horizontal direction. Thus, in the transition region and for the same change of the mean effective stress, the proposed model predicts almost double volumetric strain for  $K_0'$ -consolidation than for  $K_0$ -consolidation. However, as expected, the slopes of the linear part of all the curves in Figs. 5.5 and 5.8 are identical and equal to  $C_c$ .

#### 5.2.6 THE PARAMETERS $\alpha$ AND $\beta$ .

The parameter  $\alpha$  (along with the friction angle in triaxial extension) controls the predicted undrained shear strength of  $K_0$ -normally consolidated triaxial extension tests. Figure 5.9 shows the effective stress path of a  $CK_0U$  triaxial extension test predicted by the proposed model for various values \*\* of the parameter  $\alpha$ . The specific value of  $\alpha$  has some effect on the slope of the effective stress path, but the major effect appears to be on the predicted undrained shear strength ( $s_u$ ).\*\*\*

Table 5.4 shows the effect of  $\alpha$  on the predicted  $s_u$  and

---

\* since the vertical direction is a preferred direction

\*\* the values of the other model parameters are those shown in Table 5.7.

\*\*\* In the context of the proposed model, the term "failure" is used for either of the Peak and Critical States. Then, the shear strength is defined as one-half of the difference between the maximum and minimum principal stresses at failure. According to this definition, the Peak and Critical State shear strengths are distinct values.

compares predictions with measured values of  $s_u$  in laboratory tests on resedimented  $K_0$ -normally consolidated samples of BBC sheared in triaxial extension and reported by Ladd and Varallyay (1965). We select the value  $\alpha = -0.75$  which provides reasonable predictions.

The parameter  $\beta$  (along with the Critical State friction angle in triaxial compression) controls the predicted Critical State undrained shear strength for  $K_0$ -normally consolidated triaxial compression tests. Figure 5.10 shows the effective stress path of a  $CK_0U$  triaxial compression test predicted by the proposed model for various values of the parameter  $\beta$ . \* The specific value of  $\beta$  has some effect on the slope of the post-peak region of the effective stress path, but the major effect appears to be on the predicted Critical State undrained shear strength ( $s_u$ ). Table 5.5 shows the effect of  $\beta$  on the predicted Critical State  $s_u$  and compares the predictions with measured values of the Critical State  $s_u$  in laboratory tests on resedimented  $K_0$ -normally consolidated samples of BBC sheared in triaxial compression and reported by Ladd and Varallyay (1965). We select the value  $\beta = -2.95$  which provides reasonable predictions.

---

\* For high values of  $\beta$ , the selected Critical State friction angle cannot be reached because the model predicts a too high rate of strain softening.



### 5.2.7 THE PARAMETER c

The parameter  $c$  controls the ratio of the axes of the yield surface of the proposed model (see Section 4.2.2). Figure 5.11 schematically shows the experimental procedure required to evaluate the parameter  $c$ . The upper diagram shows the required stress paths in the effective stress space  $(\bar{\sigma}, S_1)$  and the lower diagram shows the corresponding relationship between the mean effective stress  $(\bar{\sigma})$  and the volumetric strain  $(\epsilon)$ . A clay sample, represented by point A in Fig. 5.11, is  $K_0$ -normally consolidated in the vertical ( $y$ ) direction with mean effective stress  $\bar{\sigma}_A$  and shear stress  $(S_1)_A = b_1 \bar{\sigma}_A$  (see Sections 4.4.2 and 4.7.2), where

$$b_1 = \sqrt{6} (1 - K_0) / (1 + 2K_0) \quad (5.5a)$$

is the amount of anisotropy in the initial  $K_0$ -consolidated state. An undrained removal of the applied shear stress (e.g. due to perfect sampling) then brings the sample to an overconsolidated isotropic stress state (point B). During this unloading, the yield surface not change shape, size or orientation and thus, when the stress state has reached point B, the yield surface is still oriented along the  $K_0$ -line. The clay sample is subsequently isotropically consolidated along the hydrostatic axis (path BFD). During the initial part of consolidation (path BF), the clay is overconsolidated whereas, in the remaining part (path FD) the clay is normally consolidated. Thus, at point F (see lower part of Fig. 5.11) an

abrupt change in the slope of the stress-strain curve will indicate the transition from an overconsolidated to a normally consolidated state, i.e., the fact that the stress point has reached the yield surface. If  $\bar{\sigma}_F$  is the mean effective stress at point F and,  $\mu = \bar{\sigma}_A / \bar{\sigma}_F$  then, the parameter c can be evaluated from the relation:

$$c = b_1 / \sqrt{\mu - 1} \quad (5.5b)$$

Hence, c can be evaluated by measuring  $K_O$  and  $\mu$  in the test described above. Unfortunately, such a test has not been performed on BBC but, for the purpose of using the proposed model, typical values of c may be obtained from similar tests on other clays: Leroueil et al (1979) report such tests on St. Alban clay which is a soft sensitive clay deposited on the northern shoreline of the Champlain sea in Canada (see Table 5.6 for classification data). They measured  $K_O$ -values of 0.50 to 0.55 and  $\mu$  values ranging between 1.30 and 1.49 which give c values between 0.75 and 1.10. Comparison of Tables 5.6 and 5.1 (classification data of BBC) shows differences in the properties of the two clays that may give different c values. We select  $c = \sqrt{3}/2 = 0.866$  for resedimented BBC as the best estimate using the available data.

The sensitivity of the proposed model predictions to the selected value of c is studied by predicting the behavior in  $K_O$ -normally consolidated undrained triaxial tests for various values of c. Figures 5.12 and 5.13 show the predicted

effective stress paths of  $K_0$ -normally consolidated undrained triaxial compression and extension tests, respectively, for  $c$  equal \* to 0.75, 0.866 and 1.0. The predicted effective stress paths show that:

- (i) The peak undrained shear strength in both triaxial compression and extension increases slightly with increasing  $c$ . This result should be expected as by increasing  $c$  the yield surface approaches a circle.
- (ii) The amount of strain softening in triaxial compression increases significantly with increasing  $c$ .

---

\* all other parameters are those shown in Table 5.7

### 5.3 THE INITIAL VALUES OF THE STATE VARIABLES

In most practical problems, the soil is initially one-dimensionally ( $K_o$ ) consolidated in the vertical (y) direction. For this condition, Table 5.7b gives the required initial values of the state variables (see Section 4.9), where:

$\bar{\sigma}_{vo}$  is the initial vertical effective stress  
 $(K_o)_{OC}$  is the  $K_o$ -value corresponding to the initial state,  
i.e.,

$$(K_o)_{OC} \equiv \bar{\sigma}_{ho} / \bar{\sigma}_{vo}$$

where  $\bar{\sigma}_{ho}$  is the initial horizontal effective stress.\*

(OCR) is the Over-Consolidation Ratio in the initial state, i.e., the ratio of the maximum vertical effective stress ( $\bar{\sigma}_{vm}$ ) ever carried by the soil, to the initial vertical effective stress ( $\bar{\sigma}_{vo}$ ) or,

$$(OCR) \equiv \bar{\sigma}_{vm} / \bar{\sigma}_{vo}$$

$(K_o)_{NC}$  is the  $K_o$ -value corresponding to a normally consolidated state.

Table 5.7 also summarizes the values of the input parameters used in the prediction of the stress-strain behavior

---

\* For a normally consolidated clay,  $(K_o)_{OC} = (K_o)_{NC}$ . For an overconsolidated clay,  $(K_o)_{OC}$  is simply the initial  $K_o$ -value.

of  $K_0$ -consolidated BBC. Finally, the proposed model requires the value of the void ratio  $e_0$  at the initial state.

Experimental data from one-dimensional consolidation tests on normally consolidated BBC reported by Ladd and Varallyay (1965) suggest  $e_0 = 0.898$  when the mean effective stress is equal to 1  $\text{kg/cm}^2$  (i.e., when  $\bar{\sigma}_{v0} = 1.45 \text{ kg/cm}^2$ ).

## 5.4 STRESS-STRAIN-STRENGTH PREDICTIONS

### 5.4.1 NORMALLY $K_0$ -CONSOLIDATED BOSTON BLUE CLAY

#### 5.4.1.1 Undrained Tests.

##### (a) Monotonic Tests.

Figures 5.14 to 5.19 compare measured and predicted stress-strain curves and effective stress paths for  $K_0$ -normally consolidated undrained tests on resedimented Boston Blue Clay (BBC). Three non-linear stress-strain soil models are used in the predictions:

- (i) The model proposed in Chapter 4 using the input parameters shown in Table 5.7.
- (ii) The Modified Cam-Clay (MCC) model (discussed in Section 3.3), using the same values of the input parameters as for the proposed model. \*
- (iii) The Prevost-Levadoux-Baligh (PLB) model, originally developed by Prevost (1977) and modified by Levadoux and Baligh (1980).

Figures 5.14 and 5.15 compare the predicted and measured stress-strain curves and effective stress paths (respectively) for undrained triaxial compression and extension tests on  $K_0$ -normally consolidated resedimented BBC. The laboratory tests reported by Ladd and Varallyay (1965) include two

---

\* evidently, only the relevant ones (see Table 3.3).

compression and four extension tests. \* There is some scatter in the results of the triaxial extension tests. More specifically, the measured value of the effective friction angle in triaxial extension ranges between  $40^\circ$  and  $50^\circ$  \*\* and the corresponding values of the normalized undrained shear strength are equal to 0.13-0.18.

The PLB model uses these stress-strain curves and effective stress paths as input (curve fitting) and thus, the agreement is excellent. The MCC model grossly overpredicts the undrained shear strength in triaxial extension (by 130%) and fails to predict the strain softening measured in triaxial compression. Finally, the proposed model provides good predictions of the undrained shear strength in both the compression and extension modes, predicts very well the rate of the post-peak strain softening in compression but, the predicted stiffness in triaxial extension is much too low for axial strains less than 3%.

Table 5.8 summarizes the measured and predicted undrained shear strengths and effective friction angles for  $K_0$ -normally consolidated triaxial tests on resedimented BBC. The proposed and the PLB models predict the Peak and the Critical State friction angles in compression and extension exactly, because all these angles are part of the input data. The Critical State undrained shear strengths in compression and extension

---

\* Extension tests 1 and 2 are stress controlled whereas, 4 and 5 are strain controlled.

\*\* see Section 5.2.4

predicted by the proposed model are affected by the selected values of the parameters  $\alpha$  and  $\beta$  (see Section 5.2.6). The MCC model overestimates the peak friction angle in compression by 30% and in extension by 20%.

Figures 5.16 and 5.17 compare the predicted and measured stress-strain curves and effective stress paths (respectively) for undrained plane strain compression and extension tests on  $K_0$ -normally consolidated resedimented BBC. After conducting an extensive program of plane strain tests on resedimented BBC, Ladd et al (1971) concluded that (i) the plane strain apparatus used to obtain the test results in Figs. 5.16 and 5.17 yields reliable data for compression tests, and (ii) stress-strain data in the extension mode are not reliable for vertical strains larger than 3+1 percent. \*

The PLB model overpredicts the undrained shear strength in compression by about 8% but the rate of post-peak strain softening is very well predicted. The MCC model grossly overpredicts the undrained shear strength in extension (by 130%) and fails to predict the strain softening measured in compression. Finally, the proposed model provides reasonable predictions of the undrained shear strength in both compression and extension but significantly underpredicts the rate of post-peak strain softening in compression.

Table 5.9 summarizes the measured and predicted undrained shear strengths and effective friction angles for  $K_0$ -normally

---

\* At larger strains, testing errors due to the side friction and sample necking lead to measured strength values that are too high.



consolidated plane strain tests on resedimented BBC. The proposed and the PLB models give reasonable predictions of the Peak Strength friction angle in compression but overpredict the Critical State friction angles. The MCC model significantly overestimates the Peak Strength and the Critical State friction angles in both the compression and extension modes.

Figures 5.18 and 5.19 compare the predicted stress-strain curves and effective stress paths respectively, for undrained Direct Simple Shear (DSS) tests \* on  $K_0$ -normally consolidated resedimented BBC, with the measured behavior in three laboratory tests reported by Ladd and Edgers (1972) using the DSS apparatus developed at the Norwegian Geotechnical Institute (Bjerrum and Landva, 1966). Several workers have discussed the stress changes that occur during a DSS test (e.g. Roscoe, 1953; Ladd and Edgers, 1972; Prevost and Hoeg, 1976; Budhu, 1979) and they all seem to agree that the relative slippage at the contact between the soil sample and the top and bottom caps, together with the lack of complementary shear stresses on the vertical sides of the sample, create non-homogeneous distributions of shear and normal stresses on the sample. To account for the difference between the maximum and the average shear stresses acting on the sample, Prevost and Hoeg (1976) suggest that the predicted (maximum) shear stress is 10% higher than the measured (average) horizontal shear stress on the sample and thus, proposed a 10% reduction of the predicted

---

\* the predictions are obtained for idealized conditions i.e., assuming that the stresses and strains in the sample are uniform.

shear stress in order to estimate the measured (average) shear stress. After this 10% reduction, the predictions of the proposed model match very well the measured behavior whereas, the PLB model overpredicts the undrained shear strength by 20% and the MCC model grossly overpredicts the undrained shear strength by 66%. Furthermore, the PLB model predicts a too "stiff" response for shear strains less than two per cent. Table 5.10 summarizes the measured and predicted undrained shear strengths and effective friction angles for  $K_0$ -normally consolidated DSS tests on resedimented BBC. Measured values of  $\phi$  are not shown because, the testing apparatus only provides measurements of the (average) normal and shear stresses on ONE plane (the horizontal) and thus, the friction angle cannot be obtained.

Figure 5.20 shows the evolution of the Mohr circle of effective stresses during a DSS test, as predicted by the proposed model. We note that:

- (i) The angle

$$\psi \equiv \arctan (\tau / \bar{\sigma}_v)$$

expresses the effective stress obliquity on the horizontal plane. The proposed model predicts a monotonic increase of  $\psi$  with shear strain and, at the Critical State,  $\psi$  reaches a limiting value of about 25°.

- (ii) At the peak strength condition (i.e., when  $\gamma/\gamma_p=1$ ) the

predicted friction angle is about  $32^\circ$  and increases to  $38.6^\circ$  at the Critical State.

(iii) The direction of the maximum principal stress (expressed by the angle  $\delta$ ) rotates rapidly with increasing shear strain and reaches the value  $\delta = 31^\circ$  at the Critical State.

(iv) The proposed model predicts that at the peak strength condition, the origin of planes  $O_p$  coincides with the point of tangency of the Mohr circle and the failure envelope (i.e.,  $\theta = \omega$ ). This means that, at the peak strength condition, the vertical plane is a plane of maximum stress obliquity and since it is also a "zero extension" plane, we can say that the proposed model predicts that at the peak strength condition, one of the zero extension directions (the vertical) coincides with one of the planes of maximum stress obliquity. This agrees with the results of theoretical analyses reported by Shield (1953) and de Josselin de Jong (1971) as well as the suggestions of Randolph and Wroth (1981). Randolph and Wroth (1981) also assume that, at the Critical State, the horizontal plane is a plane of maximum stress obliquity which requires that  $\theta = \psi$  at the Critical State. However, the proposed model predictions do not agree with this assumption of Randolph and Wroth (1981) for the Critical State.

## (b) Effect of Stress Reversals

Although the proposed model was developed mainly to study the stress-strain-strength behavior of normally consolidated clays under monotonic stress paths, it is interesting to investigate the predictions of the proposed model for stress paths involving stress reversals. The idealized \*  $K_0$ -normally consolidated undrained Direct Simple Shear (DSS) test was selected because, in this test, the sample is initially isotropic with respect to positive or negative shear stress applications and thus, any predicted strength change after a stress reversal, is due exclusively to the applied stress reversal and not to some initial strength anisotropy (e.g. such as between compression and extension in a triaxial test).

Figure 5.21 shows the proposed model predictions for certain undrained DSS tests on a  $K_0$ -normally consolidated clay with the same properties as BBC. In the first test (path OABC), an initially  $K_0$ -normally consolidated sample is sheared up to a shear strain  $\gamma = 2\%$  (point A) and then, the shear stress is reversed until failure is reached. In the second test (path OADEFG), an initially  $K_0$ -normally consolidated sample is sheared up to a shear strain  $\gamma = 5\%$  (point D) and then the shear stress is reversed until failure. These tests allow one to investigate:

- (i) The effect of the level of the applied shear strain  $\gamma$  on the stiffness of the linear part of the shear

---

\* i.e., assuming uniform distribution of stresses and strains in the sample

stress-strain curves during a stress reversal. The proposed model predicts a 25% decrease of the elastic stiffness  $G/\bar{\sigma}_{v0}$  for  $\gamma = 2\%$  and a 40% decrease for  $\gamma = 5\%$ . This is due to the fact that according to the proposed model, the elastic  $G$  is proportional to the mean effective stress and, the mean effective stress decreases during undrained shear (i.e., along the curve OAD).

- (ii) The effect of the level of the applied shear strain  $\gamma$  on the predicted undrained shear strength following a reversal of the shear stress. The proposed model predicts a 10% decrease \* of the peak shear stress (i.e.,  $\tau_{\max}/\bar{\sigma}_{v0} = 0.20$ ) when the shear stress direction is reversed at  $\gamma = 2\%$ , and a 20% decrease of the peak shear stress (i.e.,  $\tau_{\max}/\bar{\sigma}_{v0} = 0.177$ ) when the shear stress direction is reversed at  $\gamma = 5\%$ . The decrease of the predicted undrained shear strength after a stress reversal is due to the rotation of the yield surface of the proposed model during plastic loading (i.e., because of kinematic hardening).

### (c) Cyclic Tests

Braathen (1966) performed a series of cyclic undrained triaxial tests on  $K_0$ -normally consolidated BBC with highly repeatable results. Figures 5.22 and 5.23 present the

---

\* with respect to the value predicted for virgin undrained shear ( $\tau_{\max}/\bar{\sigma}_{v0} = 0.22$ )

stress-strain curve and the effective stress path (denoted by open circles for loading and dark circles for unloading) respectively, of one of his tests (P15). In Fig. 5.22, the normalized deviatoric stress  $(\bar{\sigma}_v - \bar{\sigma}_h)/2\bar{\sigma}_{v0}$  is plotted against the "generalized" strain which, in the case of a triaxial test, is the sum of the absolute values of the vertical strain increments. The values of the model parameters used in the predictions of the monotonic tests (see Table 5.7) are also used in the predictions of the cyclic tests with the exception of the elastic shear modulus  $G$ . In the monotonic tests,  $G$  only affects the predicted stiffness at very low strain levels and thus, the selected value is based on measurements of the shear modulus at such strain levels (see Section 5.2.2). In the cyclic tests,  $G$  also affects the predicted stiffness of the unloading portion of the stress-strain curve, which is a constant until yielding occurs in the reverse direction (see Fig. 5.22). In the cyclic tests performed by Braathen (1966), the strain levels associated with the unloading portions of the measured stress-strain curves are much higher \* than the strain levels used to evaluate  $G$  in the case of the monotonic tests, which means that one would expect a lower value of the secant modulus during these unloading paths. Thus, a lower value of  $G$  ( $G/\bar{\sigma}_{v0} = 65$  instead of 150) is used in the predictions of the cyclic tests. The continuous line in Figs. 5.22 and 5.23 represents the prediction of the proposed model. The predicted stress-strain curve fits very well the

---

\* typically one order of magnitude higher

experimental data for the first two cycles of loading and unloading shown in Fig. 5.22, whereas, Fig. 5.23 shows that the proposed model underpredicts the excess pore pressures.

#### 5.4.1.2. Drained Strain Controlled Tests

Figure 5.24 presents the proposed model predictions of the effective stress paths for various drained strain controlled tests that can be performed in the triaxial apparatus starting from a  $K_0$ -normally consolidated state on a clay with the same properties as BBC (see Table 5.7). The ratio of the applied horizontal to vertical strain (i.e.,  $\epsilon_h/\epsilon_v$ ) is kept constant in each of these tests and ranges between infinity (for the  $K_0'$ -consolidation path) and -0.5 (for the undrained triaxial compression test). As expected, the  $K_0'$ -consolidation stress path asymptotically approaches the  $K_0'$ -consolidation line, whereas, the isotropic consolidation path (i.e., when  $\epsilon_h = \epsilon_v$ ) approaches the isotropic consolidation line.

#### 5.4.2 $K_0$ -OVERCONSOLIDATED TESTS ON BOSTON BLUE CLAY

Although the proposed model is developed to study mainly the stress-strain-strength behavior of normally consolidated clays and the model parameters are evaluated solely from  $K_0$ -normally consolidated tests, in the following the model is used to predict the stress-strain curves and the effective stress paths of undrained tests on overconsolidated BBC (OCR=2). The values of the input parameters are again those

used in the predictions of the normally consolidated BBC (see Table 5.7). \* For an overconsolidated clay, the initial state (denoted by A in Figs. 5.24 to 5.27) is represented by a point inside the yield surface and thus, upon shearing, the initial response is linear elastic until the yield surface is reached.

Figure 5.25 shows the shear stress-strain curve and the effective stress path predicted by the proposed model for  $K_0$ -consolidated undrained triaxial compression and extension tests on overconsolidated BBC (OCR=2). The proposed model predicts a normalized peak strength  $s_u/\bar{\sigma}_{v0}=0.63$  in triaxial compression and  $s_u/\bar{\sigma}_{v0}=0.275$  in triaxial extension. Unfortunately, experimental data for  $K$ -consolidated undrained triaxial tests (at OCR=2) are not available for this clay.

Figure 5.26 shows the shear stress-strain curve and the effective stress path predicted by the proposed model and compares the prediction to the experimentally measured response of  $K_0$ -consolidated undrained plane strain compression and extension tests on overconsolidated BBC (OCR=2) reported by Ladd et al (1971). The predicted values of the normalized peak undrained shear strength in plane strain ( $s_u/\bar{\sigma}_{v0}=0.68$  in compression and 0.32 in extension) are slightly higher than those predicted for the triaxial tests (about 8% in compression and 16% in extension) and, in general, the trends predicted in

---

\*

For OCR=2,  $K_0 = 0.72$ . Also the value  $G/\bar{\sigma}_{v0}=65$  was used instead of 150, because of the large elastic region inside the yield surface (see also Section 6.4.1.1c).



the plane strain tests are similar to those predicted in the triaxial tests. In plane strain compression, the predicted stress-strain curve and effective stress path poorly match the measured behavior: the proposed model overpredicts the undrained shear strength in compression by 20% and predicts an increase of the mean effective stress in the post-peak region of the effective stress path, whereas, the laboratory data indicate a decreasing mean effective stress. This is partly due to the linear behavior predicted by the proposed model for stress points inside the yield surface and also due to the adopted flow rule for the part of the yield surface that may be reached during undrained shear starting from overconsolidated states. In plane strain extension the agreement between prediction and measurement is better.

Figure 5.27 compares measured values \* and proposed model predictions of the stress-strain curves and the effective stress paths for  $K_0$ -consolidated undrained Direct Simple Shear (DSS) tests on overconsolidated resedimented BBC (OCR=2). The proposed model predicts reasonably well the peak value of the applied shear stress (predicted  $\tau_{\max} / \bar{\sigma}_{v0}$  equal to 0.378 \*\* vs. measured values equal to 0.35-0.40) but poorly matches the measured effective stress path (see Fig. 5.27b). This is again due to the linear behavior predicted by the proposed model for stress points inside the yield surface. Figures 5.25 through

---

\* test data reported by Ladd and Edgers (1972)

\*\* After a 10% reduction to account for non-homogeneity of stresses (Prevost and Hoeg, 1976).

5.27 do not show the predictions of the PLB model because this model cannot predict the behavior of overconsolidated clays using the input parameters obtained from tests on normally consolidated clays. \* These Figures also do not show the predictions of the MCC model because they overlap with the linear portions of the corresponding curves predicted by the proposed model since, for undrained tests with  $OCR=2$ , the MCC model predicts linear behavior up to the Critical State. Table 5.11 compares the values of the undrained shear strength for overconsolidated BBC ( $OCR=2$ ) predicted by the MCC model \*\* and the proposed model, to the experimentally measured values (shown in Figs. 5.26 and 5.27). The MCC model grossly overestimates the undrained shear strength in all plane strain modes of deformation (e.g. by 100% in the Plane Strain Extension and the DSS tests and, by 40% in the Plane Strain Compression test) whereas, the proposed model gives more realistic predictions of the measured strengths.

---

\* since it is a total stress model

\*\* using the same parameters as in the predictions for the normally consolidated clay

## 5.5 SUMMARY AND CONCLUSIONS

This Chapter evaluates the soil model proposed in Chapter 4 by comparing the model predictions to results of laboratory tests on  $K_0$ -consolidated resedimented Boston Blue Clay (BBC) and, to the predictions of the Modified Cam-Clay (MCC) and the Prevost-Levadoux-Baligh (PLB) models.

The MCC model has certain interesting characteristics (e.g. volumetric hardening, the Critical State concept, few parameters that are easy to obtain, etc), but it does not give realistic predictions of the measured stress-strain-strength behavior of  $K_0$ -consolidated BBC. More specifically, it does not predict the strain softening and strength anisotropy and grossly overestimates the measured undrained shear strength in all plane strain modes of deformation. \*

The PLB model can describe the post-peak strain softening observed in certain modes of deformation and, when the necessary parameters are evaluated from cyclic triaxial tests, it can predict the stress-strain behavior of clays under repeated loading. \*\* The model also gives reasonably good predictions of the undrained shear strength in Plane Strain Compression and Extension, but overestimates the strength in the DSS test. However, because of its nature (i.e., a total stress model), the model is limited to undrained stress paths,

---

\* actually the model predicts the same value of the undrained shear strength for all Plane Strain modes

\*\* Levadoux and Baligh (1980) show that the model can give reasonably good predictions for the first 3 to 4 cycles of load application

i.e., it cannot be used to study consolidation or drained paths. Furthermore, the model cannot predict the stress-strain behavior of overconsolidated clays based on the values of the soil parameters obtained from tests on (say) the normally consolidated clay but, requires additional tests for ALL overconsolidation ratios to be studied. Finally, the model requires a large number of input parameters (typically 130-200, depending on the number of yield surfaces used).

The proposed model has certain advantages compared to the PLB model:

- (i) It can be used to solve Boundary Value problems involving consolidation and drained loading because it is an effective stress model. \*
- (ii) It gives predictions similar to those of the PLB model for Undrained tests on  $K_0$ -normally consolidated BBC. More specifically, the proposed model predicts the undrained shear strength and the effective friction angles in the Triaxial and Plane Strain modes of deformation with the same degree of accuracy and, it gives significantly better predictions in the DSS mode of deformation compared to the PLB model.
- (iii) It can predict the stress-strain behavior of overconsolidated clays and the behavior of clays during cyclic tests, based on the values of the parameters obtained from monotonic tests on the normally consolidated clay whereas, the PLB model requires

---

\* it can also be used to study undrained problems

additional monotonic and cyclic tests for each overconsolidation ratio to be analysed.

- (iv) It requires a reasonable number of input parameters (typically 11, compared to 130-200 required by the PLB model) and, it is computationally more efficient than the PLB model (typically it requires 7-10 times less CPU time depending on the stress path).

In the present form, the proposed model gives reasonable predictions for  $K_0$ -normally consolidated undrained monotonic shear tests in the Triaxial, Plane Strain and the Direct Simple Shear apparatuses, as well as during the first couple of cycles of one series of undrained cyclic triaxial tests on the  $K_0$ -normally consolidated clay. For undrained shear tests on the slightly overconsolidated clay (OCR=2), the model overpredicts the strength in the Compression modes but gives reasonable predictions in the Extension and in the DSS modes. The discrepancies in the predictions for the overconsolidated clay are mainly due to the assumption that stress states inside the yield surface \* give a linear elastic stress-strain response. This simplifying assumption does not have significant consequences when studying monotonic stress paths on normally consolidated clays but affects the predicted response for cyclic tests and tests on overconsolidated clays. In these cases, improvements can be achieved by using a more sophisticated law to describe the stress-strain behavior inside

---

\* such states may be reached during a load reversal (i.e., for a cyclic test) and during a rebound leading to an overconsolidated state.

the yield surface (i.e., for elastic states) which basically means introducing more parameters obtained from cyclic tests and tests on overconsolidated samples. It is also interesting to note that, since the stress-strain behavior inside the yield surface is basically uncoupled from the behavior at states located on the yield surface (i.e., elastoplastic states), these improvements can be incorporated in the model with only minor modifications of the existing computational algorithm.

BOSTON BLUE CLAY			
PROPERTY	BATCH NUMBER		
	S-4	S-5	S-6
Specific Gravity, $G_s$	-	2.78	-
Liquid Limit (%)	32.6	33.3	32.8
Plastic Limit (%)	19.5	20.4	20.3
Plasticity Index (%)	13.1	12.9	12.5
Shrinkage Limit (%) (remolded)	-	16.9	-
Salt Content, g/l NaCl	-	16.8	16.0

Table 5.1: Classification Data of  
Boston Blue Clay  
(after Ladd and Varallyay, 1965)

	Test Number	$\lambda \equiv -\Delta e / \Delta \ln \bar{\sigma}$	$\lambda$ Average	Standard Deviation
Isotropic Consolidation	CIUC - 1	0.205	0.163	0.043
	CIUC - 2	0.167		
	CIUC - 3	0.118		
	CIUE - 1	0.105		
	CIUE - 2	0.209		
	CIUE - 3	0.173		
$K_o$ Consolidation ( $K_o \approx 0.534$ )	CK <sub>o</sub> UC - 1	0.097	0.175	0.080
	CK <sub>o</sub> UC - 2	0.101		
	CK <sub>o</sub> UUC - 1	0.298		
	CK <sub>o</sub> UUC - 2	0.299		
	CK <sub>o</sub> URE - 1	0.164		
	CK <sub>o</sub> URE - 2	0.158		
	CK <sub>o</sub> URE - 4	0.124		
	CK <sub>o</sub> URE - 5	0.161		
$\frac{1}{K_o}$ Consolidation ( $\frac{1}{K_o} \approx 1.871$ )	C( $\frac{1}{K_o}$ )UE - 1	0.177	0.157	0.067
	C( $\frac{1}{K_o}$ )UE - 3	0.131		
	C( $\frac{1}{K_o}$ )URC - 2	0.104		
	C( $\frac{1}{K_o}$ )URC - 4	0.282		
	C( $\frac{1}{K_o}$ )URC - 5	0.143		
	C( $\frac{1}{K_o}$ )URC - 6	0.104		

**Table 5.2: Measured  $\lambda$  Values from Consolidation Tests on Normally Consolidated Boston Blue Clay (Data from Ladd and Varallyay, 1965)**



$\overline{CK}_O \overline{U}$	Failure Condition	Test Number	$K_\sigma$	$K_\sigma$ Average	$\overline{\phi}$	$S_1/\overline{\sigma}$
TC	Peak	CK <sub>O</sub> UC - 1	0.3861	0.3922	25.88°	0.83423
		CK <sub>O</sub> UC - 2	0.3984			
	Critical ( $\epsilon_y = 8\%$ )	CK <sub>O</sub> UC - 1	0.3082	0.2899	33.40°	1.10084
		CK <sub>O</sub> UC - 2	0.2717			
TE	Peak & Critical ( $\epsilon_y = 8\%$ )	CK <sub>O</sub> UE - 1	8.00	6.10	45.91°*	-0.9464
		CK <sub>O</sub> UE - 4	4.20			

Note:  $K_\sigma \equiv \overline{\sigma}_x / \overline{\sigma}_y$  ;  $\overline{\sigma}_x = \overline{\sigma}_z$  (triaxial)

\* see discussion in Section 5.2.4

Table 5.3: Data at Peak and Critical Conditions  
From  $\overline{CK}_O \overline{U}(C)$  and  $\overline{CK}_O \overline{U}(E)$  Triaxial Tests on  
Normally Consolidated Boston Blue Clay  
(Data from Ladd and Varallyay, 1965)

(a)		(b)	
MEASUREMENT (Ladd and Varallyay, 1965)		PROPOSED MODEL PREDICTION	
Test Number	Normalized Undrained Shear Strength $s_u/\bar{\sigma}_{vo}$	$\alpha$	Normalized Undrained Shear Strength $s_u/\bar{\sigma}_{vo}$
CK <sub>O</sub> URE-1	0.124	-1.50	0.09
CK <sub>O</sub> URE-2	0.116	-0.75	0.14
CK <sub>O</sub> URE-4	0.165	0.0	0.18
CK <sub>O</sub> URE-5	0.137		
AVERAGE	0.136		

Table 5.4: Evaluation of the Parameter  $\alpha$  of the Proposed Model from the Undrained Shear Strength of  $\overline{CK}_O\bar{U}$  Triaxial Extension Tests on Normally Consolidated BBC.

(a) MEASUREMENT (Ladd and Varallyay, 1965)		(b) PROPOSED MODEL PREDICTION	
Test Number	Normalized Critical State Undrained Shear Strength $s_u/\bar{\sigma}_{vo}$	$\beta$	Normalized Critical State Undrained Shear Strength $s_u/\bar{\sigma}_{vo}$
CK <sub>0</sub> UC-1	0.224	-3.40	0.280
CK <sub>0</sub> UC-2	0.211	-2.95	0.215
AVERAGE	0.217	-2.50	0.170

Table 5.5: Evaluation of the Parameter  $\beta$  of the Proposed Model from the Critical State Undrained Shear Strength  $\overline{CK}_0^U$  Triaxial Compression Tests on Normally Consolidated BBC.

St. Alban (Champlain) Clay		
Property	Depth 3m	Depth 5.7m
Liquid Limit (%)	50	40
Plastic Limit (%)	27	23
Plasticity Index (%)	23	17
Sensitivity by Field Vane	14	22
Salt Content, g/l, NaCl	0.7	0.3

Table 5.6: Classification Data of  
St. Alban (Champlain) Clay  
(Data from Leroueil et al, 1979)

INPUT PARAMETERS	
Symbol	Selected Value
$\lambda$	0.170
$\kappa$	0.034
$G/\bar{\sigma}_{vo}$	150
$K_o$	0.5344
$\bar{\phi}_{TC}^D$	25.88°
$\bar{\phi}_{TC}^C$	33.40°
$\bar{p} = \bar{\phi}_{TE}^C$	45.91°
$\psi$	14.0
$c$	0.866
$\alpha$	-0.75
$\beta$	-2.95

(a)

INITIAL VALUES OF THE STATE VARIABLES
$\bar{\alpha} = \frac{1}{6} [1 + 2(K_o)_{NC}] (OCR) \bar{\sigma}_{vo}$
$b_1 = \sqrt{6} \{1 - (K_o)_{NC}\} / [1 + 2(K_o)_{NC}]$ $b_2 = b_3 = b_4 = b_5 = 0$
$\bar{\sigma} = \frac{1}{3} [1 + 2(K_o)_{OC}] \bar{\sigma}_{vo}$ $S_1 = \frac{2}{\sqrt{6}} [1 - (K_o)_{OC}] \bar{\sigma}_{vo}$ $S_2 = S_3 = S_4 = S_5 = 0$
$e_o = 0.898$ for $K_o$ -normally consolidated clay when $\bar{\sigma}_{vo} = 1.45 \text{ kg/cm}^2$

(b)

Table 5.7: Input Parameters and Initial Values of the State Variables Used in the Predictions of the Stress-Strain-Strength Behavior of  $K_o$ -consolidated Boston Blue Clay

K <sub>0</sub> -NORMALLY CONSOLIDATED UNDRAINED TRIAXIAL TESTS ON BOSTON BLUE CLAY									
COMPRESSION					EXTENSION				
Prediction	Undrained Shear Strength $s_u/\sigma_{vo}$		Effective Friction Angle $\phi$		Undrained Shear Strength $s_u/\sigma_{vo}$		Effective Friction Angle $\phi$		Critical State
	Peak	Critical State	Peak	Critical State	Peak	Critical State	Peak	Critical State	
Average Measured Value Ladd and Varallyay (1965)	0.325	0.215	25.9	33.4	0.13-0.18	0.13-0.18	40-50**	40-50**	
Proposed Model	0.320	0.212	25.9*	33.4*	0.142	0.142	45.9*	45.9*	
MCC Model	0.320	0.320	33.4*	33.4*	0.320	0.320	60.4	60.4	
PLB Model	0.325*	0.220*	25.9*	33.4*	0.140*	0.140*	45.9*	45.9*	

\* Value used as input to the model

\*\* see discussion in Section 5.2.4

Table 5.8: Measured and Predicted Undrained Shear Strengths and Effective Friction Angles for K<sub>0</sub>-Normally Consolidated Undrained Triaxial Tests on Boston Blue Clay.

K <sub>0</sub> -NORMALLY CONSOLIDATED UNDRAINED PLANE STRAIN TESTS ON BOSTON BLUE CLAY									
	COMPRESSION					EXTENSION			
	Undrained Shear Strength $s_u/\sigma_{vo}$		Effective Friction Angle $\phi$		Undrained Shear Strength $s_u/\sigma_{vo}$		Effective Friction Angle $\phi$		
	Peak	Critical State	Peak	Critical State	Peak	Critical State	Peak	Critical State	Critical State
Average Measured Value Ladd et al (1971)	0.338	0.215	29.0	32.7	≈0.19	~0.19	34-46*	34-46*	34-46*
Proposed Model	0.344	0.283	31.6	42.6	0.165	0.164	34.7	36.0	36.0
MCC Model	0.369	0.369	51.1	51.1	0.369	0.369	51.1	51.1	51.1
PLB Model	0.363	0.220	32.0	42.0	0.160	0.160	35.0	35.0	35.0

\* suggested value equal to 40°

Table 5.9: Measured and Predicted Undrained Shear Strengths and Effective Friction Angles for K<sub>0</sub>-Normally Consolidated Undrained Plane Strain Tests on Boston Blue Clay.

K <sub>0</sub> -NORMALLY CONSOLIDATED UNDRAINED DIRECT SIMPLE SHEAR TESTS ON BOSTON BLUE CLAY				
	Undrained Shear Strength $\tau/\sigma_{vo}$		Effective Friction Angle $\bar{\phi}$	
	Peak	Critical State	Peak	Critical State
Average Measured Value Ladd and Edgers (1972)	0.200	0.193	-	-
PREDICTION	Proposed Model	0.193	31.9	38.6
	MCC Model	0.332	51.1	51.1
	PLB Model	0.238	32.0	41.8

NOTE: A 10% reduction is applied to the predicted shear strength to account for non-homogeneity of stresses (Prevost and Hoeg, 1976).

Table 5.10: Measured and Predicted Undrained Shear Strengths and Effective Friction Angles for K<sub>0</sub>-Normally Consolidated Undrained Direct Simple Shear Tests on Boston Blue Clay.



K <sub>O</sub> -OVERCONSOLIDATED UNDRAINED TESTS ON BOSTON BLUE CLAY (OCR = 2)						
PEAK UNDRAINED SHEAR STRENGTH $s_u / \sigma_{vo}$						
	TRIAXIAL		PLANE STRAIN		Direct Simple Shear	
	Compression	Extension	Compression	Extension		
Measured Values	-	-	0.54 - 0.58	≈ 0.38	0.35 - 0.40	
Predicted Values	0.630	0.275	0.680	0.320	0.378*	
MCC Model	0.674	0.674	0.780	0.780	0.702*	

NOTE: For OCR = 2 the MCC model predicts linear behavior up to the Critical State.

\*Values reduced by 10% to account for stress inhomogeneity (Prevost and Hoeg, 1976).

Table 5.11: Measured and Predicted Peak Undrained Shear Strengths for K<sub>O</sub>-Overconsolidated Undrained Tests on Boston Blue Clay (OCR = 2)

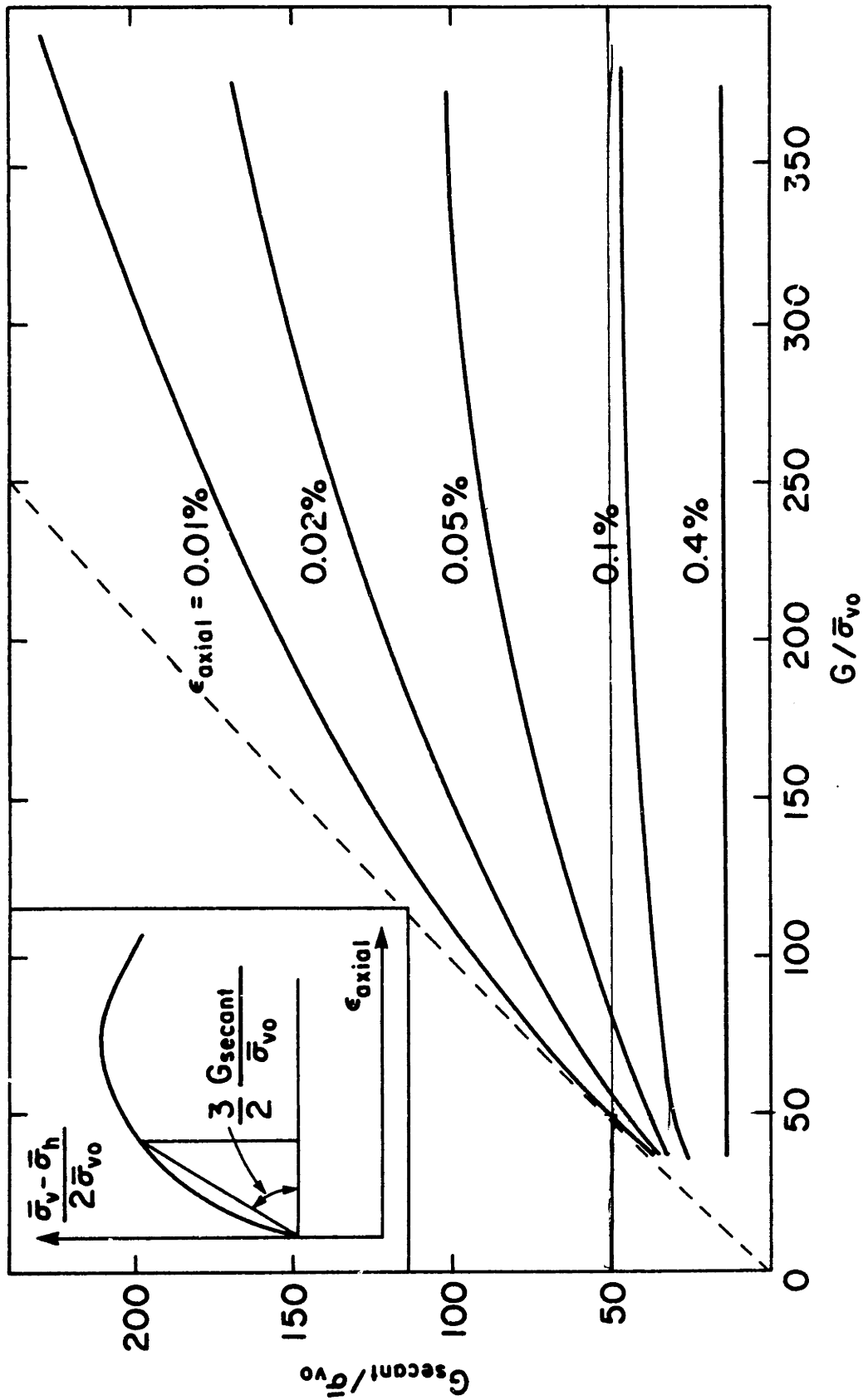
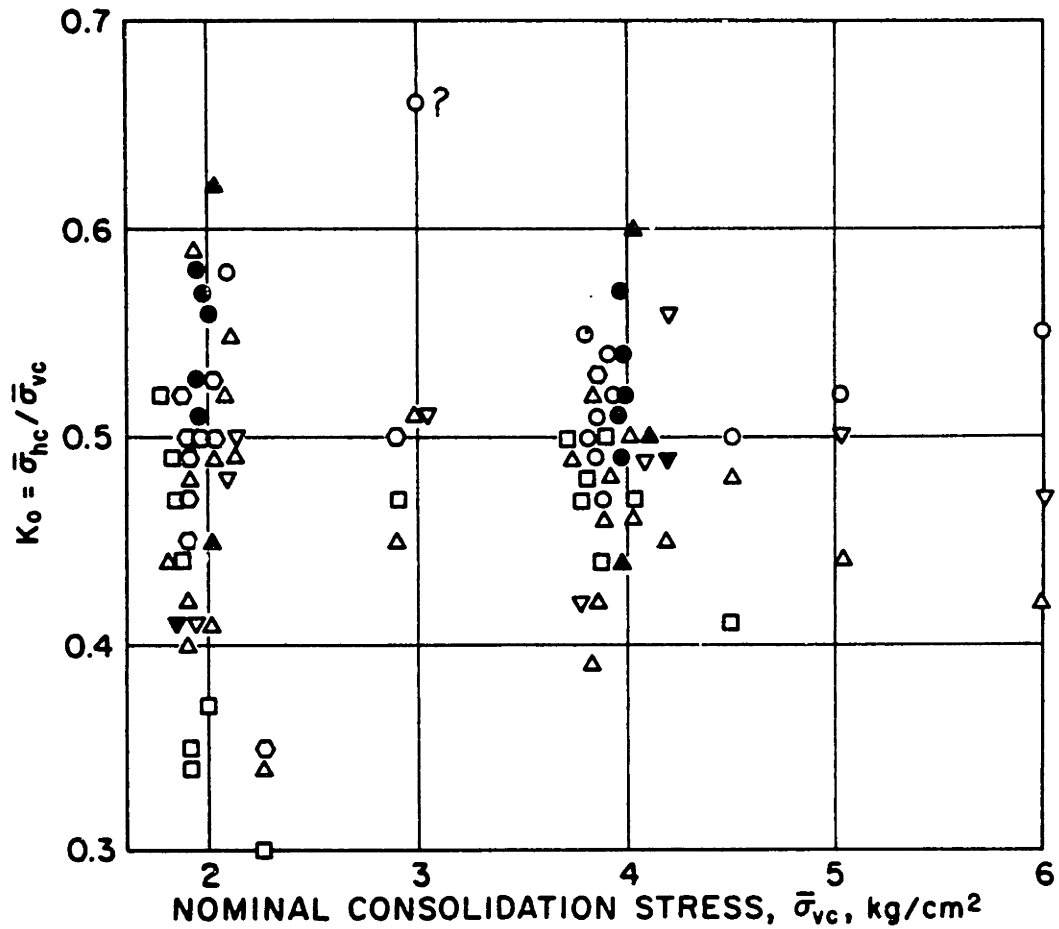


Fig. 5.1: Secant shear modulus predicted by the proposed model at various levels of axial strain during  $K_0$ -consolidated undrained triaxial compression tests on a clay with properties similar to normally consolidated Boston Blue Clay



$K_0$ measured by	Device	
	P	B
Cell pressure	○	●
Side platen	○	
Front end pressure plate	□	
Front end pressure transducer	▽	▼
Back end pressure transducer	△	▲

**Fig. 5.2:** Measured  $K_0$ -Values of resedimented normally consolidated samples of Boston Blue Clay using two Plane Strain Apparatuses (Models P and B). After Ladd et al (1971).

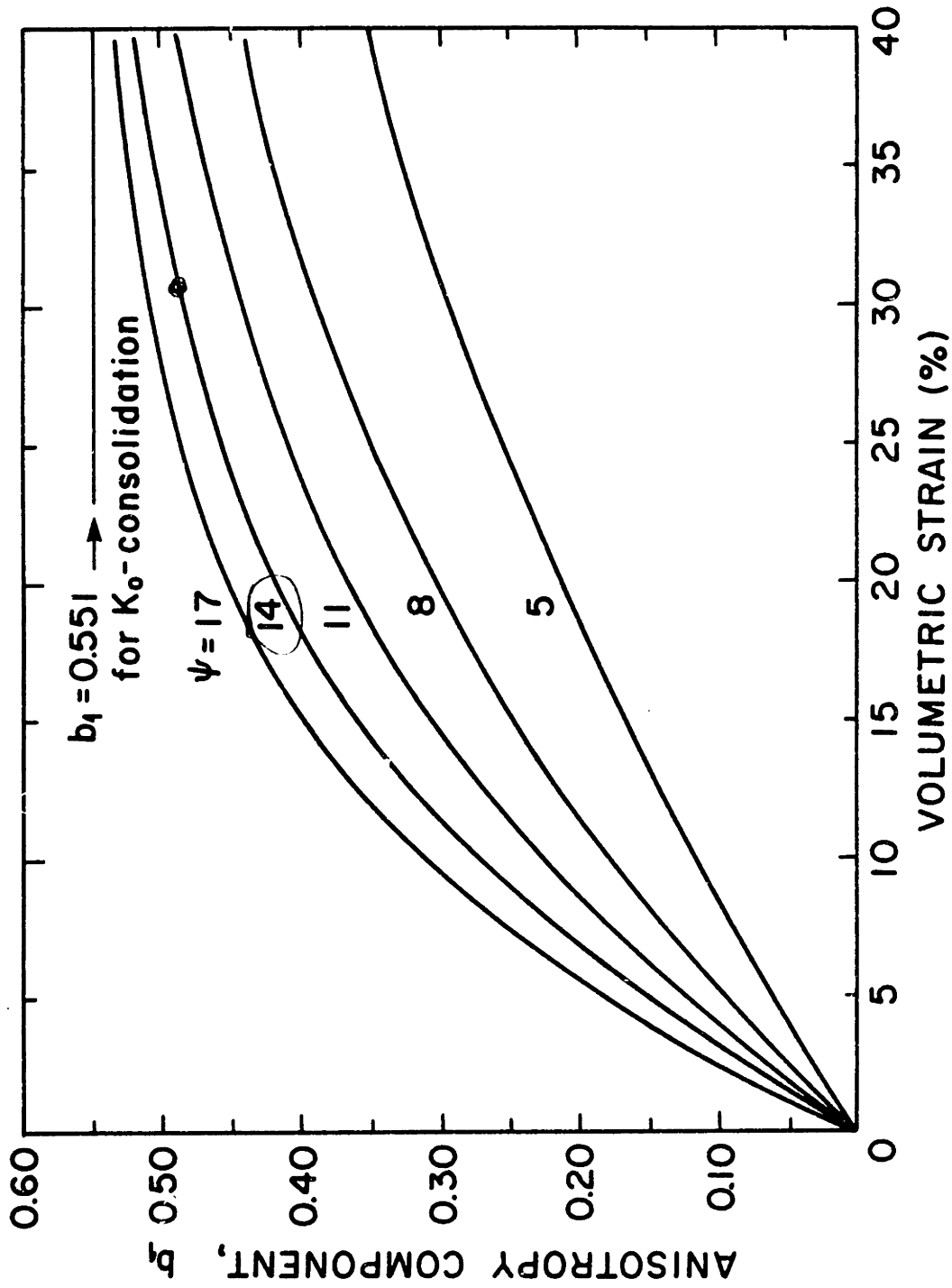


Fig. 5.3: Proposed model prediction of the change in anisotropy during one-dimensional ( $K_0$ ) consolidation of an initially isotropically normally consolidated sample

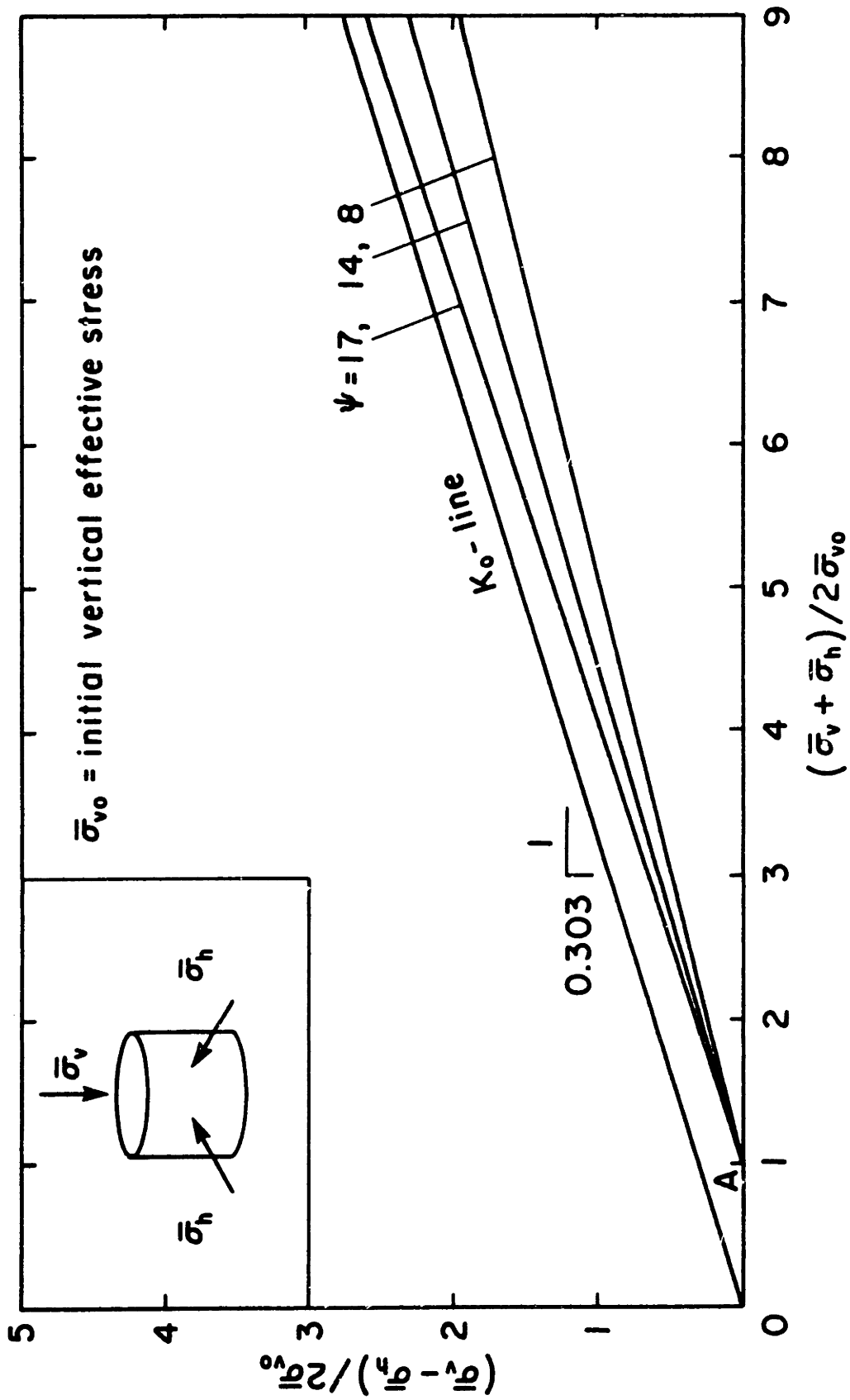
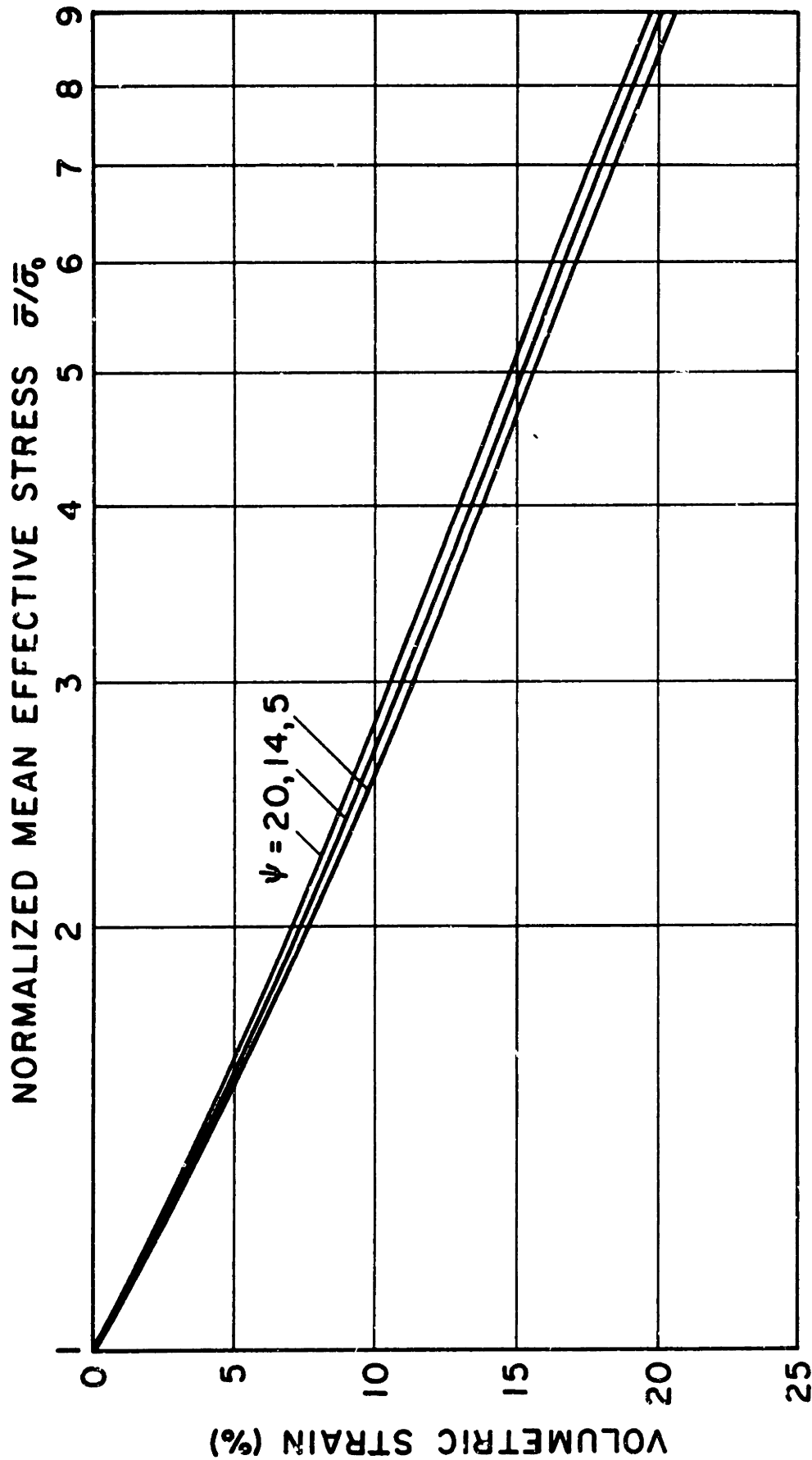
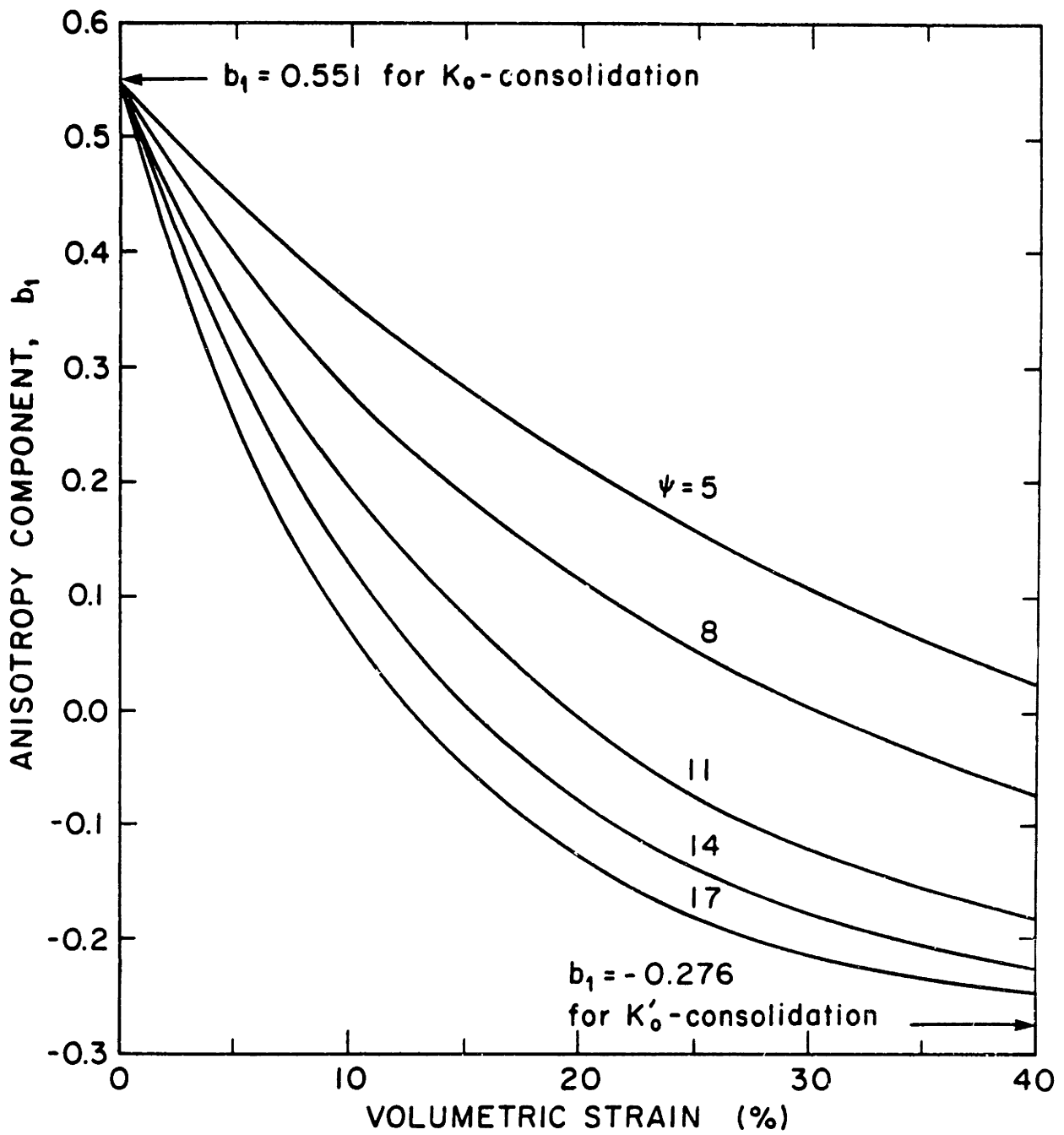


Fig. 5.4: Proposed model prediction of the effective stress path during one-dimensional straining of an initially normally consolidated sample



**Note:  $\bar{\sigma}_0$  is the initial mean effective stress**

**Fig. 5.5:** Proposed model prediction of the mean effective stress vs. volumetric strain curves during one-dimensional straining of an initially isotropic normally consolidated sample



**Fig. 5.6:** Proposed model prediction of the change in anisotropy during  $K'_0$ -consolidation of an initially  $K_0$ -consolidated sample with properties similar to Boston Blue Clay.

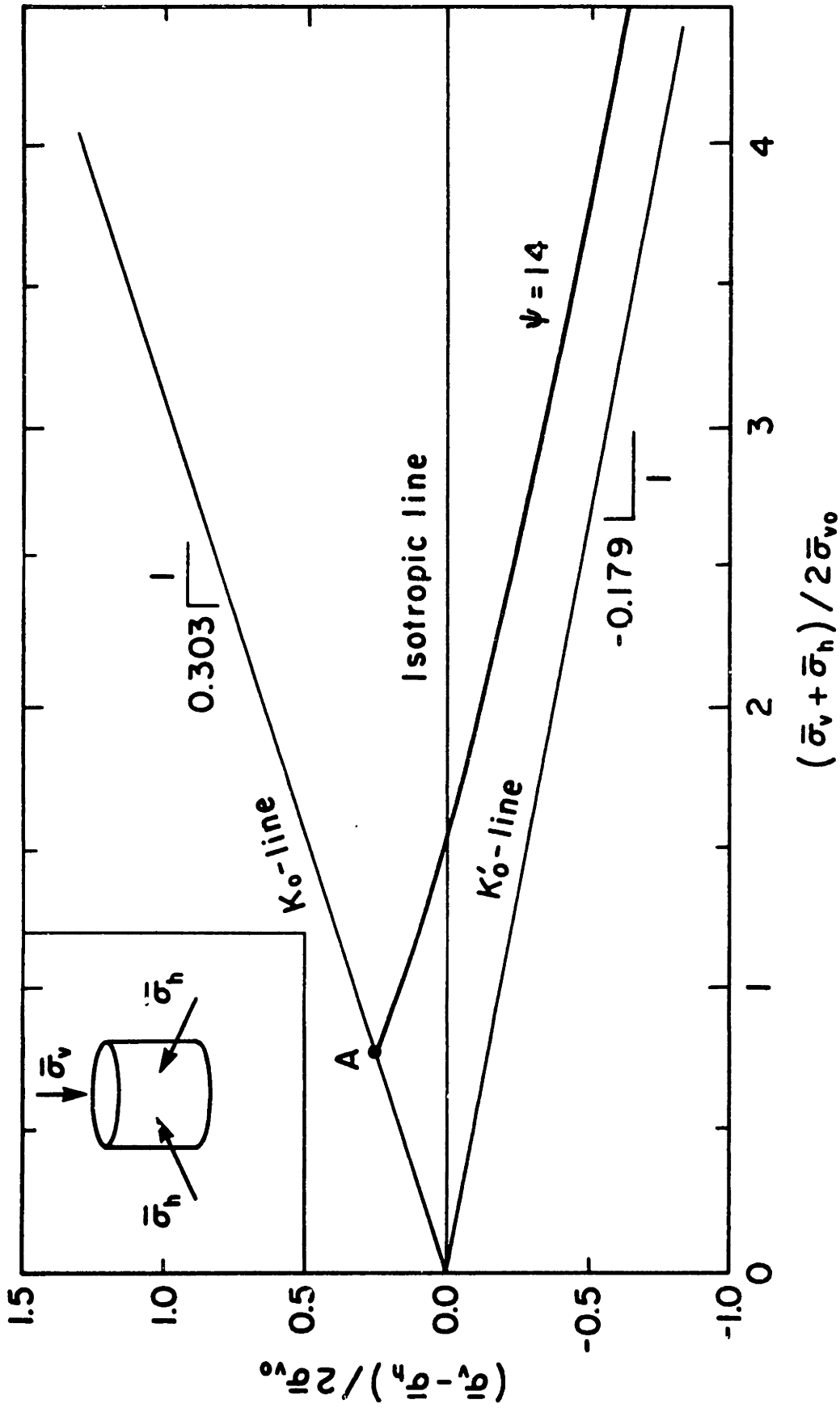


Fig. 5.7: Proposed model predictions of the effective stress path during  $K'_0$ -consolidation of an initially  $K_0$ -consolidated sample



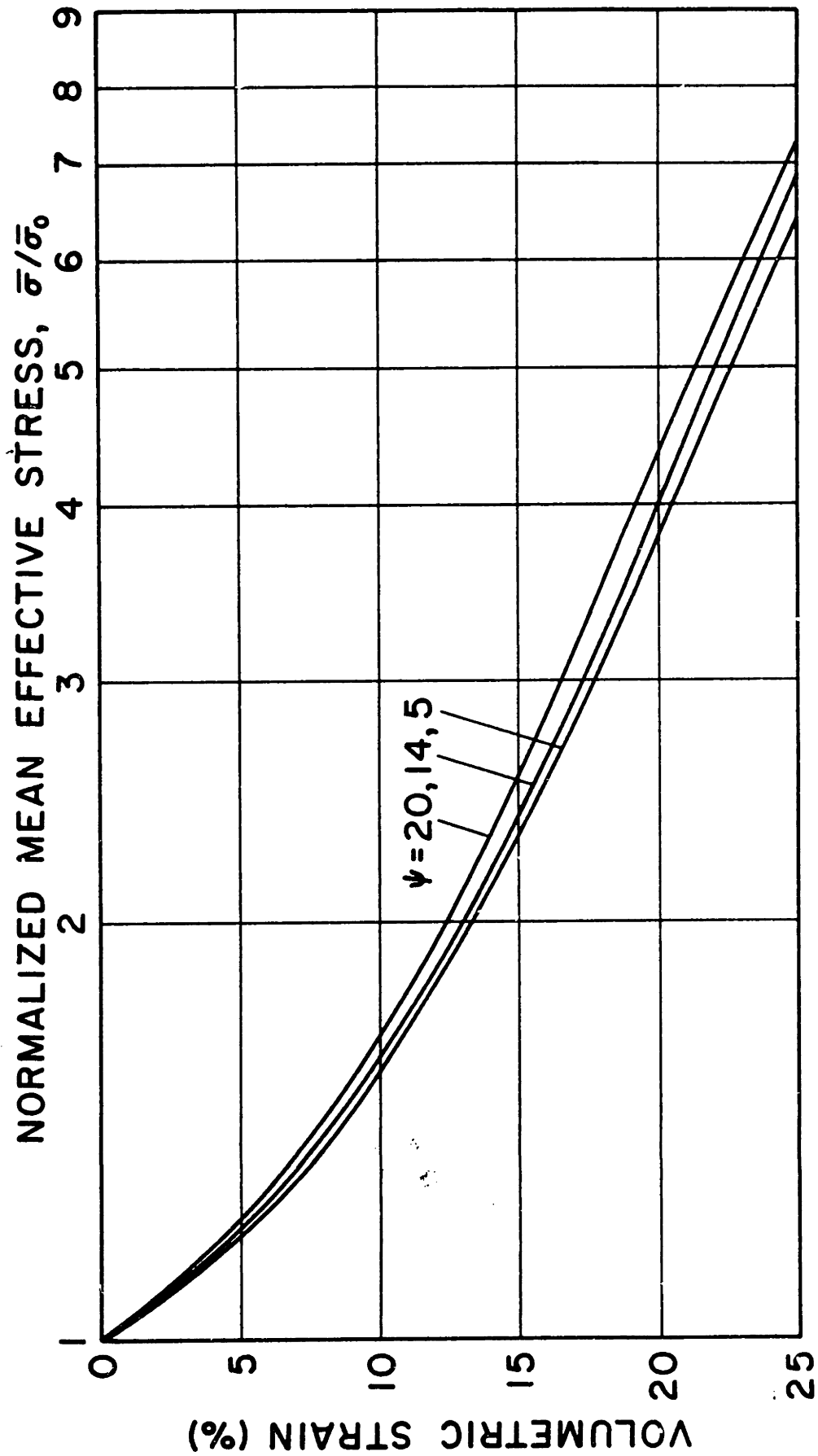


Fig. 5.8: Proposed model prediction of the mean effective stress vs. volumetric strain curves for  $K_0$ -consolidation of an initially  $K_0$ -consolidated sample

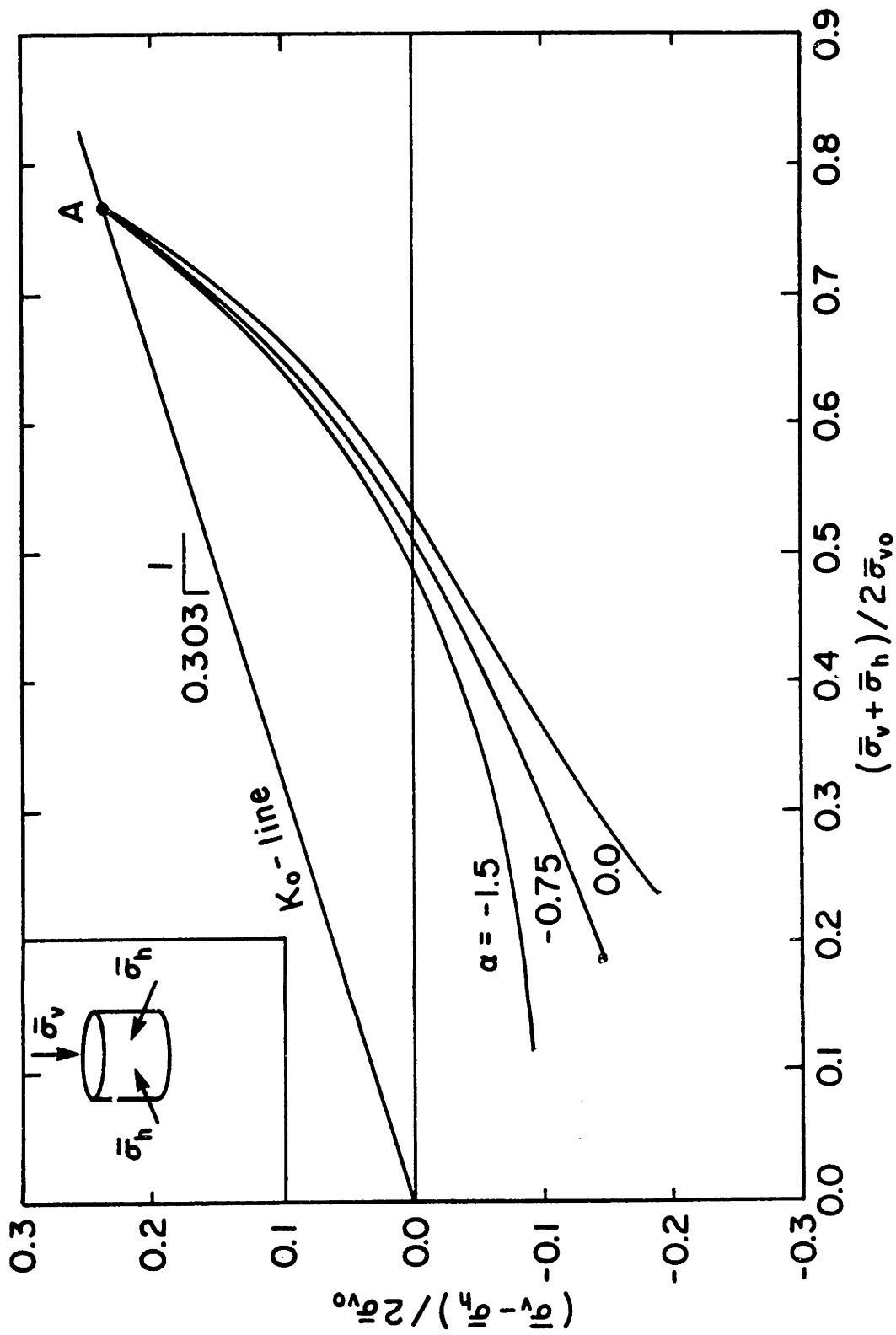


Fig. 5.9: Proposed model prediction of the effective stress paths of  $K_0$ -consolidated undrained triaxial extension tests on normally consolidated Boston Blue Clay

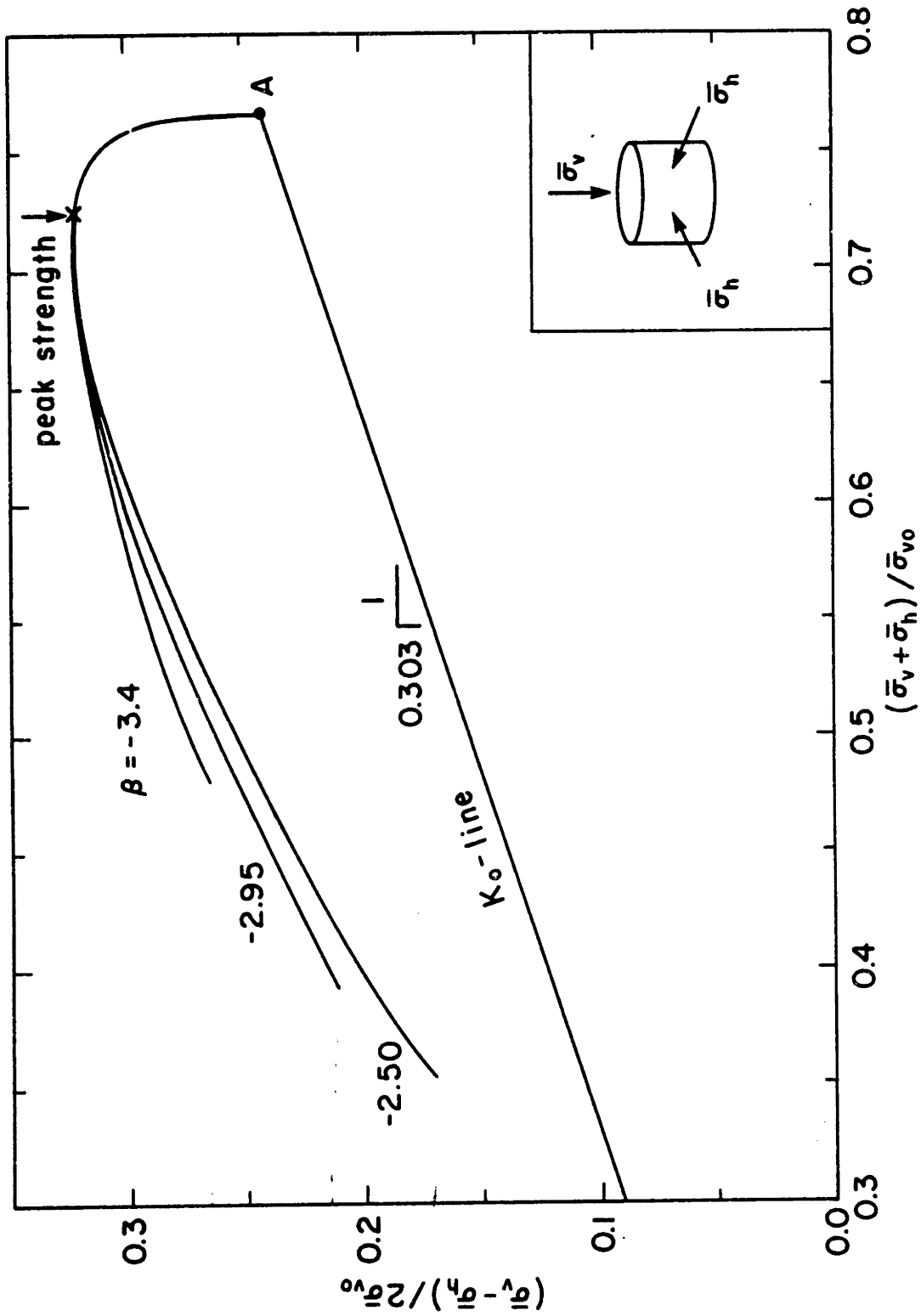
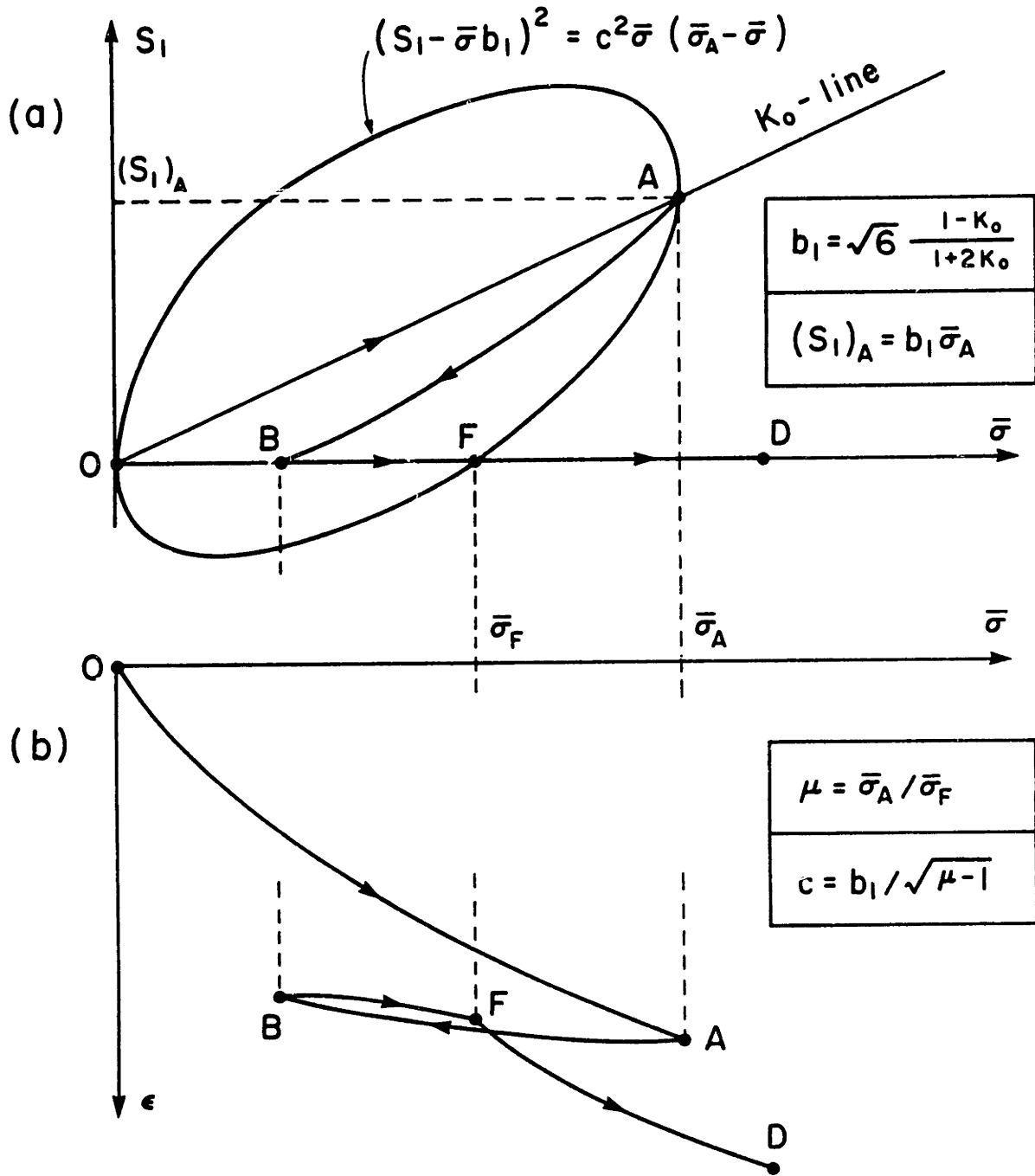


Fig. 5.10: Proposed model prediction of the effective stress paths of  $K_0$ -normally consolidated undrained triaxial compression tests for various values of the parameter  $\beta$



**Fig. 5.11:** Schematic procedure for evaluating the parameter  $c$  of the proposed model

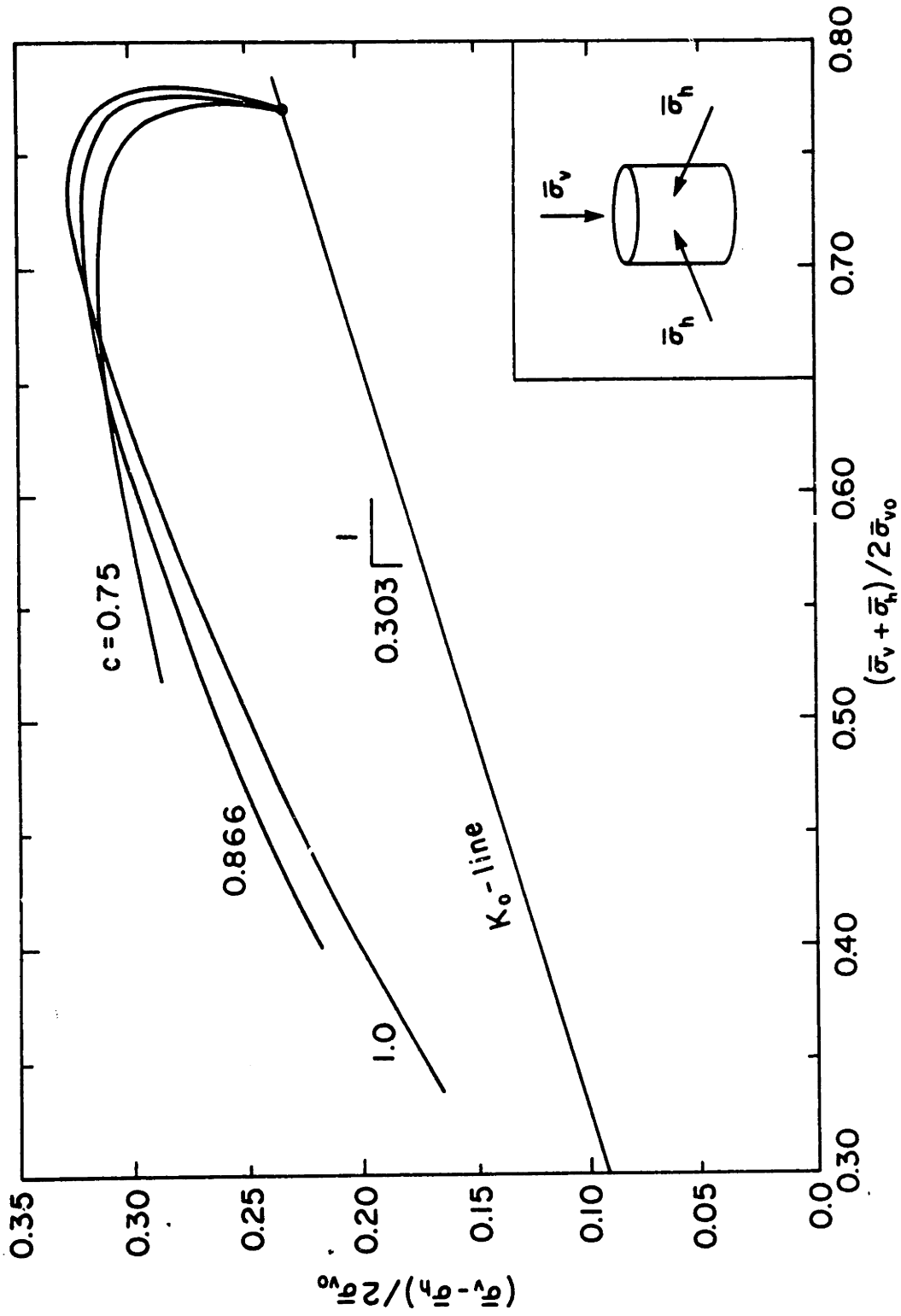


Fig. 5.12: Proposed model prediction of the effective stress paths of  $K_0$ -normally consolidated undrained triaxial compression tests for various values of the parameter  $c$

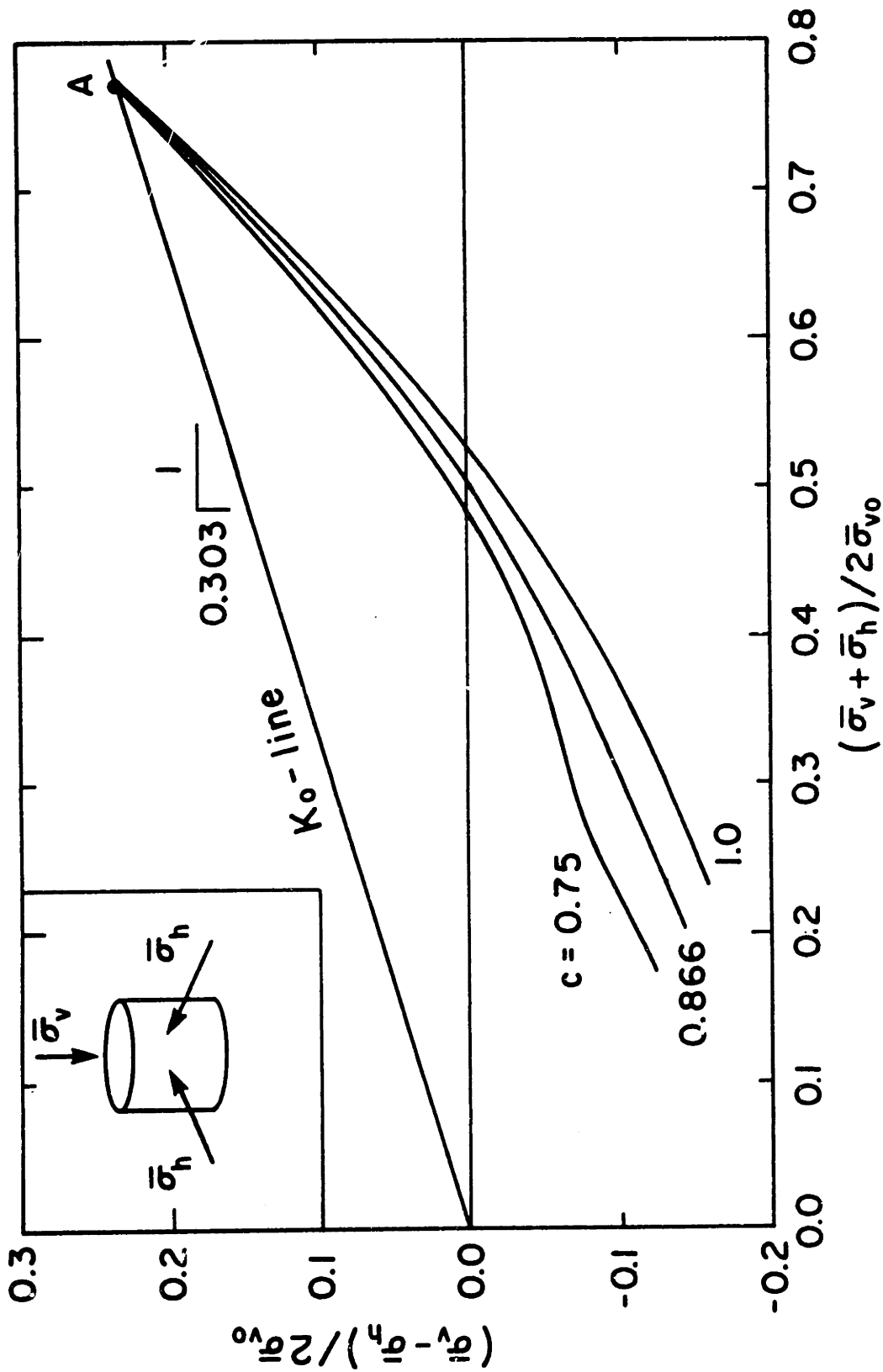


Fig. 5.13: Proposed model prediction of the effective stress paths of  $K_0$ -normally consolidated undrained triaxial extension tests for various values of the model parameter  $c$ .

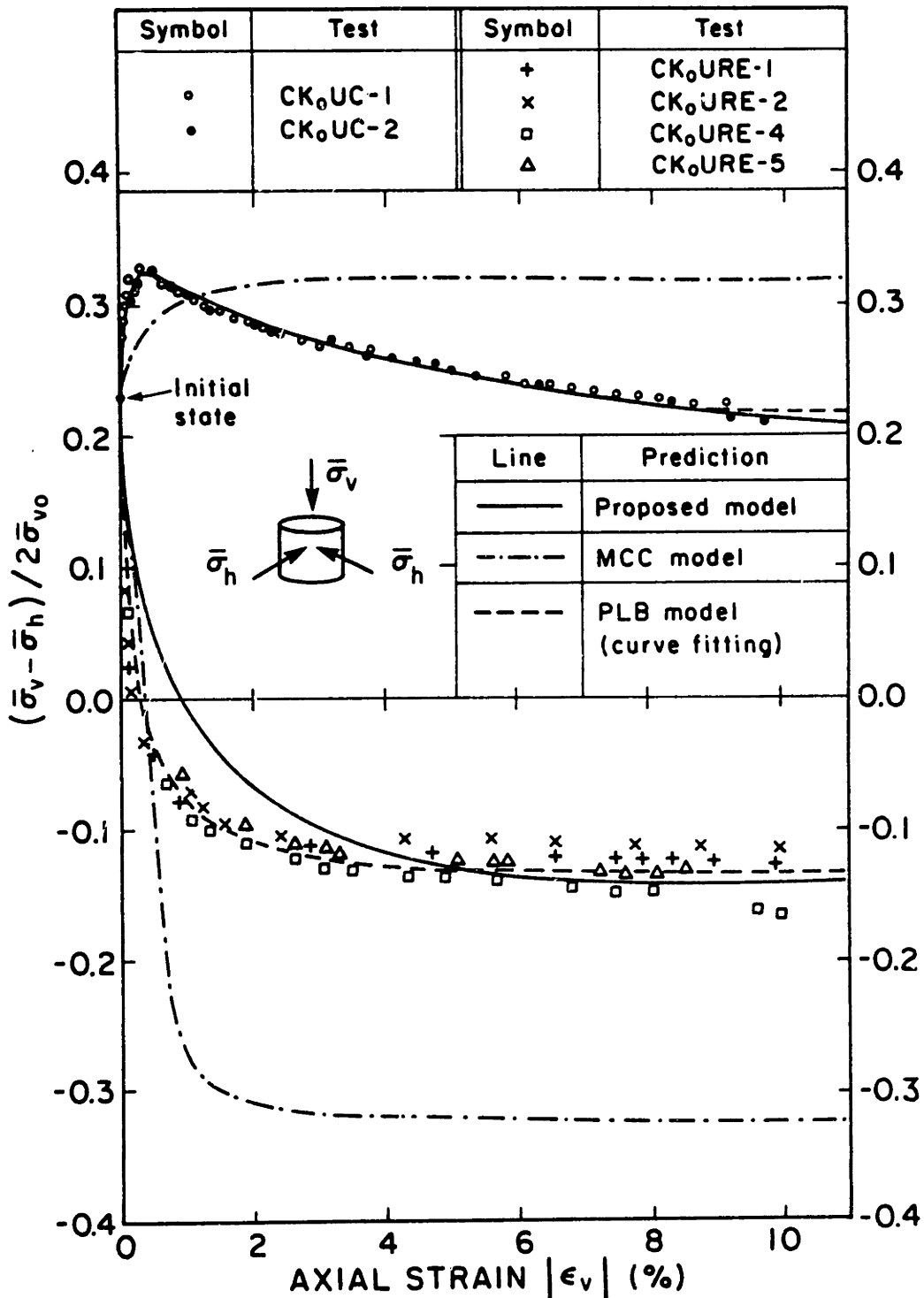


Fig. 5.14: Predicted and measured stress-strain curves for undrained triaxial compression and extension tests on  $K_0$ -normally consolidated resedimented Boston Blue Clay (data from Ladd and Varallyay, 1965)

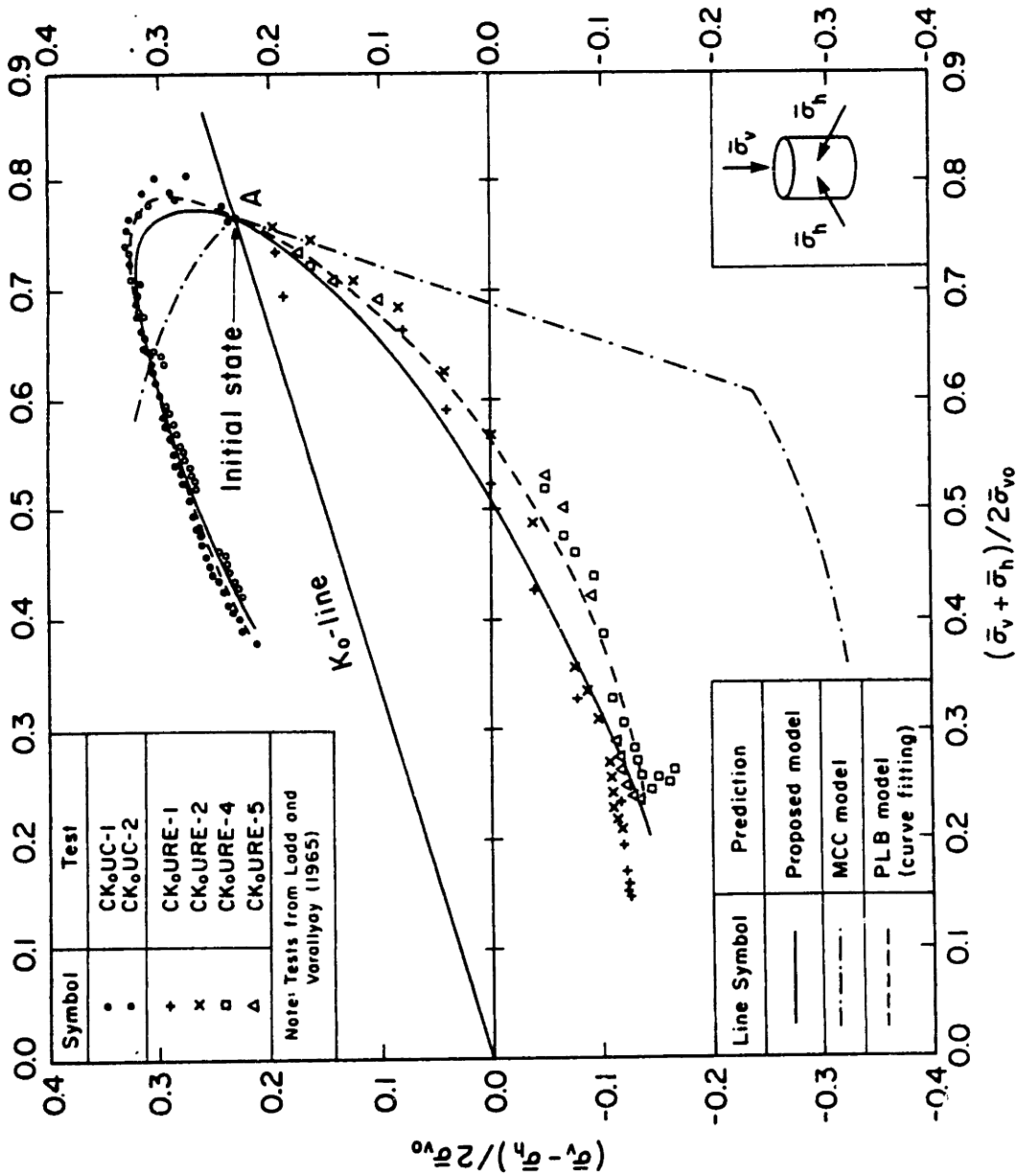
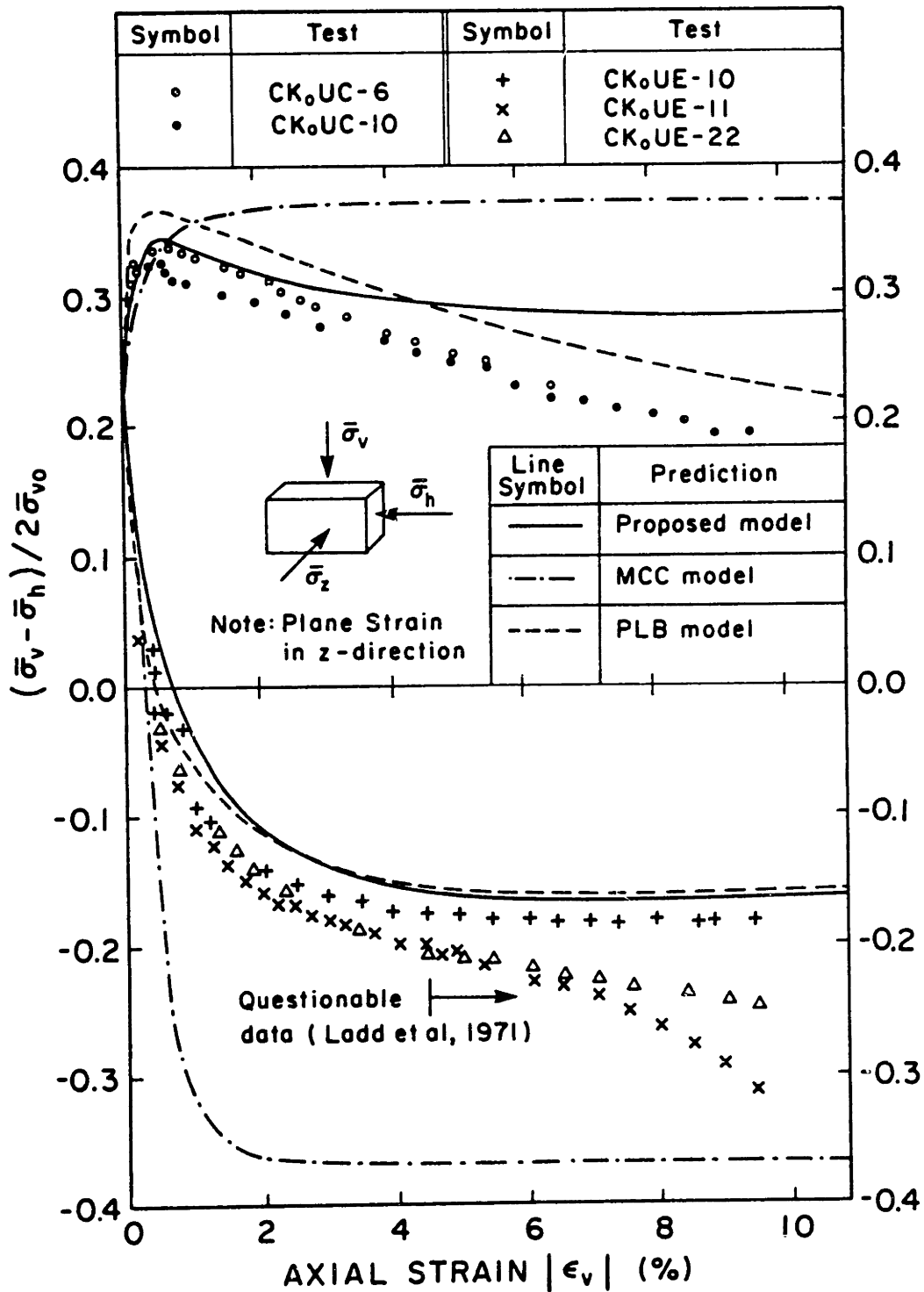
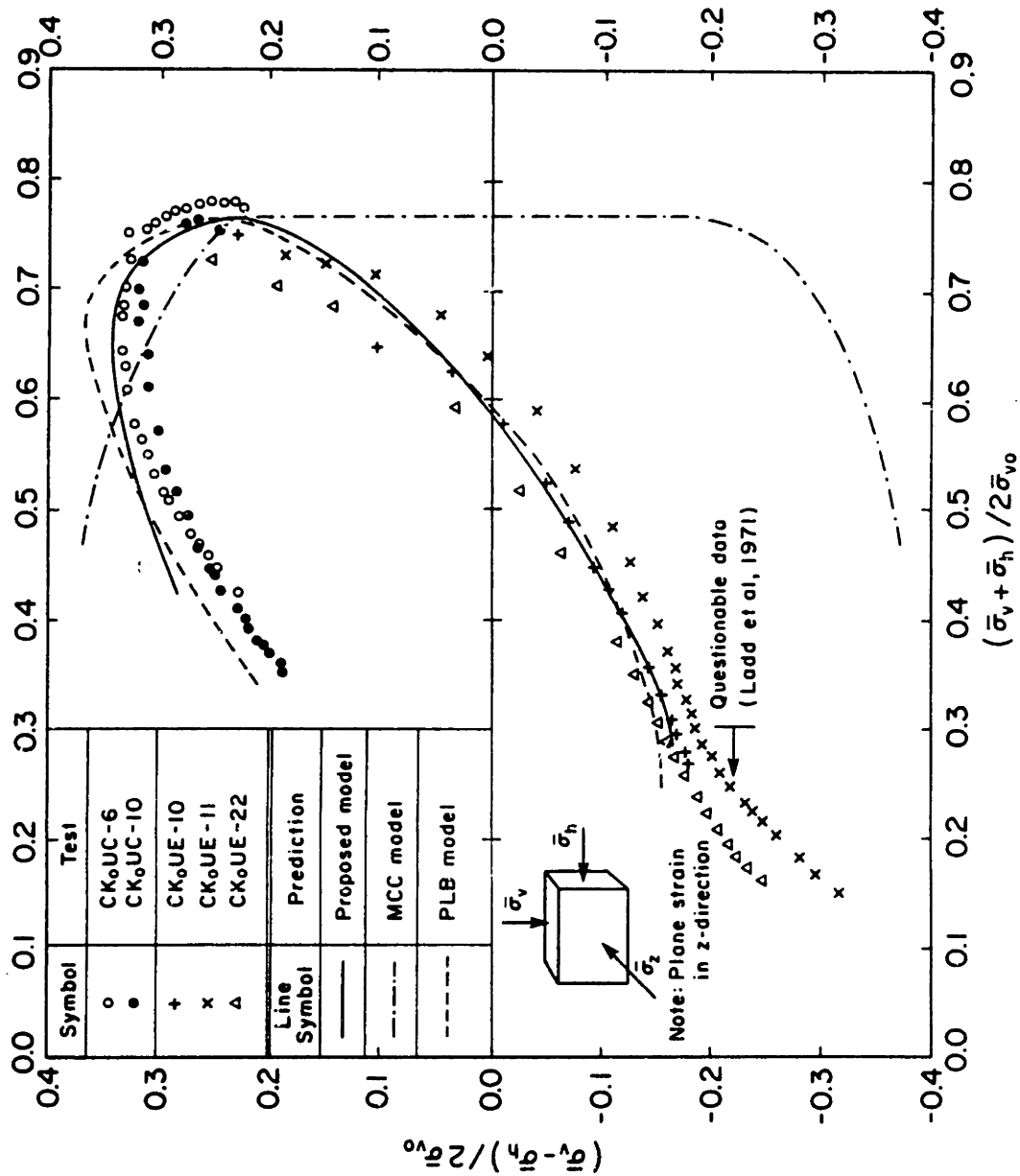


Fig. 5.15: Predicted and measured effective stress paths for undrained triaxial compression and extension tests on  $K_0$ -normally consolidated resedimented Boston Blue Clay.





**Fig. 5.16:** Predicted and measured stress-strain curves for undrained Plane Strain compression and extension tests on  $K_0$ -normally consolidated resedimented Boston Blue Clay (data from Ladd et al, 1971)



**Fig. 5.17:** Predicted and measured effective stress paths for undrained Plane Strain compression and extension tests on  $K_0$ -normally consolidated Boston Blue Clay (data from Ladd et al, 1971)

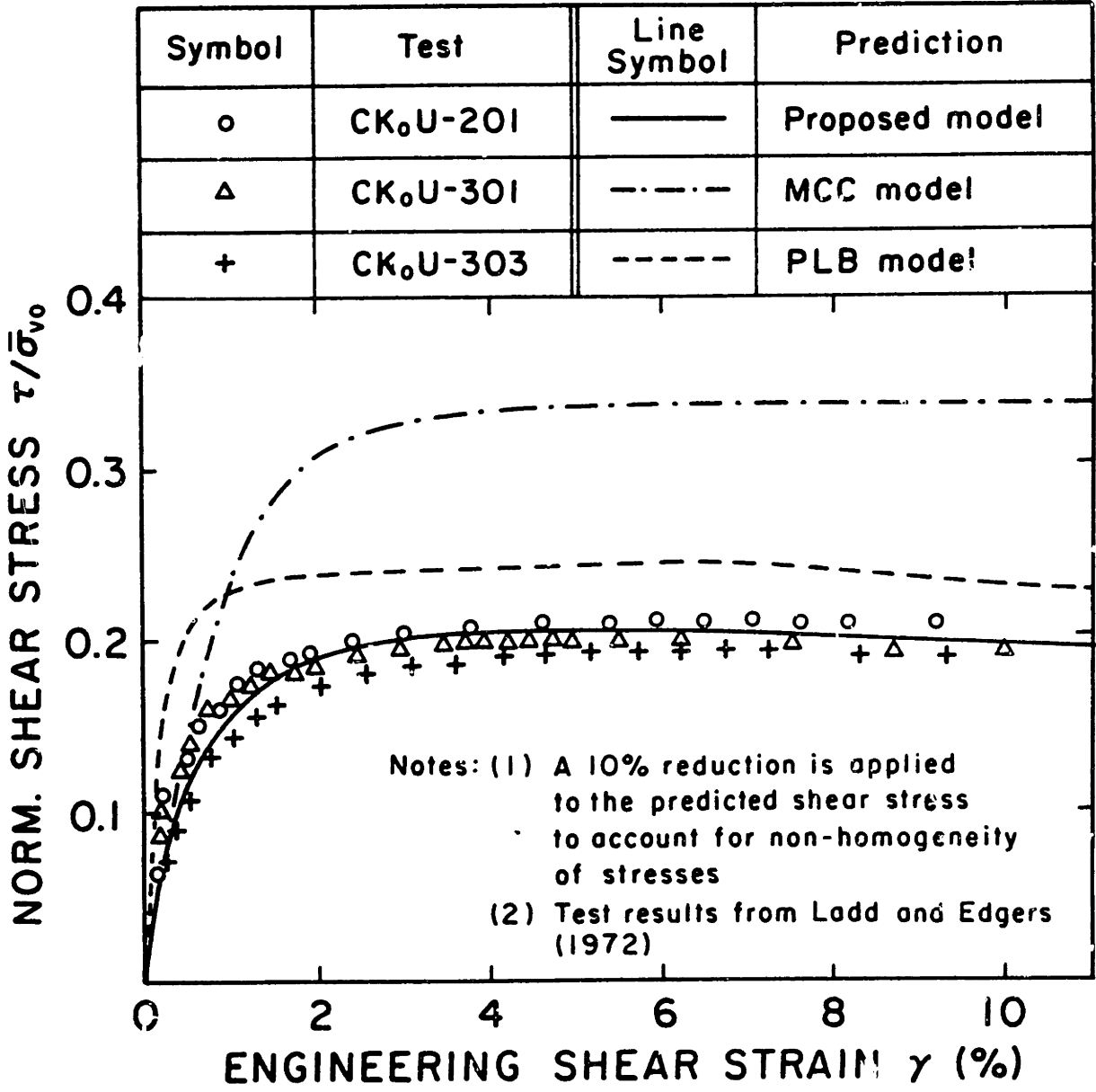


Fig. 5.18: Predicted and measured stress-strain curves for undrained Direct Simple Shear tests on K<sub>0</sub>-normally consolidated resedimented Boston Blue Clay

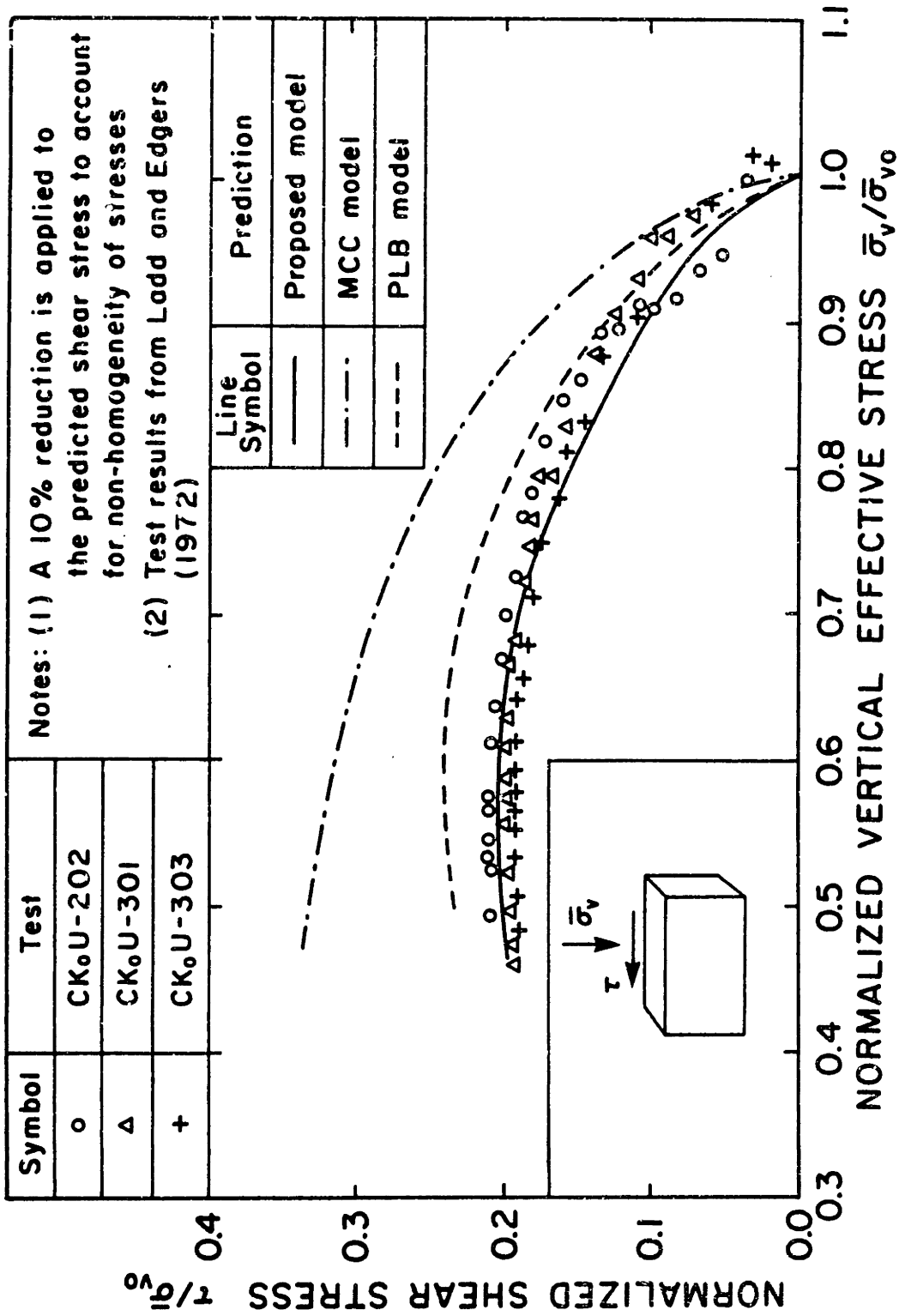
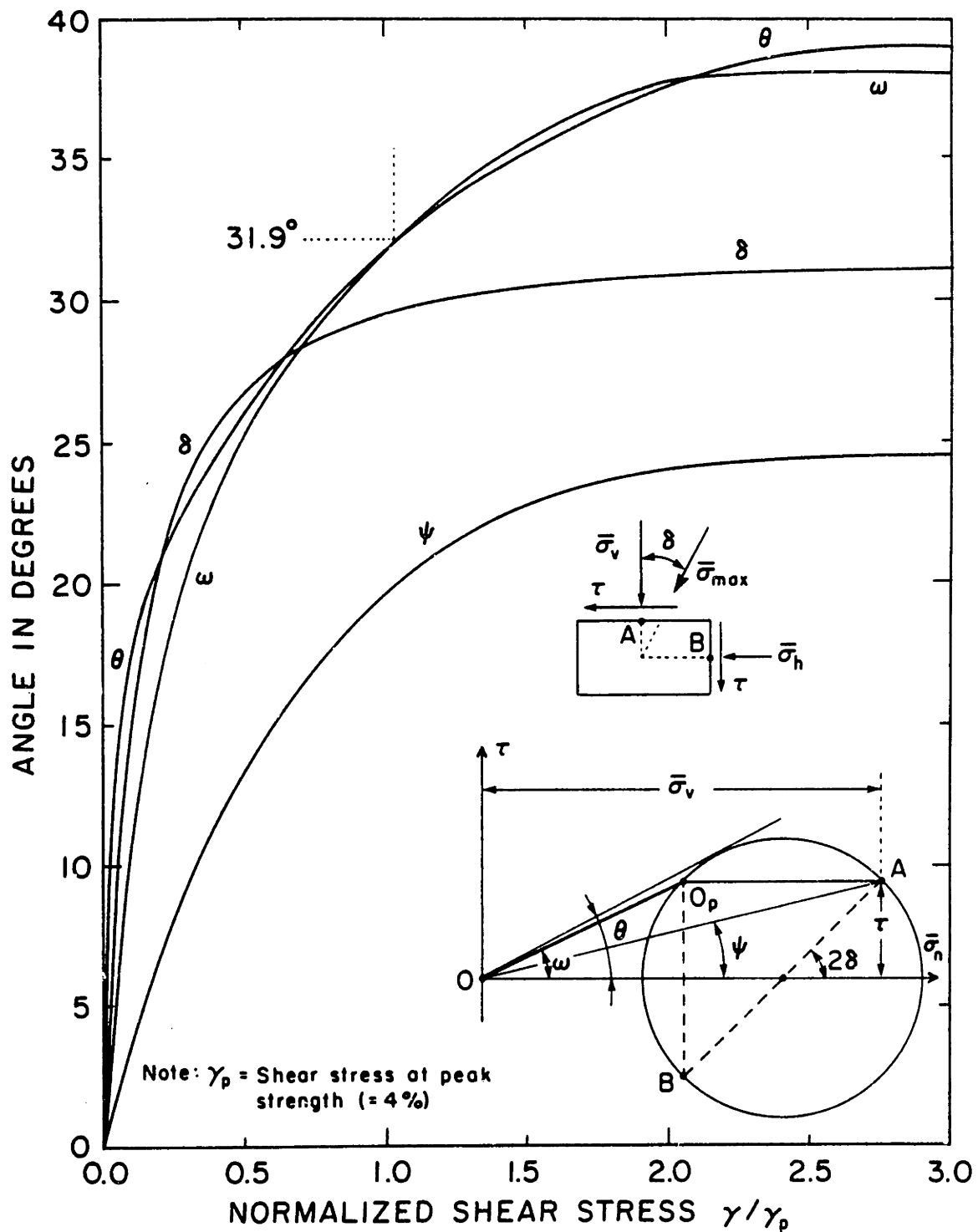


Fig. 5.19: Predicted and measured effective stress paths for undrained Direct Simple Shear tests on K<sub>0</sub>-normally consolidated resedimented Boston Blue Clay



**Fig. 5.20:** Proposed model prediction of the evolution of the Mohr circle of stress during a  $K_0$ -normally consolidated undrained Direct Simple Shear test on resedimented Boston Blue Clay.

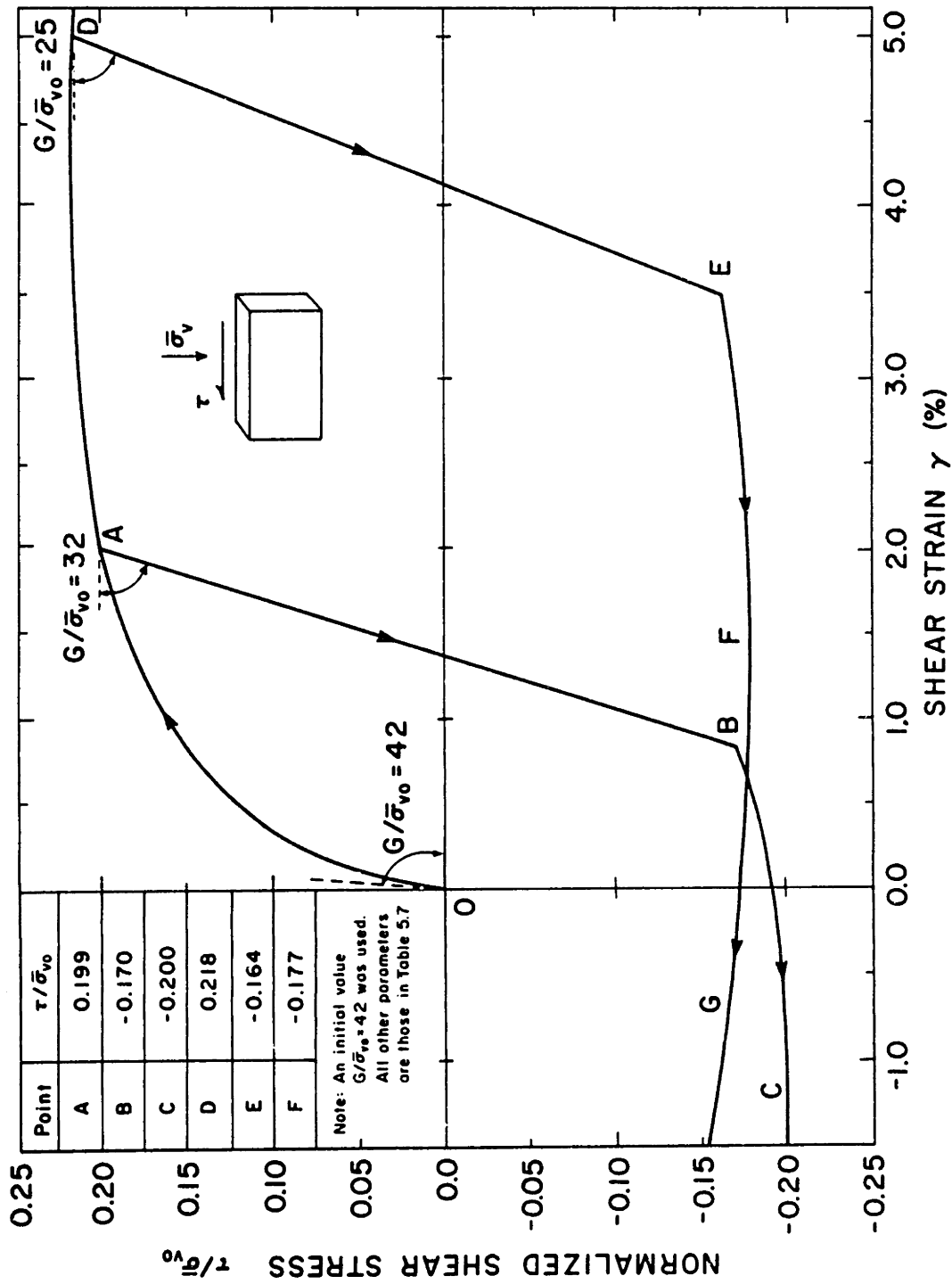
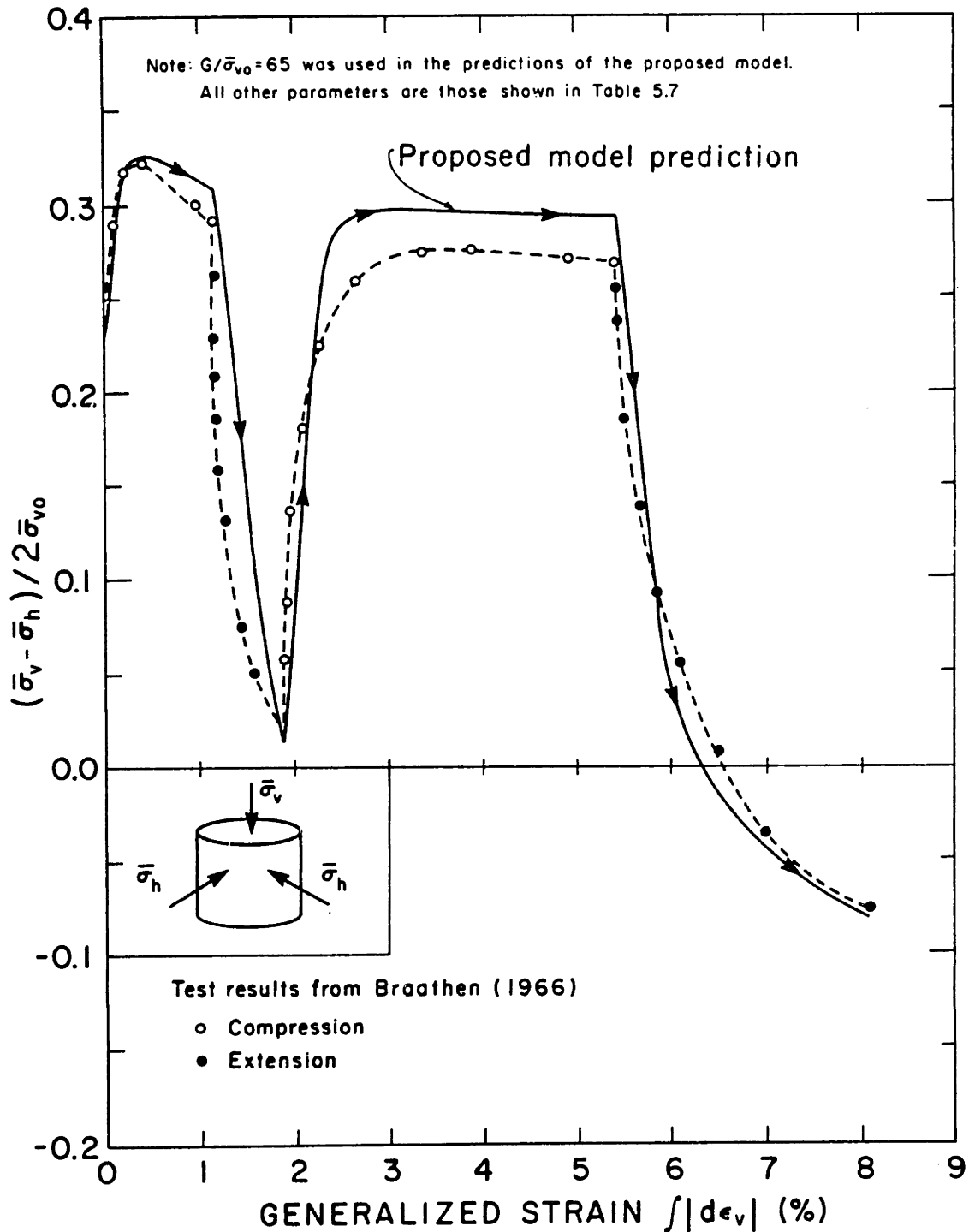
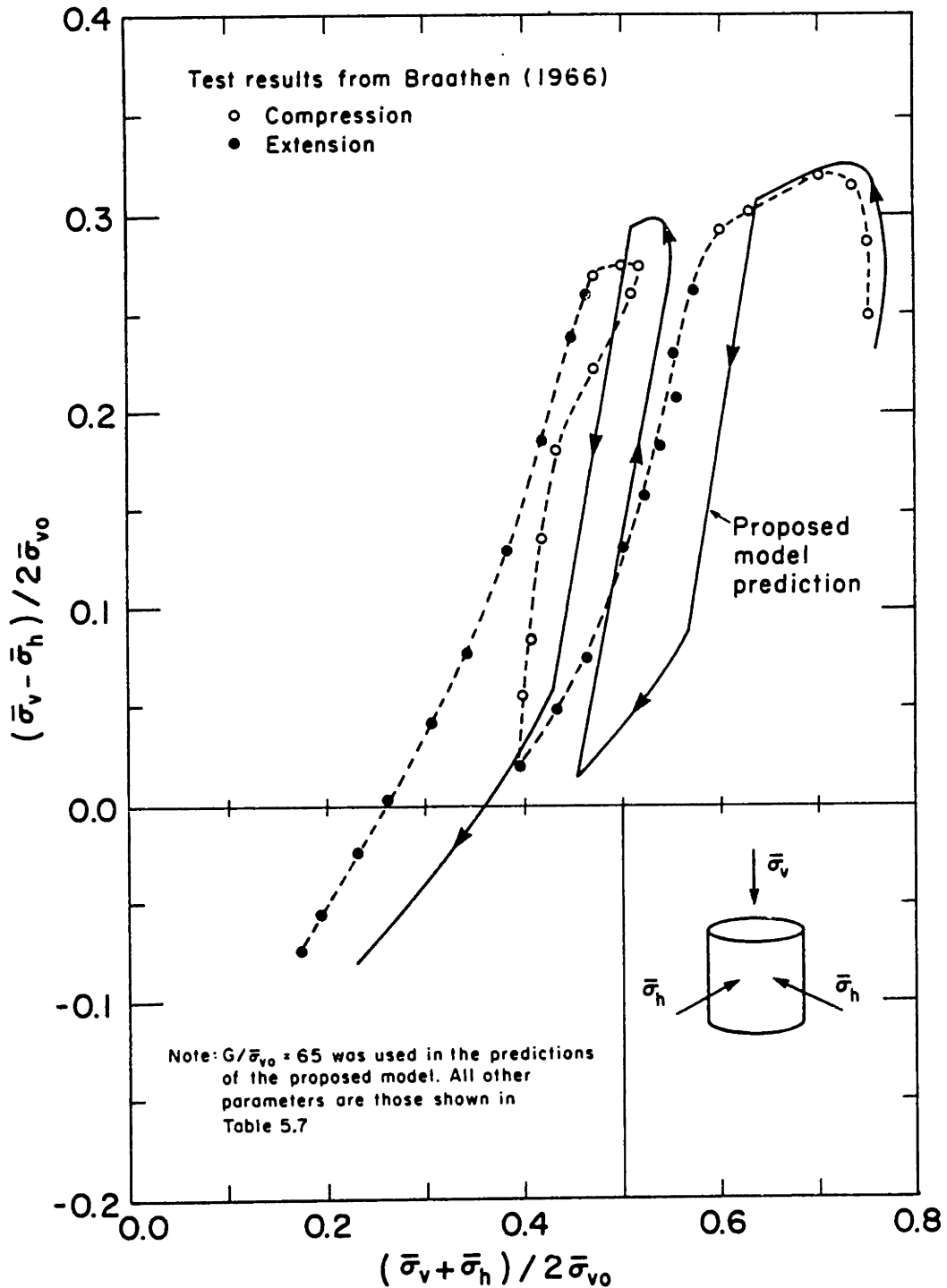


Fig. 5.21: Proposed model prediction of the effect of shear stress reversal during undrained Direct Simple Shear tests on a  $K_0$ -normally consolidated clay with properties similar to Boston Blue Clay



**Fig. 5.22:** Measured and predicted stress-strain curves for an undrained cyclic triaxial test on  $K_0$ -normally consolidated resedimented Boston Blue Clay



**Fig. 5.23:** Measured and predicted effective stress paths for an undrained cyclic triaxial test on  $K_0$ -normally consolidated resedimented Boston Blue Clay



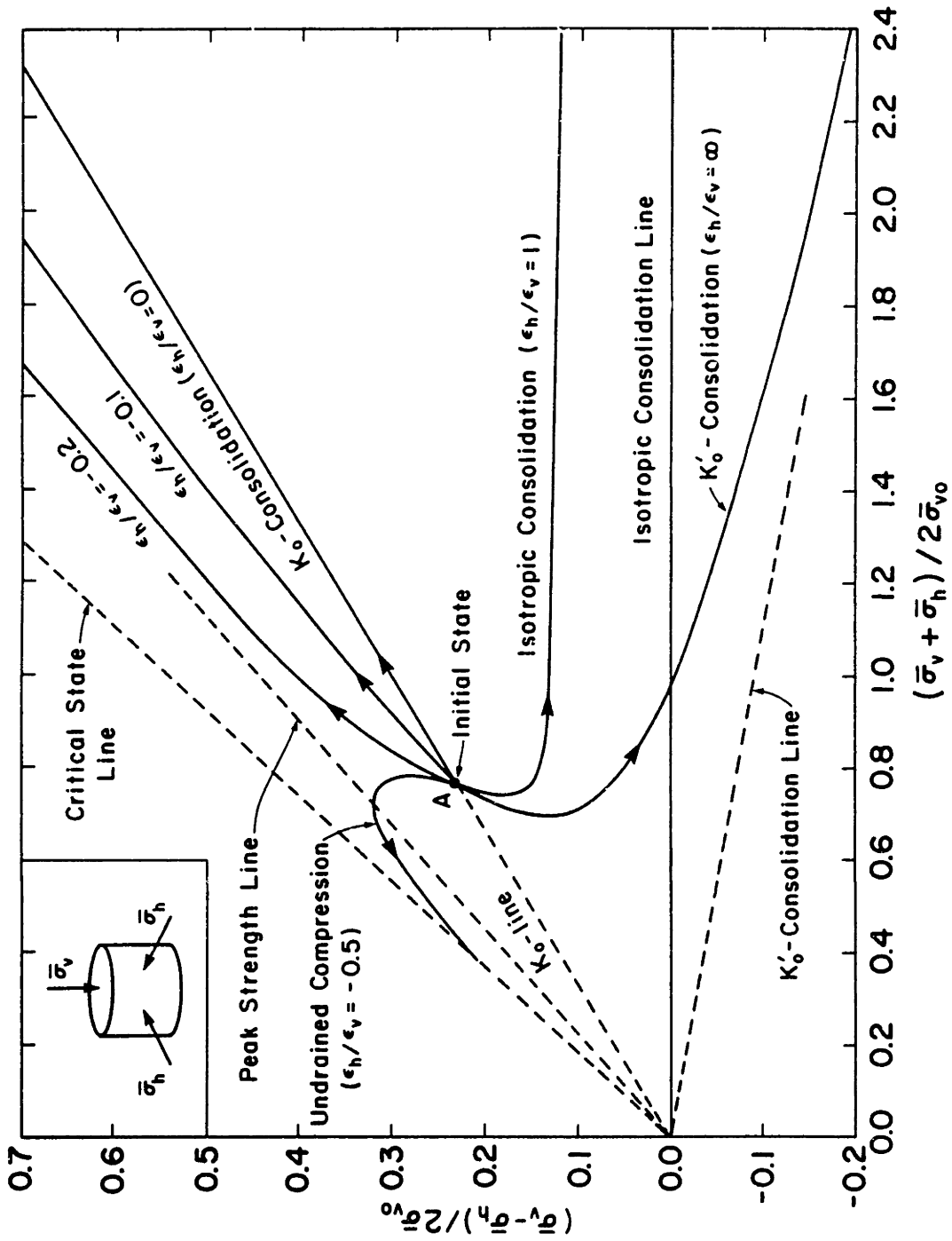


Fig. 5.24: Proposed model predictions of the effective stress paths for various consolidation tests on an initially  $K_0$ -normally consolidated clay with properties similar to Boston Blue Clay

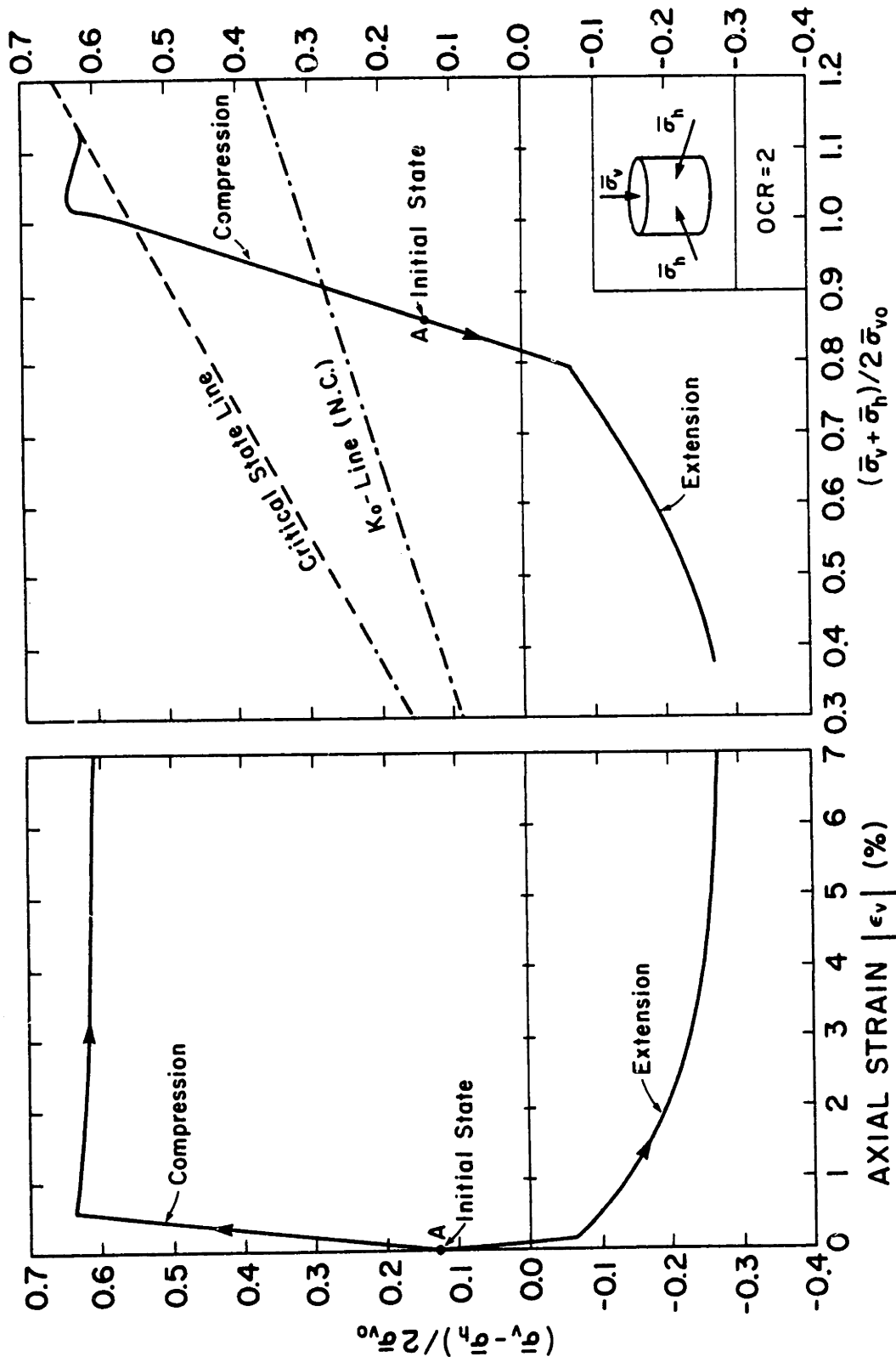


Fig. 5.25: Proposed model predictions of the stress-strain curves and the effective stress paths of  $K_0$ -consolidated undrained triaxial compression and extension tests for overconsolidated resedimented Boston Blue Clay (OCR = 2)

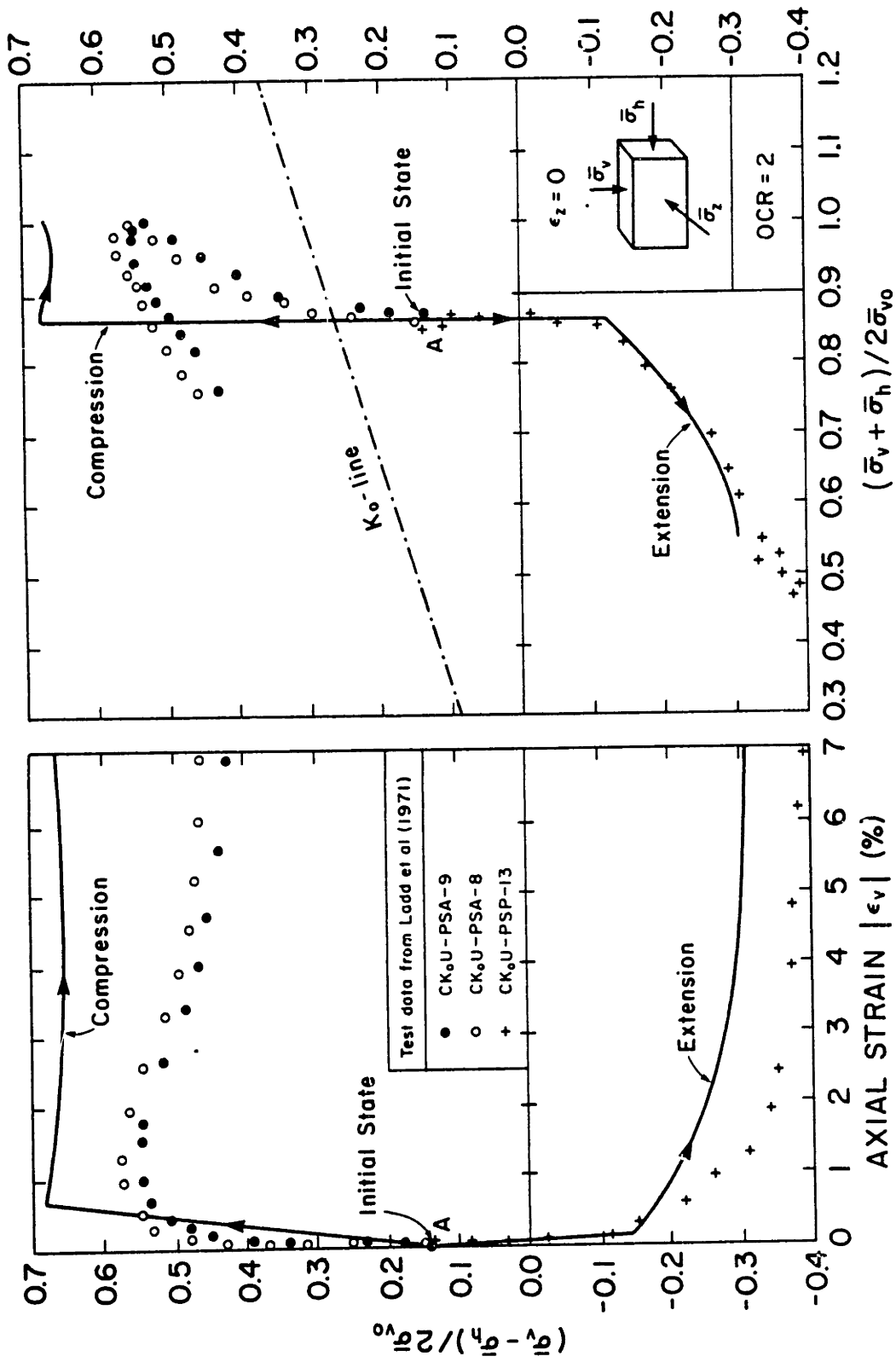


Fig. 5.26: Measured values and proposed model predictions of the stress-strain curves and the effective stress paths of  $K_0$ -consolidated undrained plane strain compression and extension tests for overconsolidated resedimented Boston Blue Clay (OCR = 2)

Note: A 10% reduction is applied to the predicted shear stress to account for non-homogeneity of stresses.  
(Prevost and Hoeg 1976)

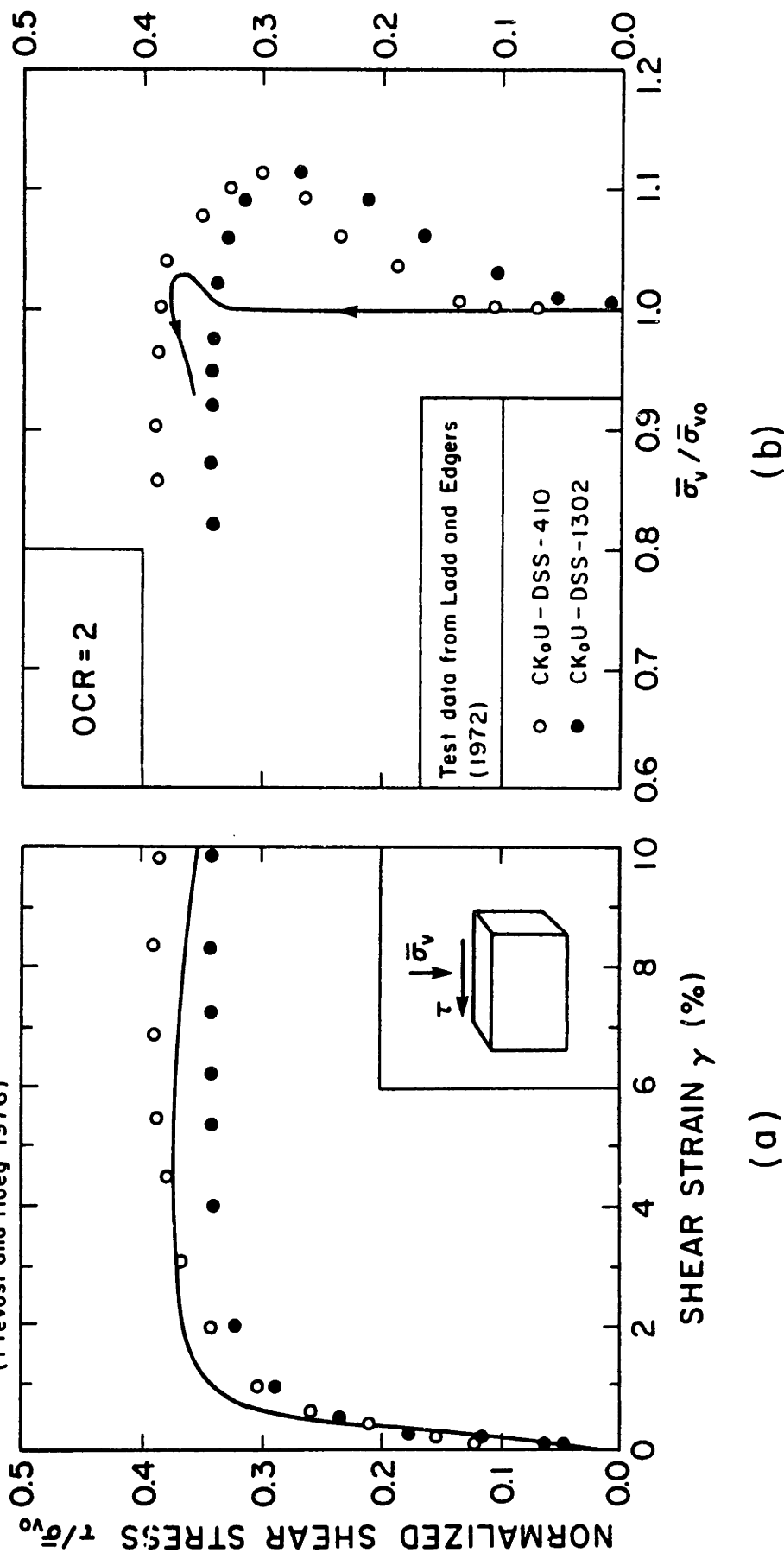


Fig. 5.27: Measured values and proposed model predictions of the stress-strain curves and the effective stress paths of  $K_0$ -consolidated undrained Direct Simple Shear tests for overconsolidated resedimented Boston Blue Clay (OCR = 2)

## CHAPTER 6

### STEADY STATE PILE INSTALLATION

#### 6.1 INTRODUCTION

The primary objective of this Chapter is to estimate the values of the excess pore pressures and the effective stresses in the soil during steady pile installation (driving). These values represent the initial conditions for the consolidation analyses and thus, they are essential in the rational interpretation of the consolidation that takes place after pile installation. More specifically, this Chapter concentrates on the estimation of the excess pore pressures and the effective stresses far behind the pile tip, since the major portion of the bearing capacity of long friction piles (commonly used offshore) is due to the shaft friction rather than the point resistance (see Chapter 2).

Chapter 2 presents the difficulties in obtaining reliable estimates of installation pore pressures and effective stresses, which are due to two major reasons:

- (i) Uncertainties in the mathematical model simulating soil behavior and, in particular, the parameters describing the in situ properties of a given soil.
- (ii) Uncertainties in the method of analysis since the complexity of the mechanism of steady pile installation

requires the use of assumptions in obtaining solutions.  
Section 6.2 discusses these uncertainties.

## 6.2 SOIL MODEL AND METHOD OF ANALYSIS

### 6.2.1 SOIL MODEL

Chapters 3, 4 and 5 discuss the use of mathematical models for the simulation of the stress-strain behavior of clays and, present and evaluate three such models:

- (i) The Modified Cam-Clay (MCC) model developed by Roscoe and Burland (1968) and discussed in Section 3.3.
- (ii) The Prevost-Levadoux-Baligh (PLB) model developed by Prevost (1977) and modified by Levadoux and Baligh (1980).
- (iii) The model proposed in Chapter 4.

Comparisons of model predictions to the measured behavior of  $K_0$ -consolidated resedimented Boston Blue Clay (BBC) in selected laboratory modes of deformation show that (see also Chapter 5):

- (i) The MCC model can be used for general stress paths (i.e., undrained, drained and partially drained), but does not give realistic predictions of the stress-strain relationships and the effective stress paths in most modes of deformation.
- (ii) The PLB model can only be used for undrained stress paths and gives realistic predictions of the stress-strain relationships and the effective stress paths in most modes of deformation.
- (iii) The proposed model can be used for general stress paths (i.e., undrained, drained and partially drained) and

gives realistic predictions of the stress-strain relationships and the effective stress paths in most modes of deformation.

For the sake of comparison, this Chapter uses all three models to predict the excess pore pressures and the effective stresses in the soil, far behind the pile tip, during installation.

### 6.2.2 METHOD OF ANALYSIS

Two methods are used to analyze the steady state pile installation:

- (i) The Undrained Expansion of a Cylindrical Cavity and,
- (ii) The Strain Path method.

The assumptions used in both methods impose kinematic constraints such that the strains in the soil around the pile can be estimated without considering the stress-strain behavior of the soil, i.e., each method predicts the same strains around the pile for any soil. The following subsections summarize these methods:

#### 6.2.2.1. Undrained Cylindrical Cavity Expansion

Pile installation is modelled as the undrained expansion of a long cylindrical cavity (e.g. Soderberg, 1962; Butterfield and Banerjee, 1970; Randolph et al, 1978). The radial displacement\*  $u$  is the only non-vanishing component of the soil deformation vector. Thus, the infinitesimal increment of

---

\* positive when directed towards the cavity, according to the Soil Mechanics sign convention.



the circumferential strain at any time during cavity expansion is given by:

$$\dot{\epsilon}_{\theta} = \dot{u} / R \quad (6.1)$$

where, R is the current radial coordinate and  $\dot{u}$  is the infinitesimal increment of u. Integration of  $\dot{\epsilon}_{\theta}$  between the initial (undeformed) and the final (after cavity expansion) states, gives the circumferential strain\*

$$\epsilon_{\theta} = \ln ( R_0 / r ) \quad (6.2)$$

of a soil element with radial coordinates  $R_0$  and r before and after cavity expansion, respectively. For soft\*\* soils undrained deformation is incompressible and, in this case  $R_0$  and r are related by:

$$R_0^2 = r^2 - r_0^2 \quad (6.3)$$

where,  $r_0$  is the radius of the cavity (pile) after expansion. Combining Eqs. 6.2 and 6.3 we get:

$$\epsilon_{\theta} = - \epsilon_r = \frac{1}{2} \ln \{ 1 - (r/r_0)^{-2} \} \quad (6.4a)$$

\* since  $\dot{u} = -\dot{R}$

\*\* i.e., when the compressibility of the soil skeleton is much larger than the compressibilities of the constituents (pore fluid and solid grains).

$$\epsilon_z = \gamma_{rz} = \gamma_{r\theta} = \gamma_{\theta z} = 0 \quad (6.4b)$$

or, using the transformed strain measures introduced in Table 4.1:\*

$$\epsilon = E_1 = E_3 = E_4 = E_5 = 0 \quad (6.5a)$$

$$E_2 = \frac{1}{\sqrt{2}} \ln \{ 1 - (r/r_0)^{-2} \} \quad (6.5b)$$

Thus, the strain in the soil around the pile after cavity expansion is estimated solely by considering the kinematics of the deformation, i.e., without assuming any stress-strain model for the soil. A soil model must, however, be used in order to compute the effective stresses corresponding to the estimated strains.

Randolph et al (1978) used a Finite Element computer program and various soil models to estimate the effective stresses during the undrained expansion of a cylindrical cavity. In order to avoid the strain singularity during the initial creation of the cavity, they used the expansion of a pre-existing cavity from  $a=a_0$  to  $a=2a_0$  to model the creation of a cavity of final radius  $r = \sqrt{3}a_0$ . However, as they admit, their method gives no knowledge of the stress components for

---

\* using a one-to-one correspondance between the cartesian axes (x,y,z) and the cylindrical axes (r,z,θ).

the soil contained in the annular region bounded on the inside by the pile wall ( $r=r_0$ ) and on the outside by the cylindrical surface  $r=2r_0/\sqrt{3}$  and thus, requires extrapolation in the region where estimates of the effective stresses are most useful (i.e., close to the pile wall).

The effective stresses around the pile can also be obtained without the use of sophisticated Finite Element programs if it is realized that, during undrained cavity expansion, all soil elements follow the same (radial) strain path,\* but each corresponds to a different point along this path depending on its distance  $r/r_0$  from the center-line of the cavity. Thus, all soil elements trace the same stress-strain curve (corresponding to the undrained cylindrical cavity expansion mode of deformation) and, their effective stress components can be directly computed from the level of strain associated with each soil element (via Eqs. 6.4 or 6.5). Figure 6.1a shows the shear stress vs radial strain curve for the undrained cylindrical cavity expansion mode of deformation as predicted by the MCC, the PLB and the proposed models for an initially  $K_0$ -normally consolidated soil with properties\*\* similar to resedimented Boston Blue Clay (BBC). The MCC and the PLB models predict values of the peak undrained shear strength which are, respectively, 70% and 20% higher than that predicted by the proposed model. Kirby and Esrig (1979) report tests on

---

\* given by Eqs. 6.4 or 6.5

\*\* the values of the model parameters used are shown in Table 5.7.

normally consolidated resedimented BBC and the measured value of the normalized undrained shear strength is equal to  $s_u / \bar{\sigma}_{vo} = 0.21$ . Wood (1981) performed True Triaxial Tests\* on resedimented BBC and followed the strain path corresponding to the undrained cylindrical cavity expansion mode of deformation, but does not report values of the undrained shear strength. Figure 6.1b shows the predicted variation of the vertical effective stress with the radial strain. Although all models predict approximately the same value of  $\bar{\sigma}_z$  at large strains, the predicted response at smaller strains is somewhat different. Finally, Fig. 6.1c presents the predicted effective stress paths. The MCC curve rises almost vertically until the Critical State is reached, indicating that the model predicts small shear induced pore pressures  $\Delta p_s$ \*\* during the undrained cavity expansion mode of deformation.

The excess pore pressures caused by pile installation can be obtained by integrating the stress equilibrium equation in the radial direction

$$\frac{dp}{dr} = \frac{\bar{\sigma}_\theta - \bar{\sigma}_r}{r} - \frac{d\bar{\sigma}_r}{dr} \quad (6.6)$$

using the effective stresses computed above.

---

\* using the apparatus described by Wood (1974)

\*\* since  $\Delta p_s = - \Delta \bar{\sigma}$  ,  $\Delta \bar{\sigma}_z = ( \Delta \bar{\sigma}_r + \Delta \bar{\sigma}_\theta ) / 2$   
and then:

$$\Delta p_s = - \Delta ( \bar{\sigma}_r + \bar{\sigma}_\theta ) / 2$$

#### 6.2.2.2. Strain Path Method

Section 2.2.3.2 (see also Fig. 2.19) presents a version of the Strain Path Method (Baligh et al, 1978) which can be used in conjunction with a total stress soil model. Figure 6.2 shows the required steps when the Strain Path method is used in conjunction with an effective stress model (such as the MCC or the proposed models). They are:

- (1) Estimation of a velocity field (consisting of the soil velocities relative to the pile) which satisfies the conservation of volume (i.e., incompressibility) requirements and the boundary conditions.
- (2) Differentiation of the velocities with respect to the spatial coordinates to obtain the strain rates along the stream-lines.
- (3) Integration of the strain rates with respect to time to obtain the strain paths along the stream-lines.
- (4) Estimation of the initial stresses and pore pressures in the soil prior to pile installation.
- (5) Estimation of the effective stress paths for the soil elements along the stream-lines using an effective stress model in conjunction with the strain paths obtained under item (3) above.
- (6) Estimation of the excess pore pressures using the equilibrium equations in conjunction with the effective stresses obtained under item (5) above.
- (7) The total stresses along the stream-lines are finally

obtained from the effective stresses and the excess pore pressures obtained under items (5) and (6) above.

In the application of the method to the problem of deep steady pile installation, soil velocities are estimated by assuming that the soil has no shearing resistance (i.e., it behaves as an ideal fluid) following the procedure discussed in detail by Levadoux and Baligh (1980). The effective stress paths are then estimated using the MCC, the PLB and the proposed models. Finally, the excess pore pressures caused by pile installation far behind the pile tip are estimated by integrating the equilibrium equation in the radial direction (Eq. 6.6).\*

The application of the Strain Path method to the problem of deep steady pile installation is only approximate because the soil velocities around the pile are commonly estimated using a stress-strain relationship which is different\*\* than that used in item (5) to estimate the associated effective stress paths.

The discussion of the application of the Strain Path method in the problem of deep steady pile installation shows that the Undrained Cylindrical Cavity Expansion method is a particular case of the Strain Path method since it follows the steps

---

\* Levadoux and Baligh (1980) discuss the issue of selecting the direction of the integration path and conclude that the radial direction may give more accurate predictions of the excess pore pressures, especially in the region far behind the tip of the pile

\*\* and usually simpler, in order to get closed form solutions that can be accurately differentiated as required in item (2) of the method.

presented above.

### 6.3 STRAINS IN THE SOIL DURING PILE INSTALLATION

Figure 6.3 shows the radial and circumferential strains far behind the tip of a long cylindrical pile as a function of the normalized radius  $r/r_0$ , estimated according to the Cavity Expansion (full line) and the Strain Path\* (dashed line) methods. The Cavity Expansion method predicts that the radial and circumferential strains are equal and opposite at all locations because the axial strain vanishes and deformation is incompressible. The predictions of the Strain Path and the Cavity Expansion methods are very similar, indicating that the effect of the (non-zero) axial strain is small. Figure 6.4 shows the axial and shear strains far behind the tip of a long cylindrical pile, as a function of the normalized radial coordinate  $r/r_0$ , estimated according to the Strain Path method.\*\* The magnitudes of these strains are much smaller than the predicted magnitudes of the radial and the circumferential strains,\*\*\* indicating that soil deformation far behind the tip of a pile is basically controlled by the cavity expansion mode of deformation.

Figures 6.3 and 6.4 show that the strain states far behind the pile tip predicted by the Cavity Expansion and the Strain Path methods are almost identical. However, these strain

---

\* using a  $60^\circ$  tip angle and the method discussed in detail by Levadoux and Baligh (1980).

\*\* evidently, both strains vanish according to the Cavity Expansion method.

\*\*\* typically one order of magnitude less at each location



states represent the final strain states after pile installation (obtained by integrating the strain increments along the stream-line followed by each soil element), and thus do not contain information for the strain paths followed by the individual soil elements until the final strain states are reached. The strain paths predicted by the Cavity Expansion and the Strain Path methods are very different: the Cavity Expansion method predicts (see Section 6.2.2.1) monotonic radial strain paths between the initial (undeformed) state and the final strain state (after pile installation) for all soil elements, whereas Levadoux and Baligh (1980) show that the Strain Path method predicts large strain reversals and complicated strain paths\* (also see Fig. 2.21), due to the effect of the pile tip which is neglected by the Cavity Expansion method. Furthermore, it is a well established fact that the effective stresses\*\* around the pile are controlled by the strain paths followed during pile installation rather than the final strain states. Thus, the effective stresses predicted by the Cavity Expansion and the Strain Path methods are expected to be different and, since estimates of the effective stresses are of main interest in studying the pile problem, the two methods of analysis are by no means equivalent. As will be illustrated shortly, the Strain Path method gives more realistic predictions of the effective

---

\* especially for soil elements located close to the pile wall ( $r/r_0 < 3-4$ )

\*\* and thus, also the excess pore pressures

stresses around the pile because it takes into consideration the effect of the pile tip (it is a two-dimensional model), whereas the Cavity Expansion method has the advantage of computational simplicity (it is a one-dimensional model). For the sake of comparison, in the following we will use both methods to predict the excess pore pressures and the effective stresses in the soil far behind the pile tip during installation.

## 6.4 PREDICTED STRESS AND PORE PRESSURE CHANGES IN THE SOIL DURING PILE INSTALLATION

Figures 6.5 through 6.9 present the predicted stress and pore pressure changes in a soil with properties similar to  $K_0$ -normally consolidated resedimented Boston Blue Clay, immediately after pile installation, far behind the tip of a cylindrical pile. The predictions are determined using the Cavity Expansion and the Strain Path methods in conjunction with the MCC, PLB and the proposed soil models.

The Cavity Expansion method predictions are obtained by means of the method described in Section 6.2.2.1. Integration of the equilibrium equation in the radial direction begins at a radius equal to 200 times the radius of the cavity where the initial ( $K_0$ ) stresses and the ambient (hydrostatic) pore pressures are imposed. Forty five intervals (i.e., 46 nodal points) are used with interval length gradually decreasing towards the cavity to provide better resolution in the zone of high strain gradients near the cavity wall. The locations of the nodal points are shown in Table 6.1.

The Strain Path method predictions are determined by means of the method described in Section 6.2.2.2 using a cylindrical pile with a  $60^\circ$  tip.\* Analyses are performed using 46 stream-lines to cover the soil mass between the pile wall and

---

\* Levadoux and Baligh (1980) show that the Strain Path method predictions far behind the pile tip are almost insensitive to variations of the magnitude of the tip angle.

150 times the pile radius in the radial direction. The stream-lines start at 200 times the pile radius in front of the pile tip and end at 15 times the pile radius behind the pile tip in the axial direction. The radial coordinates of the last point (i.e., far behind the pile tip) on each stream-line are shown in Table 6.1. The excess pore pressures are computed using the same numerical integration scheme used in the Cavity Expansion method.

Figures 6.5 through 6.9 indicate that:

- (1) All models and methods of analysis predict that the disturbance caused by pile installation is negligible at radial distances larger than 60 times the pile radius (i.e., for radial strains less than 0.015%) which means that, at large radial distances the stresses approach the initial  $K_0$  stress conditions.
- (2) The Strain Path and the Cavity Expansion methods predict\* comparable stress and pore pressure changes in the soil for radial distances larger than 10-20 times the pile radius. This means that the disturbance caused by the pile tip\*\* does not extend to radial distances larger than 10-20 times the pile radius.
- (3) For the same method of analysis, there are small differences in the predicted distributions of the stresses and excess pore pressures, which are due to the different stiffness, undrained shear strength and rate of strain

---

\* for the same soil model

\*\* neglected by the Cavity Expansion method

softening of each model (see e.g. Fig. 6.1).

- (4) For the same soil model, major differences exist between the predictions of the radial effective stress according to the Cavity Expansion and the Strain Path methods in the zone close to the pile (i.e., for  $r/r_o < 10$ ), indicating that the effect of the pile tip, which is neglected by the Cavity Expansion method, is very significant (see Fig. 6.5). According to the Strain Path method, soil elements located close to the pile are subjected to significant strain reversals which cause unloading in shear, and reduced effective stresses (e.g., at the pile wall, the various soil models predict a radial effective stress between 0.0 and 0.12 times the initial vertical effective stress). On the contrary, according to the Cavity Expansion method all soil elements follow identical, radial, monotonic\* strain paths and thus, the predicted value of the radial effective stress in the region close to the pile (for  $r/r_o < 4-6$ ) is constant (i.e., the Critical State is reached). More specifically, the PLB and the proposed models predict almost identical values of the normalized radial effective stress (equal to 0.50 and 0.48 times the initial vertical effective stress, respectively), whereas the MCC model prediction is significantly higher because this model predicts a higher value of the undrained shear strength at the Critical State (see Fig. 6.1a). Similar remarks are applicable in Fig. 6.6 which represents

---

\* i.e., involving no unloading

the predictions of the maximum shear stress in the  $r-\theta$  plane.

- (5) The Cavity Expansion method predicts a continuous decrease of the axial effective stress with decreasing distance from the cavity (see Fig. 6.7). When the Strain Path method is used, the PLB and the proposed models also predict decreasing values of the axial effective stress with decreasing distance from the pile, whereas the MCC model predictions initially decrease, then increase and, at the pile wall, the predicted axial effective stress is almost equal to its value before pile installation.
- (6) Figure 6.8 presents the predicted excess pore pressure distribution far behind the pile tip. All Cavity Expansion solutions predict an almost logarithmic\* increase of the excess pore pressure in the region close to the cavity (i.e., for  $r/r_0 < 10$ ) because, in this region, the stresses are approximately constant\*\* (see Figs. 6.5 and 6.6) and thus, the integration of the stress equilibrium equation (Eq. 6.6) gives a logarithmic variation of the excess pore pressure. The slope of the linear part of these curves is proportional to the predicted undrained shear strength at the Critical State and, as expected,\*\*\* the slope of the MCC model prediction is larger than that of the PLB model prediction which is again slightly larger than the

---

\* shown as linear in the semi-log plot

\*\* indicating that the Critical State is reached

\*\*\* see e.g. Fig. 6.1a

prediction obtained using the proposed model. The Strain Path method predicts an almost constant distribution of the excess pore pressure in the immediate vicinity of the pile (i.e., for  $r/r_0 < 3-4$ ) for all soil models. In this region, the excess pore pressure predicted by the Strain Path method is significantly lower than the prediction of the Cavity Expansion method (typically the MCC, PLB and the proposed models predict 25.4%, 34.2% and 18.5% lower values at the pile wall, respectively).

- (7) Figure 6.9 presents the predicted radial total stress\* distributions in the soil far behind the pile tip. All Cavity Expansion solutions predict a logarithmic\*\* increase of the total radial stress in the region close to the cavity (i.e., for  $r/r_0 < 10$ ) because, in this region, the effective radial stress is approximately constant (see Fig. 6.5) and thus, the predicted change of the total radial stress is approximately equal to the excess pore pressure which is logarithmically distributed (see the upper part of Fig. 6.8). The total radial stress at the pile wall, predicted by the Strain Path method, is significantly lower than the prediction of the Cavity Expansion method (typically, the MCC, PLB and the proposed models predict 48.5%, 46.8% and 40% lower values, respectively). This is due to the lower values of the excess pore pressure (see Fig. 6.8) and of the radial effective stress (see Fig. 6.5)

---

\* minus the ambient (hydrostatic) pore pressure

\*\* shown as linear in the semi-log plot

predicted by the Strain Path method compared to the Cavity  
Expansion method.



## 6.5 COMPARISON WITH MEASUREMENTS

### 6.5.1 THE SHAPE OF THE PORE PRESSURE DISTRIBUTION

Measurements of the excess pore pressure caused by pile installation can be used to evaluate the Cavity Expansion and the Strain Path methods, since the two methods predict different shapes of the excess pore pressure distribution in the soil around the pile. Figure 6.8 shows that in the immediate vicinity of the pile (i.e., for  $r/r_0 < 5$ ) and, regardless of the soil model used in the analysis of pile installation, the Cavity Expansion method predicts an almost logarithmic increase of the excess pore pressure, whereas the Strain Path method predicts an almost constant value. Figure 6.10 presents the excess pore pressure\* on the shaft and in the soil far behind the pile tip measured during pile installation in various clays having different properties (e.g. overconsolidation ratio, undrained shear strength, Plasticity Index, sensitivity, etc.). The data show that close to the pile wall and regardless of the properties of the clay, there exists a region of almost constant excess pore pressure indicating that the shape of the excess pore pressure distribution predicted by the Strain Path method is more realistic than that predicted by the Cavity Expansion method.

---

\* normalized with the vertical effective stress before pile installation

## 6.5.2 COMPARISON BETWEEN MEASUREMENTS AND PREDICTIONS IN BOSTON BLUE CLAY

The excess pore pressure and the radial stress at the pile wall far behind the pile tip were measured during the MIT field testing program performed at the site of the partially completed Interstate Highway I-95 in Saugus, Massachusetts. The testing site overlies deep deposits of Boston Blue Clay (BBC). The clay between depths 25 and 75 ft. is clearly overconsolidated with an OCR decreasing from 7 to 1.4. Below 75 ft., the clay is reasonably uniform with an  $OCR=1.3\pm 0.1$ . All field measurements in BBC reported in this Section are obtained in this uniform clay (i.e., below 75 ft.). The field program performed in June 1980 included the installation of a model pile, 3.8 cm in diameter, having a  $60^\circ$  tip angle. Measurements were obtained by means of a new device, the Piezo-Lateral Stress (PLS cell) recently developed at MIT. The PLS cell is a cylindrical device (having the same diameter as the model pile), installed along the shaft of the pile about one meter behind the tip. It can measure simultaneously the total radial stress and the pore pressure at the location of the device, i.e., on the shaft of the pile and thus, it can also provide the radial effective stress. This Section compares the values of the excess pore pressure and the radial stress at the pile wall, far behind the pile tip, measured during the 1980 MIT field testing program,\* to the corresponding values

---

\* in the deposit of BBC below 75 ft, where the clay is uniform with an  $OCR=1.3\pm 0.1$ .

predicted by means of the MCC, PLB and the proposed models (see Section 6.4), for a soil with properties similar to  $K_0$ -normally consolidated resedimented BBC. The measurements are compared to the predictions obtained by means of the Strain Path method because this method is believed to be superior to the Cavity Expansion method, since:

- (i) It takes into consideration the effect of the pile tip, which is neglected by the Cavity Expansion method (see Section 6.2.2) and,
- (ii) It predicts the correct shape of the excess pore pressure distribution in the soil (see Section 6.5.1).

Table 6.2 presents the values of the excess pore pressure and the radial (total and effective) stress at the pile wall,\* measured by means of the PLS cell and shows that the measured excess pore pressure ranges between 2.0 and 2.13 times the vertical effective stress in the soil before pile installation. The predicted values of the excess pore pressure at the pile wall according to the MCC, the proposed and the PLB models are equal to 1.32, 1.10 and 1.02 times the vertical effective stress in the soil before pile installation\*\* i.e., the predictions underestimate the measured values by almost a factor of two. The discrepancy between the measured and predicted excess pore pressures is also reflected in the total

---

\* at depths 84.5, 99.5 and 114.5 feet in the uniform deposit of BBC

\*\* the higher value predicted by the MCC model is evidently due to the fact that this model significantly overestimates the strength of the clay (see Fig. 6.1)

radial stresses. The measured total radial stress at the pile wall ranges between 2.23 and 2.37 times the vertical effective stress in the soil before pile installation, whereas the corresponding predicted values according to the MCC, the PLB and the proposed models are equal to 1.36, 1.13 and 1.10, respectively.

A series of self-boring pressuremeter tests\* performed at the same site (in the uniform clay below 75 ft), also shows a poor agreement between the predicted and measured total radial stress at the cavity wall. Levadoux and Baligh (1980) modelled the self-boring pressuremeter test by the undrained expansion of a pre-existing cylindrical cavity and, using the PLB model, predicted a value of the total radial stress at the cavity wall\*\* equal to 1.75 times the initial vertical effective stress in the soil whereas, the measured values range between 3.0 and 3.1 times the initial vertical effective stress in the soil. They conclude that the discrepancies are mainly due to:

- (i) Non-cylindrical expansion during the self-boring pressuremeter test.
- (ii) Partial drainage.
- (iii) The fast rate of expansion of the probe compared to the rate of straining during the laboratory tests used in the predictions.
- (iv) A possible underprediction of the stiffness of the clay

---

\* reported by Ladd et al (1979)

\*\* at 15% increase of the volume of the cavity

at very low strain levels (less than 0.1%), comparable to the strain levels in the soil far away from the cavity.

- (v) A slight overconsolidation of the clay below 75 ft., since  $OCR=1.3\pm 0.1$  instead of the normally consolidated clay assumed in obtaining the predictions.

Levadoux and Baligh (1980) discuss these issues in detail for the case of the pressuremeter test, but their conclusions\* also apply in the case of pile installation.

Figure 6.11 shows the effect of varying the overconsolidation ratio (OCR) and the elastic shear modulus,\*\* on the predicted distributions of the excess pore pressure far behind the tip of a pile, computed according to the Strain Path method in conjunction with the proposed model.\*\*\* When the OCR is increased from unity to 1.35,\*\*\*\* the proposed model predicts 18% higher excess pore pressure at the pile wall.\*\*\*\*\* Similarly, for a three-fold increase of the elastic stiffness (from 150 to 500), the proposed model predicts 10% higher excess pore pressure at the pile wall, which is almost totally

---

\* except the first one

\*\* and thus, also the secant shear modulus at low strain levels (see Fig. 5.1).

\*\*\* Figure 6.12 shows the proposed model prediction for the effect of the OCR on the stress-strain curves and the effective stress paths during the undrained cylindrical cavity expansion mode of deformation.

\*\*\*\* which is a more reasonable value for the uniform clay below 75 ft.

\*\*\*\*\* For OCR equal to 1.0 and 1.35 the predicted values of the excess pore pressure are equal to 1.1 and 1.3 respectively.

due to increased predicted excess pore pressures in the region between 20 and 60 times the pile radius (i.e., for radial strains between 0.1% and 0.01%).

The small improvements in the predicted excess pore pressures obtained for a slightly overconsolidated clay or by assuming a larger secant shear modulus at very small strain levels, are not sufficient to justify the almost two-fold underprediction of the excess pore pressure at the pile wall. Levadoux and Baligh (1980) performed similar parametric studies and reached the above conclusion. They believe that the remaining discrepancy might be explained by:

- (i) The OCR of the clay is actually higher than 1.35 and hence the in situ strength is higher than estimated.
- (ii) The in situ clay has a significantly different behavior from the resedimented BBC used to determine the model parameters. In particular, the in situ clay has very high peak shear strength and/or initial stiffness that affect pile installation. This proposition is supported by the more sensitive behavior of the in situ clay (as detected by consolidation tests and suggested by the low salt concentration in the pore water), but is hard to evaluate or even prove satisfactorily.
- (iii) Strain rate effects which tend to underestimate the field strength measured by pile installation tests performed at higher rates than laboratory tests.

Despite the large discrepancy between measurement and prediction in the excess pore pressure and the total radial

stress, the effective radial stress at the pile wall is reasonably well predicted especially since the (small) measured radial effective stress is obtained by the difference of two large numbers\* which are almost equal to each other. Table 6.2 shows that the measured radial effective stress at the pile wall ranges between 0.21 and 0.26 times the vertical effective stress in the soil before pile installation, whereas the corresponding predicted values are equal to 0.12, 0.05 and 0.0 according to the PLB, MCC and the proposed models, respectively.

Figures 6.13 and 6.14 present the distributions (in the radial direction) of:\*\* (a) the radial effective stress, (b) the vertical effective stress, (c) the radial total stress and (d) the maximum shear stress difference in the  $r-\theta$  plane and, Fig. 6.15 shows the radial, axial and circumferential effective stresses far behind the pile tip, immediately after pile installation, predicted according to the Strain Path method (in conjunction with the proposed model) for a clay with properties similar to BBC and overconsolidation ratios equal to 1.0, 1.2 and 1.35. These stress and pore pressure distributions are used in Chapter 8 as initial conditions in the non-linear consolidation analyses (see Chapter 8) for the following reasons:

- (i) The radial effective stress at the pile wall immediately

---

\* i.e., the radial total stress and the excess pore pressure

\*\* the distribution of the excess pore pressure is presented in Fig. 6.11.

after installation is reasonably well predicted\* and, it is widely accepted that the single most important parameter in estimating pile capacity is the radial effective stress at the pile wall immediately after installation and its changes during consolidation.

- (ii) The normalized\*\* distribution of the excess pore pressure is reasonably well predicted (see Section 6.5.2) and previous work (e.g. Levadoux and Baligh, 1980) has shown that excess pore pressure dissipation rates appear to depend primarily\*\*\* on this normalized distribution rather than the absolute magnitudes of the excess pore pressure.

---

\* especially in view of the uncertainties in the measurements

\*\* with the value of the excess pore pressure at the pile shaft.

\*\*\* evidently, they also depend on the soil characteristics (i.e., the coefficient of consolidation).



## 6.6 SUMMARY AND CONCLUSIONS

The primary objective of this Chapter is to estimate the values of the excess pore pressures and the effective stresses in the soil during steady pile installation (driving). These values represent the initial conditions for the consolidation analyses and thus, they are essential for the rational interpretation of the consolidation that takes place after pile installation. More specifically, this Chapter concentrates on the estimation of the excess pore pressures and the effective stresses far behind the pile tip, since the major portion of the bearing capacity of long friction piles (commonly used offshore) is due to the shaft friction rather than the point resistance.

File installation analyses are performed using two methods:

- (i) The Undrained Expansion of a Cylindrical Cavity.
- (ii) The Strain Path method.

Both methods are based on assumed (simplified) soil velocity fields obtained mainly by kinematic considerations (i.e., incompressibility), without solving the Boundary Value problem of pile installation. In the case of the Strain Path method, the assumed velocity field does not conform with the constitutive behavior of the soil. The basic difference between the two methods is that the Strain Path method takes into consideration the effect of the pile tip, whereas the Cavity Expansion method neglects this effect and treats pile installation as an one-dimensional problem. Thus, the Strain

Path method is expected to give more realistic predictions of the effective stresses and the excess pore pressures in the soil immediately after pile installation. Both methods give very similar strains in the soil far behind the pile tip, whereas the predicted strain paths of the individual soil elements are very different: the Cavity Expansion method predicts monotonic radial strain paths for all soil elements and, the Strain Path method predicts large strain reversals and complicated strain paths.\*

The stress and excess pore pressure distributions in the soil far behind the pile tip are estimated\*\* by means of three non-linear soil models:

- (i) The Modified Cam-Clay (MCC) model.
- (ii) The Prevost-Levadoux-Baligh (PLB) model.
- (iii) The model proposed in Chapter 4.

Pile installation analyses show that:

- (i) For radial distances less than 10 times the pile radius, there are major differences in the stress and pore pressure changes predicted by means of the Cavity Expansion and the Strain Path methods. These differences indicate that the effect of the pile tip (which is neglected by the Cavity Expansion method) is very significant. More specifically, in the region close to the pile wall, the Strain Path method predicts

---

\* especially close to the pile wall

\*\* using the strain paths predicted by the Cavity Expansion and the Strain Path methods for a soil with properties similar to normally consolidated resedimented Boston Blue Clay

significantly smaller values of the excess pore pressure and the total (and effective) radial stress, compared to the Cavity Expansion method. Furthermore, the predicted distributions in the radial direction have different shapes: in the region close to the pile wall, the Cavity Expansion method predicts a logarithmic distribution of the excess pore pressure and of the total radial stress, whereas the Strain Path method predicts approximately constant values of the excess pore pressure and of the total radial stress. Field measurements in a variety of clays support the shape of the excess pore pressure distributions predicted by the Strain Path method.

- (ii) The Strain Path and the Cavity Expansion methods predict comparable stress and excess pore pressure changes in the soil, for radial distances larger than 10-20 times the pile radius. This means that the effect of the pile tip does not extend to radial distances larger than 10-20 times the pile radius.

The values of the excess pore pressure and of the total radial stress at the pile wall (far behind the pile tip), estimated\* according to the Strain Path method, underpredict the values measured in Boston Blue Clay\*\* by almost a factor of two. On the contrary, the measured value of the effective radial stress at the pile wall is reasonably well predicted.

---

\* using any of the three soil models above for a soil with properties similar to normally consolidated Boston Blue Clay

\*\* at depths below 75 ft., where the clay is reasonably uniform with  $OCR=1.3\pm 0.1$ .

The poor agreement between the predicted and measured values of the excess pore pressure and the total radial stress at the pile wall is mainly due to:

- (i) The fast rate of straining during pile installation compared to the rate of straining during the laboratory tests used in the predictions.
- (ii) A possible underprediction of the stiffness of the clay at very low strain levels (less than 0.1%), comparable to the strain levels in the soil far away from the pile.
- (iii) A slight overconsolidation of the clay below 75 ft., since  $OCR=1.3\pm 0.1$  instead of the normally consolidated clay assumed in obtaining the predictions.

The effects of varying the overconsolidation ratio and the initial stiffness of the clay are small. When the OCR is increased from unity to 1.35, the proposed model predicts 18% higher excess pore pressure at the pile wall. Similarly, for a three-fold increase of the elastic stiffness, the proposed model predicts 10% higher excess pore pressure at the pile wall. These improvements are not sufficient to justify the underprediction of the excess pore pressure at the pile wall by almost a factor of two. However, the predicted distributions of stresses and pore pressures around the pile\* are used as initial conditions in the consolidation analyses (see Chapter 8) for the following reasons:

- (i) The radial effective stress at the pile wall is reasonably well predicted and, it is widely accepted

---

\* for OCR equal to 1.0, 1.2 and 1.35

that the single most important parameter in estimating pile capacity is the radial effective stress at the pile wall immediately after installation and its changes during consolidation.

- (ii) The normalized\* distribution of the excess pore pressure is reasonably well predicted and previous work (e.g. Levadoux and Baligh, 1980) has shown that excess pore pressure dissipation rates appear to depend primarily\*\* on this normalized distribution rather than the absolute magnitudes of the excess pore pressure.

---

\* with the value of the excess pore pressure at the pile shaft.

\*\* evidently, they also depend on the soil characteristics (i.e., the coefficient of consolidation).

Node	$r/r_0$	Node	$r/r_0$
1	1.00000	24	3.44803
2	1.00549	25	3.73601
3	1.02013	26	4.12262
4	1.04426	27	4.60904
5	1.07723	28	5.09805
6	1.11815	29	5.83500
7	1.16632	30	6.57485
8	1.22074	31	7.56437
9	1.28073	32	8.55629
10	1.34554	33	9.54987
11	1.41438	34	11.04240
12	1.48729	35	12.53670
13	1.56264	36	14.03220
14	1.64065	37	16.02750
15	1.72094	38	18.02390
16	1.80321	39	20.02100
17	1.92977	40	25.01590
18	2.05947	41	30.01260
19	2.23637	42	40.00870
20	2.46245	43	50.00660
21	2.69274	44	70.00430
22	2.92625	45	100.00300
23	3.16225	46	150.00000

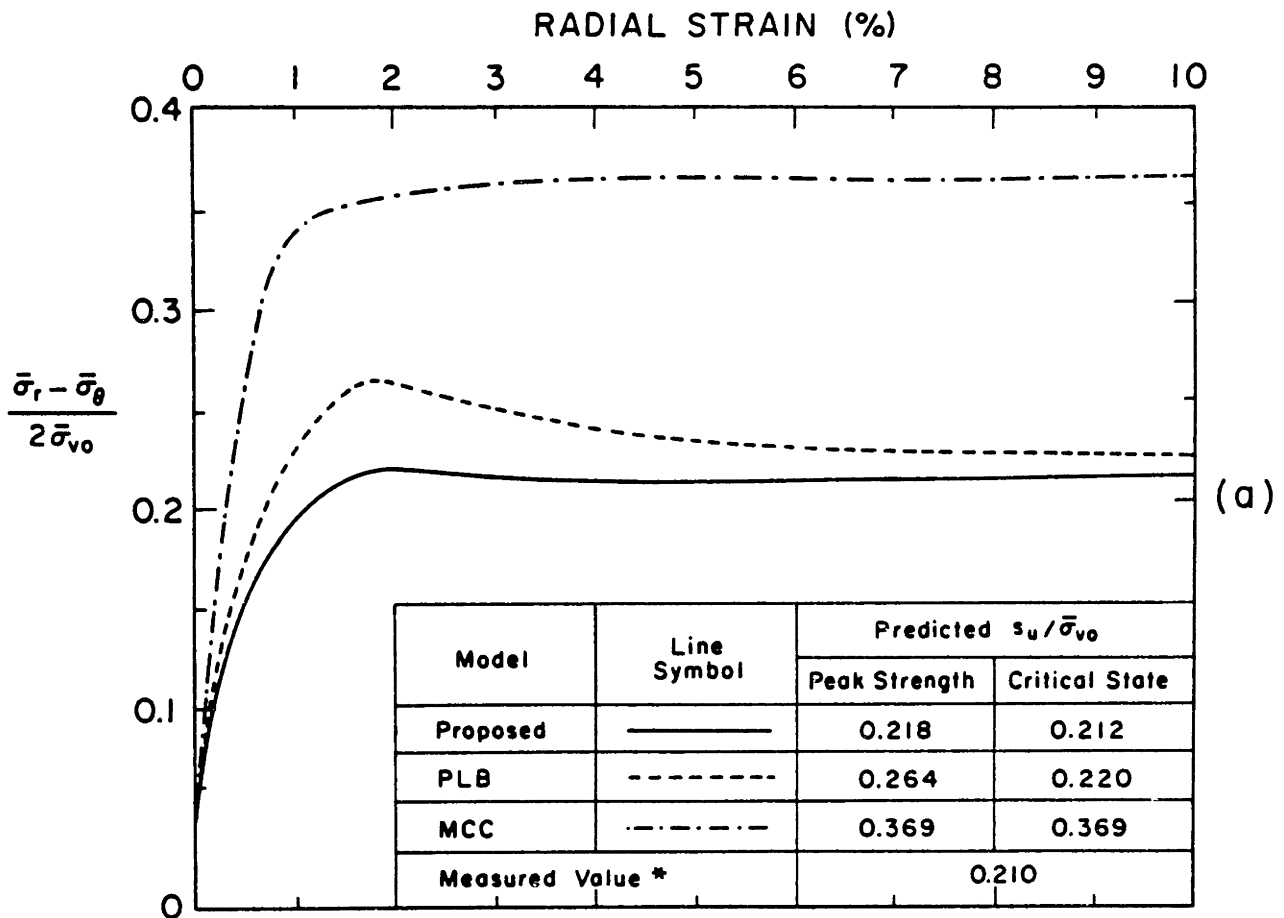
Table 6.1 : Radial coordinates of the nodal points far behind the tip of the pile, used to model pile installation via the Cavity Expansion and the Strain Path methods.

MEASUREMENTS IN BOSTON BLUE CLAY

Depth (ft)	Measured $\frac{\sigma_r - p_0}{\bar{\sigma}_{vo}}$	Measured $\frac{p - p_0}{\bar{\sigma}_{vo}}$	Computed $\frac{\bar{\sigma}_r}{\bar{\sigma}_{vo}}$
84.5	2.234	1.997	0.237
99.5	2.331	2.126	0.205
114.5	2.374	2.118	0.256

Note:  $\bar{\sigma}_{vo}$  is the vertical effective stress in the soil before pile installation.

Table 6.2: Measured values of the excess pore pressure and of the radial stress at the pile wall in Boston Blue Clay



\* Reported by Kirby and Esrig (1979)  
Complete testing information not available.

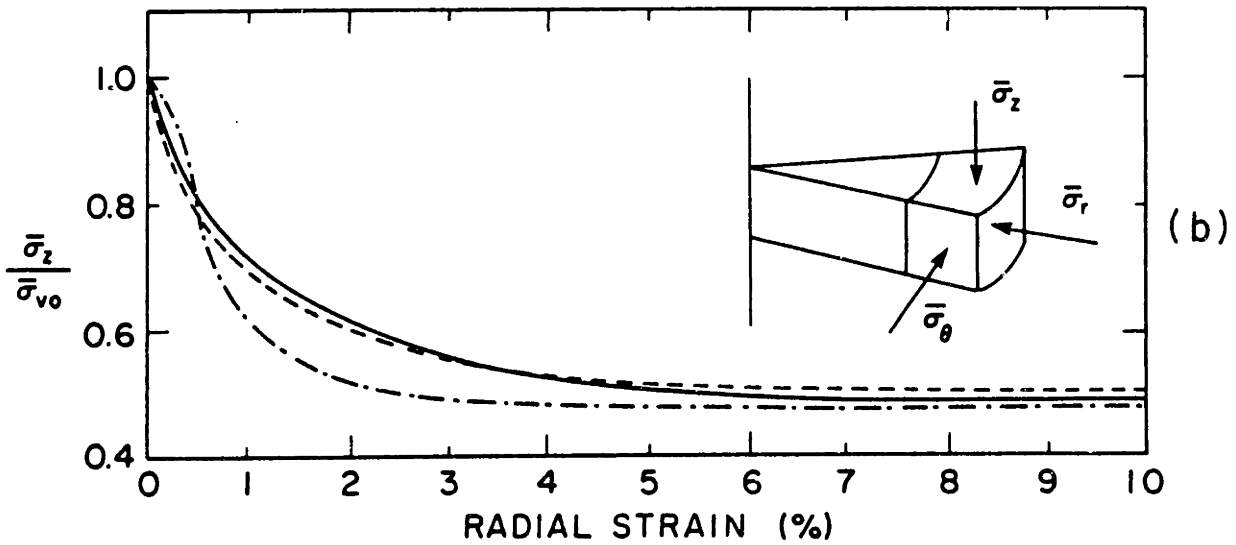


Fig. 6.1: Stress-strain curves predicted by various models during an undrained cylindrical cavity expansion in normally consolidated BBC.



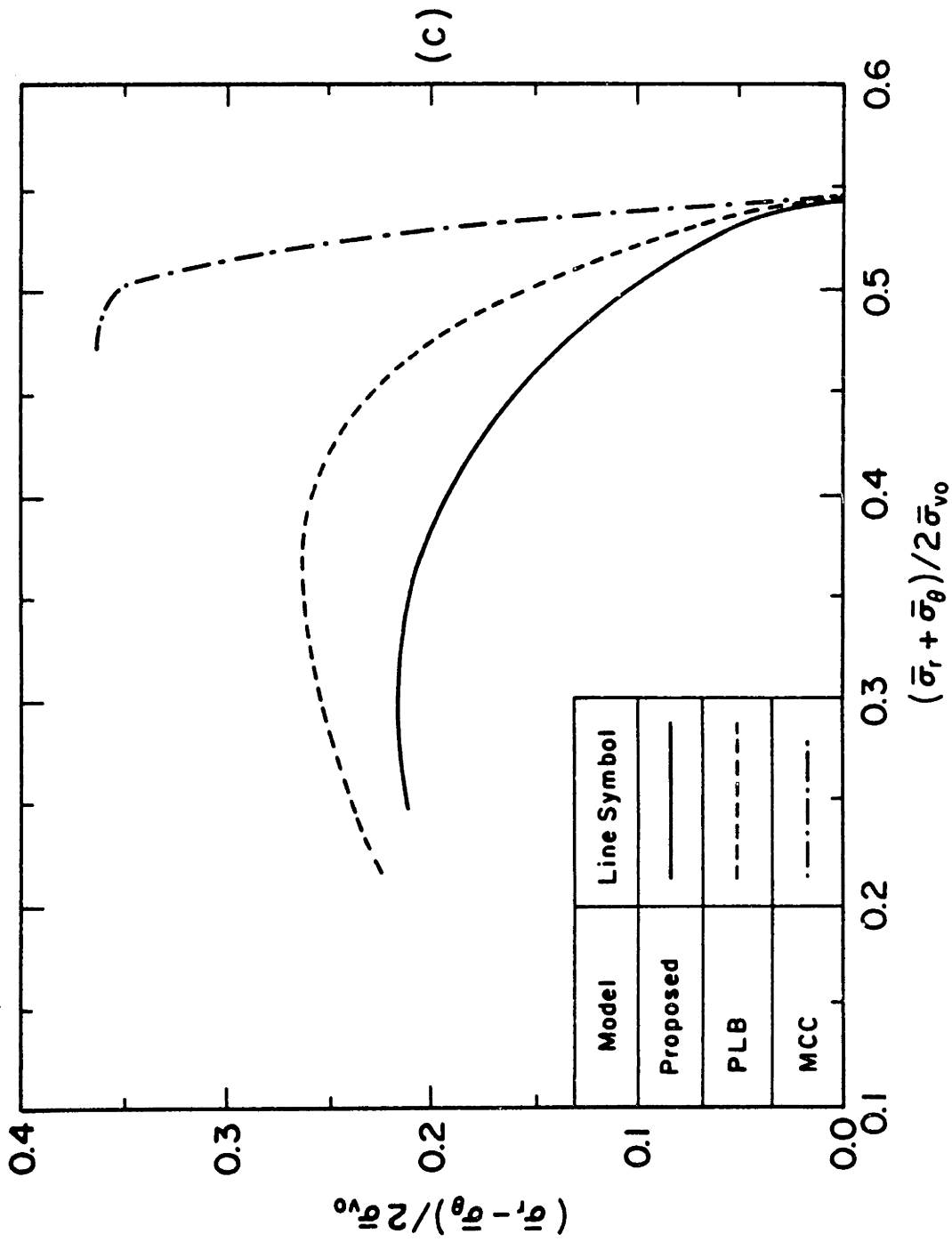
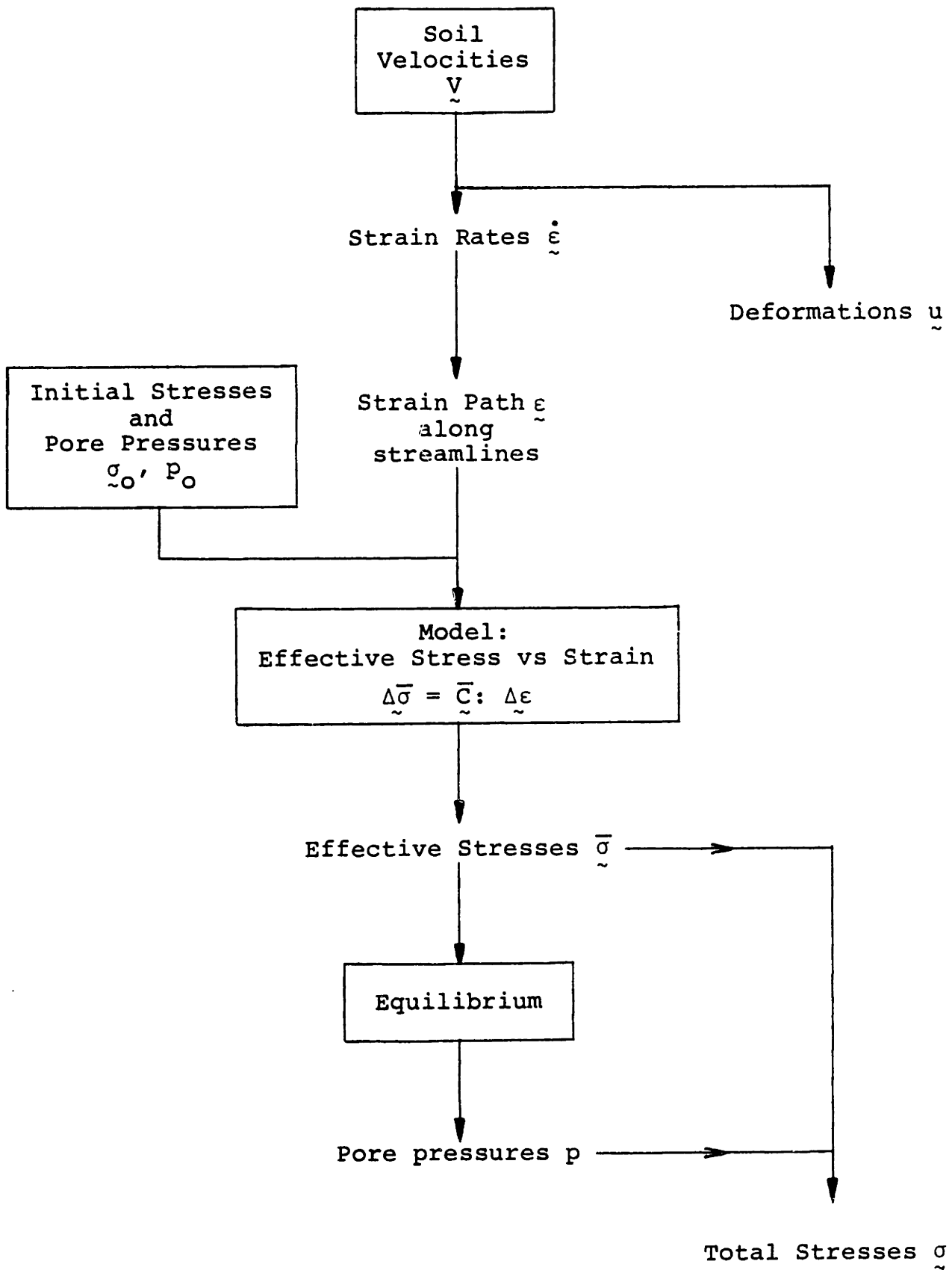


Fig. 6.1 (continued): Effective stress paths predicted by various models during an undrained cylindrical cavity expansion in normally consolidated BBC.



**Figure 6.2:** Application of the Strain Path method to deep steady pile installation using an effective stress model

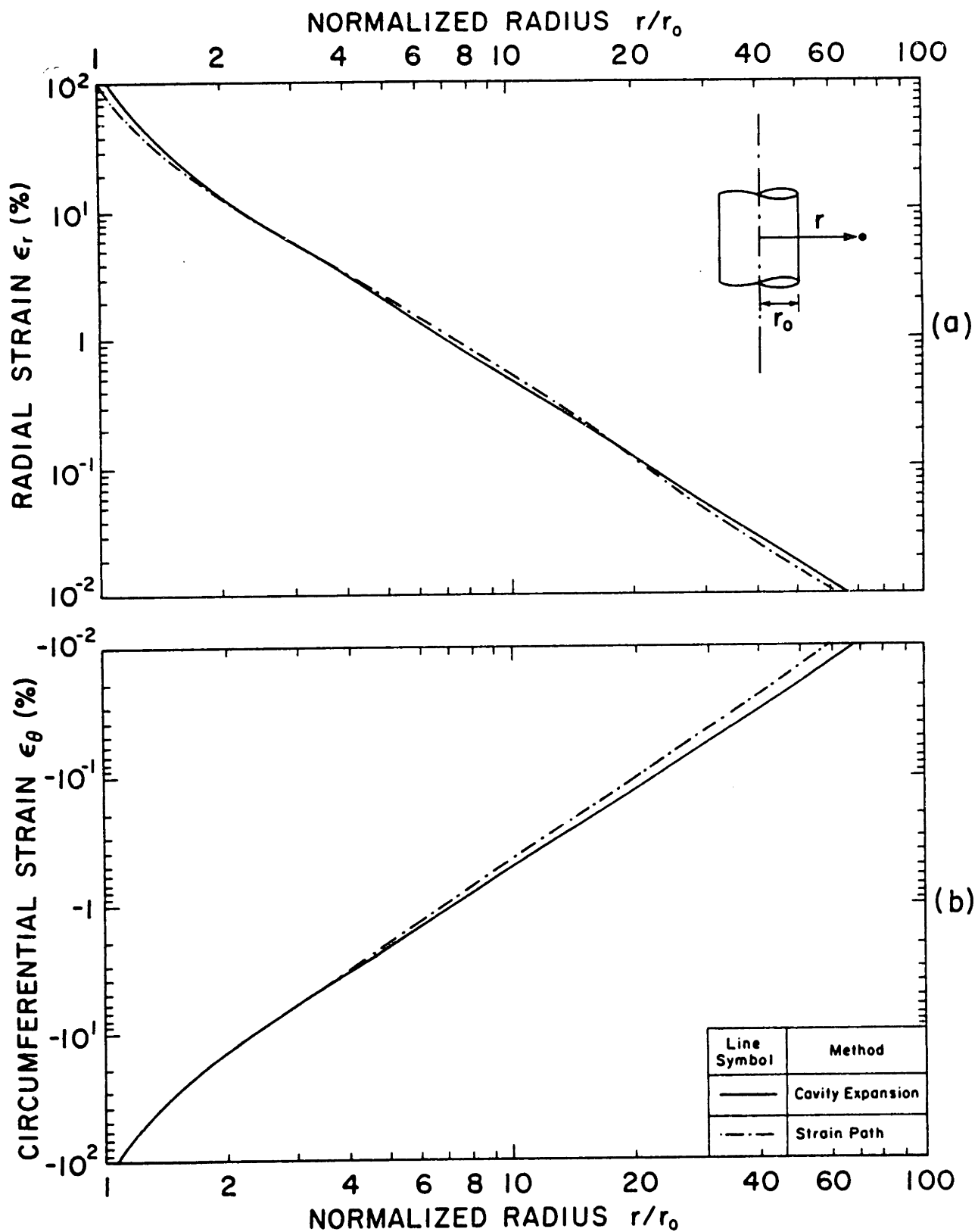


Fig. 6.3: Distribution of (a) the radial and (b) the circumferential strains far behind the pile tip, predicted according to the Cavity Expansion and the Strain Path methods.

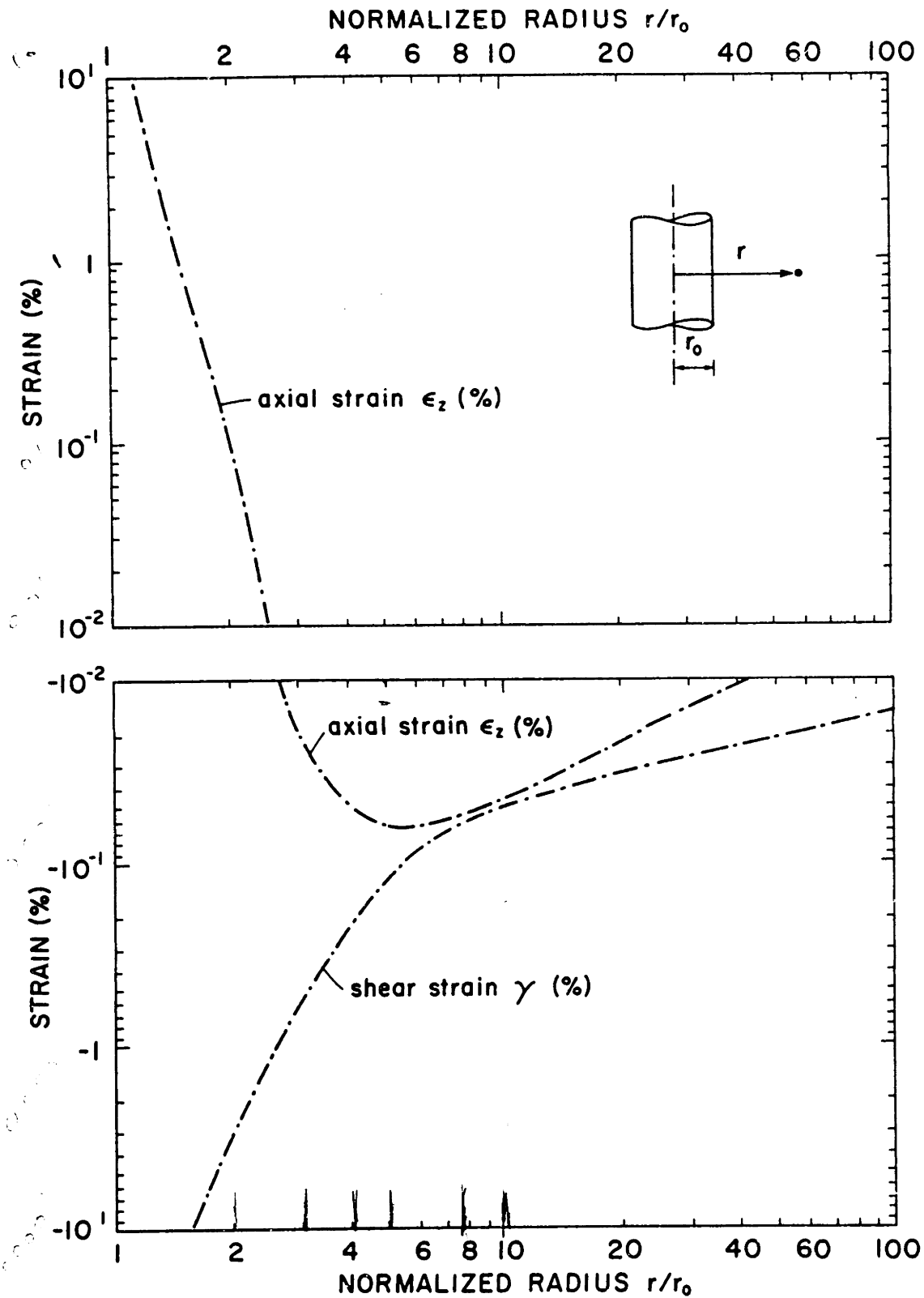


Fig. 6.4: Axial and shear strain far behind the pile tip, predicted according to the Strain Path method.

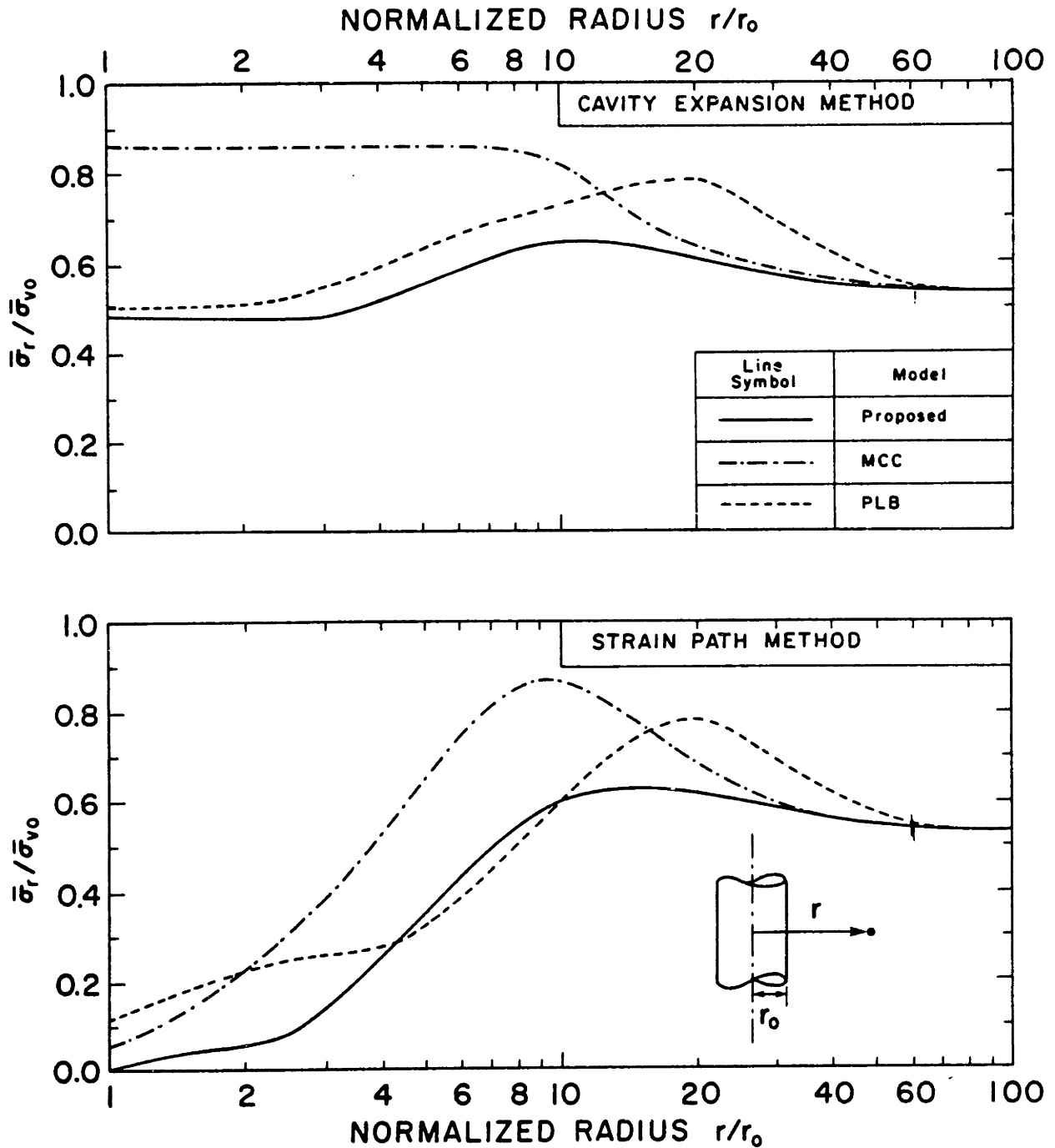


Fig. 6.5: Distributions of the radial effective stress far behind the pile tip, predicted according to the Cavity Expansion and the Strain Path methods.

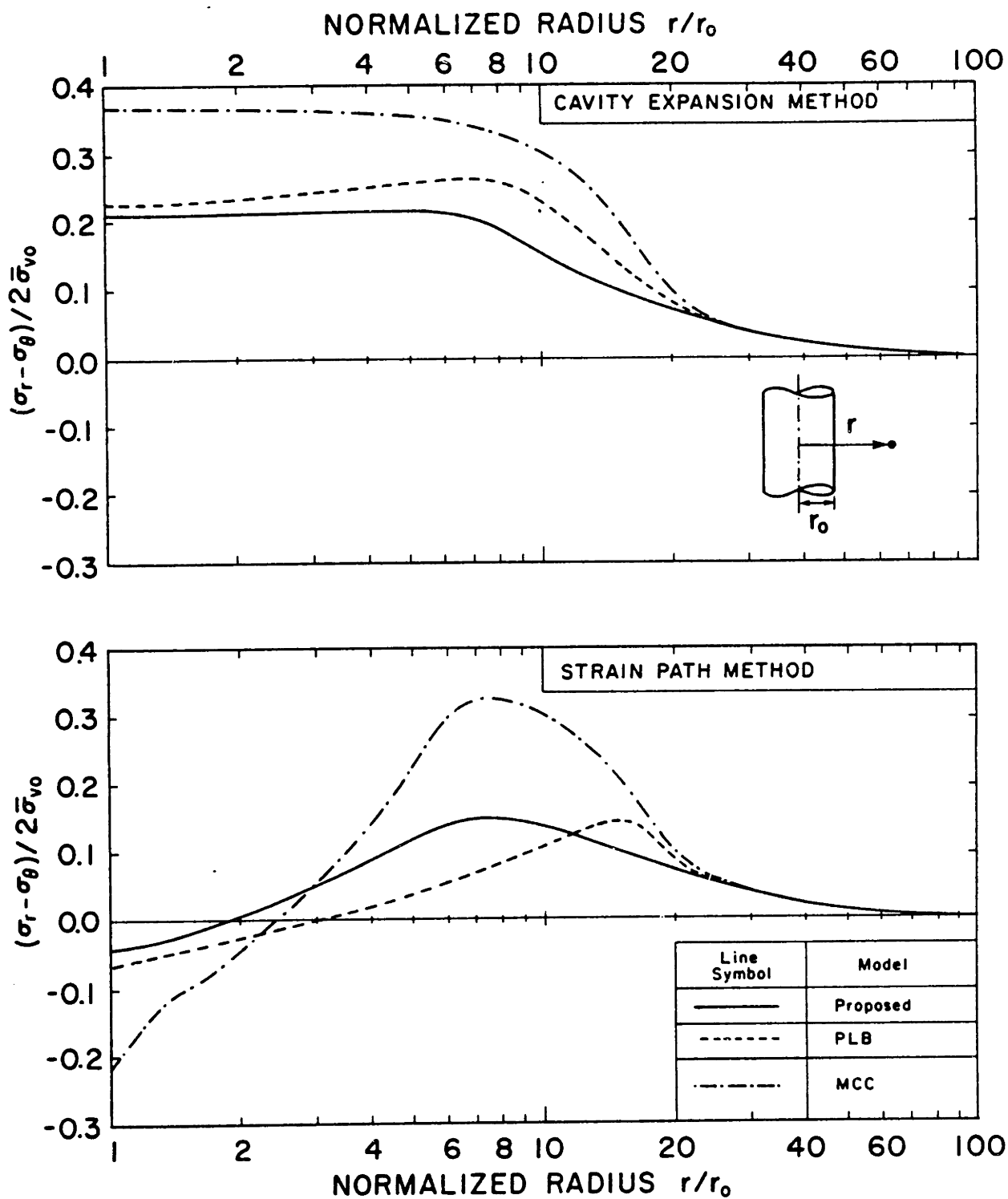


Fig. 6.6: Distributions of the shear stress in the horizontal plane, far behind the pile tip, predicted according to the Cavity Expansion and the Strain Path methods.

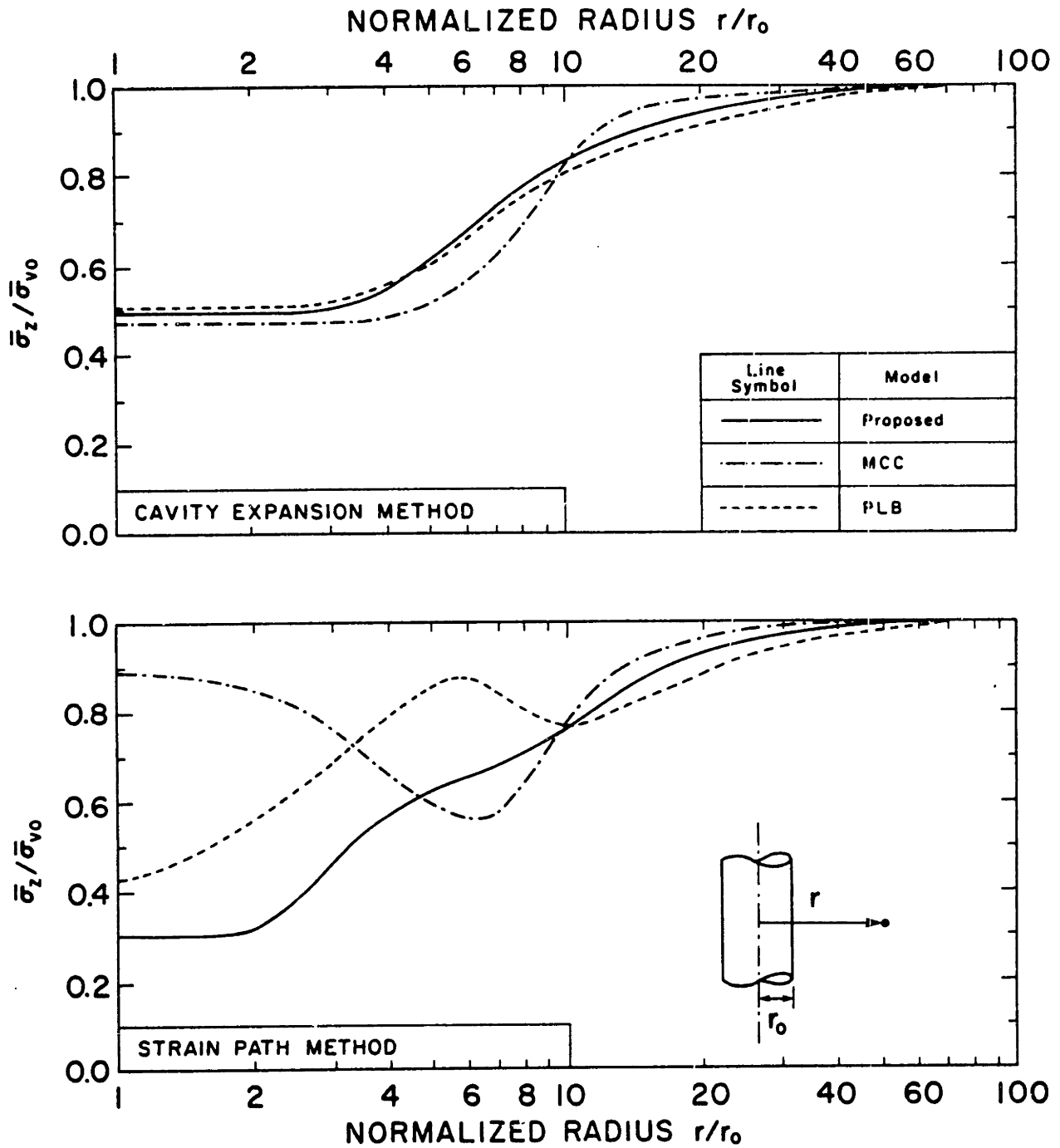


Fig. 6.7: Distributions of the axial effective stress far behind the pile tip, predicted according to the Cavity Expansion and the Strain Path methods.

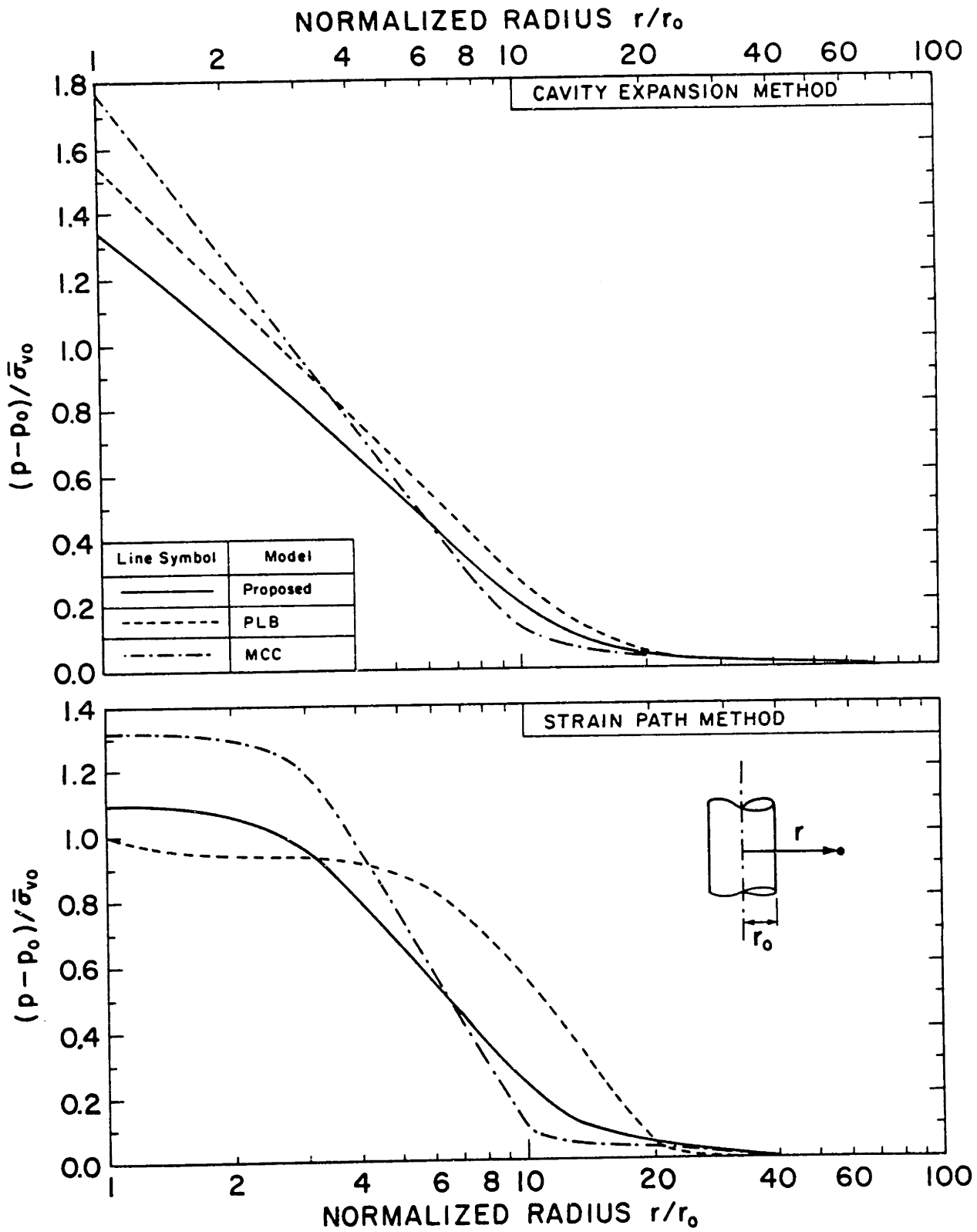


Fig. 6.8: Distributions of the excess pore pressure far behind the pile tip, predicted according to the Cavity Expansion and the Strain Path methods.



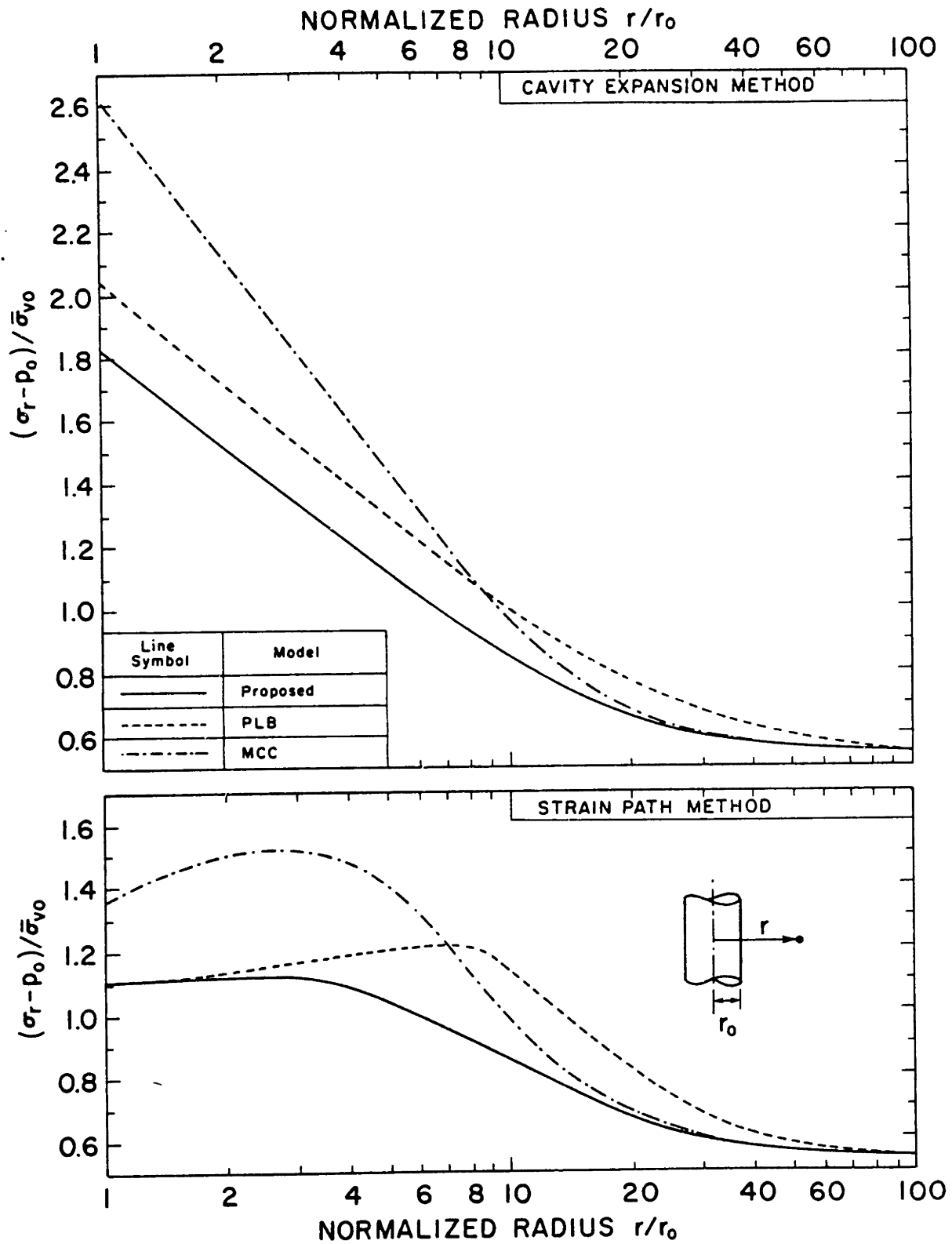


Fig. 6.9: Distributions of the radial total stress far behind the pile tip, predicted according to the Cavity Expansion and the Strain Path methods.

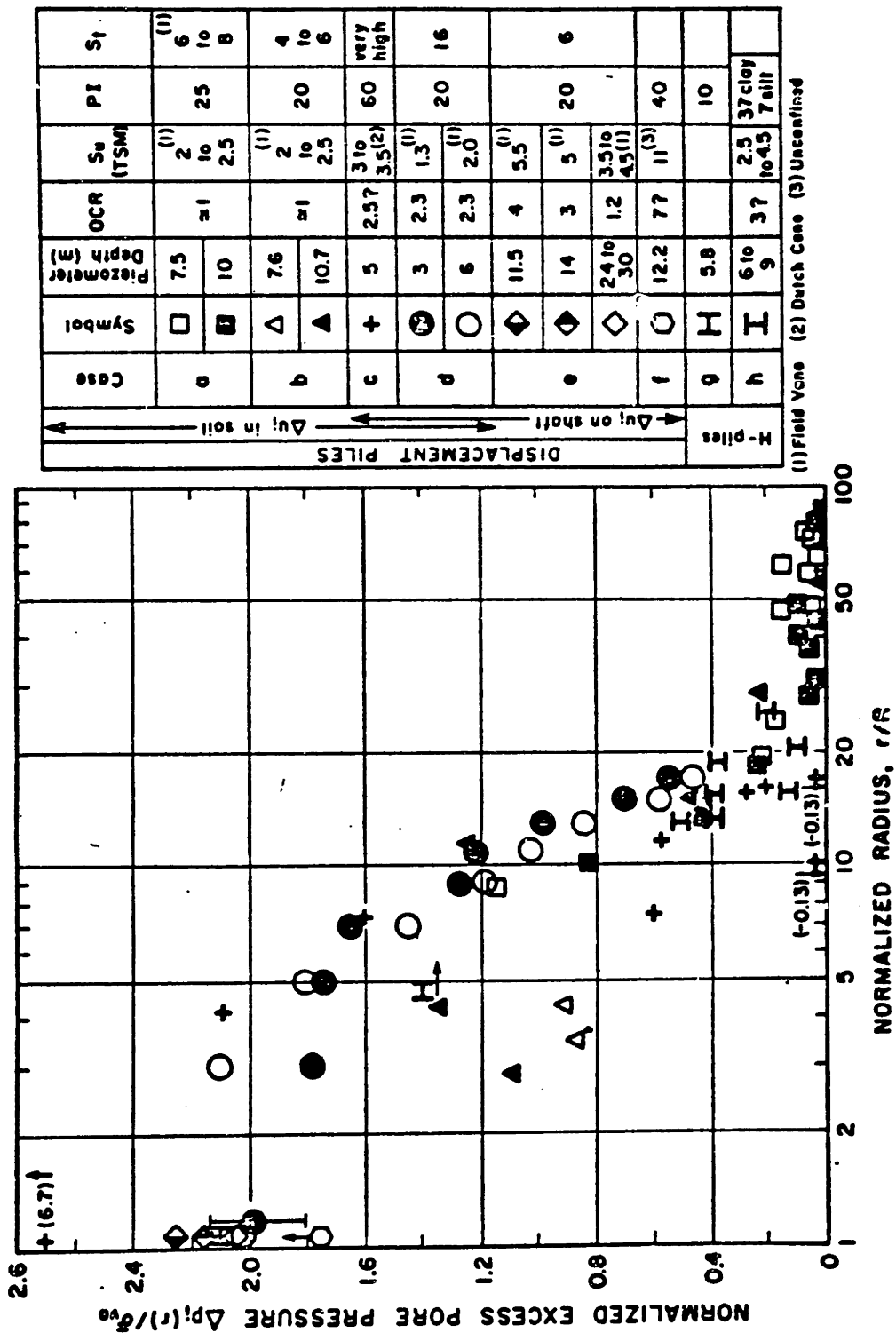


Fig. 6.10: Excess pore pressure measurements due to pile installation in clays - Case histories.

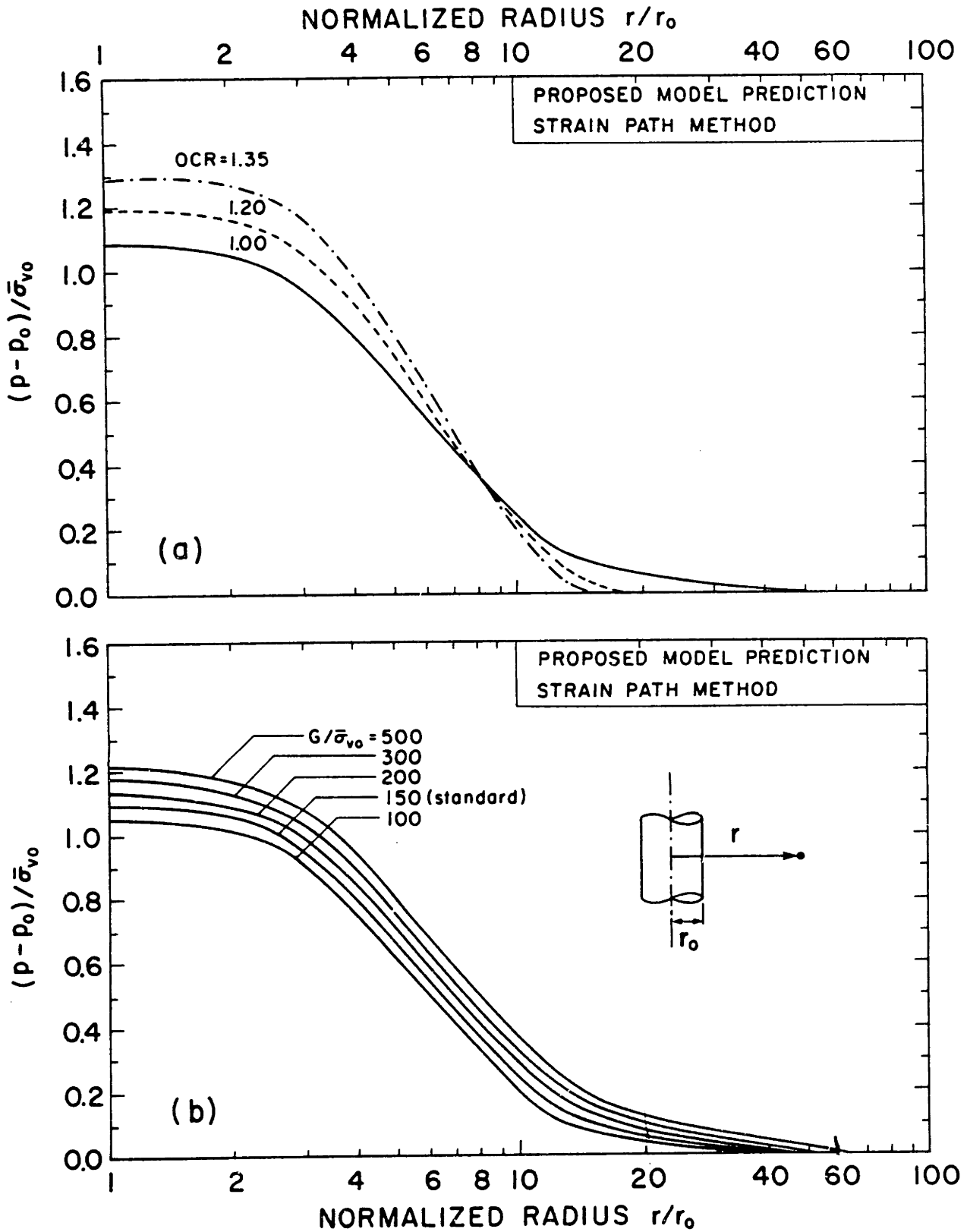


Fig. 6.11: Effect of (a) the Overconsolidation Ratio and (b) the elastic shear modulus on the distributions of the excess pore pressure predicted according to the Strain Path method, using the proposed model.

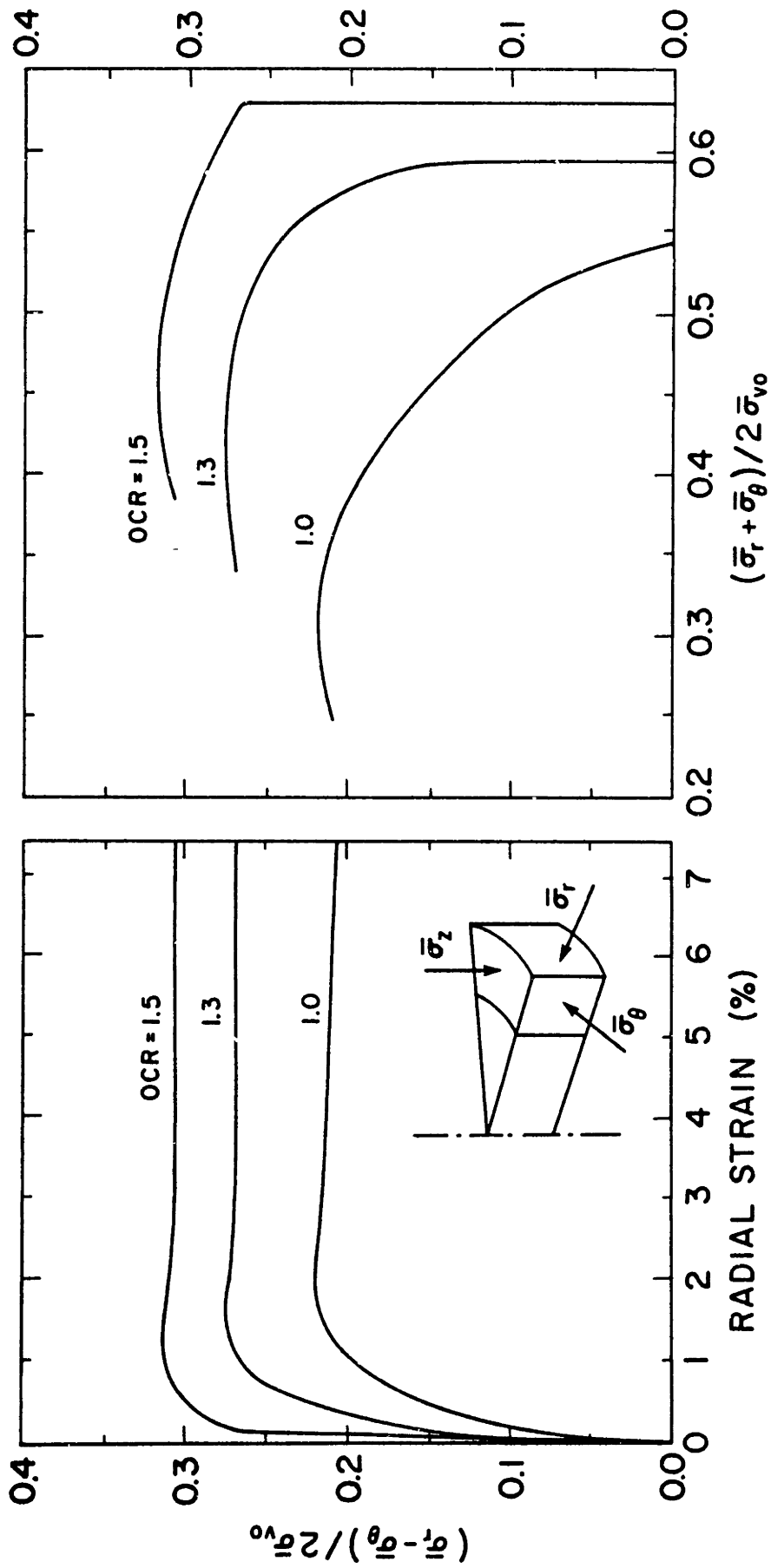


Fig. 6.12: Proposed model prediction of the stress-strain curves and the effective stress paths during an undrained cylindrical cavity expansion in BBC for various overconsolidation ratios.

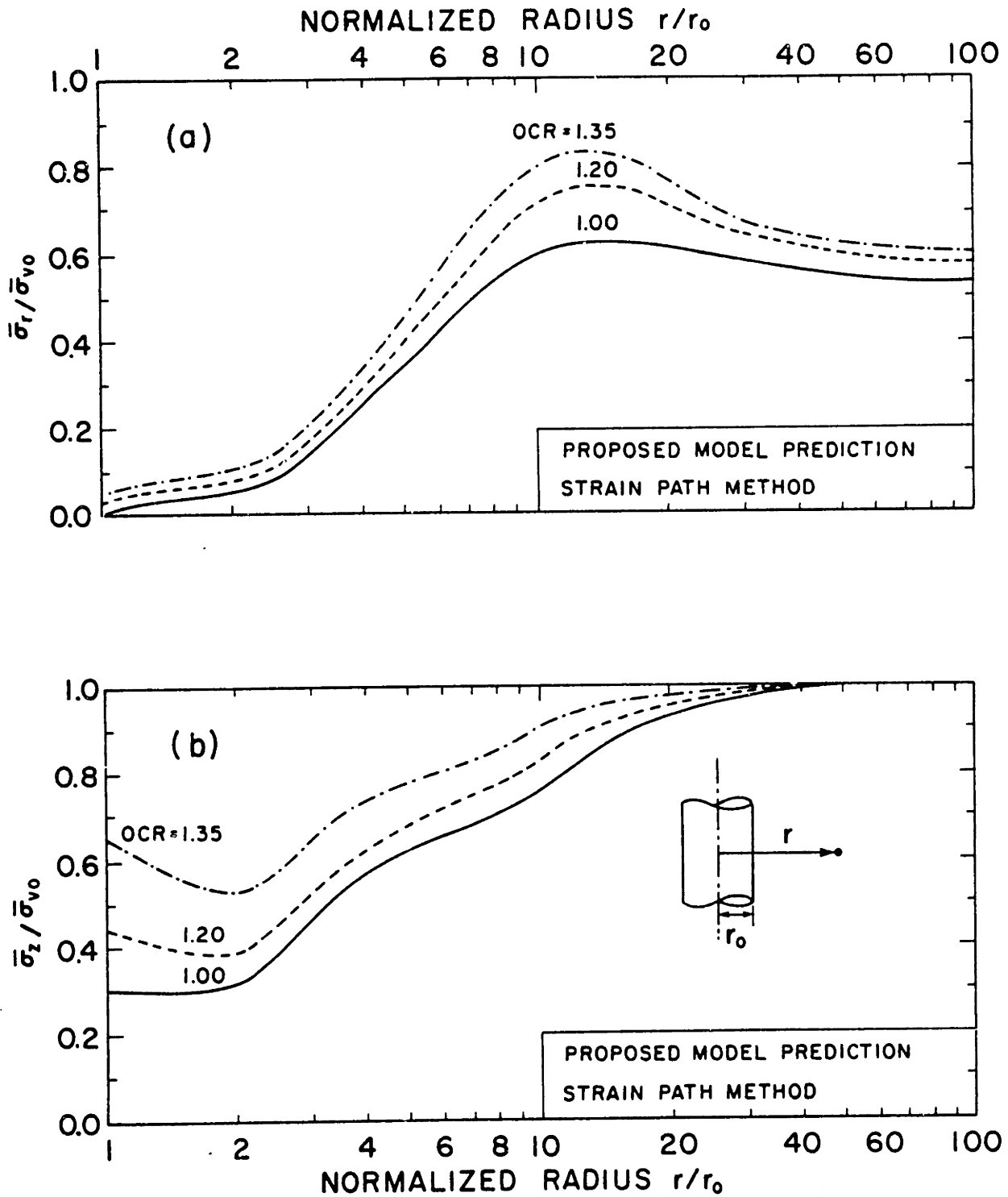


Fig. 6.13: Effect of the OCR on the distributions of (a) the radial effective stress and (b) the axial effective stress predicted according to the Strain Path method using the proposed model.

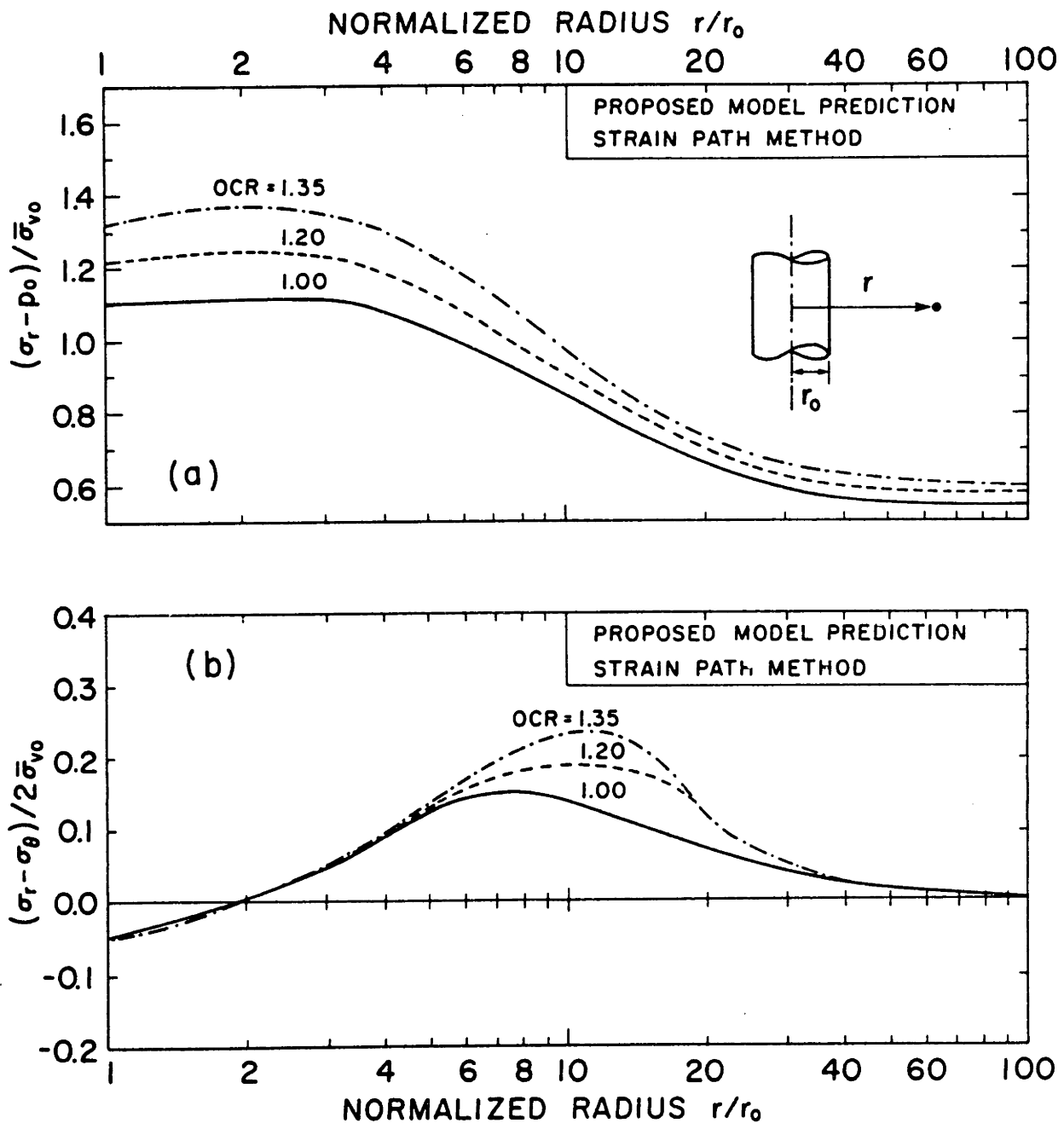


Fig. 6.14: Effect of the OCR on the distributions of (a) the total radial stress and (b) the shear stress in the horizontal plane, predicted according to the Strain Path method using the proposed model.

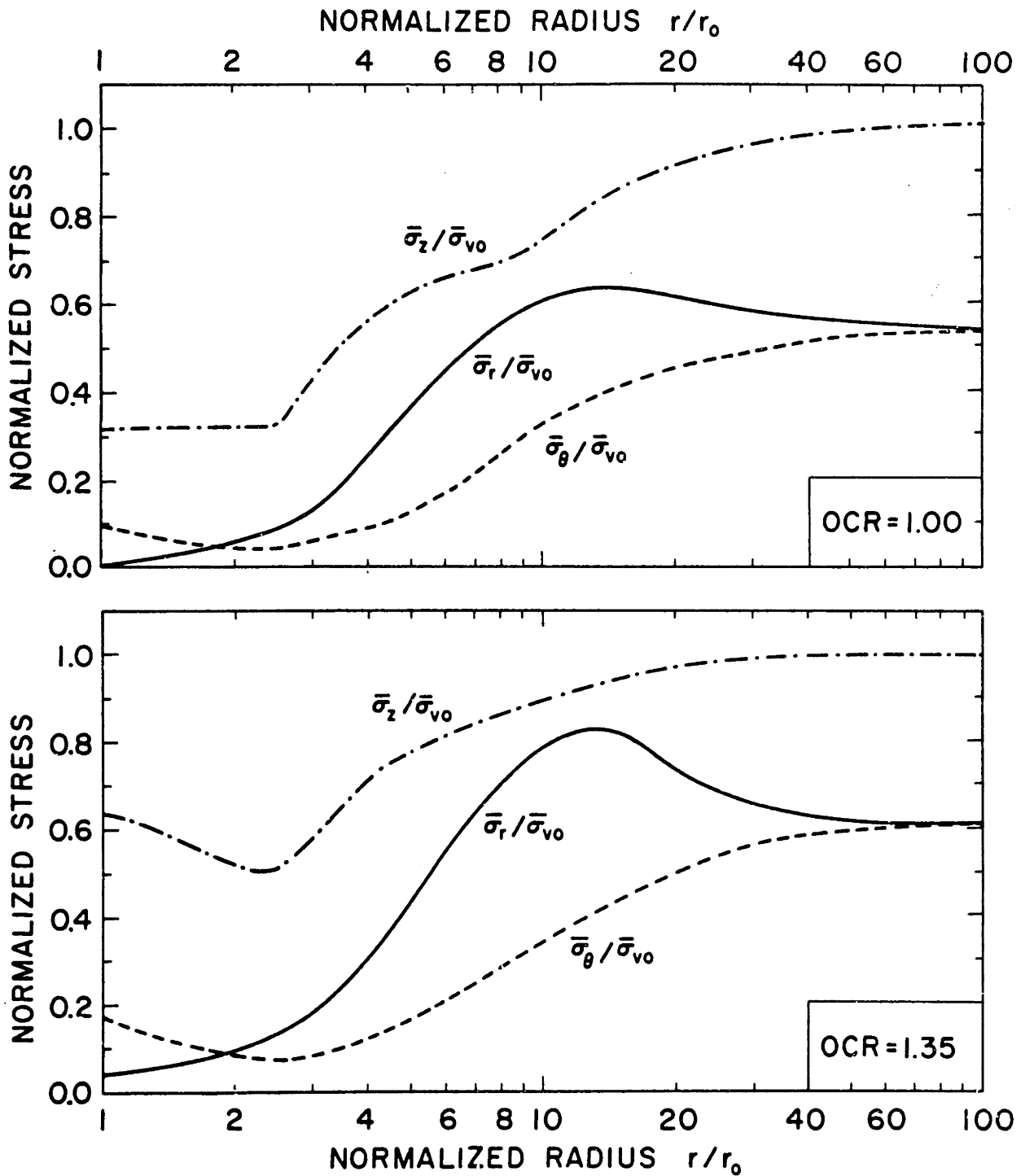


Fig. 6.15: Effective stresses immediately after pile installation predicted by the proposed model (in conjunction with the Strain Path method) for  $K_0$ -consolidated Poston Blue Clay.

## CHAPTER 7

### LINEAR AND NON-LINEAR SOIL CONSOLIDATION

#### 7.1 INTRODUCTION

Consolidation of a fluid infiltrated soil, commonly refers to the process of soil deformation and excess pore pressure dissipation due to unsteady fluid flow through the pores of the soil.

Terzaghi (1923) formulated the one-dimensional\* consolidation theory to rationalize observations of time-dependent settlements of soils. His theory still represents the backbone of consolidation analyses in geotechnical engineering and is based on the assumption that, at any time, the strain in the soil is proportional to the change of the corresponding effective stress, which is assumed to be equal to the pore pressure already dissipated. To avoid the oversimplification of one-dimensionality, Rendulic (1936) formulated a three-dimensional consolidation theory based on the assumption that the mean total stress  $\sigma$  does not change during consolidation. This assumption uncouples the equations governing consolidation and thus, the pore pressure dissipation profiles can be computed without considering the associated soil deformation and the changes of the effective stresses during consolidation. Rendulic's (or uncoupled) consolidation theory, has limited

---

\* for the case when lateral strains are prevented, i.e., for an oedometer type situation.



applications in practical problems mainly because of the assumption that  $\sigma$  is constant during consolidation. For example, the theory cannot predict the so-called Mandel-Cryer effect (Mandel, 1953, Cryer, 1963) which causes an increase in the pore pressure at early times and has been observed experimentally during consolidation of a spherical sample (Gibson et al, 1963).

Biot (1935) formulated a general (coupled) linear, elastic, isotropic three-dimensional consolidation theory and later refined it to include cross-anisotropic, linear, elastic soils and compressible pore fluids (Biot, 1941, 1955, 1956). Schiffman et al (1969) used Biot's theory to investigate the plane strain consolidation under a flexible strip footing resting on a linear isotropic half-space and found that significant Mandel-Cryer effects take place under the load and close to the surface. These effects, however, decrease in magnitude when (i) the permeability of the soil decreases\* and (ii) the drained Poisson ratio increases. Viggiani (1970) and Davis and Poulos (1970) show that in a wide range of practical problems and, except for the occurrence of the Mandel-Cryer effect during the early stages of consolidation, Rendulic's theory predicts fairly well the pore pressure dissipation profiles but has serious limitations in predicting the changes of the effective stresses during consolidation. Hence, in

---

\* thus, they are very significant in sands

problems where the changes of the effective stresses (rather than the pore pressures) are of main interest\*, Biot's (coupled) consolidation theory should be used. Furthermore, Rendulic's theory should not be used in studying consolidation of non-linear soils because, the basic assumption of the theory (i.e.,  $\sigma = \text{constant}$ ) does not justify any sophistication in the constitutive description of the soil. Sills (1975) showed that Biot's and Rendulic's consolidation theories give the same governing equations for a class of problems that includes one-dimensional linear consolidation (Terzaghi, 1923) and consolidation around spherical and cylindrical cavities in a linear isotropic soil extending to infinity.

---

\* as in the problem of consolidation around pile shafts

## 7.2 BIOT'S THEORY OF CONSOLIDATION

### 7.2.1 GENERAL

Section 7.2 presents a modern version of Biot's Theory of Consolidation that can be used to develop a numerical scheme for the solution of non-linear consolidation problems via the Finite Element Method. Soil consolidation is governed by the conservation laws of Mechanics which are\*:

- (i) The Conservation of Momentum and,
- (ii) The Conservation of Mass.

In the presentation of the theory it is assumed that:

- (i) The soil is saturated, i.e., air and other gases are not present in the pores.
- (ii) Soil deformation is associated with infinitesimal strains and rotations, i.e., geometric non-linearities are neglected. However, non-linearities resulting from the constitutive law are included.
- (iii) Soil deformation and pore fluid flow occur under quasi-static conditions, i.e., inertia forces are neglected.
- (iv) Consolidation occurs under isothermal conditions, which means that the conservation of energy law is redundant.

---

\* in the case of isothermal deformation

The following sections study the conservation laws for the case of soil consolidation, using the standard Soil Mechanics sign convention, i.e., compressive stresses, strains and pore pressures are positive.

### 7.2.2 THE CONSERVATION OF MOMENTUM

The Conservation of Momentum Law gives the stress equilibrium equations which have the following tensorial form (e.g., see Malvern, 1969):

$$\underline{\nabla} \cdot \underline{\sigma} + \underline{\hat{f}} = \underline{0} \quad (7.1)$$

at each point in the volume  $V$  occupied by the soil under consolidation, where,  $\underline{\sigma}$  is the total stress tensor,  $(\underline{\nabla} \cdot)$  is the divergence operator and  $\underline{\hat{f}}$  is the vector of the prescribed body forces per unit volume of soil. Using Terzaghi's effective stress principle (Terzaghi, 1973), the total stress ( $\underline{\sigma}$ ) can be decomposed in the effective stress ( $\underline{\bar{\sigma}}$ ) and the pore pressure ( $p$ ):

$$\underline{\sigma} = \underline{\bar{\sigma}} + p\underline{I} \quad (7.2)$$

where  $\underline{I}$  is the unit isotropic second order tensor (Kronecker delta).

The Boundary Conditions associated with the stress equilibrium equations are:

### 1. Essential Boundary Conditions:

The Essential Boundary Conditions prescribe the values of the soil displacement  $\underline{u}$  on a certain part of the total boundary  $S$  (denoted by  $S_u$ ), i.e.:

$$\underline{u} = \hat{\underline{u}} \quad (7.3)$$

where  $\hat{\underline{u}}$  are the prescribed values of the displacement on  $S_u$ .

### 2. Natural Boundary Conditions:

The Natural Boundary Conditions prescribe the values of the surface traction vector  $\underline{T}$  on the remaining part of the total boundary  $S$  (denoted by  $S_\sigma \equiv S - S_u$ ), i.e.:

$$\underline{n} \cdot \underline{\sigma} = \hat{\underline{T}} \quad (7.4)$$

where  $\hat{\underline{T}}$  are the prescribed values of the surface traction on an infinitesimal element of  $S_\sigma$  with unit normal vector  $\underline{n}$ .

#### 7.2.3 THE CONSERVATION OF MASS

In the case of a Lagrangian description of the deformation process, the Mass Conservation Law is automatically satisfied for one-phase materials (e.g. metals) because, following the motion of the material elements, no mass can be "lost". For soils, however, following the motion of the soil skeleton, the Mass Conservation Law is required to express the mass balance for the pore fluid as it moves inside the pores (rela-

tive to the soil skeleton). More specifically, the Mass Conservation Law suggests that the time rate of decrease of the pore fluid mass in a volume  $V$  of soil, is equal to the pore fluid mass flowing through the surface  $S$  of the volume  $V$  per unit time, i.e.:

$$-\frac{\partial}{\partial t} \int_V m dV = \int_S \underline{n} \cdot \underline{q} dS \quad (7.5)$$

where:

$m$  is the fluid mass content, defined as the mass of pore fluid per unit volume of soil, i.e.:

$$m = \rho \eta \quad (7.6)$$

where  $\rho$  is the pore fluid density and  $\eta$  is the soil porosity.

$\underline{n}$  is the unit vector normal to the element  $dS$  of the surface  $S$  and,

$\underline{q}$  is the fluid mass flux vector which is related to the velocity  $\underline{v}$  of the pore fluid with respect to the soil skeleton by the equation (see Appendix D):

$$\underline{q} = \rho \underline{v} \quad (7.7)$$

Using the divergence theorem:

$$\int_S \underline{n} \cdot \underline{q} \, dS = \int_V \underline{\nabla} \cdot \underline{q} \, dV \quad (7.8)$$

and combining with Eq. 7.5 for an arbitrary volume  $V$  of soil, we get:

$$\underline{\nabla} \cdot \underline{q} + \frac{\partial m}{\partial t} = 0 \quad (7.9)$$

which is the differential form of the mass conservation equation for saturated soils.

The pore pressure ( $p$ ) can be introduced in Eq. 7.9 since, the fluid flux ( $\underline{q}$ ) is caused by the gradient of the excess pore pressure  $\underline{\nabla}(p - p_0)$  where,  $p_0$  is the ambient (hydrostatic) pore pressure. Darcy's law gives the simplest possible (i.e., linear) form of such a relationship:

$$\underline{q} = - \frac{1}{g} \underline{k} \cdot \underline{\nabla}(p - p_0) \quad (7.10)$$

where  $g$  is the acceleration of gravity and  $\underline{k}$  is a second order symmetric permeability tensor\*. Combining Eqs. 7.9 and 7.10 we get:

$$\underline{\nabla} \cdot \{ \underline{k} \cdot \underline{\nabla}(p - p_0) \} = g \frac{\partial m}{\partial t} \quad (7.11)$$

---

\* The components of the permeability tensor have dimensions: length/time.

which is a form of the mass conservation equation valid for spatially variable permeability as well as for compressible soil particles and pore fluids.

The Boundary Conditions associated with the mass conservation equation (Eq. 7.11) are:

1. Essential Boundary Conditions:

The Essential Boundary Conditions prescribe the values of the pore pressure on a certain part of the total boundary  $S$  (denoted by  $S_p$ ), i.e.:

$$p = \hat{p} \quad (7.12)$$

where  $\hat{p}$  are the prescribed values of the pore pressure on  $S_p$ .

2. Natural Boundary Conditions:

The Natural Boundary Conditions prescribe the values of the normal component  $q_n \equiv \underline{n} \cdot \underline{q}$  of the fluid flux on the remaining part of the total boundary  $S$  (denoted by  $S_q \equiv S - S_p$ ), i.e., using Eq. 7.10:

$$\underline{n} \cdot \underline{k} \cdot \underline{\nabla}(p - p_0) = -g \hat{q}_n \quad (7.13)$$

where  $\hat{q}_n$  are the prescribed values of  $q_n$  on  $S_q$ .

In the case of soft soils (e.g., clays), the compressibility of the soil skeleton is much larger than the compressibility of both the soil particles and the pore fluid and thus,



the soil particles and the pore fluid can be assumed incompressible\*. This means that:

$$\epsilon_s = \frac{\partial \rho}{\partial t} = 0 \quad (7.14)$$

where  $\epsilon_s$  is the volumetric strain of the soil particles. Using the chain rule of differentiation in Eq. 7.6 we get:

$$\frac{\partial m}{\partial t} = \eta \frac{\partial \rho}{\partial t} + \rho \frac{\partial \eta}{\partial t} = \eta \frac{\partial \rho}{\partial t} + \rho \left\{ (1 - \eta) \frac{\partial \epsilon_s}{\partial t} - \frac{\partial \epsilon}{\partial t} \right\} \quad (7.15)$$

where  $\partial \epsilon / \partial t \equiv \dot{\epsilon} \equiv \dot{\underline{\underline{\epsilon}}}$  is the volumetric strain rate of the soil skeleton. Combining Eqs. 7.14 and 7.15 we get:

$$\frac{\partial m}{\partial t} = -\rho \dot{\epsilon} \quad (7.16)$$

which relates  $m$  and  $\dot{\epsilon}$  in the case of incompressible soil particles and pore fluid. Combining Eqs. 7.16 and 7.11 we get the following form of the mass conservation equation, valid for incompressible soil constituents (i.e., particles and fluid):

$$\underline{\underline{\nabla}} \cdot \{ \underline{\underline{k}} \cdot \underline{\underline{\nabla}}(p - p_0) \} = -\rho g \dot{\epsilon} \quad (7.17)$$

Equation 7.17 cannot be solved for the pore pressure  $p$  because, the evolution of the pore pressure field is coupled with the

---

\* i.e., Skempton's B parameter (Skempton, 1954) is equal to unity.

deformation variables (since the volumetric strain rate appears in Eq. 7.17). Thus, the conservation of mass (Eq. 7.17) and the conservation of momentum (Eq. 7.1) must be solved simultaneously and in conjunction with an appropriate constitutive law describing the stress-strain behavior of the soil skeleton.

#### 7.2.4 RENDULIC'S (1936) CONSOLIDATION THEORY

In the case of a linear isotropic soil:

$$\dot{\epsilon} = \frac{1}{K} \dot{\bar{\sigma}} = \frac{1}{K} (\dot{\sigma} - \dot{p}) \quad (7.18)$$

where  $\dot{\bar{\sigma}}$  is the time rate of change of the mean effective stress and  $K$  is the (elastic) bulk modulus of the soil skeleton (i.e. the drained bulk modulus). Rendulic (1936), assumed that the mean total stress  $\sigma$  does not change during consolidation, i.e.:

$$\dot{\sigma} = 0 \quad (7.19)$$

Thus, combining Eqs. 7.19, 7.18 and 7.17 we get:

$$\frac{K}{\rho g} \nabla \cdot \{ \underline{k} \cdot \nabla (p - p_0) \} = \frac{\partial p}{\partial t} \quad (7.20)$$

which is the equation governing soil consolidation according to Rendulic's theory. The pore pressure  $p$  is the only unknown in Eq. 7.20 and hence, it can be solved (with the appropriate boundary and initial conditions on  $p$ ) without con-

sidering the associated soil deformations and stress changes, i.e., the pore pressure is not coupled to soil deformation. In the special case of spatially constant and isotropic permeability (i.e.,  $k = k_I$ ), Eq. 7.20 gives:

$$c_R \nabla^2 (p - p_0) = \frac{\partial p}{\partial t} \quad (7.21a)$$

where:

$$\nabla^2 \equiv \frac{\partial^2}{\partial x^2} + \frac{\partial^2}{\partial y^2} + \frac{\partial^2}{\partial z^2} \quad (7.21b)$$

is the Laplacian operator and,

$$c_R \equiv \frac{K k}{\rho g} \quad (7.21c)$$

is Rendulic's coefficient of consolidation. Equation 7.21 is the well known Terzaghi-Rendulic equation of consolidation, and is based on Rendulic's simplifying assumption.

### 7.3 AN ANALYTICAL SOLUTION FOR THE LINEAR CONSOLIDATION AROUND PILES

Sills (1975) applied Biot's theory of consolidation in the case of a linear, elastic soil having isotropic and spatially constant moduli and permeability. She specifically studied a class of problems having the following additional features:

- (i) The displacement field is irrotational, i.e., there exists a scalar function such that

$$\underline{\underline{u}} \equiv \underline{\underline{\nabla}} \phi \quad (7.22)$$

- (ii) The soil extends to infinity, and
- (iii) The body forces are constant during consolidation.

For these problems it can be shown\* that the mass conservation equation (Eq. 7.17) uncouples (i.e., it can be solved for  $p$ ) because the volumetric strain rate ( $\dot{\epsilon}$ ) can be expressed in terms of  $\dot{p}$  without Rendulic's simplifying assumption. The resulting equation for the pore pressure is:

$$c \nabla^2 (p - p_0) = \frac{\partial p}{\partial t} \quad (7.23a)$$

where\*\*

$$c \equiv \frac{3(1 - \bar{\nu})}{(1 + \bar{\nu})} \left( \frac{K k}{\rho g} \right) = \frac{3(1 - \bar{\nu})}{(1 + \bar{\nu})} c_R \quad (7.23b)$$

---

\*The proof is given in Appendix E.

\*\* $\bar{\nu}$  is the drained Poisson's ratio

i.e., Eq. 7.23 has the same form as Eq. 7.21 (obtained by using Rendulic's assumption) but introduces a different coefficient of consolidation ( $c$  instead of  $c_R$ ). For  $\bar{v} = 0.25$  (say), Eq. 7.23b gives:

$$c_R/c = 0.56$$

which means that Rendulic's theory underestimates the coefficient of consolidation by 44% (for  $\bar{v} = 0.25$ ). Evidently, the difference is due to Rendulic's assumption which is not realistic at least for the problems studied by Sills (1975).

The problem of the radial consolidation in a linear, isotropic, elastic soil\* with isotropic and spatially constant permeability around a long cylindrical vertical pile, fulfills the requirements of the analysis by Sills (1975) since,

- (i) The radial component of the displacement field is the only non-vanishing component and thus, the displacement field is irrotational.
- (ii) The soil extends to infinity and,
- (iii) Gravity forces (i.e., the only body forces applied) do not vary during consolidation.

In this case, the governing field equation (Eq. 7.23) can be written in cylindrical coordinates as,

---

\* extending to infinity

$$c \left[ \frac{\partial^2 p}{\partial r^2} + \frac{1}{r} \frac{\partial p}{\partial r} \right] = \frac{\partial p}{\partial t} \quad (7.24a)$$

where,  $r$  is the radial coordinate ( $r_0 \leq r < \infty$ ) and  $r_0$  is the pile radius. Equation 7.24a is subject to the following boundary conditions:

(i) Free drainage at infinity, i.e.,

$$p = p_0 \text{ at } r = \infty \quad (7.24b)$$

(ii) Impermeable pile, i.e.,

$$\frac{\partial p}{\partial r} = 0 \text{ at } r = r_0 \quad (7.24c)$$

Appendix F presents the closed form solution for the normalized pore pressure

$$P(R, T) \equiv [p(r, t) - p_0] / [p(r_0, 0^+) - p_0] \quad (7.25a)$$

where,

$$R \equiv r/r_0 \quad (7.25b)$$

is the normalized radius and,

$$T \equiv ct/r_0^2 \quad (7.25c)$$

is the dimensionless time factor, for any arbitrary initial distribution of the pore pressure given by the function

$$f(R) \equiv [p(r,0^+) - p_0]/[p(r_0,0^+) - p_0] \quad (7.26)$$

The solution involves zero and first order Bessel functions of the first kind (see, e.g., Abramowitz and Stegun, 1965, pp. 369-370) and requires the numerical evaluation of an infinite integral (see, e.g., Berezin and Zhidkov, 1965).

The limitations of the analytical solution are obvious: the soil is assumed linear, elastic and isotropic, which, as shown in Chapter 5 is not a realistic assumption for soils. Thus, the main reason for presenting the analytical solution is to check the results\* of the Finite Element numerical scheme discussed in Section 7.4 rather than to obtain realistic predictions for the pore pressure dissipation rates.

---

\* i.e., rate of convergence, accuracy, number of elements required, etc.

7.4 A WEIGHTED RESIDUALS FORMULATION FOR  
NON-LINEAR CONSOLIDATION AND ITS  
FINITE ELEMENT IMPLEMENTATION

7.4.1 INTRODUCTION

It is a well established experimental fact (see, e.g., Chapter 5) that the stress-strain behavior of soils is non-linear and inelastic. Thus, sophisticated non-linear soil models are required in the solution of practical problems (e.g., soil consolidation). When non-linear soil models are used, analytical solutions of most practical boundary value problems are intractable and thus, numerical solutions are necessary. The Finite Element method, which has proved to be a powerful tool in the solution of linear and non-linear Solid Mechanics problems, can also be used to solve soil consolidation problems. Kavvadas and Baligh (1980) review the various methods that have been used to develop Finite Element schemes for soil consolidation: Sandhu and Wilson (1969) used a Gurtin type Variational Principle (Gurtin, 1964) and Booker (1973) used a Variational Principle involving the Laplace transforms of the field variables. In the present study, it proves convenient to adopt\* an approach based on the method of Weighted Residuals (Connor and Brebbia, 1976).

---

\* A version of this method was used by Small, Booker and Davis (1976).



## 7.4.2 A WEIGHTED RESIDUALS FORMULATION FOR SOIL CONSOLIDATION

### 7.4.2.1 Definitions

Consider a function  $f$  defined in the domain  $V$  and a differential equation

$$L(f) = 0 \quad (7.27)$$

for the function  $f$  in  $V$ . We say that the differential equation 7.27 is weighted\* with respect to arbitrary variations of another function  $g$  (also defined in the domain  $V$ ) when:

$$\int_V L(f) \cdot \delta g \cdot dV = 0 \quad (7.28)$$

where  $\delta(\dots)$  denotes the variation of the function following it.

### 7.4.2.2 Conservation of Momentum

A Weighted Residuals Variational form of the Conservation of Momentum Law is obtained if the Equilibrium Equations (Eq. 7.1) and their Natural Boundary Conditions (Eq. 7.4) are weighted with respect to arbitrary\*\* variations  $\delta \underline{u}$  of the displacement field  $\underline{u}$ , i.e.:

---

\* see Connor and Brebbia (1976)

\*\* The displacement field  $\underline{u}$  needs only to satisfy the Essential Boundary conditions (Eq. 7.3), i.e.:

$$\delta \underline{u} = 0 \text{ on } S_u \quad (7.29)$$

$$\int_V [\underline{\nabla} \cdot \underline{\sigma} + \underline{\hat{f}}] \cdot \delta \underline{u} \, dV + \int_{S_\sigma} [\underline{\hat{T}} - \underline{n} \cdot \underline{\sigma}] \cdot \delta \underline{u} \, dS = 0 \quad (7.30)$$

Applying Gauss' theorem,

$$\int_V (\underline{\nabla} \cdot \underline{\sigma}) \cdot \delta \underline{u} \, dV = \int_S \underline{n} \cdot \underline{\sigma} \cdot \delta \underline{u} \, dS - \int_V \underline{\sigma} : \underline{\nabla}(\delta \underline{u}) \, dV \quad (7.31)$$

since,

$$\underline{\sigma} : \underline{\nabla}(\delta \underline{u}) = \underline{\sigma} : \delta \underline{\varepsilon} \quad (7.32)$$

and combining Eqs. 7.29 to 7.32 we get:

$$\int_V \underline{\sigma} : \delta \underline{\varepsilon} \, dV = \int_V \underline{\hat{f}} \cdot \delta \underline{u} \, dV + \int_{S_\sigma} \underline{\hat{T}} \cdot \delta \underline{u} \, dS \quad (7.33)$$

Finally, using Terzaghi's effective stress principle (Eq. 7.2), we get:

$$\int_V \underline{\bar{\sigma}} : \delta \underline{\varepsilon} \, dV + \int_V p \, \delta \varepsilon \, dV = \int_V \underline{\hat{f}} \cdot \delta \underline{u} \, dV + \int_{S_\sigma} \underline{\hat{T}} \cdot \delta \underline{u} \, dS \quad (7.34)$$

where  $\delta \varepsilon$  is the variation of the volumetric strain. Equation 7.34 is the Principle of Virtual Work for a saturated soil. The left-hand-side member, is the internal virtual work and the right-hand-side member is the virtual work of the body forces and the surface tractions.

Specifically in the case of soil consolidation due to an initial known pore pressure field under constant body forces and surface tractions, the Principle of Virtual Work (Eq. 7.34)

can be further simplified: Applying Eq. 7.34 for the initial state (with known effective stresses  $\bar{\sigma}^0$  and pore pressures  $p^0$ ) and for an (arbitrary) state at time  $t$  and, comparing the two forms we get:

$$\int_V \bar{\sigma} : \delta \underline{\underline{\epsilon}} dV + \int_V p \delta \epsilon dV = \int_V \bar{\sigma}^0 : \delta \underline{\underline{\epsilon}} dV + \int_V p^0 \delta \epsilon dV \quad (7.35)$$

or,

$$\int_V \bar{\sigma}^0 : \delta \underline{\underline{\epsilon}} dV + \int_V p^0 \delta \epsilon dV = 0 \quad (7.36)$$

where,

$$\bar{\sigma}^0 \equiv \bar{\sigma} - \bar{\sigma}^0 \quad (7.37a)$$

$$p^0 \equiv p - p^0 \quad (7.37b)$$

are the effective stress and pore pressure relative to the initial state (at  $t = 0$ ).

#### 7.4.2.3 Conservation of Mass

A Weighted Residuals Variational form of the Conservation of Mass Law is obtained if the mass conservation equation\* (Eq. 7.17) and its Natural Boundary Conditions (Eq. 7.13) are

---

\* Eq. 7.17 is valid for incompressible soil particles and pore fluid which is a good assumption for soft soils.

weighted with respect to arbitrary\* variations  $\delta p$  of the pore pressure field  $p$ , i.e.:

$$\int_V [\underline{\nabla} \cdot \{ \underline{k} \cdot \underline{\nabla}(p - p_0) \} + \gamma \dot{\varepsilon}] \delta p \, dV - \int_{S_q} [g \hat{q}_n + \underline{n} \cdot \underline{k} \cdot \underline{\nabla}(p - p_0)] \delta p \, dS = 0 \quad (7.39)$$

where  $p_0$  is the ambient (hydrostatic) pore pressure and  $\gamma \equiv \rho g$  is the unit weight of water.

Applying Gauss' theorem,

$$\int_V \underline{\nabla} \cdot \{ \underline{k} \cdot \underline{\nabla}(p - p_0) \} \delta p \, dV = \int_S \underline{n} \cdot \underline{k} \cdot \underline{\nabla}(p - p_0) \delta p \, dS - \int_V \underline{\nabla}(\delta p) \cdot \underline{k} \cdot \underline{\nabla}(p - p_0) \, dV \quad (7.40)$$

and combining Eqs. 7.38, 7.39 and 7.40 we get:

$$\int_V \dot{\varepsilon} \delta p \, dV - \frac{1}{\gamma} \int_V \underline{\nabla}(\delta p) \cdot \underline{k} \cdot \underline{\nabla}(p - p_0) \, dV = \frac{1}{\rho} \int_{S_q} \hat{q}_n \delta p \, dS \quad (7.41)$$

In most practical problems, the boundary  $S_q$  where the fluid flux is prescribed, is impermeable (i.e.,  $\hat{q}_n = 0$ ) and then,

---

\* they only need to satisfy the Essential Boundary Conditions (Eq. 7.12), i.e.:

$$\delta p = 0 \text{ on } S_p \quad (7.38)$$

Eq. 7.41 gives:

$$\int_V \dot{\epsilon} \delta p \, dV - \frac{1}{\gamma} \int_V \underline{\nabla}(\delta p) \cdot \underline{k} \cdot \underline{\nabla}(p - p_0) \, dV = 0 \quad (7.42)$$

The pair of Eqs. 7.36 and 7.42 fully describe soil consolidation\* due to an initial known pore pressure field, under constant body forces and surface tractions and will be used to develop a numerical solution scheme via the Finite Element method.

In the development of the Finite Element scheme, the matrix form of Eqs. 7.36 and 7.42 is more convenient than their tensorial form which has been used up to now for efficiency in the mathematical expressions of the field equations. Equations 7.36 and 7.42 can be written in matrix form as follows:

$$\int_V \delta \underline{\epsilon}^T \underline{\sigma} \, dV + \int_V \delta \epsilon \, p \, dV = 0 \quad (7.43a)$$

$$\int_V \delta p \, \dot{\epsilon} \, dV - \frac{1}{\gamma} \int_V [\underline{\nabla}(\delta p)]^T \underline{k} [\underline{\nabla}(p - p_0)] \, dV = 0 \quad (7.43b)$$

where, matrices are denoted with underbars, using the same symbol as in their tensorial representation and, right superscript T denotes the transpose of the matrix. Table 7.1

---

\* of a soil with incompressible constituents and impermeable  $S_q$  boundary

presents the Cartesian form of the various matrices describing the field quantities above.

#### 7.4.3 THE FINITE ELEMENT IMPLEMENTATION

A Standard Isoparametric Finite Element interpolation scheme is introduced (see e.g., Bathe and Wilson, 1976) for the displacement and the pore pressure fields:

$$\underline{u} = \underline{N} \underline{U} \quad (7.44a)$$

$$p = \underline{L} \underline{P} \quad (7.44b)$$

where,  $\underline{U}$  and  $\underline{P}$  are column matrices storing the values of the displacement components and the pore pressure (respectively) at the nodes of the Finite Elements (in which the soil region is discretized) and,  $\underline{N}$  and  $\underline{L}$  are "shape functions" relating the values of the displacements and pore pressure (respectively) at the nodes of the Finite Elements with the corresponding values at any point in the soil region under consideration.

Appendix G presents the details of the proposed Finite Element scheme and more specifically:

- (i) It gives the definitions of the matrices that appear in the calculations.
- (ii) It presents the numerical scheme that is used to march the solution in time. A Crank-Nickolson type integration scheme\*

---

\* see, e.g., Bathe and Wilson (1976)

that introduces a parameter  $\alpha$  ( $0 \leq \alpha \leq 1$ ) is used. The scheme is purely explicit if  $\alpha = 0$  and purely implicit if  $\alpha = 1$ . Booker and Small (1975) studied the stability of this time integration scheme for the various values of  $\alpha$ , and concluded that the scheme is unconditionally stable for  $\alpha \geq 1/2$ . For  $\alpha < 1/2$  the scheme is only conditionally stable, which means that, there is an upper limit of the time step size\*  $\Delta t$  which when exceeded, makes the marching scheme unstable. On the contrary, an unconditionally stable scheme has no restrictions on the maximum time step size for stability reasons. However, in all schemes, the time step size should be sufficiently small to give accurate results. For this reason, the analytical closed form solution of the linear problem\*\* can be used as a guide in deciding on the accuracy of the results of the Finite Element solution and thus help us decide on the size of the time step  $\Delta t$  to be used in the algorithm.

---

\* depending on the properties of the soil, the geometry of the problem and the size of the finite elements

\*\* presented in Section 7.3

(iii) It describes the iterative scheme that is used to achieve equilibrium of stresses and fluxes in each time step of the non-linear algorithm. The approach used is basically a "residual force" method\* where, in each iteration step, the out-of-balance residual forces act as additional (fictitious) nodal forces\*\* required to bring the assumed displacement and pore pressure pattern in nodal equilibrium. Thus, we get improved estimates of the displacement and pore pressure fields that will be used as out-of-balance forces in the next iteration step until convergence is achieved when the magnitude of the out-of-balance forces does not exceed a specific tolerance. In computing the improved estimates of the displacement and pore pressure fields, a constant, linear, positive definite stiffness matrix  $\underline{K}^e$  is used. Nayak and Zienkiewicz (1972) suggest that the advantages of such a constant stiffness matrix are not only economic\*\*\*

---

\* e.g., Argyris and Scharpf (1969) or Nayak and Zienkiewicz (1972)

\*\* in the right-hand-side of the equation

\*\*\* In fact, the stiffness matrix need only be triangularized once and then the solution in each iteration step is obtained by back-substitution.



but also permit the computation to include strain softening materials and non-associated flow rules. More specifically, for the problem of consolidation around piles, we think that the use of a constant elastic stiffness matrix has further advantages because, as it will be shown in Chapter 8, a certain part of the soil\* is loading plastically (i.e., it has soft response) and the remaining part of the soil is unloading elastically (i.e., it has a stiff response) during consolidation. This kind of behavior can cause problems in formulations based on the tangent stiffness.

Appendix G also presents the steps that need to be followed in the solution of the consolidation problem. The set of equations that need to be solved in each iteration of each time step is (see Eq. G.14):

$$\begin{bmatrix} \underline{\underline{K}}^e & \underline{\underline{H}} \\ \underline{\underline{H}}^T & -\alpha \Delta t \underline{\underline{k}} \end{bmatrix} \begin{Bmatrix} d\underline{\underline{U}}^{(i)} \\ \Delta \underline{\underline{P}}^{(i)} \end{Bmatrix} = \begin{Bmatrix} \underline{\underline{0}} \\ \Delta t \underline{\underline{k}} \underline{\underline{t}}_P \end{Bmatrix} - \begin{Bmatrix} \int_V \underline{\underline{B}}^T \Delta \underline{\underline{\sigma}}^{(i-1)} dV \\ \underline{\underline{H}}^T \Delta \underline{\underline{U}}^{(i-1)} \end{Bmatrix} \quad (7.45)$$

---

\* close to the pile

with unknowns  $\underline{dU}^{(i)}$  and  $\underline{\Delta P}^{(i)}$ .

The ordering of the displacement and pore pressure degrees of freedom does not affect the accuracy, but significantly influences the efficiency of the algorithm. The bandwidth should in general be kept at a minimum. Submatrices  $\underline{K}^e$  and  $\underline{\bar{K}}$  are in general close-coupled\* whereas, submatrix  $\underline{H}$  introduces non-zero elements far away from the diagonal. In order to decrease the bandwidth, an optimized ordering of the degrees of freedom must be adopted. Equation 7.45 has grouped all the displacement and pore pressure degrees of freedom separately. This facilitates the assembly of the global stiffness matrix but wastes a lot of storage by storing useless zeroes. A more efficient ordering sequence can be obtained if each pore pressure degree of freedom is ordered immediately after the displacement degrees that are coupled with it.

The choice of the finite elements also needs special attention. Since effective stresses and pore pressures are additive quantities\*\*, it seems reasonable that their polynomial expansions in each element should be of the same order. However, effective stresses result from the displacements by differentiation with respect to the spatial coordinates. So, if the displacement expansions in each element are one order higher than the pore pressure expansions, we can achieve

---

\* i.e., elements far away from the diagonal are zero

\*\* their sum is the total stress

the same order of approximation for both the stresses and the pore pressures.

Sandhu and Wilson (1969) used a composite element consisting of a six-node triangle for the displacement expansion and having linear expansion for the pore pressure. Hwang et al (1971) and Desai and Saxena (1977) used the same type of element in linear problems. Yokoo et al (1971) employed several different elements, all of which used the same expansion for the displacements and for the pore pressures and thus do not conform with the remarks made above. They studied linear problems and gave examples for a two-node bar element, a three-node axisymmetric ring element and a four-node rectangular element.

#### 7.4.4 FINITE ELEMENT IMPLEMENTATION FOR THE RADIAL CONSOLIDATION AROUND PILES

Radial consolidation around a cylindrical pile can be studied as a one-dimensional problem because of axisymmetric and plane strain conditions. In the Finite Element implementation, a three-node bar element is used in interpolating displacements and a two-node bar element in the pore pressure interpolations, which gives equal order of expansions for the pore pressure and the effective stresses. Table 7.2 presents the basic "shape functions" for this choice of elements, where  $s$  ( $-1 \leq s \leq 1$ ) is the transformed radial coordinate, related to the natural radial coordinate  $r$  by:

$$r = \frac{\ell}{2} s + r_M \quad (7.46)$$

where  $\ell$  is the length and  $r_M$  the natural radial coordinate of the mid-node of each Finite Element. Using the basic matrices in Table 7.2, the matrices  $\underline{H}$ ,  $\underline{\bar{k}}$  and  $\underline{K}^e$  can be evaluated numerically using Eqs. G.4a, G.4b and G.10 respectively, where the volume integrals extend over the length of the element, i.e.:

$$dV = \frac{1}{2} r \ell ds \quad (7.47)$$

for  $-1 \leq s \leq 1$ .

Chapter 8 presents predictions of the pore pressure dissipation rates and the effective stress changes for radial consolidation around a cylindrical impermeable pile due to a known initial excess pore pressure distribution, computed via the Finite Element scheme discussed above, using 45 elements, and a purely implicit scheme (i.e.,  $\alpha = 1$ ).

<p><u>Stress:</u></p> $\underline{\sigma}^T \equiv \{ \bar{\sigma}_x \quad \bar{\sigma}_y \quad \bar{\sigma}_z \quad \bar{\sigma}_{yz} \quad \bar{\sigma}_{zx} \quad \bar{\sigma}_{xy} \}$
<p><u>Strain:</u></p> $\delta \underline{\epsilon}^T \equiv \{ \delta \epsilon_x \quad \delta \epsilon_y \quad \delta \epsilon_z \quad \delta \gamma_{yz} \quad \delta \gamma_{zx} \quad \delta \gamma_{xy} \}$
<p><u>Pore Pressure Gradient:</u></p> $(\underline{\nabla}p)^T \equiv \left\{ \frac{\partial p}{\partial x} \quad \frac{\partial p}{\partial y} \quad \frac{\partial p}{\partial z} \right\}$
<p><u>Displacement:</u></p> $\underline{u}^T \equiv \{ u_x \quad u_y \quad u_z \}$
<p><u>Permeability:</u></p> $\underline{k} \equiv \begin{bmatrix} k_x & & & & & \\ & k_{xy} & & & & \\ & & k_y & & & \\ & & & & & \\ & & & & & \\ & & & & & k_{zz} \end{bmatrix}$

Table 7.1: Cartesian Components of the Various Matrices Describing Field Quantities

$$\underline{N} = \left\{ \frac{1}{2} s(s-1) \quad -(s+1)(s-1) \quad \frac{1}{2} s(s+1) \right\}$$

$$\underline{B} = \begin{bmatrix} \frac{1}{\ell} (2s-1) & -\frac{4}{\ell} s & \frac{1}{\ell} (2s+1) \\ \frac{1}{2r} (s-1)s & -\frac{1}{r} (s+1)(s-1) & \frac{1}{2r} (s+1)s \end{bmatrix}$$

$$\underline{D} = \left\{ \frac{1}{\ell} (2s-1) + \frac{1}{2r} (s-1)s \quad -\frac{4}{\ell} s - \frac{1}{r} (s+1)(s-1) \right. \\ \left. \frac{1}{\ell} (2s+1) + \frac{1}{2r} (s+1)s \right\}$$

$$\underline{L} = \left\{ \frac{1}{2} (1-s) \quad \frac{1}{2} (1+s) \right\}$$

$$\underline{M} = \left\{ -\frac{1}{\ell} \quad \frac{1}{\ell} \right\}$$

**Table 7.2:** Basic Shape Functions for  
One-Dimensional Bar Elements

## CHAPTER 8

### RADIAL CONSOLIDATION ANALYSES AROUND A PILE DRIVEN IN BOSTON BLUE CLAY

#### 8.1 INTRODUCTION

This Chapter performs linear and non-linear radial (one-dimensional) consolidation analyses for a pile driven in normally consolidated and slightly overconsolidated\* Boston Blue Clay (BBC) using the following soil constitutive models:

- (i) The Linear Elastic Isotropic model.
- (ii) The Modified Cam-Clay (MCC) model.
- (iii) The model proposed in Chapter 4.

and initial stress and excess pore pressure distributions obtained by means of (see Chapter 6):

- (i) The Undrained Cylindrical Cavity Expansion method
- (ii) The Strain Path method.

Solutions are obtained by means of a Finite Element computer program (developed by the author for the purposes of this thesis) based on the non-linear consolidation algorithm described in Chapter 7. Appendix H presents a User's Manual and a complete listing of this program. Table 8.1 shows the radial

---

\* OCR=1.20 and 1.35

coordinates of the corner nodes of the Finite Elements\* used to obtain the results presented in this Chapter.

The Finite Element computer program is checked against the closed form analytical solution for the linear consolidation around a cylindrical pile discussed in Section 7.3. Figure 8.1 presents the Finite Element prediction of the excess pore pressure dissipation and the radial stress changes at the pile wall during linear\*\* consolidation using the initial stress and excess pore pressure distributions computed via the Strain Path method (in conjunction with the proposed model) for normally consolidated BBC. The maximum error of the Finite Element solution\*\*\* is less than 0.1% at all times, indicating that the Finite Element scheme is sufficiently accurate. Figure 8.1 shows that the total radial stress at the pile wall remains constant during consolidation\*\*\*\* which means that, at each time, the change of the radial effective stress at the pile wall is equal to the pore pressure already dissipated. Hence, after consolidation is completed, the radial effective stress at the pile wall is increased by an amount equal to the excess

---

\* for details on the type of the Finite Elements used, see Chapter 7

\*\* Poisson's ratio equal to 0.2 and

$$K + 4G/3 = 55.8 * \bar{\sigma}_0$$

was used, where  $\bar{\sigma}_0$  is the initial mean effective stress before pile installation

\*\*\* A standard five point Gaussian quadrature was used to compute the integrals appearing in the analytical solution

\*\*\*\* Baligh and Kavvadas (1980) theoretically prove that this is always true in the case of linear consolidation around a cylindrical pile.



pore pressure caused by pile installation. Chapter 2 shows that such a change of the radial effective stress at the pile wall is too high and results in significant overestimation of the bearing capacity of piles. Thus, non-linear consolidation analyses are necessary obtain realistic predictions of the radial effective stress at the pile wall and hence, provide reasonable estimates of the bearing capacity of friction piles in clays. The following Sections of this Chapter present the results of such non-linear consolidation analyses.

## 8.2 NON-LINEAR CONSOLIDATION ANALYSES IN NORMALLY CONSOLIDATED BOSTON BLUE CLAY

Non-linear Finite Element solutions show that during consolidation, the soil around the pile consists of two characteristic regions:

(i) A region close to the pile wall where the soil loads plastically\* i.e., it exhibits a soft response and,

(ii) the remaining region (away from the pile) where the soil unloads elastically\* i.e., it exhibits a stiff response.

The Elasto-Plastic Boundary (i.e., the boundary between the two regions) changes position during consolidation and, in general, moves away from the pile. Figure 8.2a presents the location of the Elasto-Plastic Boundary as a function of the dimensionless equivalent time factor\*\*, predicted according to the MCC and the proposed models for a clay with the properties of normally consolidated BBC. Figure 8.2a shows that the method used to compute the initial stress and excess pore pressure distributions has a significant effect on the predicted positions of the Elasto-Plastic Boundary during consolidation. Consolidation analyses with initial conditions computed via the Strain Path method (denoted with full lines in Fig. 8.1a)

---

\* Section 3.2.2.3 defines 'plastic loading' and 'elastic unloading'.

\*\* it is called 'equivalent' because the vertical effective stress in the soil before pile installation is used as a stiffness measure (see the definition of the equivalent coefficient of consolidation  $c$  in Fig. 8.1)

predict that for time factors less than 0.1-0.3 the whole soil around the pile unloads elastically and, at later times, a certain region close to the pile loads plastically. On the contrary, consolidation analyses with initial conditions computed via the Cavity Expansion method (denoted with dashed lines in Fig. 8.1a) predict that, at all times, a certain region close to the pile wall loads plastically. The differences in the results of these consolidation analyses are due to differences in the initial conditions computed via the Cavity Expansion and the Strain Path methods (see Chapter 6) i.e., to the effect of the pile tip which is neglected by the Cavity Expansion method.

For values of the time factor larger than 0.3, all consolidation analyses predict that the Elasto-Plastic Boundary moves away from the pile and finally stabilizes at 3.5-9.5 times the pile radius depending on the soil model and the method used to compute the initial conditions.

Figure 8.2b presents the location of the Elasto-Plastic Boundary as a function of the time factor, predicted according to the proposed model\* and initial conditions computed via the Strain Path method for various values of the overconsolidation ratio (OCR). The size of the plastic region at large values of the time factor and the values of the time factor when Plasticity is initially induced in the soil increase with increasing values of the OCR.

Figure 8.3 shows the proposed model predictions of the

---

\* for soils with the properties of BBC.

excess pore pressure dissipation and the (total and effective) radial stress changes at the pile wall during consolidation of a soil with the properties of normally consolidated BBC for initial conditions computed via (a) the Cavity Expansion and (b) the Strain Path methods. One can note that:

- (i) The predicted value of the radial effective stress at the pile wall after consolidation is completed is controlled by the method used to compute the initial conditions, since the predicted change of the radial effective stress during consolidation is the same (equal to 0.40) in parts (a) and (b) of Fig. 8.3. Thus, the final values (equal to 0.88 and 0.40) directly reflect the differences between the initial values (equal to 0.49 and 0.0) computed via the Cavity Expansion and the Strain Path methods, respectively.
- (ii) Figure 8.3b shows that for  $T < 0.1$  the radial effective stress at the pile wall increases rapidly and the corresponding total stress only changes slightly, whereas for  $T > 0.1$  the behavior is reversed. This is because the proposed model predicts that Plasticity is only induced for  $T > 0.1$  (see Fig. 8.2a) which means that for  $T < 0.1$  the soil around the pile behaves elastically. However, the elasticity of the proposed model is non-linear\* and thus, although the predicted consolidation curves are similar to the linear

---

\* The elastic moduli of the proposed model are proportional to the mean effective stress which increases during consolidation.

consolidation curves for  $T < 0.1$  (see Fig. 8.1), the total radial stress decreases slightly. For  $T > 0.1$ , the soft plastic zone close to the pile causes a significant decrease of the total radial stress while the rate of increase of the radial effective stress is small.

Figure 8.3a does not show the features described above because, when the initial conditions are computed via the Cavity Expansion method, the proposed model predicts that a soft plastic zone exists close to the pile at all times (see Fig. 8.2a). Thus, the slope of the radial effective stress curve is uniform and the total radial stress decreases significantly even at small values of the time factor.

Figure 8.4 shows the MCC model predictions of the excess pore pressure dissipation and the (total and effective) radial stress changes at the pile wall during consolidation of a soil with the properties of normally consolidated BBC for initial conditions computed via (a) the Cavity Expansion and (b) the Strain Path methods. Figure 8.4b shows that for  $T < 0.3$  the radial effective stress at the pile wall increases rapidly and the corresponding total stress changes only by a small amount, whereas for  $T > 0.3$  both the total and effective radial stresses remain almost constant. This is due to the fact that, the MCC model predicts that Plasticity is only induced for  $T > 0.3$  (see Fig. 8.2a) which means that for  $T < 0.3$  the soil around the pile behaves elastically and thus, remarks similar to those made in the discussion of Fig. 8.3 apply. For  $T > 0.3$  the soft plastic

zone close to the pile tends to cause a decrease of the radial total stress. However, at  $T=0.3$  most of the excess pore pressure has already dissipated and thus, the effect of the development of the plastic zone on the subsequent stress changes is small. Figure 8.4a does not show the features described above for reasons similar to the ones described in the discussion of Fig. 8.3a.

Figures 8.5 and 8.6 show the proposed and MCC model predictions of the excess pore pressure dissipation curves at various time factors during consolidation of a soil with the properties of normally consolidated BBC. One can note that:

- (i) Regardless of the initial shape of the excess pore pressure curve, a zone of almost constant pore pressure develops close to the pile wall at later times due to the fact that the pile is assumed impermeable.
- (ii) The pore pressures predicted by the Cavity Expansion method dissipate faster than those predicted by the Strain Path method because of the larger initial pore pressure gradients close to the pile wall predicted by the Cavity Expansion method.
- (iii) In the region close to the pile (i.e., for distances less than about 6 times the pile radius) the excess pore pressure decreases monotonically during consolidation, whereas in the remaining soil the excess pore pressure first increases and then decreases.

Figure 8.7 presents the proposed model predictions of the radial effective stress changes around a pile (at various time

factors), during consolidation of a soil with the properties of normally consolidated BBC for initial conditions computed via (a) the Cavity Expansion and (b) the Strain Path methods. One can note that:

- (i) In the region close to the pile (i.e., for distances less than 4-6 times the pile radius) the radial effective stress increases, whereas in the remaining soil it decreases during consolidation.
- (ii) At each location, the change of the radial effective stress during consolidation is approximately the same in Figs. 8.7a and 8.7b. Thus, the values of the radial effective stress in the beginning of consolidation control the corresponding values after consolidation is completed which means that, in the region close to the pile the Cavity Expansion method predicts significantly larger radial effective stresses.

Figure 8.8 presents the MCC model predictions of the radial effective stress changes around the pile at various time factors. Figures 8.7 and 8.8 show that, when compared to the proposed model, the MCC model predicts larger changes of the radial effective stress in the region close to the pile, especially when the initial conditions are computed via the Strain Path method. This is mainly because the MCC model predicts that the development of the plastic zone close to the pile\* occurs during the final stages of consolidation,

---

\* which retards further increases of the radial effective stress (see Figs. 8.3 and 8.4)

whereas the proposed model predicts that this plastic zone develops at earlier times (see Fig. 8.2a).

During consolidation, a soil element located at the pile wall is subjected to one-dimensional straining in the radial direction, because the axial and circumferential strains vanish. Figure 8.9 presents (a) the effective stress path\* and (b) the mean effective stress vs volumetric strain curve predicted by the proposed model during one-dimensional straining (in the radial direction) for a soil element located at the pile wall and having the properties of normally consolidated BBC. The initial stress state (point A) is the proposed model prediction of the stress state at the pile wall immediately after pile installation computed via the Strain Path method. Figure 8.9a also shows the Critical State Line corresponding to a friction angle equal to\*\* 38.6°. The initial stress state lies beyond the Critical State Line; because the stress path followed during pile installation involves significant stress reversals which can lead to stress states located inside (or on) the yield surface beyond the Critical State Line. The initial portion of the effective stress path corresponds to unloading in shear and gives small volumetric strains (stiff response). After this initial transition region, the shear stress increases and the effective

---

\*  $\bar{\sigma}_0$  is the mean effective stress in the soil before pile installation. Table 4.1 gives the definitions of the shear stress components  $S_i$ .

\*\* This is the proposed model prediction for the undrained cylindrical cavity expansion mode of deformation



stress path approaches the predicted radial one-dimensional consolidation line\*. After the initial stiff portion of the mean stress vs. volumetric strain curve, the soil yields and the stiffness decreases drastically. Non-linear consolidation analyses performed using the proposed model\*\* predict that, during consolidation, a soil element located at the pile wall follows the effective stress path and the stress-strain curve shown in Fig. 8.9 and, after consolidation is completed, the predicted stress state corresponds to point F which means that:

- (i) The final stress state approximately coincides with the point of minimum shear stress along the effective stress path for one-dimensional straining in the radial direction.
- (ii) At the end of consolidation, the volumetric strain\*\*\* of the soil element located at the pile wall is approximately equal to 6%.

Figure 8.10 presents (a) the effective stress path and (b) the mean effective stress vs. volumetric strain curve predicted by the MCC model during one-dimensional straining in the radial direction for a soil element located at the pile wall and having the properties of normally consolidated BBC. The initial stress state (point A) is the MCC model prediction of the stress state at the pile wall immediately after pile

---

\* This is a straight line through the origin of stresses and corresponds to a friction angle equal to  $17.8^\circ$ .

\*\* and initial conditions computed via the Strain Path method

\*\*\* which is equal to the radial strain

installation computed via the Cavity Expansion method. Figure 8.10a shows that the initial stress state lies on the Critical State Line corresponding to a friction angle equal to\* 51.1°. The initial portion of the effective stress path indicates some unloading in shear and small volumetric strains (stiff response). After this initial transition region, the shear stress increases and the effective stress path approaches the predicted one-dimensional consolidation line\*\*. After the initial stiff portion of the mean stress vs. volumetric strain curve, the soil yields and the stiffness decreases. Non-linear consolidation analyses performed using the MCC model\*\*\* predict that during consolidation, a soil element located at the pile wall follows the effective stress path and the stress-strain curve shown in Fig. 8.10 and, after consolidation is completed, the predicted stress state corresponds to point F which means that:

- (i) The final stress state has almost reached the stress state of a virgin soil sample one-dimensionally consolidated in the horizontal direction. Comparing Figs. 8.9a and 8.10a one can note that the MCC model prediction of the stress state at the pile wall after consolidation is completed, lies closer to the

---

\* This is the MCC model prediction for the undrained cylindrical cavity expansion mode of deformation

\*\* This is a straight line through the origin of stresses and corresponds to a friction angle equal to 15.4°.

\*\*\* and initial conditions computed via the Cavity Expansion method

one-dimensional straining line than the corresponding proposed model prediction. This is mainly because the proposed model needs to reorient the yield surface to the new stress state\*, whereas the yield surface of the MCC model does not change orientation in the effective stress space.

- (ii) After consolidation is completed, the volumetric strain of the soil element located at the pile wall is equal to 3.8% i.e., it is smaller than the proposed model prediction.

---

\* which requires significant straining

### 8.3 NON-LINEAR CONSOLIDATION ANALYSES IN SLIGHTLY OVERCONSOLIDATED BOSTON BLUE CLAY

This Section presents the results of non-linear consolidation analyses far behind the tip of a pile driven in slightly overconsolidated BBC (OCR=1.20 and 1.35), obtained by means of the soil model proposed in Chapter 4 and the initial stress and excess pore pressure distributions computed via the Strain Path method (see Chapter 6).

Section 8.2 discussed that the major portion of the increase of the radial effective stress at the pile wall during consolidation occurs while the soil around the pile is elastic, i.e., before Plasticity is induced in the region close to the pile (see e.g. Figs. 8.3b and 8.2a). Furthermore, Fig. 8.2b shows that the value of the time factor, when Plasticity is initially induced in the soil close to the pile, increases with increasing OCR, which means that the soil remains elastic for a longer period of time. Thus, it is expected that the radial stress at the pile wall after consolidation is completed increases with increasing OCR. Figure 8.11 shows that in fact, the value of the radial stress\* at the pile wall after consolidation is completed increases with increasing OCR\*\* (e.g. it is equal to 0.40, 0.56 and 0.80 for OCR equal to 1.00, 1.20 and 1.35 respectively). One can also notice the abrupt

---

\* normalized with the vertical effective stress in the soil before pile installation

\*\* see Fig. 8.3b for OCR=1

change in the slope of the predicted radial effective stress curve (indicating that Plasticity is induced in the soil close to the pile), which occurs at time factors increasing with increasing OCR\*.

The excess pore pressure dissipation curves predicted for a slightly overconsolidated clay (see Fig. 8.12) have the same characteristics as the dissipation curves predicted for the normally consolidated clay (see Fig. 8.5b), i.e., in a region close to the pile, the excess pore pressure decreases monotonically during consolidation whereas, in the remaining soil, the excess pore pressure first increases and then decreases.

The radial effective stress changes predicted for the slightly overconsolidated clay (see Fig. 8.13) have the same characteristics as the predictions for the normally consolidated clay (see Fig. 8.7b), i.e., in a region close to the pile, the radial effective stress increases during consolidation and, after consolidation is completed, the radial stress at all locations around the pile is approximately equal to the in-situ horizontal stress before pile installation.

Figure 8.14 presents the proposed model predictions for the effective stresses in the soil, after consolidation is completed, for OCR equal to 1.00 and 1.35. One can note that:

- (i) At the pile wall, the vertical stress is the maximum effective stress and, the radial and circumferential are the intermediate and minimum principal stresses,

---

\* also compare to Fig. 8.2b

respectively.

- (ii) The minimum value of the radial effective stress occurs at a distance equal to 2.5-3.0 pile radii and the effect is more pronounced in the overconsolidated clay.

## 8.4 COMPARISON WITH MEASUREMENTS

### IN BOSTON BLUE CLAY

This Section compares the results of the non-linear consolidation analyses described in Sections 8.2 and 8.3 to the excess pore pressure and radial stress changes at the pile wall during consolidation, measured during the 1980 MIT field testing program\* in Saugus, Massachusetts, using the Piezo-Lateral Stress (PLS) cell (see Section 6.5).

Figure 8.15 compares the measured normalized excess pore pressure dissipation curves at three different depths (equal to 84.5, 99.5 and 114.5 ft.) to the proposed model predictions for a soil with the properties of BBC. Because of the large discrepancy between the predicted and measured values of the excess pore pressure at the pile wall immediately after installation (see Section 6.5.2), the pore pressure dissipation curves are normalized with the value of the excess pore pressure at the pile wall in the beginning of consolidation\*\*. The time variable is expressed in terms of the dimensionless time factor  $T$  which appears naturally in the problem of consolidation around a cylindrical pile (see Appendix G). A specific value of the permeability coefficient  $k$  is required in converting from the real time\*\*\* to the

---

\* in the BBC deposit below 75 ft. where the clay is uniform with  $OCR=1.3\pm 0.1$

\*\* Thus, all curves start from unity in the beginning of consolidation ( $T=0$ ).

\*\*\* since the data are measured at real times

corresponding value of the dimensionless time factor. Laboratory permeability tests performed at MIT using undisturbed BBC samples from the test site in Saugus, Mass., indicate that the coefficient of permeability (in the horizontal direction) in the uniform clay below 75 ft. is equal to\*  $3-6 \times 10^{-8}$  cm/sec. A value of the permeability coefficient equal to  $3 \times 10^{-8}$  cm/sec is used in plotting the data in Figs. 8.15, 8.16 and 8.17. This value provides the best match of the measured data and the predicted pore pressure and radial effective stress curves (Figs. 8.15 and 8.16), whereas when considered individually, values of the permeability coefficient equal to  $1.5 \times 10^{-8}$  and  $5 \times 10^{-8}$  cm/sec provide the best match in Figs. 8.15 and 8.16, respectively. The pore pressure dissipation data at depths equal to 84.5 and 99.5 ft. show a small increase of the excess pore pressure at the pile wall in the early stages of consolidation\*\*, indicating that the peak value of the excess pore pressure immediately after installation is at some location away from the pile. Thus, in the early stages of consolidation, pore water migrates towards the pile wall and causes increased excess pore pressures. Figure 6.11a shows that, in the case of the normally consolidated clay, the proposed model predicts that the maximum excess pore pressure occurs at the pile wall, whereas, in the case of the slightly overconsolidated clay (OCR=1.35) there is

---

\* range of results of five tests

\*\* the data obtained at depth equal to 114.5 ft. do not show this effect



a small increase of the predicted excess pore pressure away from the pile. However, this increase is very small and thus, the predicted excess pore pressure dissipation curves (Fig. 8.15) are almost horizontal in the early stages of consolidation for all overconsolidation ratios.

Figure 8.16 compares the measured radial effective stress changes at the pile wall (at depths equal to 84.5, 99.5 and 114.5 ft.) to the proposed model predictions for a soil with the properties of BBC. The data show that in the early stages of consolidation the radial effective stress decreases and approaches a zero value for time factors approximately equal to 0.01. On the contrary, the proposed model predicts that the initial value of the radial effective stress at the pile wall is close to zero (see Chapter 6) and remains practically constant for time factors less than 0.01. The discrepancy between the predicted and measured radial effective stress response at early times is related to the differences between the predicted and measured pore pressure dissipation curves at early times (see Fig. 8.15) i.e., an increase of the excess pore pressure at early times causes the radial effective stress to decrease. For time factors larger than 0.01, the agreement between measurement and prediction is reasonable and the measured value of the radial effective stress after consolidation is completed corresponds to the predicted value for an OCR equal to 1.25, which is a reasonable value for the clay below 75 ft.

Figure 8.17 compares the measured normalized total radial

stress changes at the pile wall (at depths equal to 84.5, 99.5 and 114.5 ft.) to the proposed model predictions for a soil with the properties of BBC. Because of the large discrepancy between the predicted and measured values of the total radial stress at the pile wall immediately after installation (see Section 6.5.2), the total radial stress curves are normalized with the corresponding value at the pile wall in the beginning of consolidation\*. The agreement between the measured and predicted value is poor indicating that the normalized curves cannot be compared i.e., the differences in the absolute magnitudes of the predicted and measured total radial stresses in the beginning of consolidation have a significant effect on the changes during consolidation.

---

\* Thus, all curves start from unity in the beginning of consolidation.

## 8.5 COMPARISON BETWEEN LINEAR AND NON-LINEAR CONSOLIDATION SOLUTIONS

Linear and non-linear consolidation solutions around a cylindrical pile exhibit certain fundamental differences: linear solutions predict that the total radial stress at the pile wall remains constant during consolidation. This means that the radial effective stress at the pile wall after consolidation is completed is equal to the total radial stress\* in the beginning of consolidation (see Fig. 8.1). These conclusions do not agree with experimental data indicating that at the pile wall:

- (i) The total radial stress decreases during consolidation.
- (ii) The radial effective stress after consolidation is significantly smaller than the total radial stress in the beginning of consolidation.

Thus, linear solutions do not give realistic estimates of the stresses at the pile wall during and after consolidation. However, linear solutions can be used to estimate the stiffness of the soil\*\*. This can be achieved via a linear elastic soil model equivalent to the proposed model for the problem of consolidation around a pile:

Figure 8.18a compares the stress and pore pressure changes at the pile wall predicted by the proposed model\*\*\* to the

---

\* minus the ambient (hydrostatic) pore pressure

\*\* or, the permeability or, the coefficient of consolidation.

\*\*\* for a clay with the properties of normally consolidated BBC

predictions of an 'equivalent' linear elastic soil model. The stiffness of the 'equivalent' model

$$K + 4G/3 = 55.8 * \bar{\sigma}_0$$

is selected by matching the predicted pore pressure dissipation curves in the early stages of consolidation (i.e., for  $T < 0.1$ ). For  $T < 0.1$ , the proposed model predicts that the soil around the pile is elastic\* (i.e., stiff) and thus, the selected stiffness of the 'equivalent' model corresponds to the recompression modulus of the clay. Figure 8.18a also shows that the pore pressure dissipation curve of the thus fitted 'equivalent' model, is very similar to the proposed model prediction at all times (i.e., not only for  $T < 0.1$ ). This is because the proposed model predicts that, at time factors larger than 0.1, two mechanisms with opposite effects on the pore pressure dissipation rate are present in the soil:

(i) A plastic (soft) zone develops close to the pile wall.

This tends to retard the pore pressure dissipation rate.

(ii) The stiffness of the soil in the elastic (and the plastic) zone increases because the effective stresses increase during consolidation\*\*. This tends to accelerate the pore pressure dissipation rate.

These two mechanisms are approximately balanced and thus, the proposed model prediction is at all times similar to the prediction of the fitted 'equivalent' model. Figure 8.18b

---

\* see Fig. 8.2

\*\* The principle of normalized behavior suggests that the moduli are proportional to the effective stresses.

presents the effect of the two mechanisms: the dash-dot line shows the predicted pore pressure dissipation curve for a soil model having stiffness proportional to the mean effective stress but without introducing Plasticity in the soil close to the pile. As expected, this model predicts dissipation rates much faster than the proposed model (for  $T > 0.1$ ) because of the lack of the soft (plastic) zone close to the pile\*.

Figure 8.19 compares the stress and pore pressure changes at the pile wall predicted by the proposed model (for slightly overconsolidated BBC) to the predictions of 'equivalent' linear elastic models with stiffnesses selected by matching the early portions of the pore pressure dissipation curves. One can note that (a) the stiffness of the 'equivalent' model increases with increasing OCR and (b) the pore pressure dissipation curve predicted by the 'equivalent' model is similar to the proposed model prediction at all times (for reasons similar to those discribed in the discussion of the normally consolidated clay).

Based on these conclusions, one can use the pore pressure dissipation data measured at the pile wall to estimate the soil stiffness (for known permeability) or, the soil permeability (for known stiffness) or, finally, the coefficient of consolidation (which is proportional to the product of stiffness and permeability).

---

\* which would tend to retard the pore pressure dissipation rates.

## 8.6 SUMMARY AND CONCLUSIONS

This Chapter performs linear and non-linear one-dimensional consolidation analyses around a pile driven in normally consolidated and slightly overconsolidated BBC (OCR=1.20 and 1.35) using the following soil constitutive models:

- (i) The Linear Elastic Isotropic model.
- (ii) The Modified Cam-Clay (MCC) model.
- (iii) The model proposed in Chapter 4.

and initial stress and excess pore pressure distributions obtained by means of:

- (i) The Undrained Cylindrical Cavity Expansion method.
- (ii) The Strain Path method.

Linear analyses show that the total radial stress at the pile wall remains constant during consolidation which means that the radial effective stress at the pile wall after consolidation is completed is equal to the total radial stress\* in the beginning of consolidation. These conclusions do not agree with experimental data and thus, non-linear analyses are required in order to obtain realistic estimates of the stresses acting on the pile wall after consolidation is completed.

Non-linear analyses using the proposed model and initial conditions estimated via the Strain Path method show that in the early stages of consolidation, the soil around the pile has a stiff (elastic) response, whereas at later times, a soft (plastic) zone develops in the region close to the pile wall.

---

\* minus the ambient (hydrostatic) pore pressure

The value of the equivalent time factor when Plasticity is first induced in the soil increases with increasing OCR and has a significant effect on the predicted changes of the radial effective stress at the pile wall during consolidation. More specifically, non-linear analyses show that the radial effective stress at the pile wall increases mainly during the early stages of consolidation (i.e., while the soil around the pile is elastic) and thus, the predicted value of the radial effective stress at the pile wall at the end of consolidation increases with increasing OCR.

Comparison of non-linear analyses shows that the method used to estimate the stress and excess pore pressure distributions in the soil in the beginning of consolidation has a significant effect on the predicted value of the radial effective stress acting on the pile wall after consolidation. Analyses using the proposed model and initial conditions estimated via the Strain Path method show that, after consolidation is completed, the radial effective stress everywhere in the soil around the pile, is approximately equal to the initial in-situ horizontal effective stress before pile installation. On the contrary, analyses using initial conditions estimated via the Cavity Expansion method show that, after consolidation is completed, the predicted value of the radial effective stress at the pile wall is significantly higher than the Strain Path prediction mainly because of differences in the corresponding values in the beginning of consolidation.

During consolidation, a soil element located at the pile wall is subjected to one-dimensional straining in the radial direction and thus, the predicted effective stress path approaches the radial one-dimensional consolidation line.

Comparison of the results of non-linear consolidation analyses\* with field measurements in slightly overconsolidated Boston Blue Clay show that the proposed model gives:

- (i) Good estimates of the permeability coefficient based on normalized\*\* pore pressure dissipation data measured at the pile wall, or on the measured changes of the radial effective stress at the pile wall.
- (ii) Reasonable estimates of the radial effective stress changes at the pile wall during consolidation (except at very small times) and good predictions of the magnitude of the radial effective stress at the pile wall after consolidation is completed.
- (iii) Poor predictions of the normalized\*\*\* total radial stress changes at the pile wall during consolidation indicating that the differences in the absolute magnitudes of the predicted and measured total radial stresses in the beginning of consolidation have a

---

\* using the proposed model and initial conditions estimated via the Strain Path method

\*\* with the value of the pore pressure at the pile wall in the beginning of consolidation

\*\*\* with the magnitude of the total radial stress at the pile wall in the beginning of consolidation



significant effect on the predicted changes during consolidation.

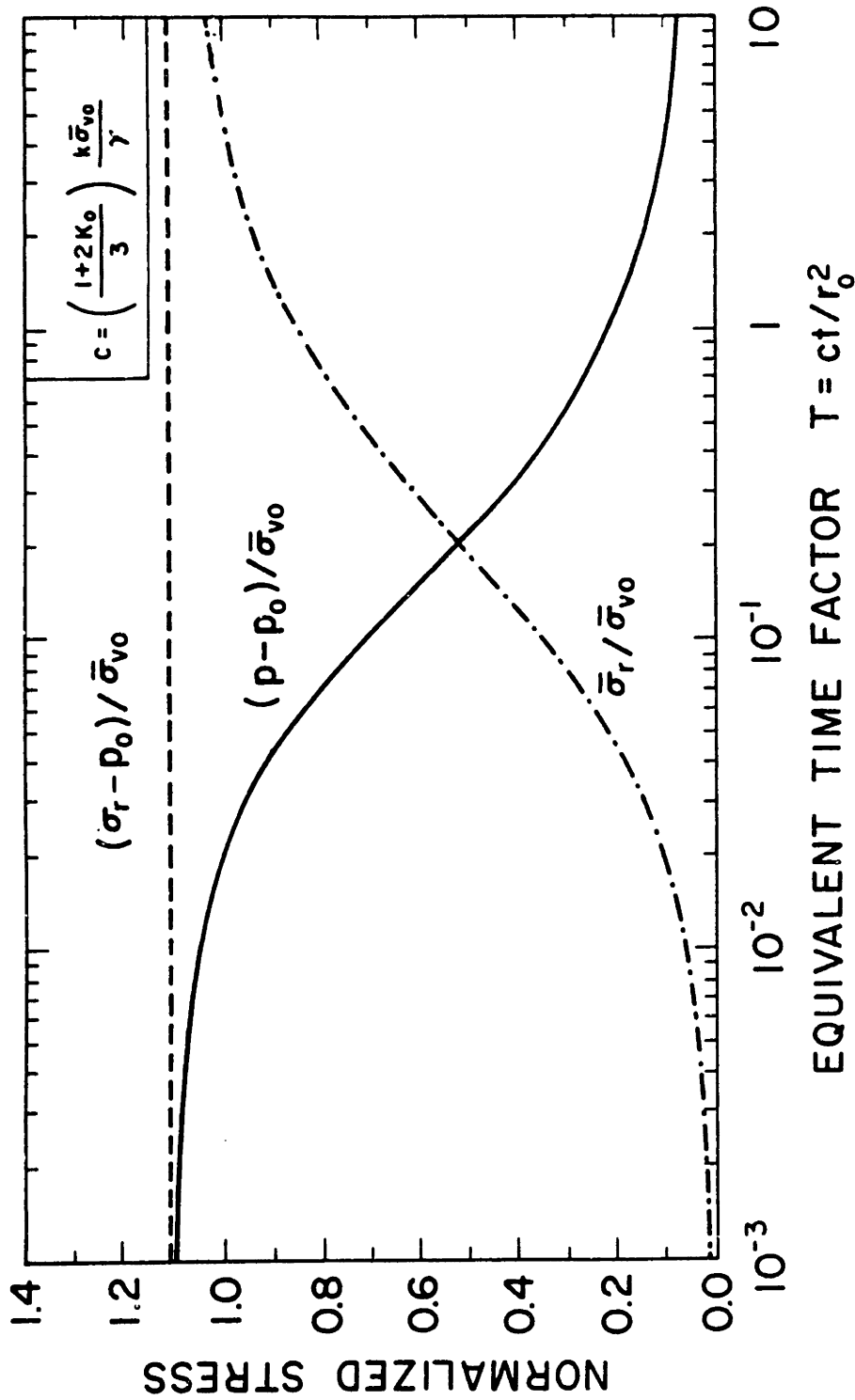
An 'equivalent' linear elastic soil model with stiffness corresponding to the recompression modulus of the clay fits reasonably well the excess pore pressure dissipation curve at all times indicating that the average stiffness of the soil around the pile remains essentially constant during consolidation. This is due to the fact that during consolidation:

- (i) A soft (plastic) zone develops close to the pile wall, tending to retard the pore pressure dissipation rates.
- (ii) The mean effective stress increases and thus, the soil stiffness increases tending to accelerate the pore pressure dissipation rates.

The combined effect of these mechanisms is that the average stiffness of the soil remains essentially constant during consolidation.

Node	$r/r_0$	Node	$r/r_0$
1	1.00000	24	3.44803
2	1.00549	25	3.73601
3	1.02013	26	4.12262
4	1.04426	27	4.60904
5	1.07723	28	5.09805
6	1.11815	29	5.83500
7	1.16632	30	6.57485
8	1.22074	31	7.56437
9	1.28073	32	8.55629
10	1.34554	33	9.54987
11	1.41438	34	11.04240
12	1.48729	35	12.53670
13	1.56264	36	14.03220
14	1.64065	37	16.02750
15	1.72094	38	18.02390
16	1.80321	39	20.02100
17	1.92977	40	25.01590
18	2.05947	41	30.01260
19	2.23637	42	40.00870
20	2.46245	43	50.00660
21	2.69274	44	70.00430
22	2.92625	45	100.00300
23	3.16225	46	150.00000

Table 8.1: Normalized radial coordinates of nodal points used in the Finite Element solution of radial consolidation around a long cylindrical pile.



Note:  $K + \frac{4}{3} G = 55.8 \times \left( \frac{1+2K_o}{3} \right) \bar{\sigma}_{v0}$  was used.

Fig. 8.1: Predicted excess pore pressure dissipation and radial stress changes at the pile wall during linear consolidation. Initial conditions computed via the Strain Path method in conjunction with the proposed model for normally consolidated Boston Blue Clay.

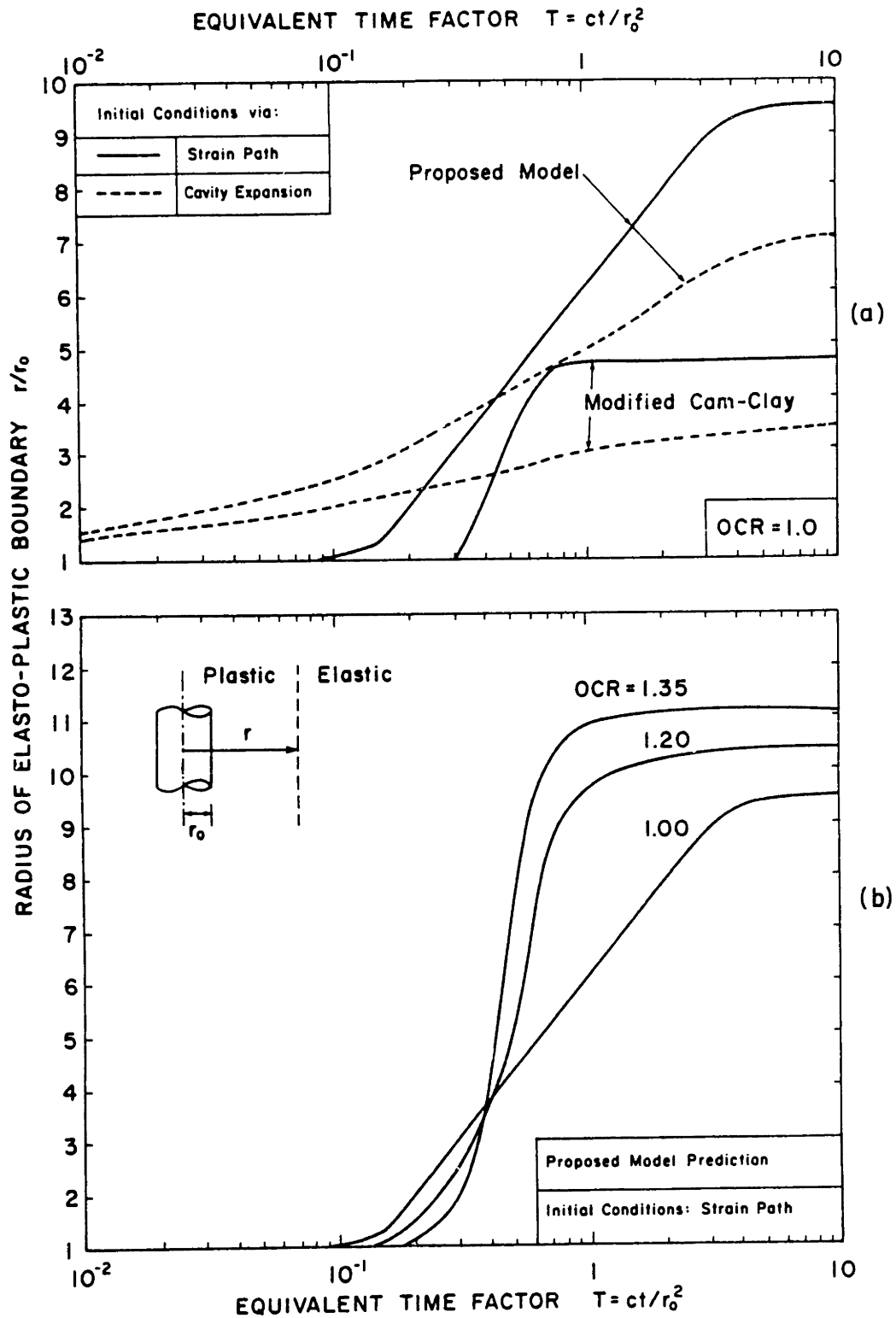


Fig. 8.2: Predicted locations of the Elasto-Plastic Boundary around a pile, during consolidation of a soil with the properties of BBC.

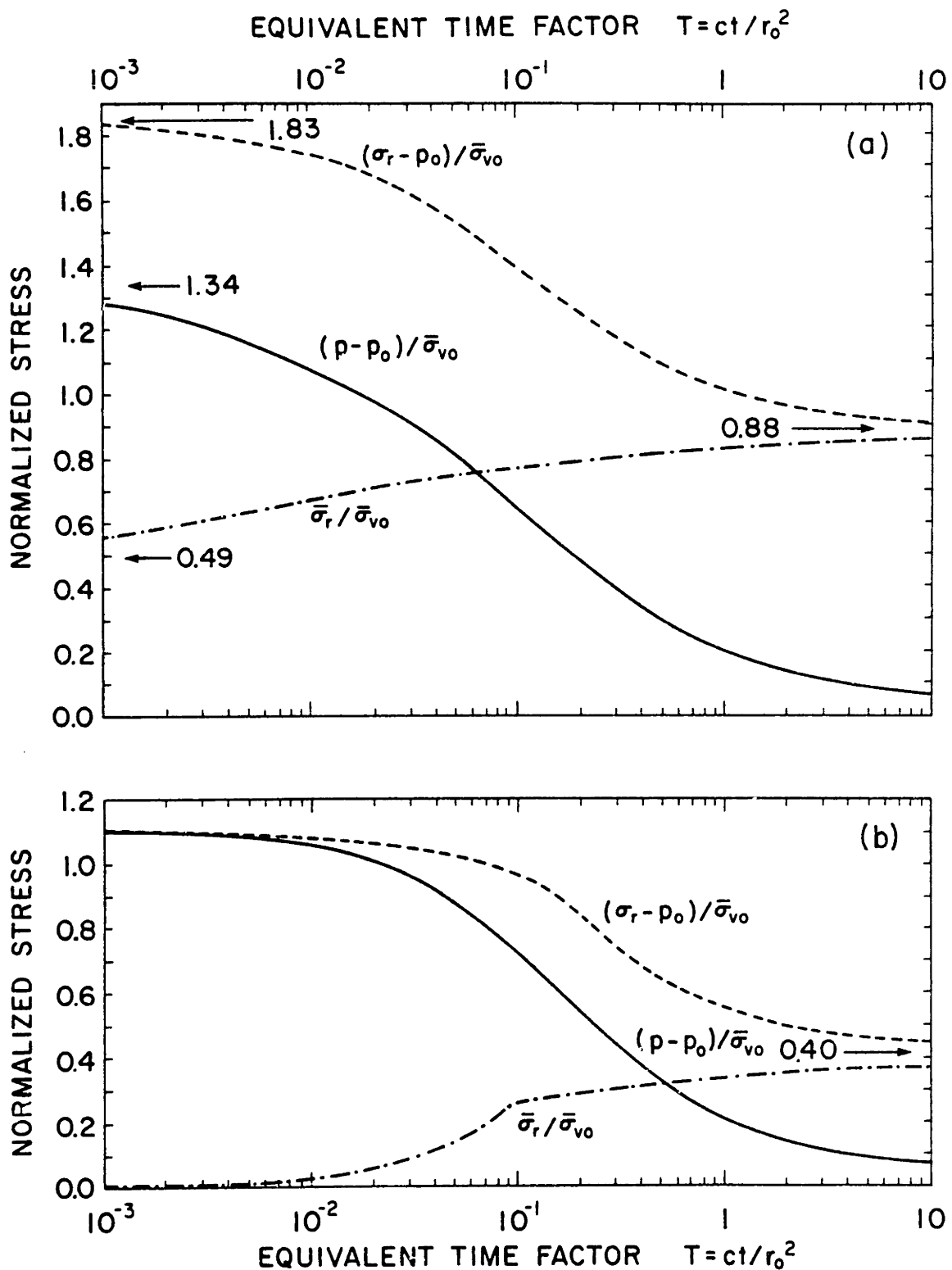


Fig. 8.3: Proposed model predictions of the pore pressure dissipation and the radial stress changes at the pile wall during consolidation of a soil with the properties of normally consolidated BBC. Initial conditions via: (a) Cavity Expansion and (b) Strain Path methods.

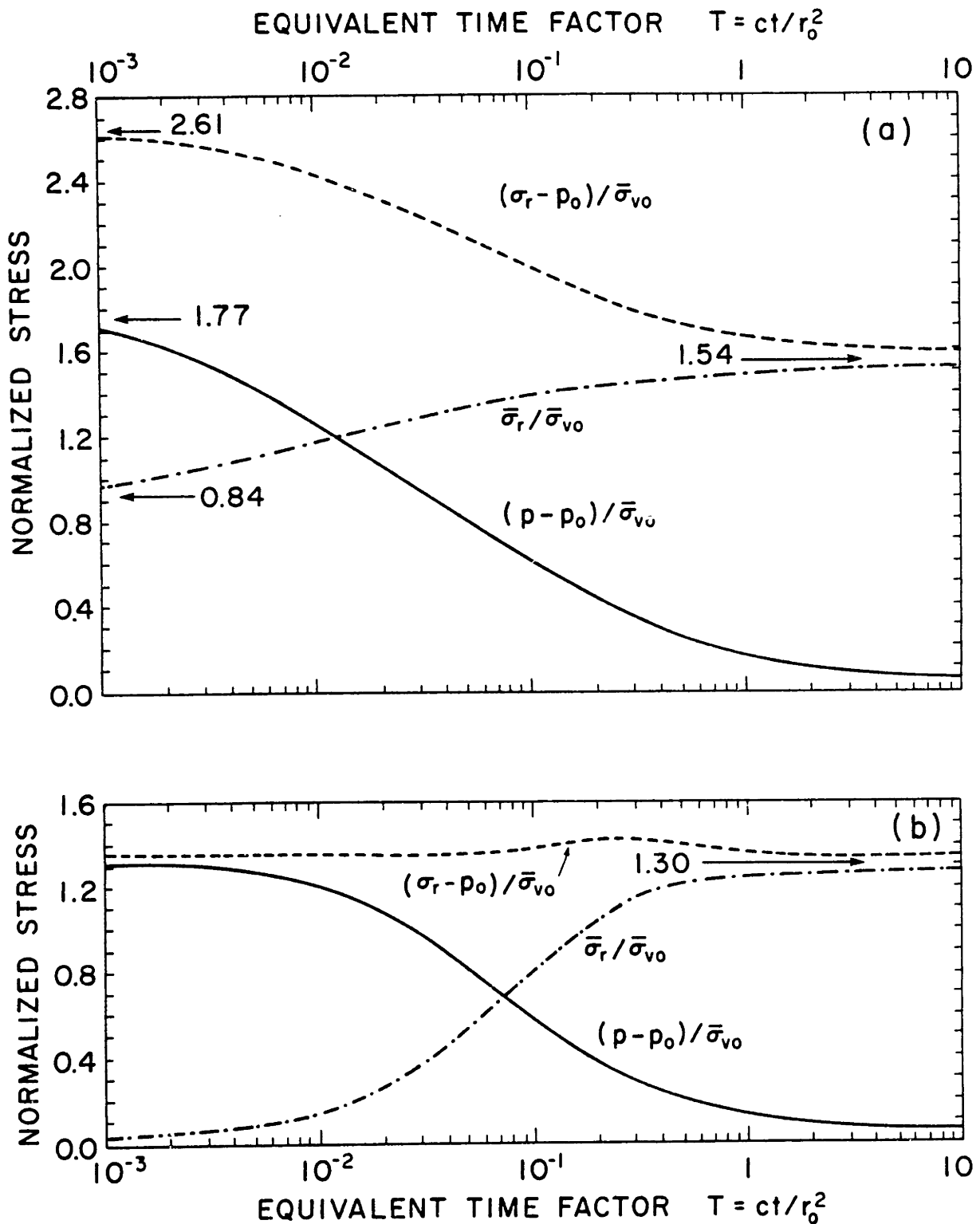


Fig. 8.4: Modified Cam-Clay model predictions of the pore pressure dissipation and the radial stress changes at the pile wall during consolidation of a soil with the properties of normally consolidated BBC. Initial conditions via: (a) Cavity Expansion and (b) Strain Path methods.

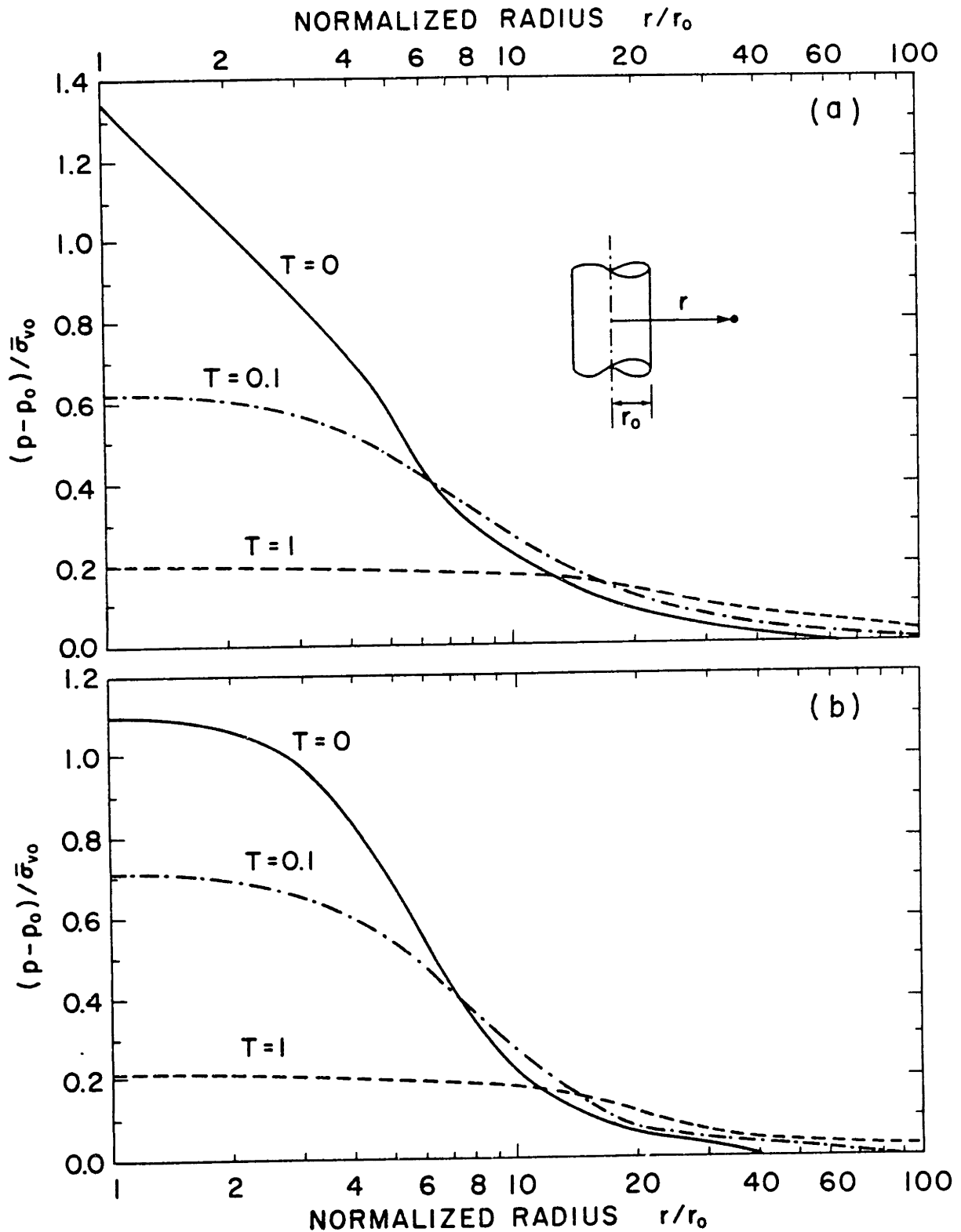


Fig. 8.5: Proposed model predictions of the excess pore pressure dissipation (at various time factors) during consolidation of a soil with the properties of normally consolidated 3BC. Initial conditions via: (a) Cavity Expansion and (b) Strain Path methods.

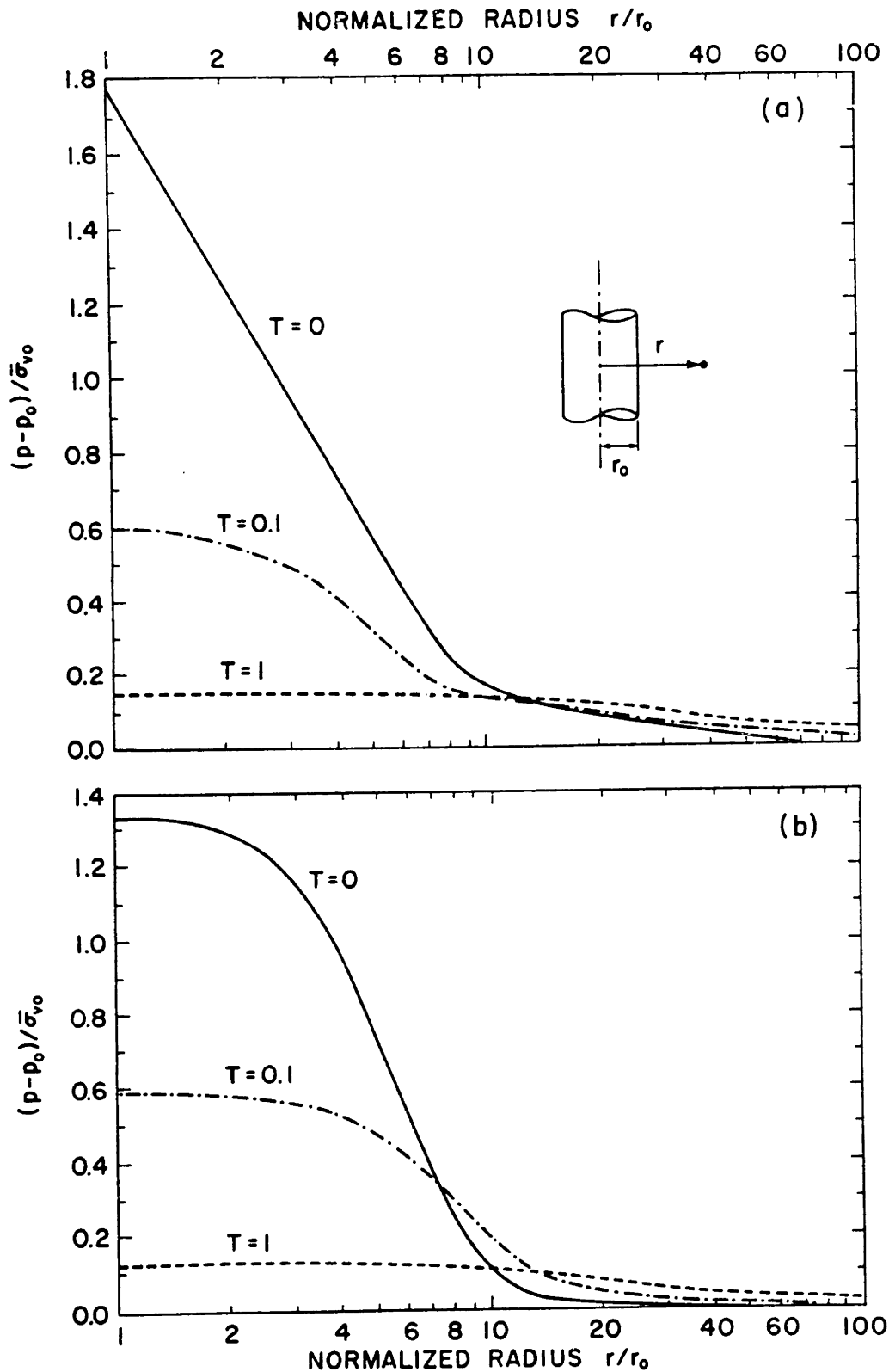


Fig. 8.6: Modified Cam-Clay model predictions of the excess pore pressure dissipation (at various time factors) during consolidation of a soil with the properties of normally consolidated BBC. Initial conditions via: (a) Cavity Expansion and (b) Strain Path methods.



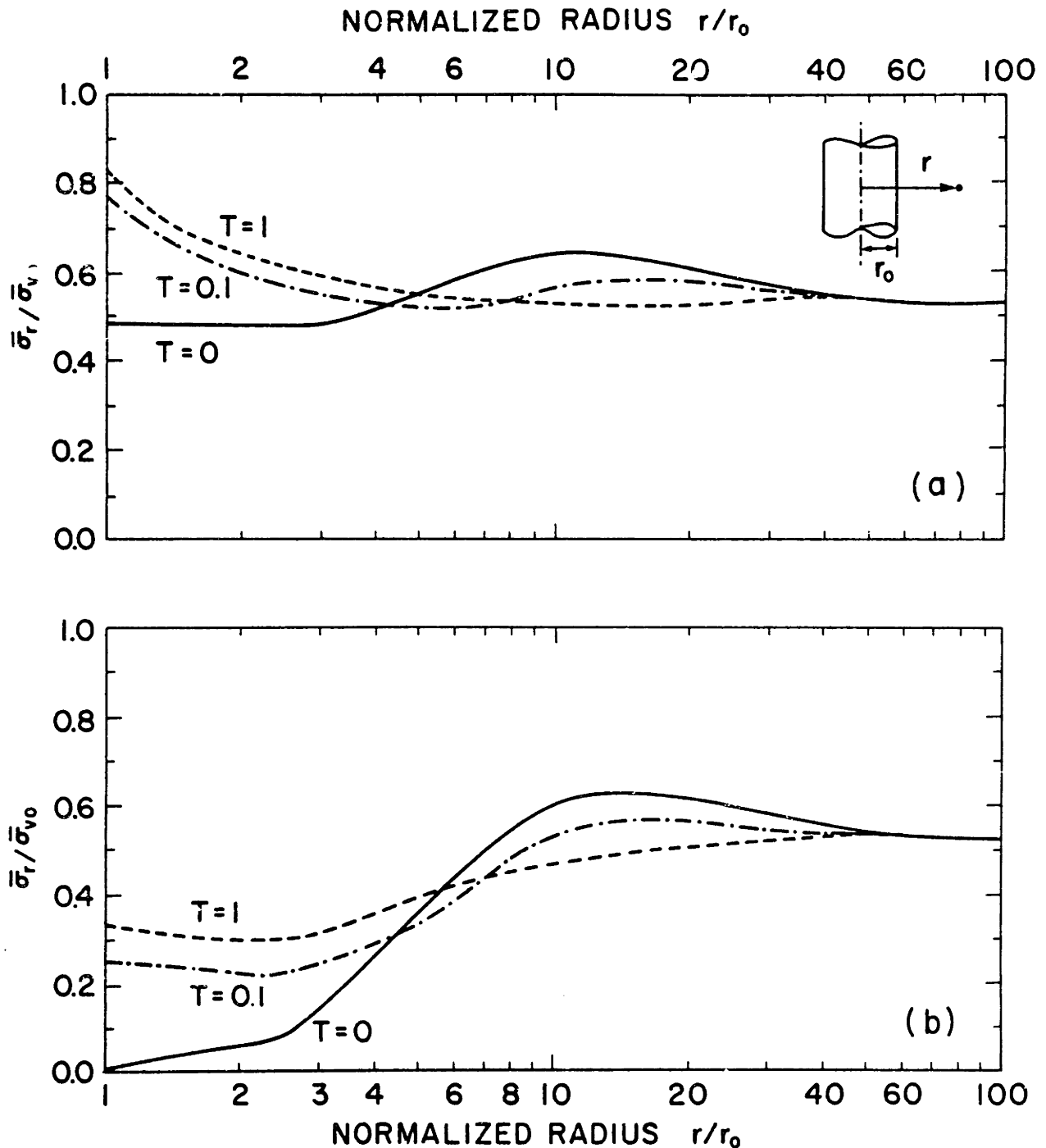


Fig. 8.7: Proposed model predictions of the radial effective stress changes (at various time factors) during consolidation of a soil with the properties of normally consolidated BBC. Initial conditions computed via: (a) Cavity Expansion and (b) Strain Path methods.

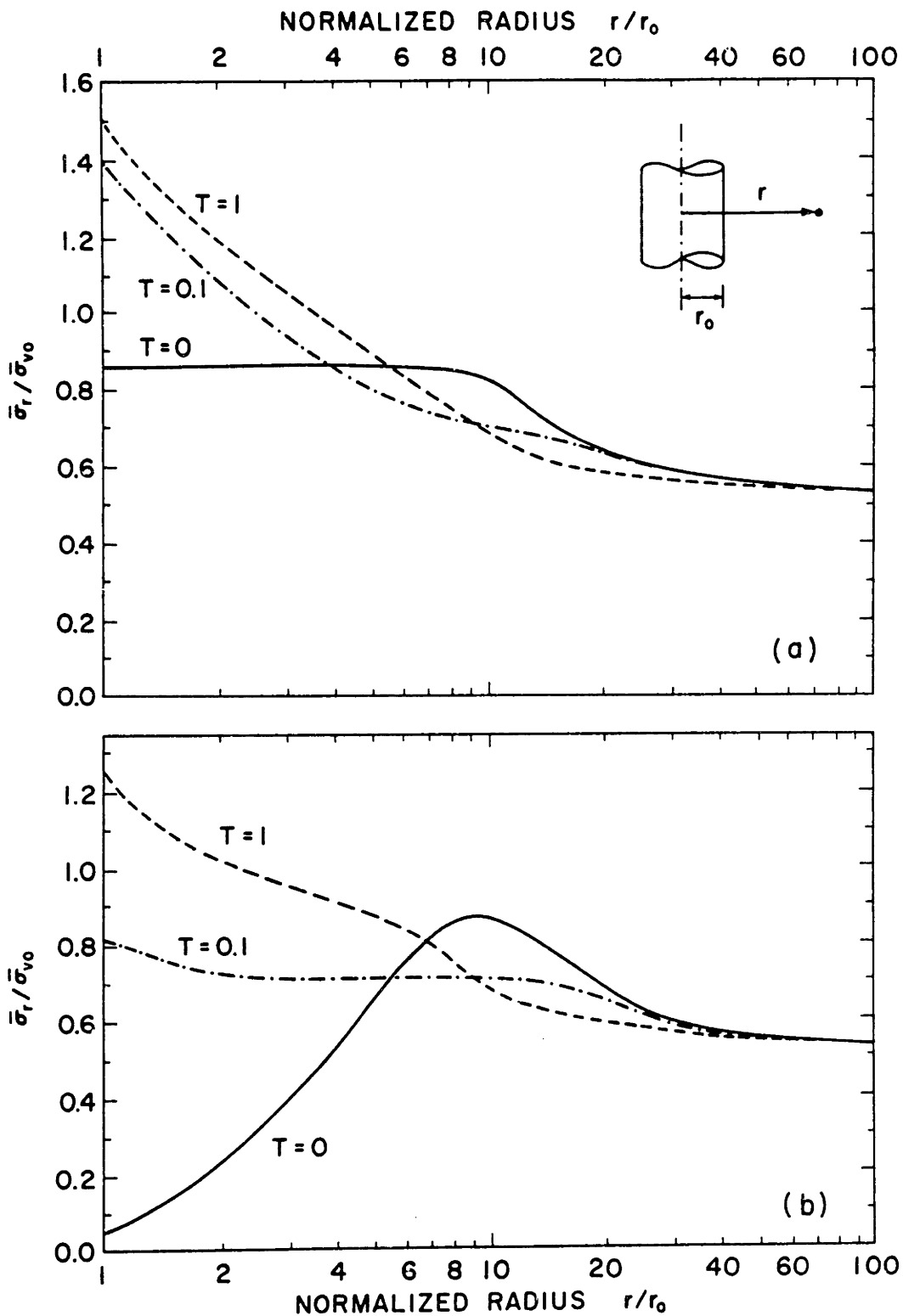


Fig. 8.8: Modified Cam-Clay model predictions of the radial effective stress changes (at various time factors) during consolidation of a soil with the properties of normally consolidated BBC. Initial conditions via: (a) Cavity Expansion and (b) Strain Path methods.

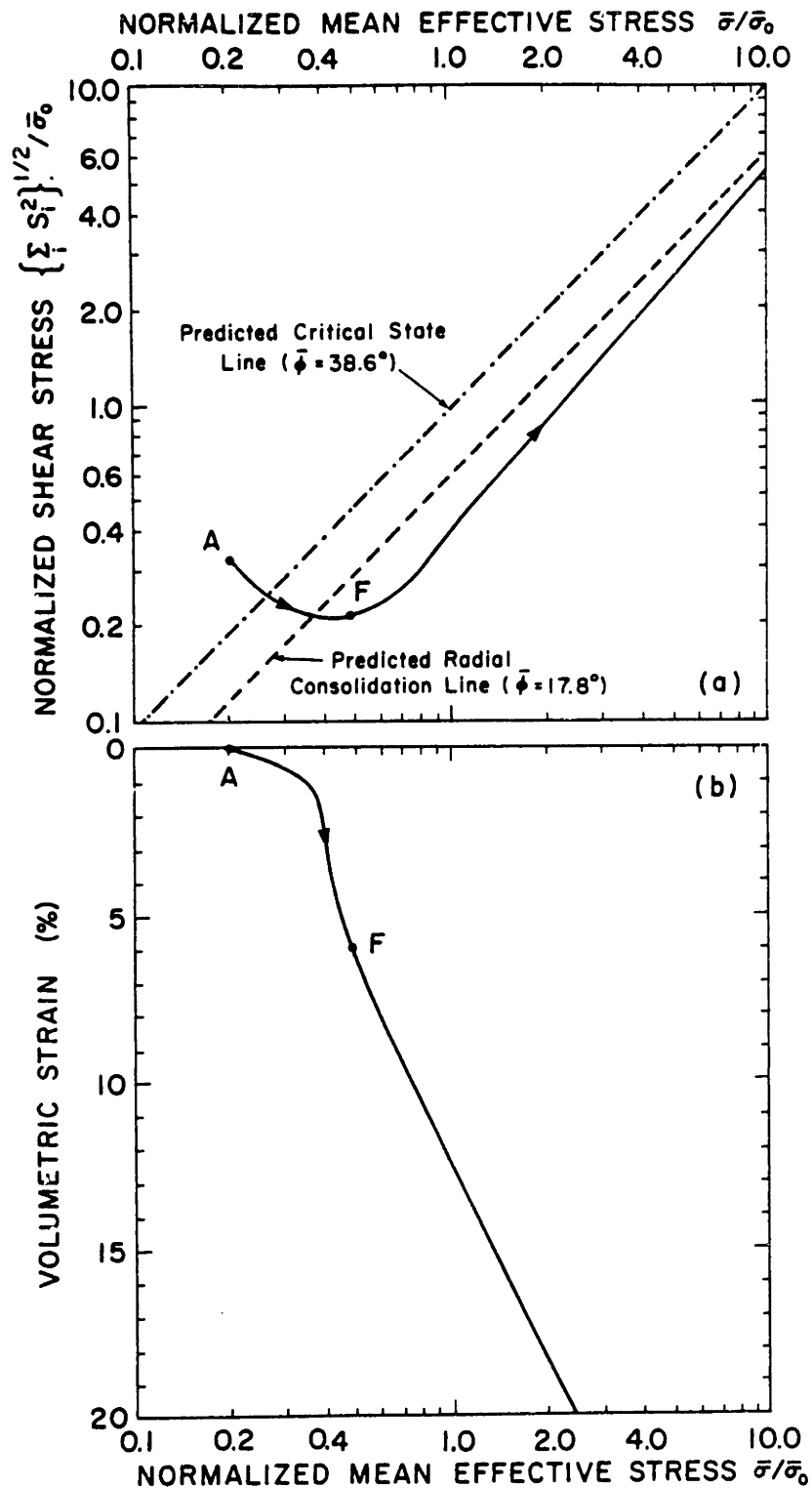


Fig. 8.9: Proposed model predictions of (a) the effective stress path and (b) the stress-strain curve for an element located at the pile wall during consolidation of a soil with the properties of normally consolidated BBC. Initial conditions via the Strain Path method.

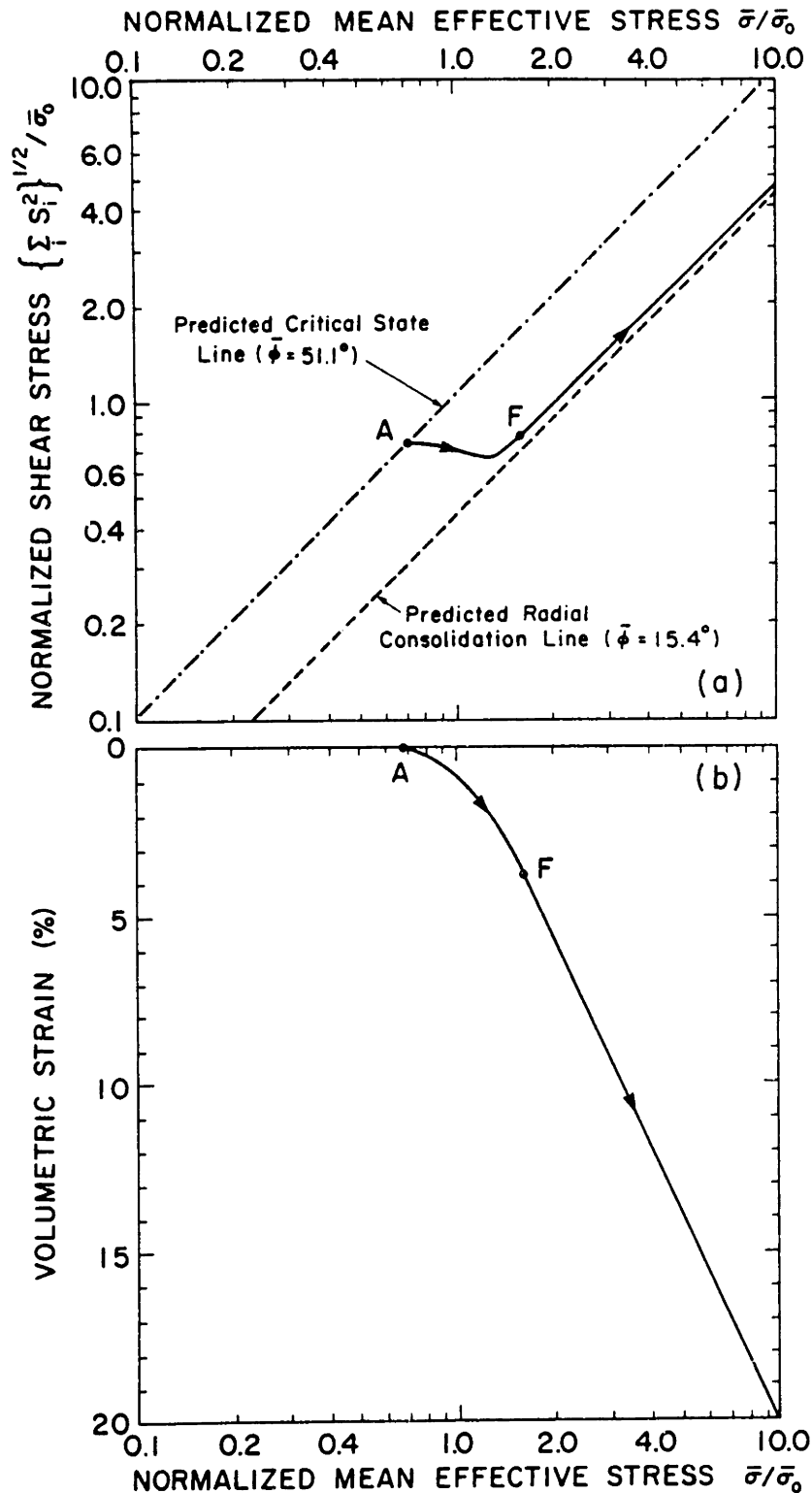


Fig. 8.10: Modified Cam-Clay model predictions of (a) the effective stress path and (b) the stress-strain curve for an element located at the pile wall during consolidation of a soil with the properties of normally consolidated BEC. Initial conditions via the Cavity Expansion method.

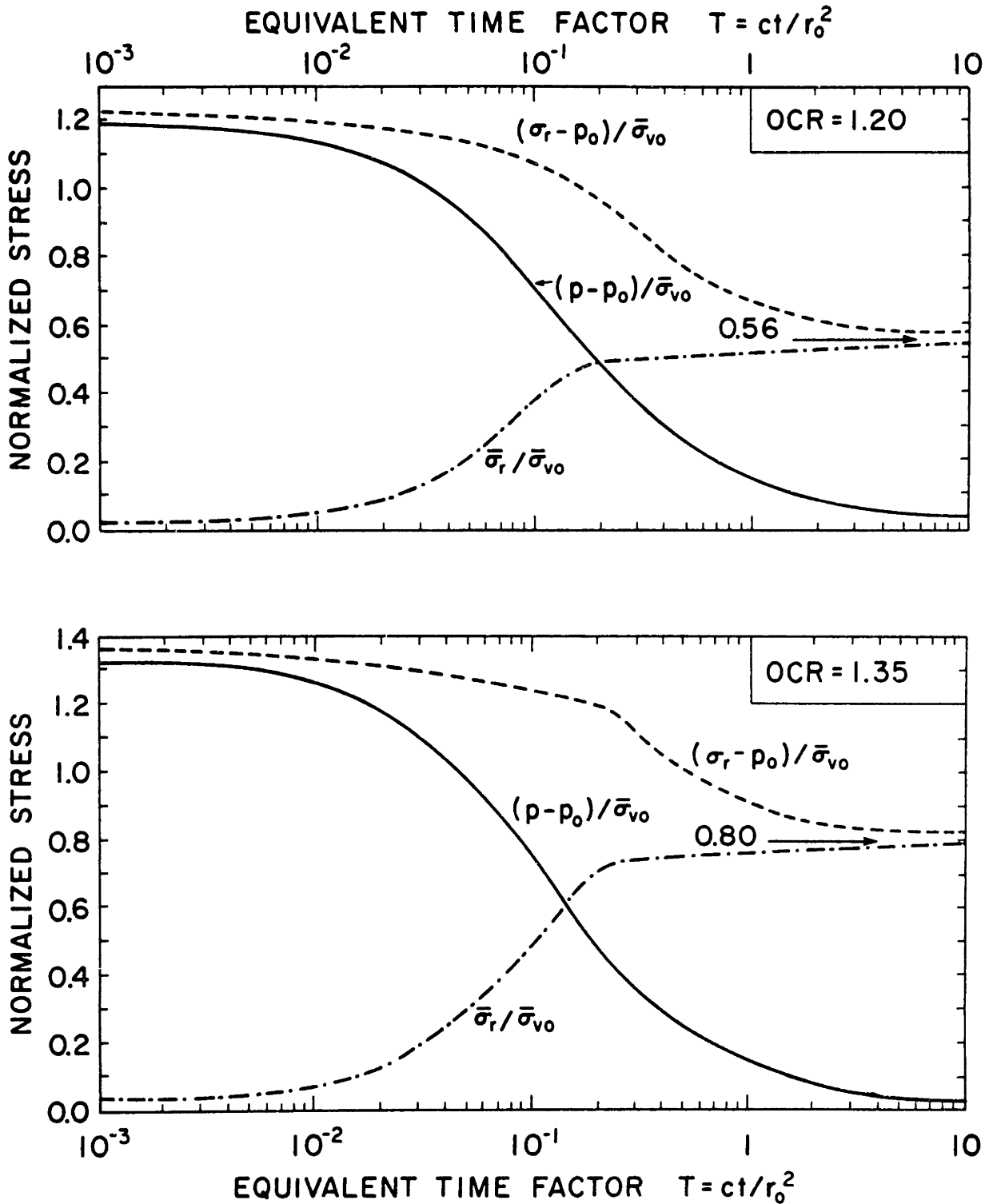


Fig. 8.11: Proposed model predictions of the pore pressure and the radial stress changes at the pile wall during consolidation of a soil with the properties of slightly overconsolidated BBC. Initial conditions computed via the Strain Path method.

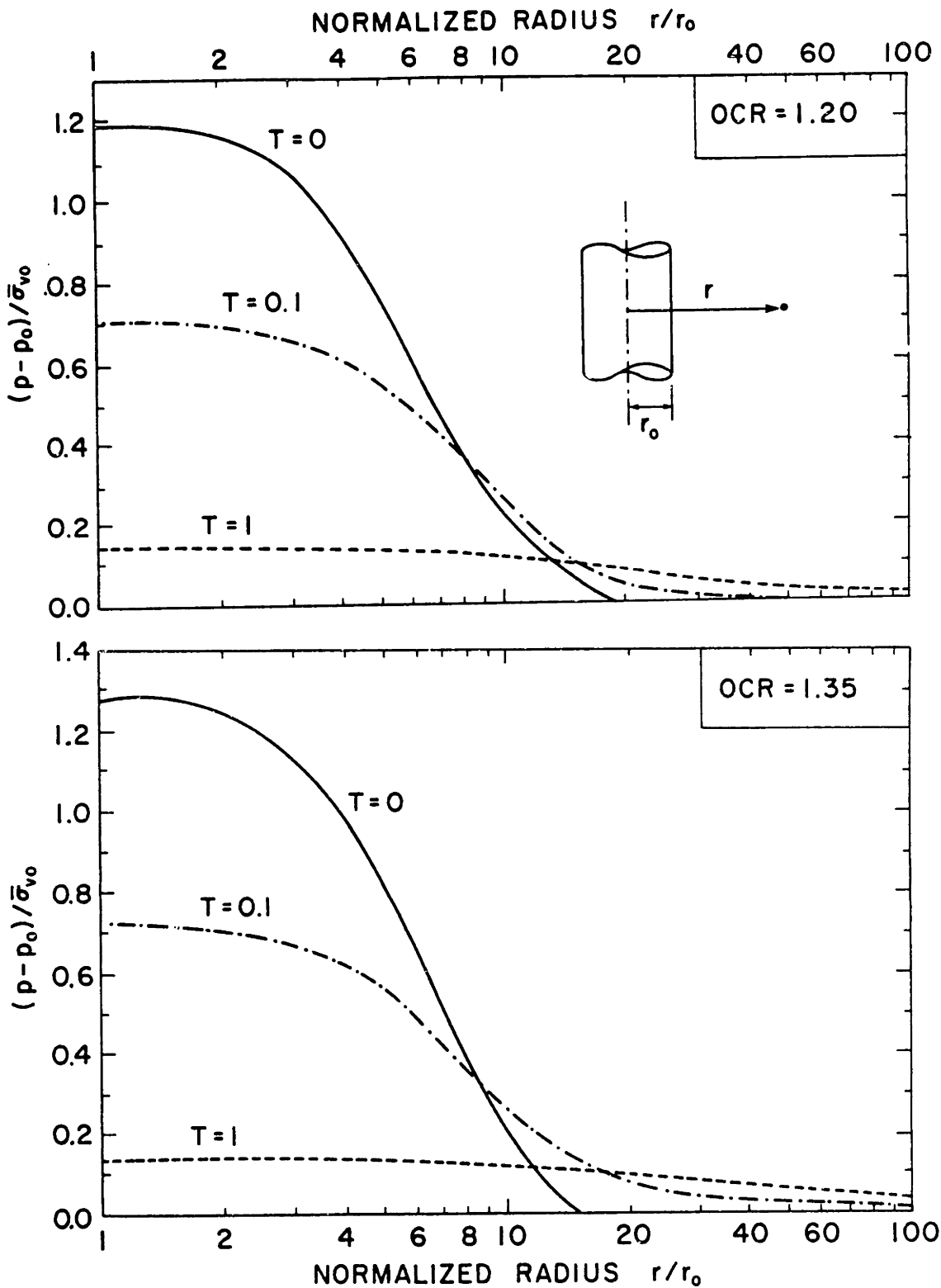


Fig. 8.12: Proposed model predictions of the pore pressure dissipation (at various time factors) during consolidation of a soil with the properties of slightly overconsolidated BBC. Initial conditions computed via the Strain Path method.

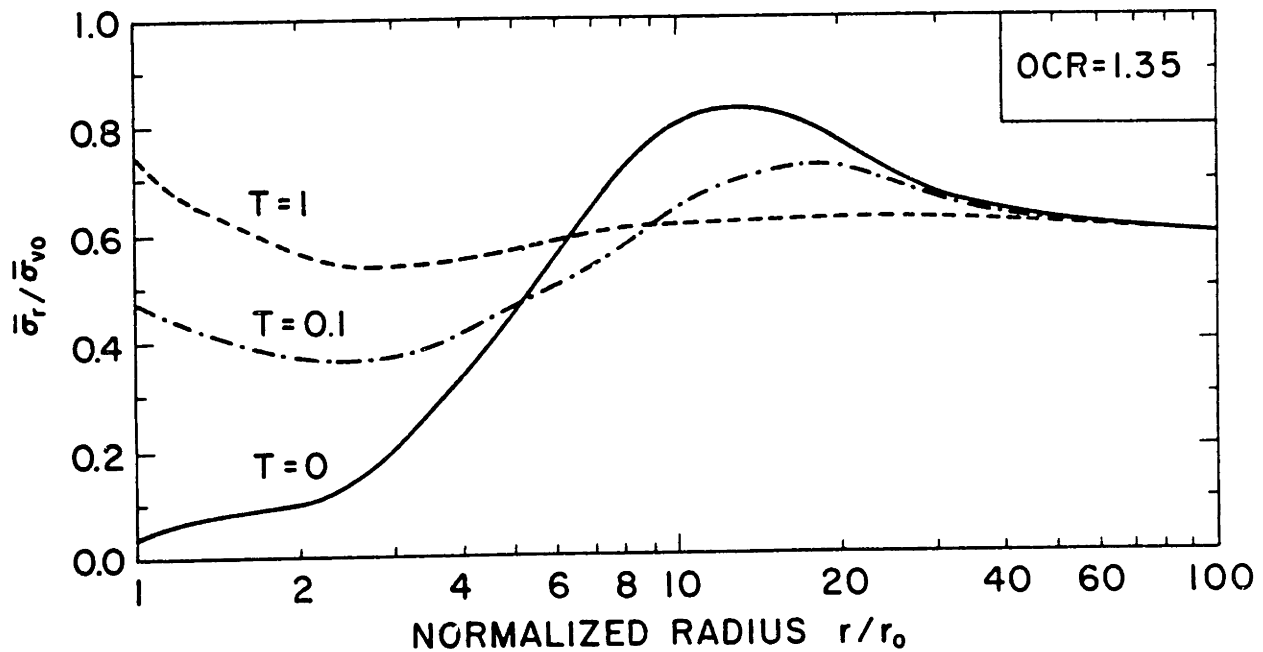
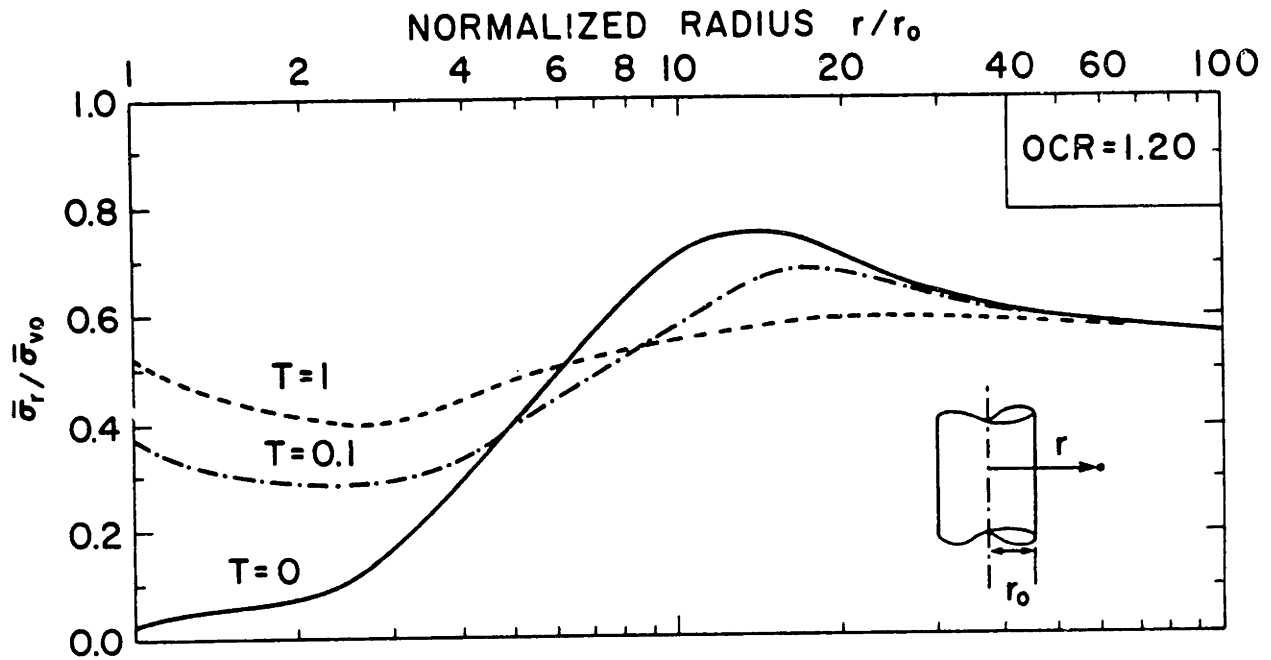


Fig. 8.13: Proposed model predictions of the radial effective stress changes (at various time factors) during consolidation of a soil with the properties of slightly overconsolidated BBC. Initial conditions computed via the Strain Path method.

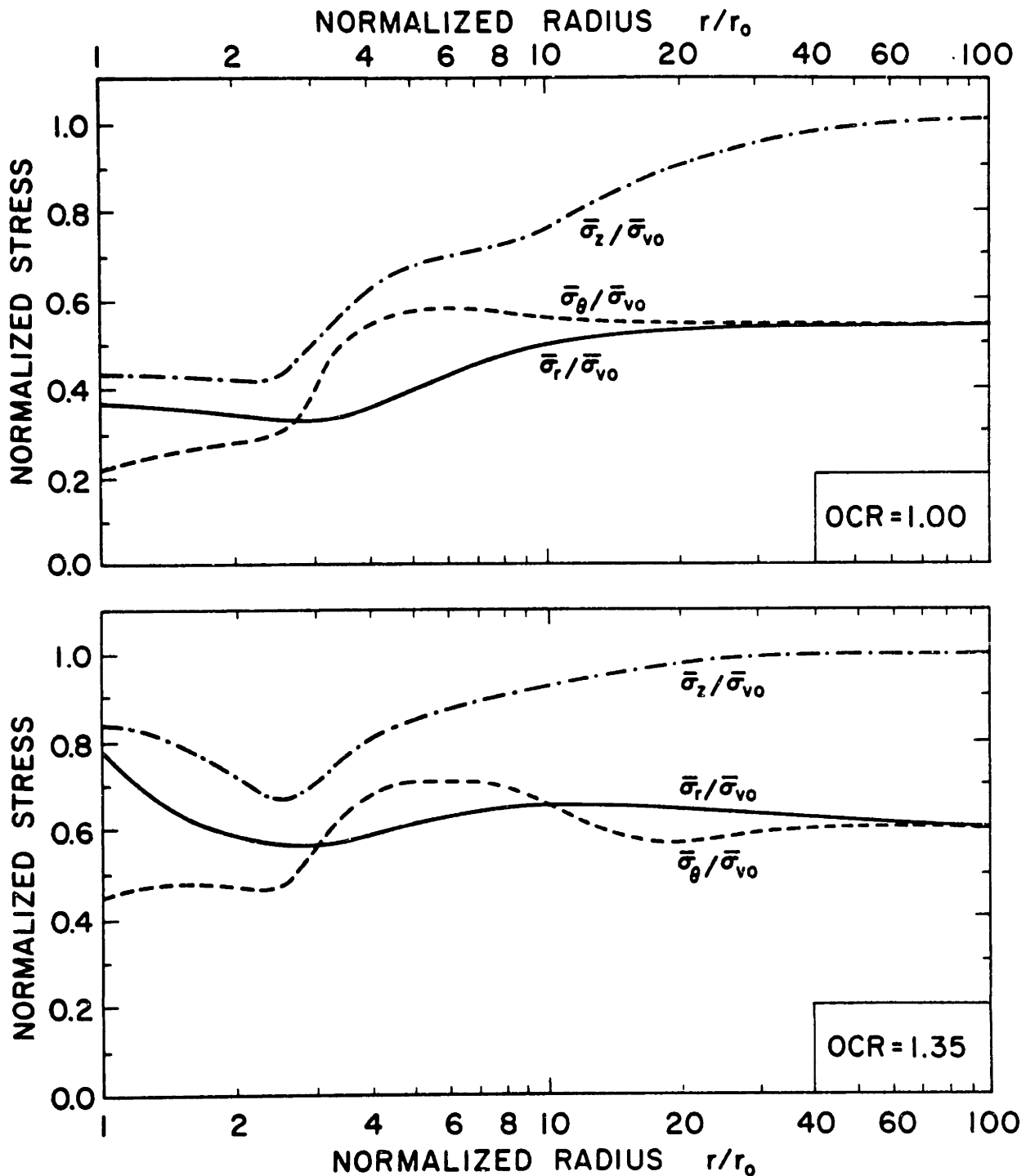


Fig. 8.14: Effective stresses after soil consolidation predicted by the proposed model (in conjunction with the Strain Path method) for  $K_0$ -consolidated Boston Blue Clay.



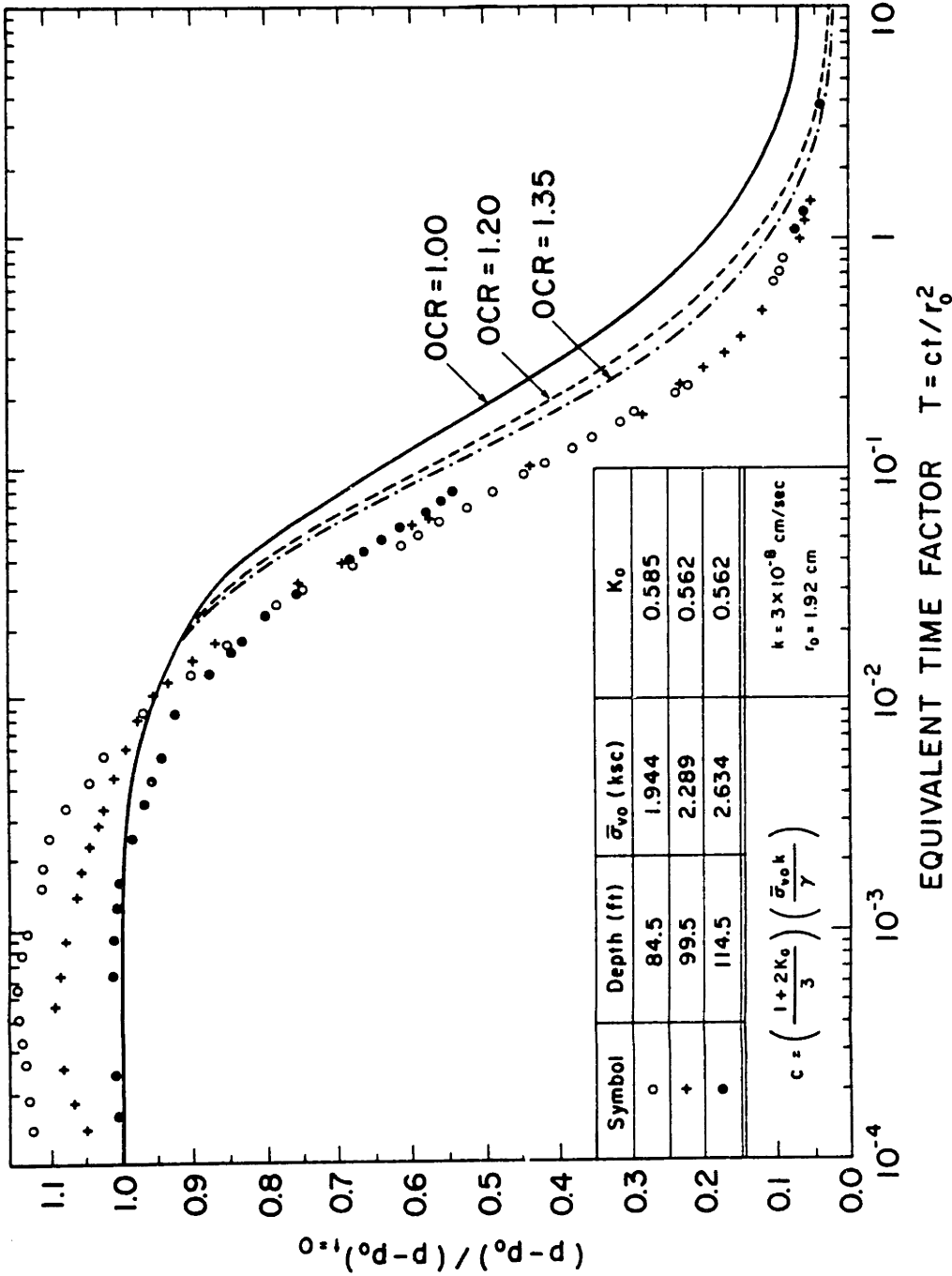


Fig. 8.15: Comparison of the measured normalized excess pore pressure dissipation curves at the pile wall, with the proposed model predictions for a soil with the properties of Boston Blue Clay and initial conditions computed via the Strain Path method.

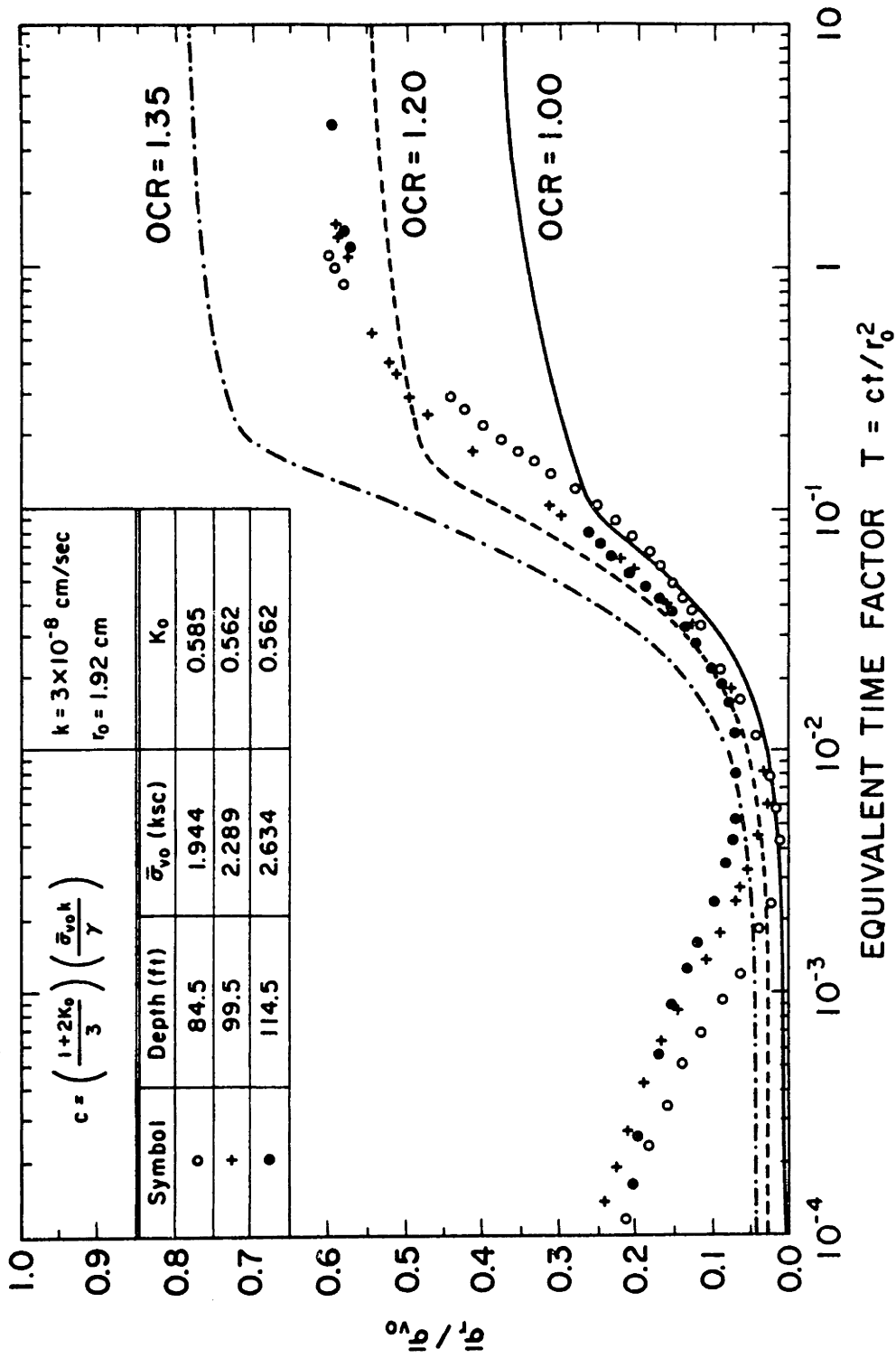


Fig. 8.16: Comparison of the measured radial effective stress at the pile wall, with the proposed model predictions for a soil with the properties of Boston Blue Clay and initial conditions computed via the Strain Path method.

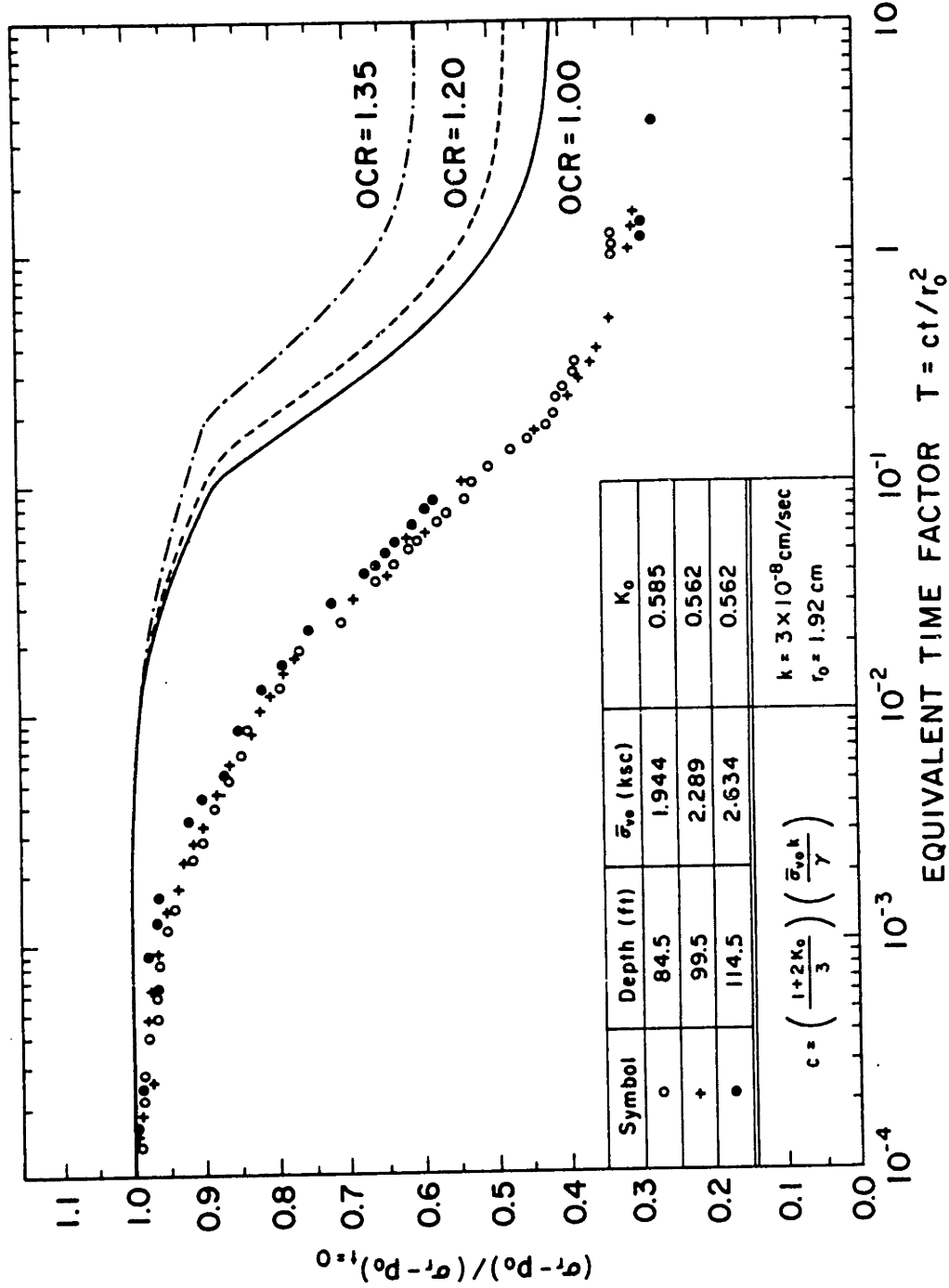
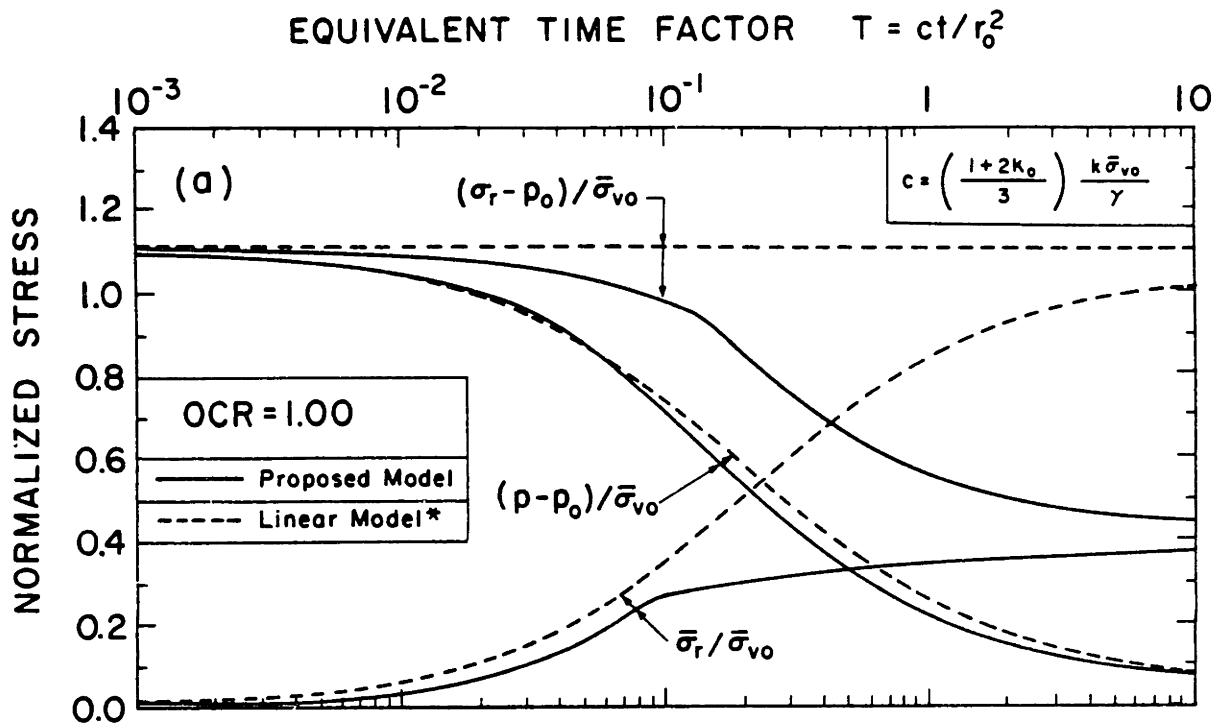


Fig. 8.17: Comparison of the measured normalized radial total stress at the pile wall, with the proposed model predictions for a soil with the properties of Boston Blue Clay and initial conditions computed via the Strain Path method.



\*  $K + \frac{4}{3}G = 55.8 \times \left( \frac{1+2K_0}{3} \right) \bar{\sigma}_{v0}$  was used.

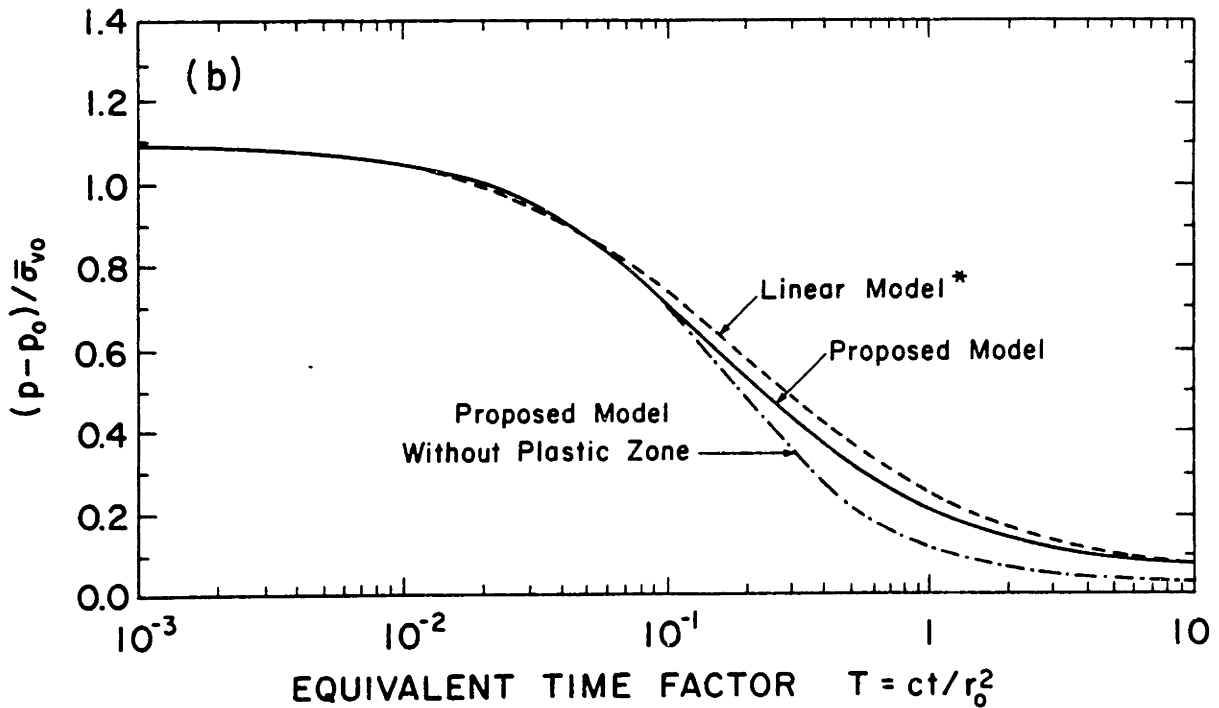


Fig. 8.18: Comparison of the stress and pore pressure changes at the pile wall predicted by the proposed model with the predictions of an 'equivalent' linear elastic soil model for a clay with the properties of normally consolidated BBC.

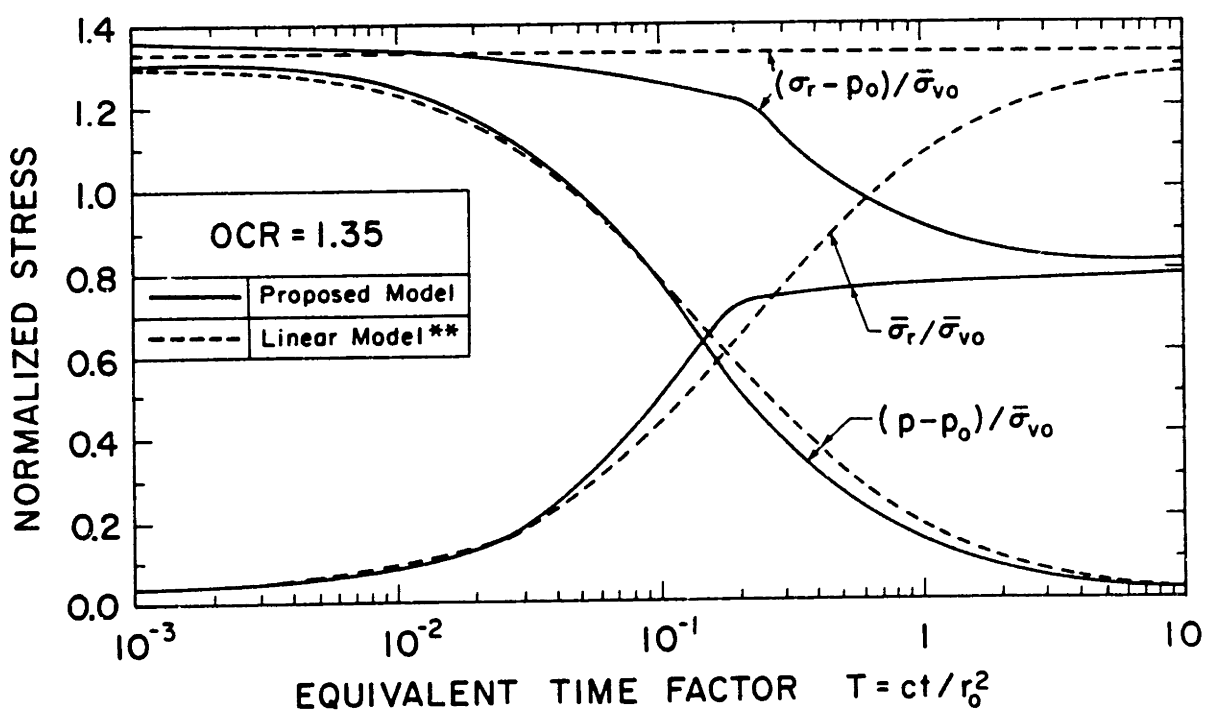
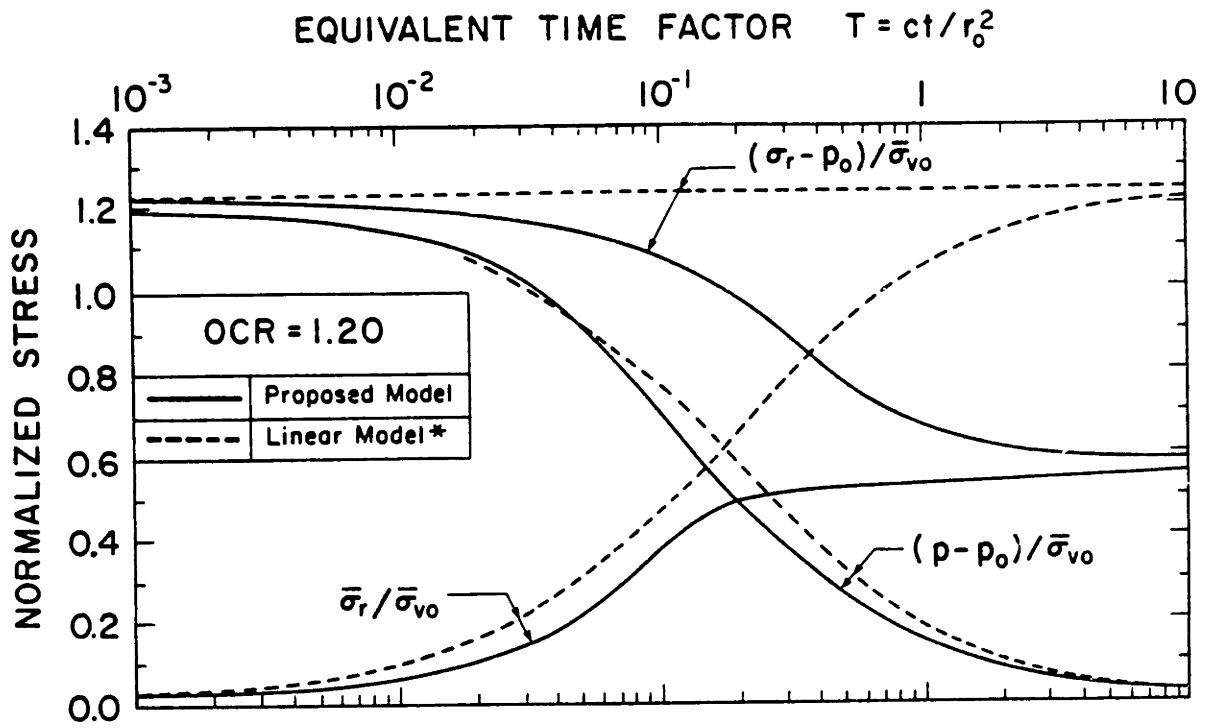


Fig. 8.19: Comparison of the stress and pore pressure changes at the pile wall predicted by the proposed model with the predictions of an 'equivalent' linear elastic soil model for slightly overconsolidated BCC.

## CHAPTER 9

### SUMMARY AND CONCLUSIONS

This research represents an effort to develop a better understanding of the mechanisms governing the development of axial capacity of piles driven in clays.

The prediction of the axial capacity of a single pile is the first step in deep foundation design and consists of the estimation of the resistance at the tip (point resistance) and along the shaft (skin friction). For long piles in clays the point resistance usually represents a small fraction of the pile capacity and, for most practical purposes, is adequately predicted by existing methods (see Chapter 1). Thus, the major portion of the axial capacity is derived from the skin friction, especially when no competent end bearing layer exists. Therefore, the limiting skin friction that can be provided by the soil is of primary importance in the design of piles.

Currently, estimates of the skin friction are obtained mainly by empirical methods (see Chapter 2) because of the complicated and very little understood mechanisms of soil deformation and stressing during pile loading to failure. These mechanisms may be understood by studying the sequence of events preceding pile loading to failure, i.e., pile installation and soil consolidation:

Pile installation changes the initial in-situ effective stresses in the soil and induces significant excess pore pressures. The dissipation of these pore pressures with time (consolidation) causes further changes of the effective stresses and, the values of the effective stresses after consolidation control the magnitude of the skin friction that can be mobilized during pile loading. Thus, the values of the effective stresses after consolidation depend on:

- (i) The initial in-situ conditions before pile installation;
- (ii) The changes of the effective stresses and pore pressures during pile installation and,
- (iii) The changes of the effective stresses during consolidation.

Estimates of the above changes of the effective stresses depend on the method used to analyze pile installation and subsequent soil consolidation as well as the soil stress-strain model employed in these analyses. Thus, this research concentrates on the following topics:

- (i) Development of a stress-strain constitutive relationship that can reliably model clay behavior under general (undrained and partially drained) loading conditions.
- (ii) Analysis of pile installation and estimation of the effective stresses and excess pore pressures in the soil immediately after pile driving.
- (iii) Analysis of soil consolidation and estimation of the effective stresses around the pile after consolidation.

## SOIL MODEL

Chapter 3 presents a modern formulation of the concepts of Plasticity Theory necessary to develop constitutive laws for soils and, as an application, discusses the Principles of the Modified Cam-Clay (MCC) model (Roscoe and Burland, 1968).

Chapter 4 proposes a non-linear, elasto-plastic, anisotropic model for clays based on Plasticity Theory. The proposed model generalizes many of the features of the MCC model in order to represent more realistically the following aspects of clay behavior:

- (i) Stress paths starting from  $K_0$ -stress conditions instead of isotropic conditions.
- (ii) Stress-strain and strength anisotropy.
- (iii) Strain softening after a peak strength condition in certain modes of deformation

The yield surface of the proposed model can be represented by a distorted ellipsoid in a general multi-dimensional effective stress space. In the case of an one-dimensionally ( $K_0$ ) consolidated clay, the yield surface is initially oriented along the  $K_0$ -line. During deformation, the yield surface in general changes in size (isotropic hardening) and rotates in the stress space (kinematic hardening). Changes in size allow the proposed model to take in consideration the influence of the void ratio on the predicted strength of the clay, whereas the orientation of the yield surface expresses the magnitude and direction of the stress-strain anisotropy.

The proposed model takes in consideration strength



anisotropy by introducing a (Critical State) failure criterion represented by a conical surface in a general multi-dimensional effective stress space; the orientation of the cone axis expresses the magnitude and direction of the Critical State strength anisotropy. An additional conical surface in the interior of the Critical State cone represents the Peak Strength condition and its orientation expresses the magnitude and direction of the Peak Strength anisotropy. The two nested conical surfaces divide the effective stress space in three domains:

- (i) The interior of the Peak Strength cone representing Strain Hardening states;
- (ii) The region between the Peak Strength and the Critical State cones representing Strain Softening states; and,
- (iii) The exterior of the Critical State cone which is inaccessible for most stress paths (e.g. monotonic paths on normally consolidated or slightly overconsolidated clays).

The proposed model is equipped with a non-associated flow rule\* such that all radial effective stress paths on the normally consolidated clay have the same virgin compression index.

The proposed model requires twelve material parameters which can be obtained from laboratory tests (see Chapter 5).

For the sake of computational efficiency, all tensorial equations of the proposed model are expressed in terms of six 'transformed' stress (and strain) measures comprised of the

---

\* which reduces to associated at the Critical State

octahedral component and five linear combinations of the deviatoric tensorial components.

Chapter 5 evaluates the proposed model by comparing its predictions to results of laboratory tests on  $K_0$ -consolidated resedimented Boston Blue Clay (BBC) and to the predictions of the Modified Cam-Clay (MCC) and the Prevost-Levadoux-Baligh (PLB) models.

The MCC model has certain interesting characteristics (e.g. volumetric hardening, the Critical State concept, few parameters that are easy to obtain, etc), but it does not give realistic predictions of the measured stress-strain-strength behavior of  $K_0$ -consolidated BBC. More specifically, it does not predict the strain softening and strength anisotropy and grossly overestimates the measured undrained shear strength in all plane strain modes of deformation\*.

The PLB model can describe the post-peak strain softening observed in certain modes of deformation and, when the necessary parameters are evaluated from cyclic triaxial tests, it can predict the stress-strain behavior of clays under repeated loading\*\*. The model also gives reasonably good predictions of the undrained shear strength in Plane Strain Compression and Extension, but overestimates the strength in the DSS test. However, because of its nature (i.e., a total

---

\* actually the model predicts the same value of the undrained shear strength for all Plane Strain modes

\*\* Levadoux and Baligh (1980) show that the model can give reasonably good predictions for the first 3 to 4 cycles of load application

stress model), the model is limited to undrained stress paths, i.e., it cannot be used to study consolidation or drained paths. Furthermore, the model cannot predict the stress-strain behavior of overconsolidated clays based on the values of the soil parameters obtained from tests on (say) the normally consolidated clay, but requires additional tests for ALL overconsolidation ratios to be studied. Finally, the model requires a large number of input parameters (typically 130-200, depending on the number of yield surfaces used).

The proposed model has certain advantages compared to the PLB model:

- (i) It can be used to solve Boundary Value problems involving consolidation and drained loading because it is an effective stress model\*.
- (ii) It gives predictions similar to those of the PLB model for undrained tests on  $K_0$ -normally consolidated BBC. More specifically, the proposed model predicts the undrained shear strength and the effective friction angles in the Triaxial and Plane Strain modes of deformation with the same degree of accuracy and, it gives significantly better predictions in the DSS mode of deformation compared to the PLB model.
- (iii) It can predict the stress-strain behavior of overconsolidated clays and the behavior of clays during cyclic tests, based on the values of the parameters obtained from monotonic tests on the normally

---

\* it can also be used to study undrained problems

consolidated clay, whereas the PLB model requires additional monotonic and cyclic tests for each overconsolidation ratio to be analysed.

- (iv) It requires a reasonable number of input parameters (twelve) compared to 130-200 required by the PLB model and it is computationally more efficient than the PLB model (typically it requires 7-10 times less CPU time depending on the stress path).

In the present form, the proposed model gives reasonable predictions for  $K_0$ -normally consolidated undrained monotonic shear tests in the Triaxial, Plane Strain and the Direct Simple Shear apparatuses, as well as during the first couple of cycles of one series of undrained cyclic triaxial tests on the  $K_0$ -normally consolidated clay. For undrained shear tests on the slightly overconsolidated clay (OCR=2), the model overpredicts the strength in the Compression modes but gives reasonable predictions in the Extension and in the DSS modes. The discrepancies in the predictions for the overconsolidated clay are mainly due to the assumption that stress states inside the yield surface\* give a linear elastic stress-strain response. This simplifying assumption does not have significant consequences when studying monotonic stress paths on normally consolidated clays but affects the predicted response for cyclic tests and tests on overconsolidated clays. In these cases, improvements can be achieved by using a more

---

\* such states may be reached during a load reversal (i.e., for a cyclic test) and during a rebound leading to an overconsolidated state.

sophisticated law to describe the stress-strain behavior inside the yield surface (i.e., for elastic states) which basically means introducing more parameters obtained from cyclic tests and tests on overconsolidated samples. It is also interesting to note that, since the stress-strain behavior inside the yield surface is basically uncoupled from the behavior at states located on the yield surface (i.e., elastoplastic states), these improvements can be incorporated in the model with only minor modifications of the existing computational algorithm.

#### PILE INSTALLATION

Chapter 6 estimates the values of the excess pore pressures and the effective stresses in the soil during steady pile installation (driving). These values represent the initial conditions for the consolidation analyses and thus, they are essential for the rational interpretation of the consolidation that takes place after pile installation. More specifically, this Chapter concentrates on the estimation of the excess pore pressures and the effective stresses far behind the pile tip, since the major portion of the bearing capacity of long friction piles (commonly used offshore) is due to the shaft friction rather than the point resistance.

File installation analyses are performed using two methods:

- (i) The Undrained Expansion of a Cylindrical Cavity.
- (ii) The Strain Path method.

Both methods are based on assumed (simplified) soil velocity fields obtained mainly by kinematic considerations (i.e.,

incompressibility), without solving the Boundary Value problem of pile installation. In the case of the Strain Path method, the assumed velocity field does not conform with the constitutive behavior of the soil. The basic difference between the two methods is that the Strain Path method takes into consideration the effect of the pile tip, whereas the Cavity Expansion method neglects this effect and treats pile installation as an one-dimensional problem. Thus, the Strain Path method is expected to give more realistic predictions of the effective stresses and the excess pore pressures in the soil immediately after pile installation. Both methods give very similar strains in the soil far behind the pile tip, whereas the predicted strain paths of the individual soil elements are very different: the Cavity Expansion method predicts monotonic radial strain paths for all soil elements and, the Strain Path method predicts large strain reversals and complicated strain paths\*.

The stress and excess pore pressure distributions in the soil far behind the pile tip are estimated\*\* by means of three non-linear soil models:

- (i) The Modified Cam-Clay (MCC) model.
- (ii) The Prevost-Levađoux-Baligh (PLB) model.
- (iii) The model proposed in Chapter 4.

File installation analyses show that:

---

\* especially close to the pile wall

\*\* using the strain paths predicted by the Cavity Expansion and the Strain Path methods for a soil with properties similar to normally consolidated resedimented Boston Blue Clay

- (i) For radial distances less than 10 times the pile radius, there are major differences in the stress and pore pressure changes predicted by means of the Cavity Expansion and the Strain Path methods. These differences indicate that the effect of the pile tip (which is neglected by the Cavity Expansion method) is very significant. More specifically, in the region close to the pile wall, the Strain Path method predicts significantly smaller values of the excess pore pressure and the total (and effective) radial stress, compared to the Cavity Expansion method. Furthermore, the predicted distributions in the radial direction have different shapes: in the region close to the pile wall, the Cavity Expansion method predicts a logarithmic distribution of the excess pore pressure and of the total radial stress, whereas the Strain Path method predicts approximately constant values of the excess pore pressure and of the total radial stress. Field measurements in a variety of clays support the shape of the excess pore pressure distributions predicted by the Strain Path method.
- (ii) The Strain Path and the Cavity Expansion methods predict comparable stress and excess pore pressure changes in the soil, for radial distances larger than 10-20 times the pile radius. This means that the effect of the pile tip does not extend to radial distances larger than 10-20 times the pile radius.

The values of the excess pore pressure and of the total radial

stress at the pile wall (far behind the pile tip), estimated\* according to the Strain Path method, underpredict the values measured in Boston Blue Clay\*\* by almost a factor of two. On the contrary, the measured value of the effective radial stress at the pile wall is reasonably well predicted. The poor agreement between the predicted and measured values of the excess pore pressure and the total radial stress at the pile wall is mainly due to:

- (i) The fast rate of straining during pile installation compared to the rate of straining during the laboratory tests used in the predictions.
- (ii) A possible underprediction of the stiffness of the clay at very low strain levels (less than 0.1%), comparable to the strain levels in the soil far away from the pile.
- (iii) A slight overconsolidation of the clay below 75 ft., since  $OCR=1.3\pm 0.1$  instead of the normally consolidated clay assumed in obtaining the predictions.

The effects of varying the overconsolidation ratio and the initial stiffness of the clay are small. When the OCR is increased from unity to 1.35, the proposed model predicts 18% higher excess pore pressure at the pile wall. Similarly, for a three-fold increase of the elastic stiffness, the proposed model predicts 10% higher excess pore pressure at the pile wall. These improvements are not sufficient to justify the

---

\* using any of the three soil models above for a soil with properties similar to normally consolidated Boston Blue Clay

\*\* at depths below 75 ft., where the clay is reasonably uniform with  $OCR=1.3\pm 0.1$ .



underprediction of the excess pore pressure at the pile wall by almost a factor of two. However, the predicted distributions of stresses and pore pressures around the pile\* are used as initial conditions in the consolidation analyses presented in Chapter 8, for the following reasons:

- (i) The radial effective stress at the pile wall is reasonably well predicted and, it is widely accepted that the single most important parameter in estimating pile capacity is the radial effective stress at the pile wall immediately after installation and its changes during consolidation.
- (ii) The normalized\*\* distribution of the excess pore pressure is reasonably well predicted and previous work (e.g. Levadoux and Baligh, 1980) has shown that excess pore pressure dissipation rates appear to depend primarily\*\*\* on this normalized distribution rather than the absolute magnitudes of the excess pore pressure.

## SOIL CONSOLIDATION

Chapter 7 presents a modern version of Biot's Theory of Consolidation and its application in the study of consolidation

---

\* for OCR equal to 1.0, 1.2 and 1.35

\*\* with the value of the excess pore pressure at the pile shaft.

\*\*\* evidently, they also depend on the soil characteristics (i.e., the coefficient of consolidation).

around piles. In the case of a linear, elastic, isotropic soil a closed form analytical solution is obtained, whereas in the case of a non-linear soil, the Theory is expressed in an Incremental Weighted Residuals Variational form. This Variational form is then used to develop a Finite Element scheme for the solution of linear and non-linear consolidation problems and, this scheme is implemented in a computer program for the case of one-dimensional linear and non-linear soil consolidation around a cylindrical pile.

Chapter 8 performs linear and non-linear one-dimensional consolidation analyses around a pile driven in normally consolidated and slightly overconsolidated BBC (OCR=1.20 and 1.35) using the following soil constitutive models:

- (i) The Linear Elastic Isotropic model.
- (ii) The Modified Cam-Clay (MCC) model.
- (iii) The model proposed in Chapter 4.

and initial stress and excess pore pressure distributions obtained by means of:

- (i) The Undrained Cylindrical Cavity Expansion method.
- (ii) The Strain Path method.

Linear analyses show that the total radial stress at the pile wall remains constant during consolidation which means that the radial effective stress at the pile wall after consolidation is completed is equal to the total radial stress\* in the beginning of consolidation. These conclusions do not agree with experimental data and thus, non-linear analyses are

---

\* minus the ambient (hydrostatic) pore pressure

required in order to obtain realistic estimates of the stresses acting on the pile wall after consolidation is completed.

Non-linear analyses using the proposed model and initial conditions estimated via the Strain Path method show that in the early stages of consolidation, the soil around the pile has a stiff (elastic) response, whereas at later times, a soft (plastic) zone develops in the region close to the pile wall. The value of the equivalent time factor when Plasticity is first induced in the soil increases with increasing OCR and has a significant effect on the predicted changes of the radial effective stress at the pile wall during consolidation. More specifically, non-linear analyses show that the radial effective stress at the pile wall increases mainly during the early stages of consolidation (i.e., while the soil around the pile is elastic) and thus, the predicted value of the radial effective stress at the pile wall at the end of consolidation increases with increasing OCR.

Comparison of non-linear analyses shows that the method used to estimate the stress and excess pore pressure distributions in the soil in the beginning of consolidation has a significant effect on the predicted value of the radial effective stress acting on the pile wall after consolidation. Analyses using the proposed model and initial conditions estimated via the Strain Path method show that, after consolidation is completed, the radial effective stress everywhere in the soil around the pile, is approximately equal to the initial in-situ horizontal effective stress before pile

installation. On the contrary, analyses using initial conditions estimated via the Cavity Expansion method show that, after consolidation is completed, the predicted value of the radial effective stress at the pile wall is significantly higher than the Strain Path prediction mainly because of differences in the corresponding values in the beginning of consolidation.

During consolidation, a soil element located at the pile wall is subjected to one-dimensional straining in the radial direction and thus, the predicted effective stress path approaches the radial one-dimensional consolidation line.

Comparison of the results of non-linear consolidation analyses\* with field measurements in slightly overconsolidated Boston Blue Clay show that the proposed model gives:

- (i) Good estimates of the permeability coefficient based on normalized\*\* pore pressure dissipation data measured at the pile wall, or on the measured changes of the radial effective stress at the pile wall.
- (ii) Reasonable estimates of the radial effective stress changes at the pile wall during consolidation (except at very small times) and good predictions of the magnitude of the radial effective stress at the pile wall after consolidation is completed.

---

\* using the proposed model and initial conditions estimated via the Strain Path method

\*\* with the value of the pore pressure at the pile wall in the beginning of consolidation

(iii) Poor predictions of the normalized\* total radial stress changes at the pile wall during consolidation indicating that the differences in the absolute magnitudes of the predicted and measured total radial stresses in the beginning of consolidation have a significant effect on the predicted changes during consolidation.

An 'equivalent' linear elastic soil model with stiffness corresponding to the recompression modulus of the clay fits reasonably well the excess pore pressure dissipation curve at all times indicating that the average stiffness of the soil around the pile remains essentially constant during consolidation. This is due to the fact that during consolidation:

- (i) A soft (plastic) zone develops close to the pile wall, tending to retard the pore pressure dissipation rates.
- (ii) The mean effective stress increases and thus, the soil stiffness increases tending to accelerate the pore pressure dissipation rates.

The combined effect of these mechanisms is that the average stiffness of the soil remains essentially constant during consolidation.

---

\* with the magnitude of the total radial stress at the pile wall in the beginning of consolidation

## REFERENCES

**NOTE:** The following abbreviations have been used:

API : American Petroleum Institute  
ASCE : American Society of Civil Engineers  
ASME : American Society of Mechanical Engineers  
ASTM : American Society of Testing Materials  
ICSMFE : International Conference of Soil Mechanics and Foundation Engineering  
IUTAM : International Union of Theoretical and Applied Mechanics  
JEMD : Journal of the Engineering Mechanics Division  
JGED : Journal of the Geotechnical Engineering Division  
JSMFD : Journal of Soil Mechanics and Foundations Division  
MIT : Massachusetts Institute of Technology  
OTC : Offshore Technology Conference

Abramowitz M. and Stegun I.A. (1965) Handbook of Mathematical Functions, Dover Publications Inc. N.Y.

American Petroleum Institute. (1975) "Recommended Practice for Planning, Designing and Constructing Fixed Offshore Platforms." API RP2A.

Argyris J.H. and Scharpf D.W. (1969) "Methods of Elasto-Plastic Analysis". ISD, ISSC Symposium on Finite Element Technology, Stuttgart, Germany.

Arthur J.R.F. and Assadi A. (1977) "Ruptured Sand Sheared in Plane Strain", Proc. 9th ICSMFE, Tokyo, Vol.1, pp. 19-22.

Arthur J.R.F., Bekenstein S., Germaine J.T. and Ladd C.C. (1980) "Stress Path Tests with Controlled Rotation of Principal Stress Directions", ASTM Symposium on Shear Strength of Soil, Chicago (Preprint).

Arthur J.R.F. and Menzies B.K. (1972) "Inherent Anisotropy in a Sand", Geotechnique, Vol. 22, No. 1, pp. 115-128.

Azzouz A.S., Levadoux J.N. and Baligh M.M. (1980) "Cavity Expansion Approaches in Deep Foundations", Research Report, Department of Civil Engineering, MIT, Cambridge, Mass.

Baguelin F. et al (1972) "Expansion of Cylindrical Probes in Cohesive Soils", JSMFD, ASCE, Vol. 98, SM11, pp. 1129-1142.

Baligh M.M. (1975) "Theory of Deep Site Static Cone Penetration Resistance", Research Report R75-56, No. 517, Department of Civil Engineering, MIT, Cambridge, Mass. 133 pp.

- Baligh M.M. and Kavvadas M. (1980) "Axial Static Capacity of Offshore Friction Piles in Clays: I. Evaluation of Existing Methods". Research Report R80-32 No. 681, Department of Civil Engineering, MIT, Cambridge, Mass. 221 pp.
- Baligh M.M. and Levadoux J.N. (1980) "Pore Pressure Dissipation After Cone Penetration", Publication No. R80-11, Order No. 662, Department of Civil Engineering, MIT, Cambridge, Mass.
- Baligh M.M., Vivatrat V. and Ladd C.C. (1978) "Exploration and Evaluation of Engineering Properties for Foundation Design of Offshore Structures", Research Report R78-40, No. 607, Department of Civil Engineering, MIT, Cambridge, Mass.
- Banerjee P.K. (1970) "A Contribution to the Study of Axially Loaded Pile Foundations". PhD Thesis, Southampton University, England.
- Bathe K.J. and Wilson E.L. (1976) Numerical Methods in Finite Element Analysis, Prentice-Hall Inc., Englewood Cliffs, N.J.
- Bea R.G. (1975) "Parameters Affecting Axial Capacity of Piles in Clays". 7th Annual OTC, Paper Number 2307, Vol. 2, pp. 611-623.
- Berezin I.S. and Zhidkov N.P. (1965) Computing Methods, Pergamon Press, Oxford, England.
- Biot M.A. (1935) "Le Probleme de la Consolidation des Matieres Argileuses sous une Charge". Annales de la Societe Scientifique de Bruxelles, Series B, 55, pp. 110-113.
- Biot M.A. (1941) "General Theory of Three-Dimensional Consolidation", Journal of Applied Physics, Vol. 12, pp. 155-164.
- Biot M.A. (1955) "Theory of Elasticity and Consolidation for a Porous Anisotropic Solid". Journal of Applied Physics, Vol. 26, pp. 182-185.
- Biot M.A. (1956) "General Solutions of the Equations of Elasticity and Consolidation for a Porous Material". Transactions, Journal of Applied Mechanics, ASME, Vol. 78, pp. 91-96.
- Bishop A.W. and Hight D.W. (1977) "The Value of Poisson's Ratio in Saturated Soils and Rocks, Stressed Under Undrained Conditions", Geotechnique, Vol. 27, 3, pp. 369-384.

- Bishop R., Hill R. and Mott N. (1945) "The Theory of Indentation and Hardness Tests", Proceedings, Physical Society, London, Vol. 57, Part 3, No. 321, pp. 147-159.
- Bjerrum L. (1973) "Problems of Soil Mechanics and Construction on Soft Clays", State-of-the-Art Report, Session 4, Proc. 8th ICSMFE, Moscow, Vol. 3, pp. 109-159.
- Bjerrum L. and Flodin N. (1960) "The Development of Soil Mechanics in Sweden, 1900-1925". Geotechnique, Vol. 10, 1, pp. 1-18.
- Bjerrum L., Hansen J.B. and Sevaldson R. (1958) "Geotechnical Investigations for a Quay Structure in Horton". Norwegian Geotechnical Publication, No. 28, Oslo, Norway.
- Bjerrum L. and Landva A. (1966) "Direct Simple Shear Tests on Norwegian Quick Clay", Geotechnique, Vol. 16, No. 1, pp. 1-20.
- Booker J.R. (1973) "A Numerical Method for the Solution of Biot's Consolidation Theory". Quarterly Journal of Mechanics and Applied Mathematics, Vol. 26, pp. 457-470.
- Booker J.R. and Small J.C. (1975) "An Investigation of the Stability of Numerical Solutions of Biot's Equations of Consolidation", Int. Journal of Solids and Structures. Vol. 11, pp. 907-917.
- Braathen N.F. (1966) "Investigation of Effect of Disturbance on Undrained Shear Strength of Boston Blue Clay", Master's Thesis, Department of Civil Engineering, MIT, Cambridge, Mass.
- Budhu M. (1979) "Simple Shear Deformation of Sands". PhD. thesis. Cambridge University, Cambridge, England.
- Burland J.B. (1967) "Deformation of Soft Clay". PhD. Thesis, Cambridge University, Cambridge, England.
- Burland J.B. (1973) "Shaft Friction of Piles in Clay; A Simple Fundamental Approach", Ground Engineering, Vol. 6, No. 3, pp. 30-32, 37-42.
- Butterfield R. and Bannerjee P.K. (1970) "The Effect of Porewater Pressures on the Ultimate Bearing Capacity of Driven Piles", Proceedings, 2nd Southeast Asian Conference on Soil Engineering, Singapore, pp. 385-394.
- Campanella R.G. and Vaid Y.P. (1972) "A Simple  $K_0$ -Triaxial Cell", Canadian Geotechnical Journal, Vol. 9, No. 3, pp. 249-260.
- Carslaw A.R. and Jaeger C.J. (1959) Conduction of Heat in



Solids, Oxford at the Clarendon Press, London.

- Carter J.P., Booker J.R. and Small J.C. (1979) "The Analysis of Finite Elasto-Plastic Consolidation". International Journal for Numerical and Analytical Methods in Geomechanics, Vol. 3, 2, pp. 107-130.
- Carter J.P., Randolph M.F. and Wroth C.P. (1978) "Stress and Pore Pressure Changes in Clay during and after the Expansion of a Cylindrical Cavity", Report No. TR 51, Department of Civil Engineering, Cambridge University, Cambridge, England.
- Carter J.P., Randolph M.F. and Wroth C.P. (1979) "Some Aspects of the Performance of Open and Closed-End Piles". Conference on Numerical Methods in Offshore Piling, Institution of Civil Engineers, London, England, pp.137-142.
- Carter J.P., Randolph M.F. and Wroth C.P. (1979) "Stress and Pore Pressure Changes in Clay during and after the Expansion of a Cylindrical Cavity". International Journal for Numerical and Analytical Methods in Geomechanics, Vol. 3, pp. 305-322.
- Carter J.P., Small J.C. and Booker J.R. (1977) "A Theory of Finite Elastic Consolidation". Int. J. of Solids and Structures, Vol. 13, pp. 467-478.
- Casagrande A. and Carillo N. (1944) "Shear Failure of Anisotropic Materials". Proc. Boston Society of Civil Engineers, Vol. 31, pp. 74-87.
- Chadwick P. (1959) "The Quasi-Static Expansion of a Spherical Cavity in Metals and Ideal Soils" Quarterly J. of Mechanics and Applied Mathematics, Vol. 12, Part I, pp. 52-71.
- Chandler R.J. (1968) "The Shaft Friction of Piles in Cohesive Soils in terms of Effective Stress", Civil Eng. and Public Works Review, Vol. 63, pp. 48-51.
- Connor J.J. and Brebbia C.A. (1976) "Finite Element Techniques for Fluid Flow" Butterworth and Co. Publishers, London.
- Cryer C.W. (1963) "A Comparison of the Three-Dimensional Consolidation Theories of Biot and Terzaghi" Quarterly J. of Mechanics and Applied Mathematics, Vol. 16, Part 4, pp. 401-412.
- Cummings A.E., Kerkhoff G.O. and Peck R.B. (1950) "Effect of Driving Piles into Soft Clay" Transactions ASCE, Vol. 115, pp. 275-286.
- Davis E.H. and Poulos H.G. (1970) Discussion of "An Analysis of Consolidation Theories" by Schiffman R.L. et al., JSMFD,

ASCE, Vol. 96, No. SM1, pp. 334-336.

Davis R.O. and Mullenger G. (1978) "A Rate-Type Constitutive Model for Soils with a Critical State" Int. J. for Numerical and Analytical Methods in Geomechanics, Vol. 2, No. 3, pp. 255-282.

de Josselin de Jong G. (1971) Discussion in Session II of the Roscoe Memorial Symposium "Stress-Strain Behavior of Soils" edited by R.H.G. Parry. pp. 258-261.

Desai C.S. and Saxena S.K. (1977) "Consolidation Analysis of Layered Anisotropic Foundations" Int. J. for Numerical and Analytical Methods in Geomechanics, Vol. 1, pp. 5-23.

Drucker D.C. (1959) "Definition of Stable Inelastic Material" J. of Applied Mechanics, Vol. 26, pp. 101-186.

Duncan J.M. and Seed H.B. (1966) "Anisotropy and Stress Reorientation in Clay", JSMFD, ASCE, Vol. 92, SM5, pp. 21-50.

Duncan J.M. and Seed H.B. (1966) "Strength Variation along Failure Surfaces in Clay" JSMFD, ASCE, Vol. 92, SM6, pp. 81-104.

Eide O., Hutchinson J.N. and Landva A. (1961) "Short and Long Term Test Loading of a Friction Pile in Clay", Proc. of the 5th ICSMFE, Paris, France, Vol. 2, pp. 45-53.

Esrig M.I. and Kirby R.C. (1978) "Soil Capacity for Supporting Deep Foundation Members in Clay", State-of-the-Art paper, in: Behavior of Deep Foundations, ASTM Special Technical Publication SPT 670, R. Lundgren editor, 43p.

Esrig M.I., Kirby R.C., Bea R.G. and Murphy B.S. (1977) "Initial Development of a General Effective Stress Method for the Prediction of Axial Capacity for Driven Piles in Clay", OTC Paper 2943, 9th Annual OTC, Houston, Texas.

Esrig M.I., Kirby R.C. and Murphy B.S. (1979) "Advances in General Effective Stress Method for the Prediction of Axial Capacity for Driven Piles in Clay", OTC Paper 3406, 11th Annual OTC, Houston, Texas.

Flaate K. (1968) "Baereevne av Friksjonspeler i Leire", om Beregning av Baereevne pa grunnlag av Geotekniske Under-sokelser, Oslo Veglaboratoriet, Norway.

Flaate K. (1972) "Effects of Pile Driving in Clays" Canadian Geotechnical Journal, Vol. 9, No. 1, pp. 81-96.

Flaate K. and Selnes P. (1977) "Side Friction of Piles in Clay", Proceedings of the 9th ICSMFE, Tokyo, Japan, Vol. 1, pp. 517-522.

- Fox D.A., Parker G.F. and Sutton V.J.R. (1970) "Pile Driving in the North Sea Boulder Clays", 2nd Annual OTC, pp. 1535-1546.
- Ghaboussi J. and Momen H. (1979) "Plasticity Model for Cyclic Behavior of Sands" 3rd Int. Conf. on Numerical Methods in Geomechanics, Aachen, Germany, pp. 423-434.
- Gibson R.E. and Anderson W.F. (1961) "In Situ Measurement of Soil Properties with the Pressuremeter" Civil Engineering and Public Works Review, Vol. 56, No 658, pp. 615-618.
- Gurtin M.E. (1964) "Variational Principles for Linear Elastodynamics" Archive of Rational Mechanics and Analysis, Vol. 16, No 1, pp. 32-50.
- Hardin B.O. (1972) "Effects of Strain Amplitude on the Shear Modulus of Soils" Technical Report No. AFWL-TR-72-201, Air Force Base, New Mexico, 63p.
- Hashiguchi K. (1979) "Constitutive Equations of Granular Media with an Anisotropic Hardening" Proceedings of the 3rd Int. Conf. on Numerical Methods in Geomechanics, Aachen, Germany, Vol. 3, pp. 435-439.
- Henkel D.J. (1960) "The Shear Strength of Saturated Remolded Clays" Proceedings of the ASCE Specialty Conference on Shear Strength of Cohesive Soils, Boulder Colorado.
- Henkel D.J. and Wade N.H. (1966) "Plane Strain Tests on a Saturated Remolded Clay" JSMFD, ASCE, Vol. 92, SM6, pp. 67-80.
- Hill R. (1950) The Mathematical Theory of Plasticity, Oxford at Clarendon Press, England.
- Hodge P.G. (1965) "The Theory of Piecewise Linear Isotropic Plasticity". Proceedings of the IUTAM Colloquium, Madrid.
- Housel W.S. (1950) Discussion of "Effect of Driving Piles into Soft Clay" by Cummings et al (1950). Transactions ASCE, Vol. 115, pp. 339-346.
- Hwang C.T., Morgenstern N.R. and Murray D.W. (1971) "On Solutions of Plane Strain Consolidation Problems by Finite Element Methods". Canadian Geotechnical Journal, Vol. 8, pp. 109-118.
- Jaky J. (1944) "The Coefficient of Earth Pressure at Rest". Journal of the Society of Hungarian Architects and Engineers. Budapest, Hungary pp. 355-358.
- Kavvas M. (1980) "Stress-Strain Relations for Soils based on Plasticity Theory". SM Thesis, Department of Civil Engineering, MIT, Cambridge, Mass. 155 pp.

- Kavvasdas M. and Baligh M.M. (1980) "Linear and Non-Linear Finite Element Techniques for Soil Consolidation around Pile Shafts". MIT Research Report R80-41, Order No. 685, Department of Civil Engineering, Cambridge, Mass.
- Kenney T.C. (1964) "Sea Level Movements and Geologic Histories of the Post-Glacial Marine Soils at Boston, Nicolet, Ottawa and Oslo", *Geotechnique*, Vol. 14, No. 3, pp.203-230.
- Kenney T.C. (1966) "Shearing Resistance of Natural Quick Clays" Ph.D Thesis, Faculty of Engineering, University of London, England.
- Kirby R.C and Esrig M.I. (1979) "Further Development of a General Effective Stress Method for Prediction of Axial Capacity for Driven Piles in Clay". Conference on Recent Development in the Design and Construction of Piles. The Institution of Civil Engineers, London, England.
- Kirby R.C. and Wroth C.P. (1977) "Application of Critical State Soil Mechanics to the Prediction of Axial Capacity for Driven Piles". Proceedings, 9th Offshore Technology Conference, Paper No. 2942, Vol. 3, pp. 483-494.
- Ko H.Y. and Sture S. (1980) "Data Reduction and Application for Analytical Modelling". State-of-the-Art Paper presented at ASTM Symposium, Chicago, Ill.
- Koutsoftas D. and Ryan C. (1970) "Comparative Analysis of Consolidation Data on Boston Blue Clay". MIT Informal Research Report, Cambridge, Mass.
- Krizek R.J. (1977) "Fabric Effects on Strength and Deformation of Kaolin Clay", Proceedings of the 9th ICSMFE, Tokyo, Vol. 1, pp. 169-176.
- Ladanyi B. (1963) "Expansion of a Cavity in a Saturated Clay Medium", *Journal of the Soil Mechanics and Foundations Division, ASCE*, Vol. 89, No. SM4, pp. 127-161.
- Ladanyi B. (1972) "In-Situ Determination of Undrained Stress-Strain Behavior of Sensitive Clay with the Pressuremeter", *Canadian Geotechnical Journal*, Vol. 9, No. 3, pp. 313-319.
- Ladd C.C. (1981) Personal Communication
- Ladd C.C. and Edgers L. (1972) "Consolidated-Undrained Direct-Simple Shear Tests on Saturated Clays", Contract Report No. 3-101, Phase Report No. 16, Department of Civil Engineering, MIT, Cambridge, Mass.
- Ladd C.C. and Foott R. (1980) "The Behavior of Embankments on Clay Foundations: Discussion", *Canadian Geotechnical*

Journal, Vol. 17, No. 3, pp. 454-460.

- Ladd C.C. and Varallyay J. (1965) "The Influence of Stress System on the Behavior of Saturated Clays During Undrained Shear", Research Report R65-11, No. 177, Dept. of Civil Engineering, MIT, Cambridge, Mass., 263 pp.
- Ladd C.C., Bovee R.B., Edgers L. and Rixner J.J. (1971) "Consolidated-Undrained Plane Strain Shear Tests on Boston Blue Clay", Research Report R71-13, No. 273, Dept. of Civil Engineering, MIT, Cambridge, Mass., 243 pp.
- Ladd C.C., Foott R., Ishihara K., Schlosser F. and Poulos H.G. (1977) "Stress-Deformation and Strength Characteristics". Proceedings 9th International Conference on Soil Mechanics Foundation Engineering, Vol. 2, pp. 421-494.
- Lade P.V. and Duncan J.M. (1978) "Elasto-Plastic Stress-Strain Theory for Cohesionless Soil", JGED, ASCE, Vol. 104, pp. 193-207.
- Lade P.V. and Musante H.M. (1978) "Three-Dimensional Behavior of Remolded Clay", JGED, ASCE, Vol. 104, No. GT2, pp. 193-209.
- Lambe T.W. (1951) Soil Testing for Engineers, John Wiley and Sons, New York, 165 pp.
- Lambe T.W. (1958) "The Structure of Compacted Clay", JSMFD, ASCE, Vol. 84, No. SM 2, Paper No, 1654, 34 pp.
- Lambe T.W. (1967) "The Stress Path Method", JSMFD, ASCE, Vol. 93, pp. 309-331.
- Lambe T.W. and Whitman R.V. (1969) Soil Mechanics, John Wiley and Sons, New York.
- Leifer S.A., Kirby R.C and Esrig M.I. (1979) "Effect of Radial Variation of Material Properties on Stress Changes due to Consolidation around a Driven Pile". Conference on Numerical Methods in Offshore Piling, Institution of Civil Engineering, London, England.
- Leroueil S. (1977) "Quelques Considerations sur le Comportement des Argiles Sensibles", Ph.D. Thesis, Department of Civil Engineering, Laval University, Quebec, Canada.
- Leroueil S. et al (1979) "Behavior of Destructured Natural Clays", JGED, ASCE, Vol. 105, No. GT6, pp. 759-778.
- Levadoux J.-N. (1980) "Pore Pressures in Clays due to Cone Penetration", Ph.D. Thesis, Department of Civil Engineering, MIT, Cambridge, Mass., 753 pp.
- Levadoux J.-N. and Baligh M.M. (1980) "Pore Pressures during

Cone Penetration in Clays", MIT Research Report, R80-15, Order No. 666, Dept. of Civil Engineering, Cambridge, Mass. 310 pp.

Lewin P.I. (1973) "The Influence of Stress History on the Plastic Potential". Symposium on Plasticity and Soil Mechanics, Cambridge, England, pp. 96-107.

Lewin P.I. and Burland J.B. (1970) "Stress Probe Experiments on Saturated Normally Consolidated Clay". Geotechnique, Vol. 20, No. 1, pp. 38-56.

Malvern L.E. (1969) Introduction to the Mechanics of a Continuous Medium, Prentice-Hall, New Jersey.

Mandel J. (1953) "Consolidation des Sols (Etude Mathematique)", Geotechnique, Vol. 3, pp. 287-299.

Martin J.B. (1975) "Plasticity: Fundamentals and General Results". MIT Press, Cambridge, Mass. 931 pp.

Massarch K.R. (1978) "New Aspects of Soil Fracturing in Clay". JGED, ASCE, Vol. 104, GT8, pp. 1109-1123.

Massarch K.R. and Broms B.B. (1977) "Fracturing of Soil Caused by Pile Driving in Clay", Proceedings, 9th International Conference on Soil Mechanics and Foundation Engineering, Vol. 1, pp. 312-345, Tokyo.

McCammon N.R. and Golder H.Q. (1970) "Some Loading Tests on Long Pipe Piles". Geotechnique, Vol. 20, No. 2, pp. 171-184.

McClelland B. (1974) "Design of Deep Penetration Piles for Ocean Structures". Proceedings, ASCE, JGED, Vol. 100, GT7, pp. 709-747.

McClelland B. and Lipscomb L. (1955) "Load Test on a 333-foot Friction Pile in Deep Underconsolidated Clays". Paper presented at the National Meeting ASCE, Dallas, Texas.

McClelland Engineers (1969) "Additional Soil Investigation, Pile Research Program, Block 100, Eugene Island Area". Report to Shell Oil Company, 212 pp.

Meyerhof G.G. (1951) "The Ultimate Bearing Capacity of Foundations". Geotechnique, Vol. 2, No. 4, pp. 301-332.

Meyerhof G.G. (1976) "Bearing Capacity and Settlement of Pile Foundations", JGED, ASCE, Vol. 102, No. GT3, pp. 197-228.

Miller T.W., Murff J.D. and Kraft L.M. (1978) "Critical State Soil Mechanics Model of Soil Consolidation Stresses around a Driven Pile". Proceedings 10th Offshore Technology Conference, Vol. 4, Paper No. 3307, pp. 2237-2242.

- Mitchell J.K. (1976) Fundamentals of Soil Behavior, John Wiley and Sons, New York, 422 pp.
- Mroz A. (1967) "On the Description of Anisotropic Workhardening", *Journal of the Mechanics and Physics of Solids*, Vol. 15, pp.163-175.
- Naghdi P.M. (1960) "Stress-Strain Relations and Thermoplasticity", *Proceedings, Second Symposium on Naval Structural Mechanics*, Pergamon Press, New York.
- Nayak G.C. and Zienkiewicz O.C. (1972) "Elasto-Plastic Stress Analysis: A Generalization for Various Constitutive Relations Including Strain Softening". *International Journal of Numerical Methods in Engineering*. Vol. 5, pp. 113-135.
- Oda M. and Koishikawa I. (1977) "Anisotropic Fabric of Sands", *Proceedings 9th ICSMFE, Tokyo*, Vol. 1, pp. 235-238.
- Ohta H. and Sekiguchi H. (1979) "Constitutive Equations Considering Anisotropy and Stress Reorientation in Clay", *3rd International Conference on Numerical Methods in Geomechanics, Aachen*, pp. 475-484.
- Ohta H. and Wroth C.P. (1976) "Anisotropy and Stress Reorientation in Clay under Load", *Proceedings International Conference on Numerical Methods in Geomechanics, Virginia Polytechnic Institute*, pp. 319-329.
- Palmer A.C. (1972) "Undrained Plane-Strain Expansion of a Cylindrical Cavity in Clay: A Simple Interpretation of the Pressuremeter Test", *Geotechnique*, Vol. 22, No. 3, pp. 451-457.
- Peck R.B. (1958) "A Study of the Comparative Behavior of Friction Piles". *Highway Research Board, Specialty Report 36*.
- Pender M.J. (1978) "A Model for the Behavior of Overconsolidated Clays". *Geotechnique*, Vol. 28, No. 1, pp.1-25.
- Prager W. (1956) "A New Method of Analyzing Stresses and Strains in Work-Hardening Plastic Solids", *Journal of Applied Mechanics, Transactions, ASME*, Vol. 78, Series E, pp. 493.
- Prevost, J.H. (1976) "Undrained Stress-Strain-Time Behavior of Clays", *Journal of the Geotechnical Engineering Division, ASCE*, Vol. 102, No.GT12, pp. 1245-1259.
- Prevost J.H. (1977) "Mathematical Modelling of Monotonic and Cyclic Undrained Clay Behavior", *International Journal for*

- Numerical and Analytical Methods in Geomechanics, Vol. 1, pp. 195-216.
- Prevost J.H. (1978) "Anisotropic Undrained Stress-Strain Behavior of Clays", Journal of the Geotechnical Engineering Division, ASCE, Vol. 104, No. GT8, pp. 1075-1090.
- Prevost J.H. (1978) "Plasticity Theory for Soil Stress-Strain Behavior", JEMD, ASCE, EM5, Vol. 104, pp. 1177-1194.
- Prevost J.H. and Hoeg K. (1975) "Effective Stress-Strain-Strength Model for Soils", JGED, ASCE, Vol. 101, GT3, pp. 259-277.
- Prevost J.H. and Hoeg K. (1975) "Soil Mechanics and Plasticity Analysis of Strain Softening", Geotechnique, Vol. 25, 2, pp. 279-297.
- Prevost J.H. and Hoeg K. (1975) "Analysis of Pressuremeter in Strain-Softening Soil", Journal of the Geotechnical Engineering Division, ASCE, Vol. 101, pp. 717-732.
- Prevost J.H. and Hoeg K. (1976) "Reanalysis of Simple Shear Soil Testing", Canadian Geotechnical Journal, Vol. 13, No. 4, pp. 418-429.
- Randolph M.F. and Carter J.P. (1979) Discussion of "Effects of Driving and Subsequent Consolidation on Behavior of Piles", by Desai, C.S. International Journal for Numerical and Analytical Methods in Geomechanics, Vol. 3, pp. 213-215.
- Randolph M.F. and Wroth C.P. (1978) "An Analytical Solution for the Consolidation around a Driven Pile", Report No. TR 50, Department of Engineering, University of Cambridge, England.
- Randolph M.F. and Wroth C.P. (1979) "An Analytical Solution for the Consolidation around a Driven Pile", International Journal for Numerical and Analytical Methods in Geomechanics, Vol. 3, pp. 217-229.
- Randolph M.F. and Wroth C.P. (1981) "Application of the Failure State in Undrained Simple Shear to the Shaft Capacity of Driven Piles", Geotechnique, Vol. 31, No. 1, pp. 143-157.
- Randolph M.F., Carter J.P. and Wroth C.P. (1978) "Driven Piles in Clay: Installation, Modelled as the Expansion of a Cylindrical Cavity", Report No. TR 53, Department of Civil Engineering, University of Cambridge, England.
- Randolph M.F., Carter J.P. and Wroth C.P. (1978) "Driven Piles in Clay - Consolidation after Driving". Cambridge University, Department of Engineering Soils, Publishing No. TR 54.



- Randolph M.F., Carter J.P. and Wroth C.P. (1979) "Driven Piles in Clay - the Effects of Installation and Subsequent Consolidation". *Geotechnique*, Vol. 29. No.4.
- Randolph M.F., Steenfelt J.S. and Wroth C.P. (1979) "The Effect of Pile Type on Design Parameters for Driven Piles", *Proceedings, 7th European Conference on Soil Mechanics and Foundation Engineering*, Brighton, England.
- Rendulic L. (1936) "Porenziffer und Poren Wasserdruck in Tonen". *Der Bauingenieur*, Vol. 17, No. 51/53, pp. 559-564.
- Roscoe K.H. (1953) "An Apparatus for the Application of Simple Shear to Soil Samples", *Proceedings, 3rd International Conference on Soil Mechanics and Foundation Engineering*, Zurich.
- Roscoe K.H. and Burland J.B. (1968) "On the Generalized Behavior of Wet Clays", *Eng. Plasticity*. Eds. J. Heymann and F.A. Leckie, Cambridge, University Press, pp. 535-609.
- Roscoe K.H. and Poorooshasb H.B. (1963) "A Theoretical and Experimental Study of Strains in Triaxial Compression Tests on Normally Consolidated Clays", *Geotechnique*, Vol. 13, pp. 12-38.
- Roscoe K.H., Schofield A.N. and Thurairajah A. (1963) "Yielding of Soils in States Wetter than Critical", *Geotechnique*, Vol. 13, No. 3, pp. 211-240.
- Roscoe K.H. Schofield A.N. and Wroth C.P. (1958) "On the Yielding of Soils", *Geotechnique*, Vol. 8, No. 1, pp. 25-53.
- Rowe P.W. (1971) "Theoretical Meaning and Observed Values of Deformation Parameters for Soil", *Proceedings, Roscoe Memorial Symposium*, Cambridge University, Editor R.H.G. Parry, pp. 143-194.
- Roy M. et al. (1979) "Behavior of a Sensitive Clay during Pile Driving", *Proceedings, 32nd Canadian Geotechnical Conference*, Quebec, pp. 4.28-4.49.
- Sandhu R.S. and Wilson E.L. (1969) "Finite Element Analysis of Seepage in Elastic Media", *JEMD, ASCE*, Vol. 95, pp. 641-652.
- Schiffman R.L., Chen A.T.F. and Jordan J.C. (1969) "An Analysis of Consolidation Theories", *Journal of the Soil Mechanics and Foundations Division, ASCE*, Vol. 95, pp. 285-312.
- Schlitt H.G. (1950) "Steel Pile Tests, Q Street Viaduct, Omaha, Nebraska", Department of Roads and Irrigation, Lincoln, Nebraska.
- Schmertmann J.H. (1963) "Outline of Approximate Method of

- Analysis for Positioning the Average Mohr Stress Circle from a NGI Direct Shear Test", Informal Memorandum, NGI, 11.
- Schofield A.N. and Wroth C.P. (1968) Critical State Soil Mechanics, McGraw Hill, New York.
- Seed H.B. and Reese L.C. (1955) "The Action of Soft Clay along Friction Piles", Trans. ASCE, Vol. 81.
- Seed H.B. and Reese L.C. (1957) "The Action of Soft Clay along Friction Piles", Transactions ASCE, Vol. 83, pp. 731-754.
- Shield R.T. (1953) "Mixed Boundary Problems in Soil Mechanics", Quarterly of Applied Mathematics, Vol. 1, pp. 61-75.
- Shield R.T. and Ziegler H. (1958) "On Prager's Hardening Rule", Zeitschrift fur Angewandte Mathematik und Physik, v.d. IXa, Fasc 3, pp. 260-276.
- Sills G.C. (1975) "Some Conditions under which Biot's Equations of Consolidation Reduce to Terzaghi's Equation", Geotechnique, Vol. 25, No. 1, pp. 129-132.
- Simpson B. and Wroth C.P. (1972) "Finite Element Computations for a Model Retaining Wall in Sand", Proceedings 5th European Conference on Soil Mechanics and Foundation Engineering, Madrid, Vol. 1, pp. 85-93.
- Skempton A.W. (1951) "The Bearing Capacity of Clays", Proceedings, British Bldg. Research Congress, Vol. 1, pp. 180-189.
- Skempton A.W. (1954) "The Pore-Pressure Coefficients A and B", Geotechnique, Vol. 4, No. 4, pp. 143-152.
- Small J.C., Booker J.R. and Davis E.H. (1976) "Elasto-Plastic Consolidation of Soil", International Journal of Solids and Structures, Vol. 12, pp. 431-448.
- Soderberg L.O. (1962) "Consolidation Theory Applied to Foundation Pile Time Effects", Geotechnique, Vol. 12, pp. 217-225.
- Stermac A.G., Selby K.G. and Devata M. (1969) "Behavior of Various Types of Piles in Stiff Clay", 7th ICSMFE, Mexico City, Vol. 2, pp. 239-245.
- Sture S. and Desai C.S. (1979) "Fluid Cushion Truly Triaxial or Multiaxial Testing Device", Geotechnical Testing Journal, ASTM, Vol. 2, No. 1, pp. 20-33.
- Tavenas F. and Leroueil S. (1977) "Effects of Stresses and Time on Yielding of Clays", Proceedings 9th ICSMFE, Tokyo, Vol. 1, pp. 319-326.

- Tavenas F. et al. (1978) "Creep Behavior of an Undisturbed Overconsolidated Clay", Canadian Geotechnical Journal, Vol. 15, No. 1, pp. 402-423.
- Tavenas F. et al. (1979) "The Use of Strain Energy as a Yield and Creep Criterion for Lightly Overconsolidated Clays", Geotechnique, Vol. 29, No. 3, pp. 285-303.
- Terzaghi K. (1923) "Die Berechnung der Durchlässigkeitsziffer des Tones aus dem Verlauf der Hydrodynamischen Spannungsercheinungen", Akademie der Wissenschaften in Win, Sitzungsberichte Mathematisch Naturwissenschaftliche Klass, Part IIa, Vol. 132, No. 3/4, pp. 125-138.
- Terzaghi K. (1936) "The Shearing Resistance of Saturated Soil and the Angle Between the Planes of Shear", Proceedings 1st ICSMFE, Vol. 1, pp. 54-56, Harvard, Mass.
- Terzaghi K. and Peck R.B. (1967) Soil Mechanics in Engineering Practice, John Wiley and Sons, New York.
- Timoshenko S. and Goodier J.N. (1951) Theory of Elasticity, McGraw-Hill, New York.
- Tomlinson M.J. (1971) "Some Effects of Pile Driving on Skin Friction", Proceedings of the Conference on Behavior of Piles, London, pp. 107-114.
- Vesic A.S. (1970) "Load Transfer in Pile-Soil Systems", Proceedings of the Conference on Design and Installation of Pile Foundations, Lehigh University, Bethlehem, Penn., pp. 47-73.
- Vesic A.S. (1972) "Expansion of Cavities in Infinite Soil Mass", Journal of the Soil Mechanics and Foundations Division, ASCE, Vol. 98, March 1972, pp. 265-290.
- Vesic A.S. (1975) "Principles of Pile Foundation Design", Proceedings, Boston ASCE Lecture Series on Deep Foundations.
- Viggiani C. (1970) "Discussion of 'An Analysis of Consolidation Theories'", by R.L. Schiffman, A.T.F. Chen and J.C. Jordan, Journal of the Soil Mechanics and Foundations Division, ASCE, Vol. 96, pp. 331-334.
- Vijayvergiya V.N. and Focht J.A. (1972) "A New Way to Predict Capacity of Piles in Clay", 4th Offshore Technology Conference, Houston, Vol. 2, pp. 865-874.
- WCC and Santa Fe Engineers (1978) "Drilled and Grouted Piles for Offshore Structures", a Three Volume Report.
- Wood D.M. (1974) "Some Aspects of the Mechanical Behavior of Kaolin under Truly Triaxial Conditions of Stress and Strain", Ph.D. Thesis, Cambridge University.

- Wood D.M. (1981) "True Triaxial Tests on Boston Blue Clay", Proceedings of the 10th International Conference on Soil Mechanics and Foundation Engineering. Stockholm, Sweden, Session 4, pp. 825-830.
- Woodward R.J., Lundgren R. and Boitano J.D. (1961) "Pile Loading Tests in Stiff Clays", Proceedings 5th ICSMFE, Paris, France, Vol. 2, pp. 177-184.
- Wroth C.P. (1975) "In Situ Measurements of Initial Stresses and Deformation Characteristics", State-of-the-Art Paper. Proceedings ASCE Spec. Conference on In Situ Measurements of Soil Properties", Raleigh Vol. II, pp. 181-230.
- Wroth C.P. (1976) "Elastic Solution for Consolidation Around Piles", Developed for Phase II Study, Predictions of Axial Capacity for Offshore Piles, Amoco Production Co.
- Wroth C.P., Carter J.P. and Randolph M.F. (1979) "Stress Changes around a Pile Driven into Cohesive Soil", Conference on Recent Development in the Design and Construction of Piles. The Institution of Civil Engineers, London.
- Wroth C.P., Thompson S.A. and Hughes J.M.O. (1974) Appendix G of the Proceedings of the Foundation Deformation Prediction Symposium.
- Yokoo Y., Kunio Y., and Nagaoka H. (1971) "Finite Element Method Applied to Biot's Consolidation Theory", Soils and Foundations, Vol. 11, No. 1, pp. 29-46.
- Yokoo y., Yamagata K. and Nagaoka H. (1971) "Variational Principles for Consolidation", Soils and Foundations, Vol. 11, No. 4, pp. 25-36.
- Yokoo Y., Yamagata K. and Nagaoka H. (1971) "Finite Element Analysis of Consolidation Following Undrained Deformation", Soils and Foundations, Vol. 11, No. 4, pp. 37-58.
- Zeevaert L. (1959) "Reduction of Point Bearing Capacity of Piles Because of Negative Friction", Proceedings of 1st Panamerican Conference on Soil Mechanics and Foundation Engineering, Mexico, Vol. 3, pp. 1145-1152.

## APPENDIX A

### INVERSION OF THE INCREMENTAL STRESS-STRAIN RELATIONS FOR ELASTO-PLASTIC SOILS

Combining Eqs. 3.10 and 3.7 we get:

$$\dot{\bar{\sigma}} = K \dot{\bar{\epsilon}}^e = K (\dot{\bar{\epsilon}} - \dot{\bar{\epsilon}}^P) \quad (\text{A.1a})$$

$$\dot{\bar{s}} = 2G \dot{\bar{\epsilon}}^e = 2G (\dot{\bar{\epsilon}} - \dot{\bar{\epsilon}}^P) \quad (\text{A.1b})$$

and using Eqs. 3.14 and 3.15:

$$\dot{\bar{\sigma}} = K (\dot{\bar{\epsilon}} - \dot{\Lambda P}) \quad (\text{A.2a})$$

$$\dot{\bar{s}} = 2G (\dot{\bar{\epsilon}} - \dot{\Lambda P}') \quad (\text{A.2b})$$

Equations A.2 suffice to compute the components  $(\dot{\bar{\sigma}}, \dot{\bar{s}})$  of the effective stress increment  $\dot{\bar{\sigma}}$  corresponding to an applied strain increment  $(\dot{\bar{\epsilon}}, \dot{\bar{\epsilon}})$ , provided that  $\dot{\Lambda}$  is expressed in terms of the components of the applied strain increment. This is described in the following: Combining Eqs. 3.16 and A.2 we get:

$$H \dot{\Lambda} = Q' : \dot{\bar{s}} + Q \dot{\bar{\sigma}} = 2G Q' : (\dot{\bar{\epsilon}} - \dot{\Lambda P}') + KQ (\dot{\bar{\epsilon}} - \dot{\Lambda P})$$

and solving for  $\dot{\Lambda}$ :

$$\dot{\Lambda} = \frac{2G(\underline{Q}' : \dot{\underline{\epsilon}}) + KQ \dot{\epsilon}}{H + 2G(\underline{Q}' : \underline{P}') + KQP} \quad (\text{A.3})$$

which gives  $\dot{\Lambda}$  in terms of the components of the applied strain increment.

## APPENDIX B

### STRAIN HARDENING AND STRAIN SOFTENING

Consider a soil element in an elastoplastic state; i.e., in a state such that the point representing the state of the soil element in the effective stress space  $(\bar{\sigma}, \underline{s})$  is located on the yield surface. We say that the soil exhibits strain hardening behavior when the effective stress increment  $\dot{\bar{\sigma}}$  corresponding to an applied strain increment  $\dot{\underline{\epsilon}}$  is directed towards the outside of the yield surface, i.e.:

$$\underline{Q} : \dot{\bar{\sigma}} \geq 0 \quad (\text{B.1a})$$

or, equivalently:

$$\underline{Q}' : \dot{\underline{s}} + Q \dot{\bar{\sigma}} \geq 0 \quad (\text{B.1b})$$

where  $\underline{Q}$  (having components  $Q'$  and  $Q$ ) is the outward normal to the yield surface. Analogously, we say that the soil exhibits strain softening behavior when, during plastic loading, the effective stress increment is directed towards the inside of the yield surface, i.e.:

$$\underline{Q} : \dot{\bar{\sigma}} < 0 \quad (\text{B.2a})$$

or, equivalently:

$$\underline{Q}' : \underline{\dot{s}} + \underline{Q} \dot{\underline{\sigma}} < 0 \quad (\text{B.2b})$$

We will now show that any soil model based on associated Plasticity (i.e., equipped with a normality flow rule) exhibits strain hardening behavior during plastic loading from any state having a non-negative elastoplastic modulus  $H$ . In fact, in the case of associated Plasticity (i.e., if  $\underline{P} \equiv \underline{Q}$ ), Eq. 3.18c can be written as:

$$\dot{\Lambda} = \frac{2G(\underline{Q}' : \underline{\dot{e}}) + KQ \dot{\underline{\sigma}}}{H + 2G(\underline{Q}' : \underline{Q}') + KQ^2} \quad (\text{B.3})$$

The denominator of the right-hand-side member of Eq. B.3 is non-negative for  $H \geq 0$  and the numerator is also non-negative during plastic loading (see Eq. 3.22b). Thus,  $\dot{\Lambda} \geq 0$ , which means that  $\underline{Q} : \dot{\underline{\sigma}} \geq 0$  (based on Eq. 3.12) or, equivalently, that the soil exhibits strain hardening behavior.



## APPENDIX C

### RADIAL STRESS PATHS IN SOFT CLAYS

Radial stress paths consist of effective stress paths where the ratio of any two effective stress components is constant along the path. These paths can be geometrically represented in an effective stress space by a straight line passing through the origin. Triaxial radial stress paths are the radial stress paths for which:

$$\bar{\sigma}_x = \bar{\sigma}_z \quad (\text{C.1})$$

$$\sigma_{xy} = \sigma_{yz} = \sigma_{zx} = 0 \quad (\text{C.2})$$

A triaxial radial stress path can be uniquely defined by the ratio:

$$K_\sigma \equiv \bar{\sigma}_x / \bar{\sigma}_y \quad (\text{C.3})$$

where  $\bar{\sigma}_y$  is the axial\* effective stress. Using the transformed stress measures introduced in Section 4.5 (see Table 4.1) for the case of triaxial radial stress paths, we get:

$$\frac{s_1}{\bar{\sigma}} = \sqrt{6} \frac{1 - K_\sigma}{1 + 2K_\sigma} \quad (\text{C.4a})$$

---

\* i.e., along the axis of a cylindrical sample

$$S_2 = S_3 = S_4 = S_5 = 0 \quad (C.4b)$$

which means that these paths can be represented in a two-dimensional transformed stress space comprised of the  $\bar{\sigma}$  and  $S_1$  components. Isotropic,  $K_0$ -consolidation and  $K'_0$ -consolidation paths are triaxial radial stress paths.

In the following, we will present experimental evidence supporting the working hypothesis of the proposed model (see Section 4.2.1) which states:

For a normally consolidated clay subjected to any radial effective stress path, there exists a linear relationship between the void ratio ( $e$ ) and the natural logarithm of the mean effective stress ( $\bar{\sigma}$ ). The slope  $\lambda$  of this line is unique for all radial stress paths.

Table C.1 presents values of the parameter  $\lambda$  measured in tests reported by Ladd and Varallyay (1965) on resedimented normally consolidated Boston Blue Clay. Three types of triaxial radial stress paths are reported: (i) Isotropic consolidation, (ii)  $K_0$ -consolidation and (iii)  $1/K_0$ -consolidation\*. Although the scatter in the measured values of  $\lambda$  in each type of path is large ( $\lambda = 0.17 \pm 0.07$ ), the average values of  $\lambda$  in each type of path are approximately equal suggesting a unique  $\lambda$  for all

---

\*  $K_\sigma = 1/K_0$

types of radial stress paths.

Figures C.1 through C.4 present the mean effective stress vs. volumetric strain curves for triaxial radial stress paths with various stress ratios ( $K_\sigma$ ) performed on undisturbed samples\* of the lean sensitive Champlain Clay in Canada and reported by Leroueil (1977). All figures show an approximately unique slope of the  $\Delta V/V_0 - \bar{\sigma}$  curves (in the normally consolidated region) for all values of  $K_\sigma$  reported, suggesting a unique value of  $\lambda$ .

---

\* mostly block samples

	Test Number	$\lambda \equiv -\Delta e / \Delta \ln \bar{\sigma}$	$\lambda$ Average	Standard Deviation
Isotropic Consolidation	CIUC - 1	0.205	0.163	0.043
	CIUC - 2	0.167		
	CIUC - 3	0.118		
	CIUE - 1	0.105		
	CIUE - 2	0.209		
	CIUE - 3	0.173		
$K_o$ Consolidation ( $K_o \approx 0.534$ )	CK <sub>o</sub> UC - 1	0.097	0.175	0.080
	CK <sub>o</sub> UC - 2	0.101		
	CK <sub>o</sub> UUC - 1	0.298		
	CK <sub>o</sub> UUC - 2	0.299		
	CK <sub>o</sub> URE - 1	0.164		
	CK <sub>o</sub> URE - 2	0.158		
	CK <sub>o</sub> URE - 4	0.124		
	CK <sub>o</sub> URE - 5	0.161		
$\frac{1}{K_o}$ Consolidation ( $\frac{1}{K_o} \approx 1.871$ )	C( $\frac{1}{K_o}$ )UE - 1	0.177	0.157	0.067
	C( $\frac{1}{K_o}$ )UE - 3	0.131		
	C( $\frac{1}{K_o}$ )URC - 2	0.104		
	C( $\frac{1}{K_o}$ )URC - 4	0.282		
	C( $\frac{1}{K_o}$ )URC - 5	0.143		
	C( $\frac{1}{K_o}$ )URC - 6	0.104		

**Table C.1:** Measured  $\lambda$  Values from Consolidation Tests on Normally Consolidated Boston Blue Clay  
(Data from Ladd and Varallyay, 1965)

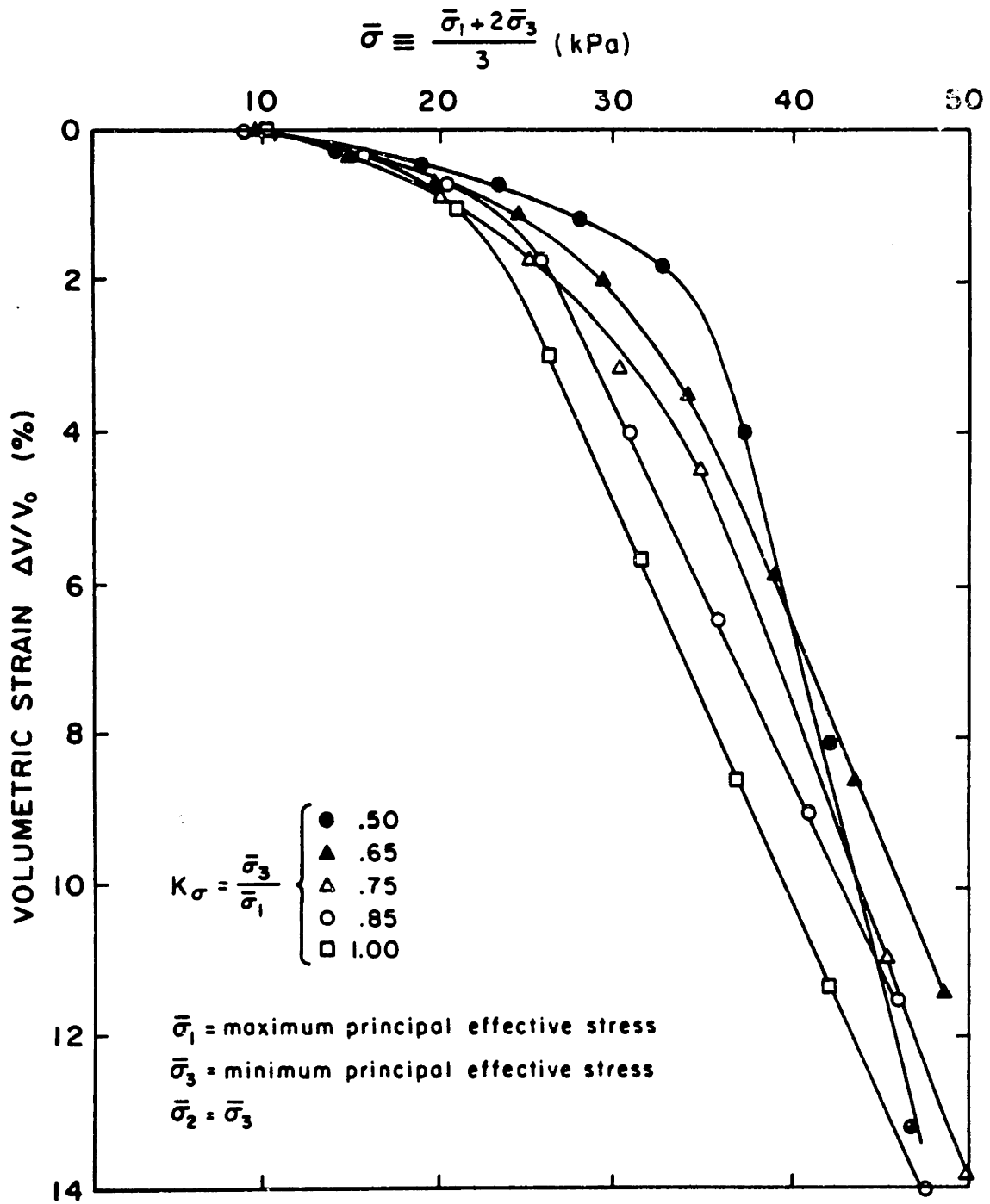


Fig. C.1: Mean effective stress vs. volumetric strain for radial stress paths with various stress ratios. St. Alban sensitive clay (depth=3m). (after Leroueil, 1977).

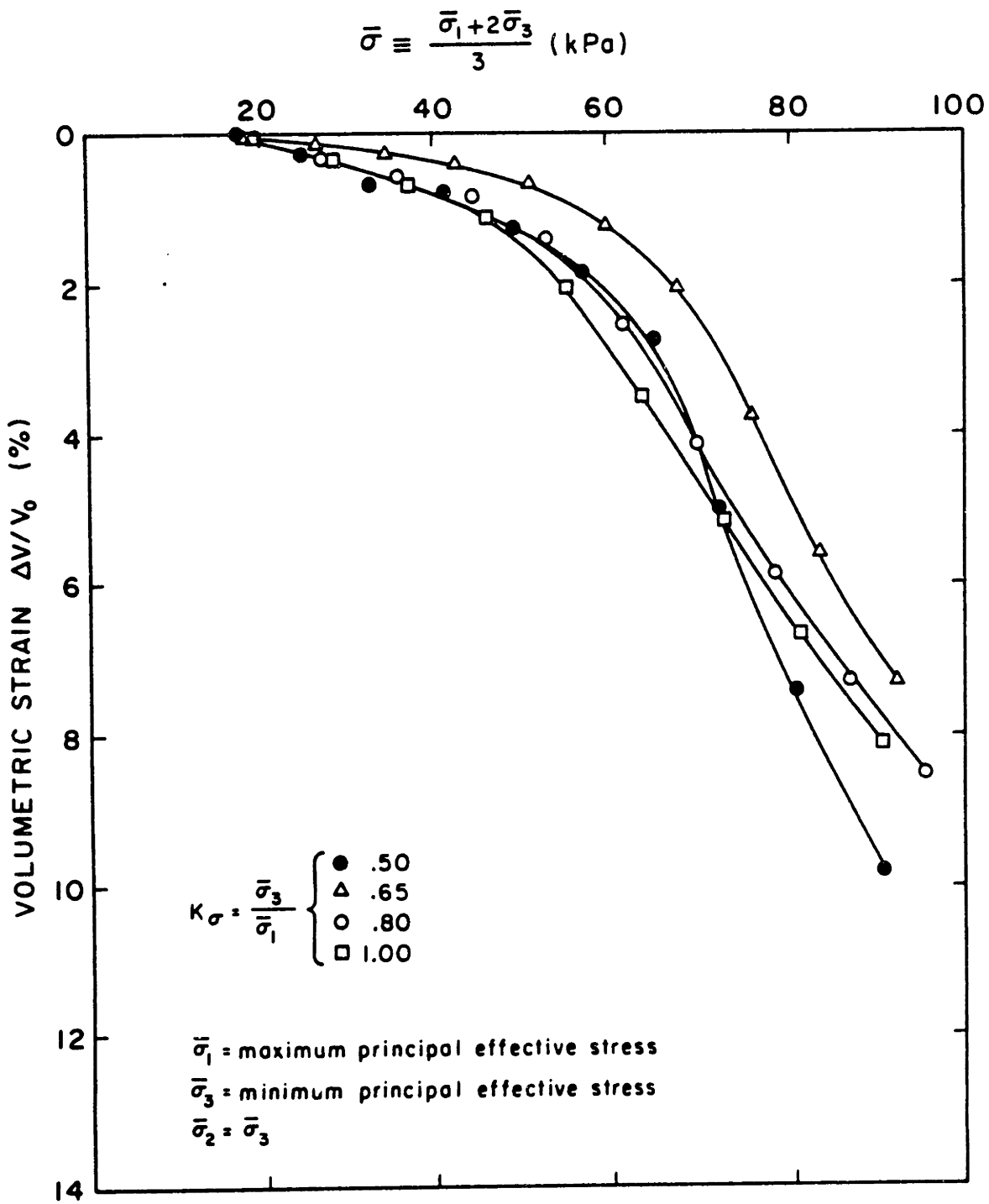


Fig. C.2: Mean effective stress vs. volumetric strain for radial stress paths with various stress ratios. St. Alban sensitive clay (depth=5.7m). (after Leroueil, 1977).

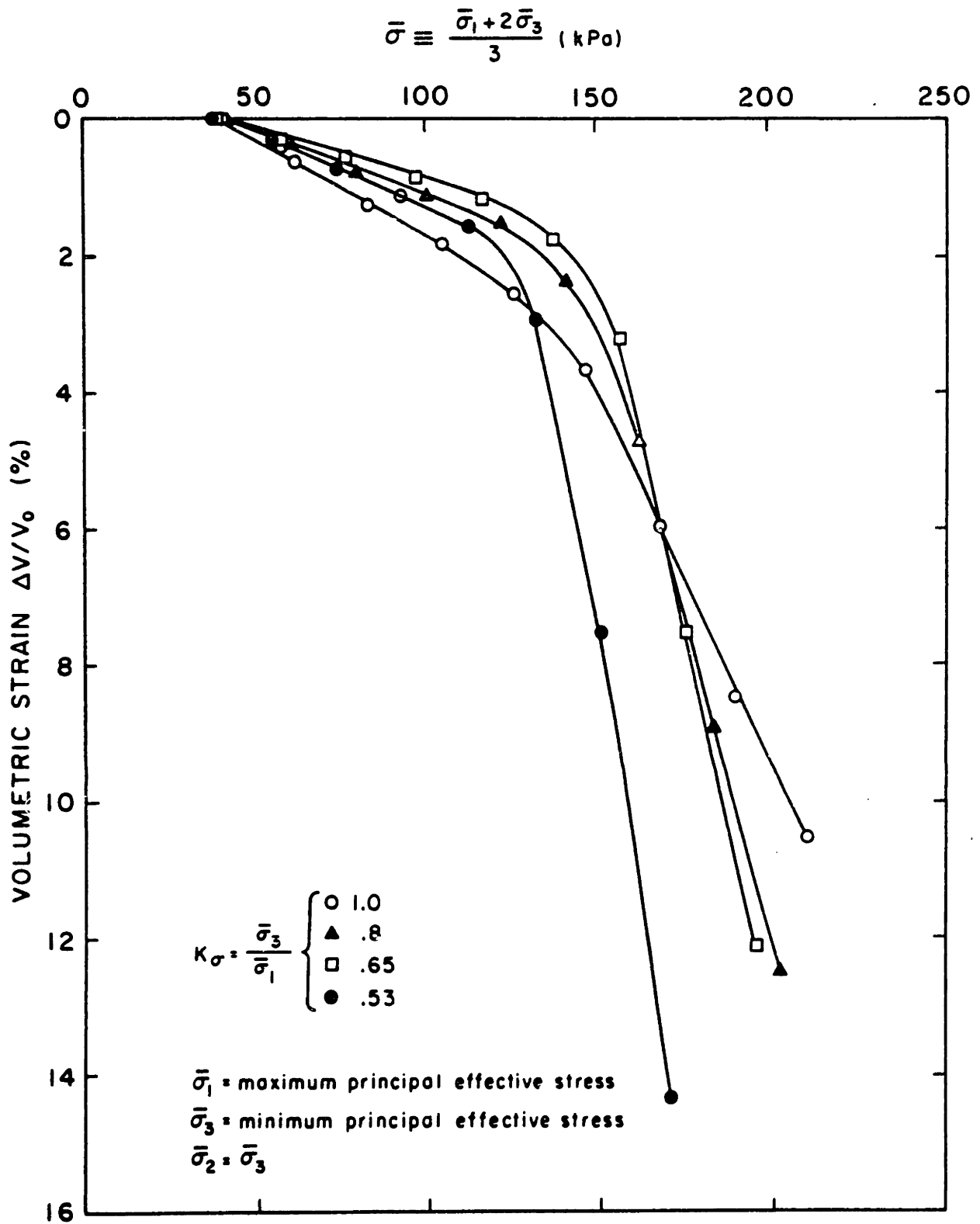


Fig. C.3: Mean effective stress vs. volumetric strain for radial stress paths with various stress ratios. St. Louis sensitive clay. (after Leroueil, 1977).

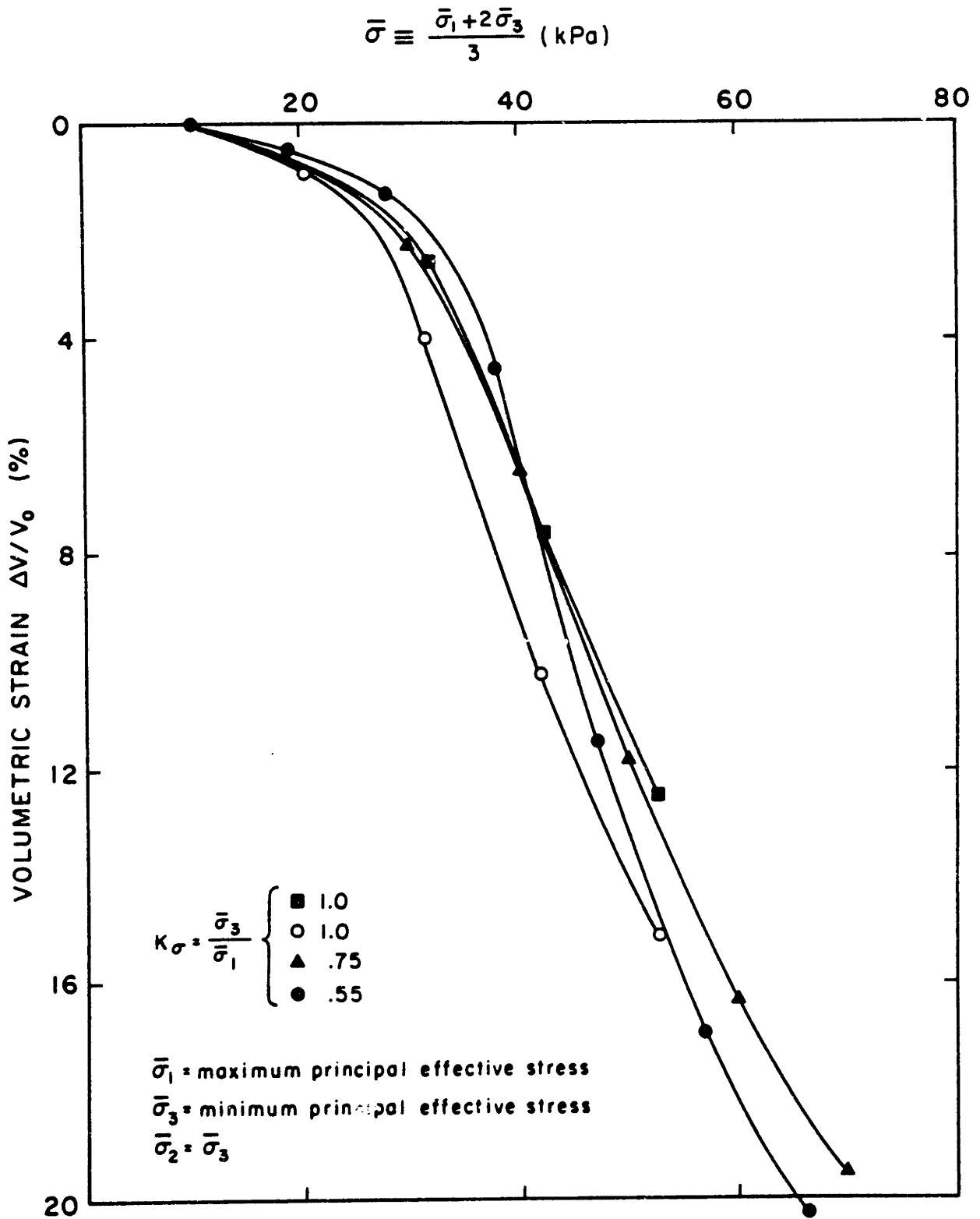


Fig. C.4: Mean effective stress vs. volumetric strain for radial stress paths with various stress ratios. Rang de Fleuve sensitive clay. (after Leroueil, 1977).



## APPENDIX D

### THE FLUID MASS FLUX VECTOR

Consider an infinitesimal surface element  $dS$  of soil with unit normal vector  $\underline{n}$ . Mass  $dM$  of pore fluid (having density  $\rho$ ) flows through the pores of the surface element  $dS$  per unit time. The "superficial" velocity\*  $\underline{v}$  of the pore fluid is then defined by the equation:

$$dM \equiv \rho(\underline{n} \cdot \underline{v}) dS \quad (D.1)$$

where  $\underline{n} \cdot \underline{v}$  is the dot product (see, e.g., Malvern, 1969) of the vectors  $\underline{n}$  and  $\underline{v}$ . The fluid mass flux vector  $\underline{q}$  is then defined by the equation:

$$\underline{q} \equiv \rho \underline{v} \quad (D.2)$$

Combining Eqs. D.1 and D.2 we get:

$$dM = \underline{n} \cdot \underline{q} dS \quad (D.3)$$

---

\* The superficial velocity  $\underline{v}$  is referred to a unit area of soil, whereas the real fluid velocity  $\underline{v}_R$  is referred to a unit area of pore space. Thus,

$$\underline{v} = \eta \underline{v}_R$$

where  $\eta$  is the soil porosity.

which means that the mass of fluid flowing through a unit surface of soil (with normal vector  $\vec{n}$ ) per unit time is equal to the dot product of  $\vec{n}$  and the fluid mass flux vector  $\vec{q}$ .

## APPENDIX E

### UNCOUPLING OF THE CONSOLIDATION EQUATION IN THE CASE OF IRROTATIONAL DISPLACEMENT FIELDS

Sills (1975) applied Biot's theory of consolidation in the case of a linear, elastic soil having isotropic and spatially constant moduli and permeability. She specifically studied a class of problems having the following additional features:

- (i) The displacement field is irrotational, i.e., there exists a scalar function  $\phi$  such that

$$\underline{u} \equiv \nabla\phi \quad (\text{E.1})$$

- (ii) The soil extends to infinity and,
- (iii) The body forces are constant during consolidation.

Combining the stress equilibrium equations (Eq. 7.1) with Terzaghi's effective stress principle (Eq. 7.2) we get:

$$\nabla \cdot \underline{\bar{\sigma}} + \nabla p + \underline{\hat{f}} = \underline{0} \quad (\text{E.2})$$

or, in rate form\*:

$$\nabla \cdot \underline{\dot{\bar{\sigma}}} + \nabla \dot{p} = \underline{0} \quad (\text{E.3})$$

---

\* assuming infinitesimal strains and rotations

because the body forces are assumed constant (i.e.,  $\dot{\hat{f}} = 0$ ).

The incremental stress-strain relationships for a linear, elastic, isotropic soil can be written:

$$\dot{\underline{\underline{\sigma}}} = 2G \left\{ \dot{\underline{\underline{\epsilon}}} + \frac{\bar{\nu}}{1 - 2\bar{\nu}} \dot{\underline{\underline{\epsilon}}} \underline{\underline{I}} \right\} \quad (\text{E.4})$$

where  $\dot{\underline{\underline{\epsilon}}}$  is the volumetric strain rate,  $\underline{\underline{I}}$  is the unit second order tensor (Kronecker delta) and  $\bar{\nu}$  is the drained Poisson's ratio. Combining Eqs. E.4 and E.5 we get:

$$2G \left\{ \nabla \cdot \dot{\underline{\underline{\epsilon}}} + \frac{\bar{\nu}}{1 - 2\bar{\nu}} \nabla \dot{\underline{\underline{\epsilon}}} \right\} + \nabla \dot{\underline{\underline{p}}} = 0 \quad (\text{E.5})$$

where  $\nabla \cdot \dot{\underline{\underline{\epsilon}}}$  is the divergence of the strain rate and  $\nabla \dot{\underline{\underline{\epsilon}}}$  is the gradient of the volumetric strain rate.

In the case of an irrotational displacement field (i.e., when Eq. E.1 holds):

$$\underline{\underline{\epsilon}} \equiv \frac{1}{2} \{ \nabla \dot{\underline{\underline{u}}} + \dot{\underline{\underline{u}}} \nabla \} = \nabla (\nabla \phi) = \nabla \dot{\underline{\underline{u}}} \quad (\text{E.6})$$

and then:

$$\nabla \cdot \dot{\underline{\underline{\epsilon}}} = \nabla \cdot (\nabla \dot{\underline{\underline{u}}}) = \nabla (\nabla \cdot \dot{\underline{\underline{u}}}) = \nabla \dot{\underline{\underline{\epsilon}}} \quad (\text{E.7})$$

Combining Eqs. E.5 and E.7 we get:

$$\nabla \left\{ 2G \left( \frac{1 - \bar{\nu}}{1 - 2\bar{\nu}} \right) \dot{\underline{\underline{\epsilon}}} + \dot{\underline{\underline{p}}} \right\} = 0 \quad (\text{E.8})$$

or,

$$2G \left( \frac{1 - \bar{v}}{1 - 2\bar{v}} \right) \dot{\epsilon} + \dot{p} = h(t) \quad (\text{E.9})$$

where  $h(t)$  is a function of time (i.e., spatially constant).

In the case of a soil extending to infinity, both  $\dot{\epsilon}$  and  $\dot{p}$  are zero at infinity which means that  $h(t) = 0$  and then, Eq. E.9 can be written:

$$2G \left( \frac{1 - \bar{v}}{1 - 2\bar{v}} \right) \dot{\epsilon} = - \dot{p} \quad (\text{E.10a})$$

or:

$$\frac{3(1 - \bar{v})}{(1 + \bar{v})} K \dot{\epsilon} = - \dot{p} \quad (\text{E.10b})$$

where  $K$  is the (drained) bulk modulus of the soil

$$K = \frac{2G}{3} \frac{(1 + \bar{v})}{(1 - 2\bar{v})} \quad (\text{E.11})$$

Equations E.10 express the volumetric strain rate ( $\dot{\epsilon}$ ) in terms of the time rate of change of the pore pressure and can be used to uncouple the consolidation equation. In fact, substituting from Eq. E.10 into the mass conservation equation (Eq. 7.17) we get:

$$\bar{v} \cdot \{ \bar{k} \cdot \bar{v} (p - p_0) \} = \frac{\rho g}{K} \frac{(1 + \bar{v})}{3(1 - \bar{v})} \dot{p} \quad (\text{E.12})$$

and, in the case of isotropic and spatially constant permeability (i.e.,  $\underline{k} = k \underline{I}$ ), Eq. E.12 gives:

$$c \nabla^2 (p - p_0) = \frac{\partial p}{\partial t} \quad (\text{E.13a})$$

where,

$$c \equiv \frac{3(1 - \bar{\nu})}{(1 + \bar{\nu})} \left( \frac{K k}{\rho g} \right) = \left( K + \frac{4G}{3} \right) \frac{k}{\rho g} \quad (\text{E.13b})$$

is the coefficient of consolidation.

## APPENDIX F

### AN ANALYTICAL SOLUTION FOR THE LINEAR CONSOLIDATION AROUND PILES

Section 7.3 shows that the problem of the radial consolidation in a linear, isotropic, elastic soil\* with isotropic and spatially constant permeability around a long cylindrical vertical pile is governed by the uncoupled consolidation equation:

$$c \left[ \frac{\partial^2 p}{\partial r^2} + \frac{1}{r} \frac{\partial p}{\partial r} \right] = \frac{\partial p}{\partial t} \quad (\text{F.1})$$

where  $r$  is the radial coordinate ( $r_0 \leq r < \infty$ ),  $r_0$  is the pile radius and,

$$c \equiv \frac{3(1 - \bar{\nu})}{(1 + \bar{\nu})} \left( \frac{K k}{\rho g} \right) = \left( K + \frac{4G}{3} \right) \frac{k}{\rho g} \quad (\text{F.2})$$

is the coefficient of consolidation. Equation F.1 is subject to the following boundary conditions:

- (i) Free drainage at infinity, i.e.,

$$p = p_0 \text{ at } r = \infty \quad (\text{F.3a})$$

- (ii) Impermeable pile, i.e.,

$$\frac{\partial p}{\partial r} = 0 \text{ at } r = r_0 \quad (\text{F.3b})$$

---

\* extending to infinity

The solution for the normalized pore pressure

$$P(R, T) \equiv [p(r, t) - p_0] / [p(r_0, 0^+) - p_0] \quad (F.4)$$

can be obtained by using Green's theorem\* and the principle of superposition and is given by:

$$P(R, T) = \int_0^{+\infty} e^{-Tx^2} J(x) \cdot \frac{Z(x, xR)}{J_1^2(x) + Y_1^2(x)} x dx \quad (F.5)$$

where:

$$R \equiv r/r_0 \quad (F.6a)$$

is the normalized radius,

$$T \equiv ct/r_0^2 \quad (F.6b)$$

is the dimensionless time factor,

$$Z(x, xR) \equiv Y_1(x) \cdot J_0(xR) - J_1(x) \cdot Y_0(xR) \quad (F.6c)$$

$$J(x) \equiv Y_1(x) \cdot J_J(x) - J_1(x) \cdot J_Y(x) \quad (F.6d)$$

$$J_J(x) \equiv \int_1^{+\infty} f(w) \cdot J_0(wx) w dw \quad (F.6e)$$

$$J_Y(x) \equiv \int_1^{+\infty} f(w) \cdot Y_0(wx) w dw \quad (F.6f)$$

---

\* see Carslaw and Jaeger (1959)



$J_0, Y_0, J_1, Y_1$  are the zero and first order Bessel functions of the first kind (see Abramowitz and Stegun, 1965, pp. 369-370) and

$$f(R) \equiv [p(r, 0^+) - p_0] / [p(r_0, 0^+) - p_0] \quad (F.6g)$$

is the initial normalized distribution of the excess pore pressure causing consolidation.

## APPENDIX G

### FINITE ELEMENT IMPLEMENTATION OF NON-LINEAR SOIL CONSOLIDATION

#### G.1 THE ALGORITHM

Section 7.4.2 presents a Weighted Residuals formulation for linear and non-linear soil consolidation\* due to an initial known excess pore pressure field, under constant body forces and surface tractions. The resulting "Virtual Work" equations (Eqs. 7.43) can be written in matrix form (see also Table 7.1):

$$\int_V \delta \underline{\underline{\epsilon}}^T \underline{\underline{\sigma}}_0 \, dV + \int_V \delta \epsilon \, {}_0p \, dV = 0 \quad (G.1a)$$

$$\int_V \delta p \, \dot{\epsilon} \, dV - \frac{1}{\gamma} \int_V [\underline{\underline{\nabla}}(\delta p)]^T \underline{\underline{k}} [\underline{\underline{\nabla}}(p - p_0)] \, dV = 0 \quad (G.1b)$$

where,  $\underline{\underline{\sigma}}_0$ ,  ${}_0p$  are the values of the effective stress and pore pressure relative to the initial state\*\* (at  $t = 0$ ),  $\dot{\epsilon}$  is the volumetric strain rate,  $\gamma$  is the unit weight of the pore fluid (usually water),  $\underline{\underline{k}}$  is the symmetric permeability matrix and  $\delta(\dots)$  denotes an arbitrary variation of the quantity following it.

---

\* of a soil with incompressible constituents and impermeable  $S_q$  boundary  
 \*\* see Eqs. 7.37

A Standard Isoparametric Finite Element interpolation scheme is then introduced (see e.g. Bathe and Wilson, 1976) for the displacement field:

$$\underline{u} = \underline{N} \underline{U} \quad (\text{G.2a})$$

where  $\underline{N}$  is a matrix of "shape functions" relating the nodal values of the displacement components  $\underline{U}$  to the values of the displacement  $\underline{u}$  at any point of each Finite Element. Using Eq. G.2a and the classical definition of strain in terms of the displacement derivatives, a relation between the strain vector  $\underline{\epsilon}$  at any point and  $\underline{U}$ , can be written as follows:

$$\underline{\epsilon} = \underline{B} \underline{U} \quad (\text{G.2b})$$

and similar relations can be written for the volumetric strain  $\epsilon$  and the volumetric strain rate:

$$\epsilon = \underline{D} \underline{U} \quad (\text{G.2c})$$

$$\dot{\epsilon} = \underline{D} \dot{\underline{U}}$$

where  $\dot{\underline{U}}$  are the nodal values of the soil velocities and  $\underline{B}$ ,  $\underline{D}$  are transformation matrices in terms of the shape functions of the Finite Element interpolation scheme.

Analogously, an Isoparametric Finite Element interpolation scheme is introduced for the pore pressure field:

$$\underline{p} = \underline{L} \underline{P} \quad (\text{G.3a})$$

where  $\underline{L}$  is a matrix of shape functions relating the nodal values of the pore pressure  $\underline{P}$  to the values of the pore pressure  $p$  at any point of each Finite Element. Using Eq. G.3a, the nodal values of the pore pressure  $\underline{P}$  can be related to the gradient of the pore pressure at any point of each Finite Element via a transformation matrix  $\underline{M}$ :

$$\underline{\nabla} p = \underline{M} \underline{P} \quad (\text{G.3b})$$

Finally, defining the auxiliary matrices:

$$\underline{H} \equiv \int_V \underline{L}^T \underline{D} \, dV \quad (\text{G.4a})$$

$$\bar{k} \equiv \frac{1}{V} \int_V \underline{M}^T \underline{k} \underline{M} \, dV \quad (\text{G.4b})$$

Eqs. G.1 can be written as:

$$\int_V \underline{B}^T \underline{\sigma} \, dV + \underline{H} \underline{P} = \underline{0} \quad (\text{G.5a})$$

$$\underline{H}^T \dot{\underline{U}} - \bar{k} (\underline{P} - \underline{P}_0) = \underline{0} \quad (\text{G.5b})$$

where:

$$\underline{P} \equiv \underline{P} - \underline{P}_0 \quad (G.6)$$

and,  $\underline{P}$  are the current nodal values of the pore pressure,  $\underline{P}_0$  are the nodal values of the pore pressure at time  $t = 0$  and  $\underline{P}_o$  are the nodal values of the ambient (hydrostatic) pore pressure.

The proposed algorithm involves:

- (i) A scheme to march the solution in time, i.e., it is assumed that the values of all quantities are known at time  $t$  and, a solution is required at time  $(t + \Delta t)$  where  $\Delta t$  is the time step. A left superscript of a quantity denotes the time instant at which the value of this quantity occurs.
- (ii) An iterative scheme to achieve equilibrium in each time step. The current iteration number is denoted by a right superscript enclosed in parentheses.

Writing Eq. G.5a for the  $i^{\text{th}}$  iteration at time  $t + \Delta t$  we get:

$$\int_V \underline{B}^T \underline{\sigma}^{(i)} dV + \underline{H} \underline{P}^{(i)} = \underline{0} \quad (G.7)$$

In our iterative scheme we will set:

$${}^{t+\Delta t} \underline{p}_{\underline{o}}(i) \equiv {}^t \underline{p}_{\underline{o}} + \Delta \underline{p}(i) \quad (\text{G.8a})$$

$${}^{t+\Delta t} \underline{\sigma}_{\underline{o}}(i) \equiv {}^t \underline{\sigma}_{\underline{o}} + \Delta \underline{\sigma}(i-1) + d \underline{\sigma}(i) \quad (\text{G.8b})$$

$$d \underline{\sigma}(i) \equiv \underline{C}^e d \underline{\varepsilon}(i) \equiv \underline{C}^e \underline{B} d \underline{U}(i) \quad (\text{G.8c})$$

where:

${}^t \underline{p}_{\underline{o}}$  are the nodal values of the pore pressure at time  $t$ , relative to the values of the pore pressure at time  $t = 0$ , i.e.:

$${}^t \underline{p}_{\underline{o}} \equiv {}^t \underline{p} - {}^0 \underline{p}$$

$\Delta \underline{p}(i)$  is the increment of the pore pressure between time  $t$  and the  $i^{\text{th}}$  iteration of time  $(t + \Delta t)$ , i.e.:

$$\Delta \underline{p}(i) \equiv {}^{t+\Delta t} \underline{p}(i) - {}^t \underline{p}$$

$${}^t \underline{\sigma}_{\underline{o}} \equiv {}^t \underline{\sigma} - {}^0 \underline{\sigma}$$

$\Delta \underline{\sigma}(i-1)$  is the increment of the effective stress between time  $t$  and the  $(i-1)^{\text{th}}$  iteration at time  $(t + \Delta t)$ , i.e.:

$$\Delta \underline{\sigma}(i-1) \equiv {}^{t+\Delta t} \underline{\sigma}(i-1) - {}^t \underline{\sigma}$$

$d\bar{\sigma}^{(i)}$  is the correction of the effective stress during the  $i^{\text{th}}$  iteration, i.e.:

$$d\bar{\sigma}^{(i)} = {}^{t+\Delta t}\bar{\sigma}^{(i)} - {}^{t+\Delta t}\bar{\sigma}^{(i-1)}$$

Furthermore, (see Eq. G.8c) the corrective increment of stress corresponds to an increment of strain  $d\bar{\epsilon}^{(i)}$  via an "elastic" material stiffness matrix  $\bar{C}^e$  and, using Eq. G.2b, the strain increment  $d\bar{\epsilon}^{(i)}$  corresponds to a displacement increment  $d\bar{U}^{(i)}$  which is the correction of the nodal displacements during the  $i^{\text{th}}$  iteration, i.e.:

$$d\bar{U}^{(i)} = {}^{t+\Delta t}\bar{U}^{(i)} - {}^{t+\Delta t}\bar{U}^{(i-1)}$$

Upon convergence of the iterative scheme, both  $d\bar{\sigma}^{(i)}$  and  $d\bar{U}^{(i)}$  become negligible.

Thus, substituting from Eqs. G.8 into Eq. G.7 we get\*:

$$\underline{K}^e d\bar{U}^{(i)} + \underline{H} \Delta \bar{P}^{(i)} = - \int_V \underline{B}^T \Delta \bar{\sigma}^{(i-1)} dV \quad (G.9)$$

---

\* We have also used that:

$$\int_V \underline{B}^T {}^t \underline{\sigma} dV + \underline{H} {}^t \underline{P} = \underline{0}$$

which means that equilibrium has been achieved at time  $t$  (see Eq. G.5a).

where  $\underline{K}^e$  is an "equivalent elastic" stiffness matrix:

$$\underline{K}^e \equiv \int_V \underline{B}^T \underline{C}^e \underline{B} dV \quad (G.10)$$

The specific value of  $\underline{K}^e$  (or equivalently,  $\underline{C}^e$ ) does not affect the accuracy of the method\* but only the rate of convergence of the iteration scheme. In fact, upon convergence of the iteration scheme,  $d\underline{U}^{(i)}$  is negligible and thus  $\underline{K}^e d\underline{U}^{(i)}$  (in Eq. G.9) is also negligible.

Writing Eq. G.5b for the  $i^{\text{th}}$  iteration at time  $t + \alpha\Delta t$  (where  $0 \leq \alpha \leq 1$ ), we get\*\*:

$$\underline{H}^T \dot{\underline{U}}^{t+\alpha\Delta t}(i) - \underline{K} (\underline{P}^{t+\alpha\Delta t}(i) - \underline{P}_0) = \underline{0} \quad (G.11)$$

A general Crank-Nickolson finite difference scheme (see, e.g., Bathe and Wilson, 1976) will be used to relate  $\dot{\underline{U}}^{t+\alpha\Delta t}(i)$  and  $\underline{P}^{t+\alpha\Delta t}(i)$  to the values of these quantities at time  $t$  and  $t + \Delta t$ , i.e.:

$$\dot{\underline{U}}^{t+\alpha\Delta t}(i) = \frac{1}{\Delta t} \{ \Delta \underline{U}^{(i-1)} + d\underline{U}^{(i)} \} \quad (G.12a)$$

$$\underline{P}^{t+\alpha\Delta t}(i) = \alpha \Delta \underline{P}^{(i)} + \underline{P} \quad (G.12b)$$

---

\* see Section G.2

\*\* assuming that permeability does not change during consolidation



where:

$$\Delta \underline{U}^{(i-1)} \equiv t + \Delta t \underline{U}^{(i-1)} - t_{\underline{U}} \quad (\text{G.12c})$$

$$d\underline{U}^{(i)} \equiv t + \Delta t \underline{U}^{(i)} - t + \Delta t \underline{U}^{(i-1)} \quad (\text{G.12d})$$

$$\Delta \underline{P}^{(i)} \equiv t + \Delta t \underline{P}^{(i)} - t_{\underline{P}} \quad (\text{G.12e})$$

Substituting from Eqs. G.12a and G.12b in Eq. G.11 we get:

$$\underline{H}^T d\underline{U}^{(i)} - \alpha \Delta t \bar{k} \Delta \underline{P}^{(i)} = \Delta t \bar{k} (t_{\underline{P}} - \underline{P}_O) - \underline{H}^T \Delta \underline{U}^{(i-1)} \quad (\text{G.13})$$

Equations G.9 and G.13 form the system of the Finite Element equations to solve non-linear consolidation. They can be written in a more compact form as:

$$\begin{bmatrix} \underline{K}^e & \underline{H} \\ \underline{H}^T & -\alpha \Delta t \bar{k} \end{bmatrix} \begin{Bmatrix} d\underline{U}^{(i)} \\ \Delta \underline{P}^{(i)} \end{Bmatrix} = \begin{Bmatrix} \underline{0} \\ \Delta t \bar{k} (t_{\underline{P}} - \underline{P}_O) \end{Bmatrix} - \begin{Bmatrix} \int_V \underline{B}^T \Delta \bar{\sigma}^{(i-1)} dV \\ \underline{H}^T \Delta \underline{U}^{(i-1)} \end{Bmatrix} \quad (\text{G.14})$$

where all quantities are known at time  $t$  and a solution is required at time  $(t + \Delta t)$ . The iterative scheme to solve Eqs.

G.14 consists of the following steps:

(1) In the first iteration ( $i=1$ ) it is assumed

that:

$$\Delta \bar{\sigma}^{(0)} = \Delta \underline{U}^{(0)} = \underline{0} \quad (\text{G.15})$$

and Eqs. G.14 are solved for  $d\underline{U}^{(i)}$  and  $\underline{\Delta P}^{(i)}$ .

- (2) A new value of the displacement increment  $\underline{\Delta U}^{(i)}$  is computed from the relation:

$$\underline{\Delta U}^{(i)} = \underline{\Delta U}^{(i-1)} + d\underline{U}^{(i)} \quad (\text{G.16})$$

- (3) Using the computed displacement increment  $\underline{\Delta U}^{(i)}$ , the corresponding strain increment is computed by the relation:

$$\underline{\Delta \underline{\epsilon}}^{(i)} = \underline{B} \underline{\Delta U}^{(i)} \quad (\text{G.17})$$

and then, the (non-linear) effective stress constitutive model is used to compute the associated effective stress increment:

$$\underline{\Delta \underline{\sigma}}^{(i)} = \underline{C} \underline{\Delta \underline{\epsilon}}^{(i)} \quad (\text{G.18})$$

- (4) Using the values of  $\underline{\Delta U}^{(i)}$  and  $\underline{\Delta \underline{\sigma}}^{(i)}$  computed in steps (2) and (3) above, we can evaluate the right-hand-side part of Eq. G.14 and proceed to the next iteration step.

Convergence is achieved when:

$$|| \underline{\Delta P}^{(i)} - \underline{\Delta P}^{(i-1)} || < \text{tolerance} \quad (\text{G.19})$$

where  $|| \dots ||$  is the norm of the associated vector. Upon convergence, the equilibrium iterations are terminated, and:

(5) The new values of the state variables are computed by:

$$t+\Delta t \underline{\sigma} = t \underline{\sigma} + \Delta \underline{\sigma}^{(n)} \quad (\text{G.20a})$$

$$t+\Delta t \underline{p} = t \underline{p} + \Delta \underline{p}^{(n)} \quad (\text{G.20b})$$

where  $n$  is the number of the last equilibrium iteration.

The time integration scheme (Eq. G.14) is purely explicit if  $\alpha = 0$  and purely implicit if  $\alpha = 1$ . Booker and Small (1975) studied the stability of this scheme and concluded that the scheme is unconditionally stable for  $\alpha \geq \frac{1}{2}$ . For  $\alpha < 1/2$  the scheme is only conditionally stable, which means that there is an upper limit of the time step size  $\Delta t$  (depending on the soil, the geometry of the problem, and the size of the finite elements), which when exceeded, makes the scheme unstable. On the contrary, an unconditionally stable scheme has no restrictions on the maximum time step size for stability reasons. However, in all schemes, the time step size should be sufficiently small to give accurate results.

## G.2 THE "ELASTIC" STIFFNESS MATRIX

The algorithm uses an iterative scheme to achieve equilibrium of stresses and pore pressures in each time step. The approach used is basically a "residual force" method\* where

---

\* e.g., Argyris and Scharpf (1969) or Nayak and Zienkiewicz (1972)

in each iteration step, the out-of-balance residual forces of the right-hand-side act as additional (fictitious) nodal forces required to bring the assumed displacement and pore pressure pattern in nodal equilibrium. We thus get improved estimates of the displacement and pore pressure fields that will be used as out-of-balance forces in the next iteration step, until convergence is achieved when the magnitude of the out-of-balance forces does not exceed a specific tolerance (Eq. G.17).

In computing the improved estimates of the displacement and pore pressure fields, a constant, linear, positive definite stiffness matrix  $\underline{K}^e$  is used. Nayak and Zienkiewicz (1972) suggest that the advantages of such a constant stiffness matrix are not only economic\* but also permit the computation to include strain softening materials and non-associated flow rules. In fact, a tangent stiffness matrix of a non-associated flow rule is non-symmetric which introduces significant problems in the inversion procedure. More specifically, for the problem of consolidation around piles, we think that the use of a constant elastic stiffness matrix has further advantages because, as it is shown in Chapter 8, a certain part of the soil\*\* is loading plastically (i.e., it has soft response) and the remaining part of the soil is unloading elastically

---

\* In fact, the stiffness matrix need only be triangularized once, and then the solution in each iteration step is obtained by back-substitution.

\*\* close to the pile

(i.e. it has stiff response) during consolidation. This kind of behavior can create problems in formulations based on the tangent stiffness.

### G.3 NON-DIMENSIONALIZATION OF THE FINITE ELEMENT EQUATION

Table G.1 presents a non-dimensional form of the Finite Element Equation (Eq. G.14) and defines the non-dimensional matrices (denoted with a ^) required in the computations. Quantities with dimension of "length" are normalized with the pile radius and quantities with dimension of "stress" are normalized with the mean effective stress in the soil before pile installation. As expected, the non-dimensional Finite Element Equation depends on time via the dimensionless time factor:

$$T \equiv ct/r_o^2 \quad (G.21a)$$

where  $t$  is the real time and

$$c \equiv k\bar{\sigma}_o/\gamma \quad (G.21b)$$

is the "coefficient of consolidation". Thus, the numerical solution of consolidation\* can be obtained in terms of the dimensionless time factor  $T$  without assuming specific values of the pile radius  $r_o$ , soil permeability  $k$ , unit weight of pore fluid  $\gamma$  and initial mean effective stress  $\bar{\sigma}_o$ .

---

\* even in the non-linear case

$\begin{bmatrix} \hat{\underline{k}}^e \\ \hat{\underline{H}}^T \\ -\alpha \Delta T \hat{\underline{k}} \end{bmatrix} \cdot \begin{bmatrix} d\hat{\underline{U}}^{(i)} \\ \Delta \hat{\underline{P}}^{(i)} \end{bmatrix} = \begin{bmatrix} \underline{0} \\ \Delta T \hat{\underline{k}} (t\hat{\underline{P}} - \hat{\underline{P}}_0) \end{bmatrix} - \left\{ \int_{-1}^{+1} \hat{\underline{B}}^T \Delta \hat{\underline{\sigma}}^{(i-1)} \frac{r' \ell'}{2} ds \right. \\ \left. \hat{\underline{H}}^T \Delta \hat{\underline{U}}^{(i-1)} \right\}$				
$\underline{N} \equiv r_0 \underline{N}$ $\hat{\underline{B}} \equiv r_0 \underline{B}$	$\hat{\underline{D}} \equiv r_0 \underline{D}$ $\hat{\underline{M}} \equiv r_0 \underline{M}$	$\hat{\underline{U}} \equiv \frac{1}{r_0} \underline{U}$ $\hat{\underline{C}}^e \equiv \frac{1}{\sigma_c} \underline{C}^e$ $\Delta T \equiv \frac{c \Delta t}{r_0}$	$\hat{\underline{P}} \equiv \frac{1}{\sigma_0} \underline{P}$ $\Delta \hat{\underline{\sigma}} \equiv \frac{1}{\sigma_0} \Delta \underline{\sigma}$ $c \equiv \frac{k \sigma_0}{\gamma}$	$r' \equiv r/r_0$ $\ell' \equiv \ell/r_0$
$\hat{\underline{H}} \equiv \int_{-1}^{+1} \underline{L}^T \hat{\underline{D}} \frac{r' \ell'}{2} ds$				
$\hat{\underline{k}} \equiv \int_{-1}^{+1} \hat{\underline{M}}^T \left( \frac{1}{\underline{k}} \right) \hat{\underline{M}} \frac{r' \ell'}{2} ds$				
$\hat{\underline{k}}^e \equiv \int_{-1}^{+1} \hat{\underline{B}}^T \hat{\underline{C}}^e \hat{\underline{B}} \frac{r' \ell'}{2} ds$				
$r_0$ = pile radius (length)		$k$ = soil permeability (length/time)		
$\gamma$ = unit weight of pore fluid (force/length cubed)		$\sigma_0$ = mean effective stress in the soil before pile installation (force/length squared)		

Table G.1: Dimensionless Finite Element Equation and Related Matrices

APPENDIX H  
COMPUTER PROGRAMS  
H.1 INTRODUCTION

Appendix H contains the descriptions, manuals and listings of various computer programs developed by the author and used in this thesis. These programs are coded according to the 1966 standard for FORTRAN, with Multics FORTRAN extensions and have been implemented at the Massachusetts Institute of Technology on a Honeywell computer (CPU model 6880) running a Multics Operating System. All programs use double precision arithmetic\* and read input in free format i.e., data fields are delimited by blanks, commas or carriage return characters. Thus, specific column fields are NOT specified in the manuals presented in this Appendix.

This Appendix contains:

- (i) A computer program for Laboratory Strain Controlled Tests.
- (ii) A computer program to compute the Effective Stresses and Excess Pore Pressures during the Undrained Expansion of a Cylindrical Cavity.
- (iii) A computer program to compute the Effective Stresses far behind the tip of a pile using the Strain Path method.

---

\*a double-word consists of eight 9-bit bytes on this computer

- (iv) A computer program to compute the Excess Pore Pressures in the radial direction far behind the tip of a Cylindrical Pile, due to a given field of Effective Stresses.
- (v) A Finite Element computer program for Non-Linear One-Dimensional Consolidation around a Cylindrical Pile due to the dissipation of a known initial Excess Pore Pressure field.
- (vi) A library containing subroutines used by the previous computer programs.



## H.2 A COMPUTER PROGRAM FOR LABORATORY

### STRAIN CONTROLLED TESTS

#### H.2.1 PROGRAM DESCRIPTION

This program computes the effective stresses during various laboratory strain controlled tests using one of the following models:

- (i) A Linear Isotropic model with different moduli in loading and unloading.
- (ii) The Modified Cam-Clay model and,
- (iii) The Proposed model (see Chapter 4).

The program reads the initial values of the state variables required by the specific model to be used, the number of strain increments that will be applied and the cartesian components of the strain applied during each strain increment.\* The program computes the effective stresses (and the remaining state variables) after each strain increment. Various effective stresses and combinations can be printed by activating or deactivating the appropriate "write" statements.

---

\*the same strain increment is applied in all steps

## H.2.2 USER'S MANUAL

The program reads input from units 09 and 28.

Unit 09 contains the input parameters of the soil model to be used in the analysis and its contents are described in Section H.7.2.

Unit 28 contains control information and is described in the following:

<u>NOTE</u>	<u>VARIABLE</u>	<u>ENTRY</u>
	model	Type of model, EQ. 1, Linear Isotropic EQ. 2, MCC EQ. 3, Proposed model
(1)	n	Dimension of the deviatoric transformed space required
	sigma	Initial mean effective stress
(2)	s(1),... s(n)	Initial deviatoric transformed stress components (Table 4.1)
(3)	nsurf	Flag for initial state EQ. 0, Elastic EQ. 1, Elastoplastic
(3),(4)	alpha	Size of the yield surface

(5)	a(1),... a(n)	Transformed components of anisotropy
(6)	sigy	Initial vertical effective stress
	increment	Number of strain increments to be applied
	fed, fed(1), fed(2) fed(3), fed(4), fed(5)	Cartesian components of the strain tensor applied during each strain increment:  x, y, z, xy, yz, zx
(7)	dlimit	Absolute maximum allowable transformed strain increment for input in the models

NOTES:

(1) 1.LE.n.LE.5

Possible Values: EQ. 1, for Triaxial test; EQ. 2, for True Triaxial test; EQ. 3, for Direct Simple Shear; EQ. 5, for the most general path.

(2) "n" values are inputted depending on the dimension of the tranformed space.

(3) Only required for model>1

(4) Equal to the initial half-length of the projection of the

axis of the yield surface on the isotropic line of the transformed space.

- (5) Only required for model>2. "n" values are inputted depending on the dimension of the transformed space used. They are:

$$a(i) \equiv a_i \equiv \bar{\alpha} b_i$$

where  $b_i$  are the transformed components of anisotropy (see Table 4.1).

- (6) Only required for normalization of stresses in the printouts.
- (7) Suggested value: 1.d-4

### H.2.3. PROGRAM LISTING

```

*****
* Program for Laboratory Strain Controlled tests.
*
* Programmed by M.J. Kavadas
* MIT April, 1980
*
* Models Implemented:
*
* model=1.....Linear Isotropic model
* model=2.....Modified Cam-Clay
* model=3.....Proposed model (my_model)
*
*****
implicit real*8(a-h,o-z)
dimension ed(5),s(5),a(5),fed(5),ds(5),tau(5)
dimension emprop(4),ccprop(4),xmmp(16)
open (28,model='in',form='formatted',ioswitch='in28_data')
Read model mode
read (28,1) model
format (v)
read space dimension (triax=1,plane_strain=2,dss=3)
read (28,1) n
Read model properties
open (9,model='in',form='formatted',ioswitch='in9_data')
call read_model_properties (model,emprop,ccprop,xmmp)
close (9)
Initialize state variables
call init_routine (model,n,sigma,s,alpha,a,nsurf)
Read normalization stress:
Usually the initial vertical effective stress
read (28,1) sigy
Read number of strain steps:
read (28,1) increment
Read cartesian components of strain increment:

```

```

C   1.e: dexx,deyy,dezz,dexy,deyz,dezxx
C   read (28,1) fevd,(fed(1),i=1,5)
C   dex=fevd
C   dey=fed(1)
C   Convert in the transformed strain measures
C   call convert (0,0,n,fevd,fed(1),fed(2),fed(3),fed(4),fed(5))
C   read (28,1) dlimit
C   Initialize here any summable measures
C   ex=0.d0
C   ey=0.d0
C   End of initialization
C   Main LOOP
C   do 900 incr=1,increment
C   evd=fevd
C   do 23 i=1,n
C   ed(i)=fed(1)
C   call model_11b (model,dlimit,n,emprop,ccprop,xmmprop,
C   &   evd,ed,sigma,s,alpha,a,nsurf,
C   &   dsigma,ds)
C   taux=sigma
C   do 24 i=1,5
C   tau(i)=s(i)
C   Convert from the transformed back to the Cartesian (cylindrical)
C   stress measures x,y,z,xy,yz,zx (or r,z,t,rz,zt,tr)
C   call convert (1,1,n,taux,tau(1),tau(2),tau(3),tau(4),tau(5))
C   Form useful quantities
C   sm=(tau(1)-taux)/(2.d0*sigy)
C   sp=(taux+tau(1))/(2.d0*sigy)
C   shear=tau(3)/sigy
C   ex=ex+100.d0*dex
C   ey=ey+100.d0*dey
C   sy=tau(1)/sigy

```

```

smp=(tau+tau(2))/(2.d0*sigy)
smm=(tau-tau(2))/(2.d0*sigy)

C
C Write quantities of interest
C Activate (or add) required quantities depending on the type of test
C
C write (6,114) ex,ey,sm.sp,smm,smp
C write (6,129) ex,smm,smp,nsurf
129 format (1x,3d16.7,2x,13)
114 format (6d16.7)
C write (31,2) nsurf,sigma,(s(1),1=1,n)
2 format (12,4d25.18)
C if (model.eq.1) go to 900
C if (model.ge.3) go to 112
C write (32,3) alpha
3 format (4d25.18)
C go to 900
112 continue
C write (32,3) alpha,(a(1),1=1,n)
C
C End of printing
C
C continue
900
C
C Print final measures of interest
C
C write (16,201) sigma,s(1),s(2)
C write (16,201) alpha,a(1),a(2)
201 format (1x,3d26.17)
C
end

```

### H.3 A COMPUTER PROGRAM FOR THE UNDRAINED EXPANSION OF A CYLINDRICAL CAVITY

#### H.3.1 PROGRAM DESCRIPTION

This program computes the effective stresses and excess\* pore pressures during the undrained expansion of a cylindrical cavity using one of the following models:

- (i) A Linear Isotropic model with different moduli in loading and unloading.
- (ii) The Modified Cam-Clay model and,
- (iii) The Proposed model (see Chapter 4).

The program reads the initial values of the state variables required by the model to be used in the analysis and the number and location of points where stresses and pore pressures will be computed. It prints the effective stresses, excess pore pressures and remaining state variables at these points.

#### H.3.2 USER'S MANUAL

The program reads input from units 09 and 28.

Unit 09 contains the input parameters of the soil model to be used in the analysis and its contents are described in Section H.7.2.

Unit 28 contains control information and is described in the following:

---

\* i.e., in excess to the hydrostatic



<u>NOTE</u>	<u>VARIABLE</u>	<u>ENTRY</u>
	model	Type of model, EQ. 1, Linear Isotropic EQ. 2, MCC EQ. 3, Proposed model
	sigma	Initial mean effective stress
	s(1),s(2)	Initial transformed deviatoric stress components (see Table 4.1)
(1)	nsurf	Flag for initial state EQ. 0, Elastic EQ. 1, Elastoplastic
(1),(2)	alpha	Size of the yield surface
(3)	a(1),a(2)	Transformed components of anisotropy
	n	Number of points where program output will be computed (maximum=46)
(4)	x(1),...x(n)	Radial coordinates (normali- zed with the pile radius) of

points where program output  
will be computed

NOTES:

- (1) Only required for model>1
- (2) Equal to the initial half-length of the projection of the axis of the yield surface on the isotropic line of the transformed space.
- (3) Only required for model>2. The values inputted are:

$$a(i) \equiv a_i \equiv \bar{\alpha} b_i$$

where  $b_i$  are the transformed components of anisotropy (see Table 4.1).

- (4) Infinity is assumed at 200 pile radii. Thus,  $x(i)<200$  for all  $i$ 's. Note that  $x(1)=1$ , is at the pile wall.

### H.3.3 PROGRAM OUTPUT

The program outputs "n" records on each of the units 07 and 08 (unit 08 is used only if model>1).

Each record on unit 07 contains information for a point, starting from the point located at the largest distance from the pile. \* It contains:

- (i) The radial coordinate (normalized with the pile radius)
- (ii) The excess pore pressure
- (iii) The mean effective stress

---

\* format used: (1x,d14.6,4d22.14)

(iv) The transformed deviatoric stress components  $s(1)$  and  $s(2)$ .

Each record on unit 08 contains information for a point, starting from the point located at the largest distance from the pile.\* It contains:

- (i) The value of the variable "nsurf".
- (ii) The value of the variable "alpha".
- (iii) The values of the variables  $a(1)$  and  $a(2)$  (only for  $model > 2$ ).

#### H.3.4 PROGRAM LISTING

---

\*format used: (1x,i4,2x,3d22.14)

```

*****
* Program to Compute Effective Stresses and Pore
* Pressures during the Undrained Expansion of a
* Cylindrical Cavity
*
* Programmed by M.J. Kavvasas
* MIT May, 1980
*
* Models implemented:
*
* model=1.....Linear Isotropic model
* model=2.....Modified Cam-Clay
* model=3.....Proposed model (my_model)
*
*****
implicit real*8(a-h,o-z)
dimension x(47),s(2),a(2),ed(2),ds(2)
dimension emprop(4),ccprop(4),xmmprop(16)

two=1/sqrt(2)
six=1/sqrt(6)

data two,six/0.7071067812d0,0.4082482905d0/
open (28,mode="in",form="formatted",ioswitch="in28_data")

Read model mode

read (28,1) model
format (v)

Read model properties

open (9,mode="in",form="formatted",ioswitch="in9_data")
call read_model_properties (model,emprop,ccprop,xmmprop)
close (9)

Initialize state variables

call init_routine (model,2,sigma,s.alpha,a,nsurf)
p=0.d0

Read number of points where output will be computed
(one more than the number of finite elements to be used
in the consolidation program). For example, if we have
45 streamlines then we have 45 elements for consolidation and
here we will read 46)

```



## H.4 A COMPUTER PROGRAM FOR PILE DRIVING USING THE STRAIN PATH METHOD

### H.4.1 PROGRAM DESCRIPTION

This program computes the effective stresses and the remaining state variables far behind the tip of a cylindrical pile, using the strain path method and one of the following soil models:

- (i) A Linear Isotropic model with different moduli in loading and unloading.
- (ii) The Modified Cam-Clay model and,
- (iii) The Proposed model (see Chapter 4).

The program processes the strains along a number of "stream-lines" around the tip of the pile and uses the specified soil model to compute the effective stresses and the remaining state variables at the end of each stream-line, i.e., far behind the tip of the pile. After processing a specific stream-line the program pauses for the user to attach the I/O switch to the file containing the strains along the next stream-line and the computations are resumed.

### H.4.2 USER'S MANUAL

The program reads input from units 09,05,11 and 28.

Unit 09 contains the input parameters of the soil model to be used in the analysis and its contents are described in Section H.7.2.

Unit 05 is by default attached to the terminal and thus,

the program prompts the user to input from the terminal:

(i) The model type (model) to be used:

EQ. 1, Linear Isotropic

EQ. 2, MCC

EQ. 3, Proposed model

(ii) The number of points (incr) along each stream-line, where strains are given, i.e., the number of records to be read in for each stream-line from unit 11.\*

Unit 11 contains "incr" number of records for each stream-line. Each record contains\*\* information for a point along the stream-line starting from points in front of the pile:

(i) The axial coordinate  $z$  (the origin is located at the tip of the pile and the positive  $z$ -axis is upwards) normalized with the pile radius.

(ii) The radial coordinate  $r$  (the origin is located along the axis of the pile) normalized with the pile radius.

(iii) The strain increments  $\Delta\epsilon_z$ ,  $\Delta\epsilon_r$ ,  $\Delta\epsilon_\theta$ , and  $\Delta\epsilon_{rz}$  between the point under consideration and the previous one.

Unit 28 contains control information and is described in the following:

---

\* Levadoux and Baligh (1980) used datasets containing 389 records for each stream-line

\*\* format: (2f10.5,4d10.3)

NOTEVARIABLEENTRY

	sigma	Initial mean effective stress
	s(1),s(2),s(3)	Initial transformed deviatoric stress components (see Table 4.1)
(1)	nsurf	Flag for initial state EQ. 0, Elastic EQ. 1, Elastoplastic
(1),(2)	alpha	Size of the yield surface
(3)	a(1),a(2),a(3)	Transformed components of anisotropy

NOTES:

- (1) Only required for model>1
- (2) Equal to the initial half-length of the projection of the axis of the yield surface on the isotropic line of the transformed space.
- (3) Only required for model>2. The values inputted are:

$$a(i) \equiv a_i \equiv \bar{\alpha} b_i$$

where  $b_i$  are the transformed components of anisotropy (see Table 4.1).



#### H.4.3. PROGRAM OUTPUT

The program outputs records on units 29 and 08 (unit 08 is used only if model>1). The number of records outputted on each unit is equal to the number of stream-lines processed. Each record contains information for the final point of the stream-line i.e., for the point far behind the tip of the pile.

Each record on unit 29 contains:\*

- (i) The radial coordinate (normalized with the pile radius)
- (ii) The mean effective stress
- (iii) The transformed deviatoric stress components  $s(1), s(2)$  and  $s(3)$ .

Each record on unit 08 contains:\*\*

- (i) The value of the variable "nsurf".
- (ii) The value of the variable "alpha".
- (iii) The values of the variables  $a(1), a(2)$  and  $a(3)$  (only for model>2).

#### H.4.4 PROGRAM LISTING

---

\* format: (f11.6,4d25.17)

\*\* format: (i3,4d25.17)

```

*****
* Program for Pile Driving using the Strain Path
* method. It computes the Effective Stresses
* far behind the tip of
* a cylindrical pile.
*
* Programmed by M.J. Kavvadas
* MIT
* May, 1980
*
* Models implemented:
*
* model=1.....Linear Isotropic model
* model=2.....Modified Cam-Clay
* model=3.....Proposed model (my_model)
*
*****
implicit real*8(a-h,o-z)
dimension ed(3),s(3),a(3),ds(3)
dimension emprop(4),ccprop(4),xmmprop(16)
write(6,301)
format(1x,'input model type')
read(5,1) model
format(v)

301
1
c
c
c
Read number of strain steps along the streamlines

write(6,302)
format(1x,'input number of increments')
read(5,1) incr

302
c
c
c
Read model properties

open(9,model='in',form='formatted',ioswitch='ing_data')
call read_model_properties(model,emprop,ccprop,xmmprop)
close(9)
open(29,model='out',form='formatted',ioswitch='out29_data')
open(8,model='out',form='formatted',ioswitch='out8_data')
continue

100
c
c
c
Initialize state variables.

open(28,model='in',form='formatted',ioswitch='in28_data')
call init_routine(model,3,sigma,s,alpha,a,nsurf)
close(28)

c
c
open(11,model='in',form='formatted',ioswitch='in11_data')

```



H.5 A COMPUTER PROGRAM TO COMPUTE PORE PRESSURES  
DUE TO GIVEN EFFECTIVE STRESSES

H.5.1 PROGRAM DESCRIPTION

This program computes the excess\* pore pressure in the radial direction, far behind the tip of a cylindrical pile, due to a given field of effective stresses. The program reads the effective stresses at various points in the radial direction, computes the pore pressures associated with these effective stresses by integrating the stress equilibrium equation in the radial direction and outputs the effective stresses and excess pore pressures.

H.5.2 USER'S MANUAL

The program reads input from units 05 and 29.

Unit 05 is by default attached to the terminal and thus, the program prompts the user to input from the terminal the number of points (npoints) at which the effective stresses are given.

Unit 29 contains \*\* "npoints" number of records. Each record contains information for one point in the radial direction, starting from the point located at the largest distance from the pile. Each record contains:\*\*\*

---

\* i.e., in excess to the hydrostatic

\*\* the file attached to unit 29 is the file outputted on unit 29 by the program described in Appendix H.4.

\*\*\* format: (f11.6,4d25.17)

- (i) The radial coordinate (normalized with the pile radius)
- (ii) The mean effective stress
- (iii) The transformed deviatoric stress components  $s(1)$ ,  $s(2)$  and  $s(3)$ .

#### H.5.3. PROGRAM OUTPUT

The program outputs "npoints" number of records on unit 07. Each record contains information for one point in the radial direction, starting from the point located at the largest distance from the pile. Each record contains:\*

- (i) The radial coordinate (normalized with the pile radius)
- (ii) The excess pore pressure
- (iii) The mean effective stress
- (iv) The transformed deviatoric stress components  $s(1)$ ,  $s(2)$  and  $s(3)$ .

#### H.5.4. PROGRAM LISTING

---

\* format: (1x,d14.6,5d22.14)



H.6. PROGRAM NON-CAP  
FOR  
NON-LINEAR ONE-DIMENSIONAL CONSOLIDATION AROUND A PILE  
USING THE FINITE ELEMENT METHOD

H.6.1 PROGRAM DESCRIPTION

This program performs Non-Linear One-Dimensional Consolidation around a Cylindrical Pile due to the dissipation of a known initial excess pore pressure field using the Finite Element method (see Chapter 7). Soil non-linearities are treated using one of the following models:

- (i) A Linear Isotropic model with different moduli in loading and unloading.
- (ii) The Modified Cam-Clay model and,
- (iii) The Proposed model (see Chapter 4).

The program uses 3-node one-dimensional isoparametric elements for the displacements and 2-node one-dimensional isoparametric elements for the pore pressures and outputs pore pressures, effective stresses and the remaining state variables, for various points in the radial direction, at various values of the dimensionless time factor  $T$ . For a description of the non-linear algorithm and other features of the program see Chapter 7. Chapter 8 presents consolidation solutions using this program.

## H.6.2 USER'S MANUAL

The program reads input from units 09, 04, 07 and 08.

Unit 09 contains the input parameters of the soil model used in the analysis and its contents are described in Section H.7.2.

Unit 04 contains control information and is described in the following:

<u>NOTE</u>	<u>VARIABLE</u>	<u>ENTRY</u>
	model	Type of model, EQ. 1, Linear Isotropic EQ. 2, MCC EQ. 3, Proposed model
	n	Number of Finite Elements
(1)	nloop	Dimension of the Transformed stress space
	elastic_cmod	Value of $K+4G/3$ used in the formulation of the "elastic" stiffness matrix
	elastic_dmod	Value of $K-2G/3$ used in the formulation of the "elastic" stiffness matrix



	dt	Standard increment of the dimensionless time factor
(2)	ngroups	Number of groups of time steps
(3)	nstep(1), multiplier(1), . . nstep(ngroups), multiplier(ngroups)	Integers controlling the length of each time step
	max_iteration	Maximum number of equilibrium iterations in each time step
(4)	tolerance	Convergence tolerance for equilibrium iterations
(5)	dlimit	Absolute maximum allowable transformed strain increment for input in the models

**NOTES:**

- (1) EQ. 2, for consolidation due to initial fields computed via the Undrained Cavity Expansion method (Appendix H.3); EQ. 3, for consolidation due to initial fields computed via the

Strain Path method (Appendices H.4 and H.5).

- (2) Output is printed after each such group of time steps.

Note that the stiffness matrix is reformed in the beginning of each such group of time steps because the increment "deltat" of the dimensionless time factor changes (see note (3) below).

- (3) "ngroups" pairs of integers are inputted. The first integer of each pair specifies the number of time steps comprising this group. The second integer of each pair is a multiplier denoting how many times is the length of the time steps of this group larger than the standard increment of the time factor "dt". Normally the multiplier should increase as consolidation goes on, because the rate of consolidation decreases.

- (4) The convergence criterion used in this version of the program is:

Convergence is achieved when the difference of the excess pore pressure at the pile wall in two successive iterations is less than "tolerance". The convergence rule is controlled by the subroutine "convergence". Suggested value: tolerance=1.d-4.

- (5) Suggested value: dlimit=1.d-4.

Units 07 and 08 contain information for the state variables at the nodes of the Finite Elements in the beginning of consolidation. Each unit contains (n+1) records, i.e., one record for each node, starting from the node located at the

largest distance from the pile and ending at the node located at the pile wall.

Each record on unit 07 contains:

- (i) The radial coordinate (normalized with the pile radius)
- (ii) The excess pore pressure
- (iii) The mean effective stress
- (iv) The transformed deviatoric stress components  $s(1), \dots, s(nloop)$ . "nloop" is equal to 2 or 3 depending on the method used to compute the initial state variables.

Unit 08 is used only if  $model > 1$ . Each record contains:

- (i) The value of the variable "nsurf".
- (ii) The value of the variable "alpha".
- (iii) The values of the variables  $a(1), \dots, a(nloop)$  (only for  $model > 2$ ).

### H.6.3 PROGRAM OUTPUT

The program prints one record of output at the end of each group of time steps. The following units receive output:

- (1) Unit 10: Effective and total radial stress at the pile wall.
- (2) Unit 11: Excess pore pressures for various points in the radial direction.
- (3) Unit 12: Values of the variable "nsurf" for various points in the radial direction.
- (4) Unit 13: Values of the mean effective stress for various points in the radial direction.
- (5) Unit 14: Values of the transformed deviatoric stress  $s(1)$

- for various points in the radial direction.
- (6) Unit 15: Values of the transformed deviatoric stress  $s(2)$  for various points in the radial direction.
  - (7) Unit 16: Values of the transformed deviatoric stress  $s(3)$  for various points in the radial direction (only for  $nloop > 2$ ).
  - (8) Unit 17: Values of the variable "alpha" for various points in the radial direction (only for  $model > 1$ ).
  - (9) Unit 18: Values of the transformed anisotropy component  $a(1)$  for various points in the radial direction (only for  $model > 2$ ).
  - (10) Unit 19: Values of the transformed anisotropy component  $a(2)$  for various points in the radial direction (only for  $model > 2$ ).
  - (11) Unit 20: Values of the transformed anisotropy component  $a(3)$  for various points in the radial direction (only for  $model > 2$  and  $nloop > 2$ ).

#### H.6.4 PROGRAM LISTING

The following listing contains:

- (i) The main program for consolidation described above.
- (ii) A set of subroutines used only by this program. It should be noted that additional subroutines which are shared among this program and the others described in this Appendix are included in the Subroutine Library discussed in Section H.7.

```

*****
*
* PROGRAM
*
*
* NON-CAP
*
*
* for NON-linear Consolidation Around a Pile
*
*
* Non-Linear
*
* One-Dimensional Consolidation in Cylindrical
* Coordinates using the Finite Element Method
* Programmed by M.J. Kavvadas
* MIT June, 1980
*
* Models implemented:
*
*
* model=1.....Linear Isotropic model
* model=2.....Modified Cam-Clay
* model=3.....Proposed model (my_model)
*
*****

```

The Program uses 3-node elements for the displacements and 2-node elements for the pore pressures.

n=number of elements

The numbering of the nodes is as follows:

- Global dof number 1: pile wall displacement.
- Global dof number 2: pile wall pressure.
- and then for the 1-th element:
- Global dof number (3\*1): middle node displacement
- Global dof number (3\*1+1): right node displacement
- Global dof number (3\*1+2): right node pore pressure

DIMENSIONING

- model state variables:
- sigma(3\*n).s(3,3\*n).alpha(3\*n).an(3,3\*n).nsurf(3\*n)
- Finite Element matrices:
- b(3\*n+2) = load vector during back substitution
- bt(3\*n+2) = part of the load vector that varies only every time step
- delu(2\*n+1) = displacement increment between time t and the 1-th iteration of time (t+deltat)
- a(12\*n+3) = compacted stiffness matrix
- maxa(3\*n+3) = stores addresses of the diagonal elements of the stiffness matrix



```

if (model.eq.1) go to 8
close (8)
number_of_step=0
call print_titles (model,nloop)
call print_output (p,sigma,s,alpha,an,nsurf,model,nloop,number_of_step)

nn=3*n+2
call form_maxx (n,maxx)

LOOP OVER GROUPS OF TIME STEPS
do 100 nng=1,ngroups
  Compute time length for this group
  ddt=dt*multiplier(nng)
  call form_stiffness_matrix (n,x,maxx,ddt,elastic_cmod,elastic_dmod,a)
  call impose_zero_b_condition (0,1,maxx,a,nn,b)
  call impose_zero_b_condition (0,nn,maxx,a,nn,b)
  call colsol (a,b,maxx,nn,0)
  call form_dt_k_p (ddt,n,x,p,bt)

LOOP OVER TIME STEPS OF THIS GROUP
do 100 itime=1,nstep(nng)
  number_of_step=number_of_step+multiplier(nng)
  do 21 i=1,nn
    b(i)=bt(i)
  do 22 i=1,2*n+1
    delu(i)=0.d0
  call impose_zero_b_condition (1,nn,maxx,a,nn,b)
  iconvergence=.false.
  old_wall=0.d0

LOOP OVER ITERATION STEPS
do 80 iteration=1,max_iteration
  call colsol (a,b,maxx,nn,1)

LOOP OVER ELEMENTS
do 23 i=1,n
  k=3*i
  k2=2*i
  delu(k2)=delu(k2)+b(k)
  delu(k2+1)=delu(k2+1)+b(k+1)
  wall=b(2)
  call convergence (iteration,wall,old_wall,tolerance,iconvergence)

```

8

C

C

C

C

C

C

C

C

C

C

21

22

C

C

C

C

C

C

23







```

C
C
C
60
C
62
C
80
C
109
C
C
C
85
C
86
119
C
C
C
C
100

```

```

add H*delu to the load vector
b(k-1)=b(k-1)+(-5.*D0*x(i))*delu(k2-1)+4.*d0*xm*delu(k2)+x(i+1)*delu(k2+1))/6.*d0
b(k+2)=b(k+2)+(-x(i))*delu(k2-1)-4.*d0*xm*delu(k2)+5.*d0*x(i+1)*delu(k2+1))/6.*d0
continue
if (i.convergence) go to 85
do 62 i=1,nn
b(1)=bt(1)-b(1)
call impose_zero_b_condition (1,1,maxa,a,nn,b)
call impose_zero_b_condition (1,nn,maxa,a,nn,b)
continue
write (6,109) max_iteration,itime,nng
format(1x,'Maximum Iteration number =',13.2x,'EXCEEDED without convergence
& at time step',14.2x,'of group',14)
PAUSE for further instruction because convergence was not achieved
pause 1
if (itime.eq.nstep(nng)) go to 86
call form_dt_k_p (ddt,n,x,p,bt)
write (6,119) iteration,itime,nng,p(1)
format (1x,'CONVERGENCE IN ITERATION',14.3x,'OF TIME STEP',
& 14.3x,'OF GROUP',14.2x,'WALL PRESSURE=',d14.5)
Print information about this time step.
call print_output (p,sigma,s,alpha,an,nsurf,model,nloop,number_of_step)
continue
end

```



```

subroutine initialization_routine
& (n,x,p,sigma,s,alpha,an,nsurf,ccprop,xmprop,
& dt,elastic_cmod,elastic_dmod,
& ngroups,nstep,multiplier,max_iteration,tolerance,
& model,dlimit,nloop)

C
C Arguments: model,ccprop,xmprop are input to the routine.
C All other arguments are outputted.
C n = number of elements (45 for the streamline solution)
C x(n+1) = radial coordinate of corner nodes of elements normalized
C          with the pile radius
C p(n+1) = pore pressures of corner nodes of the elements
C          normalized with the mean effective stress at infinity.
C sigma(3*n) = mean effective stress at integration points (3) norma-
C             lized with the mean effective stress at infinity.
C s(3,3*n) = s1 s2 and s3 at integration points (3 per element) norma-
C             lized with the mean effective stress at infinity.
C alpha(3*n) = size of the yield surface at integration points norma-
C             lized with the mean effective stress at infinity.
C an(3,3*n) = anisotropy coefficients a1 a2 a3 at integration points
C             (3 per element) normalized with the mean effective stress
C             at infinity
C nsurf(3*n) = flag. Defined at the integration points.
C             For the elastoplastic models:
C             1=ON the Y.S., 0=INSIDE the Y.S.
C             For the elastic model:
C             1=loading, 0=unloading
C dt = standard increment of the time factor
C          time factor=c*deltat/(pile radius)**2
C          c=(mean effective stress at infinity)*(permeability)/
C             (unit weight of water)
C elastic_cmod= "effective" (K+4G/3) normalized with the mean effective
C               stress at infinity.
C elastic_dmod= "effective" (K-2G/3) normalized with the mean effective
C               stress at infinity.
C ngroups = number of groups of time steps where the length of
C           the time step will change and thus the stiffness
C           matrix will be reformed.
C nstep(ngroups)= number of time steps in each group.
C multiplier(ngroups)= integer denoting how many times the length
C                   of the time steps of this group is larger than the
C                   standard 'dt'
C max_iteration= maximum number of iterations allowed in each time step
C tolerance = convergence tolerance for the displacements (Euclidean
C            norm of the displacement vector at all nodes
C            divided by the number of nodes)
C            must not exceed "tolerance" in order to have convergence
C model= type of model to be used in the analysis.

```

```

C
C dlimit= maximum transformed strain step for the models
C nloop= 2 or 3 specifying the required dimension of the deviatoric
C transformed space
C (Full 3-D problem would have nloop=5)
C
implicit real*8(a-h,o-z)
dimension x(1),p(1),sigma(1),s(3,1),alpha(1),an(3,1),nsurf(1)
dimension nstep(1),multiplier(1)
dimension xg(3)
dimension cprop(1),xmmprop(1)
dimension ssp(3),ss1(3),ssp(3),ssm(3),ss(3)
dimension aar(3),aal(3),aap(3),aam(3),aa(3)
data xg/-0.7745966692d0,0.d0,0.7745966692d0/
read (4,1) n
format (v)
read (4,1) nloop
nn=n+1
C
C read values at outermost streamline
read (7,1) x(nn),p(nn),sigr,(ssr(mm),mm=1,nloop)
if (model.eq.1) go to 12
if (model.ge.3) go to 11
read (8,1) nsurfr,alpr
go to 12
11 read (8,1) nsurfr,alpr,(aar(mm),mm=1,nloop)
12 do 100 i=n,1,-1
C
C read values at inward end of each element starting from outermost
read (7,1) x(i),p(i),sigl,(ssl(mm),mm=1,nloop)
if (model.eq.1) go to 22
if (model.ge.3) go to 21
read (8,1) nsurfi,alpi
go to 22
21 read (8,1) nsurfi,alpi,(aal(mm),mm=1,nloop)
C
C Compute values of the state variables at the integration
C points knowing their values at the nodes.
C
C
22 sigp=(sigr+sigl)/2.d0
sigma=(sigr-sigl)/2.d0
do 23 kk=1,nloop
ssp(kk)=(ssr(kk)+ss1(kk))/2.d0
ssm(kk)=(ssr(kk)-ss1(kk))/2.d0
if (model.eq.1) go to 32
iflag=1
if (nsurfr.eq.0.or.nsurfi.eq.0) iflag=0
alpp=(alpr+alpi)/2.d0
alpm=(alpr-alpi)/2.d0
if (model.eq.2) go to 32
do 24 kk=1,nloop

```

```

24      aap(kk)=(aar(kk)+aa1(kk))/2.d0
32      aam(kk)=(aar(kk)-aa1(kk))/2.d0
      k=3*(i-1)
      do 15 j=1,3
      sig=sigm*xg(j)+sigp
      do 25 kk=1,nloop
25      ss(kk)=ssm(kk)*xg(j)+ssp(kk)
      if (model.eq.1) go to 43
      alp=alpm*xg(j)+alpp
      if (model.eq.2) go to 42
      do 26 kk=1,nloop
26      aa(kk)=aam(kk)*xg(j)+aap(kk)
42      call adj_stress (iflag,jflag,model,ccprop,xmprop,sig,ss,alp,aa,nloop)
43      sigma(k+j)=sig
      do 27 kk=1,nloop
27      s(kk,k+j)=ss(kk)
      if (model.eq.1) go to 15
      nsurf(k+j)=1
      if (jflag.eq.0) nsurf(k+j)=0
      alpha (k+j)=alp
      if (model.eq.2) go to 15
28      do 28 kk=1,nloop
15      an(kk,k+j)=aa(kk)
      continue
      sigr=sigl
      do 29 kk=1,nloop
29      srr(kk)=ss1(kk)
      if (model.eq.1) go to 100
      nsurf=nsurf1
      alpr=alpl
      if (model.eq. 2) go to 100
      do 30 kk=1,nloop
30      aar(kk)=aal(kk)
      continue
      Read remaining parameters

      read (4,1) elastic_cmod,elastic_dmod
      read (4,1) dt
      read (4,1) ngroups
      do 10 j=1,ngroups
10      read (4,1) nstep(j),multiplier(j)
      read (4,1) max_iteration
      read (4,1) tolerance
      read (4,1) dlimit
      return

```

end





```
11 db=db+zum*zum
    zum=c*sigma
    db=db/(zum+zum)
    zum=2.d0/((1.d0+db)+dum)
    sigma=zum*sigma
    do 21 i=1,n
    s(i)=zum*s(i)
    return
    end
```

21

subroutine impose\_zero\_b\_condition (iflag,k,maxa,a,nn,b)

```

C
C      Imposes a zero Boundary Condition
C      iflag=1..... modify load vector
C      iflag=0..... modify stiffness matrix
C      k..... degree of freedom to be constrained
C      nn..... total number of equations
C      maxa..... contains addresses of diagonal elements
C      b..... load vector
C      implicit real*8(a-h,o-z)
C      dimension maxa(1),a(1),b(1)
C      if (iflag.eq.1) go to 50
C      modify stiffness matrix
C      ma=maxa(k)
C      a(ma)=1.d0
C      if (k.eq.1) go to 10
C      mma=maxa(k+1)-maxa(k)-1
C      if (mma.eq.0) go to 10
C      do 5 i=1,mma
C      ma=ma+1
C      a(ma)=0.d0
C      ma=nn-k
C      if (ma.eq.0) return
C      do 20 i=1,ma
C      j=((maxa(k+1+1)-maxa(k+1)).1t.(i+1)) go to 20
C      a(j)=0.d0
C      continue
C      return
C      modify load vector
C      b(k)=0.d0
C      return
C      end

```

C

C

C

C

C

C

C

C

C

C

C

C

C

C

C

C

C

C

C

C

C

C

C

C

C

C

C

C

C

C

C

C

C

C

C

C

C

C

C

C

C

C

C

C

C

C

C

C

C

C

C

C

C

C

C

C

C

C

C

C



```

if (i.gt.1) go to 2
a(j-3)=xk1
a(j-2)=fum
a(j-1)=-d56*x(1)
go to 3
2 a(j-9)=a(j-9)+xk1
a(j-5)=a(j-5)+fum
3 a(j-4)=a(j-4)-d56*x(1)
a(j)=xk2
a(j+1)=d23*xm
a(j+2)=xk3
a(j+3)=xk4
a(j+4)=xk5
a(j+5)=d16*x(i+1)
a(j+6)=xk6
a(j+7)=fum
a(j+8)=d56*x(i+1)
a(j+9)=-a(j+1)
a(j+10)=-fum
a(j+11)=-d16*x(1)
return
end
10

```

subroutine form\_maxa (n,maxa)

```
implicit real*8(a-h,o-z)
dimension maxa(1)
maxa(1)=1
maxa(2)=2
maxa(3)=4
do 5 i=1,n
  j=3*i+1
  maxa(j)=maxa(j-1)+3
  maxa(j+1)=maxa(j)+4
  maxa(j+2)=maxa(j+1)+5
return
end
```

c

5

```
subroutine form_dt_k_p (dt,n,x,p,b)
```

```
  Computes dt*k*p and all the zeroes of the load vector X  
  p(n+1)= normalized (with the stress measure) pore pressures.  
  b(3*n+2) = load vector to be formed
```

```
  implicit real*8(a-h,o-z)  
  dimension x(1),p(1),b(1)  
  b(1)=0.d0  
  b(2)=0.d0  
  do 10 i=1,n  
    xm=(x(i+1)+x(i))/2.d0  
    xlen=x(i+1)-x(i)  
    zum=dt*xm*(p(i)-p(i+1))/xlen  
    j=3*i  
    b(j-1)=b(j-1)+zum  
    b(j)=0.d0  
    b(j+1)=0.d0  
    b(j+2)=-zum  
  return  
end
```

```
C  
C  
C  
C  
C
```

```
10
```



```

110      if (a(kn)) 140,120,140
120      write (6,2000) n
2000     format (ix,'STOP-zero pivot for equation',14)
140     stop
       continue
       return
       reduce load vector
150     do 180 n=1,nn
         k1=maxa(n)+1
         ku=maxa(n+1)-1
160     if (ku-k1) 180,160,160
         k=n
         c=0.d0
         do 170 kk=k1,ku
           k=k-1
           c=c+a(kk)*v(k)
           v(n)=v(n)-c
170     continue
       Back substitute
180     do 200 n=1,nn
         k=maxa(n)
         v(n)=v(n)/a(k)
200     if (nn.eq.1) return
         n=nn
         do 230 l=2,nn
           k1=maxa(n)+1
           ku=maxa(n+1)-1
210     if (ku-k1) 230,210,210
           k=n
           do 220 kk=k1,ku
             k=k-1
             v(k)=v(k)-a(kk)*v(n)
220     n=n-1
230     return
       end

```





end

```

subroutine print_output (p,sigma,s,alpha,an,nsurf,model,nloop,number_of_step)
implicit real*8(a-h,o-z)
dimension p(1),sigma(1),s(3,1),alpha(1),an(3,1),nsurf(1)
data six,two/0.4082482905d0,0.7071067812d0/
data xol,xpol/0.11270167d0,0.88729833d0/
six=1/sqrt(6)
two=1/sqrt(2)
sigr=sigma(1)-s(1,1)*six-s(2,1)*two
press=pol*p(1)+xol*p(2)
tot_sigr=sigr+press
write (10,105) number_of_step,sigr,tot_sigr,press
write (11,103) number_of_step,p(1),p(6),p(11),p(17),p(21),p(25),
& p(28),p(30),p(32),p(35),p(38),p(41),p(44)
write (12,104) number_of_step,(nsurf(1),i=1,135)
write (13,103) number_of_step,(sigma(1),i=2,134,11)
write (14,103) number_of_step,(s(1,1),i=2,134,11)
write (15,103) number_of_step,(s(2,1),i=2,134,11)
if (nloop.eq.2) go to 5
write (16,103) number_of_step,(s(3,1),i=2,134,11)
if (model.eq.1) return
write (17,103) number_of_step,(alpha(1),i=2,134,11)
if (model.eq.2) return
write (18,103) number_of_step,(an(1,1),i=2,134,11)
write (19,103) number_of_step,(an(2,1),i=2,134,11)
if (nloop.eq.2) return
write (20,103) number_of_step,(an(3,1),i=2,134,11)
format (14,1x,3d21.10)
format (14,d13.5,9d12.4,3d11.3)
format (14,2x,13511)
return
end

```

C

C C

5

105  
103  
104

## H.7 SUBROUTINE LIBRARY

### H.7.1 PROGRAM DESCRIPTION

This library contains subroutines shared by most of the previous programs. Among these subroutines, are the drivers and associated routines for the soil models implemented in this research, i.e.:

- (i) A Linear Isotropic model with different moduli in loading and unloading (subroutine elastic\_model).
- (ii) The Modified Cam-Clay model (subroutine cam\_clay) and,
- (iii) The Proposed model (subroutine my\_model).

### H.7.2 CONTENTS OF UNIT 09

Unit 09 contains the input parameters of the implemented models. The contents of this unit depend on the soil model to be used in the analysis (i.e., the value of the variable "model").

### H.7.2.1 Linear Isotropic Model

In the case of a Linear Isotropic model (model=1), unit 09 contains:

<u>NOTE</u>	<u>VARIABLE</u>	<u>ENTRY</u>
	bulke	Bulk modulus for unloading
	bulkp	Bulk modulus for loading
	two_ge	Twice the shear modulus for unloading
	two_gp	Twice the shear modulus for loading

### H.7.2.2. Modified Cam-Clay model

In the case of the MCC model (model=2) unit 09 contains  
(see Chapter 3):

<u>NOTE</u>	<u>VARIABLE</u>	<u>ENTRY</u>
	elk	$(1 + e_o) / (\lambda - \kappa)$
	ek	$(1 + e_o) / \kappa$
(1)	xnu	
	xm	M

NOTES:

$$(1) \quad xnu = \frac{6 \kappa}{(1 + e_o) [1 + 2 (K_o)_{0C}]} \left( \frac{G}{\sigma_{vo}} \right)$$

### H.7.2.3. Proposed Model

In the case of the proposed model (model=3) unit 09 contains (see Table 5.7a):

<u>NOTE</u>	<u>VARIABLE</u>	<u>ENTRY</u>
	xlk	$\lambda/\kappa$
	elk	$(1 + e_o)/(\lambda - \kappa)$
	ek	$(1 + e_o)/\kappa$
(1)	xnu	
(2)	x	
	c	c
	psi	$\psi$
	beta	$\beta$
	gama	$\gamma$
	alfa	$\alpha$

xmm

Suggested value 0.40

ambg

$(\alpha - \beta) / \gamma$

sip

$\xi^P$

sic

$\xi^C$

xkp2

$(k^P)^2$

xkc2

$(k^C)^2$

NOTES:

$$(1) \quad xnu = \frac{6 \kappa}{(1 + e_o) [1 + 2(K_o)_{OC}]} \left( \frac{G}{\sigma_{vo}} \right)$$

$$(2) \quad x = \frac{1}{(x\ell k - 1)} \left\{ (x\ell k) \frac{1 + 2(K_o)_{NC}}{3[1 - (K_o)_{NC}]} - \frac{1}{xnu} \right\}$$

H.7.3 PROGRAM LISTINGS





```

subroutine convert (iflag,mode,n,x,y,z,xy,yz,zx)
C
C This routine converts stress (if mode=1) or strain (if mode=0)
C measures.
C If iflag=0, it converts standard measures x,y,z,xy,yz,zx (or
C r,z,t,rz,zt,tr for polar coordinates) to the 'equivalent'
C -Greek,1,2,3,4,5- . If iflag=1 it does the inverse conversion
C The variable n denotes the space (stress and strain) of
C interest. Note that the routine does NOT adjust the remaining
C shear stresses if n<5.
C
C implicit real*8(a-h,o-z)
data two,six,three/0.707106781d0,0.408248290d0,0.333333333d0/
C
C two=1/sqrt(2)
C three=1/3
C six=1/sqrt(6)
C dum=1.d0
C
C zum=three
C if (mode.eq.1) go to 5
C dum=three
C zum=1.d0
C if (iflag.eq.1) go to 15
C fum=x
C
C x=zum*(x+yz)
C y=six*(2.d0*y-fum-z)
C z=two*(z-fum)
C if (n.le.2) return
C xy=xy/two
C if (n.eq.3) return
C yz=yz/two
C if (n.eq.4) return
C zx=zx/two
C return
C fum=dum*x
C x=fum-six*y-two*z
C z=fum-six*y+two*z
C y=fum+2.d0*six*y
C if (n.le.2) return
C xy=two*xy
C if (n.eq.3) return
C yz=two*yz
C if (n.eq.4) return
C zx=two*zx
C return
C end

```



```

c
c
c
      subroutine model_lib (model,dlimit,n,emprop,ccprop,xcprop,xmprop,
      &   evd,ed,sigma,s,alpha,a,nsurf,dsigma,ds)
      It calls the appropriate model according to the value of "model".
      implicit real*8(a-h,o-z)
      dimension emprop(1),ccprop(1),xmprop(1),s(1),a(1)
      dimension ed(1),ds(1)
      dsigma=sigma
      do 55 i=1,n
      ds(i)=s(i)
      go to (1,2,3,   ),model
      call elastic_model (evd,ed,emprop(1),emprop(2),emprop(3),emprop(4),sigma,s,nsurf,n)
      go to 10
      call cam_clay (evd,ed,dlimit,
      &   ccp(1),ccprop(2),ccprop(3),ccprop(4),
      &   sigma,s,alpha,nsurf,n)
      go to 10
      call my_model (evd,ed,dlimit,
      &   xmprop(1),xmprop(2),xmprop(3),xmprop(4),xmprop(5),xmprop(6),xmprop(7),
      &   xmprop(8),xmprop(9),xmprop(10),xmprop(11),xmprop(12),
      &   xmprop(13),xmprop(14),xmprop(15),xmprop(16),
      &   sigma,s,alpha,a,nsurf,n)
      go to 10
      Any other models can be added here
      dsigma=sigma-dsigma
      do 15 i=1,n
      ds(i)=s(i)-ds(1)
      return
      end
55
1
2
3
c
c
c
10
15

```

```

subroutine read_model_properties (model,emprop,ccprop,xmmprop)
reads the model properties for the various models

implicit real*8 (a-h,o-z)
dimension emprop(1),ccprop(1),xmmprop(1)
if (model.ne.1) go to 2
read (9,1) emprop(1),emprop(2),emprop(3),emprop(4)
format (v)
return
if (model.ne.2) go to 3
read (9,1) ccprop(1),ccprop(2),ccprop(3),ccprop(4)
return
read (9,1) xmmprop(1),xmmprop(2),xmmprop(3),xmmprop(4)
read (9,1) xmmprop(5),xmmprop(6),xmmprop(7),xmmprop(8)
read (9,1) xmmprop(9),xmmprop(10),xmmprop(11),xmmprop(12)
read (9,1) xmmprop(13),xmmprop(14),xmmprop(15),xmmprop(16)
return
end

```

c

c

1

2

3

```
subroutine elastic_model (evd,ed,bulke,bulkp,two_ge,two_gp,sigma,s,nsurf,n)
```

```
  Elastic model with moduli:
```

```
  For loading:
    bulkp=K
    two_gp=2G
  For unloading:
    bulke=K
    two_ge=2G
```

```
  implicit real*8 (a-h,o-z)
  dimension ed(1),s(1)
  r=0.d0
  sum=0.d0
  do 1 i=1,n
    r=r+s(i)*ed(i)
    sum=sum+s(i)*s(i)
  q=(sigma-sum/sigma)/2.d0
  two_g=two_ge
  bulk=bulke
  nsurf=0
  r=two_g*r+bulk*q*evd
  if (r.lt.0.d0) go to 10
  two_gp=two_gp
  bulk=bulkp
  nsurf=1
  sigma=sigma+bulk*evd
  do 11 i=1,n
    s(i)=s(i)+two_g*ed(i)
  return
end
```

```
  C
  C
  C
  C
  C
  C
  C
  C
```

```
  1
```

```
 10
```

```
 11
```



```

10 do 10 i=1,n
C ed(i)=ed(1)/float(ndiv)
C
C MAIN LOOP
C
do 999 i times=1,ndiv
fevd=evd
do 15 i=1,n
fe(i)=ed(1)
call cc_driving_routine (ek,ek,xnu,xm,sigma,s,alpha,nsurf,fevd,ed,n)
continue
999 return
end
C *****
C *****
C subroutine cc_driving_routine (ek,ek,xnu,xm,sigma,s,alpha,nsurf,fevd,ed,n)
C The routine requires the following INPUT:
C
C (a) MATERIAL CONSTANTS
C *
C * eik=(1+e0)/(lamda-kappa) ; lamda='compression ratio' [=0.170]
C * ek=(1+e0)/kappa ; kappa='swelling ratio' [=0.034]
C * xnu= computed via the "elastic" shear modulus.
C * xm= ratio of the axes of the yield surface
C xm=sqrt(6)*(1-Kf)/(1+2*Kf) ; Kf=tan2(45-phi/2) ; phi=33.40
C (b) STATE VARIABLES
C * sigma.s(1,2,3,4,5) ; effective stresses
C * alpha Equal to the half-length of the sigma axis of the ellipse
C * nsurf ; index(1=on yield surface, 0=inside yield surface)
C (c) STRAIN INCREMENT
C * evd,ed(1,2,3,4,5)
C (d) AUXILIARY
C * n ; range of the do loops (stress space dimension)
C
C On OUTPUT the routine:
C (a) Leaves material constants intact
C (b) Returns the new value of the stress variables
C (c) Destroys the value of the strain increment
C (d) Leaves n intact
C
implicit real*8(a-h,o-z)
dimension s(1),ed(1)
dimension p(5),sd(5),q(5)
b=ek*sigma
two_g=xnu*b
sigmaad=b*evd
do 1 i=1,n

```



```

1      sd(i)=two_g*ed(i)
      if (nsurf.eq.0) go to 10
      r=0.d0
      do 2 i=1,n
2         q(i)=2.d0*s(i)
         r=r+q(i)*sd(i)
         qpp=2.d0*xm*xm*(sigma-alpha)
         r=qpp*sigmad+r
10        if (r.ge.0.d0) go to 20
         pb=sigma+sigmad
         f=0.d0
         do 3 i=1,n
3            p(i)=s(i)+sd(i)
            f=f+p(i)*p(i)
            dum=pb*(2.d0*alpha-pb)
            f=f-xm*xm*dum
40           if (f) 30,40,50
            nsurf=1
            go to 60
30          nsurf=0
60          sigma=pb
         do 4 i=1,n
4            s(i)=p(i)
            go to 70
50          call cc_intersection_with_surface (xm,sigma,s.alpha,s.alpha,nsurf,sigmad,ed,n,pb)
           call cc_modify_temporary (xm,ek,xnu,sigma,s.alpha,sigmad,ed,ed,n,
           & pb,q,qpp,b,two_g,r)
20          call cc_plastic (ek,xm,sigma,s.alpha,qpp,q,ed,ed,two_g,b,r,n)
70          call cc_adjust_stresses (xm,sigma,s.alpha,n)
           return
           end

```

```

subroutine cc_intersection_with_surface (xm,sigma,s,alpha,nsurf,sigmad,sd,n,z)
implicit real*8(a-h,o-z)
dimension s(1)
dimension sd(5)
sxx=0.d0
sxxd=0.d0
sxdxd=0.d0
do 1 i=1,n
sxx=sxx+s(i)*s(i)
sxxd=sxxd+s(i)*sd(i)
sxdxd=sxdxd+sd(i)*sd(i)
dum=xm*sigmad
ab=sxdxd+dum*dum
z=-2.d0*(sxxd-dum*xm*(alpha-sigma))/ab
if (nsurf.eq.1) return
nsurf=1
cb=sxx-xm*xm*(2.d0*alpha-sigma)*sigma
zum=dsqrt(z*z-4.d0*cb/ab)
z=(z+zum)/2.d0
return
end
c *****
c *****
subroutine cc_modify_temporary (xm,ek,xnu,sigma,s,alpha,sigmad,sd,evd,
& ed,r,z,q,qpp,b,two_g,r)
implicit real*8(a-h,o-z)
dimension s(1),ed(1)
dimension sd(5),q(5)
sigma=sigma+z*s.gmad
do 1 i=1,n
s(i)=s(i)+z*sd(i)
q(i)=2.d0*s(i)
qpp=2.d0*xm*xm*(sigma-alpha)
z=1.d0-z
evd=z*evd
dum=0.d0
do 2 i=1,n
ed(i)=z*ed(i)
dum=dum+q(i)*ed(i)
b=ek*sigma
two_g=xnu*b
r=b*qpp*evd+two_g*dum
return
end
c *****
c *****
subroutine cc_plastic (ek,xm,sigma,s,alpha,qpp,q,evd,ed,two_g,b,r,n)
implicit real*8(a-h,o-z)

```

```

1      dimension s(1),ed(1)
      dimension q(5),sd(5)
      phi=elk*qqp
      hh=2.d0*xm*xm*sigma*alpha*phi+b*qqp*qqp
      tt=0.d0
      do 1 i=1,n
        tt=tt+q(1)*q(1)
        tt=two_g*tt
        xl=r/(hh+tt)
        sigmaad=b*(evd-xl*qqp)
      do 2 i=1,n
        sd(1)=two_g*(ed(1)-xl*q(1))
        s(1)=s(1)+sd(1)
        z=1.d0+phi*xl
        alpha=z*alpha
        sigma=sigma+sigmaad
      return
      end
C *****
C *****
      subroutine cc_adjust_stresses (xm,sigma,x,alpha,n)
      implicit real*8(a-h,o-z)
      dimension s(1)
      y=C.d0
      do 1 i=1,n
        y=y+s(1)*s(1)
        dum=xm*sigma
        y=y+dum*dum
        y=2.d0*dum*xm*alpha/y
        sigma=y*sigma
      do 2 i=1,n
        s(1)=y*s(1)
      return
      end
2

```





```

c      * sigma,s(1,2,3,4,5) ; effective stresses
c      * alpha,a(1,2,3,4,5) ; anisotropy
c      * nsurf ; index(1=on yield surface, 0=inside yield surface)
c      (c) STRAIN INCREMENT
c      * evd,ed(1,2,3,4,5)
c      (d) AUXILIARY
c      * n ;range of the do loops (stress space dimension)

c      On OUTPUT the routine:
c      (a) Leaves material constants intact
c      (b) Returns the new value of the stress variables
c      (c) Destroys the value of the strain increment
c      (d) Leaves n intact

c      implicit real*8(a-h,o-z)
c      dimension s(1),a(1),ed(1)
c      dimension p(5),sd(5),q(5)

c      b=ek*sigma
c      two_g=xnu*b
c      sigmad=b*evd
c      do 11 i=1,n
c      sd(i)=two_g*ed(i)
c      if (nsurf.eq.0) go to 10
c      dum=sigma/alpha
c      r=0.d0
c      qa=0.d0
c      do 21 i=1,n
c      q(i)=2.d0*(s(i)-dum*a(i))
c      r=r+q(i)*sd(i)
c      qa=qa+q(i)*a(i)
c      qpp=2.d0*c*c*(sigma-alpha)-qa/alpha
c      r=qpp*sigmad+r
c      if (r.ge.0.d0) go to 20
c      pb=sigma+sigmad
c      dum=pb/alpha
c      f=0.d0
c      do 31 i=1,n
c      p(i)=s(i)+sd(i)
c      r=p(i)-dum*a(i)
c      f=f+r*r
c      dum=pb-alpha
c      f=f+c*c*(dum*dum-alpha*alpha)
c      if (f) 30,40,50
c      nsurf=1
c      go to 60
c      nsurf=0
c      sigma=pb

```

```

41 do 41 i=1,n
s(i)=p(1)
go to 70
50 call intersection_with_surface (c,sigma,s,alpha,a,nsurf,sigmad,sd,n,pb)
call modify_temporary (c,ek,xnu,sigma,s,alpha,a,sigmad,sd,emd,ed,n,
& pb,q,qpp,b,two_g,r)
20 call cone (sip,xkp2,sigma,alpha,a,n,q,rp)
call cone (sic,xkc2,sigma.alpha,a,n,q,rc)
c
c
c Here should be the restriction for rc only when
c extremely large strains are expected
c
c if (rc.lt.0.05d0) rc=0.d0
c
c call plastic (x1k,elk,c,psi,x,xmm,alfa,beta,ambg,gama,sigma,s,alpha,
& a,qpp,q,svd,ed,rc,rp,two_g,b,r,n)
call adjust_stresses (c,sigma,s,alpha,a,n)
return
end
70

```

## BIOGRAPHY

The author was born on August 22, 1954 in Thessaloniki, Greece. He entered the National Technical University of Athens (NTUA) in September 1972 and was awarded a 'Diploma' in Civil Engineering in June 1977. In September 1977 he commenced graduate studies at the Massachusetts Institute of Technology and received a Master of Science degree in Civil Engineering in May 1980.

The author can be reached in the following addresses:

Department of Civil Engineering

Room 1-371

Massachusetts Institute of Technology

Cambridge, Mass 02139 USA Tel. (617) 253-5043  
(617) 547-2128

or,

6 Xifiou St.

Athens, 708 GREECE

Tel. 30-1-643-7796